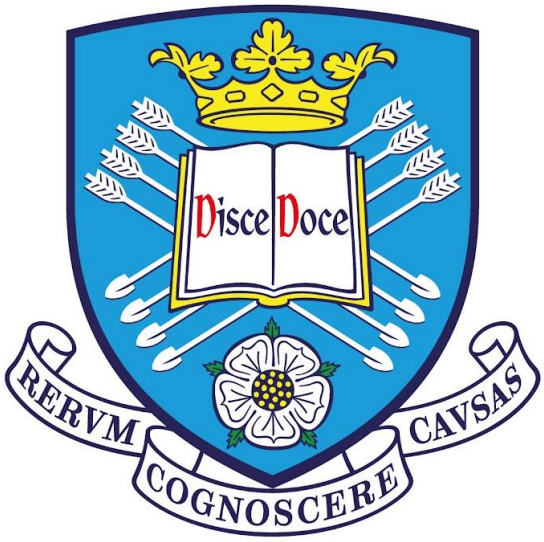

Characterisation of the Neuroinflammatory Response in Human Sporadic Motor Neuron Disease

Bridget Allison Ashford

Submitted for the degree of Doctor of Philosophy (PhD)

Department of Neuroscience

Sheffield Institute for Translational Neuroscience

September 2022

Abstract

Microglia are highly involved in the pathogenesis of Motor Neuron Disease (MND). Their activation correlates with several features of disease. However, how microglia contribute to human MND is not currently known. *We aim to elucidate the role of immunity in sporadic MND (sMND) by examining gene expression in post-mortem tissue.*

The inflammatory transcriptome was characterized in the ventral horn of the spinal cord and the motor cortex in sMND and control cases using the NanoString Neuroinflammation panel. Pre-published data sets were re-analysed and compared with the NanoString data: to identify key pathways. Immunohistochemistry was allied with tissue microarray technology the examine the inflammatory response in the spinal cord, precentral gyrus, and regions across the brain.

In the spinal cord, significant inflammation was observed in sMND cases, however, less immune gene dysregulation was observed in the motor cortex compared to control cases. Examination of differentially expressed genes highlighted TREM2, TYROBP, APOE, and CD163 signalling as well as phagocytic pathways. In sMND spinal cord, significant microglial reactivity, and an upregulation of APOE and TYROBP was observed. Motor white matter tracts showed significant immune activation, the severity of which equal to or exceeding the ventral horn. Expression of TREM2 did not differ between control and sMND cases, but increased TREM2 expression in the white matter, was associated with longer survival. The precentral gyrus of sMND cases showed little change in immune reactivity compared to control cases.

The spinal cord is a more immune environment in sMND compared to the precentral gyrus, with the motor white matter tracts of the spinal cord showing significant microglial activity in sMND. Developing a greater understanding of the TREM2/ TYROBP/ APOE signalling pathway on microglial phenotype and the role of inflammation in white matter in sMND may be of importance in the development of potential treatments.

Acknowledgements

I would first like to thank my supervisors Robin and Julie for their endless support and enthusiasm throughout this project. Your patience and ability to keep me (mostly) calm throughout has been truly appreciated. To Robin, your ability to stay to always see the bright side throughout, has kept me motivated, particularly through the writing up process. To Professor Delphine Boche, thank you for your role both in the development of this project, and microglial advice throughout. You have been a huge inspiration and I am so grateful to have had the opportunity to work with you.

I would also like to thank Lynne Baxter, Dan Fillingham, Rachel Davenport, Paul Heath, and Charlie Appleby-Mallinder, this project would not have been possible without the help and support you provided.

Thank you to my funders, the Pathological Society, and to those who donated to the Sheffield Brain and Tissue Bank and their families. Thank you for making this research possible.

To Martyna, Katy, Sarah, and Rachel (or TBRiS), we did it, we got through a pandemic PhD! You've been there through all these last 4 years have thrown and have made this whole experience so much fun. Thank you for all the lunches, coffee breaks, pub trips and games nights. I feel so lucky to have met such wonderful people, and to see us grow as researchers together.

To Helen, your pep talks have really kept me going, you are such an inspiration. Fritha thank you for all our phone calls and can't wait to celebrate you finishing your PhD!

To my family, thank you all for being my personal cheerleaders. I wouldn't be with here without you all. I would particularly like to thank my grandfather Roger, who has always seen big things in my future. To my dad, sister and brother, you have been so supportive and sent me so much encouragement particularly while writing up. Your daily phone calls, photos and letters have meant so much! Additionally, to the Lamont family, you have all kept me going and supported me like one of your own.

To my grandfather, Prof. Norman Ashford, you are missed every day and I know you would have provided me so much advice throughout this stage. You have been such an inspiration, both in your determination and sense of humour.

Finally, to Siôn you seen me through three degrees and been my best friend and biggest fan throughout. You have celebrated every success and given me endless encouragement. I cannot thank you enough for all you have done to support me through this PhD, including watching many presentations, endless proofreading and keeping me fed and in clean clothes. I would not be where I am without all you have done, thank you so much … and this is the last degree, I promise!

Contents

Tables

Figures

Abbreviations

ABC	Avidin Biotinylated Enzyme Complex
AD	Alzheimer's Disease
ALS	Amyotrophic Lateral Sclerosis
AMPA	A-Amino-3-Hydroxy-5-Methyl-4-Isoxazolepropionic Acid
AP	Alkaline Phosphatase
APOE	Apolipoprotein E
ATP	Adenosine Triphosphate
BAX	BCL2 Associated X
BBB	Blood-Brain Barrier
BDNF	Brain Derived Neurotrophic Factor
BAX	Bcl-2 Associated X
C9orf72	Chromosome 9 Open Reading Frame 72
CD	Cluster Of Differentiation
CNS	Central Nervous System
CPM	Counts Per Million
CSF	Cerebrospinal Fluid
CTSS	Cathepsin S
CV%	Coefficient Of Variation
DAB	3,3′-Diaminobenzidine
DAM	Disease-Associated Microglia
DAMPS	Damage-Associated Molecular Patterns
DC	Dorsal Column

dH_2O	Distilled H_2O
DPR	Dipeptide Repeat
ECL	Enhanced Chemiluminescence
EDTA	Ethylenediaminetetraacetic Acid
EEAT2	Excitatory Amino Acid Transport Receptor 2
FACS	Fluorescence-Activated Cell Sorting
FC	Fold Change
FFPE	Formalin-Fixed Paraffin-Embedded
fMND	Familial Motor Neuron Disease
FTD	Frontotemporal Dementia
FUS	Fused In Sarcoma
GFAP	Glial Fibrillary Acidic Protein
GM	Grey Matter
GRASPS	Genome-Wide RNA Analysis of Stalled Protein Synthes
HLA-DR	Human Leukocyte Antigen – DR Isotype
HRP	Horse-Radish Peroxidase
IBA1	Ionized Calcium Binding Adaptor Molecule 1
IFNγ	Interferon γ
IHC	Immunohistochemistry
IL	Interleukin
iPSC	Induced Pluripotent Stem Cell
ITAM	Immunoreceptor Tyrosine Activation Motif
LCST	Lateral Corticospinal Tract
LPS	Lipopolysaccharide

MCF1	Monocyte Chemoattractant Protein-1
MCT1	Monocarboxylate Transporter 1
MDMi	Monocyte-Derived Microglia-Like Cells
MHCII	Major Histocompatibility Complex II
MND	Motor Neuron Disease
mRNA	Messenger Ribonucleic Acid
MS	Multiple Sclerosis
mSOD1	Mutant Superoxidase Dismutase 1
mTDP-43	Mutant TDP-43
NADPH	Nicotinamide Adenine Dinucleotide Phosphate
NF-κB	Nuclear Factor Kappa-Light-Chain-Enhancer of Activate
NMDA	N-Methyl-D-Aspartate
NOX2	NADPH Oxidase 2
NRF2	Nuclear Factor Erythroid 2 Related Factor 2
NTC	No Template Control
PAMPS	Pathogen-Associated Molecular Patterns
PCR	Polymerase Chain Reaction
PKD	Proteinase K Digestion Buffer
PMD	Post-Mortem Delay
pTDP-43	Phosphorylated Transactive Response DNA Binding Pr
q	Adjusted P Value
QC	Quality Control
RBC buffer	Red Blood Cell Buffer
RIN	RNA Integrity Number

RNA	Ribonucleic Acid
RNASeq	RNA Sequencing
ROI	Region Of Interest
RT-qPCR	Real Time Quantification Polymerase Chain Reaction
SBTB	Sheffield Brain And Tissue Bank
SC	Spinal Cord
SDS	Sodium Dodecyl Sulphate
SDS-PAGE	Sodium Dodecyl Sulphate–Polyacrylamide Gel Electrop
SRA	Sequence Read Archive
sMND	Sporadic Motor Neuron Disease
SOD1	Superoxide Dismutase 1
STING	Stimulator Of Interferon Genes
TBS	Tris Buffered Saline
TBS-T	Tris Buffered Saline with Tween
TDP-43	Transactive Response DNA Binding Protein 43 KDa
TLR	Toll-Like Receptor
TMA	Tissue Microarray
TNFα	Tumour Necrosis Factor A
Treg	Regulatory T Cells
TREM2	Triggering Receptor Expressed on Myeloid Cells 2
TSC	Tri-Sodium Citrate
TYROBP	TYRO Protein Tyrosine Kinase-Binding Protein
UV	Ultraviolet
VEGF	Vascular Endothelial Growth Factor

VH	Ventral Horn
WM	White Matter
WT	Wild-type

Chapter 1 Introduction

1.1 Motor Neuron Disease

Motor Neuron Disease (MND) is a fatal neurodegenerative condition, characterised by the progressive degeneration of motor neurons. Degeneration of upper motor neurons, originating in the precentral gyrus or motor cortex with axons descending through the corticospinal tract of the spinal cord, results in weakness, spasticity, and rigidity (Ince, Highley and Wharton, 2015). Degeneration of lower motor neurons, located in the ventral horns of the spinal cord and the cranial nerve motor nuclei, results in muscular atrophy, cramping, weakness and fasciculations (Ince, Highley and Wharton, 2015).

MND has a global incidence of 1-3 cases per 100,000 people, and a prevalence of 1-9 cases per 100,000 (Rojas *et al.*, 2020). MND has four clinical subtypes (Bilsland *et al.*, 2010; Arora and Khan, 2021): Amyotrophic lateral sclerosis (ALS), primary lateral sclerosis, progressive bulbar palsy and progressive muscular atrophy (Table 1.1).

Table 1.1 Summary of the Motor Neuron Disease Phenotypes

MND Phenotype	Site of Motor Neuron Degeneration	% of MND cases	Summary of main symptoms
Amyotrophic Lateral Sclerosis (ALS)	Upper and lower	60-70%	Muscle atrophy, weakness, spasticity, stiffness, cramps, reduced reflexes, fasciculations
Primary Lateral Sclerosis (PLS)	Purely upper	1-2%	Muscle atrophy, weakness, rigidity
Progressive Bulbar Palsy (PBP)	Bulbar lower	20%	Weakness and stiffness of the tongue, dysphagia, slurred speech.
Progressive Muscular Atrophy (PMA)	Spinal lower	10%	Loss of muscle tone, muscle weakness, atrophy, fasciculations

ALS is the most common type of MND accounting for 80-90% of MND cases and has an incidence of 1.5-2 diagnoses in 100,000 people per year, and a prevalence of 5-7 cases per 100,000 people worldwide (Ludolph *et al.*, 2015). Throughout the literature, the terms ALS and MND are often used synonymously. From here the term MND will be used.

1.2 Clinical Features of MND

Diagnosis of MND normally occurs at approximately 50-65 years of age, although this varies greatly (Ince, Highley and Wharton, 2015), for example, 5% of cases will have an onset before 30 years of age (Zarei *et al.*, 2015). Depending on the site of first symptoms, MND is usually classified as limb, bulbar or respiratory onset (Wood-Allum and Shaw, 2010; Hobson *et al.*, 2016). Limb onset is the most prevalent, with symptoms usually beginning in distal muscles (Turner *et al.*, 2010). Bulbar onset accounts for 25% to 30% of cases (Masrori and Van Damme, 2020). Patients initially present with dysphagia, dysarthria and dysphonia. Prognosis is usually poorer compared to limb onset. A small proportion of cases (3%) are classified as respiratory onset, which presents with diaphragm weakness resulting in dyspnoea at rest and exertion. These cases have the poorest prognosis (Masrori and Van Damme, 2020).

MND is sometimes described as a diagnosis of exclusion: diagnosis is made based on a set of clinical and electrophysiological evidence of upper and lower motor neuron signs, which cannot be explained by another diagnosis. Clinical criteria for diagnosis have been developed in the revised El Escorial Criteria (Brooks *et al.*, 2000).

Death is usually the result of respiratory failure (Foster and Salajegheh, 2018). Survival time varies from just a few months to decades, although 80% of patients survive only two to five years after diagnosis (Westeneng et al., 2018).

Many patients additionally experience non-motor symptoms: These include changes in executive function, cognitive impairment, neuropsychiatric symptoms, sleep disturbances, fatigue, changes in saliva production and/or clearance, weight loss and pain (Benbrika *et al.*, 2019; Beswick *et al.*, 2022; Essat *et al.*, 2022) .

Approximately 50% of patients will experience cognitive impairment, but in 10-15% of MND cases, patients will also go on to receive a diagnosis of frontotemporal dementia (FTD; Phukan, Pender and Hardiman, 2007). FTD is a rare type of dementia associated with personality and behavioural changes, executive dysfunction and/ or aphasia, with memory being relatively spared (Ferrari *et al.*, 2011). Conversely, a substantial proportion of patients initially presenting with FTD will also have motor symptoms, and between 5-10% of those will be diagnosed with MND (Rosso *et al.*, 2003; Johnson *et al.*, 2005; Seelaar *et al.*, 2007). MND and FTD are thought to represent either ends of a diagnostic spectrum, as both conditions share genetic and molecular mechanisms, as well as pathology.

1.3 Treatments for MND

Currently there is no cure for MND, and disease-modifying treatment options are limited. Riluzole was the first drug to enter the field, following clinical trials in 1993-1995 (Lacomblez *et al.*, 1996). Riluzole has a modest survival effect, increasing survival by only 2-3 months (Lacomblez *et al.*, 1996; Miller, Mitchell and Moore,

2012). Edaravone was approved for the treatment of MND first in Japan in 2015, followed by the United States of America in 2017, but is yet to be approved in the United Kingdom (Abe *et al.*, 2017). Edaravone has a small effect in slowing decline in patients when administered early in the disease progression (Abe *et al.*, 2017). For both drugs, the mechanisms of action are poorly understood, and their modest effect on survival highlights the importance of further research to understand the complex nature of MND. Symptom management varies patient-to-patient but includes placement of a gastrostomy tube to treat dysphagia and weight loss, alternative means of communication for dysarthria, as well as medications to treat pain, spasticity, and cramps (Foster and Salajegheh, 2019).

1.4 Pathology in MND

At *post-mortem*, the brain and spinal cord of MND patients does not show striking macroscopic changes. Patients may have atrophy of the precentral gyrus, thinning of the spinal ventral roots, or sclerosis and pallor in the corticospinal tracts (Ince, Highley and Wharton, 2015).

MND is characterized by degeneration of the pyramidal tract, from the upper motor neurons in the precentral gyrus to spinal and bulbar lower motor neurons. Furthermore, myelinated axon loss is observed in both the lateral and anterior corticospinal tracts in the spinal cord. Motor neuron degeneration and loss are seen, accompanied by gliosis, and the presence of protein inclusions. In the majority of cases, these inclusions are largely formed of ubiquitylated phosphorylated TAR DNA-binding protein 43kDa (TDP-43).

TDP-43-positive inclusions are almost universal in MND, apart from cases associated with *Fused in Sarcoma (FUS)* and most *Super Oxidase Dismutase 1 (SOD1)* mutations, or atypically presenting cases (Borthwick *et al.*, 2006; Saberi *et al.*, 2015). Pathology/disease progression varies slightly depending on the patient's genetic status – see Section 1.5).

1.5 Causes and Genetics of MND

MND cases are classified as either familial MND (fMND) or sporadic MND (sMND). Familial cases are defined as having a family history of MND, potentially associated with the inheritance of a known genetic mutation associated with MND. In the majority of cases, inheritance is dominant, although other patterns of inheritance have occasionally been reported (Siddique and Ajroud-Driss, 2011; Mathis *et al.*, 2019). Sporadic cases do not have a family history of MND or obvious inheritance of MND-associated mutations.

Sporadic cases account for approximately 90-95% of cases. Familial cases, which account for between 5-10% of cases, tend to have an earlier onset, approximately ten years earlier than sporadic cases (Longinetti and Fang, 2019).

Over the last 40 years, increasing numbers of mutations have been linked to the development of MND, the most commonly occurring and well-studied are mutations in *SOD1, TARDBP, FUS and C9orf72.* There is overlap in familial and sporadic MND in terms of genetics with some sporadic cases carrying disease-causing mutations, which may be the result of incomplete family history or *de-novo* mutations. While

many genes have been implicated in MND, the top 4 most frequently implicated with MND are discussed below.

1.5.1 Superoxidase Dismutase 1

In 1993, the first gene associated with fMND was discovered, superoxidase dismutase 1 (*SOD1*; Rosen *et al.*, 1993). As such, *SOD1* mutations are among the most well-characterised of MND associated genes. Mutations in this gene are associated with approximately 20% of fMND and between 1-5% of sMND cases, with over 180 mutations now described (Mathis *et al.*, 2019; Müller *et al.*, 2022).

SOD1 is a cytosolic metalloenzyme, which has a copper and a zinc binding site. Through the binding of these ions, SOD1 catalyses the reduction of free superoxidase radicals into hydrogen peroxide and oxygen. Disease-causing mutations result in protein instability and misfolding. Misfolded SOD1 forms aggregates in the cytoplasm of neurons across the motor regions of the central nervous system (CNS). In turn, pathogenic SOD1 may be able to misfold the wild-type (WT) protein in a prion-like manner (Ayers *et al.*, 2016).

The pathogenicity of mutant SOD1 (mSOD1) has not been fully established but is believed to be independent of the loss of the protein's enzymatic action, and through a toxic gain of function: Knockdown or enzyme inactivation does not result motor neuron loss (Andersen *et al.*, 1995; Reaume *et al.*, 1996). Furthermore, transgenic mice expressing high levels of human mSOD1 develop paralysis resulting from motor neuron loss, but wild-type (WT) SOD1 enzyme activity was not altered (Gurney *et al.*, 1994). Additionally, motor neuron loss is observed both in

mouse models which carry mutations that confer full enzymatic action such as G378R, and in transgenic models with mutations which do not provide enzymatic dismutase activity (H46R/H48Q) (Wong *et al.*, 1995; Wang *et al.*, 2002).

In MND cases with *SOD1* mutations, the disease course varies with the mutation. The D90A mutation (the most common) is associated with slow progression (Andersen *et al.*, 1995). However, cases caused by the A4V mutation, have a much faster and more aggressive course (Cudkowicz *et al.*, 1997). Furthermore, *SOD1* MND cases are distinct from other MND types: Most MND cases with *SOD1* mutations do not develop the hallmark TDP-43 inclusions seen in almost all other cases of MND. In addition, patients with *SOD1* mutations rarely develop cognitive symptoms observed in other forms of MND (Andersen *et al.*, 1997).

Models of SOD1-MND

Mutations in SOD1 are some of the best characterised and have been used to generate the most widely used animal models of MND. In 1994, Gurney *et al.* developed the first mouse model of MND, using a glycine to alanine substitution at position 93 (henceforth m*SOD1*^{G93A}). Since the development of this model, several others have been created with varying mutations, transgene numbers, and resultant phenotype. However, the m*SOD1*^{G93A} mouse model remains the most widely used (Philips and Rothstein, 2015).

SOD1 models recapitulate many key disease features, including selective motor neuron degeneration, gliosis and microglial activation, weight loss (or failure to gain weight), muscle weakness and atrophy (Gurney *et al.*, 1994). *In-vivo* models have

provided great insight into disease processes taking place both before and after symptom onset (Gurney *et al.*, 1994; Hall, Oostveen and Gurney, 1998; Olsen *et al.*, 2001).

However, there have been concerns over their use as a model of human MND. First, many of these models vastly overexpress mSOD1 (some up to 24-fold), resulting in a severe disease phenotype (Shibata, 2001). To rectify this, models have been developed with a lower gene copy number, which have delayed symptom onset and slower disease progression, but fail to recapitulate many key features of disease such as focal symptom onset (Acevedo-Arozena *et al.*, 2011). Secondly, mice expressing WT human *SOD1* also show abnormalities. Human WT SOD1 was found in high concentrations in vacuolated mitochondria, resulting in mitochondrial dysfunction, a feature seen in mice carrying mSOD1 mutations (Jaarsma *et al.*, 2001). Finally, despite being a hallmark of *SOD1* MND cases, many *mSOD1* models do not develop SOD1 aggregates (Philips and Rothstein, 2015).

Furthermore, mSOD1 models recapitulate a very specific form of MND. They do not develop the hallmark cytoplasmic TDP-43 mutations. Approximately 90% of MND is sporadic in nature, and only 5% of these cases are associated with mutations in *SOD1. A*s such these models' applicability to the other types of MND, such as sMND is questionable. This may reflect some of the difficulty in translating drugs developed in mSOD1 mice to successful treatment of human MND (Benatar, 2007; Lutz, 2018).

1.5.2 TDP-43

The trans-activation response (TAR) DNA-binding protein 43 kDa, which is coded for by the *TARDBP* gene, is one of the primary components of the pathological hallmark

of MND - ubiquitin-positive TDP-43 cytoplasmic inclusions (Arai *et al.*, 2006; Neumann *et al.*, 2006). Aggregates of TDP-43 are observed in approximately 97% of MND cases. Subsequentially, mutations in *TARDBP* were later discovered in fMND (Gitcho *et al.*, 2008; Sreedharan *et al.*, 2008), although these mutations are present in a relatively small number of MND cases: 4% of fMND and 1% of sMND cases (Scotter, Chen and Shaw, 2015).

TDP-43 is a ubiquitously expressed RNA/DNA binding protein (Ou *et al.*, 1995), which has several roles in RNA metabolism including transcription, translation, and mRNA transport and stability, as well as exon splicing and stress granule formation (Prasad *et al.*, 2019).

Structurally, the TDP-43 protein has a nuclear localisation signal at the N terminal, two RNA recognition motifs, a nuclear export signal, and a glycine rich C terminal (Ayala *et al.*, 2008). The C terminal domain contains repetitive functional domains (Van Deerlin *et al.*, 2008; Suk and Rousseaux, 2020). Repetitive functional domains often referred to as prion-like domains, are thought to mediate gene regulation through phase separation, and can also drive protein aggregation (Hennig *et al.*, 2015; Afroz *et al.*, 2017). Notably, pathological mutations of TDP-43 are clustered in this gene region (Sreedharan *et al.*, 2008; Van Deerlin *et al.*, 2008; Scotter, Chen and Shaw, 2015).

TDP-43-mediated toxicity is thought to come from the loss of the protein’s nuclear functions such a nuclear RNA processing, as well as toxic gains of functions (Hergesheimer *et al.*, 2019).

TDP-43 Pathology in MND

TDP-43 is primarily located in the nucleus but has the ability to shuttle between the nucleus and the cytoplasm, due to the presence of export signals and nuclear localisation signal in the protein structure (Ayala *et al.*, 2008). In MND, a cleaved, hyperphosphorylated and ubiquitinated form of TDP-43 becomes mislocalised to the cytoplasm (often referred to as phosphorylated TDP-43 or pTDP-43). This can be observed in cells as pre-inclusions – diffuse cytoplasmic pTDP-43 with a clear absence of nuclear TDP-43 – and as the hallmark dense aggregates. Neuroinflammation, oxidative stress and excitotoxicity have all been found to cause TDP-43 delocalisation to the cytoplasm (Ayala *et al.*, 2011; Cohen *et al.*, 2012; Feiler *et al.*, 2015; Liu *et al.*, 2015; Bozzo *et al.*, 2016; Ederle and Dormann, 2017). Inclusions are observed in the cytoplasm of remaining motor neurons and in glia, predominantly oligodendrocytes.

In MND, TDP-43 proteinopathy spreads through the CNS in a sequential manner, comparable to that of tau pathology in Alzheimer's disease (AD, Braak and Braak, 1991), and alpha synuclein in Parkinson's disease (PD, Braak *et al.*, 2003) allowing the creation of a staging system by Brettschneider *et al.* (2013, 2014). In Stage 1, pathology is observed in the motor cortex, brain stem motor nuclei, and spinal cord motor neurons. In Stage 2, pathology is observed in the prefrontal cortex (middle frontal gyrus) and increasingly in the brainstem (reticular formation, precerebellar nuclei, and red nucleus). In Stage 3, the burden increases in the prefrontal cortex (gyrus rectus and orbital gyri), and pathology is observed in the post central cortex and striatum. At Stage 4, the temporal lobe and hippocampus show pathology.

In more advanced MND or in cases where patients are ventilated for long periods, pathology has been observed more widely throughout the CNS. Inclusion pathology has been noted in the oculomotor system, in non-motor regions of the spinal cord, and regions of the brain including the globus pallidus, subthalamic nucleus, substantia nigra, thalamus, and amygdala (Hayashi and Kato, 1989; Sasaki et al., 1992; Kato, Oda and Hayashi, 1993; Brettschneider et al., 2014). This led to the addition of Stage 5 in the Brettschneider classification system in 2014 (summarised in Table 1.2). The relationship between affected CNS regions and TDP-43 pathology has been further explored (Tan *et al.*, 2015; Nelson *et al.*, 2019), however these data may be more relevant to other TDP-43 proteinopathies, such as FTD and AD .

Table 1.2 Stages of Brettschneider Staging System of TDP-43 Pathology in MND.

Stage	Site of TDP-43 Protienopathy
Stage 1	Motor Cortex (Brodmann areas 4 & 6): neurons of layers II, III, V, VI Motor neurons in the ventral horns of the spinal cord Somatomotor nuclei of cranial nerves XII-X, VII and V Medulla oblongata: hypoglossal nuclei (XII)
Stage 2	Middle Frontal Gyrus Precerebellar nuclei Inferior olive, medullary reticular formation Red nucleus
Stage 3	Prefrontal cortex (gyrus rectus and orbitofrontal gyri) Post central cortex Striatum Thalamus
Stage 4	Hippocampus Anteromedial portions of the temporal lobe
Stage 5	Oculomotor system Loss of substantia nigra pigmentation Dentate nucleus involvement

TDP-43 pathology is not unique to MND and is observed in a number of neurodegenerative conditions including forms of dementia such as FTD, PD,

Huntington's disease (reviewed by De Boer *et al.*, 2021), as well as limbic-predominant age-related TDP-43 encephalopathy (Nelson *et al.*, 2019). Pathologically, there is a disease continuum whereby some cases show pathology purely in motor regions, ranging to others with purely non-motor region pathology (Frontotemporal Lobar Degeneration; Arai et al., 2006). This is reflected clinically, as some patients who present pure motor symptoms and others present pure cognitive symptoms, mostly as FTD.

1.5.3 Fused in Sarcoma

Fused in Sarcoma (FUS) is a ubiquitously expressed gene which encodes for an RNA/DNA binding protein similar to TDP-43. Mutations were first discovered in MND cases in 2009 and are observed in approximately <1% of sMND cases, and 5% of fMND cases (Kwiatkowski *et al.*, 2009; Vance *et al.*, 2009; Lattante, Rouleau and Kabashi, 2013). FUS is part of the heterogeneous ribonucleoprotein family. Like TDP-43, FUS is mostly located in the nucleus, but shuttles between the nucleus and the cytoplasm (Zinszner *et al.*, 1997; Andersson *et al.*, 2008; Vance *et al.*, 2009). In the nucleus, FUS is involved in multiple levels of RNA processing including transcriptional regulation, DNA repair, RNA shuttling and alternative splicing (Kamelgarn *et al.*, 2016). In the cytoplasm FUS, like TDP-43, is involved in formation of stress granules, and RNA transport granules (Dormann *et al.*, 2010; Yasuda *et al.*, 2013; Kamelgarn *et al.*, 2016).

As was the case with TDP-43, most of the mutations in *FUS* observed in MND are in the C terminal (DeJesus-Hernandez *et al.*, 2010; Mackenzie, Rademakers and Neumann, 2010; Drepper *et al.*, 2011; Naumann *et al.*, 2019). This region is

responsible the protein's DNA and RNA binding ability, as well as the moderation of alternative splicing (Zinszner *et al.*, 1997). In MND, FUS is mislocated from the nucleus and forms cytoplasmic inclusions in both neurons and glia (Beutner *et al.*, 2013). These inclusions are composed of large messenger ribonucleoproteins which are immunonegative for TDP-43. On rare occasions these aggregates are also observed in the nucleus (Mackenzie, Rademakers and Neumann, 2010; Mackenzie and Neumann, 2016). Pathogenicity likely results from loss of nuclear functions in alternative splicing and transcriptional regulation, and gain of toxic functions such as altered protein-protein interactions and atypical RNA processing, resulting in neuronal dysfunction (Sun *et al.*, 2015; Ederle and Dormann, 2017; Ishigaki and Sobue, 2018). The similarities both structural and functional, between FUS and TDP-43 highlight a role for RNA and DNA processing in MND pathogenesis.

1.5.4 C9orf72

In 2011, two studies independently identified a repeat expansion in the *Chromosome 9 open reading frame 72 (C9orf72)* gene, which has now been identified as the most common mutation associated with both MND and FTD (DeJesus-Hernandez *et al.*, 2011; Renton *et al.*, 2011). Mutations in C9orf72 are present in approximately 40% of fMND cases and 7% of sMND cases (Majounie *et al.*, 2012). The corresponding protein is associated with endosomal (Farg *et al.*, 2014) and membrane trafficking (Yang *et al.*, 2016).

The gene contains a hexanucleotide repeat (GGGGCC or G_4C_2) in intron 1, surrounded by 2 non-coding exons. Three hexanucleotide repeats are considered normal, 4-27 are considered an intermediate range – the pathological effect of which

is unknown. More than 30 repeats is considered MND-causing (García-Redondo *et al.*, 2013), however individuals with C9orf72 type MND or FTD tend to carry repeats in the range of 700 and 1500 repeats (Buchman *et al.*, 2013). Interestingly, unlike other repeat expansion disorders, such as Huntington's disease, repeat number does not correlate with onset age or disease progression rate (Dols-Icardo *et al.*, 2014). C9orf72 mutations are inherited in an autosomal dominant manner. Sporadic mutations likely develop as a result of the instability of the G_4C_2 expansion.

C9orf72 mutations are believed to cause toxicity through two main mechanisms: toxic gains of function and haploinsufficiency.

Toxic Gain of Function

C9orf72 repeat expansions result in toxicity through RNA toxicity (via the sequestration and aggregation of RNA processing proteins) and via the formation of dipeptide repeats. *In-vitro* studies have shown the hexanucleotide repeat is able to form a hairpin structure with g-quadruplex secondary structures with complementary DNA. This in turn is able to bind nucleic acid-binding proteins, including nucleolin an essential nuclear protein. The sequestration of nucleoin results in nucleolar stress (Haeusler *et al.*, 2014).

Furthermore, the G_4C_2 repeat results in bidirectional repeat-associated non-ATG translation, which results in the production of dipeptide repeat proteins (DPRs), both sense and antisense. These dipeptide repeat proteins form in addition to RNA foci. They are p62-positive but TDP-43-negative and accumulate across the CNS (Ash *et al.*, 2013; Gendron *et al.*, 2013; Mori *et al.*, 2013). There are 5 possible dipeptide repeat species. Arginine-Glycine containing DPRs have been found to be directly

toxic to mouse neurons (Verdone *et al.*, 2022). Furthermore the expression of the DPR in mice resulted in a sex-specific MND phenotype including motor neuron loss (Verdone *et al.*, 2022).

C9orf72 Haploinsufficiency

Expansions in the hexanucleotide repeat result in insufficient translation to mRNA resulting in loss of the protein's function. Transcription of the *C9orf72* genes usually results in three mRNA transcripts or variants. Two of these, Variant 2 and Variant 3, encode for one isoform (461aa C9orf72L), and the other transcript, Variant 1 encodes the second isoform (222aa, C9orf72S) (DeJesus-Hernandez *et al.*, 2011). In Variant 2, the repeat expansion falls within the promotor region of the gene, resulting in reduced expression. C9orf72 protein expression has been found to be reduced in induced pluripotent stem cell (iPSC)-derived neurons from MND patients carrying *C9orf72* mutations, and in *post-mortem* in the frontal and motor cortex, cerebellum and cervical spinal cord (Donnelly *et al.*, 2013; van Blitterswijk *et al.*, 2015; Rizzu *et al.*, 2016).

C9orf72 insufficiency has been found to result in neurodegeneration. First, C9orf72 depletion in murine neurons, resulted in impaired autophagy and in turn aggregation of TDP-43 and p62 (Sellier *et al.*, 2016). Furthermore, Shi *et al. (*2018) used viral overexpression of spinal motor neuron transcription factors to change C9orf72 MND patient-derived iPSCs into induced motor neurons. C9orf72 was found to be critical for normal vesicle trafficking. Furthermore, C9orf72 haploinsufficiency resulted in accumulation of glutamate receptors resulting in excitotoxicity and impaired DPR clearance.

Haploinsufficiency as a pathogenic mechanism in MND has also been supported by studies in invertebrate models. In zebrafish, knockdown of the C9orf72 homolog resulted motor deficits, which were rescued with expression of human C9orf72 (Ciura *et al.*, 2013). Similarly, deletion of the *C. Elegans* C9orf72 orthologue, *alfa-1*, resulted in paralysis, cell-specific degeneration of motor neurons and increased susceptibility to environmental stress (Therrien *et al.*, 2013).

The Role of C9orf72 in Immunity

There is substantial evidence linking C9orf72 to immune function and regulation. C9orf72 is expressed in most tissue but widely expressed within the brain and spinal cord, and in the immune system (DeJesus-Hernandez *et al.*, 2011; Renton *et al.*, 2011; Rizzu *et al.*, 2016). In the CNS, microglia express the highest amounts of C9orf72 compared to other cells (Sharma *et al.*, 2015; Zhang *et al.*, 2016). Peripherally, C9orf72 expression is particularly high in myeloid cells, and to a lesser extent macrophage and lymphoid cells (O'Rourke *et al.*, 2016; Rizzu *et al.*, 2016).

Homozygous knockdown or knock out of the mouse C9orf72 ortholog results in an autoimmune condition. C9orf72$^{-/-}$ mice, had enlarged macrophages, enlarged spleen and lymph nodes, increased autoantibody production, microglia and macrophage dysfunction and increased cytokine production (Atanasio *et al.*, 2016; Burberry *et al.*, 2016; Jiang *et al.*, 2016; O'Rourke *et al.*, 2016; Sudria-Lopez *et al.*, 2016; Sullivan *et al.*, 2016; Ugolino *et al.*, 2016).

Deficits in lysosomal and endosomal function were observed in C9orf72$^{-/-}$ mice, characterised by a build-up of macrophages in the spleen with accumulations of p62 and LC3 proteins, both components of the autophagy pathway, (O'Rourke *et al.*, 2016). Furthermore, microglia from the spinal cord of C9orf72$^{-/-}$ mice had enlarged

vesicles positive for LAMP1, a component of the lysosomal membrane (Atanasio *et al.*, 2016; Burberry *et al.*, 2016; O'Rourke *et al.*, 2016). Together, these data highlight the importance of functional C9orf72 in autophagy and lysosomal mechanisms.

Depletion of C9orf72 in myeloid derived-cells alone was sufficient to produce the full C9orf72 knockout immune phenotype (McCauley *et al.*, 2020) validating the importance of C9orf72 in the functioning of myeloid cells. In these C9orf72$^{-/-}$ mice, dendritic cells were found to have increased and early production of type 1 interferons in response to activators of the Stimulator of Interferon Genes (STING) protein (McCauley *et al.*, 2020). STING protein is a key protein involved in the regulation of the innate immune response to cytosolic DNA (Zhang *et al.*, 2013). Usually STING is regulated by autolysosomal degradation, however this process was impaired in C9orf72-deficient cells, resulting in the hyperreactive interferon response observed (McCauley *et al.*, 2020). Furthermore, blood and brain tissue from *C9orf72*-mutatation carrying MND patients was found to have increased type 1 interferon expression, highlighting the role C9orf72 plays in regulating the inflammatory response through the lysosomal pathway.

1.6 Glial Pathology in MND

Glia are the resident non-neuronal cells within the CNS and make up between 33 and 66% of the cells within the human brain (Azevedo *et al.*, 2009; Herculano-Houzel, 2014; Jäkel and Dimou, 2017). Glia form a supportive network surrounding neuronal soma and axons. Their main functions are to provide structural support and supply nutrients and oxygen to neurons, supporting neuronal health, electrical insulation, maintain homeostasis and offer protection from potential pathogens (Cragnolini *et al.*, 2020). There are four main types of glia: oligodendrocytes, astrocytes, ependymal cells, and microglia.

Oligodendrocytes coat axons forming the myelin sheath, the main purpose of which is to provide electrical insulation, allowing more efficient signal propagation (Baumann and Pham-Dinh, 2001). Oligodendrocytes also provide metabolic support to the axon (Griffiths *et al.*, 1998; Lappe-Siefke *et al.*, 2003)

Astrocytes are the most abundant glial cell and have processes which connect to both blood vessels and neurons. Astrocytes play an important role in the blood brain barrier, whilst supplying neurons with energy substrates and purines such as ATP, growth and trophic factors, and transmitters (Sofroniew and Vinters, 2010). Furthermore, astrocytes help maintain the optimum environment for neurons by clearing excess neurotransmitters and ions and regulating synaptic formation and function. Astrocytes are also an important player in the inflammatory response.

Ependymal cells are form of ciliated epithelioid glial cells which line the ventricular system and the spinal canal. They form a barrier between the cerebrospinal fluid (CSF) and brain tissue and beat their cilia to circulate CSF around the CNS, helping to maintain homeostasis, and clear waste (MacDonald *et al.*, 2021).

Microglia will be discussed in greater detail below (Section 1.9), but briefly they are the resident immune cells of the brain, and are involved in synaptic pruning and form the brains primary immune response (Ashford *et al.*, 2020).

MND is not a motor neuron autonomous condition, and glial cells contribute to disease both actively and through loss of their supportive functions. The importance of glia in MND was highlighted by Clement *et al.* (2003) who developed chimeric mSOD1^{G93A} mice. Motor neurons expressing mSOD1 showed improved survival when surrounded by WT glia, while WT motor neurons showed MND pathology when surrounded by m*SOD1* glia.

The role that oligodendrocytes, astrocytes and microglia play in MND will now be considered.

1.7 Oligodendrocytes in MND

Jean-Martin Charcot first described ALS/MND in 1869, identifying spinal cord white matter pallor as a key feature (Rowland, 2001). Loss of the white matter is observed in the corticospinal and spinothalamic tracts of spinal cord (Hayashi *et al.*, 2001; Kassubek *et al.*, 2009; Ishaque *et al.*, 2022) and the precentral gyrus (Kassubek *et al.*, 2009; Ishaque *et al.*, 2022), and can extend to non-motor regions of the cortex (Kassubek *et al.*, 2009; Ishaque *et al.*, 2022). Additionally, pTDP-43 aggregates are observed in oligodendrocytes as well as neurons (Mackenzie *et al.*, 2007; Philips *et al.*, 2013).

Using mSOD1^{G93A} rats, Niebroj-Dobosz *et al.* (2007) observed changes in oligodendrocytes before symptom onset, indicating oligodendroglial function is impacted early in disease. Electron microscopy revealed changes in the myelin sheath, including detachment, separation, dissolution, and vacuolisation the myelin lamellae in the late pre-symptomatic stages of disease, leading to myelin loss in the end stages of disease.

Oligodendrocytes may also contribute to neuronal dysfunction in MND, through loss of their metabolic support. Oligodendrocytes provide axons with trophic support through the release of lactate, via the expression of Monocarboxylate transporter 1 (MCT1, Lee *et al.*, 2012). Reduction of MCT1 is fatal to neurons both *in-vivo* and *in-vitro*, and expression has been found to be reduced both in MND patients and in models of MND (Lee *et al.*, 2012). MCT1 expression was improved upon deletion of the mSOD^{G37R} in oligodendrocyte precursor cells, delaying symptom onset and improving length of survival in mice (Kang *et al.*, 2013).

1.8 Astrocytes in MND

Reactive astrogliosis, the accumulation of reactive, activated astrocytes, is observed at the key sites of degeneration in human MND and animal models of MND (Kushner, Stephenson and Wright, 1991; Schiffer *et al.*, 1996; Bruijn *et al.*, 1997; Hall, Oostveen and Gurney, 1998). In some mSOD1 models, astrocyte-specific expression of mSOD1 was insufficient to induce neuronal dysfunction alone (Gong *et al.*, 2000). However, in several studies, knockdown of mSOD1 in astrocytes and/or microglia specifically, resulted in a significant increase in mouse survival time (Boillée *et al.*, 2006; Yamanaka *et al.*, 2008; Wang *et al.*, 2009; Wang, Gutmann and Roos, 2011). These data highlight the importance of astrocytes and microglia in the progression of MND. Astrocytes likely contribute to MND pathology through several different means.

1.8.1 Astrocyte-Mediated Inflammation and Toxicity

Inflammation is a key response in MND, and although astrocytes are not the primary cells associated with immunity, astrocytes do play an important role in the inflammation. Haidet-Phillips *et al.* (2011) derived astrocytes from neural progenitor cells from the *post-mortem* spinal cord of MND patients to examine their toxicity. These astrocytes showed increased expression of proinflammatory cytokines and chemokines compared to controls, and co-culture with mouse motor neurons resulted in neuron death. Furthermore, the addition of cultured medium from astrocytes expressing mSOD1 proved toxic to mouse motor neurons, more so than medium from human WT SOD1 expressing and non-transgenic astrocytes (Nagai *et al.*, 2007). The soluble factors released by mSOD1 astrocytes did not affect

interneurons or dorsal root ganglia neurons. Furthermore, the media of other glia cells was not toxic. Motor neuron degeneration occurred through a Bcl-2 associated X (BAX) dependent mechanism: mSOD1 astrocytes expressed a soluble inhibitor of the pro-death protein BAX, resulting in the initiation of apoptosis.

Ziff *et al.* (2022) examined the transcriptomic response in human iPSC astrocytes and compared these data to published data from MND models and data from MND cases with varying mutations. MND astrocytes showed an increase in genes associated with the immunity. Both human and mouse MND astrocytes showed upregulation in proinflammatory markers such as IL-1a and TNF, as well as complement pathway elements. Further, markers of protective functions were downregulated. Astrocyte expression of interferon gamma (IFNγ), a proinflammatory cytokine, increased with disease progression in mSOD1^{G93A} mice. IFNγ induced motor neuron death *in-vitro* (Aebischer *et al.*, 2011). Another member of the interferon protein family – interferon stimulated gene 15 was found to be upregulated in the mSOD1^{G93A} mouse and sMND patient spinal cord. Knockdown of its receptor IFN-α receptor 1 increased mouse survival.

1.8.2 Mitochondrial Dysfunction

Mitochondrial dysfunction is a key mechanism in motor neuron dysfunction (Kodavati, Wang and Hegde, 2020), but is also observed in astrocytes in MND. Astrocytic mitochondria from mSOD1^{G93A} rats showed evidence of mitochondrial dysfunction including reduced oxygen consumption and decreased membrane potential (Cassina *et al.*, 2008). In addition, mSOD1 astrocyte mitochondria produced increased amounts of superoxide radicals, both in culture and in the spinal

cord. Culture of these astrocytes with motor neurons proved toxic but was rescued by pre-treatment with antioxidants and nitric-oxide synthase inhibitors, indicating toxicity was the result of free radical production. Likewise, human embryonic stem cell-derived astrocytes overexpressing mSOD1^{G37R} also show increased production of reactive oxygen species, as well as inducible nitrous oxide and the super oxide producing enzyme NOX2 – both of which are proinflammatory (Marchetto et al., 2008). Overexpression of NRF2, a transcription factor which increases antioxidant production, by astrocytes resulted in neuroprotection, reducing neuronal apoptosis in culture (Vargas *et al.*, 2006, 2008).

1.8.3 Glutamate Toxicity

One of the most important astrocytic functions is the regulation of extracellular glutamate. Excess glutamate in the synaptic cleft can cause excess neuronal firing, resulting in a toxic influx of calcium ions (Yamanaka and Komine, 2018).

The excitatory amino acid transport receptor 2 (EAAT2) is expressed in high levels on the membrane of astrocytes and is responsible for the clearance of approximately 90% of CNS extracellular glutamate (Danbolt, Storm-Mathisen and Kanner, 1992). Loss of EAAT2 has been observed in both familial and sMND, as well as astrocytes in mSOD1 mouse models, with resultant deficiencies in glutamate uptake (Rothstein, Martin and Kuncl, 1992; Rothstein *et al.*, 1995; Bruijn *et al.*, 1997; Howland *et al.*, 2002; Guo *et al.*, 2003; Pardo *et al.*, 2006).

Astrocytes from rats expressing mSOD1 have shown reduced ability to regulate the expression of the Glutatmate Receptor 2 (GluR2) subunit of neuronal α-amino-3-

hydroxy-5-methyl-4-isoxazolepropionic acid (AMPA) receptors (Van Damme *et al.*, 2007). This in turn, increased motor neuron vulnerability to glutamate excitotoxicity.

Finally, astrocytes release a form of the amino acid serine – d-serine- which coactivates N-methyl-D-aspartate glutamate receptors. D-serine is increased in the spinal cords of sMND and fMND patients (Sasabe *et al.*, 2012). Increased D-serine results in further glutamate signalling and excitotoxicity. Further, a mutation (R199W DAO) in the gene encoding D-amino acid oxidase, which regulates D-serine expression, has been found in fMND cases (Mitchell *et al.*, 2010). The induction of this mutation into neurons resulted in the formation of protein aggregates, evidence of DNA fragmentation and reduced neuronal survival. A similar effect was observed with WT neurons co-cultured with astrocytes expressing the R199W DOA mutation.

1.8.4 Loss of Homeostatic Functions

Astrocytes may contribute to neurodegeneration through loss of homeostatic function. Astrocytes provide neurons with energy through lactate. Astrocyte lactate production has been found to be reduced in MND, as well as deficits in the shuttling of lactate between astrocytes and motor neurons (Cassina *et al.*, 2008; Ferraiuolo *et al.*, 2011; Madji Hounoum *et al.*, 2017).

Furthermore, astrocytes are also responsible for maintaining calcium homeostasis: This process is impaired in MND. In culture, mSOD1^{G93A} mouse astrocytes released increased calcium from the endoplasmic reticulum into cell medium upon purinergic stimulation (Kawamata *et al.*, 2014). Extracellular calcium is toxic to neurons.

1.9 Microglia in MND

1.9.1 Introduction to Microglia

Microglial Function

Microglia are the resident immune cells of the CNS, and account for between 5-12% of cells within the brain. Microglial density varies greatly with brain region and differs between white and grey matter (Mittelbronn *et al.*, 2001; Herculano-Houzel, 2014). Unlike neurons and other glial cells which derive from the ectoderm, microglia are of myeloid origin and derive from haematopoietic stem cells from the yolk sac, which infiltrate into the CNS during development (Chan, Kohsaka and Rezaie, 2007). These highly active cells serve several functions in development, homeostasis, and innate immunity (summarised in *Table 1.3*).

Table 1.3 Microglial Functions in the Brain and Spinal Cord

Process	Microglial Function	References
CNS Development	Promote maturation, and synaptic pruning. Contribute to developmentally regulated neuronal apoptosis and aid neurogenesis via the release of trophic factors	(Blinzinger and Kreutzberg, 1968; Wakselman *et al.*, 2008; Paolicelli *et al.*, 2011; Hoshiko *et al.*, 2012; Schafer *et al.*, 2012; Cunningham, Martínez-Cerdeño and Noctor, 2013; Ueno *et al.*, 2013; Mazaheri *et al.*, 2014; Shigemoto-Mogami *et al.*, 2014; Kim *et al.*, 2016; Miyamoto *et al.*, 2016)
Surveillance and Pathogen Recognition	Microglia are spread evenly throughout the parenchyma forming a matrix throughout the CNS. Microglia continuously scan for signals of pathogens or cellular distress through cell surface receptors (e.g., Toll-like receptors). Microglia are also able to recognise extracellular protein aggregations or dying cells, which may be toxic.	(Aloisi, 2001; Nimmerjahn, Kirchhoff and Helmchen, 2005; Kigerl *et al.*, 2014; Santoni *et al.*, 2015)
Phagocytosis	Able to ingest and destroy several items such as: degenerating neurons and damaged cells, micro-organisms, virally infected cells, and the products following haemorrhage	(Witting *et al.*, 2000; Schilling *et al.*, 2005; Weinhard *et al.*, 2018)
	Clear cellular debris, which facilitates neuroplasticity and remodelling, synaptogenesis, and repair	
	Linked to the destruction of myelin through phagocytosis	
Antigen Presentation	Microglia present pathogens bound to major histocompatibility complex (MHC) proteins, to activate T lymphocytes.	(Hayes, Woodroofe and Cuzner, 1987; Hickey and Kimura, 1988)
Extracellular Matrix Remodelling	Involved in the remodelling of the extracellular matrix by the release of various proteases such as Matrix metalloproteinases.	(Könnecke and Bechmann, 2013; Das and Chinnathambi, 2021)
Modulation of inflammation and immunity	Release of chemokines which attract other inflammatory cells, and the release of inflammatory/anti-inflammatory molecules	*Please see Table 1.4 for further details*
Cytotoxicity	Release of reactive oxygen and nitrogen species and inflammatory cytokines.	*Please see Table 1.4 for further details*
Stem Cell Regulation	Can trigger neurogenesis and oligodendrogenesis through chemical signalling. Interestingly, the inflammatory response from microglia can also block adult neurogenesis. In turn, stem cells regulate microglial polarisation.	(Monje, Toda and Palmer, 2003; Butovsky *et al.*, 2006; Sierra *et al.*, 2010; Xu *et al.*, 2017)
Lipid Metabolism and Transport	Microglia phagocytose and metabolise myelin. Secrete lipoproteins, which aid delivery of lipids to neurons. This aids cell membrane maintenance and facilitates neuron growth and plasticity.	(Xu *et al.*, 2000; Hayashi *et al.*, 2004; Nugent *et al.*, 2020)
Tumours	Can be destructive to cancer cells, but they can facilitate cancer invasion and growth through secretion growth factors and cytokines	(Hambardzumyan, Gutmann and Kettenmann, 2016; Wu and Watabe, 2017)
Synaptic Plasticity	As well as clearing cellular debris, microglia also secrete Brain Derived Neurotrophic Factor (BDNF), which supports synaptic plasticity and function.	(Parkhurst *et al.*, 2013)

This table was adapted from Ashford et al. 2021 with permission.

Microglial Morphology

Under physiological conditions, microglia have a ramified morphology with small soma and fine processes, that constantly extend, retract, and reform in order to survey the local microenvironment (Figure 1.1; Nimmerjahn, Kirchhoff and Helmchen, 2005). In pathological conditions, microglia have functions in pathogen destruction, the resolution of inflammation and the promotion of healing and cell growth. Microglia react to signals from potential pathogens (Pathogen-Associated Molecular Patterns; PAMPs), and signals expressed by damaged endogenous cells (Damage-Associated Molecular Patterns; DAMPS), via the activation of pattern recognition receptors (Geloso et al., 2017). In response, microglial cytoplasmic processes swell and shorten (hyper-ramification) and at the extreme end of the spectrum, adopt a large, ‘amoeboid’ morphology.

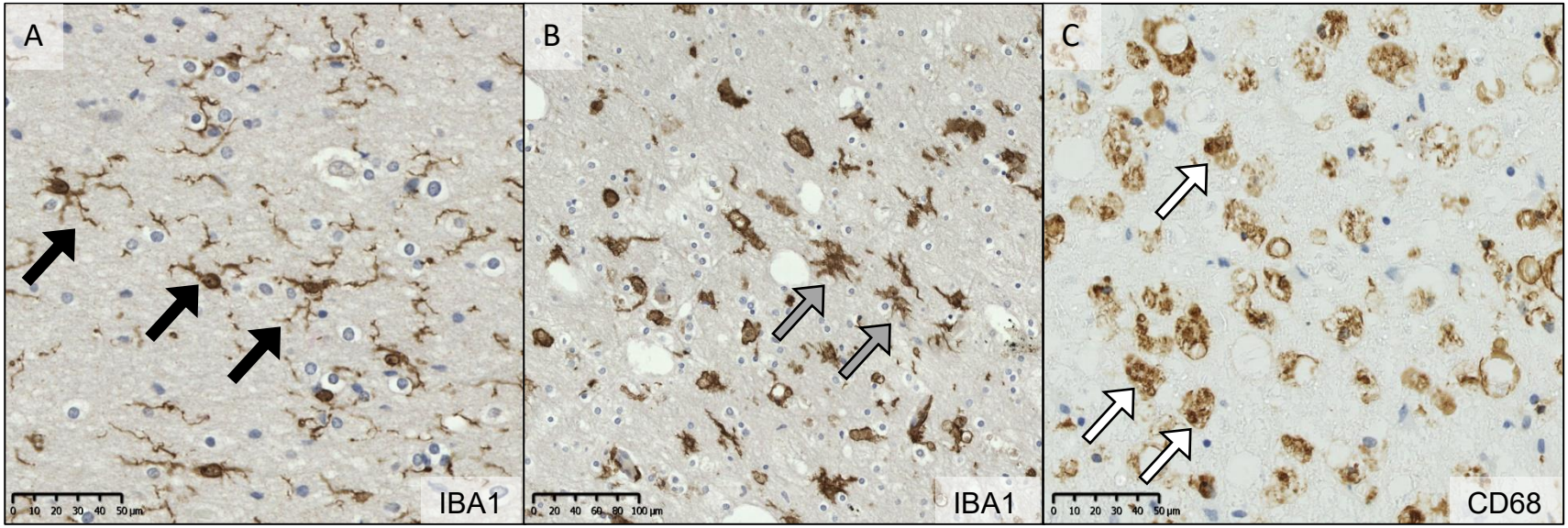

Figure 1.1 Variations in Microglial Morphology

*In their resting state microglia, display a ramified morphology (**A**), with small soma and thin branching processes. Once activated, these cytoplasmic processes start to swell (hyper-ramification, **B**) and form a large amoeboid morphology (**C**). Once the activating stimuli is resolved, microglia revert to their resting, ramified state.*

Scale bars for Figures A and C are 50µM, and 100µM for Figure B.

Microglial Phenotype and the Inflammatory Response

Microglia present a multifaceted inflammatory response. This includes the release of toxic pro-inflammatory cytokines, and reactive oxygen and nitrogen species to aid the destruction of pathogens and damaged cells. Chemokines may be released to further activate and recruit glial and immune cells to the site of injury, and encourage microglial proliferation (Boche, Perry and Nicoll, 2013). Microglia also have functions relating to inflammation resolution and debris clearance. Firstly, via the release of anti-inflammatory cytokines and trophic factors which promote healing, repair, and tissue remodelling. Secondly, via the increase in surface scavenger receptors to promote phagocytosis of pathogens and debris (Mueller *et al.*, 2002; Cherry, Olschowka and O'Banion, 2014).

Historically, activated microglia have been classified as pro-inflammatory (M1) or anti-inflammatory (M2). However, with advancements in gene expression analysis, this binary system has received criticism. Single-cell-based analyses of microglia from both mouse and human cortex, have revealed several transcriptionally-distinct phenotypes which differ from the M1/M2 phenotypes (Friedman *et al.*, 2018; Böttcher *et al.*, 2019). It was suggested activated microglia may fall on a spectrum, with some being purely M1 and pro-inflammatory through to some cells which show a purely M2 anti-inflammatory phenotype. However, genome-wide exome profiling of *ex-vivo* microglia, isolated from mouse models of various neurodegenerative conditions, failed to find evidence of an M1/M2 disease spectrum (Chiu, Morimoto, *et al.*, 2013; Wes *et al.*, 2016). This indicates the microglial transcriptome is too complex to be defined via this binary classification system. Therefore, it is important to independently assess many markers of microglial function, rather than relying on individual markers to infer the functional phenotype.

A summary of the main molecules associated with microglial expression and activation are given in Table 1.4. Microglial phenotype is highly complex and changes with several factors including the region of the CNS (Grabert *et al.*, 2016), age (Galatro *et al.*, 2017), and, activating stimuli and disease (Friedman *et al.*, 2018). Differences in the microglial transcriptome are present between murine and human microglia (Galatro *et al.*, 2017). Furthermore, culturing microglia has also been found to alter their transcriptome and response to stimuli (Caldeira *et al.*, 2014), in particular impacting genes associated with neurodegeneration (Gosselin *et al.*, 2017). Cell culture and examination of microglia from animal models has been crucial to developing our understanding of microglia and their behaviour in disease. However, these methodological differences should be accounted for. As such it should be noted that Table 1.4 represents a brief summary with a focus on makers associated with neurodegeneration. Markers derived from *in-vivo* research, as well as information of mouse and human expression has been highlighted.

Table 1.4 Brief Summary of Microglial Functions, Activating Stimuli, and Typical Markers for Identification

Associated Functions	***Homeostatic state and pathogen detection***	***Pathogen Destruction-associated with inflammation***	***Inflammation Suppression and Phagocytosis***	***Tissue Remodelling and Extracellular Matrix Deposition***
Upregulated Cytokines		TNF-α, IL-1β, IL-1α, IL-6, IL-12a, IL-12b, IL-15, IL-18, **IL-23**, IL-33, IFN-γ	**IL-4,** IL-10, **IL-13 ARG1*, TGF-β**, **FIZZ1***	IL-10
Chemokines		CCL1, CCL2 (MCP-1), CCL3, **CCL4,** CCL5, **CCL8**, CCL12 (MCP-5), **CXCL2**, **CXCL4,** CXCL9, CXCL10, CXCL13	CXCL16, **CCR2 (CD192),**	CXCL13
Enzymes	HEXB+,	NOX2 (CYBB), NOS2, iNOS, CASP1 (ICE), **COX2**		MMP-12, **ARG1*?, YM1*?**
Receptors and Transmembrane Proteins	TGFBR1+, P2RY12+, P2RY13+, FCRLS*, TMEM119+, GPR34+, SIGLEC-H+, CD11b (ITGAM), Iba1(AIF1*), CXC3R1, CSF1R	MHC II receptors including HLA-DR, IFNar1, IFNar2, CD45, CD119 (IFNgr1), CD14, TLR-2, **CCR8**,	CD163, CD204, IFNAR1, IFNAR2, IL-10RA, CD68, IFITM3, CD16 (FcγRIII), CD32 (FcγRII), **CD33**, CD64, TREM2*?	MHCII, **CCR8**
Growth Factors			IGF1	BDNF
Transcription and signalling factors	SALL1+, PU.1,	IRF1, **STAT3**		
Other	OLFML3+, GLUT5, ROS	S100A8, S100A9, IRAK1	OPTN, TYROBP(DAP12), GRN,	
References	(Gautier *et al.*, 2012; Butovsky *et al.*, 2014; Bennett *et al.*, 2016; Friedman *et al.*, 2018; Hickman *et al.*, 2018)	(Simpson *et al.*, 2007; Michelucci *et al.*, 2009; Kawamura *et al.*, 2012; Boche, Perry and Nicoll, 2013; Chiu *et al.*, 2013; Walker and Lue, 2015; Friedman *et al.*, 2018; Hickman *et al.*, 2018; Wang *et al.*, 2019)	(Michelucci *et al.*, 2009; Chiu *et al.*, 2013; Walker and Lue, 2015; Friedman *et al.*, 2018; Hickman *et al.*, 2018)	(Krumbholz *et al.*, 2006; Boche, Perry and Nicoll, 2013; Chiu *et al.*, 2013; Hickman *et al.*, 2013; Walker and Lue, 2015; Friedman *et al.*, 2018)

Key: mouse specific*; Human expression uncertain*?; **Result from In-vitro study*;*** Microglial Marker/Signature Gene+

Note. This table was used with permission from Ashford *et al.* (2020)

Microglial Markers

Genes/proteins expressed my microglia are often used to identify microglia from other cells and can give insights into the activation state. The mostly widely used markers will be explored.

IBA1 (Ionized calcium Binding Adapter molecule 1), is calcium and actin binding adapter molecule, which plays a role in membrane ruffling and phagocytosis. IBA1 is expressed relatively uniformly across the cell and is expressed in homeostatic microglia but expression is increased in activated and phagocytic microglia (Boche, Perry and Nicoll, 2013). IBA1 is often described as a pan microglial marker. However, populations of IBA1-negative/CD68-positive microglia have been observed (Waller *et al.*, 2019).

CD68 (Cluster of Differentiation 68) is a transmembrane glycoprotein expressed by monocyte lineage cells and is particularly associated with macrophages including microglia. CD68 protein is localised to endosomes and lysosomes, and functions as a scavenger receptor, promoting phagocytosis. Therefore, expression of CD68 is commonly considered a marker of phagocytic, activated microglia, although some resting microglia express CD68.

HLA-DR (Human Leukocyte Antigen- DR isotype) is a cell surface receptor from the MHC-II family. MHC-II molecules are present on many immune cells, and are responsible for antigen presentation, the process by which antigens from pathogens are presented on the cell surface for recognition by T-cells (Schetters *et al.*, 2018). Under pathological conditions, microglia are the primary cells within the brain's parenchyma to express MHC-II proteins, and as such expression of these is

commonly seen as a marker of microglial activation (Motataianu, Barcutean and Balasa, 2020).

Other markers include TMEM119 which is thought to be microglial-specific. TMEM199 is expressed by homeostatic microglia and is downregulated in inflammation (Satoh *et al.*, 2016). In cell sorting studies, a combination of CD11b and CD45 are used to identify microglia and distinguish them from other macrophage cells. Homeostatic microglia are considered to be CD11b high expressing and CD45 low expressing whereas macrophages are high expressing for both (Ford *et al.*, 1995). Finally, CX3CR1 is the fractalkine receptor located on the membrane of macrophages including microglia, monocytes and lymphocytes. Fractalkine is a transmembrane receptor for the fractalkine ligand and also acts as a chemokine involved in adhesion and migration (Wolf *et al.*, 2013).

Microglia in Neurodegeneration

Microglia act as a “double-edged sword” in neurodegenerative conditions. In AD, they facilitate the clearance of neuronal plaques, via phagocytosis, endocytosis, and the release of Beta-amyloid degrading enzymes, (El Khoury *et al.*, 1996; Hickman, Allison and El Khoury, 2008; Frenkel *et al.*, 2013). However, continued interaction with these aggregates results in the development of a more inflammatory and cytotoxic phenotype (Coraci *et al.*, 2002; Venegas *et al.*, 2017), resulting in synapse loss and neuronal death (Hong *et al.*, 2016). This double-edged sword characteristic of microglia is seen in other neurodegenerative conditions including Chronic Traumatic Encephalopathy, PD, Progressive Supranuclear Palsy, Cortico-basal Degeneration, FTD and Prion disease (see review Hickman *et al.*, 2018). In

summary, microglia have both neuroprotective and toxic roles in neurodegenerative disease.

The Cycle of Pro-Inflammatory Microglial Activation and Neuron Death

The microglial response is critical for CNS protection, through the destruction and removal of damaged or dysfunctional cells or pathogens and the provision of trophic support. This response is highly effective. However, where the initial trigger is not resolved, a destructive cycle of microglial activation and neuron death is initiated (Figure 1.5). Briefly, this cycle can be triggered by PAMPs causing microglial cytotoxicity. Alternatively, if neuronal damage is triggered by processes such as protein aggregation or excitotoxicity, DAMP release can cause inflammatory microglial activation again resulting in neuronal death (Block, Zecca and Hong, 2007). This is seen as a driver of progression in neurodegeneration (Cho et al., 2006; Fuhrmann et al., 2010; Howell et al., 2010; Frakes et al., 2014; Wu, 2014; Tang and Le, 2016).

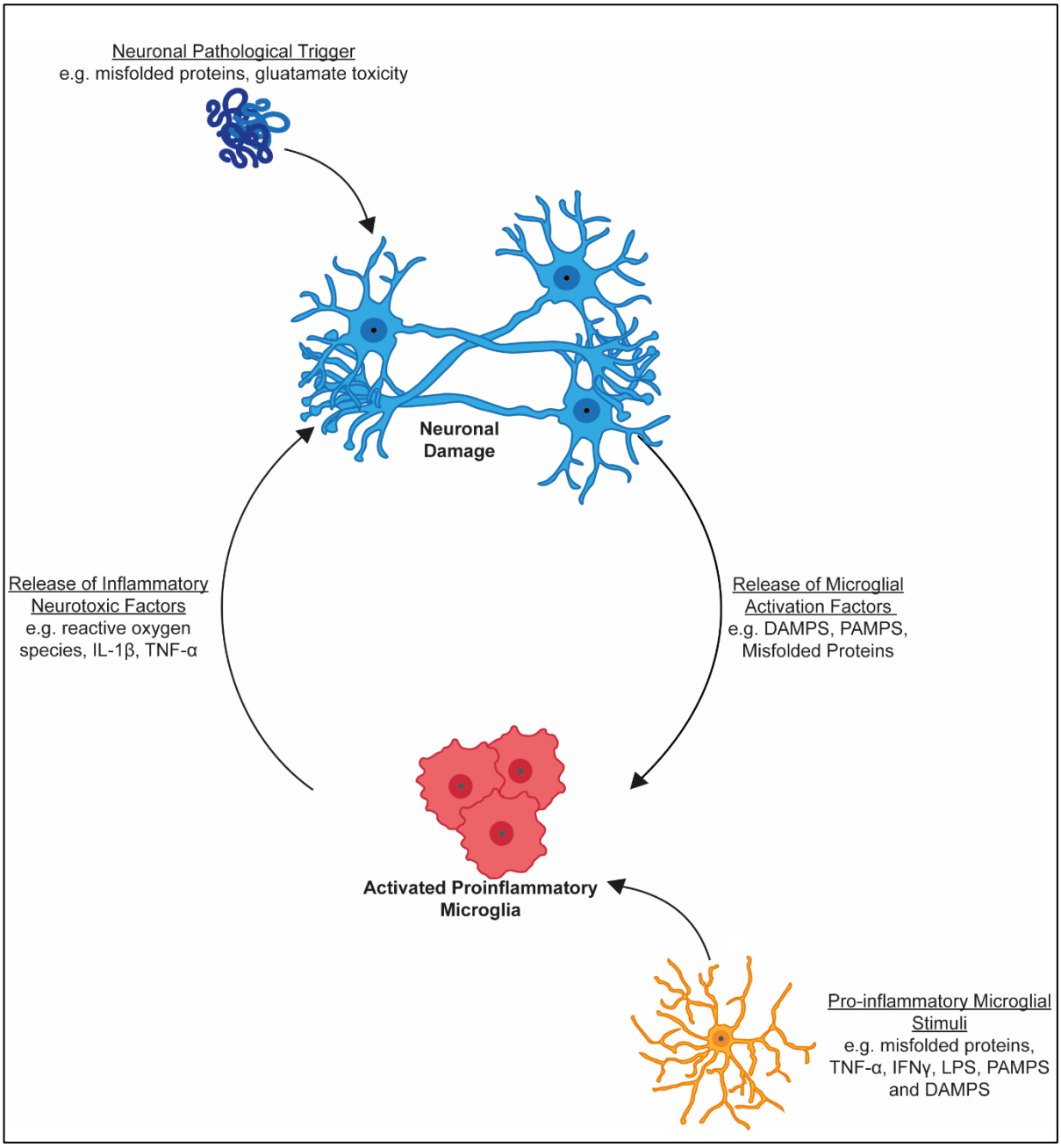

Figure 1.2. The Cycle of Pro-Inflammatory Microglial Activation and Neuron Death

The toxicity cycle can be activated in two ways. First, an external stimulus directly activates microglia, which become pro-inflammatory, releasing cytotoxic factors that can cause neuronal damage. Secondly, neuronal damage can be initiated by neuronal pathological triggers, resulting in the release of DAMPS. These in turn activate microglia resulting in a toxic environment for other neurons (reactive microgliosis). This results in a self-perpetuating cycle of microglial over-activation and neuronal damage. Figure adapted with permission from Ashford et al. (2020).

Disease-Associated Microglia

Microglia adopt various phenotypes in response to external signalling and stimuli. With aging and neurodegeneration, microglia tend to lose their homeostatic signature and functions, and become inflammatory (Holtman *et al.*, 2015). However, in the last ten years several studies have identified microglia with a unique signature associated with neurodegeneration referred to as disease-associated microglia or DAM.

The homeostatic microglial phenotype is associated with expression of markers including CX3CR1, TMEM119, and TGFβ (Krasemann *et al.*, 2017; Deczkowska *et al.*, 2018). DAM are associated with a downregulation of these homeostatic genes and an increase in genes associated with inflammation, lipid metabolism, and phagocytosis and lysosomal pathways.

DAM were initially identified in mouse models, particularly of AD, and were observed in regions of the brain associated with pathology and not in unaffected regions (Holtman *et al.*, 2015; Kamphuis *et al.*, 2016; Krasemann *et al.*, 2017; Ajami *et al.*, 2018; Mrdjen *et al.*, 2018). DAM transcriptomic signatures have been observed in a number of mouse models of other neurodegenerative disease including MND (Chiu *et al.*, 2013; Holtman *et al.*, 2015; Keren-Shaul *et al.*, 2017; Krasemann *et al.*, 2017; Friedman *et al.*, 2018; Spiller *et al.*, 2018), providing evidence this microglial signature is a response to neurodegeneration rather than a specific disease response. *Post-mortem* studies have also found evidence of the DAM signature in AD (Keren-Shaul *et al.*, 2017; Friedman *et al.*, 2018). However, this DAM phenotype has not yet been examined in other human neurodegenerative conditions.

Krasemann et al. (2017) proposed a TREM2 (Triggering Receptor Expressed on Myeloid Cell 2) / APOE (Apolipoprotein E) signalling pathway which may be responsible for the switch from homeostatic microglia to DAM (Figure 1.3). Microglia were isolated from mouse models of aging, MND, AD, and multiple sclerosis (MS). Through transcriptomic analysis, *in-vivo* and *in-vitro* studies, Krasseman et al. found that following phagocytosis of apoptotic neurons, microglia increased expression of APOE, through TREM2/TYROBP signalling. This resulted in a reduction of the TGFβ-mediated microglial homeostatic phenotype, and an increase in DAM-associated genes.

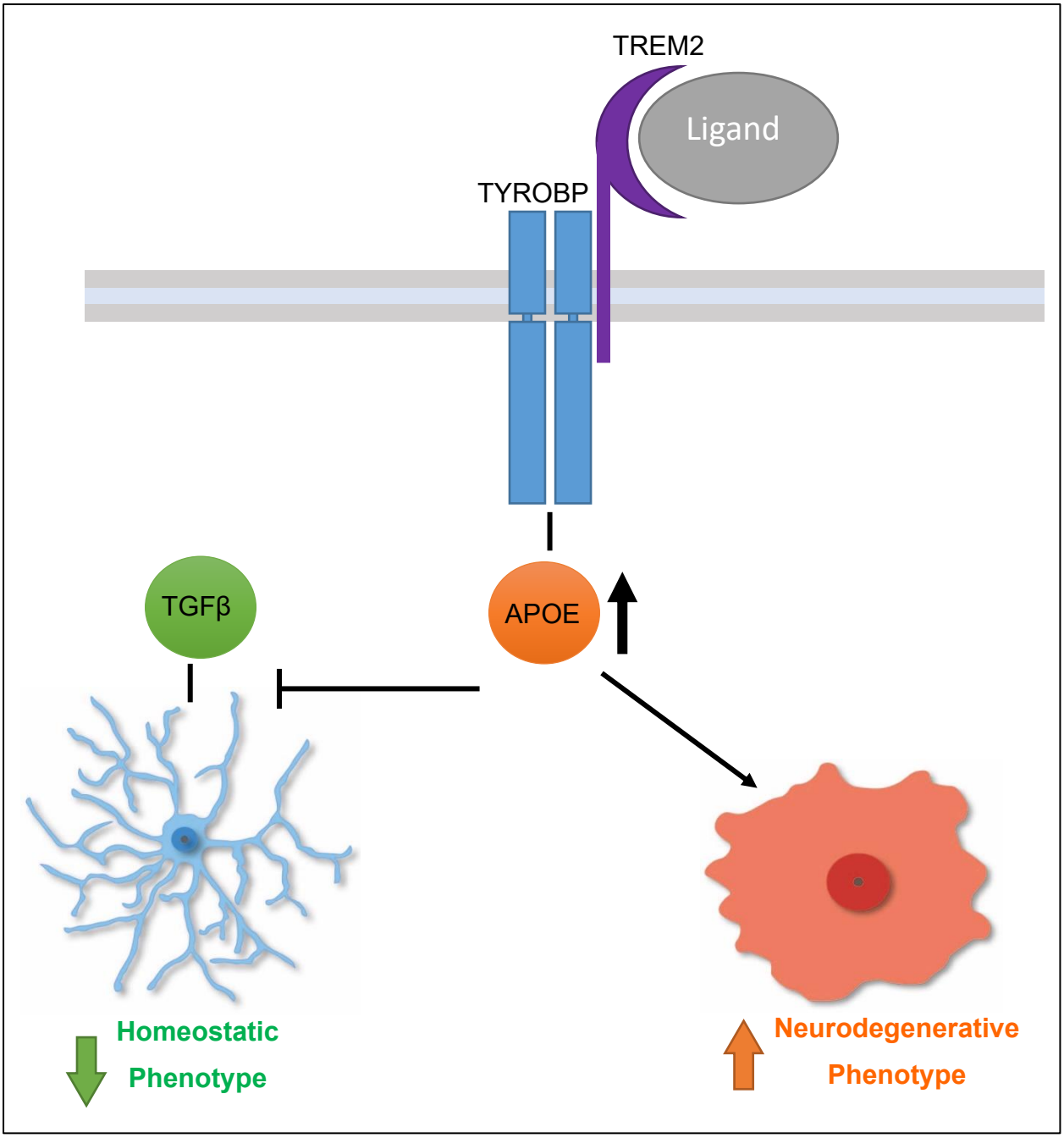

Figure 1.3 The Disease-Associated Microglial Phenotype

The gene expression signature of homeostatic microglia is mediated by TGFβ signalling and characterised by low expression of APOE. Microglial TREM2 receptors can be activated by an anion phospholipids/APOE complex from the surface of phagocytosed neurons or cellular debris (shown here by the orange circle). This signalling cascade results in an upregulation of APOE which in turn downregulates the homeostatic microglial phenotype and microglia switch to neurodegenerative disease phenotype (also referred to as the "microglial neurodegenerative phenotype" Krasemann et al., 2017, and also Disease-Associated Microglia or DAMs). This degenerative phenotype has been observed across murine models of various neurodegenerative diseases and ageing.

1.9.2 Microglia in Human MND

Neuroinflammation is a Key Feature of MND

Neuroinflammation is a key feature of human MND. It is mediated by the production of various cytokines, reactive oxygen and nitrogen species, chemokines, and signalling molecules by microglia, as well as extensive signalling with surrounding neurons and glia. CSF from MND patients has high levels of inflammatory cytokines (Babu *et al.*, 2008; Mitchell *et al.*, 2009; Zhang *et al.*, 2009), the expression of which has been correlated with the disease progression rate (Süssmuth *et al.*, 2010; Tateishi *et al.*, 2010; Liu, Gao and Zang, 2015). Furthermore, transcriptomic analysis of *post-mortem* spinal cord has highlighted inflammation as one of the most altered pathways (Dangond *et al.*, 2004; Offen *et al.*, 2009; Figueroa-Romero *et al.*, 2012; Cirulli *et al.*, 2015; Brohawn, O'Brien and Bennett, 2016; Andrés-Benito *et al.*, 2017; Cooper-Knock *et al.*, 2017). Interestingly, Dangond et al. (2004) found it possible to distinguish between fMND and sMND from their gene expression profiles, highlighting the significant differences between the two types of MND. The motor cortex has been less widely examined in *post-mortem* transcriptomic studies of MND. Wang *et al.* (2006) found only 10 genes to be upregulated in the motor cortex in sMND, and 265 down regulated, with inflammation being one of the key down-regulated processes. In contrast, Lederer *et al.* (2007) and (Aronica *et al.*, 2015) found a significant upregulation of inflammatory transcripts in MND motor cortex compared to controls. The discrepancy in inflammatory signalling in the motor cortex indicates a requirement for further investigation.

Microglial Activation Correlates with Clinical Features in Post-mortem Studies

Post-mortem spinal cord from MND patients showed raised levels of Monocyte Chemoattractant Factor 1, a key recruiter of microglia (Henkel *et al.*, 2004). At sites of neuronal loss, CD68 and Iba1 immunohistochemistry (IHC) revealed microglia that have transitioned from their ramified morphology to the 'activated' morphology in both fMND and sMND (Henkel *et al.*, 2004; Brettschneider, Libon, *et al.*, 2012; Brettschneider, Toledo, *et al.*, 2012). Increased CD68 microglial immunoreactivity implicates the importance of phagocytic activity in these regions.

In-vivo positron emission tomography (PET) with the TSPO PK11195 tracer to image microglia has shown increased signal in both motor and extra motor regions in MND (Turner *et al.*, 2004). A further PET study showed microglial activation in MND to be associated with cortical thinning and a worse disease phenotype (Alshikho *et al.*, 2016). In addition, human autopsy studies have shown microglial activation correlates with the extent of TDP-43 inclusion pathology, executive dysfunction, upper motor neuron loss and upper motor neuron dysfunction-associated symptoms, and the rate of disease progression (Brettschneider, Toledo, *et al.*, 2012; Alshikho *et al.*, 2016). Microarray analysis of mRNA from MND spinal cord found genes associated with microglial activation, which were able to predict the rate of disease progression (Cooper-Knock *et al.*, 2017).

Genetic Studies have highlighted the Role of Microglia in MND

Genetic studies have also implicated microglia in MND. TREM2 is an immunoglobulin superfamily cell surface receptor expressed on the surface of many monocyte lineage cells (Yeh, Hansen and Sheng, 2017). TREM2 is thought to

regulate microglial activation, cytokine production, proliferation, motility and phagocytosis (Konishi and Kiyama, 2018). However, the downstream effects of TREM2 activation vary depending on the type and affinity of the binding ligand (Konishi and Kiyama, 2018). Additionally, TREM2 can be cleaved by ADAM10 or ADAM17 to form a soluble form of TREM2 (sTREM2) which can also bind to monocytes causing an inflammatory response through PI3K/Akt signalling, resulting in improved microglial survival (Zhong *et al.*, 2017). Furthermore, sTREM2 may regulate TREM2 through competitive binding to activating substrates.

TREM2, was found to be more highly expressed in MND patient spinal cord compared to controls, and showed a modest inverse correlation with the length of patient survival (Cady *et al.*, 2014). In contrast, expression of sTREM2 has been found to be highly expressed in CSF in the early stages of MND and diminishes in later stage patient CSF (Cooper-Knock *et al.*, 2017). In the late stages of disease, soluble TREM2 expression positively correlated with survival time. As sTREM2 is thought to regulate membrane-bound TREM2, these data could indicate that increased production of sTREM2 may be protective in MND, though regulation of the membrane-bound TREM2

A rare missense variant (R47H) in *TREM2* has been identified as a risk factor for neurodegenerative conditions including AD, (Jonsson *et al.*, 2013), although results have varied in MND (Cady *et al.*, 2014; Lill *et al.*, 2015). While TREM2 is associated with microglial activation in mice (Schmid *et al.*, 2002; Hickman *et al.*, 2013), the expression of TREM2 by human microglia has recently been questioned: Immunohistochemistry on human cortical tissue found that TREM2 was overwhelmingly expressed by infiltrating monocytes (in 284/299 cases), and little

expression was observed in microglia (Fahrenhold *et al.*, 2018), suggesting a key species-specific difference in microglia, strengthening the need for human research as well as animal models.

To further support the role of microglia in human MND, a variant (V2491) in the microglial fractalkine receptor, *CX3CR1* is associated with more rapid disease progression (Lopez-Lopez *et al.*, 2014; Calvo *et al.*, 2018). The fractalkine receptor interacts with the fractalkine chemokine which is expressed by neurons (Cardona *et al.*, 2006). Fractalkine and its receptor mediate the neuron-microglial interactions associated with inflammation and provides neurons with protection by preventing toxic microglial activation (Arnoux and Audinat, 2015). V2491 is associated with reduced numbers of fractalkine binding sites resulting in loss of function. As such, this finding indicates microglia are able to cause damage to neurons through inflammation, due to impaired neuron-microglial signalling.

APOE is an important protein in the metabolism and transport of lipids throughout the body (Sing and Davignon, 1985; Mahley, 1988; Bennet *et al.*, 2007). In the brain, APOE is most widely expressed by astrocytes and microglia, with lesser expression by neurons (Pitas *et al.*, 1987; Xu *et al.*, 2000; Harris *et al.*, 2004; Mahley, 2016; Lanfranco *et al.*, 2021). In the CNS, APOE is involved in lipid transport, and is important for neuronal survival and plasticity and neurite outgrowth (Holtzman *et al.*, 1995; LaDu *et al.*, 2001; White *et al.*, 2001; Lanfranco *et al.*, 2021). APOE has been linked to modulation of the immune response through MHC class proteins (Tenger and Zhou, 2003) and the switch from homeostatic to the DAM microglial phenotype (Krasemann *et al.*, 2017).

Possession of one or two copies of the ε4 *APOE* allele is considered the largest risk factor in the development of AD (Bertram *et al.*, 2007) and is associated with poorer

outcome in a number of other conditions such as MS (Chapman *et al.*, 2001) and chronic traumatic brain injury (Jordan *et al.*, 1997). The ε4 allele is associated with impaired protein clearance by microglia, increased inflammatory cytokine expression and deficient debris clearance (Vitek, Brown and Colton, 2009; Fernandez *et al.*, 2019).

APOE expression and allele status has been examined in relation to MND. Several studies have indicated there is no link between possessing the ε4 allele and overall risk of developing MND (Moulard *et al.*, 1996; Siddique *et al.*, 1998; Govone *et al.*, 2014). This said, the ε4 allele has been associated with increased risk of developing the bulbar onset (as opposed to other forms) of MND (Praline *et al.*, 2011) in whom onset was on average 6 years earlier (Moulard *et al.*, 1996). Carrying the ε2 allele, which is broadly protective in AD, was found to delay symptom onset by approximately 3 years (Li *et al.*, 2004). APOE expression has consistently been found to be upregulated in *post-mortem* spinal cord for MND patients (Offen *et al.*, 2009; Andrés-Benito *et al.*, 2017; Oeckl *et al.*, 2020).

Interestingly, of the microglial/ immunity-associated genetic variations discussed, all result in worsened phenotype or faster disease progression but do not confer risk, which indicates microglia may act as disease modifiers as opposed to causative factors.

In summary, human pathology, imaging, and genetic studies have supported a role for microglia in MND. However, attempts to determine microglial functions in human MND have been sparse.

1.9.3 Microglia in Animal Models of MND

Attempts to determine the molecular behaviours of microglia in MND with greater specificity have predominantly utilised transgenic animal models. The most characterised and widely used models, are the aforementioned m*SOD1* mouse models (Gurney *et al.*, 1994; Ripps *et al.*, 1995; Wong *et al.*, 1995; Bruijn *et al.*, 1997). More recently, models have been created which contain transgenic mutations in *TARDBP, FUS, C9orf72, PFN1*, and *UBQLN2* (summarised by Lutz, 2018), as well as in other species including rats (Philips and Rothstein, 2015) and zebrafish (Costa *et al.*, 2014; Ramesh, Shaw and McDearmid, 2014; Shaw *et al.*, 2018).

Microglia in Early Disease Progression

Transgenic mSOD1^{G93A} mice show evidence of peripheral nerve and motor neuron dysfunction early in disease course, prior to the appearance of macrophages and microglia in the muscle and spinal cord respectively, which occurred at symptom onset (Kano *et al.*, 2012). Similarly, Shiraishi *et al.* (2021) observed activation of microglia in the ventral horn which was concomitant with the development of mSOD1 pathology in this region in the spinal cord of mSOD1^{G93A} mice. Gerber *et al.* (2012) found a decrease in the number of IBA1^{+} microglia in mSOD1^{G93A} mouse spinal cord compared to control littermates, prior to symptom onset using fluorescence activated flow cytometry (FACS). In the early, symptom-onset stage, the mSOD1^{G93A} mice showed little difference in the number of microglia in the spinal cord, contradicting the above findings of Kano et al. (2012). In contrast, mSOD1^{G93A} rats showed increased numbers of microglia in the spinal cord before symptom onset, as

determined by flow cytometry of immunomagnetically-isolated microglia (Nikodemova *et al.*, 2014), in contrast to the findings of Gerber et al.

The reported time of onset of microglial activation varies greatly in mSOD1 models, such that it is difficult to determine whether microglial activation precipitates MND symptoms and/or inclusion pathology or *vice versa*.

Anti-inflammatory and Trophic Roles of Microglia in sMND

In the early stages of most diseases, microglia are activated by signals from dying neurons (Glass *et al.*, 2010). In MND, these signals are likely to include ATP, chemokines and DAMPS (Yiangou *et al.*, 2006; Zhao, Beers and Appel, 2013). Microglia isolated from 11-week-old mSOD1^{G93A} mice, were found to express high levels of Ym1 and CD163 mRNA, markers of anti-inflammatory and phagocytic microglia, as well as BDNF, a neurotrophin which promotes neuronal survival (Liao *et al.*, 2012). Co-culture of these microglia with WT motor neurons resulted in little difference to neuronal health than co-culture of WT microglia and motor neurons. However, on incubation with WT motor neurons and WT astrocytes, motor neuron survival increased, over that of the motor neurons co-cultured with WT microglia only group, indicating a powerful neuroprotective astrocyte-mediated microglial response. In addition, microglia from presymptomatic mSOD1^{G93A} mice showed a 16-fold increase in the production of IL-10, a cytokine responsible for the downregulation of inflammation (Gravel *et al.*, 2016). Targeted over-expression of IL-10 in the spine resulted in delayed symptom onset and extended survival. Furthermore, blocking IL-10 receptors using the mIL-10R1 antibody resulted in rapid precipitation of symptoms in presymptomatic mice. These high levels of IL-10 were associated with

reduced Toll like Receptor 2 activity, which upon activation promotes the production of inflammatory cytokines via microglia (Henkel *et al.*, 2009).

Inflammatory and Toxic Roles of Microglia in MND

As with other neurodegenerative diseases, MND displays a prominent and sustained inflammatory response orchestrated by glia, including microglia, and peripheral immune cells, which contributes to neuron death (Henkel *et al.*, 2014). This response can also induce protein misfolding in motor neurons (Glass *et al.*, 2010). Transcriptomic analysis of microglia from late-stage mSOD1^{G93A} mice, showed diminished protective markers and high levels of nitric oxide. Co-culture of these late-stage microglia with WT motor neurons induced neuronal death (Liao *et al.*, 2012). Nitric oxide induced motor neuron death, by increasing motor neuron sensitivity to glutamate, potentially results in excitotoxicity. Additionally, these microglia were shown to inhibit astrocytic uptake of glutamate in culture (Zhao *et al.*, 2004), indicating inflammatory microglia could diminish the protective ability of other glial cells.

In addition, transcriptional analysis of mSOD1^{G93A} mouse spinal cord homogenate showed a significant upregulation of inflammatory genes including cathepsin D and TNF-α, at 11 weeks of age compared to non-transgenic littermates (Yoshihara *et al.*, 2002). Yoshihara and colleagues, conclude this as evidence of an inflammatory response in the pre-symptomatic stage. However, symptom onset has been observed as early as 8.5 weeks of age in this model (Gerber *et al.*, 2012), implying the inflammatory microglial phenotype observed occurred in the early stages of disease. Furthermore, these results contradict the findings of aforementioned research by Liao et al. (2012), who found an increase in the expression of anti-

inflammatory cytokines at 11 weeks, utilising the same mSOD1^{G93A} model. These results highlight the variation observed in from this model.

Microglia expressing mSOD1 appear to be more neurotoxic than WT inflammatory microglia. Upon stimulation with LPS, a PAMP that induces a neurotoxic phenotype, microglia over-expressing mSOD1^{G93A} released more nitric oxide and super oxidase (toxic agents), than microglia overexpressing WT SOD1, and WT microglia (Beers *et al.*, 2006; Xiao *et al.*, 2007). These mSOD1 microglia induced more neuronal death in co-culture with motor neurons than their WT counterparts. However, these microglia were isolated from neonatal mice and cultured. Consequentially they may no longer reflect the aged microglia found in MND.

Interestingly, Weydt *et al.* (2004) performed a similar experiment, but compared primary microglia isolated from 3-day old mice and 60-day old mice (early symptomatic). Upon stimulation with LPS, only the older mSOD1^{G93A} microglia showed a significant difference to WT, by increasing the production of TNF-α and reducing expression IL-6 compared to WT microglia: This response was sustained over 24 hours. This suggests aged mSOD1-expressing microglia are more neurotoxic than WT microglia, even under the same treatment conditions.

This heightened response by aged mSOD1 microglia compared to WT may reflect a so-called ‘microglial priming’ response, whereby microglia display an exaggerated response to stimuli, after prior activation (Perry and Holmes, 2014), such as repeated exposure to mSOD1. Microglial priming is particularly observed in aging and neurodegenerative conditions such as AD (Norden and Godbout, 2013): These microglia are also less responsive to anti-inflammatory agents. Transplantation of WT microglia into mSOD1^{G93A} mice, via bone marrow transplant, resulted in reduced motor neuron loss and extended survival time (Beers *et al.*, 2006). This indicates that

in mSOD1 mice, treatment with WT microglia is sufficient to benefit motor neurons and consequentially mouse survival.

The expression of mutant TDP-43 (mTDP-43) by microglia produces a more toxic response to stimulation with LPS compared to WT microglia, *in-vitro* (Swarup *et al.*, 2011). mTDP-43 appears to activate microglia through the nuclear factor kappa-light-chain-enhancer of activated B cells (NF-κB) pathway (Zhao *et al.*, 2015). This pathway is a master regulator of inflammation, and is highly upregulated in MND patient spinal cord, and mSOD1 mice (Swarup *et al.*, 2011; Frakes *et al.*, 2014). When activated (by inflammatory cytokines or reactive oxygen species), the NF-κB complex relocates to the nucleus, inducing further expression of inflammatory cytokines and chemokines (Ghosh and Karin, 2002). However, the NF-κB pathway can be induced directly via the truncated WT TDP-43 and even more potently by mTDP-43 in WT primary mouse microglia (Zhao *et al.*, 2015). This results in the production of inflammatory cytokines which are toxic in co-culture with MNs (Frakes *et al.*, 2014; Zhao *et al.*, 2015). Additionally, NF-κB-activated mSOD1 microglia have been shown to phagocytose healthy synapses *in-vitro*, a feature not observed in NF-κB stimulated WT microglia (Frakes *et al.*, 2014).

The Role of Microglial Phagocytosis and Protein Clearance in Animal Models of MND

Microglia play in important role in the clearance of misfolded proteins and cellular debris. Animal models of MND indicate this process of may be dysfunctional in MND.

The phagocytosis of pathological proteins in MND, triggers an inflammatory response by microglia. Phagocytosis of extracellular mSOD1 has been shown to activate microglia, producing an amoeboid, toxic phenotype (Zhao *et al.*, 2010). Real-time quantitative Polymerase Chain Reaction (RT-qPCR) revealed an increase in the expression of the inflammatory factors *TNF-α, IL-1β, NADPH oxidase 2 (NOX2)* and *superoxidase*, and a concomitant decreased expression of the repair factor *IGF-1*. When co-cultured with primary mSOD1^{G93A} mouse motor neurons, these microglia proved neurotoxic, compared to un-primed mSOD1 ^{G93A} microglia. This effect was rescued using TLR2, TLR4 and CD14 blocking antibodies.

Dysfunctional microglia may contribute to the pathological translocation of TDP-43 from the nucleus to the cytoplasm. Using transgenic zebrafish, which co-expresses green fluorescent protein with TDP-43, and microglia which express mCherry, Svahn *et al.* (2018) were able to visualise the nucleocytoplasmic translocation of TDP-43 with green fluorescence, and microglial dynamics *in-vivo*. After the initiation of motor neuron death via UV, microglia rapidly approached the damaged neuron and phagocytosed the soma. Microglia also phagocytosed TDP-43 in the nucleus. Microglial populations were depleted via morpholinos targeted at the hematopoietic transcription factor, PU.1. After initiation of motor neuron death in the absence of functional microglia, motor neurons showed a more typical pattern of neurodegeneration characterised by swelling of the soma. Microglial depletion also resulted in the translocation of TDP-43 from the nucleus to the cytoplasm, a key feature of MND pathobiology. Although this is quite an artificial model of motor neuron death, it indicates dysfunctional microglial phagocytosis may contribute to the TDP-43 pathology observed in models of MND and human pathology.

Inconsistencies in Findings in Animal Models

Research characterising microglia in animal models of MND have highlighted both toxic and neuroprotective microglial functions. However, there has been considerable inconsistencies within the literature. Older studies indicated a tendency towards an early increase in trophic and anti-inflammatory expression prior to symptom onset (Hensley *et al.*, 2002; Beers *et al.*, 2006; Liao *et al.*, 2012; Gravel *et al.*, 2016), followed by a switch to a more toxic, proinflammatory phenotype (Hensley *et al.*, 2002; Henkel *et al.*, 2006; Xiao *et al.*, 2007; Zhao *et al.*, 2010; Liao *et al.*, 2012; Funikov *et al.*, 2018). In contrast, more recent studies have provided evidence indicating microglia express both protective and toxic factors consistently throughout disease. Flow cytometry and RNA sequencing of microglia from m*SOD1*^{G93A} mouse spinal cord over different disease time points have revealed simultaneous upregulation of inflammatory genes such as *Tumour Necrosis Factor* (*TNF) -α, Interleukin (IL) -1β,* and receptors for various interferons (IFNs) and *NADPH oxidase 2* (*NOX2)*, as well anti-inflammatory genes such as Interferon Growth Factor (*IGF) -1, Progranulin* and *Triggering Receptor Expressed on Myeloid Cells 2* (*TREM2*; Chiu *et al.*, 2013).

Furthermore, RT-qPCR characterisation of microglia from m*SOD1*^{G93A} rat spinal cord did not find microglial activation in the presymptomatic stages of disease (Nikodemova *et al.*, 2014). However, at disease onset and late-stage disease, m*SOD1* microglia showed a simultaneous upregulation of *galectin* and *osteopontin*, factors involved in macrophage activation and chemotaxis, which can be both neurotoxic and protective. The pro-survival factor *Vascular Endothelial Growth Factor (VEGF)* was also upregulated. This was accompanied by the concomitant

downregulation of the classic inflammatory marker *TNF-α,* and anti-inflammatory markers *Brain-derived neurotrophic factor* (*BDNF), IL-6* and *arginase-1.*

The same study found microglial function to vary according to location: The above differences were only seen in spinal cord, but not cortex.

1.10 Aims and Hypotheses

MND is a non-cell autonomous condition, where glia play a large role in pathogenesis. Inflammation is a key feature and is primarily mediated by the microglial response.

Human *post-mortem,* and genetic studies have highlighted a role for microglia in the pathology of MND, with their activation being correlated with disease progression. The majority of research which has attempted to characterise the microglial inflammatory response has used animal models of MND.

While such models have provided great insight into the pathology of MND, they model fMND which accounts for only a very small proportion of MND cases. Furthermore, the majority of existing data comes from models of MND containing *SOD1* mutations, which in humans presents with unique pathology, compared to other familial and sporadic MND cases. The variability in findings from mSOD1 mice, although representative of the heterogeneity in human SOD1-MND, make findings from mSOD1 mice difficult to apply to human MND.

As such, this project looks to characterise the neuroinflammatory and microglial phenotype across the CNS in human sMND. The following aims will be addressed:

Aim 1. Perform transcriptomic analysis of the motor regions of the CNS (ventral horn of the spinal cord and precentral gyrus – motor cortex) from control and sMND cases to identify a neuroinflammatory signature.

Hypothesis 1. *There will be an increase in inflammatory gene expression, both protective and toxic, in sMND cases, compared to control. The microglial response will not conform to a strict M1 or M2 phenotype but will instead show a mixture of pro-inflammatory and anti-inflammatory functions.*

Aim 2. Data from sMND cases with long and short survival will be compared to identify potentially harmful and beneficial microglial responses.

Hypothesis 2. *There will be greater expression of neurotoxic markers in cases with shorter survival, and increased expression of neuroprotective markers will be observed in cases with longer survival.*

Aim 3. Immunohistochemistry will then be used to examine these changes in gene expression at the protein level, characterise changes in microglial morphology, and examine the relationship between expression genes of interest with clinical features such as length of survival.

Hypothesis 3. *Immunohistochemistry will validate these gene expression changes; microglial activation will be increased in areas associated with neurodegeneration. There will be a relationship between microglial markers and genes of interest.*

Chapter 2 Materials and Methods

2.1 Tissue Collection

Formalin-fixed Paraffin-embedded Spinal Cord

Formalin-fixed Paraffin-embedded (FFPE) *post-mortem* cervical spinal cord tissue was obtained from the Sheffield Brain and Tissue Bank (SBTB), which has ethical permission to function as a Research Tissue Bank granted by the Scotland A Research Ethics Committee (19/SS/0029; All ethics certificates for this research are given in Appendix E). This cohort consisted of 16 sporadic motor neuron disease (sMND) cases of varying survival times from diagnosis to death (median age at death: 67.5 years, median survival times: 98 months), and 8 approximately age- and sex-matched neurologically normal control cases (median age at death: 66 years; see Table 2.1). sMND cases which showed no comorbidity for other neurological conditions were selected, and control cases were checked to ensure the cause of death would have caused minimal pathology within the CNS.

Table 2.1 FFPE Spinal Cord Full Cohort Details

Case Number	Sex	Status	Onset age	Duration (months)	Age at Death (Years)	Site of Symptom Onset	Post-mortem Delay (hours)
085/2007	f	control			59		5
335/1990	f	control			29		20
035/1996	f	control			87		14
014/1999	f	control			86		52
056/1990	m	control			51		25
309/1990	m	control			82		24
144/1991	m	control			65		34
098/2007	m	control			67		63
009/2017	f	sALS		6	78		-
025/2013	f	sALS	71	22	72	Respiratory	60
723/1989	f	sALS	62	23	64	Limb	40
105/2007	f	sALS	81	24	83	Bulbar	44
041/2008	f	sALS	57	38	60	-	18
023/2010	f	sALS	34	89	42	Limb	24
004/2006	f	sALS	64	66	69	Limb	12
059/2009	f	sALS	72	104	80	Bulbar	50
072/2005	m	sALS	66	10	66	Limb	8
094/2006	m	sALS	71	9	71	Limb	53
094/2009	m	sALS	62	14	63	Bulbar	48
005/2010	m	sALS	38	32	40	Limb	96
091/2008	m	sALS	50	44	53	Limb	16
074/2009	m	sALS	65	46	69	Bulbar	48
072/2002	m	sALS	46	61	51	Limb	48
099/2009	m	sALS	74	63	79	Limb	24

Average Age at death (Mean Years & SD):	***Average post-mortem delay at death (Mean Hours & SD):***	***Sex Split (F/M):***
sMND = 65 (13.05) *Control = 65.75 (19.79)* *T-test Age comparison between sMND and Control t(22)= 0.011, p=0.91* *t(22)=0.01116, p=0.9121*	*sMND = 39.27 (22.97)* *Control = 29.63 (19.38)* *T-test Age comparison between sMND and Control t(21)=0.046, p=0.673*	*sMND = 8/8* *Control = 4/4*

***Note**: dash symbol (-) indicates information is not known.*

Frozen Spinal Cord and Motor Cortex

Fresh frozen *post-mortem* cervical spinal cord and motor cortex tissue samples were also obtained from the SBTB. The interval between death and *post-mortem* ranged from 4 to 50 hours for the spinal cord and between 5 and 96 hours for the motor cortex. For each region, the cohort consisted of 16 sMND cases of varying survival times and 8 control cases. Demographic details are given (Table 2.2 and 2.3).

Table 2.2 Frozen Spinal Cord Cohort

Case ID	Sex	Disease Status	Onset age	Duration (months)	Age at Death (Years)	Post-mortem Delay (Hours)	Site of Symptom Onset
085/2007	f	control			59	5	
080/1992	f	control			62	36	
071/1992	f	control			75	16	
135/1982	f	control			89	24	
109/1995	m	control			46	20	
1028/1989	m	control			56	34	
025/1995	m	control			67	20	
138/1994	m	control			75	17	
150/1993	f	sALS	52	4	52	37	limb
050/2008	f	sALS	68	26	70	35	bulbar
037/2000	f	sALS	78	29	81	16	bulbar
041/2008	f	sALS	57	38	60	18	limb
024/2008	f	sALS	59	46	63	36	limb
209/1995	f	sALS	54	48	58	4	limb
023/2010	f	sALS	34	89	42	24	limb
059/2009	f	sALS	72	104	80	50	bulbar
295/1991	m	sALS	52	2	53	10	bulbar
141/2003	m	sALS	75	7	75	24	bulbar
261/1990	m	sALS	68	13	69	9	bulbar
024/2004	m	sALS	58	19	60	4	bulbar
115/2002	m	sALS	50	25	52	<24	limb
034/2005	m	sALS	60	38	63	16	limb
131/1995	m	sALS	63	53	67	6	limb
072/2002	m	sALS	46	61	51	48	limb

Average Age at death (Mean Years & SD):	***Average post-mortem delay at death (Mean Hours & SD):***	***Sex Split (F/M):***
sMND = 62.25 (11.01) *Control = 66.13 (13.40)* *T-test Age comparison between sMND and Control* *t(22)=0.757, p=0.457*	*sMND = 22.47 (15.49)* *Control = 21.50 (10)* *T-test Age comparison between sMND and Control* *t(21)=0.159, p=0.875*	*sMND = 8/8* *Control = 4/4*

Table 2.3 Frozen Motor Cortex Cohort

Case ID	Sex	Disease Status	Onset age	Duration (months)	Age at Death (Years)	Post-mortem Delay (Hours)	Site of Symptom Onset
335/1990	f	control			29	20	
178/1995	f	control			63	24	
072/1992	f	control			76	32	
023/1992	f	control			84	39	
147/1995	m	control			47	15	
111/1990	m	control			52	13	
293/1991	m	control			65	17	
309/1990	m	control			82	24	
150/1993	f	sALS	52	6	52	37	limb
223/1999	m	sALS	50	5	50	35	multifocal
193/1990	f	sALS	58	10	59	30	limb
261/1990	m	sALS	68	13	69	9	bulbar
203/1994	f	sALS	57	19	58	5	multifocal
069/2006	m	sALS	48	22	50	48	bulbar
050/2008	f	sALS	68	26	70	35	bulbar
005/2010	m	sALS	38	32	40	96	limb
041/2008	f	sALS	57	38	60	18	limb
024/2008	f	sALS	59	46	63	36	limb
088/1996	m	sALS	66	48	70	86	limb
209/1995	f	sALS	54	48	58	6	limb
131/1995	m	sALS	63	53	67	6	limb
150/1997	m	sALS	27	60	32	27	limb
043/2005	m	sALS	31	66	37	35	limb
137/1996	f	sALS	56	99	65	9	multifocal

Average Age at death (Mean Years & SD):	***Average post-mortem delay at death (Mean Hours & SD):***	***Sex Split (F/M):***
sMND = 56.25 (11.90) *Control = 62.25 (18.91)* *T-test Age comparison between sMND and Control* *t(22)=0.955, p=0.350*	*sMND = 23.00 (8.848)* *Control = 32.38 (26.71)* *T-test Age comparison between sMND and Control* *t(22)=0.958, p=0.349*	*sMND = 8/8* *Control = 4/4*

2.2 Tissue Preparation

Formalin-fixed paraffin embedded (FFPE) Tissue

For the FFPE spinal cord tissue, 10 sections of 50µM thickness were cut per case using a microtome, ensuring the top sections of the tissue block were discarded to reduce contaminants. The superficial blood vessels, leptomeninges, dorsal horns and white matter (WM) were dissected off and discarded using a disposable scalpel to isolate the ventral horn, using a head loupe magnifier visor by a qualified neuropathologist, RJH (Figure 2.1). All surfaces and scalpels were sterilised with 70% methylated spirits before and after each case to prevent cross-contamination. Multiple sections were chosen over fewer thicker sections to average out any disparities in dissection method. The dissected sections were immediately placed in a sterile RNase-free tube.

Frozen Tissue

All frozen tissue was stored at -80^{o}C and brought up to -20^{o}C for dissection. Grey matter from the motor cortex was isolated from snap-frozen coronal slices by RJH. Superficial blood vessels, leptomeninges and white matter were dissected off and discarded using a razor blade. Grey matter was taken from at least two different areas of the motor cortex coronal slice.

For the spinal cord samples, the ventral horn was dissected from frozen cervical cord in a similar manner to that for FFPE tissue (Figure 2.1). All dissection was completed in a freezer cabinet, pre-chilled to -20^{o}C. All tools and cutting surfaces were sterilised using 70% methylated spirits. Approximately 20-40mg of tissue was collected per case. All

tissue samples were placed in sterile RNAse-free 1.5mL microcentrifuge tubes and kept at -80^{o}C until RNA extraction.

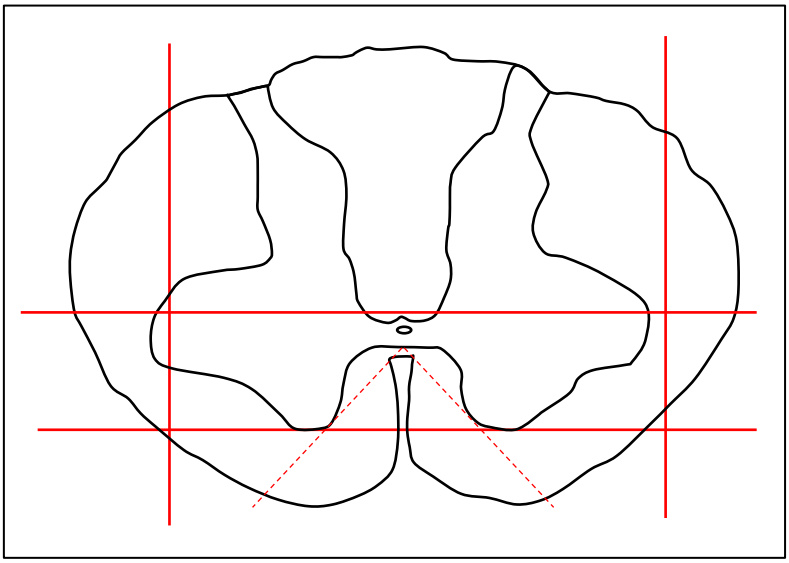

Figure 2.1 Dissection of Spinal Cord to Isolate Ventral Horns

Schematic diagram showing the method of dissection used to isolate the ventral horns form FFPE and frozen cervical spinal cord tissue. Leptomeninges and white matter were removed.

2.3 RNA extraction

2.3.1 RNA extraction from FFPE Tissue

Materials

Table 2.4 FFPE RNA Extraction Materials

Reagent/ Kit		Supplier	Catalogue Number
Qiagen® RNeasy FFPE Kit	RNeasy MinElute® Spin Columns	Qiagen®	73504
	Collection Tubes		
	50 Buffer RBC		
	Buffer PKD (Proteinase K Digestion)		
	Proteinase K		
	RNase-Free DNase I (lyophilized)		
	RNase-Free Water (1.5mL to rehydrate RNase-free DNase)		
	DNase Booster Buffer		
	Buffer RPE		
	RNase-Free Water		
	Absolute Ethanol	VWR™	20821.365DP
	Xylene (97%)	Fisher Scientific	10784001

Methods

The total RNA was extracted using the Qiagen® RNeasy FFPE RNA extraction kit as per the manufacturer's guidelines by a laboratory colleague (Dr Charlie Appleby-Mallinder). First, the samples were deparaffinised by adding 500µL of xylene in a fume hood. These samples were vortexed for 10 seconds and centrifuged at 17960×g for 2 minutes. The supernatant was removed in a fume hood, ensuring the pellet was not disturbed, and 500µL of absolute ethanol added. This solution was vortexed again for 10 seconds to mix and centrifuged at 17960×g for 2 minutes. The supernatant was removed, and pellet allowed to dry for ten minutes at room temperature. To the pellet,

150µL PKD were added, and was vortexed to re-suspend the pellet. To this 10µL of Proteinase K was added and mixed via pipetting. This solution was incubated at 56^{o}C for 15 minutes on a heating block and transferred to a pre-heated heating block at 80^{o}C for 15 minutes. Samples were briefly vortexed every 3-5 minutes over the heated incubation period to ensure the solution was well mixed.

After heating, the samples were cooled on ice for 3 minutes to prevent RNA degradation. The samples were centrifuged for 15 minutes at 20,000×g. The supernatant was transferred to a fresh sterile and RNase-free 1.5mL microcentrifuge tube, and the pellet discarded. From here, all samples were kept on ice. To this solution, 16µL of DNAse and 10µL of DNAse stock solution was added. The solution was mixed via inversion and collected via microcentrifugation. Solutions were incubated for 15 minutes at room temperature, and 320µL of buffer RBC was added and mixed via pipetting. To this 720µL of absolute ethanol was added and mixed to wash the RNA. This solution was transferred to a sample spin column and spun through by centrifuging for 15 seconds at 8,000×g. All flow-through was discarded. The filter top of the transfer column was washed with 500µL of RPE buffer, and centrifuged with for 15 seconds at 8,000×g. Again, all flow-through was discarded. Another, 500µL of RPE buffer was added and centrifuged for 2 minutes, and the flow-through again discarded. The column was placed in a new sterile and RNase-free 1.5mL microcentrifuge tube and centrifuged at 17960×g for 5 minutes with the lid of the tube open to dry the filter. All flow-through and the collection tube were discarded. The column was put in a new 1.5µL tube, and the filter washed through with 20µL of RNAse-free water and centrifuged at 17960×g for 1 minute to elute.

RNA extraction was completed in two batches. Cases were randomly assigned into a batch to prevent any differences in RNA extraction efficiency between batches confounding later analyses.

2.3.2 RNA extraction from Frozen Tissue

Materials

Table 2.5 Reagents for Frozen Tissue RNA Extraction

Reagent/ Kit		***Supplier***	***Catalogue/Product Number***
Direct-zol™ RNA Miniprep Kit	Direct-zol RNA PreWash	Zymo Research	R2050
	RNA Wash Buffer		
	DNase/RNase-free Water		
Absolute Ethanol		VWR™	20821.365DP
TRIzol™		Invitrogen, Thermo Fisher	15596026
Pellet Pestle® Cordless Motor		Kimble®	749540-0000
Disposable Pellet Pestles® With Microtubes		Kimble®	749520-0500

Note. Direct-zol RNA PreWash and RNA Wash Buffer were made up to working concentration using absolute ethanol as directed.

Methods

For the frozen tissue RNA extraction, the Direct-zol™ RNA Miniprep Kit was used, as per manufacturer's guidelines. Following a brief optimisation, it was determined RNA of a higher concentration could be achieved, when the extraction was performed on smaller volumes of tissue (20mg compared to 40mg) and the samples were broken up into smaller pieces, allowing more complete tissue homogenisation. The tissue was cut

into smaller sections at -20^{O}C, using a scalpel, and placed in a sterile RNAse-free 1.5mL microcentrifuge tube. From here, all samples were kept on ice. In a ventilation hood, 100µL of Trizol was added to each case and the tissue homogenised using the Pellet Pestle® Cordless Motor and a sterile Pellet Pestles® mortar, for one minute. Once homogenised, a further 100µL of Trizol was added and mixed via pipetting. These samples were spun down using a mini-centrifuge, and the supernatant isolated and placed into a fresh tube. To this Trizol/homogenate solution, 200µL of absolute ethanol was added and mixed via pipetting. The solution was added to a Zymo-Spin IIC Spin Column, which was placed in a collection tube. The column was centrifuged for 50 seconds at 16,000×g. The flow-through was discarded and 400µL of Direct-zol RNA PreWash was added to the column and centrifuged again at for 50 seconds at 16,000×g. This wash step was repeated. To the column, 700µL of RNA wash buffer was added, and the columns were centrifuged at 16,000×g for two minutes, to ensure all wash buffer was removed from the filter. All flow-through was discarded, and the columns were placed in sterile 1.5mL microcentrifuge tubes. RNA was eluted by adding 50µL of DNase/RNase-free water and centrifuging for 50 seconds at 16,000×g and stored at -80^{o}C. RNA extraction was performed over several small batches to ensure the tissue would stay cold during the entire process. As before, cases were randomly assigned into a batch to prevent any differences in RNA extraction efficiency between batches confounding later analyses.

2.4 RNA Quality Control Measures

2.4.1 Nanodrop Spectrophotometer

For all RNA samples, the quantity and purity were checked using a Nanodrop Spectrophotometer. This reads the absorption of light through a column of sample at different wavelengths: 230nM (background and potential contaminants), 260nm (nucleic acids) and 280nm (protein). These are used to create 260:280, and 260:230 optical density ratios which can indicate the presence of contaminants. NanoString recommends using RNA with optical density values of 1.7-2.3 for the 260:280 ratio, and 1.8-2.3 for the 260:230 ratio (NanoString Technologies, 2016). The RNA was stored in RNase-free tubes at -80^{o}C.

2.4.2 Agilent Bioanalyser

For the frozen tissue, an RNA integrity number (RIN) for each case was determined using the Agilent Bioanalyzer 2100. This capillary electrophoresis system measures the quality and the fragmentation of RNA, by separating RNA through a system of microchannels, by size into separate species. The different fragments and species of RNA are visualised as electropherograms.

RNA quality analysis was completed according to manufacturer guidelines briefly described below. All motor cortex and most spinal cord samples were assessed by nanochip. Five spinal cord samples (071/1992, 109/1995, 025/1995, 150/1993, 261/1990) were assessed by picochip, which is more accurate for RNA samples of

lower concentration. These samples were determined to have lower RNA concentrations using the Nanodrop Spectrophotometer.

Bioanalyser Nanochip Protocol

Materials

Table 2.6. Reagents for Nanochip Bioanalyzer Protocol

Reagents/Equipment		***Supplier***	***Catalogue/Product Number***
2100 Bioanalyzer Instrument		Agilent	-
Agilent RNA 6000 Nano Kit	Aglient RNA 6000 NanoChips	Agilent	5067-1511
	*RNA 6000 ladder		
	RNA 6000 Nano Dye concentrate		
	RNA 6000 Nano Marker		
	**RNA 6000 Nano Gel Matrix		
	Electrode Cleaner Chip		
	Chip priming station and Syringe		
IKA MS3 Basic Shaker (vortexer with chip fitting)			
RNaseZAP		Ambion, Inc.	9780

** RNA 6000 Nano ladder previously denatured at 70^{O}C for 2 minutes, aliquoted and stored at -80^{o}C*

***RNA 6000 Nano Gel Matrix was centrifuged at 1500xg for 10 minutes through a spin filter. Filtered gel was aliquoted into 65µL aliquots and stored at 4^{O}C*

Method

The RNA dye and gel aliquots were allowed to come to room temperature for 30 minutes before use and kept under foil to protect from light. To the 65µL gel matrix aliquot, 1µL of dye was added. This was vortexed to mix and centrifuged at 13000×g for 10 minutes at room temperature. During this time, the electrodes in the Bioanalyzer

were cleaned by adding 350µL of RNaseZap into the electrode cleaner chip, and this was placed into the Bioanalyser for 5 minutes.

The RNA chip was placed into the chip priming station and 9µL of the gel-dye mix was pipetted into the directed well. The chip priming station was closed, and the syringe plunger was compressed for exactly 30 seconds to spread the gel. The clip was released and after 5 seconds, the plunger was released. Gel was added to the other marked wells. Following this, 5µL of RNA marker was added to all 12 sample wells and the ladder marked well. To the ladder well, 1µL of RNA ladder was added, and 1µL of RNA was added to each sample well. The chip was vortexed for one minute at 2000rpm. The chip was run within 5 minutes in the Agilent Bioanalyzer 2100 to prevent evaporation of reagents from the chip, which could affect the quality of data produced.

Bioanalyser Picochip Protocol

Materials

Table 2.7 Reagents for the Pico Chip Bioanalyzer Protocol

Reagents/Equipment		***Supplier***	***Catalogue/Product Number***
2100 Bioanalyzer Instrument		Agilent	-
Agilent RNA 6000 Pico Kit	Aglient RNA 6000 PicoChips	Agilent	5067-1513
	*RNA 6000 ladder		
	RNA 6000 Pico Dye concentrate		
	RNA 6000 Pico Marker		
	**RNA 6000 Pico Gel Matrix		
	RNA 6000 Pico Conditioning Solution		
	Electrode Cleaner Chip		
	Chip priming station and Syringe		
IKA MS3 Basic Shaker (vortexer with chip fitting)			
RNaseZAP		Ambion, Inc.	9780

** RNA 6000 Pico ladder previously denatured at 70^{O}C for 2 minutes, 90µL of RNase-free water was added and solution aliquoted and stored at -80^{o}C*

***RNA 6000 Pico Gel Matrix was centrifuged at 1500xg for 10 minutes through a spin filter. Filtered gel was aliquoted into 65µL aliquots and stored at 4^{O}C*

Methods

As described above, the RNA Pico dye and Pico Gel aliquots were brought to room temperature, and 1µL of the pico dye was added to gel aliquot, and vortexed to mix, and centrifuged for 10 minutes at 1300×g at room temperature. Electrodes were cleaned as described above.

The RNA Pico chip was placed into the chip priming station and 9µL of the gel-dye mix was pipetted into the directed well. The chip priming station was closed, and the syringe plunger depressed for exactly 30 seconds to spread the gel. The clip was released and after 5 seconds the plunger was released. Gel was added to the other marked wells. To the well labelled “CS”, 9µL of Pico conditioning solution was added, and 5µL of Pico RNA marker was added to all 11 sample wells, and the well labelled ladder. To the ladder well, 1µL of RNA ladder was added, and 1µL of RNA was added to each sample well. The chip was vortexed for one minute at 2000rpm. The chip was run using the Agilent Bioanalyzer.

2.5 NanoString nCounter Gene Expression Assay

2.5.1 FFPE Spinal Cord NanoString Run

Materials

Table 2.8 NanoString nCounter Materials

Reagent/ Kit		***Supplier***	***Catalogue/Product Number***
nCounter® Human Neuroinflammation Panel	Reporter Code Set	NanoString	XT-CSO-HNROI1-12
	Capture Probeset		
	Hybridisation Buffer		
nCounter® SPRINT Profiler		NanoString	NA

Method

To characterise the gene expression profile in sMND, the NanoString Sprint Profiler gene expression assay was used. The human neuroinflammation panel was used, which assesses 784 targets: 757 probes assess immune pathways and cells; 13 probes for normalisation; eight probes are negative controls, which should bind no sequences; and six are spike-in positive controls.

Probe hybridisation was completed using the nCounter XT CodeSet Gene Expression Assay protocol outlined by NanoString Technologies (2016). RNA samples were thawed on ice. Aliquots of the Reporter CodeSet and Capture ProbeSet were thawed at room temperature, inverted several times to mix and spun down. A master mix was created by adding 70µL of the hybridisation buffer to the Reporter CodeSet tube. The master mix was inverted to mix and briefly spun down. To individual sterile and RNase-free hybridisation tubes, 8µL of the master mix was added, followed by 5µL of the extracted RNA samples. The Capture ProbeSet was again inverted and spun down to ensure the probes were suspended in the solution, and 2µL were added to each of the tubes. The tubes were closed, flicked to mix, briefly spun down and immediately placed in a pre-warmed thermal cycler at 65^{o}C. The assays were left to incubate at 65^{o}C for 18 hours and 20 minutes to allow the probes to hybridise.

The nCounter cartridges were removed from the freezer 15 minutes before the incubation was due to finish and allowed to come to room temperature, to evaporate off any condensation in the chip. The assays were removed from the incubator and immediately spun down. The reaction volume was made up to 30µL with hybridisation buffer. The incubation assays were centrifuged and 30µL loaded into each lane of the

cartridge ensuring full depression of the pipette to create an air gap behind the sample. The cartridge was wiped to remove excess liquid. The cartridge loading ports were sealed using the included transparent stickers and the cartridge immediately placed into the nCounter SPRINT Profiler and run using the nCounter Neuroinflammation Panel RLF files.

2.5.2 Frozen NanoString Run

The NanoString Neuroinflammation Gene Expression assay was performed as described in Methods 2.5.1. Following conversations with NanoString technicians, the recommend input concentration was set to approximately 100ng of RNA while and the maximum volume of RNA which can be added is 5µL. Therefore, RNA samples with a concentration greater than 20ng/µL were diluted to this concentration to prevent over saturation. All motor cortex samples were run at 20ng/µL.

Five spinal cord cases with low RNA concentration (071/1992, 109/1995, 025/1995, 150/1993, 261/1990) were concentrated using a centrifugal evaporator to approximately 20ng/µL to ensure 100ng of RNA could be inputted.

All frozen spinal cord cases were run at 20ng/µL except for case 135/1982 for which RNA was added undiluted to the hybridisation reaction, as advised by NanoString. This sample did not reach the 1.7 RIN recommended by NanoString, and the RNA was therefore more fragmented. Increasing the concentration increased the percentage of RNA fragments long enough to bind to the probes.

Following the hybridisation process previously described in Methods 2.5.1, the NanoString experimental chips were loaded and run as described.

2.6 Analysis of FFPE Spinal Cord Data

Materials

Table 2.9 NanoString Analyses Software

Software	***Software Developers***
nSolver 4.0	NanoString Technologies
nCounter Advanced Analysis 2.0	
R Version 3.3.2	R Core Team (2016)

***Note**: R 3.3.2 was required to run the NanoString Analyses Software*

Software	***Software Developers***
GraphPad Prism 8	GraphPad Software, Inc.
R version 3.6.0	R Core Team (2016)
RStudio Desktop 1.2.1335	RStudio, Inc
Qlucore	Qlucore AB

CRAN R Packages	***Used For***
ggplot	Creating Figures
ggrepel	Labelling genes on volcano plots
limma	DE Analysis
survival: Survival Analysis	Length of Survival Analyses

Methods

FFPE Initial Analysis using nSolver Software

Initially the data were analysed using the standard protocol advised by NanoString. Quality control of the raw count data was performed using the accompanying NanoString nSolver data analysis software. The raw count data was run through the

quality control wizard, which assessed binding density, imaging, positive control linearity and the limits of detection. This highlighted two cases, which had low binding density meaning the number of readable probe barcodes was below the lower threshold. This could indicate there was potentially too little input RNA, or the RNA was too fragmented in these cases. Therefore, these cases were removed from further analysis. No other quality control issues were raised by the software.

The data was run through the basic analysis package, using settings advised by NanoString. This performs basic normalisation and provides descriptive statistical analysis. First, the data was normalised to the positive controls to account for lane-to-lane variability. This step was completed by summarising the positive control counts to the geometric mean, which used a scaling factor to adjust count values relative to each case.

The data was normalised against five of the thirteen normalisation genes so that the nSolver package could be used for preliminary analyses. These were selected based on their low coefficient of variation (CV%) – indicating stable expression across cases, and non-significant difference in expression between groups, as determined by t-test (GraphPad Prism v8), to ensure expression was not affected by disease status.

From here, basic plots were made, which allowed a descriptive overview of the data. From here, the data moved forward to the Advanced Analysis wizard for statistical analysis.

The advanced analysis package allows inferential statistical analysis, and control over the type of analyses performed and potential coefficients. This involved feeding in the

un-normalised data into the program. Case annotations were added by uploading a Comma Separated Values file, detailing sex, age, and the length of survival. The Advanced Analysis wizard normalised the data according to the top 10 probes (as determined by the Advanced Analysis wizard). The software selected all normalisation genes that had been selected manually, and therefore this was not altered. Age at death was controlled for, as well as sex, as sex differences have been previously noted in immune reaction type and function of microglia and other immune cells (Scotland *et al.*, 2011; Klein and Flanagan, 2016; Guneykaya *et al.*, 2018). The Advanced Analysis package performed several analyses generating a list of differentially expressed genes, as well as various plots including heatmaps, principal component analysis diagrams, cell type quantification, and pathway analysis among others, as well as further quality control analyses.

Additional Quality Control Data Checks for FFPE Spinal Cord Data

It was noted that normalisation genes showed low count levels, indicating they were not suitable to be utilised for normalisation. Following correspondence with NanoString bioinformaticians, further quality control checks were implemented. The background noise threshold for each case was calculated for each case, using the following formula:

$$background\ threshold\ count = \ Mean\ of\ counts\ for\ negative\ control\ probes + 2\ Standard\ Deviations.$$

Across cases, the maximum background threshold calculated was 40.8 counts which was rounded to 50 counts. This suggesting probes with counts lower than 50 were the

result of background noise. Genes with counts lower than 100 counts may show greater variance and therefore be less robust. The number of endogenous genes (genes being measured) and normalisation genes above this threshold was determined. Further quality control check data is summarised in Table 2.10. Very few normalisation genes were above this threshold. On average, 15% of endogenous genes were above this threshold.

The positive spike-in control counts should range in count level from POS_F, which should be low in count number (near the background threshold level) and increase in linear fashion to probe POS_A, which should be the highest. In accordance with this, all cases showed high positive control probe counts, which increased in a stepwise manner as described above. The endogenous genes with counts above threshold showed high counts also, indicating probe hybridisation and the running of the assay had not failed. Consequentially, alternative methods of normalisation and data analysis were required.

Table 2.10 Control and MND FFPE Further Data Analysis Checks

Disease Status	Control							
Case	085/2007	807/90	309/90	035/1996	335/1990	014/1999	114/1991	098/2007
background noise	12.7506	20.6416	33.0585	27.4508	26.7589	25.0079	18.7184	19.4185
endogenous genes detected per sample	31	76	23	7	67	0	0	96
housekeeping genes detected per sample	0	0	0	0	0	0	0	0
percentage of endogenous genes detected	4.095	10.040	3.038	0.925	8.851	0	0	12.682

Disease Status	sMND															
Case	009/2017	077/1986	041/2008	004/2006	072/2002	091/2008	094/2009	072/205	105/2007	023/2010	059/2009	099/2009	005/2010	094/2006	025/2013	074/2009
background noise	26.744	24.619	27.854	27.980	18.605	27.461	40.874	29.865	23.152	15.224	23.476	14.189	18.629	33.802	30.212	23.484
endogenous genes detected per sample	114	0	245	197	123	183	171	191	156	198	79	145	118	41	77	108
housekeeping genes detected per sample	0	0	2	0	0	0	0	1	0	1	0	0	0	0	0	0
percentage of endogenous genes detected	15.059	0.000	32.365	26.024	16.248	24.174	22.589	25.231	20.608	26.156	10.436	19.155	15.588	5.416	10.172	14.267

***Note**. Case highlighted in red indicates highest background level. This case was used to decide overall background level for the FFPE spinal cord NanoString data.*

Voom-Limma Analysis of FFPE Spinal Cord Data

Dr Wenbin Wei (*Durham University*) was consulted for alternative methods of data normalisation and analyses. As the NanoString assay produces count type data similar to that produced by RNA sequencing (RNAseq), an RNAseq data analysis method, Voom Limma analysis, was adopted to normalise and analyse these data. Limma (Ritchie *et al.*, 2015) is an R package that was originally developed for differential expression analysis of microarray data. The Voom (Law *et al.*, 2014) function was added for analysis of RNAseq data to convert the read/count type data to a usable format. Further iterations of the Limma package have now been utilised for the analyses data from other methodologies including NanoString data (Ritchie *et al.*, 2015).

The data normalisation process is part of the Voom-Limma analysis process, and therefore is performed automatically. The analysis process is summarised in Figure 2.2.

Briefly, data is normalised using the Trimmed the Mean of M Values method. In this method, observations that are closest to the average are labelled reference observations and the rest are labelled test observations. All test samples are scaled using a scaling factor calculated using the weighted mean of log ratios between the test and reference observations. All extremely high and low observations for each gene, and all those with high log ratios are removed. This method reduces the influence of extreme data points.

The Voom package transforms the data using the Counts per Million (CPM) method, which is summarised by the formula below. This also converts the data to a Log_2 format.

$$Counts\ per\ Million = \frac{Count\ Number\ per\ Gene}{Total\ Number\ of\ Counts} \times 1{,}000{,}000$$

The Log_2 count data is fitted to a linear regression model. From this model, weights are calculated based on the difference in the actual y value, from the predicted value based on the regression line equation. The data is fitted to a per-gene linear model and contrasts are made between the groups to generate fold changes (FCs). The data is smoothed using Empirical Bayes smoothing to reduce the standard error for each contrast.

As low count number had been an issue with the normalisation genes, count number per case was also checked. As the threshold for background count number had been calculated as approximately 100 counts, the three cases (two control [014/1999, 114/1991], one MND case [077/1986]) with a maximum count below this level were removed from analysis. The effect of age and sex were controlled for by adding these as covariates in the Voom-Limma analysis. Tests for significance are performed, and a Benjamini-Hochberg test was used to create adjusted p values for the false discovery rate. All gene expression analysis for the FFPE spinal cord NanoString data is summarised in Figure 2.3.

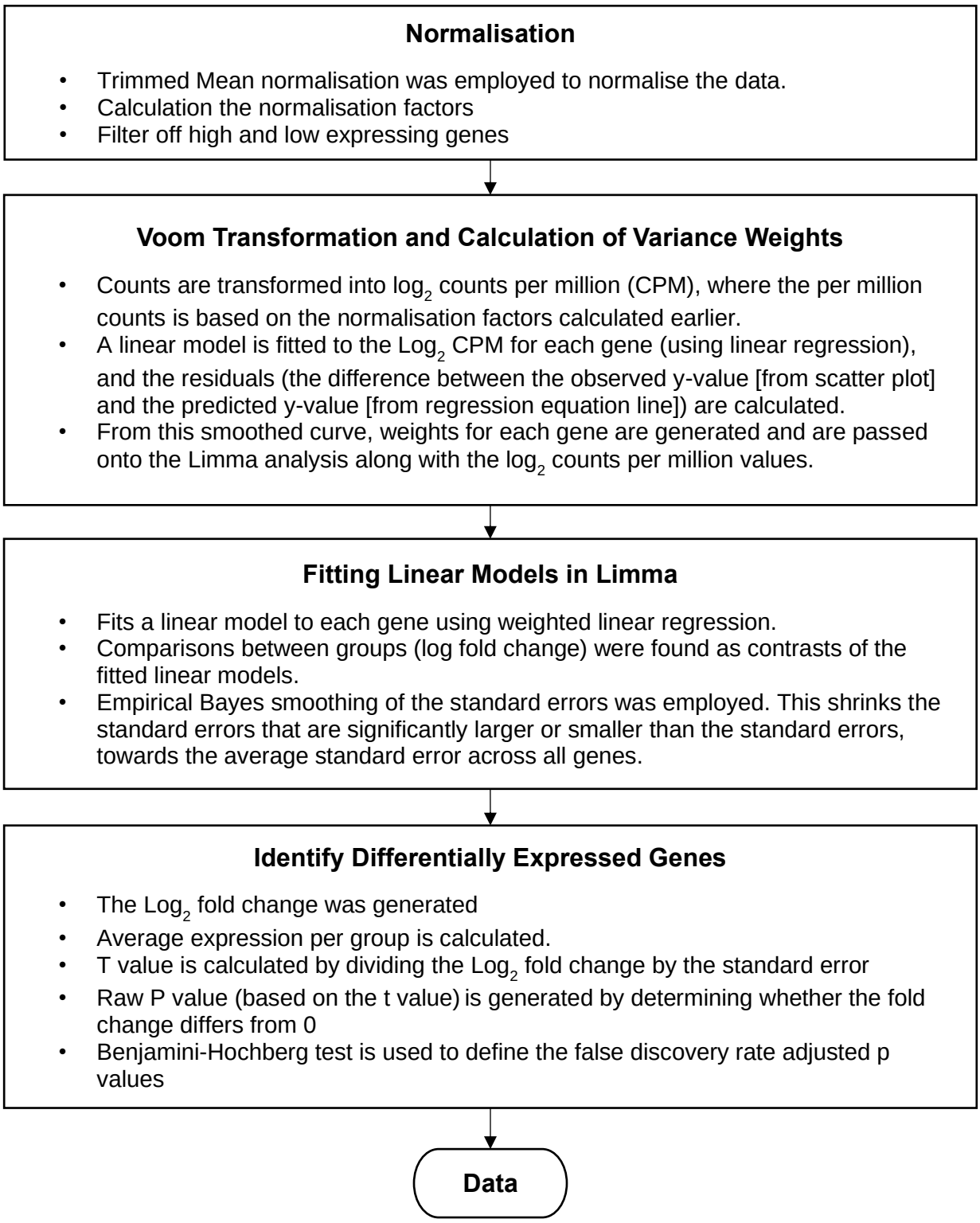

Figure 2.2. Flow chart depicting the major steps in the Voom-Limma Data Analysis Pipeline

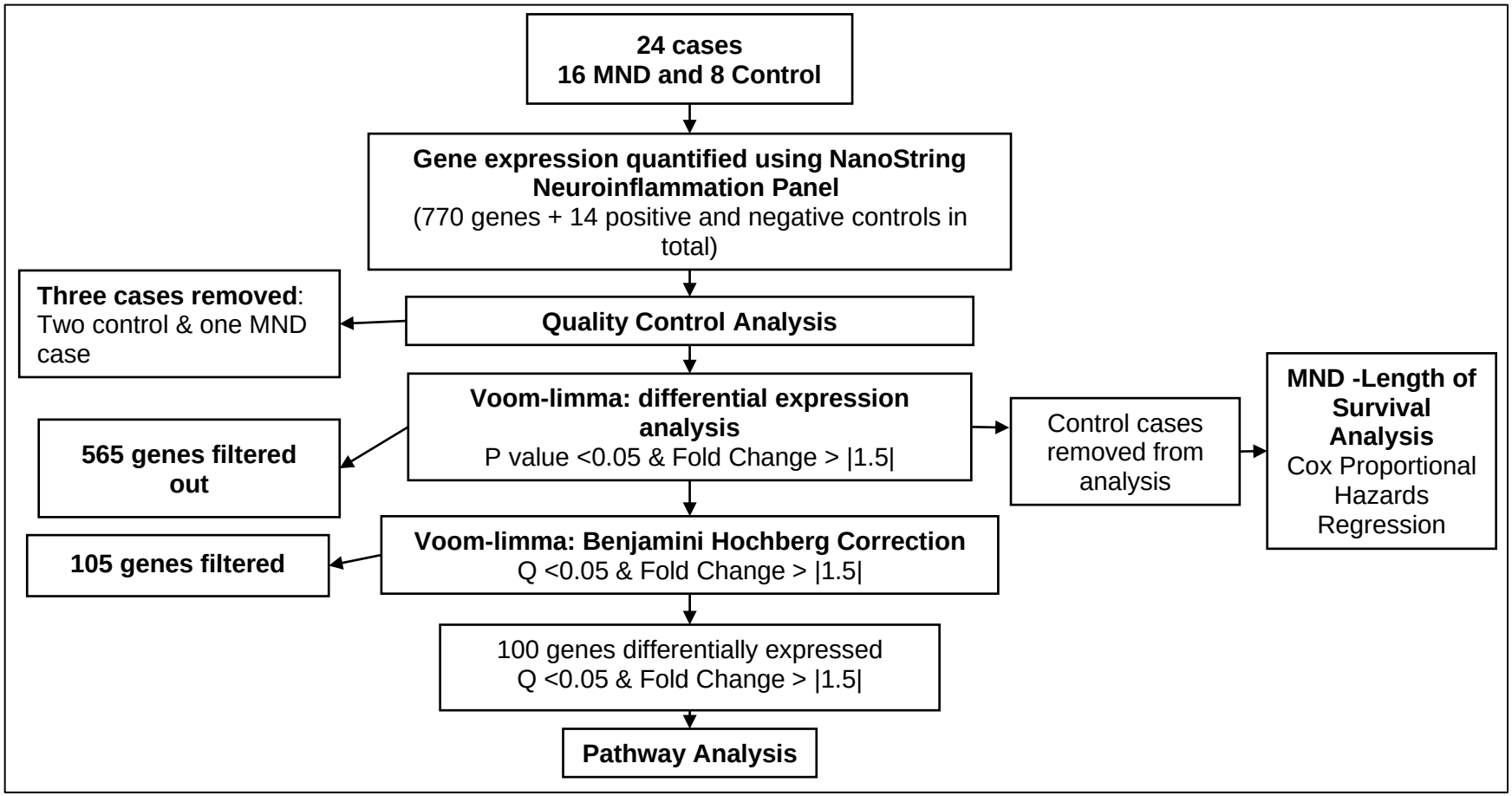

Figure 2.3 Summary of the Data Analysis Pipeline for the Transcriptomic Profile from FFPE Spinal Cord derived from MND and Control Cases.

Initially, all 16 sMND and 8 control cases went through gene expression analysis using the NanoString assay. Three cases were removed due their count values, which approached the background threshold value. Voom Limma analysis revealed 205 genes with a FC> |1.5| and p<0.05, 100 of which were significant following FDR correction. These genes went through for pathway analysis. The sMND cases were also taken forward for separate analysis, using Cox Proportional Hazards Regression to highlight those genes associated with length of survival.

2.7 Frozen tissue NanoString Data Analysis

2.7.1 Initial Quality Control Data Checks

For the frozen NanoString data, quality control checks were run similarly to that described in Section 2.5.1. First, the basic quality control wizard was run using the nSolver software. All cases from the motor cortex case passed this quality control analysis apart from case 293/1991, which showed zero counts across all genes, indicating this reaction had not run properly. Therefore, this case was removed from further analysis. Similarly, all spinal cord cases passed basic nSolver quality control checks apart from one case (209/1995). This case had two flags, one for binding density and one for limit of detection. This case was retained, for reasons detailed below.

Further quality control checks on the raw data were carried out as described in Section 2.6.1 (shown below in Tables 2.11 and 2.12). The background threshold was calculated and rounded up to nearest ten for the spinal cord data (40 counts) and motor cortex data (50 counts).

Table 2.11 Frozen Spinal Cord Data quality control Checks

Disease Status	Control							
Case	085/2007	080/1992	135/1982	1028/1989	138/1994	071/1992	109/1995	025/1995
background noise	8.046	16.709	13.428	22.181	5.527	20.692	17.866	18.565
endogenous genes detected per sample	374	534	325	524	370	508	557	714
housekeeping genes detected per sample	8	13	8	13	7	13	13	13
percentage of endogenous genes detected	49.406	70.542	42.933	69.221	48.877	67.107	73.580	94.320

Disease Status	MND															
Case	050/2008	041/2008	209/1995	141/2003	024/2004	131/1995	072/2002	150/1993	037/2000	024/2008	023/2010	295/1991	261/1990	115/2002	034/2005	059/2009
background noise	17.149	17.565	31.367	23.038	23.612	21.113	21.009	21.758	24.461	16.484	16.104	22.105	12.708	14.622	21.759	19.115
endogenous genes detected per sample	501	578	656	593	616	562	566	602	617	332	526	521	519	551	714	451
housekeeping genes detected per sample	11	12	13	13	13	13	12	13	13	8	12	12	13	13	13	10
percentage of endogenous genes detected	66.182	76.354	86.658	78.336	81.374	74.240	74.769	79.524	81.506	43.857	69.485	68.824	68.560	72.787	94.320	59.577

Note. *Case highlighted in red indicates highest background level. This case was used to decide overall background level for the frozen spinal cord NanoString data.*

Table 2.12 Frozen Motor Cortex Data quality control Checks

Disease Status	control							
Case	178/1995	023/1992	111/1990	309/1990	335/1990	072/1992	147/1995	293/1991
background noise	30.941	31.274	31.565	23.658	28.350	28.031	24.471	1.832
endogenous genes detected per sample	420	555	595	557	496	509	547	0
housekeeping genes detected per sample	13	13	13	13	13	13	13	0
percentage of endogenous genes detected	55.482	73.316	78.600	73.580	65.522	67.239	72.259	0

Disease Status	sMND															
Case	223/1999	261/1990	069/2006	005/2010	041/2008	024/2008	209/1995	137/1996	150/1993	193/1990	203/1994	050/2008	088/1996	131/1995	150/1997	043/2005
background noise	28.171	14.470	19.070	26.403	22.758	25.858	22.552	23.390	29.961	27.449	24.160	40.887	26.845	27.146	21.589	19.418
endogenous genes detected per sample	504	567	543	545	495	450	584	583	525	444	555	515	565	513	509	517
housekeeping genes detected per sample	13	13	13	13	13	12	13	13	13	13	13	13	13	13	13	13
percentage of endogenous genes detected	66.579	74.901	71.731	71.995	65.390	59.445	77.147	77.015	69.353	58.653	73.316	68.032	74.637	67.768	67.239	68.296

***Note**. Case highlighted in red indicates highest background level. This case was used to decide overall background level for the frozen motor cortex NanoString data*

2.7.2 Voom-Limma Analysis

Differential expression analysis of sMND compared to control was performed as using the Voom-Limma method as described before in 2.7. The Benjamini-Hochberg test was used to correct the false discovery rate. Significance was set at $q<0.05$ and absolute fold change >1.5. For the motor cortex data, all cases were used in analysis with the exception of 293/1991 which was removed from analysis during basic quality control checks (see above). For the spinal cord, all cases were kept in analysis. As previously discussed, (Methods 2.7.1) case 209/1995 was flagged in initial quality control checks. As stated in the NanoString manual (NanoString Technologies, 2016) data flags suggest potential but not definite issues with data but further analysis is required. As such, the Voom-Limma analysis was repeated both with and without this case, and addition of this case had little impact on the results overall, therefore this case was kept in the analysis. All data analysis for the frozen spinal cord and motor cortex is summarised in Figures 2.4 and 2.5.

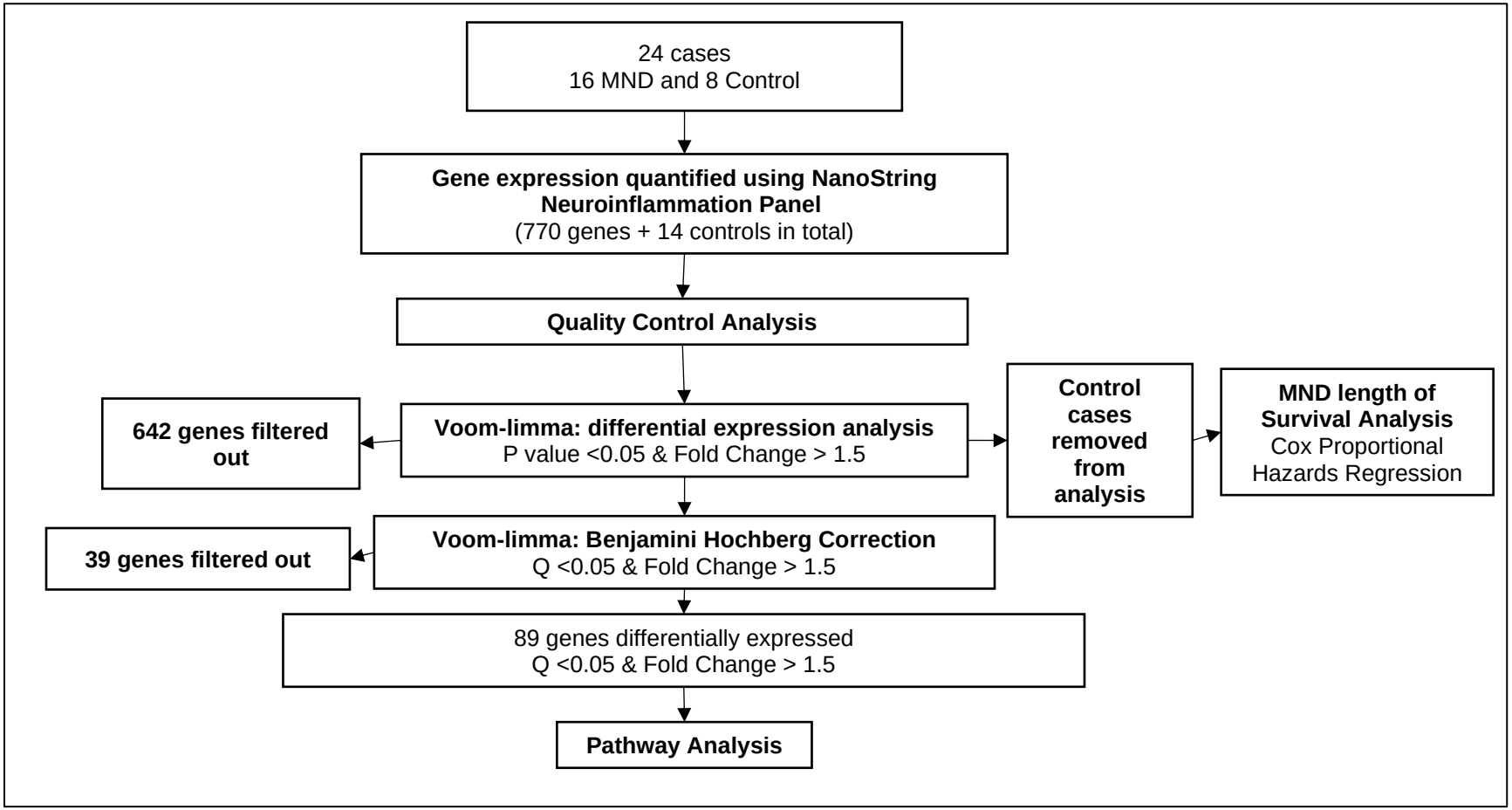

Figure 2.4 Summary of the Data Analysis Pipeline for the Transcriptomic Profile from Frozen Spinal Cord derived from sMND and Control Cases.

Sixteen sMND and eight control cases went through gene expression analysis using the NanoString assay. Voom-limma analysis revealed 128 genes with a FC> 1.5 and p<0.05, 89 of which were significant following FDR correction. These genes went through for pathway analysis. The sMND cases were also taken forward for separate analysis, using Cox Proportional Hazards Regression to highlight those genes associated with length of survival.

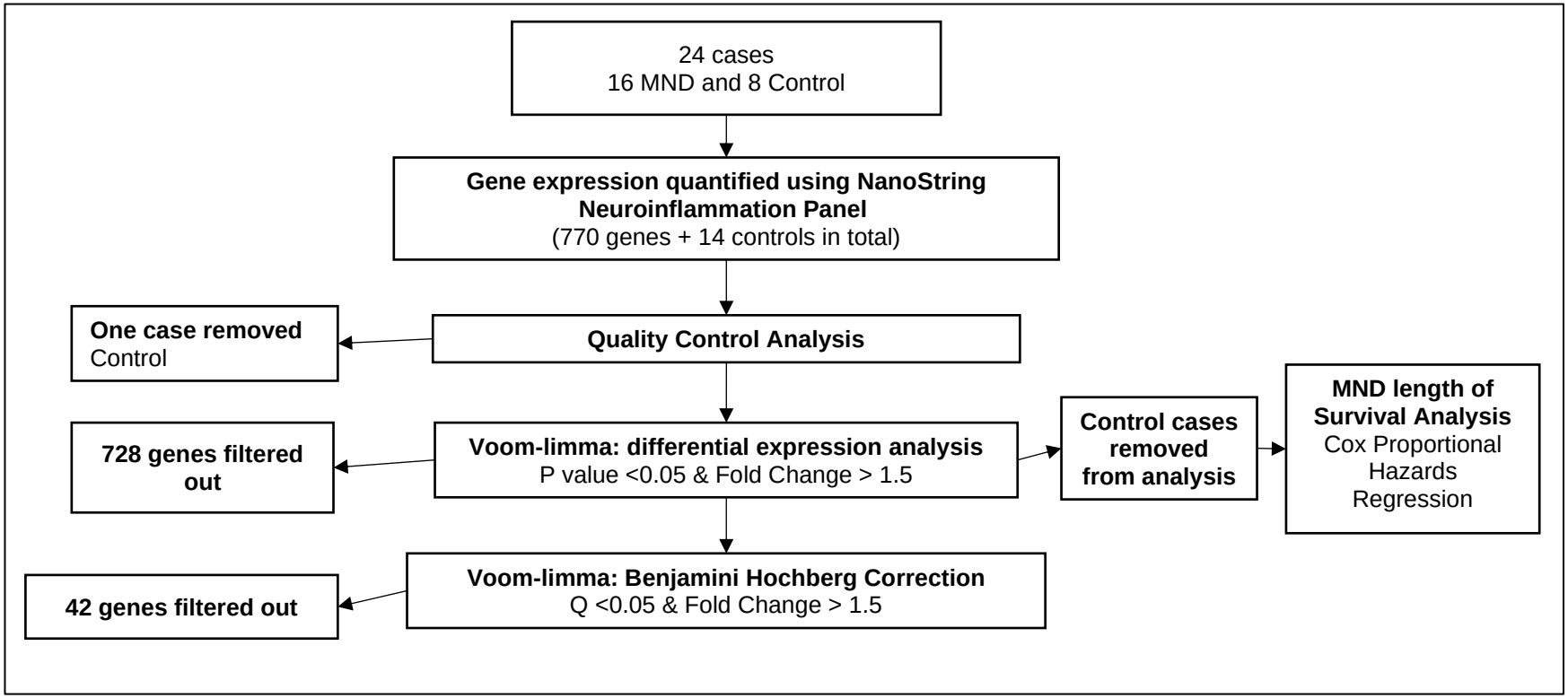

Figure 2.5 Summary of the Data Analysis Pipeline for the Transcriptomic Profile from Frozen Motor Cortex derived from sMND and Control Cases.

Sixteen sMND and eight control cases went through gene expression analysis using the NanoString assay. Initial quality control analysis revealed one case, which had not successfully run, and showed no counts. This case was consequently removed from further analysis. Voom-limma differential expression analysis revealed 42 genes which were differentially expressed. No genes were significant once the Benjamini-Hochberg correction for multiple comparisons was applied. The sMND cases were also taken forward for separate analysis, using Cox Proportional Hazards Regression to highlight those genes associated with length of survival.

2.8 Pathway Analysis

To identify cellular and biological functions, pathway analysis was used. Commonly used methods of pathway analysis, such as Database for Annotation, Visualization and Integrated Discovery (DAVID) (Huang, Sherman and Lempicki, 2009), require entering the significantly differentially expressed genes from a large-scale gene expression study that samples the entire genome. From these data, the likelihood of a set of genes from a pathway being differentially expressed is compared to the likelihood of being differentially expressed to the entire genome. This is calculated using the Fisher Exact test to give significance values.

As our gene expression study was performed using a gene background which was centred around a specific gene expression theme (770 specific genes related to neuroinflammation), these conventional methods of pathway analysis were not possible. Initially, the specific panel background was entered into such systems, but due to the small number of genes on the panel -comparative to whole genome data such as microarray- the resulting pathways were too broad to provide useful targets. For example, one pathway this method highlighted was “inflammation”.

As such an alternative method of identifying key themes from the gene expression data was sought. The NanoString Neuroinflammation panel is provided with a set of gene annotations, including KEGG pathways associated with each gene. As an alternative to conventional pathway analysis, the KEGG pathways from all significant genes (FC>|1.5|, q<0.05) were counted to identify those which appeared most frequently. The top 15 pathways from each data set were taken forward for more detailed consideration. Of these, many were related more to other general conditions also associated with inflammation e.g., cancers, viral infections, and allowing a more flexible threshold allowed more biologically relevant pathways to be included.

Pathway analysis was not performed on the motor cortex as no genes reached significance following false discovery rate correction.

2.9 Length of Survival Analyses

To determine which genes were associated with the length of survival from onset to death, all sMND cases that had undergone Voom-Limma normalisation were taken forward for survival analysis using Cox Proportional Hazards Regression in R (R Core Team, 2019, Version 3.5.3). As this test requires data organized by category, cases were split into high- or low-expressing groups, for each gene, based on the median expression across cases. The median was selected to create two groups of near equal size.

The analysis compares the risk of an incident occurring (in this case death) related to independent factors (high or low expression of the gene of interest), producing a coefficient. A negative coefficient indicates a negative relationship between the independent factor (expression of the gene) and the risk of death, whereas a positive coefficient indicates a positive relationship between gene expression and the risk of death. To test for significance between the high and low expressing groups per gene, the non-parametric Log Rank test was used ($p<0.05$). For each gene with a significant difference, Kaplan–Meier diagrams were plotted in R, showing the proportion of cases against the length of survival in months,

To control for the potential confounding effects of age and sex, the analysis was repeated using age, sex, and, age and sex combined, as the independent factor. No significant relationship was found for these variables, indicating these factors did not have a significant influence on patient survival time.

2.10 Microglial/ Macrophage deconvolution

Those genes most associated with microglial/macrophage expression were determined using the online Brain RNASeq tool (https://www.brainrnaseq.org/; Zhang et al., 2016). Each of the differentially expressed genes was entered into the database, and the Fragments per Kilobase of transcript per Million mapped reads for the main glial/ CNS cell types is given. A gene was determined to be microglial/macrophage specific if expression was greatest to the microglial/macrophage population and not highly expressed by any other cell population, (see Figure 2.6 for examples of rejected and accepted genes).

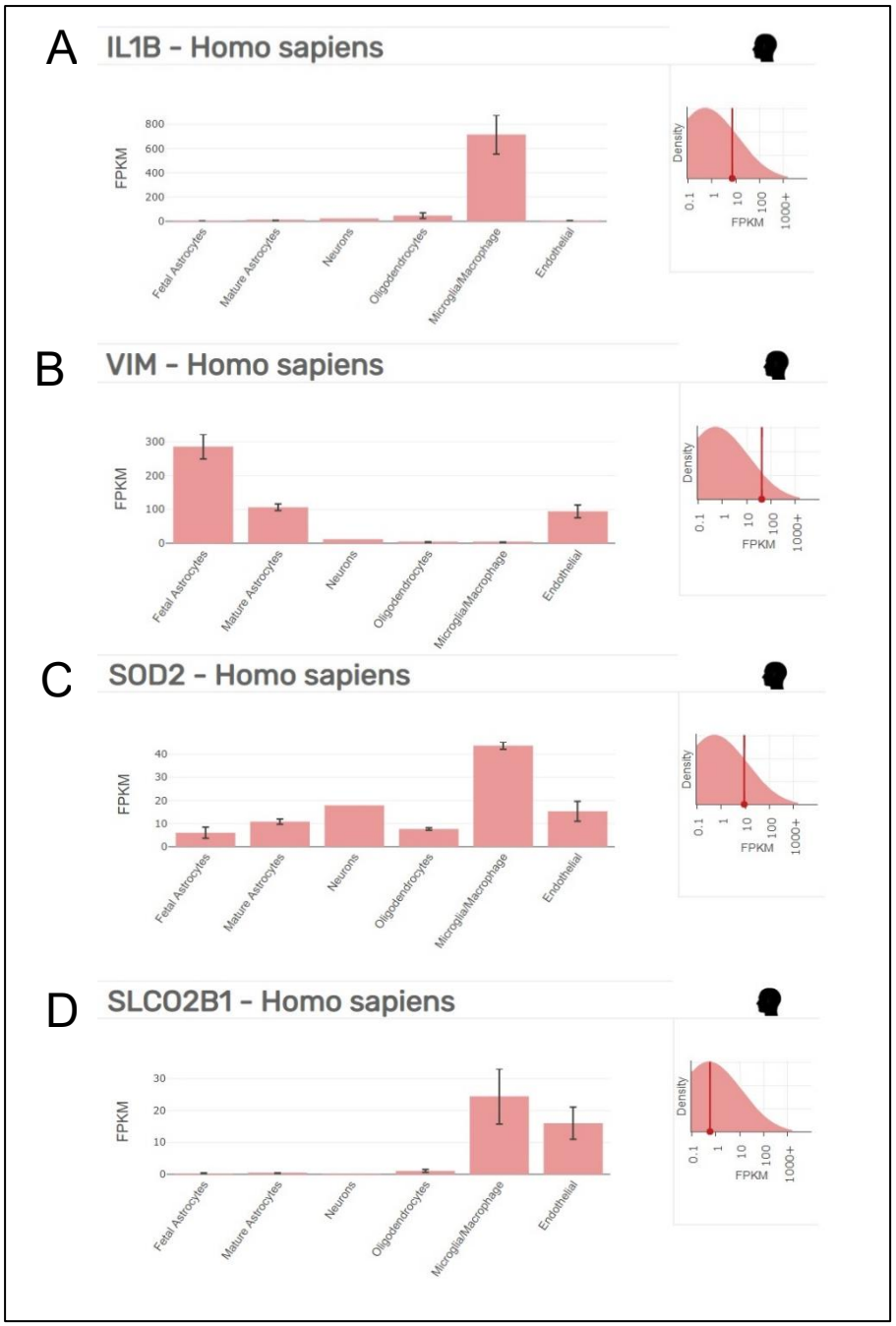

Figure 2.6 Using Brain RNASeq to determine those gene most associated with microglial/macrophage expression.

A. *An example of an accepted gene: expression of IBA1 is almost entirely found in the microglia/macrophage cell population.*

B. *A rejected gene example: almost no expression in the macrophage cell population.*

C. *C&D. Both SOD2 and SLCO2B1 are most expressed by the microglial/macrophage expression, but as expression is found in other glial populations, these genes were rejected.*

2.11 Validation of NanoString Data

2.11.1 Search for Validation Data Sets

The scientific literature search engines PubMed and google scholar, as well as ArrayExpress and the National Centre for Biotechnology Information Gene Expression Omnibus (Barrett *et al.*, 2013), were used to search for studies with publicly-available gene expression data, which could be re-analysed to validate our NanoString findings. Search criteria limited studies to those which had used high-throughput gene expression methods such as RNA Sequencing (RNAseq) and microarray, in tissue isolated from the motor cortex or spinal cord from human sMND cases and controls. All datasets were ranked according to each data set's closeness to the NanoString methods including the location of the tissue used (favouring motor cortex and cervical spinal cord) and tissue type (grey matter /ventral horn favoured over total tissue homogenate), as well as cohort size and whether age- and sex-matching of control cases to MND cases was used.

2.11.2 Cohort Data

Motor Cortex

Based on these criteria, an Agilent microarray (Whole Human Genome Microarray 4x44K. Agilent-014850) data set was selected (E-MTAB-2325, Array Express, Aronica *et al.*, 2015). The cohort consisted of 31 sMND cases (12 female, 29 male) with a median age of 58 years and 10 control cases (1 female, 9 male) with a median age of 58.5 years. (Full details are given in Appendix A).

Spinal Cord

For the spinal cord validation, an RNASeq data set (SRP064478, NCBI sequence read archive, Aronica *et al.*, 2015) was chosen based on the above criteria. The cohort consisted of six sMND cases (3 male and 3 female) with a median age of 68.5 years, and eight control cases (4 male, 4 female) with a median age of 66.5 years. Full cohort details are given in Appendix B. One case (ALS4 – male) was removed from the original studies cohort prior to analysis as although the case had no familial history of MND, genetic analysis showed this case has a pathogenic SOD1 genetic missense variant.

To generate these data, total RNA had been extracted from frozen cervical spinal cord homogenate using miRNeasy Mini (Qiagen) RNA extraction kit according to the manufacture's instruction. To construct the RNA library, Illumina Truseq Stranded Total RNA HT Sample Prep Kit and run using Illumina Nextseq 500 lane for multiplex sequencing at Cofactor Genomics system. For full details of the protocol, refer to Brohawn, O'Brien and Bennett (2016).

2.11.3 Analysis of Pre-Published Raw Data

Motor Cortex Microarray Data - Pre-processing and Differential Expression Analysis

Dr Mark Dunning (Bioinformatics Department, University of Sheffield) performed differential expression analysis on the microarray data. Initially, the raw data was downloaded into R (R Core Team, 2020, version 4.0.2) with R studio (RStudio Team, 2020) using the ArrayExpress package. Principal component analysis was performed to identify potential outliers (Figure 2.7). This led to the removal of nine

cases (59, 51bis, 71, 53, 45, 57, 69bis, 3, 33) from further analysis due to their separation from the rest of the cohort.

The remaining samples were normalised using quantile normalisation, which sets the expression values for each sample to follow the same distribution. As microarrays utilise more than one probe per gene, the best probe for use was determined using the interquartile range across the data set to remove non-informative probes. Further filtering removed 129 genes with low expression leaving 641 genes for differential expression analysis.

Differential expression was performed using the Limma package (Ritchie *et al.*, 2015). In brief, a linear model is used to compute robust average expression levels for each gene in each sample group. Significance is assessed using a modified version of the t-test. The control group was used as the baseline and positive log-fold changes were interpreted as higher expression in the sMND group.

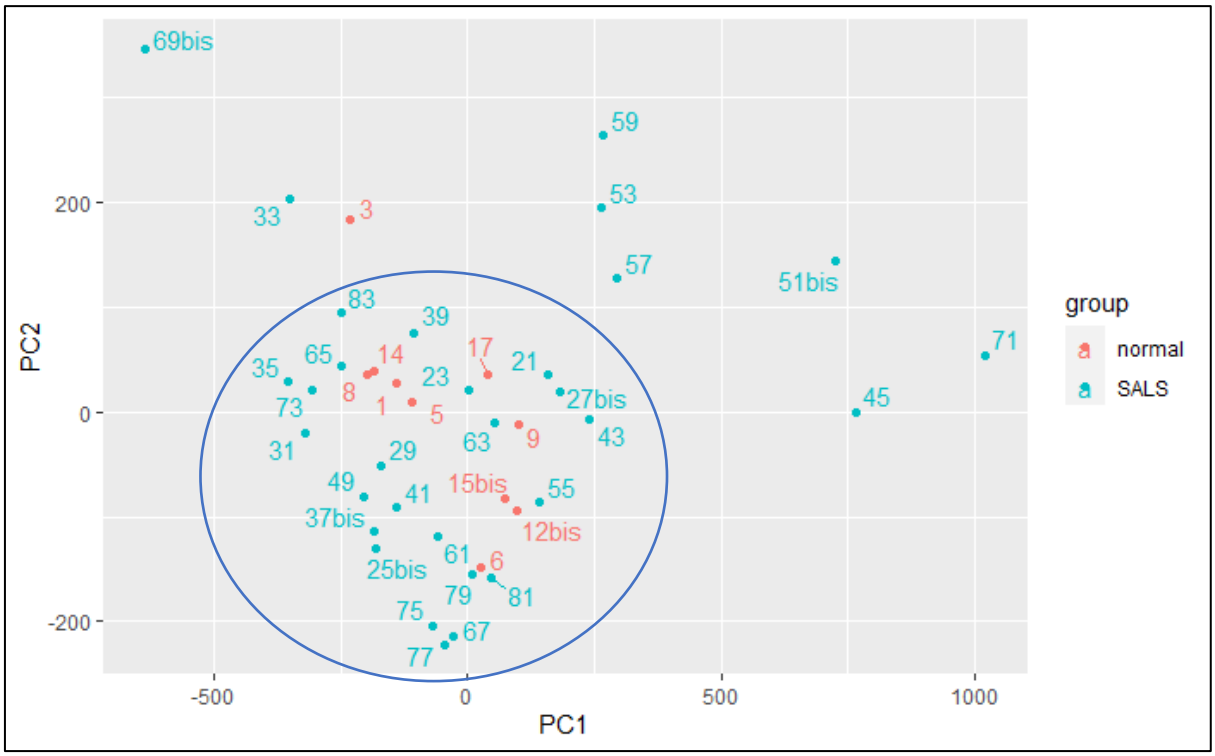

Figure 2.7 Principal Component Analysis Graph of Motor Cortex Microarray Data

PCA plot highlighting cases for removal (59, 51bis, 71, 53, 45, 57, 69bis, 3, 33). These cases were removed from analysis due to their separation from the main cluster of data points (highlighted by the blue circle) upon the advice of bioinformatician Dr Mark Dunning.

Spinal Cord RNASeq Data Pre-processing and Differential Expression Analysis

Raw RNASeq data files were downloaded as FASTQ files by entering the SRA accession number (SRP064478) into SRA explorer https://sra-explorer.info/# to generate bash codes. These codes were run in the console in R studio (RStudio Team, 2020).

The Salmon method was used to quantify and align the RNASeq raw reads using the command prompt in a virtual pc generated via Docker.

In R studio, the quant files were read, and aligned to the human genome. Genes expressed over background in less than two cases were classes as low expressing and as such were filtered out. Box plots were used to visualise the spread of the raw data and normalised data, which showed similar distribution across all samples. Heat maps were plotted and PCA performed to look for outliers. However, no clear outliers were identified therefore all cases were kept.

Differential expression was performed using the DESeq2 method as described in the R vignette, using the control group as the baseline. In short, this method generates a models comparing the counts per gene from two group (control and sMND) based on data normalisation, dispersion and group differences (Love, Huber and Anders, 2014).

2.12 *Post-mortem* tissue for Immunohistochemistry

2.12.1 Tissue source

FFPE *post-mortem* tissue from the motor, prefrontal (middle frontal), temporal and occipital cortices, basal ganglia, and cervical spinal cord were obtained from the SBTB for immunohistochemical analysis. Ethical approval for this study was given by the Management Committee of the SBTB (see appendix E). For this work, two groups were compared: cases with a confirmed diagnosis of sMND and neurologically normal cases. Patients with sMND were selected with a range of ages at death and survival time. Age and sex matching was attempted with control cases, however due to the small number of control cases donated to SBTB this was not possible. All control cases available were used, whose cause of death was not likely to have led severe brain inflammation and were within a similar age range to those in the sMND cases.

2.12.3 Spinal Cord

Table 2.13 sMND Spinal Cord immunohistochemistry cohort

Case Number	Block Number	Sex	Disease Status	Age at death	Survival time (Months)
261/1990	B	M	sMND	69	13
187/1991	D	M	sMND	60	38
175/1995	C	F	sMND	75	13
099/2003	R	M	sMND	78	10
043/2005	AB	M	sMND	31	66
042/2005	AB	M	sMND	60	57
049/2005	T	F	sMND	61	42
049/2006	V	M	sMND	91	97
088/2006	X	F	sMND	51	23
027/2008	AB	F	sMND	70	44
075/2008	V	F	sMND	61	82
096/2008	AA	F	sMND	69	50
098/2008	V	F	sMND	75	50
059/2009	AB	F	sMND	80	104
099/2009	Ab	M	sMND	79	63
005/2010	X	M	sMND	41	32
023/2010	AA	F	sMND	41	89
041/2010	AA	F	sMND	69	38
064/2010	S	M	sMND	79	24
082/2010	W	F	sMND	75	20
005/2011	Z	F	sMND	76	52
036/2012	A27	M	sMND	65	19
048/2012	A27	M	sMND	43	34
054/2015	A21	F	sMND	62	20
060/2016	A29	M	sMND	75	26
046/2013	A25	M	sMND	78	11
058/2012	A28	F	sMND	65	62
008/2013	A23	M	sMND	71	17

Table 2.14 Control spinal cord immunohistochemistry cohort

Case Number	Block Number	Sex	Disease Status	Age at death
109/1995	C	M	control	46
014/1999	Z	F	control	86
098/2007	V	M	control	68
135/2018	A28	F	control	85
335/1990	F	F	control	29
019/1991	B	M	control	54
118/1993	D	M	control	51
072/1992	C	F	control	76
144/1991	CL	M	control	65
025/1995	C	M	control	67
023/1992	C	F	control	84
147/1995	C	M	control	47
035/1996	V	F	control	87
129/1994	H	M	control	63

2.12.4 Motor Cortex Cohort

Table 2.15 sMND Motor Cortex Cohort

Case Number	Block Number	Sex	Age at death	Suvival time (Months)	*Post-mortem* Delay
027/2008	a	F	70	44	24
043/2005	b	M	31	66	35
087/1992	a2	M	72	48	18
088/2006	c	F	49	23	24
034/2005	l	M	60	38	16
099/2009	b	M	74	63	24
042/2005	e	M	60	57	9
064/2009	a	M	63	43	30
098/2008	c	F	71	50	24
096/2008	g	F	67	21	40
014/2008	j	F	73	31	48
075/2008	d	F	55	82	24
099/2003	b	M	78	10	-
023/2010	c	F	34	89	24
041/2010	d	F	65	38	72
054/2015	a1	F	76	20	96
064/2010	c	M	76	24	30
082/2010	a	F	73	20	48
005/2010	c	F	71	17	48
094/2006	a	M	71	9	53
008/2013	a23	F	71	17	48
005/2011	a	F	71	52	40
036/2012	a4	M	58	19	24
048/2012	a3	M	39	34	48
046/2013	a3	M	78	11	48
058/2012	a4	F	65	62	24
049/2006	e	M	83	97	44
060/2016	a4	M	75	26	96
054/2005	a	M	80	24	96
049/2005	a	M	91	97	44
261/1990	x1	M	68	13	9
175/1995	u	F	74	13	48
187/1991	b1	M	60	38	39
104/2004	b	M	63	26	-
168/2018	a1	F	66	26	120
062/2016	a1	M	72	24	96
138/2014	a1	M	78	-	100+
055/2012	a1	F	71	-	48
077/2011	a	M	60	21	66
014/2011	c	M	49	28	40
128/2014	a1	F	29	65	96
046/2017	b	-	-	-	-
086/2008	b	M	64	21	46
050/2008	b	F	68	26	35
024/2008	a	F	59	46	36
105/2014	a4	M	-	-	80+
009/2008	d	M	76	11	-
187/1996	w	F	51	32	5
066/1996	j1	F	70	37	10
141/1993	a1	F	66	21	13
345/1990	x1	M	68	18	11
026/1994	p1	M	56	32	-
223/2005	l1	-	-	-	-
082/1999	n1	-	-	-	-
150/1997	e1	M	27	60	39
015/1998	h1	F	86	5	13
212/1999	j1	M	60	40	32

086/2006	4b	M	49	5	55
200/1997	e1	M	69	47	18
072/2005	b	M	66	10	8
113/2008	a	M	49	29	48
025/2013	a3	F	72	22	60
026/2013	A2	M -	62	15	90

Table 2.16 Control Motor Cortex Cohort

Case Number	Block Number	Sex	Age at death	*Post-mortem* interval
224/2016	a28	F	82	-
135/2018	a3	F	85	72
005/2007	af	M	63	-
085/2007	b & c	F	59	5
058/2022	a19	F	68	91
018/2009	o	M	69	-

For the basal ganglia, prefrontal, temporal, and occipital cortex cohorts see Appendix D.

2.13 Tissue Microarray Construction

Materials

Table 2.17 Reagents used to construct Tissue Microarrays

Reagent/ Consumables/ Equipment	***Supplier***	***Catalogue/ Model Number***
Embedder	Lecia	Model: EG1150
Moulds	Lecia	
System II Hex Cassette	ProMarc cassettes	EAD-0102-03A
Beecher MTA-1 Tissue Microarrayer	Beecher	Contact Supplier
MP20, 2.0mm Core Stylets	Mitogen	
Renata 2450 batteries	Renata	-
Xylene (97%)	Fisher Scientific	10784001

Methods

Tissue microarrays (TMAs) were constructed for each CNS region of interest from sMND and control tissue. TMAs were generated using tissue from the precentral gyrus (motor cortex), middle frontal gyrus (prefrontal cortex), temporal cortex, occipital cortex, and the basal ganglia (Figure 2.8). For each of the cortical regions, separate TMAs were constructed with white and grey matter. TMAs were also constructed for the basal ganglia. For this region, the putamen was sampled as it was the easiest region to access. In cases where the white and grey matter, or region of interest were not easily distinguishable, a Luxol Fast Blue stain (see section 2.21) was performed on a tissue section taken from the block. Due to the small anatomical structures within the spinal cord, this region was not used for TMAs, as this would have led to the destruction of the tissue block (Figure 2.8). Instead, immunohistochemistry was performed on conventional tissue sections. During image analysis specific regions of the spinal cord were selected (the ventral horns, dorsal column and lateral corticospinal tracts) – see Section 2.22.2 for further information.

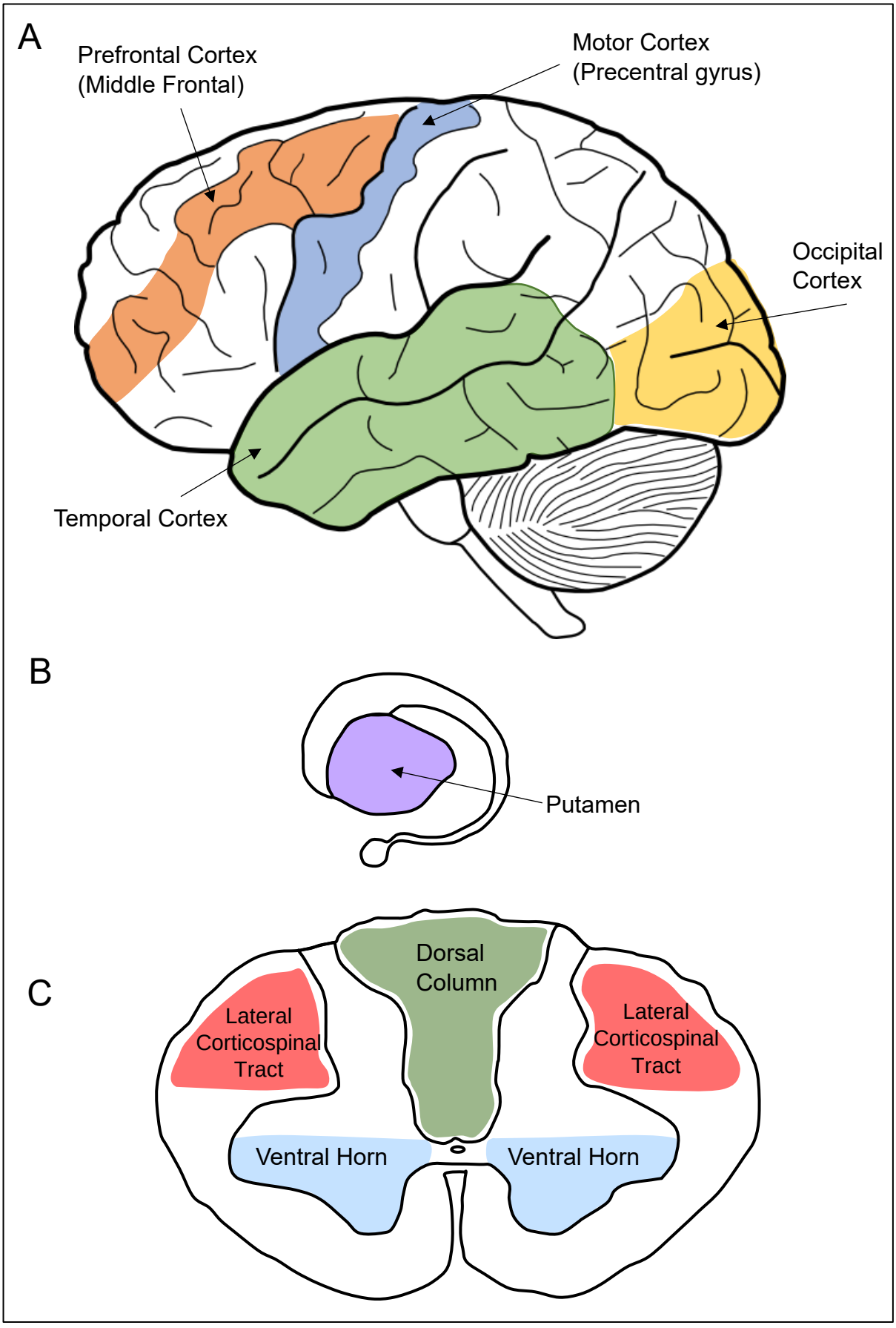
A
Prefrontal Cortex
(Middle Frontal)
Motor Cortex
(Precentral gyrus)
Occipital
Cortex
Temporal Cortex
B
Putamen
C
Dorsal
Column
Lateral
Corticospinal
Tract
Lateral
Corticospinal
Tract
Ventral Horn
Ventral Horn

Figure 2.8 Brain and Spinal Cord Regions Examined via Immunohistochemistry

A. *From the cortex, white and grey matter were sampled from each region for TMAs. Cores were taken from the middle frontal region of the prefrontal cortex (orange), the precentral gyrus (motor cortex, shown in blue), the occipital cortex (yellow) and the temporal cortex (green).*

B. *From the basal ganglia, the putamen was selected for sampling (shown here in purple). This region was sampled due to its ease of access for punches to be taken compared to other basal ganglia regions.*

C. *From cervical spinal cord, conventional sections were used for immunohistochemistry. During image analysis, the ventral horns (grey matter, shown here in light blue)., the dorsal column (dark green), and the lateral corticospinal tracts (shown in red) were selected for analysis.*

Tissue Microarrays were constructed using the Beecher MTA-1 Tissue Microarrayer. Blank ‘recipient’ paraffin blocks were prepared by pouring liquid paraffin into a base mould. A slotted cassette was placed on top, and a small volume of paraffin was added to ensure the cassette was attached to the block, and the mould was allowed to cool until the paraffin was solid. Moulds with a depth of 5-10mm were selected, with a cassette depth of 8mm. This was to allow enough space for the donor core to be seated (cores should ideally be 5mm in length), with sufficient space (~0.5 - 1mm) between the base of the core and the cassette. This prevented damage to the core itself and prevented the base of the block from separating from the cassette.

Prior to construction, the donor block was warmed for 15 minutes in an incubator at 37^{o}C. This initial warming was to prevent the paraffin from fracturing (Fedor and De Marzo, 2005). When the block became too cool, the warming process was repeated. Using the recipient stylet, which is slightly larger in diameter than the donor stylet, holes were punched into the recipient block. Three-millimetre spaces were left between each punch to prevent the block bulging, which would prevent an even cutting face later in the protocol. A 2.5-3mm perimeter of un-sampled wax was left around the edge of the recipient block to prevent the wax from cracking.

The donor stylet was then used to sample cores from the donor tissue blocks. Following the guidance from previous optimisation (Wilson *et al.*, 2021) donor tissue cores with a diameter of 2mm were selected, as cores with a smaller diameter were found to be too small to accurately represent the microglial pathology observed on the whole tissue section. Areas of white and grey matter in the FFPE tissue were confirmed by JRH prior to punching.

Most donor cores were inserted into the donor block using the stylet. However, in some cases where the tissue was particularly brittle or contained a large amount of wax cores were removed from the donor stylet, trimmed of excess wax using a scalpel and inserted into using fine point tweezers.

Tissue microarrays were constructed to hold up to 33 donor cores, 1 core per case was taken. To ensure easy identification of tissue cores, two extra cores of FFPE chicken muscle were added to block. These sections were quickly recognisable as non-brain tissue, even before staining due to differences in the tissue structure. Additionally, the core layout was such that there were no planes of symmetry (Figure 2.9) which allowed easier orientation of the block once sectioned, should the chicken cores be lost. It should be noted that some TMAs had less than 33 cores, however the same structure principles were applied.

Stylets were cleaned after each block was made by wiping with a xylene-soaked tissue. With each punch, paraffin begins to build up on the stylet, blunting the end. Therefore, more force is required to complete each punch, which risks cracking the donor and recipient blocks.

To prevent cores from being lost during sectioning, the microarray blocks were placed upside down onto a glass slide and warmed in an incubator at 37^{o}C for 10 minutes. Gentle pressure was applied to the slide to ensure the top surface of the tissue microarray was flat. This annealing step was repeated 3-5 times. This ensured the paraffin of the donor block was firmly moulded around the cores.

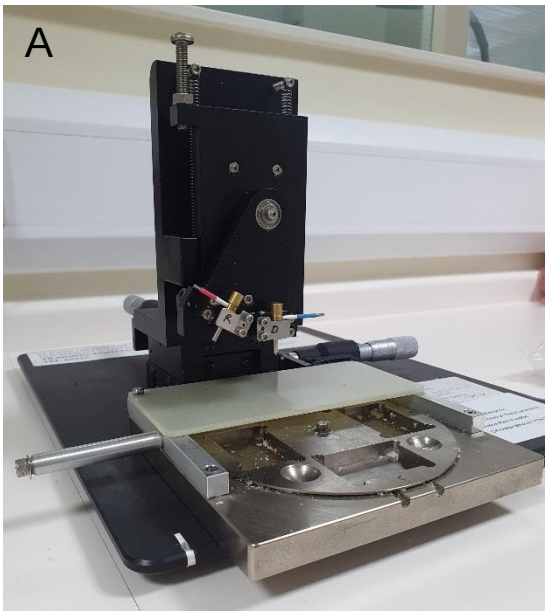

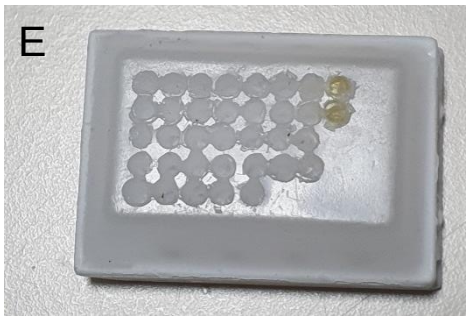

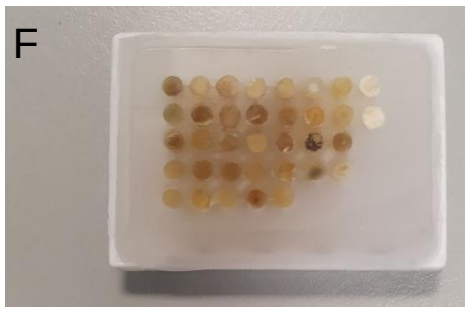

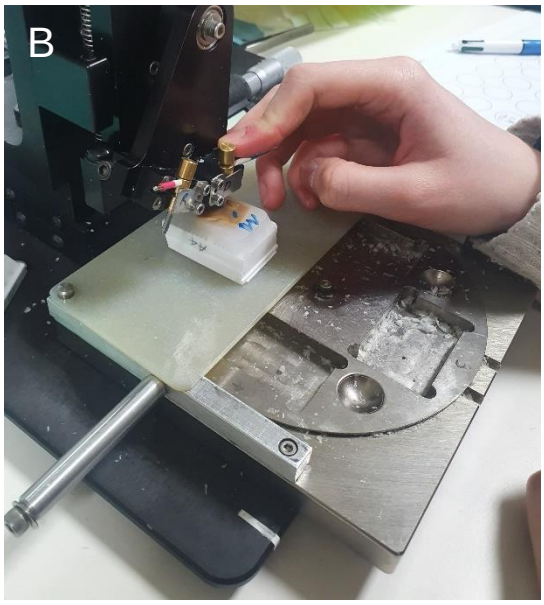

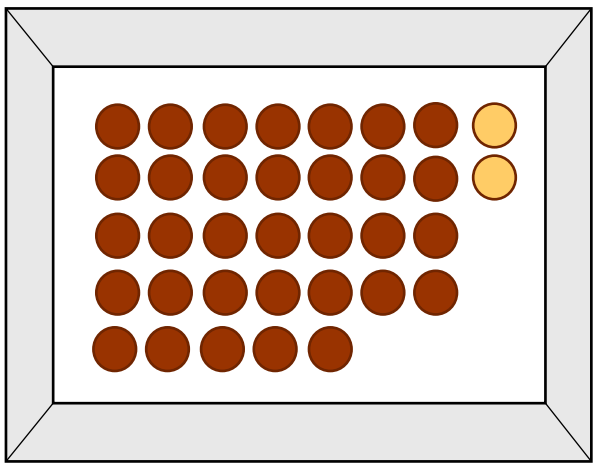

Key:

Human Tissue Core

Chicken Muscle Core

Figure 2.9 Construction of Tissue Microarrays

Tissue microarrays were constructed using the Beecher Tissue Microarrayer. Paraffin blocks were punched using the recipient stylet to create a blank TMA. FFPE brain tissue was sampled using the donor stylet and inserted into the blank TMA, along with cores of FFPE non-human non-CNS tissue (chicken muscle) for orientation.

A. *The Beecher Tissue Microarrayer used to create TMAs. The recipient stylet is marked with the letter R, the donor stylet is shown with the letter D.*

B. *Sampling of white and grey matter from a FFPE block of cortical tissue.*

C. *Paraffin block used to create blank TMAs.*

D. *Blank TMA showing grid formation of holes ready for tissue insertion.*

E. *Blank TMA with non-CNS tissue inserted.*

F. *Completed TMA following the annealing process.*

G. *Diagrammatic representation of TMA layout for human tissue microarrays. Cores of non-CNS tissue were placed in top corner. The short row at the bottom of the TMA, with the addition of non-CNS tissue removed any planes of symmetry. These factors made orientation TMA easier following sectioning.*

2.14 Immunohistochemistry

Immunohistochemistry was used to visualise the expression of antigens of interest within *post-mortem* tissue. The avidin/biotinylated enzyme complex (also known as ABC) method was used. In this method, the primary antibody binds specifically to an antigen of interest within the tissue. Biotinylated secondary antibodies bind to the primary antibody. The avidin and an enzyme are preincubated to form a complex, most commonly horse-radish peroxidase (HRP) or alkaline-phosphatase (AP). Avidin has a high affinity for biotin and has four biotin binding sites allowing large complexes to form (Figure 2.10). The ABCs binds to the biotinylated secondary antibody. Visualisation of the complex is completed using a chromophore, most commonly 3,3′-Diaminobenzidine (DAB). The HRP enzyme facilitates the conversion of DAB from colourless to a brown colour. The high complex to antibody ratio amplifies the biological signal allowing indirect visualisation of the protein.

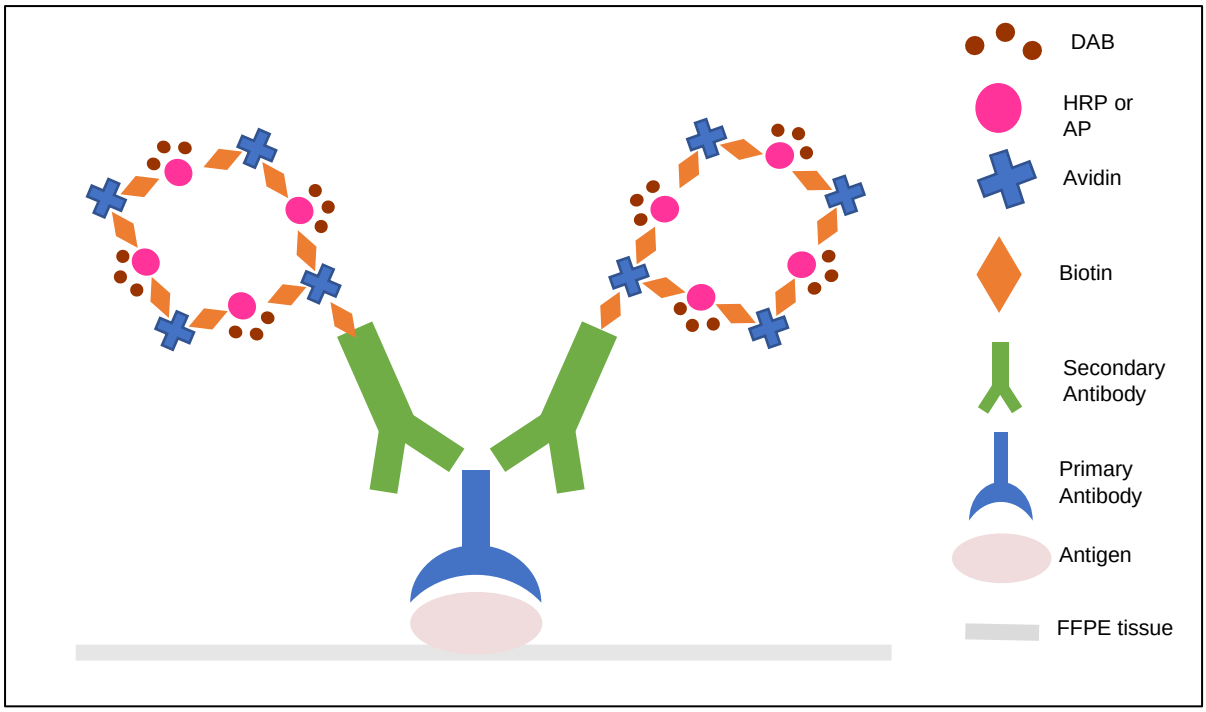

Figure 2.10 Avidin-Biotin Complex Method of Immunohistochemistry

The primary antibody (blue) binds to the antigen (grey) in the tissue. The biotinylated secondary antibody (antibody shown in blue, biotin molecule shown in orange) binds to the primary antibody. The avidin and biotinylated enzyme are preincubated to form the ABC complex, which binds to the biotinylated secondary antibody. Once DAB is added, it reacts with the enzyme (HRP), resulting in a colour change from clear to brown, allowing indirect visualization of the antibody.

Materials

Table 2.18 Immunohistochemistry Reagents

Reagent/Kit	Components	Supplier	Catalogue reference
Xylene (97%)		Fisher Scientific Inc.	X/0200/17
Antigen Access solutions	Reveal Decloaker (pH6)	Biocare Medical	RV1000
	Borg Decloaker (pH9.5)		BD1000
	3g Tri-sodium citrate (TSC) in 1L of dH_2O at pH6	Fisher	S/3320/60
	0.3g of ethylenediaminetetraacetic acid (EDTA) in 1L of dH_2O at pH9	Thermo Scientific	17892
Tris Buffered Saline (TBS) pH 7.4	85g Sodium Chloride 60.5g of Tris-base 10L of dH_2O	Fisher Scientific Melford	S/3320/60 T60040-5000.0
Graded Alcohols (100%, 100%, 90%, 70%)	Absolute Ethanol diluted to appropriate concentration with distilled H_2O (dH_2O)	VWR™	20821.365
3% Hydrogen Peroxide (H_2O_2) Solution	12mL H_2O_2 388mL Methanol	Fisher Scientific Sigma Aldrich	H/1750/15 32213-2.5l-M
Vectastain ABC-AP Kit, Peroxidase kit	Normal Serum Biotinylated Secondary Antibody Avidin Biotinylated Horseradish Peroxidase Complex (ABC-HRP)	Vector Laboratories Inc.	Rabbit: PK-4001
			Mouse: PK-4002
			Goat: PK-4005
Diaminobenzidine (DAB) Peroxidase Substrate Kit	DAB Reagent 1 (Buffer Solution) DAB Reagent 2 (DAB Stock Solution) DAB Reagent 3 (Hydrogen Peroxide)	Vector Laboratories Inc.	SK-4100
VFM Harris haematoxylin stain (acidified)		Medica Pacifica PTE limited.	RBA-4205-00A
Scotts Tap water	Magnesium Sulphate (50g) Sodium Bicarbonate (8.75g) Tap H_20 2.5L	Sigma Aldrich Sigma	M7506-5009 S7277-2509

Table 2.19 Reagents and equipment used to section tissue, mount, and image slides.

Reagent/ Consumables/ Equipment	***Supplier***	***Catalogue/Model Number***
Charged Series 2 Advanced Adhesive	Trajan	472042491
Coverslips (24x50mm)	CellPath, Ltd	SAB-2450-03A
Distyrene Plasticizer Xylene (DPX), (Phthalate Free) Mounting Medium	Fisher Scientific	SEA-1304-00A
Xylene (97%)	Fisher Scientific Inc.	X/0200/17
Waterbath (45^{O}C)	Leica	Model: RM2245
Microtome	Hamamatsu	
NanoZoomer XR Slide Scanner	NanoZoomer Digital Pathology (NDP) View	
Accompanying Software:		NDP. View 2.9.25

Table 2.20 Antibodies used for Immunohistochemistry

Protein of Interest	Manufacturer	Catalogue Reference	Species	Clone Name	Isotype	Clone	Optimised Antigen Retrieval Conditions	Optimised Primary Antibody Concentration
APOE	Abcam	ab1906	Mouse	D6E10	IgG1	Monoclonal	Pressure Cooker with Borg Decloaker buffer (pH 9.5)	1:1000
CD163	BioRad	MCA1853	Mouse	edhu1	IgG1	Monoclonal	Pressure Cooker with Reveal buffer (pH 6)	1:1000
CD68	DAKO	M0876	Mouse	PGM1	IgG3	Monoclonal	Microwave with TSC (pH6) buffer	1:100
CTSS	Sigma	HPA002988	Rabbit	-	IgG	Polyclonal	Pressure Cooker with Reveal buffer (pH 6)	1:800
HLA-DR	DAKO	m0746	Mouse	TAL.1B5	IgG	Monoclonal	Pressure Cooker with Reveal buffer (pH 6)	1:100
IBA1	Abcam	ab5076	Goat	-	IgG	Polyclonal	Microwave with TSC (pH6) buffer	1:200
TREM2	LSBio	LS-B16999	Mouse	-	IgG	Monoclonal	Pressure Cooker with Reveal buffer (pH 6)	1:1600
TYROBP	Thermofisher	PA5-83577	Rabbit	-	IgG	Polyclonal	Pressure Cooker with Borg Decloaker buffer (pH 9.5)	1:100
GFAP	DAKO	Z0334	Rabbit	-	IgG	Polyclonal	Microwave with TSC (pH6) buffer	1:2000
Mouse IgG	Vector	I-1000-5	-	-	IgG	-	-	Prepared to match the working concentration of the primary antibody
Rabbit IgG	Vector	I-2000-1						
Goat IgG	Vector	I-5000-5						

2.14.2 Tissue Sectioning

Each block containing FFPE tissue was chilled on ice prior to sectioning. This hardens the wax, providing more support for harder tissue, allowing thinner sections to be obtained. Tissue sections were cut at 5µM using a microtome, floated on a 45^{O}C water bath, and mounted on Trajan charged series 2 advanced adhesive slides. Slides were then dried in a slide oven at 37^{O}C for 24 hours.

2.14.3 Antigen Retrieval

Microscope slides with FFPE tissue sections were dewaxed in xylene for two intervals of 5 minutes and rehydrated through a graded series of alcohols at 100%, 100%, 95% and 70% concentrations for 5 minutes each, followed by tap water for a further 5 minutes. Slides were incubated in 3% hydrogen peroxide and methanol for 20 minutes to block endogenous peroxidases in the tissue, preventing non-specific staining. Slides were washed in running tap water for approximately 5 minutes and transferred to the appropriate antigen retrieval buffer ensuring slides were fully covered (details of conditions are given in Table 2.20). For microwave-based antigen retrieval, slides were covered in the appropriate buffer and heated in the microwave on full power for 10 minutes. For pressure-based antigen retrieval, placed into the antigen retrieval unit, along with 500mL of dH_2O. The antigen retrieval unit was run, allowing the temperature to reach 125^{o}C and 20 pounds per square inch for 30 minutes. Following completion, slides were allowed to cool and then rinsed in water.

2.14.4 Kit Preparation

Avidin-Biotin Complex- Horse Radish Peroxidase (ABC-HRP) Kit

The ABC-HRP kit raised in the appropriate species was prepared as follows: 1.5% blocking serum was prepared by adding 150µL of serum to 10mL of TBS. The biotinylated secondary antibody was prepared by adding 50µL of biotinylated secondary antibody to 150µL of serum and 10mL of TBS. The ABC-HRP solution was prepared by adding 100µL of Avidin and 100µL of Biotin to 5mL of TBS. This solution was prepared and allowed to stand for at least 30 minutes before use.

Diaminobenzidine (DAB) Kit

To prepare, 100µL of hydrogen peroxide, 100µL of DAB buffer and 200µL DAB were added to 5mL of dH_2O. Solution was prepared and used immediately to prevent precipitation of DAB out of solution prior to its incubation on tissue.

2.14.5 Immunohistochemistry

Following antigen retrieval, the cooled slides were placed into a staining tray with a humid chamber and washed using TBS for 5 minutes. The TBS was tapped off and slides were incubated in enough blocking serum (approximately 150µL) to cover the tissue for 30 minutes. Slides were drained, and the sides wiped to remove excess liquid. Slides were incubated in 150µL of the desired primary antibody over night at 4◦C. Slides were covered with sealing film (Parafilm) over the course of the incubation to ensure even coverage of the primary antibody and prevent evaporation. All primary antibodies were diluted to the desired concentration (see Table 2.20) in blocking serum.

Following primary antibody incubation, slides were washed in TBS for two five-minute intervals. TBS was tapped off and slides were incubated in ABC for 30 minutes. Slides were washed twice in TBS for 5 minutes per wash.

To visualise the reaction, slides were incubated in the DAB solution immediately after its preparation for up to 10 minutes. Slides were checked under the microscope to determine whether staining was visible. Once the desired colour change was reached, slides were washed in dH_2O to quench the reaction, followed by tap water for 5 minutes.

Cell nuclei were counter-stained in Harris Haematoxylin for 2 minutes until nuclei had a purple colour. Slides were washed in tap water for 1 minute, and finally transferred to Scotts tap water for approximately 10 seconds until the nuclei changed from purple to blue and were washed in tap water for 1 minute. With each run of immunohistochemistry, a tissue section known to express the protein of interest was run as a positive control, as well as a negative (primary antibody omitted) control.

Slides were rapidly rehydrated through serial alcohols (70%, 90%, 100% and 100%) for 30 seconds per concentration and cleared in xylene for 5 minutes. Slides were cover slipped using DPX and placed in a 37◦C slide oven overnight to harden.

2.14.6 Slide Digitisation

Slides that underwent immunohistochemistry were scanned using the Hamamatsu nanoZoomer slide scanner (Hamamatsu, Photonics, Japan) to create digital images of the entire tissue area.

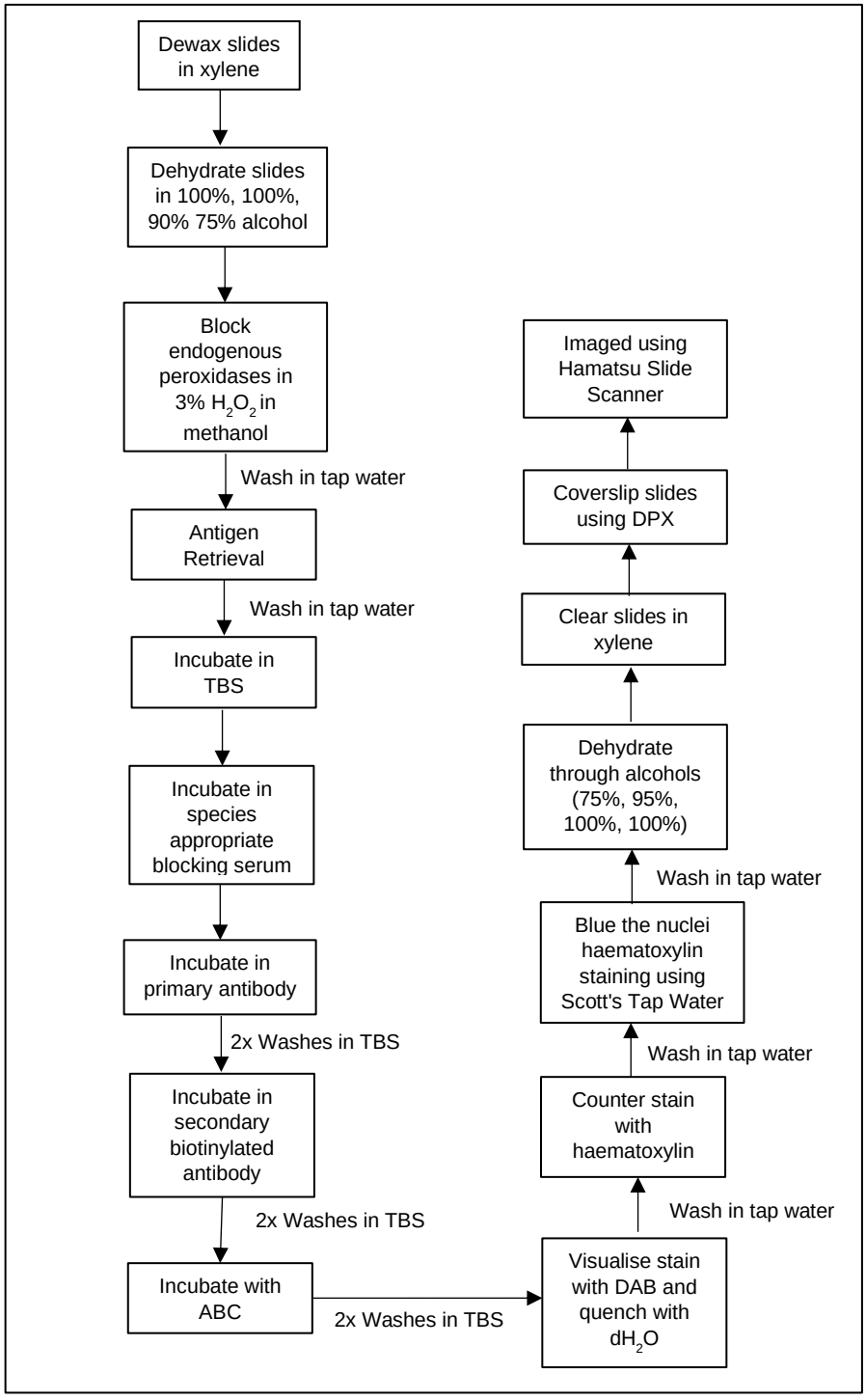

Figure 2.11 Flow Chart Depicting Immunohistochemistry Protocol.

Following sectioning, slides were prepared for immunohistochemistry by removing the paraffin in xylene and rehydrated. Endogenous peroxidases were blocked using hydrogen peroxide, followed by antigen retrieval to remove crosslinks from the formalin preservation. The tissue was blocked in serum to prevent non-specific antibody/ reagent binding. The primary antibody was then allowed to bind the antigen of interest followed by the secondary biotinylated antibody, and the ABC. Reactivity was visualised using DAB, followed by a haematoxylin counter stain to visualise cell nuclei. Slides were then dehydrated and cleared using xylene. Finally, slides were cover slipped and imaged.

2.15 Primary Antibody Optimisation

Optimisation was performed to identify the best method of antigen retrieval and primary antibody concentration to enable specific immunoreactivity, and minimal non-specific staining. All optimisations were performed on FFPE cortical tissue taken from the site of a stroke. This case was selected for optimisation as it is well characterised and shows areas of both high and low levels of inflammation and microglial activation making it ideal to optimise such markers. In some cases, further optimisation was performed in spinal cord tissue, in cases where the antibody showed differential staining according to brain region.

For each antibody, optimisation was run using the standard immunohistochemistry protocol using a range of concentrations. The concentration range was based upon that recommended by the manufacturer or referenced papers using the antibody where available. In cases where the antibody had been routinely used by peers, the recommended usage conditions were trialled to confirm staining effectiveness. In all cases, an isotype control and negative (no primary antibody) control were run to ensure staining observed was not the result of non-specific antibody interactions with the tissue or due to the detection system. Unless otherwise recommended, all antibodies were initially trialled using the pressure cooker method of antigen retrieval first; optimisation of the Tissue Microarrays (TMA's) conducted by MSc student Laura Heraty (Heraty, 2019) showed reduced tissue loss using this method of antigen retrieval compared to microwave and as such this would be the preferred method of antigen retrieval for later immunohistochemistry staining.

2.16 Primary Antibody Absorption

A primary antibody absorption assay was performed to assess the binding specificity of primary antibodies. This assay involves incubating the primary antibody with the target protein, prior to incubation with the tissue. The binding of the protein to the primary antibody should prevent the antibody being able to bind to antigens within the tissue if the antibody was specific to the protein of interest. If a DAB signal is observed this could indicate non-specific binding of the primary antibody.

This assay was to be performed on the three non-microglial markers (TREM2, TYROBP and APOE, however the protein for TYROBP antibody was not commercially available from the antibody.

Materials

Table 2.21 Proteins used for Primary Antibody Absorption

Protein of Interest	Manufacturer	Catalogue Reference
Recombinant Human APOE	Abcam	ab55210
Recombinant Human TREM2	LSBio	LS-G48318

For immunohistochemistry reagents please see section 2.14.

Methods

For each antibody of interest, preparations of the primary antibody solution in species appropriate blocking serum were prepared the working concentration using blocking serum of the appropriate species (for primary antibody concentrations and species please see table 2.18). To the primary antibody dilution, the protein was added at a 10x concentration. The primary antibody dilution without the target

protein, and the primary antibody/protein dilution were incubated over night at 4^{O}C with agitation.

Standard immunochemistry (Section 2.14) was performed substituting the primary antibody for either antibody/protein solution or the antibody solution incubated overnight. A primary antibody omission condition was used (protein only) to determine whether the secondary antibody was able to bind to the peptide directly.

2.17 Antibody Validation through SDS-Polyacrylamide Gel Electrophoresis and Western Blotting

To examine the epitope specificity of the primary antibodies for immunohistochemistry, Sodium dodecyl sulphate (SDS) polyacrylamide gel electrophoresis (SDS-PAGE) and western blotting was performed. This process demonstrates whether the antibody binding product is at the expected mass (kDA) and therefore binding to the correct protein, and whether the antibody is specific to the protein of interest or results in several products (Bordeaux *et al.*, 2010).

Materials

Table 2.22 Reagents for SDS-Polyacrylamide Gel Electrophoresis and Western Blotting

Reagent/ Kit	Supplier	Catalogue reference
5x Reporter Lysis Buffer	Promega	E397A
Protease Inhibitor	Sigma	1.084E-10
PMSF protease inhibitor	Thermo Fisher Scientific	25530049
Bradford Reagent	ThermoFisher Scientific	23236
ProtoGel (30%) Acrylamide Bisacrylamide Stabilized Solution	National Diagnostics	SKU: EC-890
Tetramethylethylenediamine (TEMED)	Melford	T18000-0.1
PageRuler™ Prestained Protein Ladder, 10 to 180 kDa	ThermoFisher Scientific	26616
Nitrocellulouse Membrane 0.2µM	Amersham	1060001
Skim Milk Powder	Millipore	70166
Tween	BDH Organics	6636e
Rabbit Secondary Antibody	Novex	A16066
Mouse Secondary Antibody	Novex	A16096
Clarity Western ECL Substrate	Bio-Rad	170-5061

Table 2.23 Preparation of Buffers for SDS-Polyacrylamide Gel Electrophoresis and Western Blotting

Buffer	Preparation
5 x Running buffer	For 5 L: 75 g Tris, 25 g SDS, 360 g Glycine.
10 % APS	1 g of Amminopersulfate in 10 ml MQ-water
Resolving buffer	For 500 mL: 90.85 g Tris/Trizma, 2 g SDS, pH 8.8 then filtered.
Stacking buffer	For 500 mL: 30.3 g Tris/Trizma, 2 g SDS, pH 6.8 then filtered.
4 x protein loading buffer	For 40 mL: 10 mL of 1M Tris-HCl, pH6.8, 16 mL glycerol, 3.2 g SDS, 0.002 g Bromophenol Blue
	(1x conc. 62.5 mM Tris-HCl, pH 6.8, 10% glycerol, 2% SDS, 0.002% Bromophenol Blue)
Transfer buffer	For 5 L: 29 g Tris Base, 14.5 g Glycine, 2 g SDS, 1 L Methanol.
10 x TBS	For 3.5 L: 84.7 g Tris Base, 280 g NaCl, pH 7.6

Table 2.24 Gel Preparation for Electrophoresis

Reagent/Buffer	5% Stacking Gel	10% Resolving Gel	15% Resolving Gel
dH2O	5.8mL	4.2mL	2.5mL
30% Acrylamide Bisacrylamide Stabilized Solution	1.7mL	3.3mL	5mL
Resolving Buffer	-	3.5mL	2.5mL
Stacking Buffer	2.5mL	-	-
10% APS	50µL	50µL	50µL
TEMED	20µL	20µL	10µL

Protein Extraction from Frozen Post-mortem Tissue

The 1x working buffer was prepared by diluting the 5x buffer in dH_20 with the protease inhibitor cocktail (20µL per mL) and PMSF protease inhibitor (20µL per mL). 500µL was added to each tissue sample in a 1.5mL Eppendorf tube, with 10 homogeniser beads. The samples were homogenised at 5500rpm twice in the Precelly Evolution homogeniser. Samples were placed on ice for 10 minutes before the homogenisation process was repeated. The samples were centrifuged at 17,000g for 10 minutes at $4^{O}C$. The supernatant containing the cell lysate was transferred to a fresh tube and kept on ice.

Bradford Assay

The protein concentration in the tissue lysate was determined by Bradford Assay. This is a colorimetric assay that uses the Coomassie Brilliant Blue G-250 dye. This dye has three forms: anionic (blue), neutral (green) and cationic (red). Under the acidic conditions in the Bradford reagent, the dye is in its cationic form. Once protein

is added to the solution, the dye binds to the protein, causing a donation of electrons from the dye to the protein. This results in the dye changing to its anionic form, producing a colour change from red/brown to blue. This is directly proportional to the amount of protein present in the sample.

The Bradford Reagent was diluted from 5x to 1x using dH_20. 2µL of cell lysate was added to 1 mL of 1x Bradford Reagent. The colour change was measured using the WPA S1200 Spectrawave Diode Array spectrometer. The spectrometer is first blanked using 1mL of 1x Bradford Reagent. For each sample 1mL was added, and the OD595 value noted. To calculate the protein concentration (mg/mL), the OD595 was multiplied by 7.5. Protein samples were diluted to the desired concentration using working buffer.

SDS-Polyacrylamide Gel Electrophoresis

To each protein sample, 5x protein loading buffer added (to produce a final concentration of 1x), and samples were boiled at approximately $100^{O}C$ for 10 minutes to denature the proteins. Samples were then quicky centrifuged to collect the sample at the base of the tube. The samples and 2µL of protein ladder were then loaded into the either 10% or 15% polyacrylamide resolving gels with 5% stacking gels (Table 2.24) which were submerged in a tank of 1x running buffer. Gels were electrophoresed at initially at 50V for approximately 20 minutes until the dye front had moved into the resolving gel. The voltage was then increased to 150V and run until the dye front reached the bottom of the gel.

Western Blotting Using Semi-Dry Transfer Method

Filter paper and 0.2µM nitrocellulose membranes where briefly soaked in ethanol-containing running buffer. The stacking gel was removed from the protein-containing resolving gels, and the resolving gels were placed onto the nitrocellulose membrane and sandwiched between three layers of filter paper on each side (see Figure 2.12). This was gently rolled to remove any potential air bubbles, which would prevent an even transfer, and placed into the electrotransfer system. Proteins were transferred onto the nitrocellulose membrane at 0.15 amps per gel, for one hour.

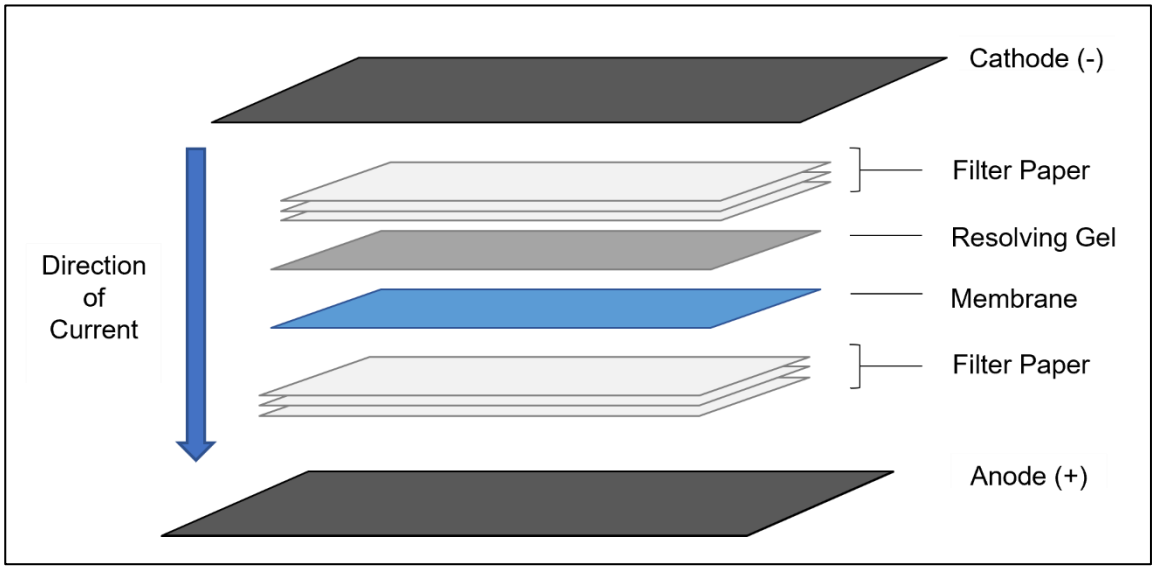

Figure 2.12 Semi-Dry Transfer Western Blot

Diagram illustrating the semi-dry transfer method. Electrical current transfers from the cathode to the anode, transferring proteins from the resolving gel to the membrane.

Once completed, the nitrocellulose membrane was incubated in 5mL of Ponceau stain solution on a shaker for approximately one minute. Once protein bands were visible, the blot was checked to ensure the transfer was successful. The Ponceau stain was washed off by in incubating in dH_2O. The membranes were incubated in 10mL of 5% powdered skimmed milk powder in TBS-T for one hour at room temperature, to block non-specific binding of the primary antibodies. The membranes

were then incubated in the primary antibody prepared in 5% milk in TBS-T overnight at $4^{O}C$.

Following incubation in primary antibodies, the membranes were washed in TBS-T for ten minutes, three times. The membranes were incubated in the species appropriate HRP conjugated secondary antibody prepared in 5% milk in for 1 hour at room temperature. Following this incubation, the membranes were washed three times in TBS-T for 10 minutes.

The blots were incubated in in equal volumes of the two enhanced chemiluminescence (ECL) solutions (750µL of ECL1 and ECL2) and imaged using the G-box Chemi-XT CCD Gel imaging system (Syngene, Cambridge, UK).

2.19 Colocalization Staining

Materials

Table 2.25 Material for Colocalization Staining

Reagent/Kit	Components	Supplier	Catalogue reference
Xylene (97%)		Fisher Scientific Inc.	
Antigen Access solutions	Reveal Decloaker (pH6)	Biocare Medical	RV1000
	Borg Decloaker (pH9.5)		BD1000
Tris Buffered Saline (TBS)	85g Sodium Chloride 60.5g of Tris-base 10L of dH_2O pH 7.4		
Graded Alcohols (100%, 100%, 90%, 70%)	Absolute Ethanol diluted to appropriate concentration with distilled H_2O	VWR™	
3% Hydrogen Peroxide (H_2O_2) Solution	12ml H_2O_2 388ml Methanol		
Vectastain ABC-AP Kit, Peroxidase kit	Normal Serum Biotinylated Secondary Antibody Avidin Biotinylated Horseradish Peroxidase Complex (ABC-HRP)	Vector Laboratories Inc.	Rabbit: PK-4001 Mouse: PK-4002 Goat: PK-4005
Diaminobenzidine (DAB) Peroxidase Substrate Kit	DAB Reagent 1 (Buffer Solution) DAB Reagent 2 (DAB Stock Solution) DAB Reagent 3 (Hydrogen Peroxide) DAB reagent 4 (Nickel - not used)	Vector Laboratories Inc.	SK-4100
ImmPACT® AMEC Red Substrate	ImmPACT AMEC Red Diluent ImmPACT AMEC Red Reagent 1 ImmPACT AMEC Red Reagent 2	Vector	SK-4285
Gill's Haematoxylin			
Scotts Tap water	Magnesium Sulphate (50g) Sodium Bicarbonate (8.75g) Tap H20 2.5L		
Distyrene Plasticizer Xylene (DPX) (Phthalate Free) Mounting Medium		CellPath, Ltd	SEA-1300-00A
VectaMount® AQ Aqueous Mounting Medium		Vector	AQ h-5501
Avidin/Biotin Blocking Kit	Avidin block solution Biotin blocking solution	Vector	SP-2001

Methods

The slides were dewaxed in xylene, rehydrated through graduate alcohols and endogenous peroxidases were blocked in 3% hydrogen peroxide for 20 mins. The slides underwent antigen retrieval, and the standard immunohistochemistry protocol was followed as described in Section 2.7, until the point of visualisation. To visualise the first protein of interest, a soluble stain was used – the ImmPACT AMEC red substrate kit. The solution was prepared in accordance with the manufacturer's guidelines by mixing 90µl of Reagent 1 and 80µl of Reagent 2 with 5ml of the dilutant reagent. This was applied to the slides for approximately 20 minutes until sufficient staining was visible under the microscope. Nuclei were counterstained with Harris' haematoxylin as described in section 2.7; however, the acid/alcohol step was avoided to prevent the dissolving of the alcohol soluble chromophore. Slides were washed in tap water and mounted immediately, using aqueous mounting media. Slides were then dried in a 37^{o}C slide oven for 24 hours.

Once dried, the slides were imaged using the Hamamatsu slide scanner. Following this, the slides were de-coverslipped by submerging in tap water in a 37^{O}C incubator until the coverslips came away completely freely without any manual removal. The dye was then dissolved by dehydrating the slides up the graduated alcohols (75%,90% and 100% ethanol), and left in the 100% alcohol until the stain was no longer visible. From here, slides were rehydrated back down alcohols to water then incubated in TBS for 5 minutes. Unbound avidin and biotin the first stain was blocked using the avidin and biotin blocking solutions for 15 mins. The slides were washed between and blocking solutions with TBS for 5 minutes twice. Slides were blocked in the primary blocking serum appropriate for the second antibody for 30 minutes. The rest of the immunohistochemistry protocol was completed as described in section

2.7. Once stained with DAB and counterstained with haematoxylin, the slides were dehydrated through the graduated alcohols, cleared in xylene, and mounted using DPX. Slides were dried for 24 hours in a 37^{o}C slide oven and scanned using the Hamamatsu scanner.

Using the NDP viewer software (v2.9.25), the two images for each slide were synchronised, allowing direct comparison of both makers in the same tissue section.

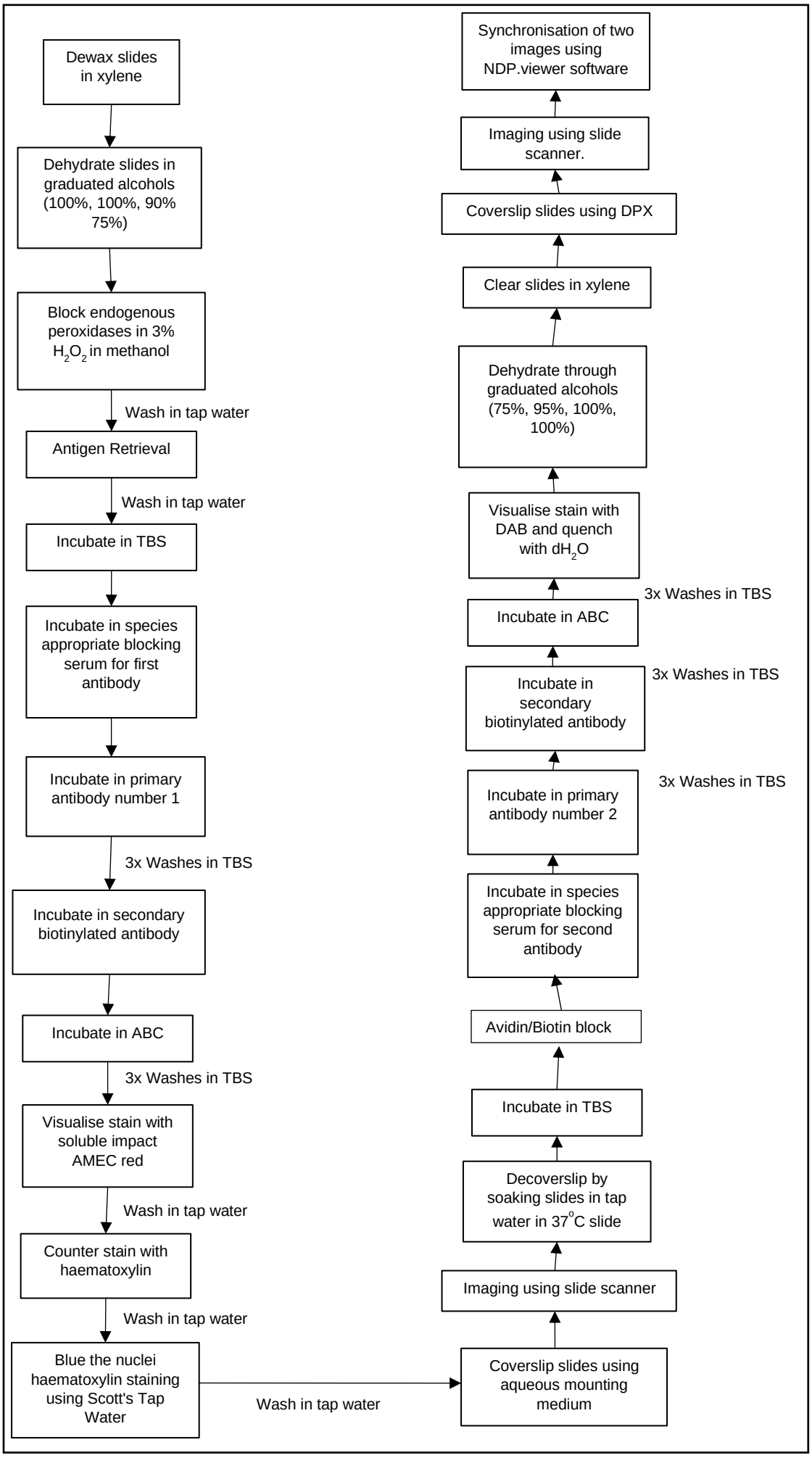
Dewax slides in xylene
Dehydrate slides in graduated alcohols (100%, 100%, 90% 75%)
Block endogenous peroxidases in 3% H_2O_2 in methanol
Wash in tap water
Antigen Retrieval
Wash in tap water
Incubate in TBS
Incubate in species appropriate blocking serum for first antibody
Incubate in primary antibody number 1
3x Washes in TBS
Incubate in secondary biotinylated antibody
Incubate in ABC
3x Washes in TBS
Visualise stain with soluble impact AMEC red
Wash in tap water
Counter stain with haematoxylin
Wash in tap water
Blue the nuclei haematoxylin staining using Scott's Tap Water
Wash in tap water
Coverslip slides using aqueous mounting medium
Imaging using slide scanner
Decoverslip by soaking slides in tap water in 37°C slide
Incubate in TBS
Avidin/Biotin block
Incubate in species appropriate blocking serum for second antibody
Incubate in primary antibody number 2
3x Washes in TBS
Incubate in secondary biotinylated antibody
3x Washes in TBS
Incubate in ABC
3x Washes in TBS
Visualise stain with DAB and quench with dH_2O
Dehydrate through graduated alcohols (75%, 95%, 100%, 100%)
Clear slides in xylene
Coverslip slides using DPX
Imaging using slide scanner.
Synchronisation of two images using NDP.viewer software

Figure 2.13 Flowchart Depicting Colocalization Staining Protocol

Following slide dewaxing and rehydrating, antigen retrieval was performed. The first round of immunohistochemistry was performed and visualised using a soluble substrate. Slides were imaged, and the stain was dissolved. The second set of stain was performed and visualised with DAB. The slides were imaged, and the images synchronised using NDP viewer software.

2.21 Luxol Fast Blue Stain

Luxol fast blue stain was used to differentiate between white and grey matter, and to identify regions of WM loss or pallor. The Luxol fast blue reagent is a copper phthalocyanine dye containing sulfonated copper. The dye is alcohol soluble and attracted to the basic elements in phospholipids. Excess dye is removed using alcohol and the stain differentiated using lithium carbonate. This results a deep blue colour in the myelin containing WM and pale blue to white colour in the grey matter.

Materials

Table 2.26 Reagents used for Luxol Fast Blue Stain

Reagent	***Supplier***	***Catalogue Number***
Luxol Fast Blue	BDH laboratory supplies	No longer in production
Lithium Carbonate (0.5%)		
Lithium Carbonate 0.25g	Sigma Aldrich	431559-50G
dH_2O 500mL		
Alcohol (Ethanol)	VWR™	20821.365DP
(Absolute ethanol was diluted with dH_2O to required concentration)		
2x Absolute		
1x 95%		
1x 70%		

Methods

Tissue sections were mounted onto Trajan slides as previously described (Section 2.14.1). Slides were deparaffinised in xylene for two intervals of 5 minutes, and rehydrated through graded alcohols starting at absolute, to 70% via incubation for 5 minutes. Slides were incubated in Luxol Fast Blue for 2 hours at 60^{O}C. The slides

were allowed to cool, and were incubated in 70% alcohol for 5 minutes, and gently washed in tap water for 1 minute. Slides were differentiated in 0.5% lithium carbonate for 1 minute or until the WM could be identified from the grey. The slides were washed in tap water for 1 minute and dehydrated through the series of alcohols again starting at 70% through to absolute. Slides were cleared in xylene and mounted with a coverslip using DPX.

2.22 Quantitative Image Analysis using Visiopharm

Visiopharm image analysis software (Visiopharm, v2018.9.5.5952, Hoersholm, Denmark) was used to quantify immunoreactivity in cervical spinal cord sections and TMA sections. Liam Wilson MSc (Wilson, 2018; Wilson *et al.*, 2021) created an APP within Visiopharm to specifically recognise DAB immunoreactivity, particularly for microglial markers. The APP had initial processing steps, (see below) but was adapted and specifically trained to recognise IBA1, CD68, HLA-DR, CD163, APOE, TREM2 and TYROBP immunolabelling for the current project.

2.22.1 Processing Steps

The APP contained the following processing steps (this work was completed by Liam Wilson MSc):

Classification:

A Bayesian classification system was used to allow the app to differentiate specific glial staining from non-specific staining or artefacts.

Pre-processing:

A haematoxylin and diaminobenzidine (HDAB) pre-processing step was added to maximise detection of DAB immunoreactivity and reduce the haematoxylin counter-stain signal strength. A 3x3 median filter was incorporated to facilitate the reduction of noise.

Post-processing:

For the microglial number measurement, a change function was used which classed any positively stained area less than 26.45µm^2 as background. This function reduced the number of transversely sectioned microglia and processes included, improving the accuracy of the microglial count. This value was based on a similar estimation of microglial size by Waller et al. (2019).

APP Adaptation

Following pre-processing, APPs were trained specifically for each protein of interest, using the training wizard in the Visiopharm software. Regions were manually selected for DAB positive regions, and background (Figure 2.14). This information was used by the wizard to improve the identification and selection of positive staining from the background.

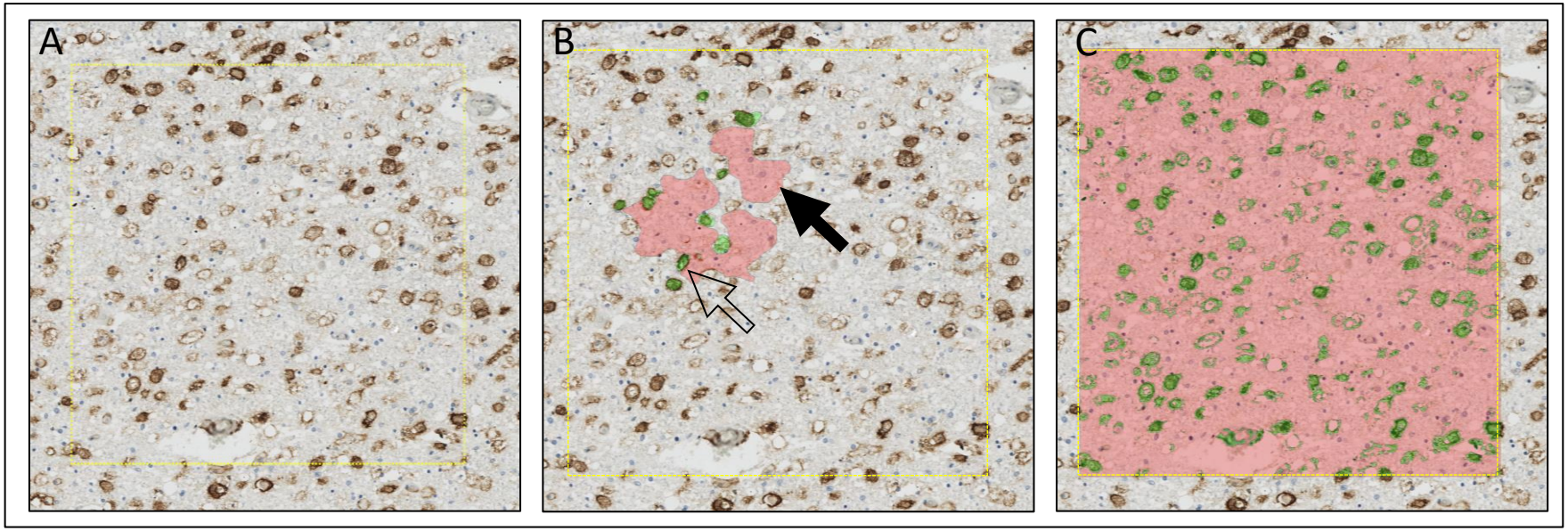

Figure 2.14 Screen Capture of APP Adaptation in Visiopharm

Each APP in the Visiopharm software was trained to recognise specific immunoreactivity from background. Images A,B,C show the same regions of lateral corticospinal tract from spinal cord with HLA-DR immunoreactivity.

A) *Region of HLA-DR immunoreactivity selected to train the HLA-DR APP, as demonstrated by the yellow box.*

B) *Regions of interest were manually selected. Background regions were selected in red (black arrow). Regions of specific immunoreactivity, in this example HLA-DR, were manually selected in green (open arrow). The manual selection was used to train the app to recognise specific staining.*

C) *App selection of background and HLA-Dr immunoreactivity following APP training.*

In spinal cord sections stained for TREM2, motor neurons showed evidence of probable artefactual lipofuscin signal (Figure 2.15). Lipofuscin is a yellow-brown pigmented granular substance found in cells, composed of lipid residues, and misfolded proteins. Lipofuscin accumulation is associated with aging and oxidative stress (Moreno-García *et al.*, 2018). This lipofuscin staining was present in most motor neurons in both control and sMND cases. Furthermore, some neurons were also stained for TREM2, while others were absent for staining. The Visiopharm software was unable to differentiate between neuronal staining and lipofuscin. To prevent bias in quantification – as sMND cases will have notably fewer motor neurons compared to control cases- the decision was made to filter out the neuronal and lipofuscin staining from the Visiopharm analysis. To do this a filter was created for the TREM2 Visiopharm APP, which re-classified DAB positive areas larger than 200µM as areas in background. Initially, this measurement was based on the average size of 50 motor neurons measured in the ventral horn (average length= 128.17µm). This value was then adjusted until all neurons and lipofuscin was removed by the APP without removing glial staining/ staining in the parenchyma.

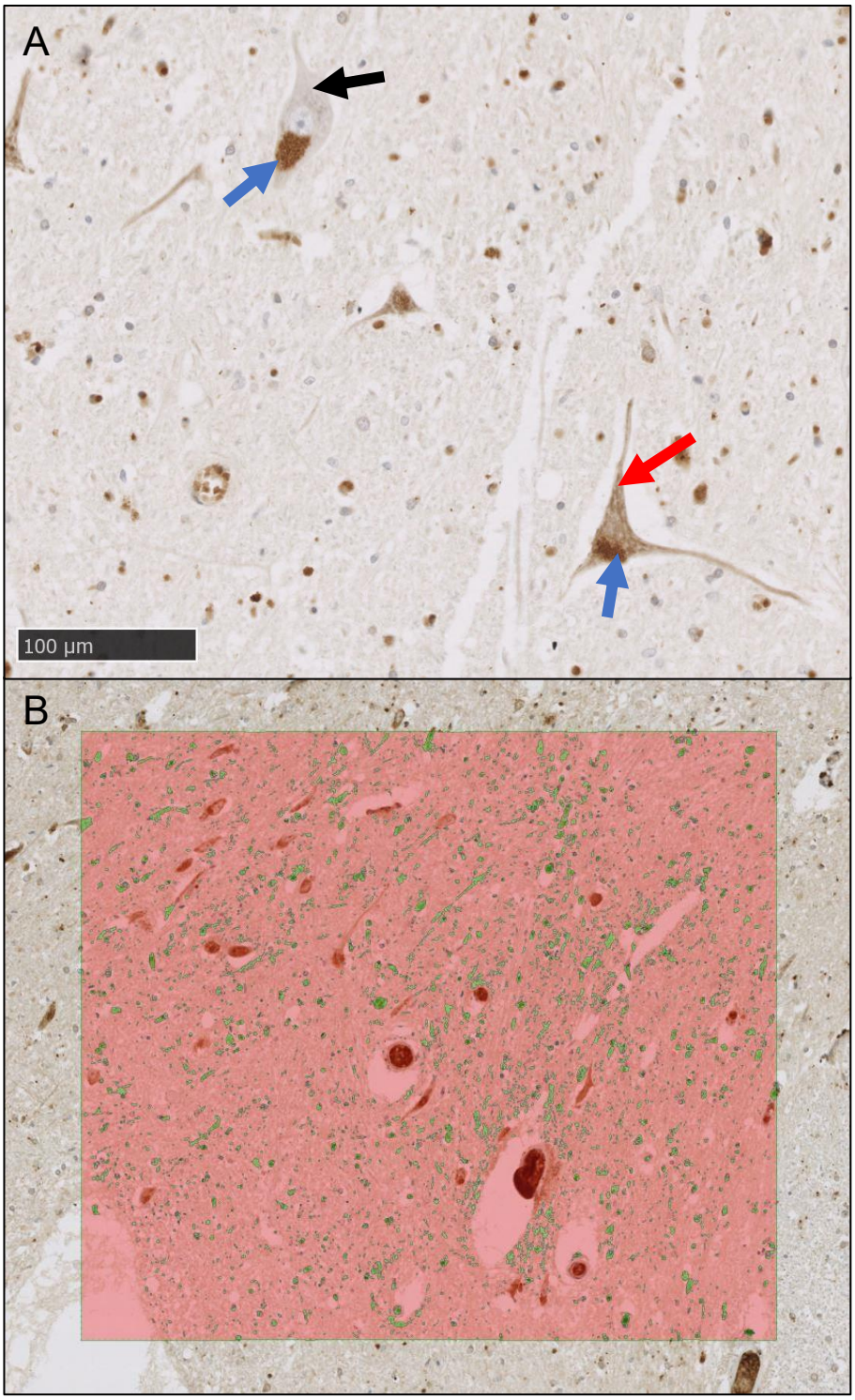

Figure 2.15 Filtering of Motor Neurons in TREM2 image analysis

A) In the spinal cord, lipofuscin artefactual signal was observed in TREM2 stained tissue as indicated by the blue arrows. Neurons showed variation in the extent of TREM2 staining. Some neurons were absent for staining (black arrow) while others were positive (red arrow). The Visiopharm software was unable to differentiate between lipofuscin and neuronal staining. As sMND cases display a loss of motor neurons from the ventral horn not seen in control ventral horn, motor neurons were removed from the Visiopharm based TREM2 analysis to prevent bias.

B) Image of the Visiopharm software with the TREM2 app and size filter. Green indicates areas positive for DAB staining. Red regions indicate the area classified as background.

2.22.2 Image Sectioning and Area Selection for Analysis

In the spinal cord, specific regions were selected for quantification: the ventral horns, the dorsal column, and the lateral corticospinal tracts (Figure 2.16). The ventral horns are a region of grey matter within the spinal cord, that contains the lower motor neurons. The dorsal column and lateral corticospinal tracts are white matter tracts. The dorsal column is an ascending tract associated with transmission of sensory information such as fine touch and vibration sensations (Al-Chalabi and Alsalman, 2018). It is thought to be relatively spared by MND pathology. The corticospinal tracts are descending tracts and contains 90% of the corticospinal fibres of the pyramidal tract, which are responsible for the control of voluntary movement in the contralateral limb (Javed and Lui, 2018). The corticospinal tract is a major site of degeneration in MND (Ellis *et al.*, 2001; Ince *et al.*, 2003; Karlsborg *et al.*, 2004).

During analysis of spinal cord, if the regions of interest could not be identified by eye, a Luxol fast blue stained section was used to identify white and grey matter (Figure 2.16). Luxol fast blue stained TMA sections were also used to identify white and grey matter. Although every effort was made to keep white and grey matter separate during TMA construction, some punches would capture both white and grey, especially in the punch was taken near a tissue boundary. If this occurred only the tissue type of interest would be selected for analysis.

For all analysis, a small border was from around the edges of all tissue was excluded from the analysis. During the staining process, reagents can become trapped under the edges of the tissue resulting in an artificially dark or non-specific stain.

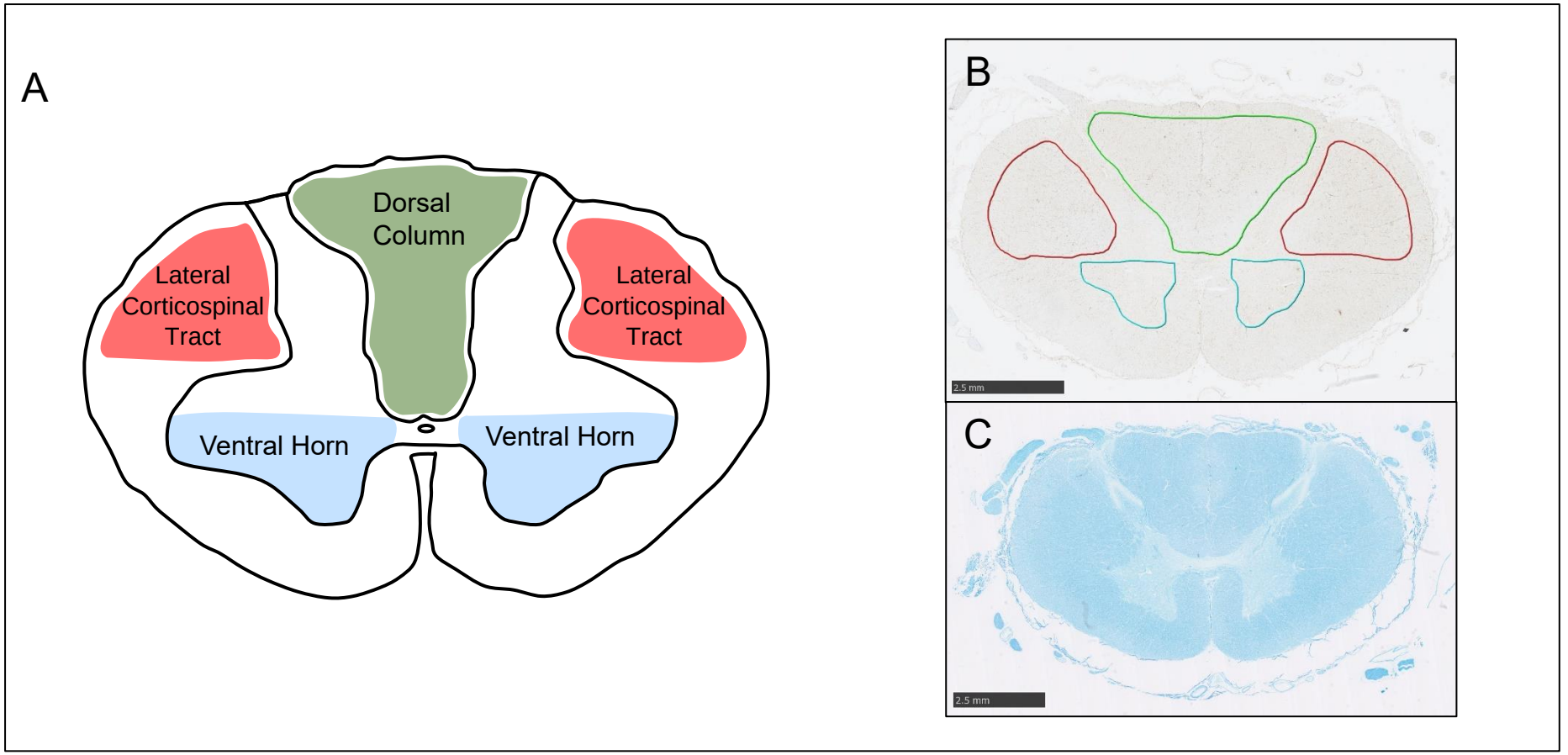

Figure 2.16 Spinal Cord Regions Selected for Quantitative Analysis

A) Schematic diagram of spinal cord regions selected for quantitative analysis of immunoreactivity: the ventral horns shown in blue, the lateral corticospinal tracts shown in red, and the dorsal column shown in green.

B) Example of the region identification in the spinal cord used for immunoreactivity quantification. Spinal cord section is of a control case stained for HLA-DR. Scale bar = 2.5mm. Ventral horns are shown in blue, lateral corticospinal tracts are shown in red and the dorsal column in shown in green.

C) Luxol fast blue stained section used to identify regions of white and grey matter for image quantification. Section is the same control case show in Figure 2.15 A. Scale bar = 2.5mm.

2.21.3 Calculation Steps

Calculation steps were added by Liam Wilson (Wilson, 2018) to the app to facilitate interpretation of the raw data. A density calculation was created using a measurement of all labels (background and DAB, see below for the formula). This calculation gave an overview off all DAB staining, including transverse sections of microglia/ processes.

$$Staining\ density = \frac{Total\ area\ of\ all\ DAB\ staining}{Total\ Area\ of\ background\ and\ DAB\ staining} \times 100$$

A count of stained microglia was conducted by removing DAB-stained areas of less than 26.45μm^2 using the post processing function. This count used to derive the average microglial label size alongside the total area positively stained for DAB using the following formula.

$$Average\ Microglial\ Label\ Size = \frac{Total\ Area\ of\ DAB\ Staining}{Number\ of\ microglial\ labels}$$

2.21.4 Statistical Analysis

All further statistical analysis was performed using GraphPad Prism (versions 7,8,9). For all statistical analysis the significance value was set at $p<0.05$.

Test for Gaussian Distribution

Before each statistical test was used, the data was checked for to see how well the data fit a gaussian distribution using the Shapiro-Wilk test to determine the most

appropriate statistical test. Where data was non-normally distributed, as indicated by a non-significant result ($p>0.05$), non-parametric tests were used.

Comparing Staining Density between control and sMND

Kruskal-Wallis one- way Analysis of Variance (ANOVA) or Kruskal-Wallis test, the non-parametric equivalent of one-way ANOVA, were used to make multiple comparisons between groups. This test compares mean ranks. Pairwise comparisons were performed using Mann-Whitney *U* tests, which is the non-parametric test equivalent to a Students t-test. Where appropriate, one tailed tests were selected as the results from Chapter 3 or previous literature had indicated the expected direction of the test outcome.

Staining Density with Length of survival

To examine the relationship between immunoreactivity and patient survival, sMND cases were split into fast or slow progressing groups. The median length of survival for each cohort, was used to split cases into groups. Staining density (% area) was compared between groups using one-way Kruskal-Wallis test. If a significant difference was observed between groups, pairwise comparisons were performed using Mann-Whitney U tests.

2.22 Semi-Quantitative Analysis of Neuronal Expression of APOE

To examine whether expression of APOE by motor neurons in the ventral horn of cervical spinal cord was affected by disease status, motor neurons were manually classified and counted. Neurons were classified as high expressing if the DAB intensity was significantly darker than the surrounding parenchyma or similar to glial expression, or low expressing if the DAB intensity was the same as the surrounding tissue or DAB staining was absent or paler than the parenchyma. Counting was completed using the 'points' function in QuPath image analysis software (QuPath v0.3.1, Bankhead *et al.*, 2017). The proportion of high to low expressing cells was expressed as a single value $(high\ expressing\ \div\ low\ expressing)$. Counts were compared between control and sMND using a Mann-Whitney U test. Statistical analysis was performed using GraphPad Prism (Version 9).

2.23 Quantitative Analysis of White Matter Pallor using QuPath

QuPath image analysis software (QuPath v0.3.1, Bankhead *et al.*, 2017) was used to quantify WM pallor in the spinal cord, using the pixel classification tool. The application was trained using five spinal cord images stained using Luxol fast blue to identify areas containing WM and areas without WM by manually selecting and labelling these regions.

As Luxol fast blue stains phospholipids in WM, areas of pallor have a similar appearance to grey matter. Therefore, to quantify pallor, regions of white matter (the dorsal column and lateral corticospinal tracts) were selected manually for analysis (Figure 2.7). The pre-trained pixel classification tool gave a measurement of the total area measured (μm^2), area of pallor (μm^2), area of WM (μm^2), and percentage area classified as WM (%) formula is given below.

$$Percentage\ WM\ pallor\ area = \frac{area\ of\ white\ matter\ pallor}{total\ area} \times 100$$

Statistical Analysis

Comparisons of percentage WM pallor area between control and sMND were performed using a Kruskal-Wallis test. Pairwise comparisons were performed using one tailed Mann-Whitney *U* test. The relationship between white matter pallor (percentage white matter pallor area) and microglial markers were tested using Spearman's Correlation. All statistical analysis was performed using GraphPad Prism (version 9).

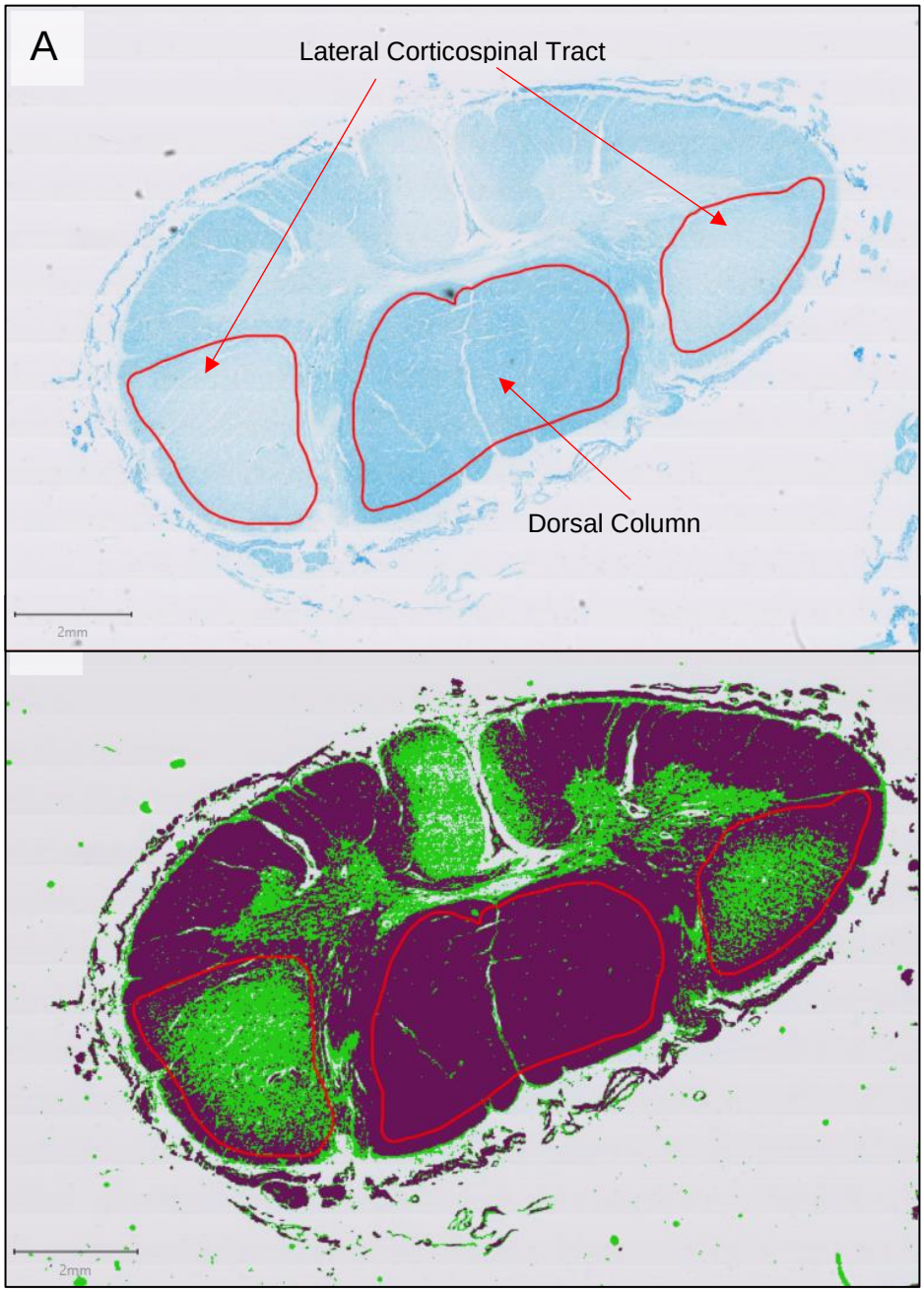

Figure 2.17 White Matter Pallor quantification using QuPath

A) Selection of the lateral corticospinal tracts and dorsal column for quantification

B) Classification of white matter (purple) and areas without myelin (green) by the pixel classification application. Areas classified as white matter pallor can be seen as green regions in the lateral corticospinal tracts

Scale bars=2mm

2.24 Semi-Quantitative Image Analysis

Additional semi-quantitative analysis was performed on APOE cervical spinal cord slide images. Motor cortex slides were analysed using semi-quantitative analysis only. Images of each region of interest (ROI; 62µm^2) were taken across the ventral horn, dorsal column, and lateral corticospinal tract. For each spinal cord region, the three images were taken at random, per case, and the case number was hidden to prevent identification of MND and control cases (Figure 2.18). For the spinal cord cases each case was then scored, using a 4-point rating scale, on the DAB intensity of the neuropil (Figure 2.19) within the highlighted region. Motor cortex cases were ranked using a 5-point scale, to better account for the higher variation of APOE staining in the cortex (Figure 2.19). To rate each region per case, one score was given, as an average of the intensity of staining across the three images per case. The rating scale was created using a range of images from APOE and cervical spinal cord and motor cortex images. This scale was created by ordering all APOE images for each region from lightest to darkest and using the lightest, first quartile, second quartile and darkest image.

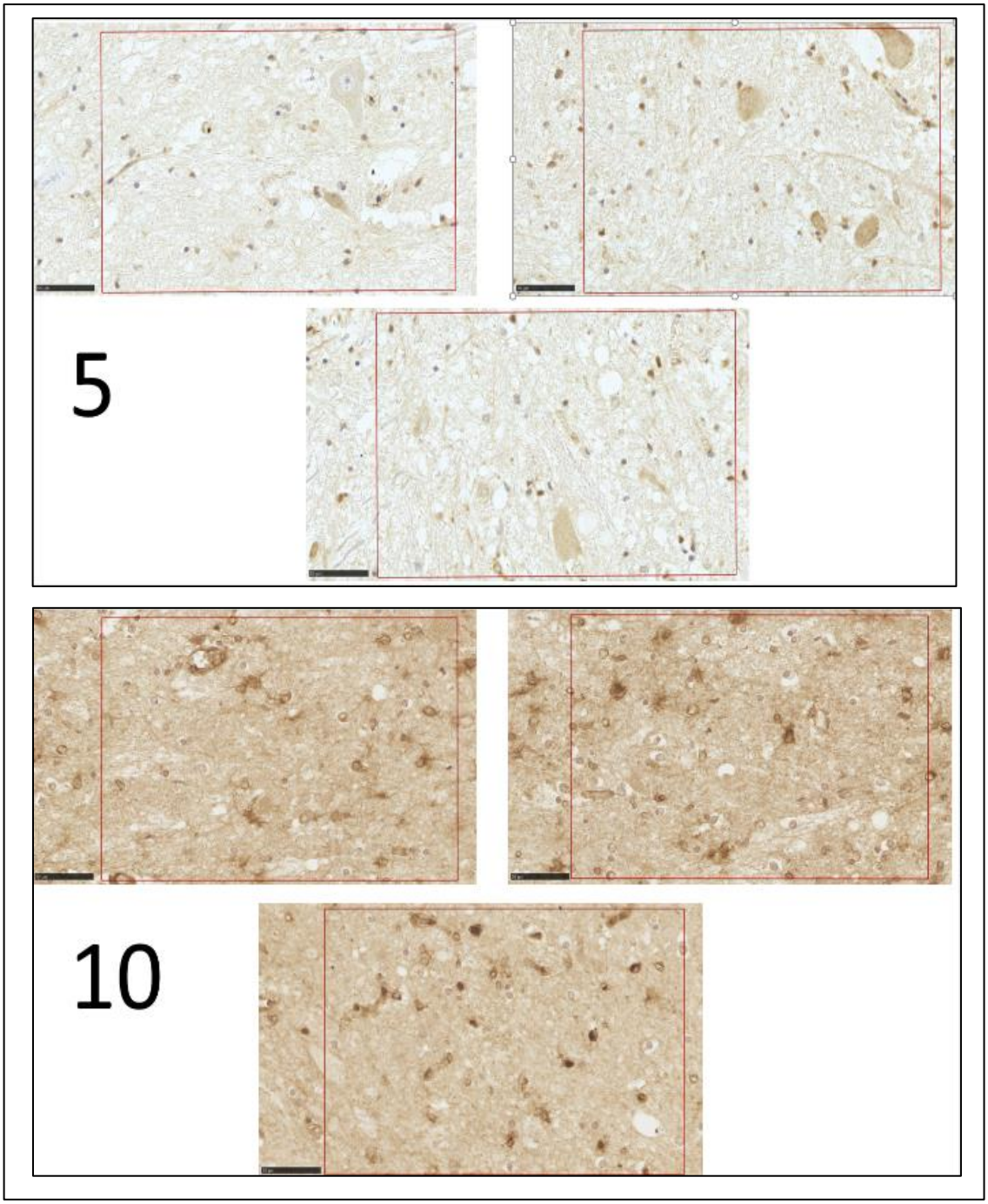

Figure 2.18 Example Images used to Semiquantitatively Score Cases.

Scorers focused on the area highlighted on the red rectangle, and were asked to give one score based on the average colour of DAB staining across all three images. Each case had three images per region to account for variability in staining.

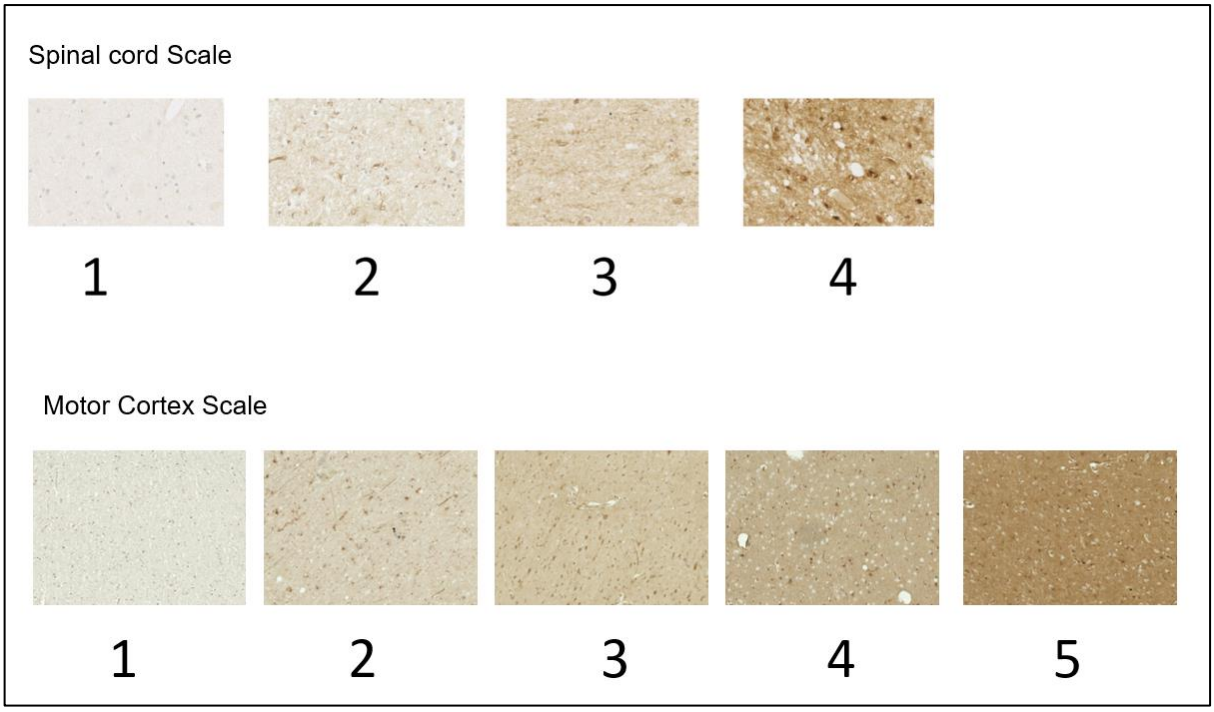

Figure 2.19 Rating scale to score DAB intensity on neuropil.

Scorers were advised to focus on overall neuropil staining rather than individual cells. Due to the greater variety of APOE immunoreactivity in the motor cortex, an extra point was added to the ranking scales.

2.24.1 Inter-Rater Reliability

Following initial scoring, another person (MMM for spinal cord, and JRH for the motor cortex cases) was asked to rate the average intensity of DAB staining in the neuropil of the cases, blind to case identity and disease status. For the motor cortex and underlying white matter, the whole TMA core image was given. For spinal cord, three fields of view were given per spinal cord region.

The cases were also scored by the author (BAA). Once the images had been scored twice, the scores for each case were compared and the percentage of

agreement was calculated for all cases, and the control and MND cases separately. Inter-rater reliability was assessed using the Cohens Kappa test (Cohen, 1960). The Cohens Kappa test is used to determine the level of agreement between the two scorers and is more robust than comparing percentage agreement as the Kappa factors in the likelihood of agreement being reached by chance.

As an ordered rating scale was used, a weighted Kappa (Cohen, 1968) was selected, as this considers not only whether the two scorers agreed or disagreed, but how close the scores were e.g., a rating of 3 and 4 is much closer than a rating of 1 and 4. These disagreements are weighted by the magnitude of different between the raters score. All cases, stained for APOE were rated. The GraphPad Prism quick calculations site was used to perform the analysis (https://www.graphpad.com/quickcalcs/kappa1/). Interpretation of the Cohens Kappa score was made using the scale shown in Table 2.22 (Landis and Koch, 1977).

Table 2.27 Interpretation of Cohen's Kappa score

Kappa Value	Level of Rater Agreement
< 0	No agreement
0.00 and 0.20	Slight agreement
0.21 and 0.40	Fair agreement
0.41 and 0.60	Moderate agreement
0.61 and 0.80	Substantial agreement
0.81 and 1.00	Almost perfect agreement

Analysis

Scorer MMMs and JRHs data was used to analyse neuropil staining as these raters was free from any bias. Immunoreactivity scores between control and sMND were compared using the Kruskal-Wallis test. Post-hoc comparisons were completed using Mann-Whitney U tests.

2.25 Genome-wide RNA Analysis of Stalled Protein Synthesis (GRASPS)

GRASPS are a novel method, currently under development by Dr Guillaume Hautbergue's laboratory, is a protocol to isolate ribosome-associated mRNA from the cytoplasm and extract these mRNA from the complex. This protocol aims to provide transcriptional data that closer represents protein expression.

Materials

Table 2.28 Buffers for GRASPS Analysis

Buffer	Components	Supplier and Catalogue Reference
Buffer A	250mM Sucrose	Melford S0809
	5mM Potassium Chloride	SIGMA P9333-500G
	50mM Tris-HCL (pH7.4)	
Buffer B	250mM Sucrose	Melford S0809
	500mM Potassium Chloride	
	50mM Tris-HCL (pH7.4)	
	5mM $MgCl_2$	
Sucrose Cushion Solution	1M Sucrose	Melford S0809
	5mM $MgCl_2$	
	50mM Tris-HCL (pH7.4)	
Ribosomal Resuspension Buffer (RRB)	50mM HEPES Buffer	HEPES (Sigma, H3375) 0.5M pH7.9
	150mM Sodium Chloride	Fisher Scientific s/316/65
	1mM DTT	
	1mM EDTA	

Table 2.29 Reagents for GRASPS

Reagent/ Kit	Stock Preparation	Supplier	Catalogue reference
Protease Inhibitor Cocktail EDTA free		Roche	4693132001
Phenylmethylsulfonyl fluoride (PMSF)	100mM	Sigma	10837091001
RNase inhibitor		Meridian	Bio-65028
NP-40	10% NP-40 made up in DEPC H2O	Sigma	9016-45-9
Potassium Chloride (4M)			
Protienase K		Thermo Fisher Scientific	25530049
Trizol (PureZole RNA Isolation Reagent, Trizole)		Bio-Rad	7326890
Chloroform			
Sodium Acetate 3M (pH5.2)			
Glycogen			
Isopropanol			
70% Ethanol in DEPC water			

Table 2.30 Cohort for GRASPS Analysis

Disease Status	Sample Number	Case	Age	Sex
Control	1	032/2000	43	M
	2	002/2000	58	M
	3	101/1992	65	F
sMND	4	135/1994	42	M
	5	089/1994	58	M
	6	1025/1989	61	F

Methods

Frozen spinal cord tissue from three control and three sMND cases underwent GRASPS RNA extraction for cDNA synthesis (Table 2.27). Permission was given for this work from the Sheffield Brain and Tissue Bank (see Appendix E). Frozen

tissue sections were cut at 5µM thick using a microtome and placed in sterile RNAse free microtubes. All blades and equipment were sterilised using methylated spirits. All steps were performed on ice, with chilled tubes. All microtubes and pipette tips were DNase free.

Spinal cord tissue was resuspended in a solution of 16µL Protease Inhibitor Cocktail, 16µL PMSF and 0.4µL RNase inhibitor. Homogenisation beads were added, and the tissue was homogenised using at 5500rpm twice in the Precelly Evolution homogeniser. Samples were placed on ice for 10 minutes before the homogenisation process was repeated. To this solution, 63µL of cold 10% NP-40 was added, and the solution was left on ice for 10 minutes, with occasional gentle mixing. From the solute, 20µL was saved for extraction

Lysates were transferred to a 6-well plate. The plate was UV-irradiated on ice at 0.3J/cm^2. Lysates were transferred to fresh microtubes, and the solutions were centrifuged at 750xg for 10 minutes at 4^oC to pellet the nuclei. The supernatant was transferred to fresh ice-cold microtubes leaving a small amount of the supernatant on top of the pellet. The supernatant was then centrifuged again to pellet the mitochondrial fraction at 12,500xg for 10 minutes at 4^oC. From this, 750µL of the post-mitochondrial fraction to a new cold microtube, to which 107µL of 4M KCL. This was mixed by gently pipetting.

To pellet the dissociated ribosomal subunits, for each sample, 1ml of the sucrose cushion solution was added to ice-cold TLA100 centrifuge tubes. The KCL-adjusted post-mitochondrial fraction was made up to 950µL with 208µL of Buffer B, and 900µL was carefully loaded on top of the sucrose cushion. Tubes were

balanced precisely at 0.01g with Buffer B and centrifuged at 250,000xg (75,000rpm) for 2 hours at 4 ^{o}C.

The supernatant was removed, and the pellet was washed with 150µL of cold dH_2O, being careful not to disturb the pellet, and the dH_2O was removed. The pellet was resuspended in 250µL of the Ribosomal Resuspension Buffer to which 1.25µL of Proteinase K and 0.5µL of RNase inhibitor. Samples were incubated in a heating block, pre-heated to 37 ^{o}C for 30 minutes, and pulse mixing the samples every 5 minutes. Following the incubation, 5µL of EDTA and 42µL of sodium acetate, and the solution was vortexed to mix.

To the solution, 750µL of Trizol was added, and the solution was thoroughly mixed by shaking. To the input samples, 80µL of Trizol was added and pipetted to mix. The solutions were then left to incubate at room temperature for 10 minutes.

Chloroform was added to the solutions at a ratio of 1:3; 3ml to the GRASPS, and 300µL to the input samples. The solutions were vigorously mixed for 30 seconds and left at room temperature for 10 minutes. The solutions were centrifuged at 13,000 rpm for 10 minutes at 4^{o}C to separate the aqueous phase from the organic phase. The aqueous phase was transferred to a new RNase free tube sodium acetate was added: 30µL for input samples and 60µL for GRASPS samples. To these solutions, 1µL of glycogen was added and the samples mixed. Isopropanol was added 300µL for the input samples and 600 µL to the GRASPS samples. The RNA was allowed to precipitate out at -20^{o}C.

Following the precipitation, the samples were centrifuged at 13,000 rpm for 20 minutes at 4^{o}C. The supernatant was discarded at the RNA pellet washed in 500µL of 70% Ethanol in DEPC water. Samples were centrifuged at 13,000 rpm for 20 minutes at 4^{o}C. The supernatant was completely removed at the pellet allowed to dry for 10 minutes to allow any alcohol to evaporate. The RNA pellet was resuspended in 15µL of DEPC water. RNA concentration was checked using the Nanodrop Spectrophotometer.

2.26 cDNA Synthesis

Materials

Table 2.31 cDNA Synthesis Kit

Reagent/ Kit	Manufacturer	Catalogue Number
Quanta qScript Supermix	Quanta BioScience	95048-025

Methods

cDNA synthesis was performed using Quanta qScript Supermix. This mix contains optimised concentrations of deoxyribonucleotide triphosphatyes, magnesium chloride, recombinant RNase inhibitor protein, qScript reverse transcriptase, random primers, oligonucleotide primer and stabilisers. To 8µL of RNA, 2µL of the qScript Supermix was added, in 0.2ml RNAse free microtubes. The solutions were pipetted to mix and briefly centrifuged to collect the contents are the base of the tubes. The samples were incubated at 25^{o}C for 5 minutes, 42^{o}C for 30 minutes, and 85^{o}C for 5 minutes, then held at 4^{o}C. To confirm cDNA synthesis was

successful reverse transcription polymerase chain reaction (PCR) was performed using Beta Actin Primers (Table 2.32).

Table 2.32 Beta Actin Primer Sequences for PCR

Gene	Primer Sequence (5'-3')	Product Size (bp)
Beta Actin	F: TCC CCC AAC TTG AGA TGT AAG	100
	R: AAC TGG TCT CAA GTC AGT GTA CAG D	

The PCR reaction mix was performed by combining 10µL 2x PCR Master Mix, 1µL each of the forward and reverse primer, 7µL of nuclease-free water, and 1µL of cDNA, into a sterile 0.2 ml Eppendorf tube. A no template control was also performed (cDNA replaced with H_2O) to check for contamination. Samples were thoroughly mixed and spun down to collect the contents at the base of the tube. The PCR reaction was performed in a thermocycler with the following programme: denaturation at 95ºC for 10 minutes then 40 cycles of (95ºC for 15 seconds, 60ºC for 60 seconds) and 72ºC for 15 minutes. The samples were held at 4 degrees and refrigerated briefly before use.

2.27 Agarose Gel Electrophoresis of PCR products

Materials

Table 2.33 Reagents for Agarose Gel Electrophoresis

Reagent/ Kit	Manufacturer	Catalogue Number
Agarose Powder	Bioline	Bio-41025
Ethidium Bromide	Sigma-Aldrich	E1510
HyperLadder V now HyperLadder 25 bp	Bioline	BIO-33057

Tris Acetate EDTA (TAE) Buffer	
50x Buffer	242 g tris base in double-distilled H_2O
	57.1 ml glacial acetic acid
	100 ml 0.5 M EDTA solution (pH 8.0)
	Adjust volume to 1 L.
50x buffer diluted to1x with dH_2O	

Methods

The beta-actin PCR products were run on an agarose gel to check for amplification. First, the agarose gel was prepared by adding 1.5g of agarose powder to 10ml tris-acetate-EDTA (1x TAE) buffer. This solution was heated in the microwave until bubbling, to dissolve the agarose. The solution was allowed to cool, and 2µL of ethidium bromide was added. The gel solution was poured into a cassette, and a comb was placed in the solution and allowed to cool for approximately 45 minutes until set. Agarose gels were placed into an electrophoresis tank and covered with 1x TAE buffer. To the gel, 5µL of Hyperladder V plus 10µL of each sample, as well as the no template control. The

gel was left to run at constant voltage (100V), for ~60 minutes and images were captured using the GENi UV light imaging system (Syngene, UK).

2.28 Real-Time Quantitative PCR

Materials

Table 2.34 Reagents and Primer Sequences for Real-Time Quantitative

Reagent/ Kit	Manufacturer	Catalogue Number
Luna® Universal Probe qPCR Master Mix	New England Bio Labs	M3004L
Multiplate Low Profile 96 well PCR plate	Bio Rad	MLL9651
Microseal 'C' film PCR plate Sealing Film, adhesive optical	Bio Rad	MSC1001

Gene Name	Primer Sequence	
Actin Beta	1	5'-ACAGAGCCTCGCCTTTG-3'
	2	5'-CCTTGCACATGCCGGCG-3'
	Probe	5'-/56-FAM/TCATCCATG/ZEN/GTGAGCTGGCGG/31ABkFQ/-3'
APOE	1	5'-TCTGAGCAGGTGCAGGA-3'
	2	5'-GTTGTTCCTCCAGTTCCGATT-3'
	Probe	5'-56-FAM/CGTCCATCA/ZEN/GCGCCCTCA/31ABkFQ-3'
TREM2	1	5'-GCTGCTCATCTTACTCTTTGTC-3'
	2	5'-TCATAGGGGCAAGACACCT-3'
	Probe	5'-56-FAM/TGTGGGCTC/ZEN/CGGACAGCTC/31ABkFQ-3'
TYROBP	1	5'-CGAGTCGCCTTATCAGGAG-3'
	2	5'-GTTGCTGACTGTCATGATTCG-3'
	Probe	5'-56-FAM/TCGCTGTAG/ZEN/ACATCCGACCTCTGA/31ABkFQ-3'

Methods

To measure gene expression, Real-Time quantitative PCR (RT qPCR) was performed using IDT PrimeTime qPCR assays. Primers were directed at Beta

Actin, APOE TREM2 and TYROBP (primer sequence see Table 2.30). A probe-based system was chosen over fluorescence dye-based systems due to the higher specificity and reduced need for optimisation.

All work was performed using sterile equipment and tubes. Each reaction was run in triplicate using the following reaction mix: 2µL of Prime-Time qPCR Assay Mix, 20µL of 2x Luna Master Mix, 3µL cDNA and 15µL of Nuclease Free Water. Luna Master Mix is light reactive, so this reagent was kept in foil during preparation. For each gene of interest, a no template control was also run to establish the background threshold and check for contamination. The master mix was thoroughly pipetted to mix and run in a 96-well plate. Care was taken not to introduce bubbles, and the plate was sealed with an optically clear sticker. Plates were spun down to collect the reaction in the base of the well. The reaction was run in a real-time thermocycler using the following protocol: 95ºC for 3 minutes and 40 cycles of 95ºC for 10 seconds, 60ºC for 30 seconds. Data was analysed using the $2^{-\Delta\Delta Ct}$ method to calculate fold change.

Chapter 3 Characterisation of the Neuroinflammatory Transcriptome

3.1 Introduction

Transcriptional analysis using human MND *post-mortem* material has highlighted the importance of inflammation as a disease process. Such studies have primarily focused on the on the spinal cord, which has shown an upregulation of inflammatory pathways compared to control cases (Dangond *et al.*, 2004; Offen *et al.*, 2009; Figueroa-Romero *et al.*, 2012; Jones *et al.*, 2015; Brohawn, O'Brien and Bennett, 2016; Andrés-Benito *et al.*, 2017; Cooper-Knock *et al.*, 2017). Furthermore, such studies have highlighted inflammation as a modifier of survival (Cooper-Knock *et al.*, 2017).

The motor cortex has been less widely examined compared to the spinal cord. Wang *et al.* (2006), showed a downregulation of inflammatory pathways. However, Lederer *et al.* (2007) and Aronica *et al.* (2015) both found an increase in inflammatory and immune transcripts in the motor cortex.

The aim of this chapter was to characterise the neuroinflammatory transcriptome in the motor regions of the CNS of human sMND. Gene expression analysis was performed on *post-mortem* ventral horn of spinal cord and the motor cortex, from sMND cases and neurologically healthy control cases.

Initially the NanoString platform was used to analyse formalin-fixed paraffin-embedded (FFPE) tissue from the cervical spinal cord, due to the large volume of cases available. Historically, extracting sufficient RNA of usable quality has proved

challenging from FFPE tissue. However, improvements in RNA extraction and quantification methods have started to allow the use of such tissue (Bibikova *et al.*, 2004; April *et al.*, 2009). Following this first trial, quality control analysis was performed, which highlighted potential complications with this method.

Following further optimisation, the NanoString analysis was repeated using cervical spinal cord and motor cortex from flash frozen tissue.

The objectives of this chapter were:

1. To define the inflammatory transcriptomic profile in the ventral horn from cervical spinal cord and the motor cortex in sMND.
2. To identify key inflammatory pathways associated with sMND.
3. To explore the relationship between inflammation and survival in sMND.
4. To identify the microglial signature in human sMND.
5. To validate these data using another expression quantification method.
6. Identify targets for further validation via immunohistochemistry.

The hypotheses underlying the characterisation were as follows:

1. The motor regions of the CNS will show an upregulation of inflammatory signalling in sMND compared to controls via the NanoString platform.
2. There will be an upregulation of pathways associated with both pro and anti-inflammatory functions.
3. In those more rapidly progressing sMND cases, there will be an upregulation of proinflammatory signalling. Cases with longer survival will be associated with anti-inflammatory and neuroprotective inflammatory signalling.

4. Genes associated with microglial/macrophage expression will not fully conform to the M1/M2 microglial classification but will show elements of both, although there may be a tendency for one of these to be favoured. The microglial signature will show an upregulation of both pro and anti-inflammatory genes, as well as those associated with phagocytosis.
5. Data from published data sets will agree with neuroinflammatory gene expression data generated using NanoString.

3.2 Results: Gene Expression Profiling of Inflammatory Signalling in FFPE Spinal Cord in sMND.

3.2.1 RNA Extraction

RNA quality was assessed immediately after extraction. The concentrations, and 260:280 and 260:220 optical density ratios for the RNA extracted from FFPE spinal cord as measured using the Nanodrop Spectrometer are shown in Table 3.1.

Most FFPE spinal cord cases achieved a good yield of RNA; the mean concentration of RNA achieved was 20.14 ng/µl (range 7.9-50.1 ng/µl). Examination of the optical density ratios showed evidence of some contamination, as indicated by the low ratio values given. Most samples (17/24) met the NanoString criteria of an optical density value for the 260:230 ratio. A low 260:280 ratio could indicate contamination of protein or phenol. All samples had low 260:230 ratios, which could be an indication of guanidine salt contamination from the TRIzol reagent, or low RNA concentration (Thermoscientific, 2012; Choi *et al.*, 2017).

Table 3.1 FFPE Spinal Cord RNA Quantity and Quality Data

Case Number	Disease Status	RNA Concentration (ng/µl)	260:280	260:230
085/2007	control	25.6	1.59	0.58
335/1990	control	18.7	1.65	1.09
035/1996	control	13.7	1.82	0.57
014/1999	control	11.6	1.45	0.74
056/1990	control	11.8	1.8	1.29
309/1990	control	11.1	1.51	0.88
144/1991	control	16.1	1.52	0.72
098/2007	control	24.9	1.78	1.16
009/2017	sMND	17.4	1.73	1.05
025/2013	sMND	8.7	1.81	0.8
072/2005	sMND	17.4	1.65	1.24
094/2006	sMND	11.6	1.93	0.92
077/1986	sMND	7.9	1.71	0.63
105/2007	sMND	26.1	1.76	1.16
094/2009	sMND	32.5	1.76	0.94
005/2010	sMND	37.4	1.83	1.16
041/2008	sMND	17.7	1.96	1.26
023/2010	sMND	37.6	1.95	1.39
091/2008	sMND	35.3	1.89	1.19
074/2009	sMND	20.9	1.61	1.11
004/2006	sMND	50.1	1.93	1.39
059/2009	sMND	16.3	2	0.75
072/2002	sMND	47.1	1.79	1.04
099/2009	sMND	21	1.98	1.19

3.2.2 Differential Gene Expression Analysis for FFPE Spinal Cord Data

The inflammatory transcription profile of FFPE spinal cord from 16 sMND cases and 8 neurologically normal control cases was generated using the NanoString Neuroinflammation panel.

To identify differentially expressed genes, the sMND transcriptional profile was compared to that of the control groups, controlling for age and sex, using Voom-Limma analysis. The Benjamini-Hochberg correction was applied to lower the false discovery rate. Transcripts were determined to be significant if the fold change was $\geq|1.5|$, with a corrected p value, $q<0.05$.

Of the 770 gene probes on the panel, 100 genes were found to be significantly differentially expressed (Figure 3.1). Of these, 62 were upregulated (Table 3.2) and 38 were downregulated (Table 3.3). Those neuroinflammatory genes with the largest absolute fold change were upregulated in sMND, indicating an upregulation of inflammatory signalling in the spinal cord in sMND.

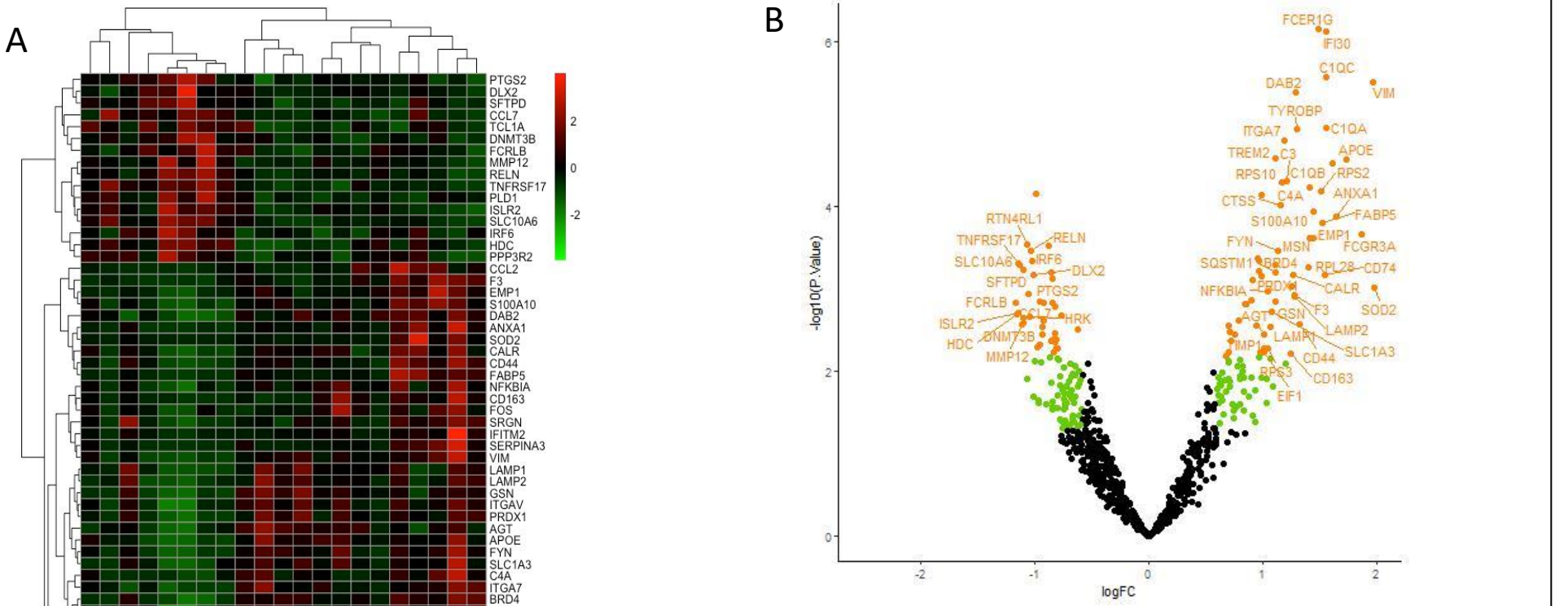

Figure 3.1 sMND is associated with an Increase in Inflammatory Signalling in the Spinal Cord – FFPE Tissue

A. Heatmap displaying the expression the top 71 significantly expressed genes (FC<1.5, p>0.05) out of 100 differentially expressed between MND and neurologically healthy cases. Hierarchal clustering group the majority of MND cases and control cases, shown on the x axis, genes are shown on the y axis.

B. Volcano plot showing fold change against the significance value. Of all the significant genes 62 were upregulated, and 38 genes were down regulated (Green Points p<0.05; FC>1.5; Orange Points FDR adjusted p<0.05; FC>1.5, labelled points FDR adjusted p<0.05; FC>2).

Table 3.2 Upregulated Genes from sMND FFPE Spinal Cord

Gene Name	Gene Symbol	Fold Change	P	Q
serpin family A member 3	SERPINA3	6.427	<0.001	0.001
secreted phosphoprotein 1	SPP1	4.744	<0.001	0.001
superoxide dismutase 2	SOD2	3.958	0.001	0.015
vimentin	VIM	3.926	<0.001	0.001
Fc fragment of IgG receptor IIIa	FCGR3A	3.662	<0.001	0.007
apolipoprotein E	APOE	3.330	<0.001	0.002
annexin A1	ANXA1	3.122	<0.001	0.005
complement C1q B chain	C1QB	3.058	<0.001	0.002
complement C1q C chain	C1QC	2.952	<0.001	0.001
complement C1q A chain	C1QA	2.951	<0.001	0.001
IFI30 lysosomal thiol reductase	IFI30	2.945	<0.001	<0.001
CD74 molecule	CD74	2.917	0.001	0.012
fatty acid binding protein 5	FABP5	2.874	<0.001	0.005
ribosomal protein S2	RPS2	2.866	<0.001	0.003
Fc fragment of IgE receptor Ig	FCER1G	2.822	<0.001	<0.001
S100 calcium binding protein A10	S100A10	2.723	<0.001	0.004
epithelial membrane protein 1	EMP1	2.719	<0.001	0.007
complement C4A (Rodgers blood group)	C4A	2.671	<0.001	0.003
moesin	MSN	2.655	<0.001	0.007
ribosomal protein L28	RPL28	2.652	0.001	0.011
CD44 molecule (Indian blood group)	CD44	2.514	0.003	0.028
transmembrane immune signalling adaptor TYROBP	TYROBP	2.468	<0.001	0.001
DAB adaptor protein 2	DAB2	2.444	<0.001	0.001
lysosomal associated membrane protein 2	LAMP2	2.437	0.001	0.018
coagulation factor III, tissue factor	F3	2.431	0.001	0.018
calreticulin	CALR	2.411	0.001	0.012
peroxiredoxin 1	PRDX1	2.384	0.001	0.015
Cluster of Differentiation 163	CD163	2.370	0.006	0.047
complement C3	C3	2.314	<0.001	0.003
integrin subunit alpha 7	ITGA7	2.275	<0.001	0.001
ribosomal protein S10	RPS10	2.250	<0.001	0.003
cathepsin S	CTSS	2.233	<0.001	0.004
FYN proto-oncogene, Src family tyrosine kinase	FYN	2.197	<0.001	0.009
bromodomain containing 4	BRD4	2.168	0.001	0.011
sequestosome 1	SQSTM1	2.164	0.001	0.012
gelsolin	GSN	2.159	0.001	0.019
triggering receptor expressed on myeloid cells 2	TREM2	2.158	<0.001	0.002
solute carrier family 1 member 3	SLC1A3	2.117	0.002	0.023
lysosomal associated membrane protein 1	LAMP1	2.091	0.003	0.029
NF-κB inhibitor alpha	NFKBIA	2.064	0.001	0.017
ribosomal protein S3	RPS3	2.061	0.005	0.044
TIMP metallopeptidase inhibitor 1	TIMP1	2.017	0.005	0.044
eukaryotic translation initiation factor 1	EIF1	2.015	0.006	0.046

angiotensinogen	AGT	2.011	0.004	0.033
coactosin like F-actin binding protein 1	COTL1	1.988	<0.001	0.003
major vault protein	MVP	1.986	0.001	0.012
ribosomal protein L29	RPL29	1.980	0.006	0.046
RAB7A, member RAS oncogene family	RAB7A	1.955	0.001	0.012
proteasome 20S subunit beta 8	PSMB8	1.955	<0.001	0.011
granulin precursor	GRN	1.949	<0.001	0.011
integrin subunit alpha V	ITGAV	1.932	0.003	0.029
junctional adhesion molecule 2	JAM2	1.889	0.001	0.013
ATPase H+ transporting V0 subunit e1	ATP6V0E1	1.870	0.001	0.019
structural maintenance of chromosomes 1A	SMC1A	1.816	0.002	0.019
BCL2 associated agonist of cell death	BAD	1.800	0.002	0.019
macrophage scavenger receptor 1	MSR1	1.730	0.002	0.027
mitochondrial antiviral signalling protein	MAVS	1.691	0.004	0.033
BCL2 associated X, apoptosis regulator	BAX	1.658	0.004	0.038
AKT serine/threonine kinase 1	AKT1	1.644	0.003	0.032
lysine methyltransferase 2C	KMT2C	1.631	0.006	0.046
TNF receptor superfamily member 1A	TNFRSF1A	1.630	0.003	0.029

Table 3.3 Down Regulated Genes from sMND FFPE Spinal Cord

Gene Name	Gene Symbol	Fold Change	P	Q
Fc receptor like B	FCRLB	-2.244	0.001	0.019
histidine decarboxylase	HDC	-2.234	0.002	0.024
solute carrier family 10 member 6	SLC10A6	-2.206	<0.001	0.011
immunoglobulin superfamily containing leucine rich repeat 2	ISLR2	-2.205	0.002	0.024
TNF receptor superfamily member 17	TNFRSF17	-2.184	<0.001	0.011
DNA methyltransferase 3 beta	DNMT3B	-2.157	0.003	0.028
surfactant protein D	SFTPD	-2.146	0.001	0.012
C-C motif chemokine ligand 7	CCL7	-2.145	0.002	0.025
matrix metallopeptidase 12	MMP12	-2.141	0.003	0.028
reticulon 4 receptor like 1	RTN4RL1	-2.087	<0.001	0.008
prostaglandin-endoperoxide synthase 2	PTGS2	-2.079	0.001	0.018
harakiri, BCL2 interacting protein	HRK	-2.058	0.002	0.025
reelin	RELN	-2.042	<0.001	0.009
interferon regulatory factor 6	IRF6	-2.032	<0.001	0.011
distal-less homeobox 2	DLX2	-2.021	0.001	0.012
suppressor of variegation 3-9 homolog 2	SUV39H2	-1.986	<0.001	0.003
CEA cell adhesion molecule 3	CEACAM3	-1.971	0.005	0.044
triggering receptor expressed on myeloid cells 1	TREM1	-1.943	0.001	0.019
cathepsin W	CTSW	-1.941	0.005	0.041
phospholipase D1	PLD1	-1.905	0.004	0.033
RAD51 paralog B	RAD51B	-1.901	0.003	0.029
lymphotoxin alpha	LTA	-1.897	0.001	0.019
E2F transcription factor 1	E2F1	-1.890	0.002	0.027
C-type lectin domain containing 7A	CLEC7A	-1.832	<0.001	0.008
ADAM metallopeptidase with thrombospondin type 1 motif 16	ADAMTS16	-1.812	0.004	0.038
flap structure-specific endonuclease 1	FEN1	-1.804	0.001	0.012
suppressor of variegation 3-9 homolog 1	SUV39H1	-1.793	0.001	0.019
family with sequence similarity 104 member A	FAM104A	-1.790	0.001	0.012
SH2 domain containing 1A	SH2D1A	-1.783	0.006	0.046
macrophage receptor with collagenous structure	MARCO	-1.768	0.004	0.039
Fas ligand	FASLG	-1.765	0.004	0.036
BLM RecQ like helicase	BLM	-1.761	0.003	0.032
solute carrier family 17 member 6	SLC17A6	-1.761	0.002	0.020
CD6 molecule	CD6	-1.758	0.005	0.044
transmembrane protein 100	TMEM100	-1.746	0.004	0.037
granulysin	GNLY	-1.736	0.005	0.044
prostaglandin E receptor 3	PTGER3	-1.705	0.002	0.025
lysine demethylase 2B	KDM2B	-1.539	0.003	0.030

3.2.3 Pathway Enrichment Analysis of the Differentially Expressed genes from sMND FFPE Spinal Cord.

To identify key cellular and biological pathways, enrichment analysis was performed by examining those KEGG pathways associated with the differentially expressed transcripts from sMND FFPE spinal cord. Pathways were ranked by the number of genes associated with each pathway and the top 15 are given (Table 3.4).

The top enriched pathway was the phagosome, other key pathways include the cyclic adenosine monophosphate (cAMP), RAS, sphingolipid and PI3K-Akt signalling pathways, and Natural Killer cell mediated cytotoxicity.

In all pathways, most genes showed increased expression indicating upregulation of these pathways in sMND.

Table 3.4 Enrichment Analysis of Differentially Expressed Genes from sMND FFPE Spinal Cord.

KEGG Symbol	KEGG Pathway	Number of Genes	Genes in Pathway	
			Upregulated Genes	Down Regulated Genes
hsa04145	Phagosome	14	ATP6V0E1, C3, CALR, CTSS, FCGR3A, HLA-E, ITGAV, LAMP1, LAMP2, MSR1 RAB7A, RAC1	CLEC7A, SFTPD
hsa05152	Tuberculosis	14	AKT1, BAD, BAX, C3, CD74, CTSS, FCER1G, FCGR3A, LAMP1, LAMP2, RAB7A, RHOA, TNFRSF1A	CLEC7A,
hsa05200	Pathways in cancer	13	AKT1, BAD, BAX, FOS, HIF1A, ITGAV, NFKBIA, RAC1, RHOA	FASLG, PLD1, PTGER3, PTGS2
hsa04380	Osteoclast differentiation	10	AKT1, FCGR3A, FOS, FYN, NFKBIA, RAC1, SQSTM1, TNFRSF1A, TREM2, TYROBP	
hsa05142	Chagas disease	10	AKT1, FCGR3A, FOS, FYN, NFKBIA, RAC1, SQSTM1, TNFRSF1A, TREM2, TYROBP	FASLG
hsa04024	cAMP signalling pathway	9	AKT1, BAD, FOS, NFKBIA, RAC1, RHOA	GRIN2B
hsa04510	Focal adhesion	9	AKT1, BAD, FYN, ITGA7, ITGAV, RAC1,	RELN
hsa05168	Herpes Simplex virus 1 infection	9	C3, CD74, FOS, HLA-E, MAVS, NFKIA, TNFRSF1A	FASLG, LTA
hsa05203	Viral carcinogenesis	9	BAD, BAX, C3, GSN, HLA-E, NFKBIA, RAC1, RHOA	HDAC4
hsa04014	Ras signalling pathway	8	AKT1, BAD, RAC1, RHOA	FASLG, GRIN2B, PLA2G4A, PLD1
hsa04071	Sphingolipid signalling pathway	8	AKT1, BAX, FCER1G, FYN, RAC1, RHOA, TNFRSF1A	PLD1
hsa04151	PI3K-Akt signalling pathway	8	AKT1, BAD, ITGA7, ITGAV, RAC1, SPP1	FASLG, RELN
hsa04650	Natural killer cell mediated cytotoxicity	8	FCER1G, FCGR3A, FYN, HLA-E, RAC1, TYROBP	FASLG, TNFRSF10B
hsa05166	Human T-cell leukemia virus 1 infection	8	AKT1, BAX, CALR, FOS, HLA-E, NFKBIA, TNFRSF1A	LTA
hsa05205	Proteoglycans in cancer	8	AKT1, CD44, HIF1A, ITGAV, MSN, RAC1, RHOA	FASLG

3.2.4 The Effect of the Length of Tissue Storage Time

Previous studies using FFPE material for gene expression analyses have noted a relationship between the length of tissue storage and poorer gene expression results (Hall *et al.*, 2012). To determine whether this relationship may have influenced the gene expression results, the length of time the FFPE spinal cord tissue have been in storage at the time of RNA extraction (years) was plotted against the maximum number of counts for each sample for the FFPE spinal cord data. The tissue storage time had a mean of 15.5 years and ranged from 2 to 33 years. A statistically significant negative correlation, with maximum count number decreasing as the length of tissue storage increased (Spearman's Correlation; $R=-0.634$, $P<0.01$, Figure 3.2) was observed. As such, after approximately 18-20 years of storage, the maximum count levels are reduced to below background noise level, which would limit the usefulness of performing gene expression work. As such, it was decided that future work would ideally be performed on cases stored for less than 18 years. As, this limited the cases eligible for cohort construction, the decision was made to use flash frozen tissue for further work, as this tissue preservation method is less damaging to RNA.

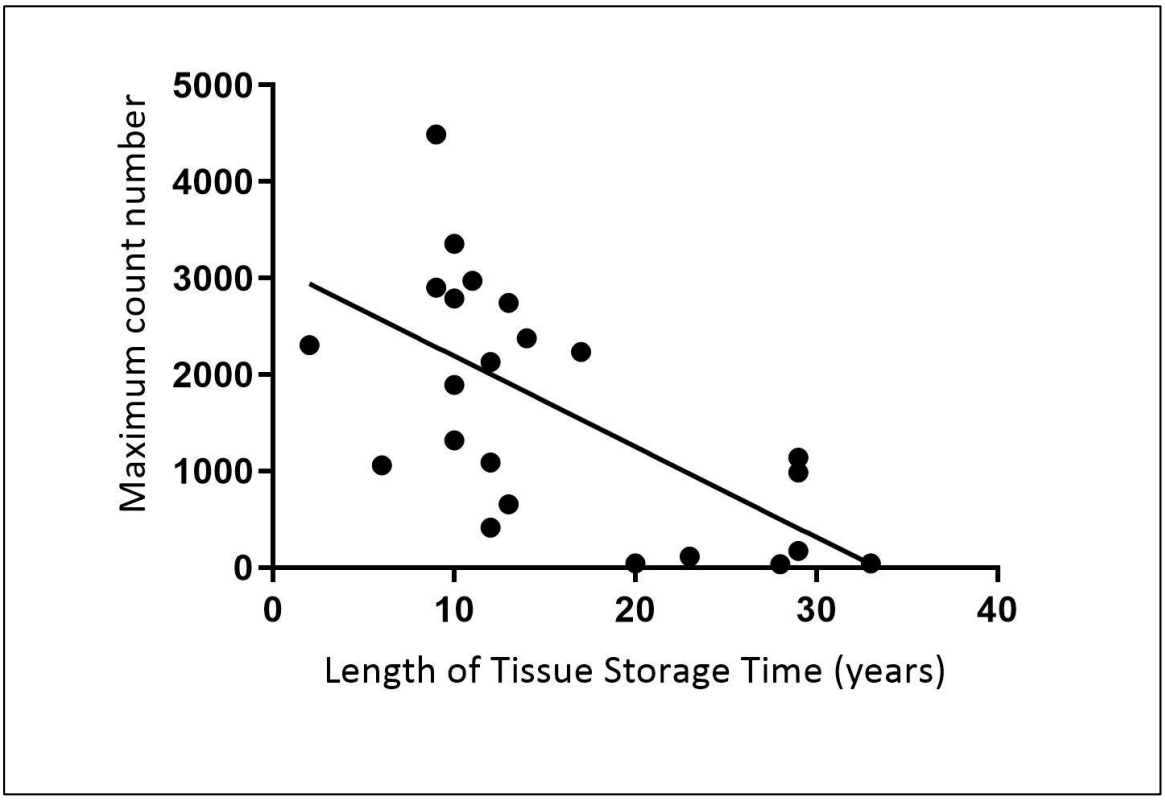

Figure 3.2 The Effect of the Length of Tissue Storage on the Maximum Count Number.

In FFPE tissue, a significant relationship was found the longer periods of tissue storage and lower maximum counts. A significant negative correlation was observed between the length of FFPE tissue storage, and the maximum count achieved for each case within the cohort.

3.2.5 Key Findings from FFPE Spinal Cord Analysis.

In summary, the NanoString platform can successfully be used to assess gene expression with FFPE archival tissue. In the spinal cord, an upregulation of neuroinflammatory signalling was observed in sMND cases compared to control. This included an upregulation of genes associated with phagocytosis and immune signalling pathways, as well as natural killer cell immunotoxicity.

In this trial, low gene expression, particularly of normalisation genes was observed. This was overcome by sourcing new methods of normalisation and differential expression – Voom Limma. A negative correlation between the length of tissue storage and the maximum count number was observed, leading to the exclusion of cases over 18 years old. However, this severely limited the number of cases usable for construction of further age and sex matched cohorts. Given the main advantage of using FFPE archival tissue over frozen tissue, was the large amount of well characterised tissue, the decision was made to use frozen tissue for further cohorts.

3.3 Gene Expression Profiling of Inflammation in Frozen Spinal Cord and Motor Cortex in sMND.

3.3.1 Comparing Age at Death across Cohorts

Aging has been associated with an exaggerated neuroinflammatory microglial response and altered microglial morphology and function (Sparkman and Johnson, 2008; Holtman *et al.*, 2015; Grabert *et al.*, 2016). As such for the NanoString gene expression cohorts, MND cases were age- and sex-matched as best as possible with the available control cases. To ensure the age at death of these cases did not significantly differ between the NanoString cohorts, the age at death was compared across the FFPE spinal cord, frozen spinal cord and frozen motor cortex cohorts using one-way ANOVA. The maximum and minimum ages, range, mean, and standard deviations are given (Table 3.5). No significant difference was found between the three cohorts ($F(2,69) = 1.661$, $p = 0.197$; Figure 3.3 A).

To examine whether the age at death for the sMND cases and control cases differed within each cohort, the age at death for the sMND cases was compared to the control cases using an unpaired t-test (Figure 3.3 B, C, D). No significant difference between age at death between sMND and control cases was found in any of the NanoString cohorts (results given in Table 3.6).

Table 3.5 Descriptive Statistics for the NanoString Cohorts.

	FFPE Spinal Cord	Frozen Spinal Cord	Frozen Motor Cortex
Minimum Age (years)	29	42	29
Maximum Age (years)	87	89	84
Mean (years)	65.25	63.54	58.25
Std. Deviation (years)	15.18	11.71	14.48

Table 3.6 T-test results comparing age at death from control and sMND cases for the NanoString cohorts

	FFPE Spinal Cord	Frozen Spinal Cord	Frozen Motor Cortex
Mean Age at death - Control (years)	65.75	66.13	62.25
Mean Age at death - sMND (years)	65	62.25	56.25
t, df	t=0.112, df=22	t=0.757, df=22	t=0.955, df=22
p value	0.912	0.457	0.350

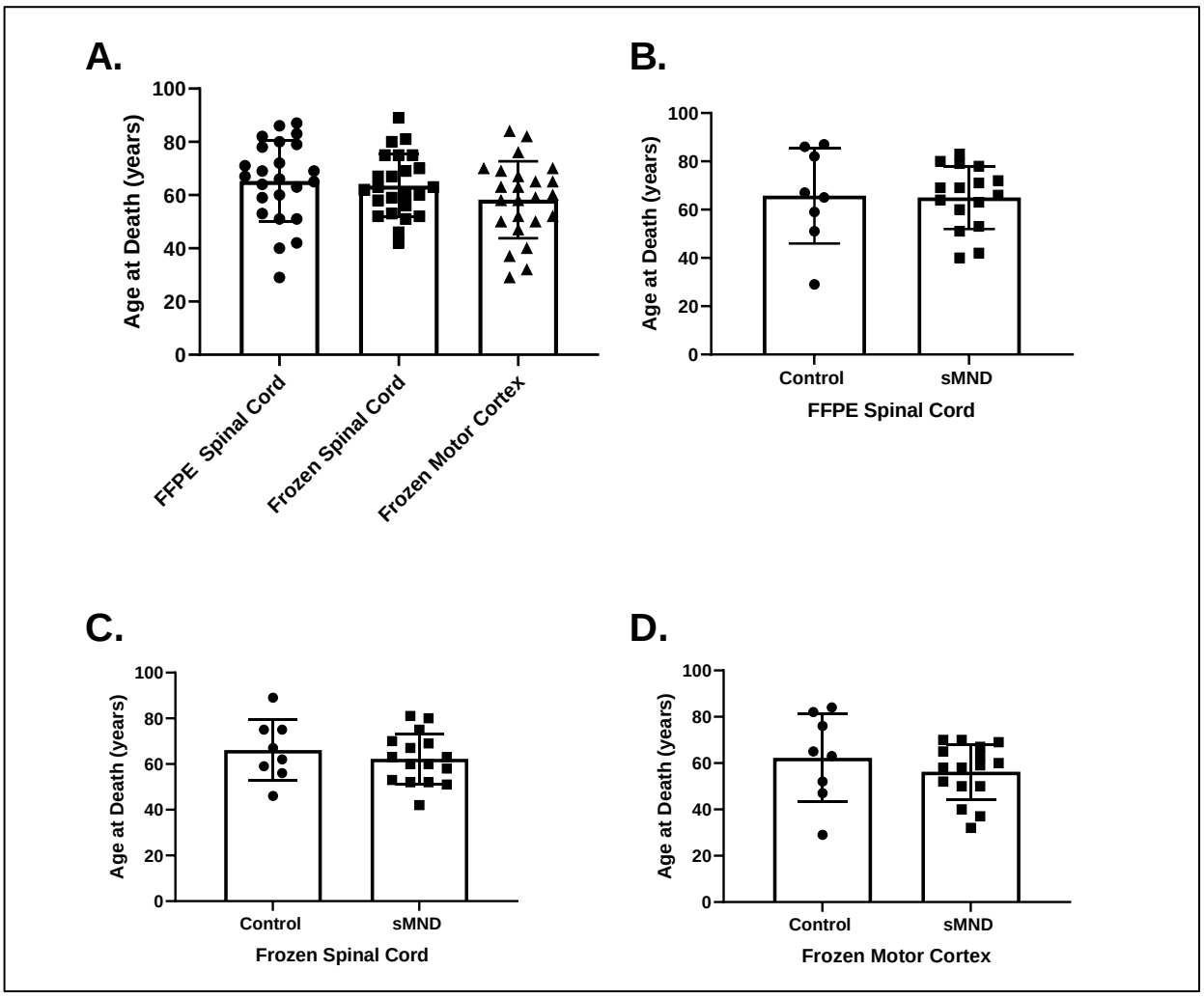

Figure 3.3 Age at Death did not significantly differ between the FFPE spinal cord, frozen spinal cord, and frozen motor cortex NanoString datasets, or between control and sMND cases.

A) Age at death was compared across the three NanoString cohorts using one-way ANOVA; no significant difference was observed ($F(2,69) = 1.661$, $p = 0.197$).

B) Comparison of age at death in control cases compared to sMND in the FFPE Spinal Cord NanoString cohort using a student's t-test. No significant difference ($t(22) = 0.112$, $p = 0.912$).

D) Comparison of age at death in control cases compared to sMND in the Frozen Spinal Cord NanoString cohort using a student's t-test. No significant difference ($t(22) = 0.757$, $p = 0.457$).

E) Comparison of age at death in control cases compared to sMND in the Frozen Motor Cortex NanoString cohort using a student's t-test. No significant difference ($t(22) = 0.955$, $p = 0.350$).

3.3.2 RNA Extraction

Following extraction from frozen tissue, RNA quality was checked using the Nanodrop spectrometer (summarised in Table 3.7). Overall, FFPE tissue yielded lower concentrations of RNA (mean, 20.14ng/µl; range, 7.9-50.1ng/ µl), than frozen spinal cord tissue (mean, 144.24ng/µl; range, 22.57-439.84ng/µl) and frozen motor (mean, 226.31ng/µl; range, 89.55-434.86ng/µl). For the motor cortex cases, all 260:280 and 260:230 ratios were close to the ideal 2 value, indicating good quality RNA with little contamination, apart from 1 case (261/1990) which showed greater absorbance at 230nm indicating some contamination. For the spinal cord cases, all 260:280 and 260:220 ratios were sufficiently close to the ideal 2 value, indicating good quality RNA with little contamination, apart from cases 071/1992, 109/1995, 150/1993, 141/2003. These cases showed greater absorbance 230nm indicating some contamination.

RNA extracted from frozen tissue shows less contamination than that from FFPE tissue as demonstrated by the average 260:280 and 260:230 ratio values.

Table 3.7 Mean Optical Density Ratios for RNA extracted from FFPE and Frozen Tissue

Mean Optical Density Ratio	FFPE Spinal Cord	Frozen Spinal Cord	Frozen Motor Cortex
260:280	1.767	2.008	1.978
260:230	1.010	1.926	1.877
Mean Yield (ng/ µl)	20.14	144.24	266.31

***Note**. For pure RNA, the 260:280 and 260:220 ratios should be ~1.8 and ~2.0-2.2, respectively (Fleige and Pfaffl, 2006).*

Further checks on RNA quality were employed by measuring the integrity of the RNA extracted from the frozen tissue; the Agilent Bioanalyser 2100 was used to generate a RIN for each case (Table 3.8 and 3.9). The majority (>90-95%) of total RNA, is made up of ribosomal RNA, whereas the mRNA is much lower in concentration and almost un-detectable in comparison. The Agilent Bioanalyser 2100 works on the principle that the quality and quantity of the ribosomal RNA should be proportional to that of mammalian mRNA. Unfragmented mammalian mRNA (28s) is ~5kb in length and ribosomal RNA (18s) is ~2kb, meaning the theoretical 28s:18s ratio should be approximately 2.7:1, although in practice 2:1 is widely accepted as pure RNA. On the electropherograms this is seen as clean, narrow 18s and 28s peaks, with the 28s peak being ideally twice the height of the 18s peak. Alterations in this ratio and the electropherograms indicate the RNA is more fragmented or digested (Figure 3.4). NanoString Technologies (2016) recommend using RNA with a RIN value of two or greater. All frozen tissue RNA samples met this criterion (except sample 135/1982 frozen spinal cord, RIN 1.7), with most samples having a RIN >7. Despite its low RIN, case 135/1982 was kept in for analysis as its RIN was only marginally lower than the pre-set threshold and showed extremely little contamination (260:280= 1.99, 260:230= 1.93). Furthermore, given the precious nature of

samples taken from *post-mortem* and rarity of donated control cases in particular, the case was included.

For seven samples, a RIN could not be generated (1 spinal cord case 209/1995; 6 motor cortex cases 150/1993, 193/1990, 203/1994, 088/1996, 131/1995, 150/1997). However, examination of the electropherograms showed clear peaks, and the optical density ratios for these cases were close to two indicating high quality RNA with minimal contamination. Therefore, these samples were deemed of high enough quality to proceed with the assay.

Table 3.8 Frozen Spinal Cord RNA Quantity and Quality Data

Case ID	Disease Status	Nanodrop Spectrometer			Agilent Bioanalyser 2100
		RNA Concentration (ng/µl)	260:280	260:230	RNA Integrity Number
085/2007	control	67.94	2.07	1.92	6.2
080/1992	control	161.23	2	1.95	6.4
071/1992	control	28.78	1.8	1.47	3.3
135/1982	control	62.6	1.99	1.93	1.7
109/1995	control	22.57	2.05	1.66	6.8
1028/1989	control	268.05	1.99	1.79	2.5
025/1995	control	24.42	1.93	1.68	2.6
138/1994	control	53.67	2.11	2.04	3.6
150/1993	sMND	27.62	2.11	1.67	3
050/2008	sMND	238.17	1.99	2.06	5.6
037/2000	sMND	113.98	2.03	2.08	7.8
041/2008	sMND	81.73	2.06	2.07	8
024/2008	sMND	180.3	2.02	2.1	8.9
209/1995	sMND	362.35	1.98	2.09	NA
023/2010	sMND	401.97	2.02	2.14	8.1
059/2009	sMND	323.43	1.99	1.95	8.1
295/1991	sMND	77.77	2.06	2.08	7.9
141/2003	sMND	63.12	1.96	1.72	6.2
261/1990	sMND	30	2.06	1.54	3.3
024/2004	sMND	90.32	1.99	2.03	3.7
115/2002	sMND	52.7	2.01	2	7.8
034/2005	sMND	439.84	1.97	2.13	2.9
131/1995	sMND	99.14	2.05	2.03	7.7
072/2002	sMND	190.02	1.96	2.09	6.7

Table 3.9 Frozen Motor Cortex RNA Quantity and Quality Data

Case ID	Disease Status	Nanodrop Spectrometer			Agilent Bioanalyser 2100
		RNA Concentration (ng/µl)	260:280	260:230	RNA Integrity Number
335/1990	control	89.55	1.96	1.72	8
178/1995	control	421.41	2.01	1.97	8.3
072/1992	control	243.04	1.97	1.93	7.2
023/1992	control	366.56	1.92	1.8	4.3
147/1995	control	246.14	2.04	2.06	8.6
111/1990	control	93.41	2.05	1.99	7.6
293/1991	control	216.88	1.95	1.75	7.6
309/1990	control	237.93	1.97	1.92	3.3
150/1993	sMND	232.17	2.01	2.05	NA
223/1999	sMND	159.58	2.01	1.96	8.6
193/1990	sMND	94.01	1.94	1.65	NA
261/1990	sMND	93.31	1.81	1.32	2.4
203/1994	sMND	148.2	2.01	1.78	NA
069/2006	sMND	94.54	1.95	1.8	7.2
050/2008	sMND	148.83	1.96	1.92	7.7
005/2010	sMND	128.89	2.02	2.06	7.1
041/2008	sMND	319.34	2.03	2.02	8.6
024/2008	sMND	434.86	2.01	1.89	3.8
088/1996	sMND	183.94	1.93	1.89	NA
209/1995	sMND	380.41	1.93	1.78	8.7
131/1995	sMND	324.84	1.99	1.92	NA
150/1997	sMND	301.27	2	1.99	NA
043/2005	sMND	164.53	2.02	2	8
137/1996	sMND	307.73	1.98	1.88	5.1

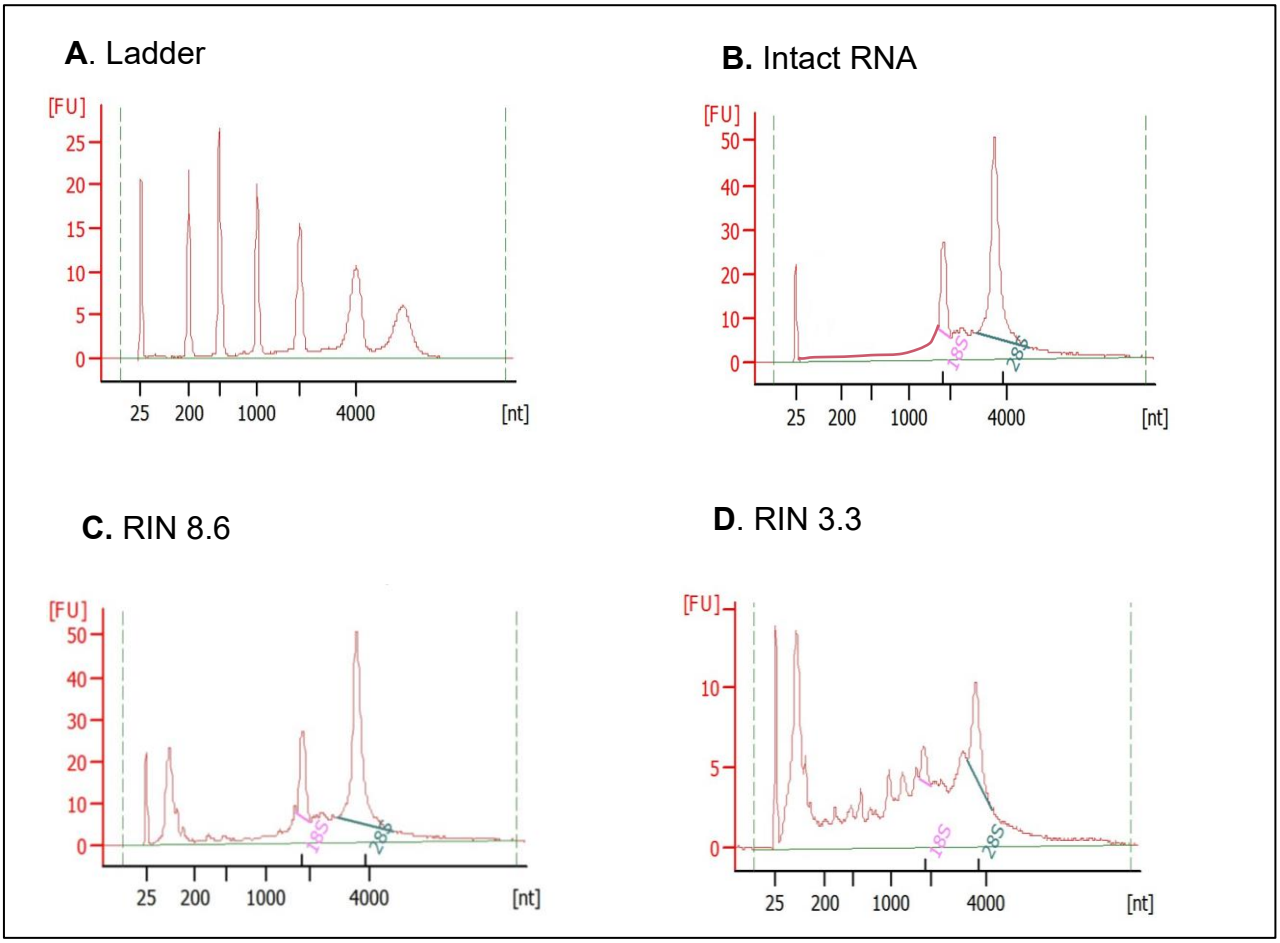

Figure 3.4. Representative Electropherograms Generated by the Agilent Bioanalyser 2100.

For all electropherograms: The y-axis represents UV absorption (FU), the x-axis represents time (seconds).

***A.** Standard RNA Ladder Graph, which is used as a reference for the RNA samples. First peak (25 seconds) represents the RNA marker. The following six peaks represent RNA peaks of increasing nucleotide length. All peaks should be well resolved.*

***B.** For comparison, a generated graph, which represents what the electropherogram for near intact total RNA would look like. The initial peak (25 seconds) is the RNA marker. Clear 18s and 28s peaks are present with the 28s peak being twice the height of the 18s peak. Little to no peaks are shown before or in between these peaks indicating there is very little fragmented or degraded RNA present.*

***C/D.** Electropherograms for total RNA samples with different levels of degradation. Sample B has a higher RIN number (8.6). After the marker, various peaks are present indicating fragments of RNA. On the more degraded case (C), the 18s and 28s case have become flattened and broader [note the axis are of different scales], indicating the presence of less intact ribosomal and mammalian RNA.*

3.3.3 The Effect of the Length of Tissue Storage Time

In Section 3.2.4, a negative relationship was found between the length of FFPE tissue storage, and the maximum number of counts achieved in the NanoString data. This analysis was repeated for the frozen spinal cord and motor cortex data.

The correlation between length of time the tissue had been in storage (until the time of RNA extraction, years) and the maximum count achieved per case was assessed using Spearman's test (Figure 3.5). For the frozen spinal cord, the mean tissue storage time was 21.29 years. No significant relationship was observed (R= 0.370, p=0.075). For the frozen motor cortex, the mean tissue storage time was 23.13 years. No significant association was observed (R= -0.244, p=0.251).

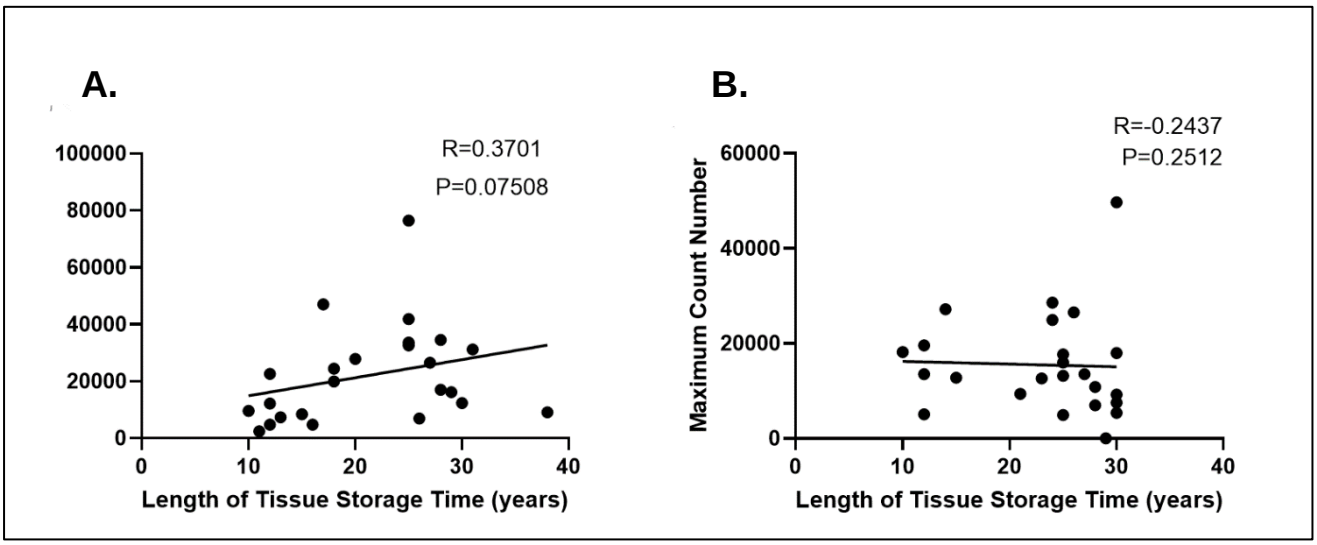

Figure 3.5 The Effect of the Length of Tissue Storage on the Maximum Count Number

In FFPE tissue, a significant relationship was found the longer periods of tissue storage and lower maximum counts. This relationship was not observed in frozen tissue.

A. No significant relationship was observed between the length of frozen spinal cord storage and the maximum count achieved per case.
B. No significant relationship was observed between the length of frozen motor cortex storage and the maximum count achieved per case.

3.3.4 Influence of *Post-mortem* Delay on Maximum Count and RNA Integrity

Increasing the length of time between death, and the autopsy and preservation of samples, or *post-mortem* interval (PMI), has been associated with reduced RNA quality (Birdsill *et al.*, 2011). However, others have found no relation between *post-mortem* interval and RNA integrity or quality (Ervin *et al.*, 2007; White *et al.*, 2018).

To determine whether *post-mortem* delay (PMD) could have influenced the gene expression results, the *post-mortem* interval (hours) was compared with the maximum count number achieved per case within each NanoString cohort using Spearman's correlation. No significant correlation was observed for any of the three datasets (Figure 3.6), indicating the length of *post-mortem* interval was unlikely to have influenced the NanoString results.

Furthermore, when the length of PMD was compared to the RIN (only available for the Frozen tissue NanoString cohorts) using Spearman's correlation, no significant result was observed (Figure. 3.7). The length of PMD was not likely to have influenced RNA integrity in frozen tissue.

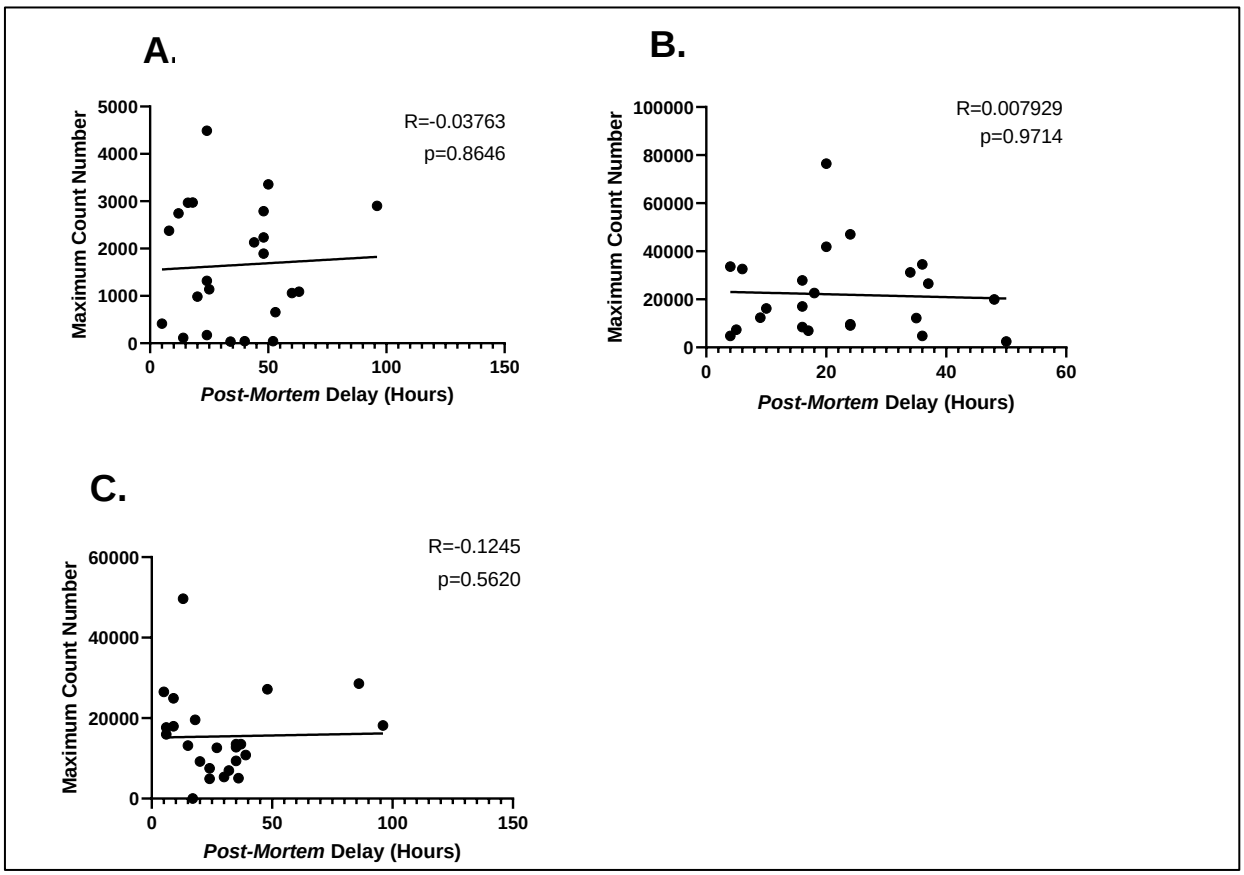

Figure 3.6 There was no relationship between post-mortem interval and maximum count number.

Spearman's correlation of the PMD (hours) and the maximum count number achieved. No correlation was observed overall, indicating the post-mortem interval did not influence the NanoString gene expression data.

- ***A.*** *Correlation of PMD and maximum count number for the FFPE spinal cord data set (R= -0.038, p=0.86).*
- ***B.*** *Correlation of PMD and maximum count number for the frozen spinal cord data set (R=0.008, p=0.971).*
- ***C.*** *Correlation of PMD and maximum count number for the frozen motor cortex data set (R=-0.125, p=0.562)*

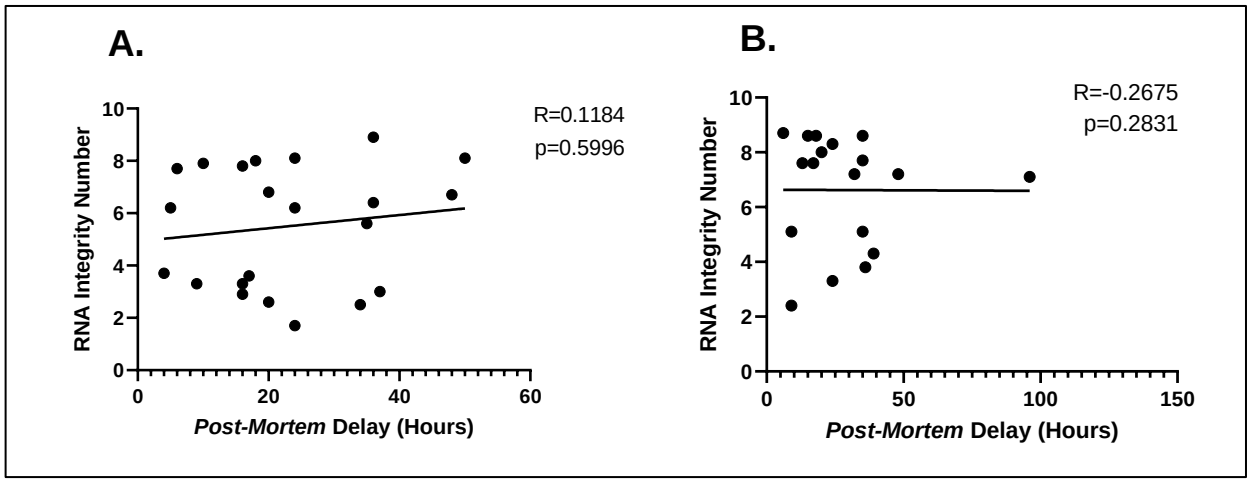

Figure 3.7 Relationship between Post-mortem interval and the RNA Integrity.

Spearman's correlation of the PMD (hours) and the maximum count number achieved. No correlation was observed overall, indicating the post-mortem interval did not influence the NanoString gene expression data.

A. *Correlation of PMD and RNA Integrity number for the frozen spinal cord data set (R=0.118, p=.600).*

B. *Correlation of PMD and maximum count number for the frozen motor cortex data set (R=-0.268, p=0.283)*

3.3.5 Main Findings from Quality Control Checks

For the NanoString data sets cohorts (FFPE and Frozen tissue), the age at death across all groups was compared. No difference in mean age observed between control cases and sMND cases, or between different datasets. As such, differences in gene expression observed between control and sMND, and between cohorts are independent of age.

A relationship between tissue storage length and reduced biological signal was observed with FFPE tissue (Section 3.2.4), however this effect was not present with frozen tissue cases.

Finally, the effect of PMD on biological signal was compared across all NanoString data sets. PMD was not significantly associated with the maximum count achieved in any NanoString cohort, or the RNA integrity for the frozen tissue cases.

These covariables are unlikely to have impacted differences in gene expression observed across the NanoString datasets.

Furthermore, following the trial of the NanoString platform with FFPE archival tissue, additional QC checks were implemented regarding the RNA quality. Optical density ratios showed significantly less contamination and higher RNA yield from frozen tissue compared to FFPE. Additionally, the integrity of the RNA extracted from tissue was investigated using the Bioanalyser. All cases used in the frozen tissue NanoString runs surpassed the quality threshold recommended by NanoString.

3.3.6 Differential Gene Expression Analysis for Frozen Spinal Cord

The neuroinflammatory transcriptional profile was assessed in in the anterior horn of frozen spinal cord and the grey matter motor cortex in sMND and neurologically normal control cases using the NanoString Neuroinflammation Chip.

To identify differentially expressed genes in sMND, the sMND transcriptional profile was compared to that of the control groups, controlling for age and sex, using Voom-Limma analysis. The Benjamini-Hochberg correction was implemented to reduce the false discovery rate. Transcripts were determined to be significant if the fold change was ≥|1.5|, with a false discovery rate corrected p value (q) <0.05.

Frozen Spinal Cord shows increased inflammatory signalling in sMND

In the spinal cord, 89 genes were found to be differentially expressed from the panel of 770 genes (Figure 3.8). Of these, 76 were upregulated and 13 were downregulated (Table 3.9 and Table 3.10) As seen in the FFPE tissue, those genes with the greatest fold change were upregulated, indicating a significant upregulation of inflammatory signalling in sMND.

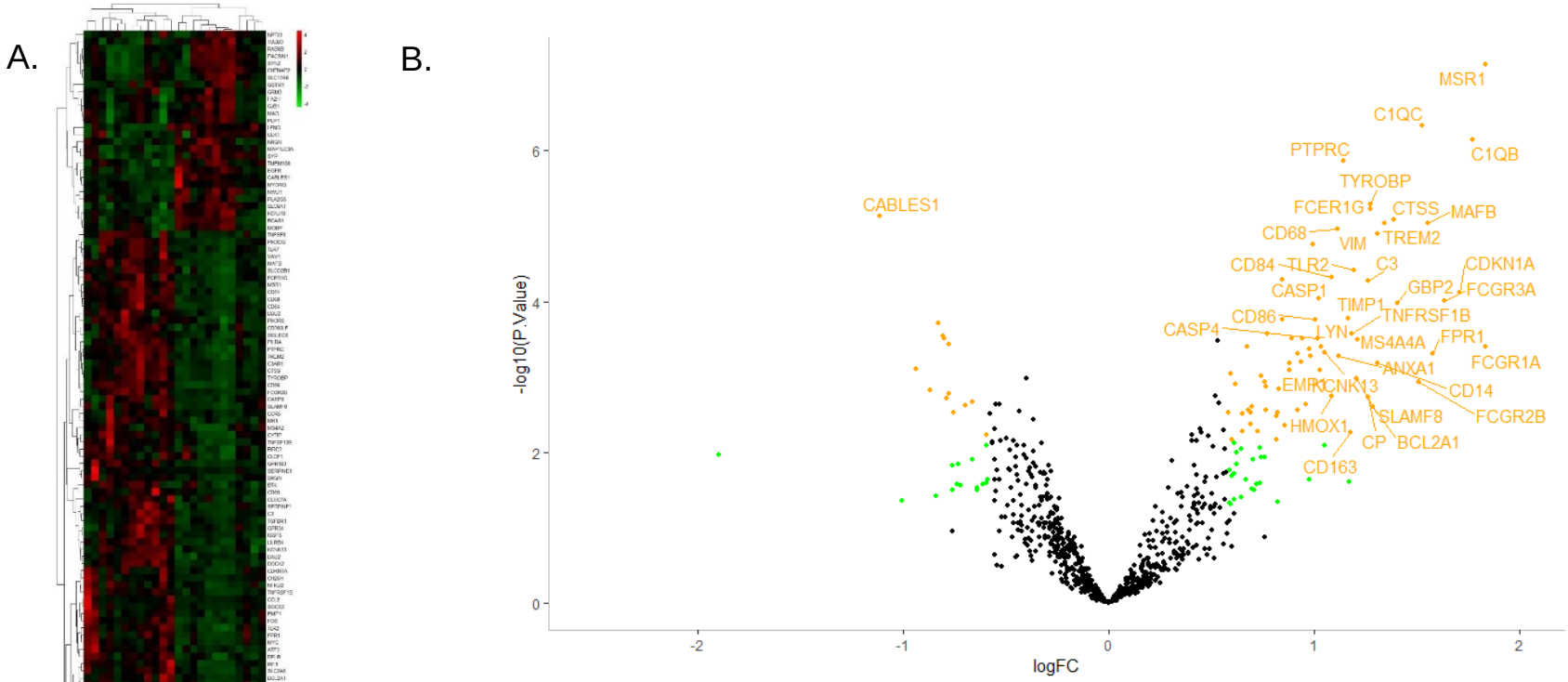

Figure 3.8 sMND is associated with an Increase in Inflammatory Signalling in the Spinal Cord – Frozen Tissue

A. *Heatmap displaying the expression the top significantly expressed genes (FC<1.5, FDR adj. p>0.05) out of 219 differentially expressed between MND and neurologically healthy cases. Hierarchal clustering grouped the majority of MND cases and control cases, shown on the x axis, genes are shown on the y axis.*

B. *Volcano plot showing fold change against the significance value. Of all the significant genes, 72 were upregulated, and 13 genes were down regulated (Green Points p<0.05; FC>1.5; Orange Points FDR adjusted p<0.05; FC>1.5, labelled points FDR adjusted p<0.05; FC>2).*

Figure 3.9 Genes Upregulated in sMND Frozen Spinal Cord.

Gene Name	Gene Symbol	Log2 Fold Change	Fold Change	P Value	Q
Serpin Family A Member 3	SERPINA3	2.367	5.157	<0.001	0.004
C-C Motif Chemokine Ligand 2	CCL2	2.330	5.029	<0.001	0.004
Suppressor Of Cytokine Signalling 3	SOCS3	2.143	4.416	0.003	0.025
IFI30 Lysosomal Thiol Reductase	IFI30	2.073	4.208	<0.001	<0.001
macrophage scavenger receptor 1	*MSR1*	3.568	1.835	<0.001	<0.001
Fc fragment of IgG receptor Ia	*FCGR1A*	3.561	1.832	<0.001	0.008
complement C1q B chain	*C1QB*	3.422	1.775	<0.001	<0.001
cyclin dependent kinase inhibitor 1A	*CDKN1A*	3.270	1.709	<0.001	0.003
Fc fragment of IgG receptor IIIa	*FCGR3A*	3.105	1.635	<0.001	0.004
formyl peptide receptor 1	*FPR1*	2.988	1.579	<0.001	0.008
MAF bZIP transcription factor B	*MAFB*	2.937	1.555	<0.001	0.001
complement C1q C chain	*C1QC*	2.880	1.526	<0.001	<0.001
Fc fragment of IgG receptor IIb	*FCGR2B*	2.844	1.508	0.001	0.015
guanylate binding protein 2	*GBP2*	2.653	1.408	<0.001	0.004
cathepsin S	*CTSS*	2.623	1.391	<0.001	0.001
triggering receptor expressed on myeloid cells 2	*TREM2*	2.536	1.342	<0.001	0.001
CD14 molecule	*CD14*	2.479	1.310	0.001	0.010
vimentin	*VIM*	2.474	1.307	<0.001	0.001
BCL2 related protein A1	*BCL2A1*	2.436	1.284	0.003	0.025
transmembrane immune signaling adaptor TYROBP	*TYROBP*	2.418	1.274	<0.001	0.001
Fc fragment of IgE receptor Ig	*FCER1G*	2.417	1.273	<0.001	0.001
complement C3	*C3*	2.405	1.266	<0.001	0.002
ceruloplasmin	*CP*	2.400	1.263	0.002	0.021
membrane spanning 4-domains A4A	*MS4A4A*	2.313	1.210	<0.001	0.007
SLAM family member 8	*SLAMF8*	2.309	1.207	0.001	0.014
toll like receptor 2	*TLR2*	2.286	1.193	<0.001	0.002
TNF receptor superfamily member 1B	*TNFRSF1B*	2.270	1.182	<0.001	0.007
Cluster of Differentiation 163	*CD163*	2.265	1.179	0.005	0.042
TIMP metallopeptidase inhibitor 1	*TIMP1*	2.249	1.169	<0.001	0.005
protein tyrosine phosphatase receptor type C	*PTPRC*	2.208	1.143	<0.001	<0.001
annexin A1	*ANXA1*	2.176	1.122	0.001	0.009
CD68 molecule	*CD68*	2.167	1.116	<0.001	0.001
heme oxygenase 1	*HMOX1*	2.126	1.088	0.002	0.021
CD84 molecule	*CD84*	2.120	1.084	<0.001	0.002
potassium two pore domain channel subfamily K member 13	*KCNK13*	2.078	1.055	<0.001	0.008

LYN proto-oncogene, Src family tyrosine kinase	*LYN*	2.046	1.033	<0.001	0.008
epithelial membrane protein 1	*EMP1*	2.045	1.032	0.001	0.012
caspase 1	*CASP1*	2.034	1.024	<0.001	0.003
caspase 4	*CASP4*	2.022	1.016	<0.001	0.007
CD86 molecule	*CD86*	2.006	1.004	<0.001	0.005
Fos proto-oncogene, AP-1 transcription factor subunit	*FOS*	1.993	0.995	<0.001	0.001
complement C1q A chain	*C1QA*	1.976	0.982	0.001	0.009
STEAP4 metalloreductase	*STEAP4*	1.970	0.978	<0.001	0.008
G protein-coupled receptor 183	*GPR183*	1.944	0.959	0.002	0.024
serpin family F member 1	*SERPINF1*	1.920	0.941	<0.001	0.007
MYC proto-oncogene, bHLH transcription factor	*MYC*	1.913	0.936	0.001	0.010
leukocyte associated immunoglobulin like receptor 1	*LAIR1*	1.897	0.924	<0.001	0.008
sialic acid binding Ig like lectin 8	*SIGLEC8*	1.897	0.924	0.003	0.027
RELB proto-oncogene, NF-kB subunit	*RELB*	1.856	0.892	<0.001	0.007
Vav guanine nucleotide exchange factor 1	*VAV1*	1.843	0.882	0.001	0.012
complement C3a receptor 1	*C3AR1*	1.841	0.880	0.001	0.010
Serglycin	*SRGN*	1.812	0.858	0.004	0.037
Fas cell surface death receptor	*FAS*	1.802	0.849	<0.001	0.002
dedicator of cytokinesis 2	*DOCK2*	1.798	0.847	<0.001	0.005
CD74 molecule	*CD74*	1.780	0.832	0.001	0.018
transforming growth factor beta receptor 1	*TGFBR1*	1.768	0.822	0.003	0.027
paired immunoglobin like type 2 receptor alpha	*PILRA*	1.765	0.820	0.003	0.029
podoplanin	*PDPN*	1.760	0.815	0.007	0.049
TNF receptor superfamily member 1A	*TNFRSF1A*	1.710	0.774	<0.001	0.007
matrix metallopeptidase 14	*MMP14*	1.702	0.768	0.001	0.017
TNF superfamily member 13b	*TNFSF13B*	1.702	0.767	0.003	0.027
sphingosine-1-phosphate receptor 3	*S1PR3*	1.698	0.763	0.001	0.015
leukocyte immunoglobulin like receptor B4	*LILRB4*	1.674	0.743	0.001	0.014
oncostatin M receptor	*OSMR*	1.654	0.726	0.005	0.042
cytohesin 1 interacting protein	*CYTIP*	1.621	0.697	0.002	0.025
lamin B1	*LMNB1*	1.619	0.695	0.003	0.027
protein tyrosine phosphatase non-receptor type 6	*PTPN6*	1.615	0.692	0.004	0.036
solute carrier family 2 member 5	*SLC2A5*	1.601	0.679	0.003	0.027
damage specific DNA binding protein 2	*DDB2*	1.601	0.679	0.003	0.027
DAB adaptor protein 2	*DAB2*	1.599	0.678	<0.001	0.008
phosphatidylinositol-4,5-bisphosphate 3-kinase catalytic subunit gamma	*PIK3CG*	1.574	0.654	0.003	0.027

baculoviral IAP repeat containing 3	*BIRC3*	1.573	0.653	0.005	0.042
WASP actin nucleation promoting factor	*WAS*	1.533	0.616	0.001	0.016
caspase 8	*CASP8*	1.516	0.600	0.007	0.049
nucleotide binding oligomerization domain containing 1	*NOD1*	1.513	0.597	0.001	0.013
solute carrier organic anion transporter family member 2B1	*SLCO2B1*	1.501	0.586	0.003	0.027

Table 3.10 Genes Downregulated in sMND Frozen Spinal Cord

Gene Name	Gene Symbol	Log_2 Fold Change	Fold Change	P Value	Q
Cdk5 and Abl enzyme substrate 1	*CABLES1*	-2.165	-1.114	<0.001	0.001
myogenesis regulating glycosidase (putative)	*MYORG*	-1.911	-0.935	0.001	0.012
NACHT and WD repeat domain containing 1	*NWD1*	-1.822	-0.865	0.001	0.018
tubulin beta 3 class III	*TUBB3*	-1.773	-0.826	<0.001	0.005
epidermal growth factor receptor	*EGFR*	-1.749	-0.806	<0.001	0.007
transmembrane protein 100	*TMEM100*	-1.741	-0.800	<0.001	0.007
solute carrier family 6 member 1	*SLC6A1*	-1.726	-0.787	0.002	0.022
phospholipase A2 group V	*PLA2G5*	-1.714	-0.778	0.002	0.020
potassium inwardly rectifying channel subfamily J member 10	*KCNJ10*	-1.712	-0.775	<0.001	0.008
LFNG O-fucosylpeptide 3-beta-N-acetylglucosaminyltransferase	*LFNG*	-1.685	-0.753	0.003	0.027
brain enriched myelin associated protein 1	*BCAS1*	-1.618	-0.695	0.002	0.025
microtubule associated protein 1 light chain 3 alpha	*MAP1LC3A*	-1.584	-0.664	0.002	0.024
myelin associated oligodendrocyte basic protein	*MOBP*	-1.509	-0.594	0.006	0.045

Pathway Enrichment Analysis of the Differentially Expressed genes from sMND Frozen Spinal Cord.

Examination of the KEGG pathways associated with the differentially expressed genes from frozen spinal cord highlighted the following key themes (Table 3.11). The top relevant pathway was the tumour necrosis factor signalling pathway, other key pathways include phagocytosis through both the phagosome and Fc Gamma mediated phagocytosis pathways, as well as MAP Kinase signalling and cytokine-cytokine receptor interaction, and the NF-κB pathway. In all pathways, most genes showed increased expression indicating upregulation of these pathways in sMND.

Table 3.11 Gene Enrichment Pathway Analysis using differentially expressed genes from sMND frozen spinal cord.

KEGG Symbol	KEGG Pathway	Number of Genes	Genes in Pathway	
			Upregulated Genes	Down Regulated Genes
hsa04380	Osteoclast differentiation	**12**	*PIK3CG, LILRB4, TNFRSF1A, TGFBR1, RELB, FOS, TYROBP, TREM2, FCGR2B, FCGR3A, FCGR1A, SOCS3,*	
hsa05142	Chagas disease	**12**	*CASP8, PIK3CG, TNFRSF1A, TGFBR1, FAS, C1QA, FOS, TLR2, C3, C1QC, C1QB, CCL2,*	
hsa05152	Tuberculosis	**11**	*CASP8, TNFRSF1A, CD74, TLR2, C3, FCER1G, CD14, CTSS, FCGR2B, FCGR3A, FCGR1A,*	
hsa04668	Tumour Necrosis Factor Signalling Pathway	**10**	*CASP8, BIRC3, PIK3CG, MMP14, TNFRSF1A, FAS, FOS, TNFRSF1B, SOCS3, CCL2,*	
hsa05168	Herpes Simplex virus 1 infection	**10**	*CASP8, TNFRSF1A, PILRA, CD74, FAS, FOS, TLR2, C3, SOCS3, CCL2,*	
hsa04145	Phagosome	**9**	*TLR2, C3, CD14, CTSS, FCGR2B, FCGR3A, FCGR1A, MSR1,*	*TUBB3*
hsa05150	Staphylococcus aureus infection	**9**	*C3AR1, C1QA, C3, FCGR2B, C1QC, FPR1, FCGR3A, C1QB, FCGR1A,*	
hsa05161	Hepatitis B virus	**9**	*CASP8, PIK3CG, DDB2, TGFBR1, FAS, MYC, FOS, TLR2, CDKN1A,*	
hsa05200	Pathways in cancer	**9**	*CASP8, BIRC3, PIK3CG, TGFBR1, FAS, MYC, FOS, CDKN1A,*	*EGFR*
hsa04010	MAPK signalling pathway	**8**	*TNFRSF1A, TGFBR1, FAS, RELB, MYC, FOS, CD14,*	*EGFR*
hsa04060	Cytokine-Cytokine Receptor Interaction	**8**	*OSMR, TNFSF13B, TNFRSF1A, TGFBR1, FAS, TNFRSF1B, CCL2,*	*EGFR*
hsa04666	Fc gamma R-mediated phagocytosis	**8**	*WAS, PIK3CG, DOCK2, VAV1, LYN, FCGR1A, FCGR3A, FCGR2B,*	
hsa05133	Pertussis	**8**	*NOD1, FOS, CASP1, CD14, C3, C1QA, C1QC, C1QB,*	
hsa04064	NF-kappa B signalling pathway	**7**	*BIRC3, TNFSF13B, TNFRSF1A, RELB, LYN, BCL2A1, CD14,*	
hsa04650	Natural killer cell mediated cytotoxicity	**7**	*PIK3CG, PTPN6, FAS, VAV1, FCER1G, TYROBP, FCGR3A,*	

Motor Cortex shows little Inflammatory Signalling in sMND

In contrast, little inflammatory signally was observed in the motor cortex. Of the 770 genes on the panel, 42 genes were significant at the FDR uncorrected p value; however, none reached significance following false discovery rate correction (Figure 3.10).

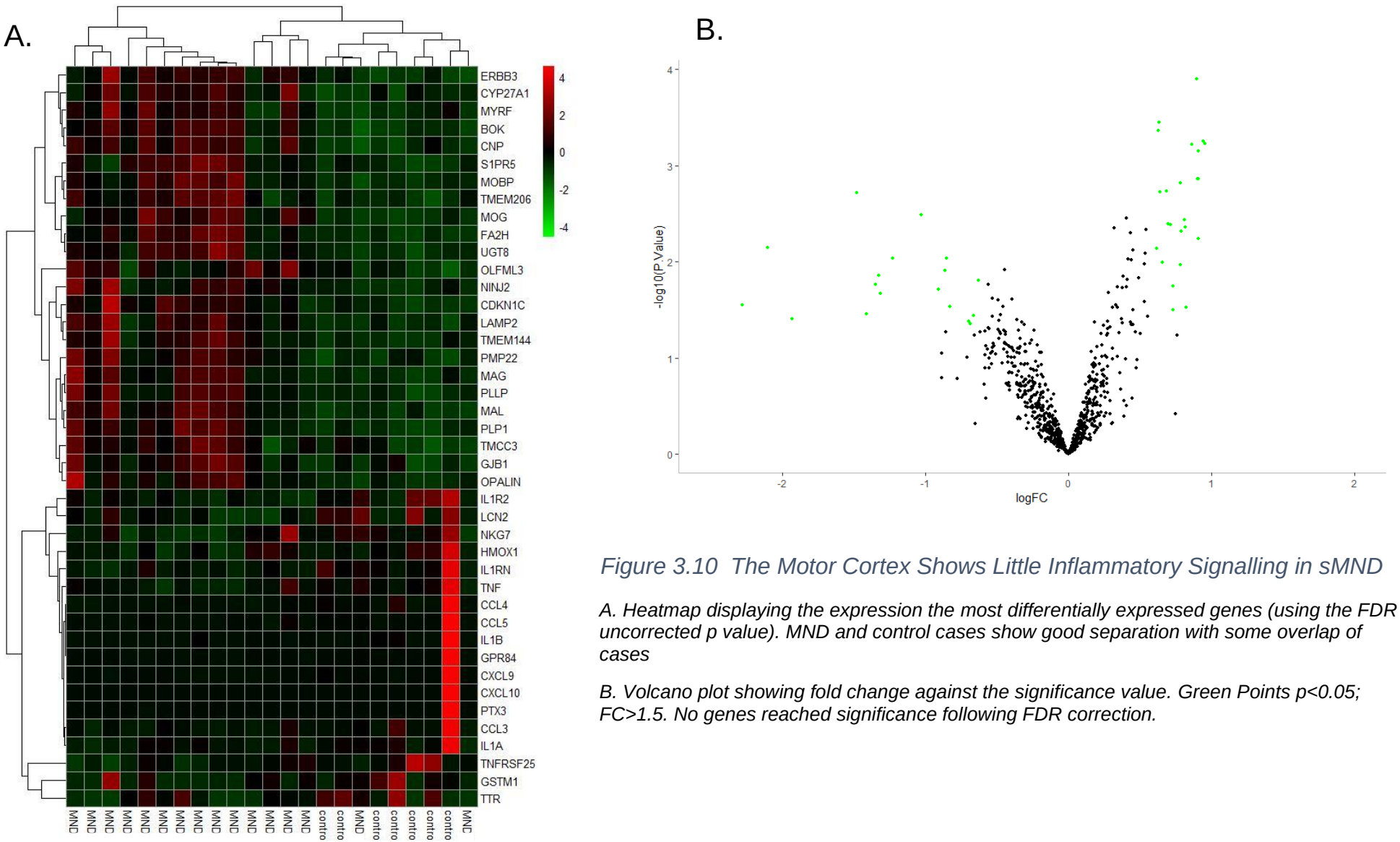

Figure 3.10 The Motor Cortex Shows Little Inflammatory Signalling in sMND

A. Heatmap displaying the expression the most differentially expressed genes (using the FDR uncorrected p value). MND and control cases show good separation with some overlap of cases

B. Volcano plot showing fold change against the significance value. Green Points p<0.05; FC>1.5. No genes reached significance following FDR correction.

3.3.6 Major Findings from Frozen Tissue NanoString Gene Expression

In the spinal cord, significant differences in neuroinflammatory gene expression profile were observed in sMND compared to control. As was also observed with FFPE tissue, most of these genes were upregulated indicating increased inflammation is a key feature within the spinal cord in sMND. Key upregulated pathways were associated with phagocytosis, cytokine signalling including TNF signalling, and the NF-KB pathway.

In contrast, very little difference in inflammatory signalling was observed in the motor cortex between sMND cases and control, indicating inflammation is not a core response in this region at the time of death. Furthermore, this is evidence that despite both regions being associated with neuronal degeneration in sMND, the inflammatory response differs by region across the CNS.

3.4 Microglial Deconvolution Analysis

To identify those genes most likely expressed by microglia, the Brain RNA-Seq database was used to sort genes via the cell type most likely to express them. This database produced by Zhang *et al.* (2016), used immunopanning to identify purified cell populations from human cortical tissue, and RNA sequencing to generate a gene profile of the main cell types within the CNS. Presented here are the deconvolution of the significantly differentially expressed genes from FFPE and frozen spinal cord.

3.4.1 FFPE Spinal Cord

Of the 100 genes differentially expressed from FFPE spinal cord, 33 showed expression specific to one cell population following removal of genes expressed by multiple cell types (Figure 3.11). Most of these genes (20) were primarily expressed by microglial/ macrophage cells. Fifteen of these genes were upregulated and associated with key themes such as phagocytic associated receptors (*FGCR3A*, *FCER1G*), antigen presentation and processing, (*CD74*, *IFI30*, *CTSS*), the complement system (*C3*, *C1QA*, *C1QB*, *C1QC*), and signalling molecules and their receptors (*MSR1*, *SSP1*, *TYROBP*, *TREM2*) among others. Those five downregulated microglial/macrophage associated genes are given below.

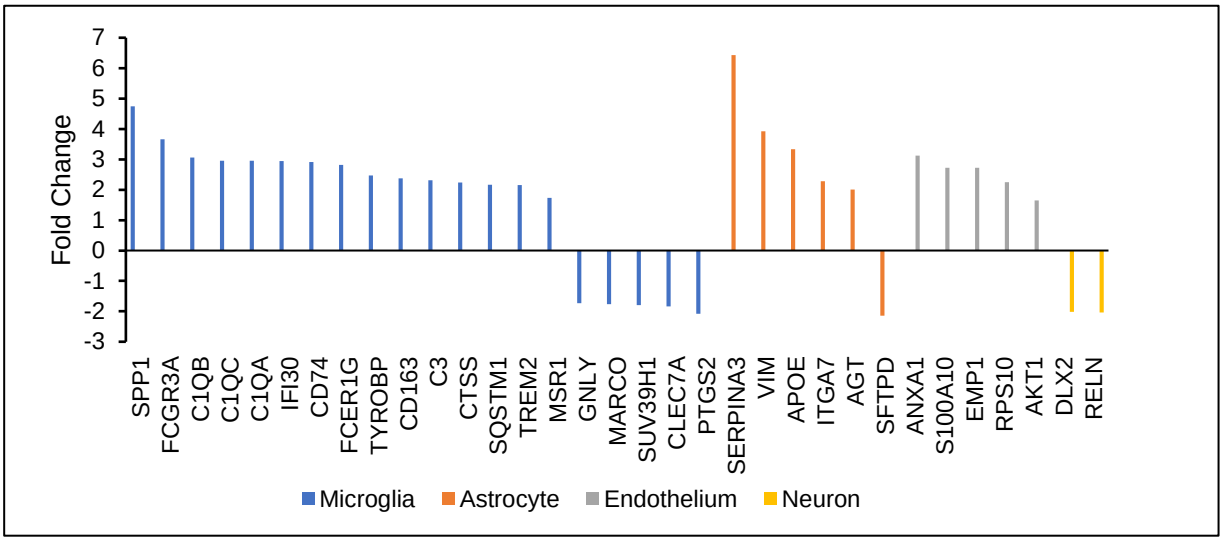

Figure 3.11 Microglial/ Macrophage associated differentially expressed genes from FFPE Spinal Cord.

Using published RNA Sequencing Data (Zhang et al., 2016), the cell type of origin was determined for each gene significantly expressed genes. From the FFPE data set, majority of differentially genes were associated with microglia/macrophages and were upregulated indicating an upregulation of microglial activity in sMND spinal cord.

3.4.2 Frozen Spinal Cord

Off the 89 significantly differentially expressed in frozen spinal cord, 72 genes showed expression predominantly associated with one cell type (Figure 3.12). Of these, 50 genes were primarily associated with microglia/macrophage cells, all of which were upregulated. Key themes include cytokines, chemokines and signalling molecules (*CCL2*, *MSR1*, *CCR5*, *TNFRSF1B*, *TNFSF8*, *WAS*), the complement system (*C1QA*, *C1QB*, *C1QC*, *C3AR1, C3*), phagocytosis (*CD14*, *CTSS*, *FCGR1A*, *FCGR3A*, *TLR2*, *CD68*), and *TREM2* signalling (*TREM2*, *TYROBP*).

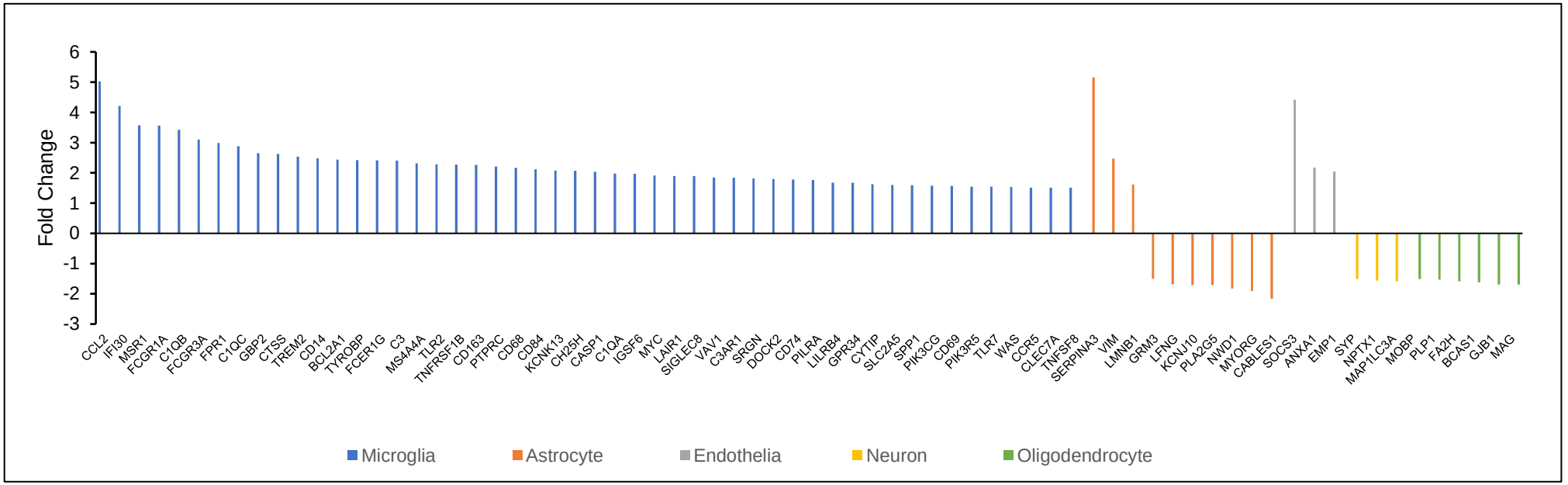

Figure 3.12 Microglial/ Macrophage associated differentially expressed genes from Frozen Spinal Cord.

Using published RNA Sequencing Data (Zhang et al., 2016), the cell type of origin was determined for each gene significantly expressed genes. Majority of genes differentially expressed were associated with microglial/macrophage gene expression. All microglial/macrophage associated genes were upregulated indicating an upregulation of microglial activity.

3.4.3 Major Findings from Microglial Deconvolution: Microglia in sMND Spinal Cord

In both FFPE and frozen spinal cord data sets, most genes associated with one cell type were linked to microglial/ macrophage expression, and most were upregulated indicating increased microglial/macrophage expression in the spinal cord in sMND. Of the two data sets, genes associated with the complement system (*C1QA, C1QB, C1QC,* and *C3*), *TREM2* and *TYROBP*, receptors linked to phagocytosis (*FCER1G, FCGR3A*), antigen presentation *(CD74, IFI30,* and *CTSS*), genes associated with regulation of the inflammatory response (*SRGN, SSP1*), and the scavenger receptor MSR1. In both data sets, microglial/macrophage associated genes did not conform to the M1/M2 macrophage phenotype classification system and instead showed a more complicated pattern of expression, with genes and pathways associated with several functions being expressed simultaneously.

3.5 Genes within the Spinal Cord and Motor Cortex are Associated with the Length of Patient Survival

In human MND, the expression of microglial markers has been found to correlate with the length of patient survival. Microarray analysis of mRNA from MND spinal cord found genes associated with microglial activation, which were able to predict disease progression (Cooper-Knock *et al.*, 2017). Furthermore assessment of microglial pathology by immunohistochemistry, revealed more extensive expression of CD68 and Iba1 in the corticospinal tract of those more rapidly progressing MND (Brettschneider, Toledo, *et al.*, 2012).

The NanoString data from the sMND cases was taken forward for further analysis using Cox Proportional Hazards Regression to identify those genes associated with slower and more rapid disease progression.

3.5.1 FFPE Spinal Cord

Using the sMND gene expression data from FFPE spinal cord, 38 genes were identified which were significantly associated with patient survival. Of these genes, 17 were upregulated in cases with longer survival (Table 3.12) and 21 of these genes were upregulated in cases with poorer survival (Table 3.13). Kaplan–Meier curves for each of these genes, demonstrating the proportion of patients alive in high and low expressing groups against time were also generated (Appendix F).

Of those 17 genes associated with longer patient survival time, *IFITM2* was the most highly expressed in those with the longest survival. *IFITM2* is associated with interferon signalling, adaptive immunity, and cytokine signalling. Those 17 genes linked to longer patient survival were associated with autophagy *(BAD, TCIRG1,*

CD44, SQSTM1, VAMP7, FCGR3A, and *CALR*), the adaptive immune response (*LAIR1, BAD, IKBKG, FCGR3A,* and *CALR*), apoptosis (*IRF3, BAD, TNFRSF1B, VIM,* and *IKBKG*) and inflammatory and cytokine signalling (*IFITM2, IRF3, TNFRSF1B, CD44, SQSTM1, IKBKG, FCGR3A*).

Of the 21 genes associated with more rapid disease progression, *TNFRSF17* was most highly expressed in those with the shortest survival times. *TNFRS17* encodes for a TNF receptor protein expressed by immune cells including microglia and is important for inflammatory signalling. This receptor binds to the ligands from the TNF superfamily, and this binding results in downstream activation NF-Kappa B and MAPK8/JNK pathway signalling. Those 17 genes linked to more rapid disease progression were associated with microglial function (*SERPINF1, NCAPH, PPFIA4, LOX, SLC2A5,* and *TMEM204*), innate immunity (*NOD1, ICAM2, IRAK2, MAP3K1, KLRD1, and IKBKE*) and adaptive immunity (*KLRD1, MAP3K1, SIGLEC8,* and *ICAM2*).

Table 3.12 Genes Associated with slower disease progression from FFPE spinal cord

Full Gene Name	Official Gene Symbol	Mean Survival (Months)		Cox Proportional Hazards coefficient	Log Rank P=
		Low Expression Cases	High Expression Cases		
Interferon Induced Transmembrane Protein 2	*IFITM2*	18.857	54	-2.775	0.001
Leukocyte Associated Immunoglobulin Like Receptor 1	*LAIR1*	19.857	53.125	-2.16	0.003
Interferon Regulatory Factor 3	*IRF3*	17.143	55.5	-1.976	0.002
BCL2 Associated Agonist of Cell Death	*BAD*	18	54.75	-1.874	0.003
T Cell Immune Regulator 1, ATPase H+ Transporting V0 Subunit A3	*TCIRG1*	23.571	49.875	-1.587	0.017
Uracil DNA Glycosylase	*UNG*	23.571	49.875	-1.587	0.017
Tumour Necrosis Factor Receptor Superfamily 1b	*TNFRSF1B*	20.857	52.25	-1.5	0.012
Cluster of Differentiation 44	*CD44*	20.857	52.25	-1.462	0.016
Peroxiredoxin 1	*PRDX1*	20.429	52.625	-1.376	0.015
Sequestesome 1	*SQSTM1*	20.429	52.625	-1.376	0.015
Thioredoxin Reductase 1	*TXNRD1*	23	50.375	-1.279	0.024
Vimentin 1	*VIM*	24.143	49.375	-1.19	0.039
Inhibitor of Nuclear Factor Kappa B Kinase Regulatory Subunit Gamma	*IKBKG*	24	49.5	-1.142	0.048
Vesicle Associated Membrane Protein 7	*VAMP7*	23.857	49.625	-1.122	0.047
Fc Fragment of Igg Receptor IIIa	*FCGR3A*	21.857	51.375	-1.118	0.044
Calreticulin	*CALR*	22.143	51.125	-1.112	0.042
DNA Mismatch Repair Protein Msh2	*MSH2*	22.143	51.125	-1.112	0.042

Table 3.13 . Genes Associated with more rapid disease progression from FFPE spinal cord

Full Gene Name	Official Gene Symbol	Mean Survival (Months)		Cox Proportional Hazards coefficient	Log Rank P=
		Low Expression Cases	High Expression Cases		
TNF Receptor Superfamily Member 17	*TNFRSF17*	59.143	18.75	2.259	0.001
Inhibitor of Nuclear Factor Kappa B Kinase Subunit Epsilon	*IKBKE*	58.857	19	1.881	0.003
Killer Cell Lectin Like Receptor D1	*KLRD1*	57.714	20	1.824	0.004
Proliferating Cell Nuclear Antigen	*PCNA*	49.857	26.875	1.682	0.026
Mitogen-Activated Protein Kinase Kinase Kinase 1	*MAP3K1*	57.571	20.125	1.675	0.005
Interleukin 1 Receptor Associated Kinase 2	*IRAK2*	56.857	20.75	1.621	0.01
Embryonic Ectoderm Development	*EED*	54.571	22.75	1.605	0.013
Sialic Acid Binding Ig Like Lectin 8	*SIGLEC8*	54.429	22.875	1.591	0.013
Serpin Family F Member 1	*SERPINF1*	53.286	23.875	1.524	0.02
DNA Ligase 1	*LIG1*	53.143	24	1.521	0.019
Leucine Rich Alpha-2-Glycoprotein 1	*LRG1*	53.429	23.75	1.436	0.026
Non-SMC Condensin I Complex Subunit H	*NCAPH*	54.714	22.625	1.365	0.02
PTPRF Interacting Protein Alpha 4	*PPFIA4*	54.714	22.625	1.365	0.02
Lysyl Oxidase	*LOX*	52.286	24.75	1.332	0.025
Intercellular Adhesion Molecule 2	*ICAM2*	50.286	26.5	1.302	0.048
Transglutaminase 1	*TGM1*	54.429	22.875	1.275	0.03
DNA Methyltransferase 3 Beta	*DNMT3B*	52.714	24.375	1.273	0.032
Solute Carrier Family 2 Member 5	*SLC2A5*	53.571	23.625	1.222	0.037
Nucleotide Binding Oligomerization Domain Containing 1	*NOD1*	50.857	26	1.203	0.043
Transmembrane Protein 204	*TMEM204*	50.857	26	1.203	0.043
Eomesodermin	*EOMES*	53	24.125	1.166	0.048

3.5.2 Frozen Spinal Cord

Using the sMND gene expression data from frozen spinal cord, 46 genes were identified which were significantly associated with patient survival. Of these genes, 23 were upregulated in cases with longer survival (Table 3.14) and 23 of these genes were upregulated in cases with more rapid disease progression (Table 3.15). Kaplan–Meier curves for each of these genes, demonstrating the proportion of patients alive in high and low expressing groups against time were also generated (Appendix G).

Of those 23 genes associated with longer patient survival time, IL2RG was the most highly expressed in those with the longest survival. The protein coded by this gene, Cytokine Receptor Common Subunit Gamma, is a key component of cytokine receptors. Those 23 genes linked to longer patient survival were associated with the innate immune response (*ATG5, TNFRSF1A, C1QA, C1QB, BID, KLRK1, NFKB1,* and *S100A12*), adaptive immune response (*IL2RG, CD3D, KLRK1,* and *NFKB1*), cytokine signalling (*IL2RG, TNFRSF1A, CXCL9,* and *NFKB1*) and growth factor signalling (*IL2RG, TNFRSF1A, CAMK4* and *NFKB1*).

Of the 23 genes associated with more rapid disease progression, *TUBB4A* was most highly expressed in those cases with the shortest patient survival. *TUBB4A* codes for beta-tubulin, a protein from the tubulin family of proteins that form and organise microtubules. Microtubules are a key component of the cytoskeleton. Those 23 genes associated with rapid disease progression are linked to adaptive immune response (*TUBB4A, EGFR, PRKCQ, IKBKG, RAC1, CSF2RB, ITGAV,* and *ERBB3*), growth factor signalling (*EGFR, IKBKG, RAC1, CSF2RB, ITGAV,* and *ERBB3*), angiogenesis (*EGFR, RAC1, CSF2RB, ITGAV,* and *ERBB3*), and oligodendrocyte function (*MOBP, FA2H, PRKCQ, CNP,* and *ERBB3*).

Table 3.14 Genes Associated with More Rapid Disease Progression from Frozen Spinal cord.

Full Gene Name	Official Gene Symbol	Mean Survival (Months)		Cox Proportional Hazards coefficient	Log Rank P=
		Low Expressing Cases	High Expressing Cases		
tubulin beta 4A class IVa	*TUBB4A*	55.75	19.75	2.36	<0.001
potassium inwardly rectifying channel subfamily J member 10	*KCNJ10*	54.75	20.75	1.87	<0.001
epidermal growth factor receptor	*EGFR*	54.875	20.625	1.54	0.01
myelin associated oligodendrocyte basic protein	*MOBP*	55.75	19.75	1.44	0.01
fatty acid 2-hydroxylase	*FA2H*	54.875	20.625	1.41	0.01
protein kinase C theta	*PRKCQ*	52.5	23	1.37	0.02
2',3'-cyclic nucleotide 3' phosphodiesterase	*CNP*	53.625	21.875	1.36	0.02
cytochrome P450 family 27 subfamily A member 1	*CYP27A1*	53.625	21.875	1.36	0.02
endothelial cell adhesion molecule	*ESAM*	51.5	24	1.33	0.03
ring finger protein 8	*RNF8*	52.375	23.125	1.28	0.03
inhibitor of nuclear factor kappa B kinase regulatory subunit gamma	*IKBKG*	54.25	21.25	1.28	0.02
peroxiredoxin 1	*PRDX1*	54.25	21.25	1.28	0.02
Rac family small GTPase 1	*RAC1*	54.25	21.25	1.28	0.02
peptidyl arginine deiminase 2	*PADI2*	53.375	22.125	1.25	0.02
cyclin dependent kinase inhibitor 1C	*CDKN1C*	54.75	20.75	1.22	0.02
colony stimulating factor 2 receptor subunit beta	*CSF2RB*	49.75	25.75	1.21	0.04
proton activated chloride channel 1	*TMEM206*	53.25	22.25	1.17	0.03
NACHT and WD repeat domain containing 1	*NWD1*	52.625	22.875	1.14	0.04
cyclin I	*CCNI*	53	22.5	1.14	0.04
integrin subunit alpha V	*ITGAV*	53	22.5	1.14	0.04
erb-b2 receptor tyrosine kinase 3	*ERBB3*	50.625	24.875	1.12	0.05
SPT7 like, STAGA complex subunit gamma	*SUPT7L*	53.5	22	1.09	0.04
IQ motif and Sec7 domain ArfGEF 1	*IQSEC1*	53.25	22.25	1.08	0.04

Table 3.15 Genes Associated with Slower Disease Progression from Frozen Spinal cord

Full Gene Name	Official Gene Symbol	Mean Survival (Months)		Cox Proportional Hazards coefficient	Log Rank P=
		Low Expressing Cases	High Expressing Cases		
interleukin 2 receptor subunit gamma	*IL2RG*	16.625	58.875	-2.65	<0.001
serine peptidase inhibitor, Kunitz type 1	*SPINT1*	17.875	57.625	-2.43	<0.001
DNA methyltransferase 1	*DNMT1*	20.875	54.625	-2.05	<0.001
autophagy related 5	*ATG5*	23.875	51.625	-1.88	0.01
Cluster of Differentiation 163	*CD163*	20.75	54.75	-1.87	<0.001
T-cell surface glycoprotein CD3 delta chain	*CD3D*	20	55.5	-1.79	<0.001
TNF receptor superfamily member 1A	*TNFRSF1A*	23.125	52.375	-1.58	0.01
complement C1q A chain	*C1QA*	23.375	52.125	-1.56	0.02
checkpoint kinase 2	*CHEK2*	20.25	55.25	-1.52	0.01
SRY-box transcription factor 4	*SOX4*	21.5	54	-1.51	0.01
serpin family A member 3	*SERPINA3*	25.25	50.25	-1.49	0.02
non-SMC condensin I complex subunit H	*NCAPH*	21.875	53.625	-1.46	0.01
complement C1q B chain	*C1QB*	24.5	51	-1.45	0.02
ceruloplasmin	*CP*	24.5	51	-1.45	0.02
FA complementation group C	*FANCC*	23	52.5	-1.38	0.02
neuroligin 2	*NLGN2*	26.25	49.25	-1.34	0.04
BH3 interacting domain death agonist	*BID*	24.875	50.625	-1.31	0.03
killer cell lectin like receptor K1	*KLRK1*	23.125	52.375	-1.28	0.03
C-X-C motif chemokine ligand 9	*CXCL9*	21.25	54.25	-1.28	0.02
calcium/calmodulin dependent protein kinase IV	*CAMK4*	22.125	53.375	-1.25	0.02
membrane spanning 4-domains A1	*MS4A1*	21.375	54.125	-1.24	0.03
nuclear factor kappa B subunit 1	*NFKB1*	20.75	54.75	-1.22	0.02
S100 calcium binding protein A12	*S100A12*	22.375	53.125	-1.14	0.04

3.5.3 Frozen Motor Cortex

Using the sMND gene expression data from frozen motor cortex, 47 genes were identified which were significantly associated with survival. Of these, 30 were upregulated in cases with longer survival (Table 3.16) and 17 were upregulated in cases with more rapid progression (Table 3.17). Kaplan–Meier curves for each of these genes, demonstrating the proportion of patients alive in high and low expressing groups against time were also generated (Appendix H).

Of those 30 genes associated with longer patient survival time, *BMI1* was the most highly expressed in those with the longest survival. *BMI1* encodes a ring finger protein, which is a major component of the polycomb group complex 1 which is essential for epigenetic repression through chromatin remodelling. It also plays a critical role in the DNA damage repair response. Those 30 genes linked to longer patient survival were associated with the innate immune response (*EP300, PIK3CG, BCL10, TMEM173, IKBKB, CHUK, TLR4, IFNAR2,* and *IRAK4*), cytokine signalling (*INPP5D, SQSTM1, EP300, BCL10, IKBKB, CHUK, IFNAR2, IRAK4*), growth factor signalling (*SQSTM1, PIK3CG, BCL10, RHOA, IKBKB, CHUK, TLR4* and *IFNAR2*), Inflammatory signalling (*GCLC, EP300, DAB2, TMEM173, IKBKB, CHUK*, *TLR4, IFNAR2*), epigenetic regulation (*BMI1, KDM3A, EP300, DOT1L, MBD2, HDAC6, SETD1A*), microglial function (*PTGER4, BLNK, BCL10, TMEM173, RPS10, HPS4, LOX*) , apoptosis (*PIK3CG, BCL10, IKBKB, CHUK, TLR4, IRAK4*) , NF- Kappa B (*BLNK, BCL10, IKBKB, CHUK, TLR4, IRAK4*), adaptive immune response (*INPP5D, PIK3CG, BLNK, IKBKB, CHUK*), cellular stress (*BMI1, EP300, HDAC6, BCL10, RPA1*), and DNA Damage (*FANCC, EP300, BCL10, RPA1, MRE11*).

Of those 17 genes upregulated in cases with more rapid disease progression in the motor cortex, *CD244* was the most highly upregulated. *CD244* encodes a cell

surface receptor expressed by natural killer cells and some T cells. This receptor is associated with the mediation of non MHC II mediated cell killing (Georgoudaki *et al.*, 2015). Those 17 genes associated with rapid disease progression are linked to cytokine signalling (*LTA, LTB, TNFRSF1B, TNF*, and *IL1RN*), growth factor signalling *(TNF, TP53, CD19, PLD2,* and *RAG1*), the innate immune response (*CD244, LTA , LY9, TNFRSF1B,* and *TNF*), microglial function (*SPINT1, TNF, CHST8, IL1RN,* and *ARHGAP24*), inflammatory signalling (*CD244, LTA, LTB,* and *TNF*), and NF-Kappa B signalling (*CD244, LTA, LTB, TNFRSF1B,* and *TNF*).

Table 3.16 Genes Associated with More Rapid Disease Progression from Frozen Motor Cortex

Full Gene Name	Official Gene Symbol	Mean Survival (Months)		Cox Proportional Hazards coefficient	Log Rank P=
		Low Expressing Cases	High Expressing Cases		
Cluster of Differentiation 244	*CD244*	52.75	21.13	2.11	0.00
forkhead box P3	*FOXP3*	52.75	21.13	2.11	0.00
lymphotoxin alpha	*LTA*	51.00	22.88	2.00	0.00
sestrin 2	*SESN2*	53.63	20.25	1.88	0.00
lymphotoxin beta	*LTB/ TNFC*	51.00	22.88	1.65	0.01
lymphocyte antigen 9	*LY9*	49.88	24.00	1.59	0.01
serine peptidase inhibitor, Kunitz type 1	*SPINT1*	50.63	23.25	1.41	0.02
TNF receptor superfamily member 1B	*TNFRSF1B*	50.00	23.88	1.40	0.02
tumour necrosis factor	*TNF*	50.38	23.50	1.40	0.02
tumour protein p53	*TP53*	49.50	24.38	1.37	0.02
carbohydrate sulfotransferase 8	*CHST8*	45.38	28.50	1.31	0.05
interleukin 1 receptor antagonist	*IL1RN*	47.63	26.25	1.17	0.05
Cluster of Differntiation 19	*CD19*	49.25	24.63	1.17	0.04
phospholipase D2	*PLD2*	49.13	24.75	1.16	0.04
recombination activating 1	*RAG1*	48.88	25.00	1.13	0.04
Spi-B transcription factor	*SPIB*	49.88	24.00	1.07	0.05
Rho GTPase activating protein 24	*ARHGAP24*	50.00	23.88	1.05	0.05

Table 3.17 Genes Associated with Slower Disease Progression from Frozen motor Cortex

Full Gene Name	Official Gene Symbol	Mean Survival (Months)		Cox Proportional Hazards coefficient	Log Rank P=
		Low Expressing Cases	High Expressing Cases		
BMI1 proto-oncogene, polycomb ring finger	*BMI1*	22.88	51	-2.03	<0.001
lysine demethylase 3A	*KDM3A*	23	50.88	-2.01	<0.001
inositol polyphosphate-5-phosphatase D	*INPP5D*	20.75	53.13	-1.92	<0.001
sequestosome 1	*SQSTM1*	24.75	49.13	-1.9	0.01
glutamate-cysteine ligase catalytic subunit	*GCLC*	22.25	51.63	-1.76	0.01
FA complementation group C	*FANCC*	21.13	52.75	-1.65	0.01
E1A binding protein p300	*EP300*	23.75	50.13	-1.61	0.01
prostaglandin E receptor 4	*PTGER4*	22.13	51.75	-1.59	0.01
DOT1 like histone lysine methyltransferase	*DOT1L*	24.63	49.25	-1.57	0.01
phosphatidylinositol-4,5-bisphosphate 3-kinase catalytic subunit gamma	*PIK3CG*	24.63	49.25	-1.57	0.01
DAB adaptor protein 2	*DAB2*	24.38	49.5	-1.56	0.01
methyl-CpG binding domain protein 2	*MBD2*	21.88	52	-1.56	0.01
B cell linker	*BLNK*	22.63	51.25	-1.51	0.01
histone deacetylase 6	*HDAC6*	22.63	51.25	-1.51	0.01
BCL10 immune signalling adaptor	*BCL10*	26	47.88	-1.49	0.02
TATA-box binding protein	*TBP*	26.88	47	-1.42	0.03
stimulator of interferon response cGAMP interactor 1	*TMEM173*	23.25	50.63	-1.41	0.02
ribosomal protein S10	*RPS10*	24.63	49.25	-1.39	0.02
ras homolog family member A	*RHOA*	27.63	46.25	-1.38	0.04
replication protein A1	*RPA1*	24.13	49.75	-1.38	0.02
inhibitor of nuclear factor kappa B kinase subunit beta	*IKBKB*	24	49.88	-1.34	0.02
component of inhibitor of nuclear factor kappa B kinase complex	*CHUK*	22.38	51.5	-1.32	0.02
adhesion molecule with Ig like domain 2	*AMIGO2*	22.5	51.38	-1.29	0.02
toll like receptor 4	*TLR4*	23.38	50.5	-1.26	0.02
HPS4 biogenesis of lysosomal organelles complex 3 subunit 2	*HPS4*	26	47.88	-1.26	0.03
lysyl oxidase	*LOX*	26.5	47.38	-1.23	0.04
SET domain containing 1A, histone lysine methyltransferase	*SETD1A*	27.13	46.75	-1.21	0.04
MRE11 homolog, double strand break repair nuclease	*MRE11*	27	46.88	-1.2	0.05
interferon alpha and beta receptor subunit 2	*IFNAR2*	23.88	50	-1.09	0.04
interleukin 1 receptor associated kinase 4	*IRAK4*	23.5	50.38	-1.08	0.04

3.5.4 Major Findings from Survival Analysis

Cox proportional hazards regression analysis has shown genes expressed within the spinal cord and motor cortex are associated with differences in the rate of disease progression.

From the FFPE spinal cord data, there was a similar number of genes whose expression was associated with both increased and reduced rate of decline. Those genes associated with increased length of survival time were associated with autophagy, adaptive immunity, cytokine signalling and apoptosis. Those genes associated with faster disease progression were associated with microglial function, and innate and adaptive immunity.

From the frozen spinal cord data set, there were an equal number of genes associated with increased and decreased length of survival. Key themes associated with longer survival included features of both the adaptive and innate immune response, cytokine signalling and growth factor signalling. Genes associated with innate and adaptive immunity, and cytokine signalling, and growth factors were associated with more rapid patient decline.

In the motor cortex, although little difference was observed in inflammatory signalling between sMND cases and control, several genes associated with the rate of disease progression. Most of these were associated with a slower decline, and were associated with DNA damage and repair, innate and adaptive immune signalling, cytokine signalling, the NF-KB pathway, microglial function, epigenetic regulation, cellular stress and growth factor signalling. Those genes associated with more rapid patient decline were associated with growth factor and cytokine signalling, microglial function, immunity, and NF-KB.

Microglial function and pathways associated with microglial signalling appear to be associated with both improved length of survival and more rapid signalling across the CNS.

3.6 Validation of NanoString Data

In the previous half of Chapter Three, two spinal cord data sets and one motor cortex data set was generated using the NanoString platform.

Initially the platform was trialled using FFPE tissue due to the large amounts of well characterised FFPE tissue available. Low gene expression, particularly of the normalisation genes, were overcome by seeking new data analysis methods. This data showed a significant upregulation of inflammatory signalling in sMND. However, older tissue was observed to have reduced biological signal, limiting the number of cases that could be used to build cohorts.

Therefore, the decision was made to use frozen tissue (spinal cord and motor cortex), and additional QC checks were added. As observed with the FFPE spinal cord data set, the spinal cord showed signification dysregulation of neuroinflammatory gene expression in sMND, with most of those genes being upregulated. In contrast the motor cortex showed very little change in inflammatory signalling compared to control.

The following sections will focus on validating the NanoString data by comparing the two spinal cord NanoString datasets, and via the comparison to publicly available data sets produced using alternative methods – microarray and RNA Sequencing (RNASeq). Furthermore, these data will be used to identify specific targets and key themes for validation via immunohistochemistry.

3.6.1 Replicability of NanoString

The fold changes of all genes (770) from the FFPE and Frozen NanoString spinal cord data sets were assessed using a non-parametric Spearman's Correlation, which showed a significant correlation ($R=0.148$, $p<0.001$, Figure 3.13 A).

All significantly differently expressed genes from the FFPE (100 genes), and Frozen (89 genes) datasets were compared for overlapping genes to identify genes differentially expressed in both. A Venn diagram showing these results is given (Figure 3.13 B). Overall, 21 genes were found to differentially expressed (absolute fold change >1.5; $q<0.05$) in both the FFPE and Frozen data sets. All genes showed fold changes of the same direction (Figure 3.13 C), indicating good agreement between the two data sets. Of those genes significant in only one of the spinal cord gene lists (frozen or FFPE), 59.18% showed changes in the same direction to the gene in the other dataset. Overall, this indicates the NanoString platform gives reliable results.

C.

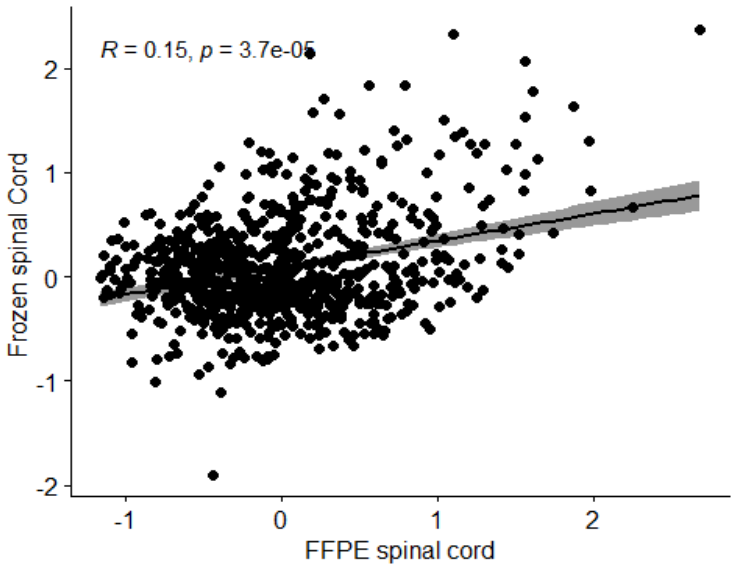

B.

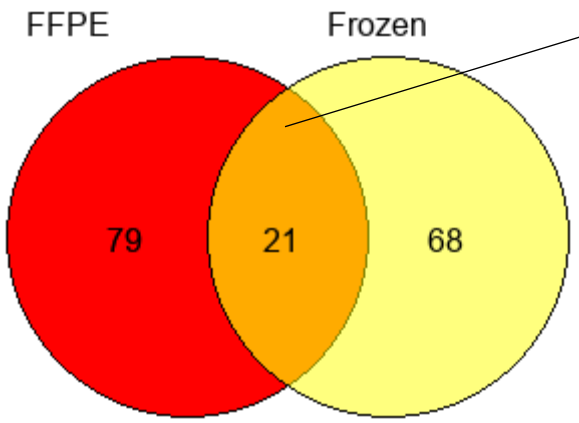

Overlap between two data sets:

ANXA1	FCGR3A
C1QA	IFI30
C1QB	MSR1
C1QC	SERPINA3
C3	TIMP1
CD163	TMEM100
CD74	TNFRSF1A
CTSS	TREM2
DAB2	TYROBP
EMP1	VIM
FCER1G	

A.

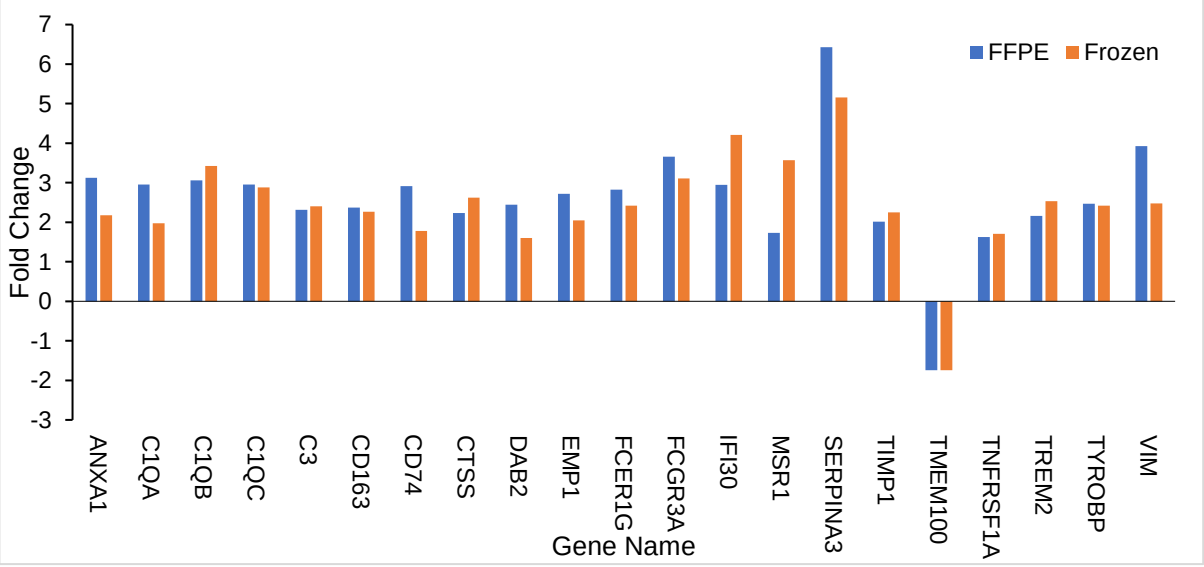

Figure 3.13 Comparison of NanoString data generated from FFPE and Frozen spinal cord.

A. *Spearman's correlation of the Log_2 Fold changes generated from FFPE and Frozen spinal cord tissue using NanoString (R=0.148, p<0.001)*
B. *Venn diagram comparing the overlapping significantly expressed genes between the two spinal cord NanoString data sets.*
C. *Bar chart comparing the fold changes from those genes common to both data sets. All genes change in the same direction indicating good alignment between the two data sets.*

3.6.2 Validity of NanoString Findings

To determine whether these gene expression results could be produced again using another gene expression platform, publicly available gene expression data sets generated using RNASeq and microarray were analysed. To validate the spinal cord NanoString data, an RNASeq data set (Brohawn, O'Brien and Bennett, 2016) was used, which compared gene expression between control and sMND groups in cervical spinal cord homogenate. To validate the motor cortex NanoString data, a microarray data set (Aronica *et al.*, 2015) which compared gene expression between control and sMND groups in motor cortex homogenate was analysed.

3.6.3 Spinal Cord Gene Expression Validation

3.6.3.1 RNASeq Data Analysis Results

Following the filtration of low expressing genes, 740 genes remained in the Spinal cord RNASeq data set from the 770 found on the original NanoString inflammation panel. Of these genes, eight reached significance (absolute fold change >1.5, adjusted p <0.05). The distribution of data is shown in Figure 3.14, with those genes with the greatest significance tending to be upregulated – a feature observed in the NanoString data.

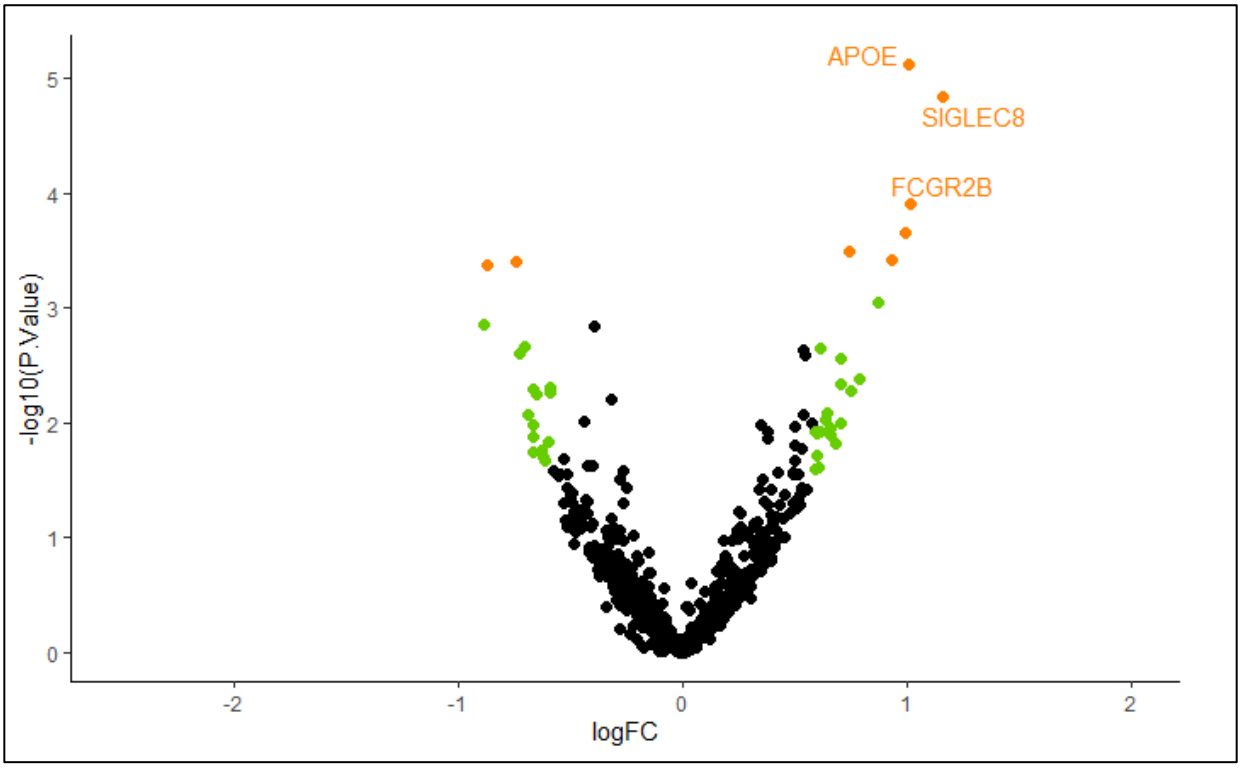

Figure 3.14 Volcano Plot of Brohawn, O'Brien and Bennett (2016) Spinal Cord RNA Seq. Validation Data

Volcano plot showing fold change against the significance value (Green Points p<0.05; FC>1.5; Orange Points FDR adjusted p<0.05; FC>1.5, Labelled Genes FDR adjusted p<0.05, FC>2).

3.6.3.2 Correlation Analysis between Spinal Cord Data from NanoString and RNASeq

The log_2 fold changes from the frozen spinal cord NanoString dataset and spinal cord RNASeq dataset were compared using Spearman's Rho correlation (Figure 3.15) showing significant correlation (R= 0.25, p<0.0011).

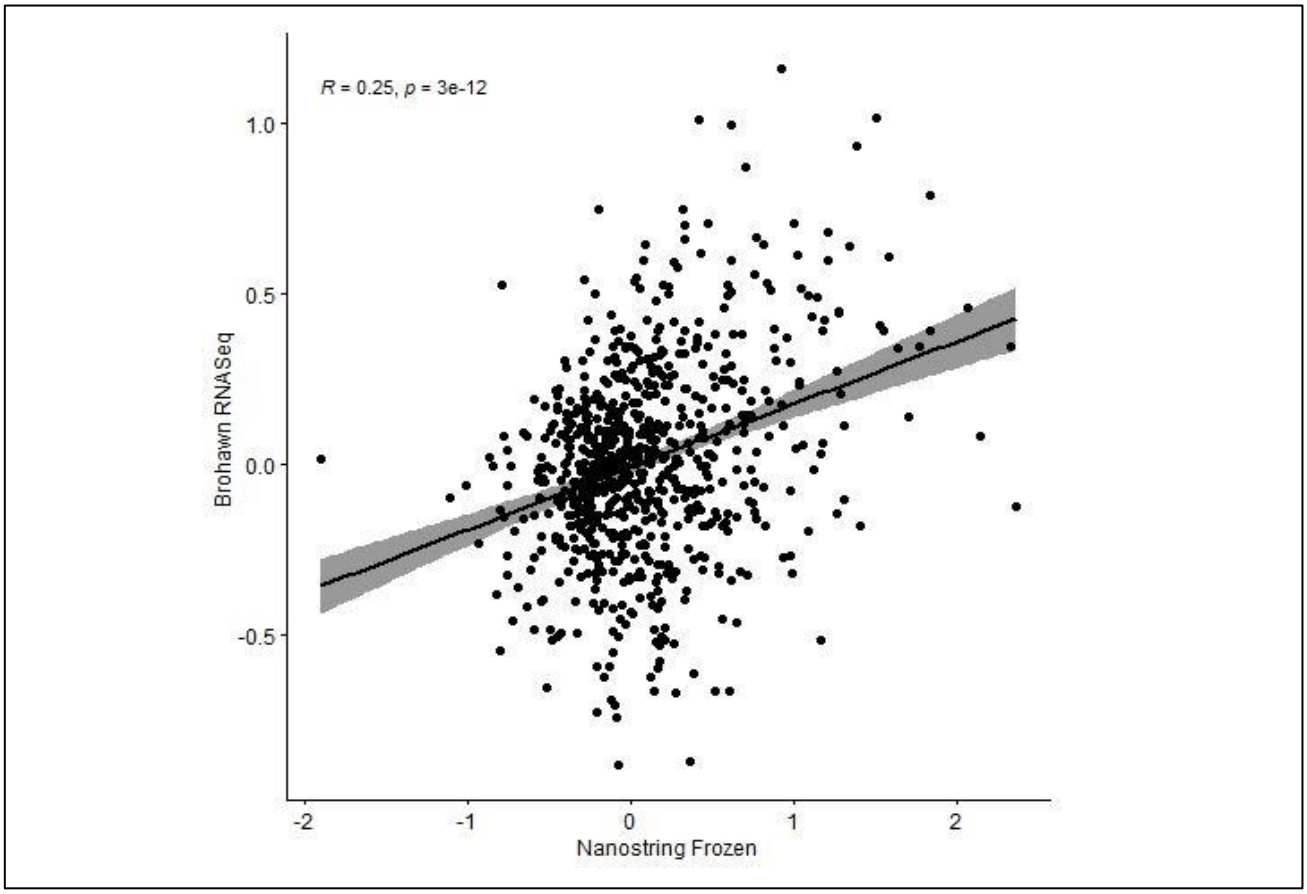

Figure 3.15 Spearman's Rho Correlation between the spinal cord NanoString dataset and the RNASeq dataset.

Spearman's correlation of the Log_2 Fold changes generated from FFPE and Frozen spinal cord tissue using NanoString (R= 0.25, p<0.0001).

Black line indicates line of best fit, grey band indicates 95% confidence interval.

Of the genes significantly differently expressed at the FDR uncorrected p value in the frozen Spinal Cord NanoString dataset and RNASeq data, 13 genes were in both data sets. Of the 13 genes, 9 genes shared the same direction of fold change (Figure 3.16).

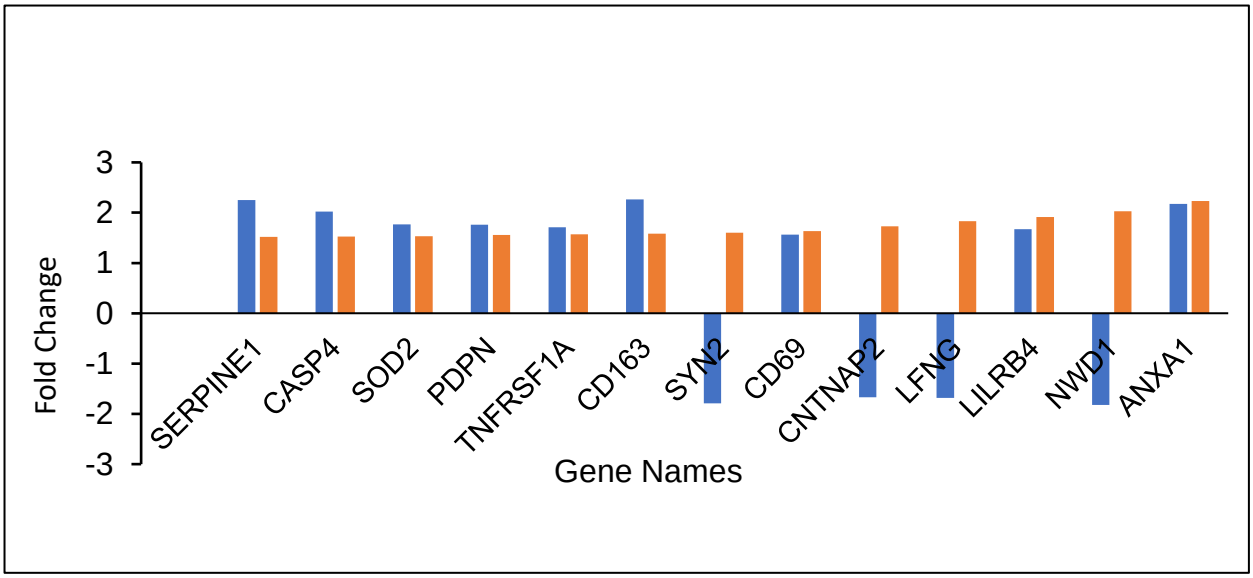

Figure 3.16 Bar graph comparing fold changes from genes common to both the spinal cord RNASeq data set and NanoString spinal cord data set.

Thirteen overlapped between the two data sets. Of those, nine genes had the same fold change direction, and four had opposite fold change directions.

Blue bars show the NanoString Spinal cord data, orange bars indicate the RNASeq spinal cord data.

3.6.4 Motor Cortex Gene Expression Validation

3.6.4.1 Microarray Raw Data Analysis Results

Of the 641 genes in the motor cortex microarray data set, 59 genes were found to be significantly different between MND and control groups (absolute fold change >1.5, adjusted p <0.05), 45 genes were upregulated and 14 downregulated. Volcano plots for both the microarray data and the motor cortex NanoString data (Figure 3.17) show a similar spread of data, with slightly more genes being upregulated then downregulated.

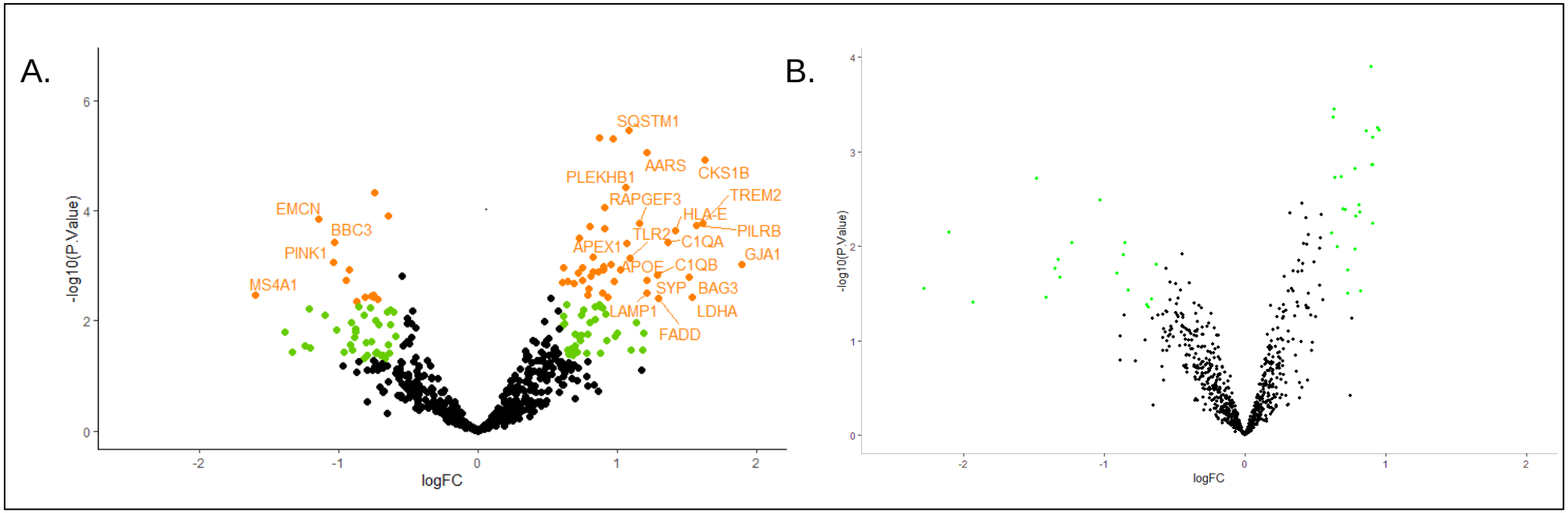

Figure 3.17 Volcano plots demonstrating the spread of data from the motor cortex microarray and NanoString datasets.

A) Volcano plot showing fold change against the significance value for the motor cortex microarray data. Of all the significant genes 114 were upregulated, and 101 genes were down regulated (Green Points p<0.05; FC>1.5; Orange Points q<0.05; FC>1.5, Labelled Genes q<0.05, FC>2). One point was removed (SERPINA3 - Fold change = 11.93, q <0.001) as it was off the scale of the graph.

B) Volcano plot showing fold change against the significance value for the motor cortex NanoString data. Green Points p<0.05; FC>1.5. No genes reached significance following FDR correction.

3.6.4.2 Correlation Analysis between Motor Cortex Data from NanoString and Microarray

The log_2 fold changes for all genes present on the NanoString neuroinflammation panel from the motor cortex NanoString dataset and motor cortex microarray dataset were compared using Spearman's Rho correlation (Figure 3.18) showing a significant correlation ($R= 0.22$, $p<0.0001$), indicating agreement between the two platforms.

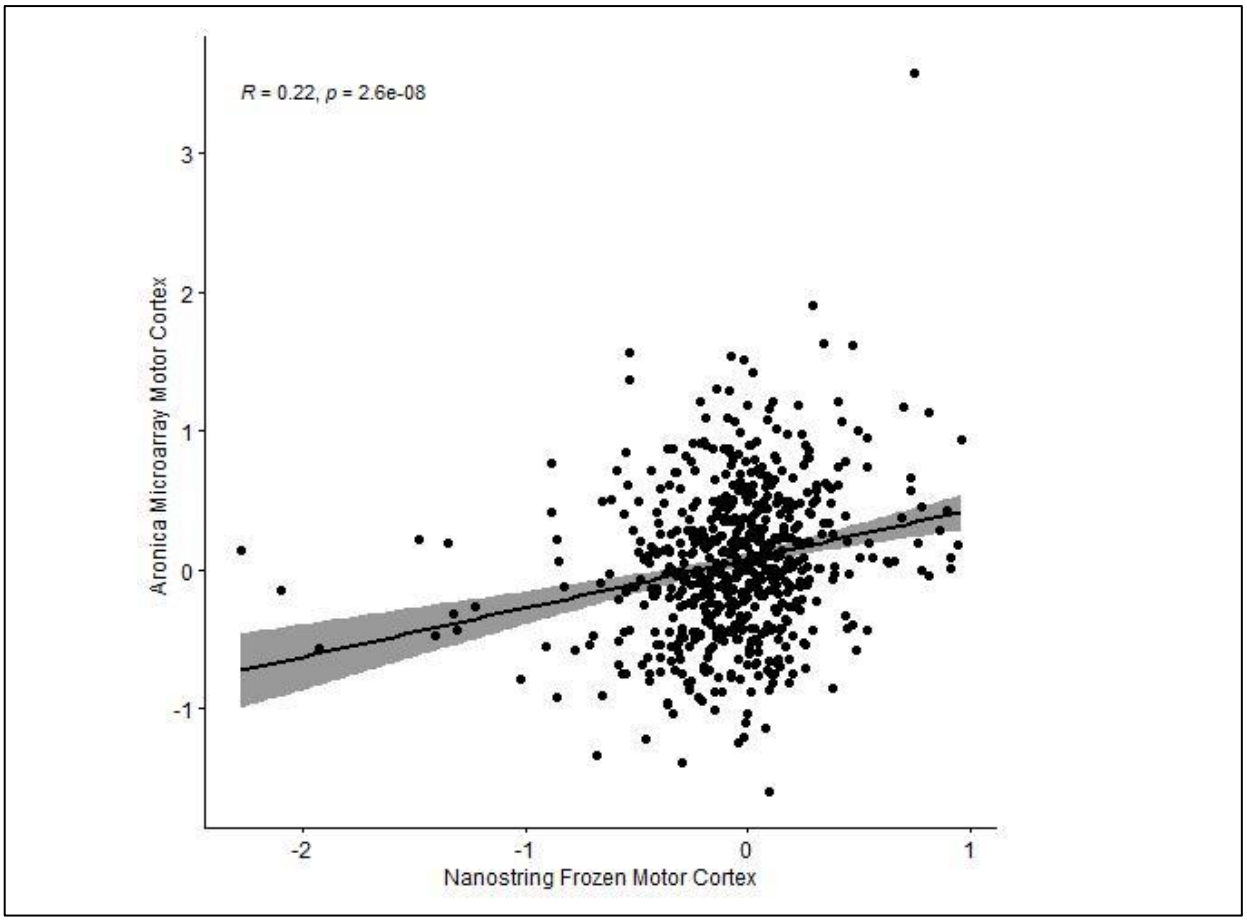

Figure 3.18 Spearman's Rho Correlation between the Motor Cortex NanoString dataset and the motor cortex microarray dataset.

Spearman's correlation of the Log_2 Fold changes generated from Motor Cortex Microarray data and Frozen Motor Cortex NanoString data (R= 0.25, p<0.0001).

The black line shows the line of best fit, and the grey band indicates 95% confidence interval.

Of the significantly differentially expressed genes at the FDR uncorrected p value in the motor cortex NanoString dataset and microarray data, seventeen genes were in both data sets. Of these seventeen genes, fourteen genes shared the same direction of change (Figure 3.19).

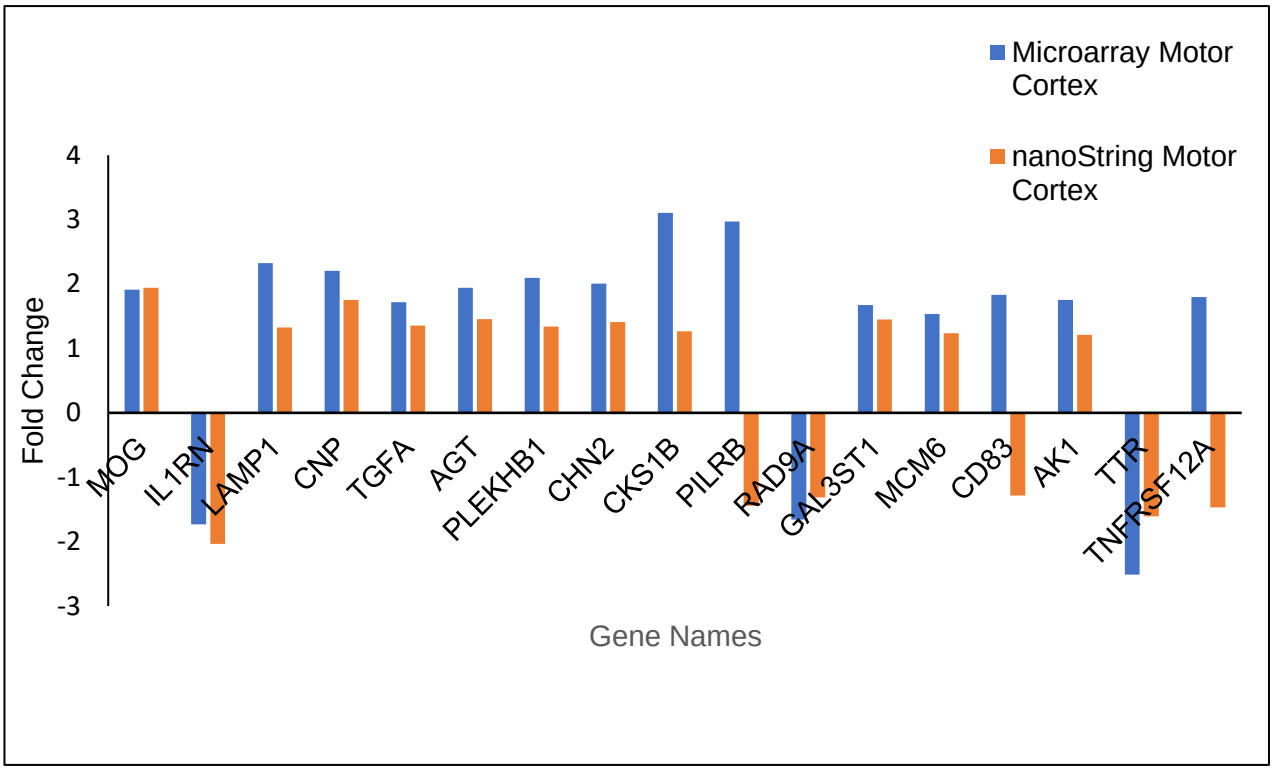

Figure 3.19 Bar graph comparing fold changes from genes common to both the motor cortex microarray data set and NanoString motor cortex data set.

Fourteen genes had the same fold change direction, and three had opposite fold change directions.

3.6.5 Major Findings of Gene Expression Validation.

To address the reliability of NanoString as a gene expression platform, the results of the FFPE and frozen spinal cord data were compared. These data were significantly correlated, with all significantly expressed changes showing fold changes of the same direction. This demonstrates the NanoString platform can produce reliable data even using different tissue types and RNA quality.

To validate the frozen NanoString data, publicly available data RNASeq and microarray datasets were re-analysed and the findings correlated with NanoString data. Regarding the spinal cord, both data sets showed a similar spread of data with the majority of gene expression being upregulated. The two data sets had a weak correlation, and genes significant at the FDR uncorrected p value showed a 70% agreement in fold change direction. In the motor cortex, the data sets correlated well with each other, and showed a similar spread of up and down regulation. Furthermore, 82% of genes significant are the FDR uncorrected p value shared the same direction of dysregulation.

3.7 Identification of Specific Targets for Further Validation

The NanoString data, as described in Section 3.2, demonstrated increased neuroinflammatory gene expression in sMND. This was primarily observed in the spinal cord with much lesser expression in the motor cortex. The next step was to assess what the key features of neuroimmunity are in sMND as implied by the gene expression data and then to validate these gene expression data at the protein level using immunohistochemistry. The following section will outline the selection of specific targets from the gene expression data, for further validation.

For the following analysis, the frozen spinal cord NanoString data serve as the main data set. However, the results from the analysis of the pre-published RNAseq data (Brohawn, O'Brien, & Bennett 2016) used in the validation of the spinal cord data, as well as the FFPE NanoString data will be consulted. The data will be examined on both a gene-by-gene basis primarily using the adjusted p value (q; the adjusted p value takes into account the magnitude of the fold change combined with the FDR uncorrected p value), and pathway analysis.

From here, all the spinal cord NanoString data sets will be referred to as FFPE and Frozen, based on the tissue type used to produce each data set. The results from the spinal cord RNAseq data by Brohawn, O'Brien, & Bennett (2016) will be referred to as the RNAseq data. Significance value will describe genes with $q<0.05$ and absolute fold change >1.5 unless otherwise stated.

3.7.1 Comparison of all Spinal Cord Data

All significantly differentially expressed genes from the three spinal cord data sets (FFPE, Frozen and RNASeq) were compared. A Venn diagram showing these results is given below (Figure 3.20). *CTSS* (Cathepsin S) was upregulated in all spinal cord data.

From the Frozen data and RNASeq data, two genes *FCGR2B* and *SIGLEC8* were also upregulated in both data sets. Those genes were dysregulated in both the FFPE and frozen NanoString data sets are listed above in section 3.2.2, and 3.3.5.

From the FFPE data and RNASeq data sets, two genes *APOE* and *PTGS2* were both significantly upregulated. The fold changes and significance values for all over lapping genes are given (Table 3.18). There was 100% agreement on the direction of change (up or down regulation in sMND) across the genes.

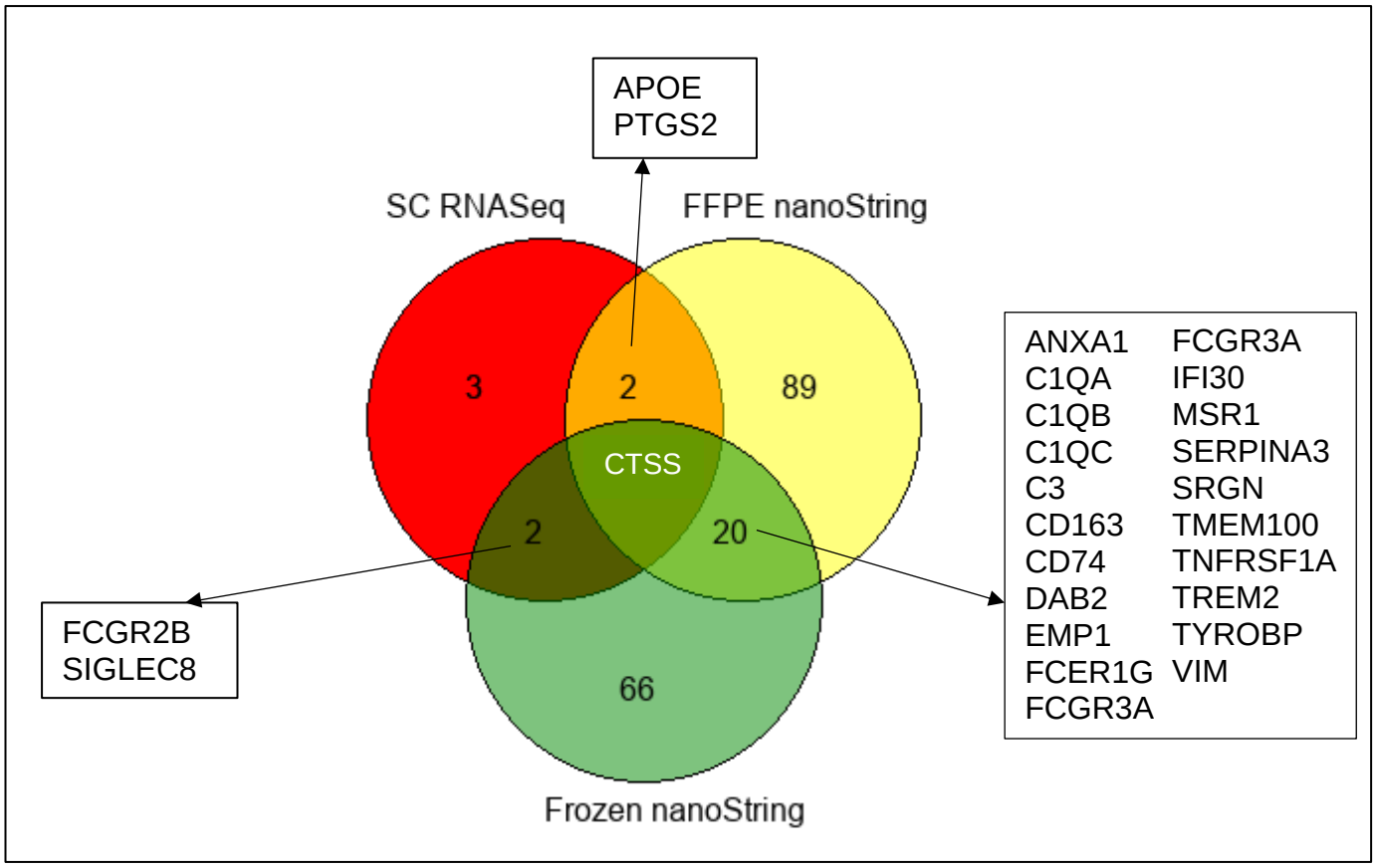

Figure 3.20 Venn diagram highlighting genes common to the spinal cord data sets.

CTSS was commonly expressed all three spinal cord data sets Two genes (APOE & PTGS2 also known as COX2) were commonly expressed in between the FFPE and RNASeq dataset, and two genes (FCGR2B and SIGLEC8) were commonly expressed in between the Frozen and RNASeq data. Those twenty genes (plus CTSS) discussed in Section 2 were commonly expressed between the FFPE and Frozen data sets.

SC = spinal cord

Table 3.18 Comparison of all overlapping genes from the frozen and FFPE spinal cord NanoString data and RNASeq Spinal Cord Data

Gene Symbol	Gene Name	Frozen Spinal cord NanoString		FFPE Spinal Cord NanoString		RNASeq Spinal Cord	
		Fold Change	Q	Fold Change	Q	Fold Change	Q
ANXA1	annexin A1	2.176	0.009	3.122	0.005	-1.008	1.004
APOE	apolipoprotein E	1.338	0.081	3.330	0.002	2.014	0.006
C1QA	complement C1q A chain	1.976	0.009	2.951	0.001	1.232	0.731
C1QB	complement C1q B chain	3.422	<0.001	3.058	0.002	1.273	0.675
C1QC	complement C1q C chain	2.880	<0.001	2.952	0.001	1.327	0.561
C3	complement C3	2.405	0.002	2.314	0.003	1.211	0.763
CD163	Cluster of Differentiation 163	2.265	0.042	2.370	0.047	1.046	0.991
CD74	Cluster of Differentiation 74	1.780	0.018	2.917	0.012	1.447	0.259
CTSS	cathepsin S	2.623	0.001	2.233	0.004	1.911	0.048
DAB2	DAB adaptor protein 2	1.599	0.008	2.444	0.001	1.109	0.916
EMP1	epithelial membrane protein 1	2.045	0.012	2.719	0.007	1.185	0.733
FCER1G	Fc fragment of IgE receptor Ig	2.417	0.001	2.822	<0.001	1.361	0.536
FCGR2B	Fc fragment of IgG receptor IIb	2.844	0.015	2.050	0.104	2.027	0.031
FCGR3A	Fc fragment of IgG receptor IIIa	3.105	0.004	2.050	0.104	1.267	0.676
IFI30	IFI30 lysosomal thiol reductase	4.208	<0.001	3.662	0.007	1.377	0.533
MSR1	macrophage scavenger receptor 1	3.568	<0.001	1.730	0.027	1.729	0.173
PTGS2	prostaglandin-endoperoxide synthase 2	1.285	0.451	-2.079	0.018	-1.824	0.039
SERPINA3	serpin family A member 3	5.157	0.004	6.427	0.001	-1.088	0.963
SIGLEC8	sialic acid binding Ig like lectin 8	1.897	0.027	1.410	0.191	2.235	0.005
SRGN	serglycin	1.812	0.037	2.300	0.054	1.424	0.435
TMEM100	transmembrane protein 100	-1.741	0.007	-1.746	0.037	-1.458	0.315
TNFRSF1A	TNF receptor superfamily member 1A	1.710	0.007	1.630	0.029	1.026	0.986
TREM2	triggering receptor expressed on myeloid cells 2	2.536	0.001	2.158	0.002	1.559	0.234
TYROBP	tyrosine binding protein	2.418	0.001	2.468	0.001	1.367	0.488
VIM	vimentin	2.474	0.001	3.926	0.001	-1.074	0.962

Note. Green indicates upregulation, Red indicates down regulation

With regard to the function of these genes, the following themes arise:

The Complement System

Three of the component proteins required for the formation of the Complement 1 (*C1*) complex (the first component of the classical complement pathway) were significantly differentially expressed (*C1QA, C1QB, C1QC*) in the NanoString analysis of frozen cord, as well as the NanoString analysis of FFPE material. Thus indicating the classical complement pathway may be significantly dysregulated in sMND. Furthermore, *C3* a key component in all complement pathways, was also differentially expressed in both NanoString data sets, further highlighting the role of the complement pathway.

Fc Receptor Mediated Signalling and Phagocytosis

In the frozen dataset, four Fc receptors were differentially expressed. Two of which (*FCERIG*, fold change=2.42, q=0.001; *FCGR3A*, fold change=3.11, q=0.004) were also highlighted in the FFPE NanoString data sets and one (*FCGR2B*, fold change=2.84, q=0.016) was also highlighted in the RNAseq dataset. Fc receptors are immune receptors, which bind to antibodies on potential pathogens or damaged cells. Depending on the receptor and binding antigen type, several potential cellular responses are stimulated by this, including phagocytosis and cytokine release.

Further highlighting the importance of phagocytosis as a key theme, *CD68*, one of the most widely used markers of phagocytosis, was highly significant in the Frozen data set (fold change=2.16, q=0.0007).

Antigen presentation

Antigen presentation was also highlighted as a key theme in the neuroinflammatory response in sMND. *CD74* (upregulated in both data sets) forms one of the key

proteins involved in antigen presentation and is involved in the formation and transport of Major Histocompatibility Class II (MHC II) peptide complexes. *CTSS* and *IFI30* (upregulated in both data sets) aid in this process by degrading antigenic proteins to peptides for presentation.

TREM2, TYROBP and APOE

TREM2 and *TYROBP* were both upregulated in in the frozen NanoString data set as well as the FFPE dataset. TREM2 is a membrane protein that forms a signalling receptor with TYROBP. TREM2-TRYOBP signalling results in a switch in microglial phenotype via *APOE* (see Section 1.9) from a homeostatic phenotype to a neurodegenerative phenotype (Krasemann *et al.*, 2017).

APOE was not significantly altered in the frozen NanoString dataset, (fold change=1.34, q=0.081) but was highlighted in both the FFPE dataset (fold change=3.59, q=0.001) and was the most significantly dysregulated gene from the RNASeq data analysis (fold change=2.01, q=0.006). *CCL2* (associated with the neurodegenerative microglial phenotype and triggered in response to *APOE* signalling) was significantly upregulated in the Frozen data (fold change = 5.02, q= 0.004). Further, while not significantly dysregulated in the frozen data, *SPP1*, a further marker of the neurodegenerative phenotype in this pathway had the second largest upregulated fold change in the FFPE dataset (fold change=5.076, q=0.00098.

Markers of the homeostatic microglial phenotype in this pathway were either upregulated (*TGFBR1* fold change=1.76, q=0.0267) or showed no significant dysregulation.

The TNF signalling pathway

TNF is a pro-inflammatory cytokine, with effects on lipid metabolism, coagulation, insulin resistance, and immune activation. Although TNF itself is expressed by most tissues, its receptors are almost exclusively expressed by immune cells, including microglia. Three receptor proteins were significantly upregulated in the frozen data set (*TNFRSF1A*, fold change=1.710, q=0.007; *TNFRSF1B*, fold change=2.27, q=0.007; and *TNFSF13B*, also known as *BAFF*; fold change=1.70, q=0.027) one of which (*TNFRSF1A*) was also upregulated in the FFPE dataset. Furthermore, in the FFPE data set, other TNF receptors were down regulated (*TNFRSF10B* fold change=-1.88, q=0.039; *TNFRSF17* fold change=-2.16, q=0.014).

SRGN was also significantly upregulated in the frozen NanoString data set as well as the FFPE dataset. This gene encodes a hematopoietic cell granule proteoglycan. Proteoglycans may be important for neutralizing hydrolytic enzymes and mediate granular apoptosis. *SRGN* has been associated with inflammatory signalling, including the modulation of TNF-a signalling (Korpetinou *et al.*, 2014).

Summary

Overall, this analysis has highlighted several key microglial and inflammatory processes including phagocytosis, antigen presentation, as well as TREM2 signalling – a key modulator of inflammation (potentially both toxic and protective) and APOE, which could potentially induce a disease-associated microglial state, and evidence of pro-inflammatory signalling has been demonstrated by the dysregulation of TNF receptors.

3.7.2 Key pathways common to the spinal cord data sets

To determine those most frequently occurring pathways the pathways from both NanoString data sets were compared using a Venn diagram (using GeneVenn). Pathway analysis was performed in Chapter 3. Results are given in Figure 3.22

Table 3.19 Results of KEGG pathway analysis from Frozen NanoString data set

KEGG Symbol	KEGG Pathway	Number of Genes	Genes in Pathway	
			Upregulated Genes	Down Regulated Genes
hsa04380	Osteoclast differentiation	**12**	PIK3CG, LILRB4, TNFRSF1A, TGFBR1, RELB, FOS, TYROBP, TREM2, FCGR2B, FCGR3A, FCGR1A, SOCS3,	
hsa05142	Chagas disease	**12**	CASP8, PIK3CG, TNFRSF1A, TGFBR1, FAS, C1QA, FOS, TLR2, C3, C1QC, C1QB, CCL2,	
hsa05152	Tuberculosis	**11**	CASP8, TNFRSF1A, CD74, TLR2, C3, FCER1G, CD14, CTSS, FCGR2B, FCGR3A, FCGR1A,	
hsa04668	**Tumour Necrosis Factor Signalling Pathway**	**10**	CASP8, BIRC3, PIK3CG, MMP14, TNFRSF1A, FAS, FOS, TNFRSF1B, SOCS3, CCL2,	
hsa05168	Herpes Simplex virus 1 infection	**10**	CASP8, TNFRSF1A, PILRA, CD74, FAS, FOS, TLR2, C3, SOCS3, CCL2,	
hsa04145	**Phagosome**	**9**	TLR2, C3, CD14, CTSS, FCGR2B, FCGR3A, FCGR1A, MSR1,	TUBB3
hsa05150	Staphylococcus aureus infection	**9**	C3AR1, C1QA, C3, FCGR2B, C1QC, FPR1, FCGR3A, C1QB, FCGR1A,	
hsa05161	Hepatitis B virus	**9**	CASP8, PIK3CG, DDB2, TGFBR1, FAS, MYC, FOS, TLR2, CDKN1A,	
hsa05200	Pathways in cancer	**9**	CASP8, BIRC3, PIK3CG, TGFBR1, FAS, MYC, FOS, CDKN1A,	EGFR
hsa04010	**MAPK signalling pathway**	**8**	TNFRSF1A, TGFBR1, FAS, RELB, MYC, FOS, CD14,	EGFR
hsa04060	**Cytokine-Cytokine Receptor Interaction**	**8**	OSMR, TNFSF13B, TNFRSF1A, TGFBR1, FAS, TNFRSF1B, CCL2,	EGFR
hsa04666	**Fc gamma R-mediated phagocytosis**	**8**	WAS, PIK3CG, DOCK2, VAV1, LYN, FCGR1A, FCGR3A, FCGR2B,	
hsa05133	Pertussis	**8**	NOD1, FOS, CASP1, CD14, C3, C1QA, C1QC, C1QB,	
hsa04064	**NF-kappa B signalling pathway**	**7**	BIRC3, TNFSF13B, TNFRSF1A, RELB, LYN, BCL2A1, CD14,	
hsa04650	**Natural killer cell mediated cytotoxicity**	**7**	PIK3CG, PTPN6, FAS, VAV1, FCER1G, TYROBP, FCGR3A,	

Table 3.20 Results of KEGG pathway analysis from FFPE NanoString data set

KEGG Symbol	KEGG Pathway	Number of Genes	Genes in Pathway	
			Upregulated Genes	Down Regulated Genes
hsa04145	**Phagosome**	13	FCGR3A, LAMP2, CALR, C3, CTSS, LAMP1, RAB7A, ITGAV, ATP6V0E1, MSR1	MARCO, CLEC7A, SFTPD
hsa05152	Tuberculosis	13	FCGR3A, CD74, FCER1G, LAMP2, C3, CTSS, LAMP1, RAB7A, BAD, BAX, AKT1, TNFRSF1A	CLEC7A
hsa05200	Pathways in cancer	10	NFKBIA, ITGAV, BAD, BAX, AKT1	PTGER3, FASLG, E2F1, PLD1, PTGS2
hsa05142	Chagas disease	9	C1QB, C1QC, C1QA, CALR, C3, NFKBIA, AKT1, TNFRSF1A	FASLG
hsa04380	Osteoclast differentiation	8	FCGR3A, TYROBP, FYN, SQSTM1, TREM2, NFKBIA, AKT1, TNFRSF1A	
hsa04151	**PI3K-Akt signalling pathway**	7	SPP1, ITGA7, ITGAV, BAD, AKT1	FASLG, RELN
hsa04510	Focal adhesion	7	SPP1, ITGA7, FYN, ITGAV, BAD, AKT1	RELN
hsa05161	Hepatitis B	7	NFKBIA, BAD, MAVS, BAX, AKT1	FASLG, E2F1
hsa05162	Measles	7	NFKBIA, FYN, MSN, MAVS, AKT1	SH2D1A, FASLG
hsa05166	Human T-cell leukaemia virus 1 infection	7	CALR, NFKBIA, BAX, AKT1, TNFRSF1A	E2F1, LTA
hsa05168	Herpes Simplex virus 1 infection	7	CD74, C3, NFKBIA, MAVS, TNFRSF1A	FASLG, LTA
hsa04071	**Sphingolipid signalling pathway**	6	FCER1G, FYN, BAX, AKT1, TNFRSF1A	PLD1
hsa04210	**Apoptosis**	6	NFKBIA, BAD, BAX, AKT1, TNFRSF1A	FASLG
hsa04610	**Complement and coagulation cascades**	6	C1QB, C1QC, C1QA, C4A, C3, F3	
hsa04650	**Natural killer cell mediated cytotoxicity**	6	FCGR3A, FCER1G, TYROBP, FYN	FASLG, SH2D1A

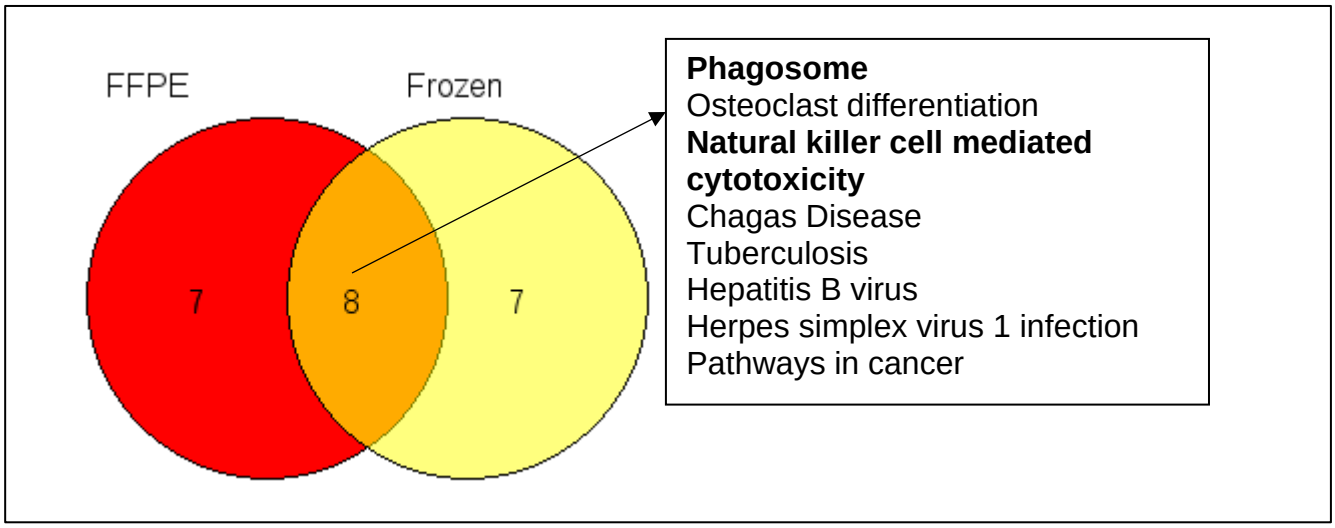

Figure 3.21 Venn diagram showing overlapping KEGG pathways between the Spinal Cord NanoString data sets.

Non-bolded pathways indicate more generic inflammation pathways.

Phagosome pathway

The phagosome pathway (Figure 3.23) describes the process of phagocytosis, which involves the engulfment and digestion of relatively large particles, such as misfolded proteins, cell debris or pathogens, via the phagosome. This process is particularly associated with pathogen destruction and immunity, and in the CNS, primarily microglia. To add support, Fc gamma R-mediated phagocytosis was also one of the top 15 pathways in the frozen NanoString data and was raised by the initial gene-by-gene analysis (Section 3.7.1).

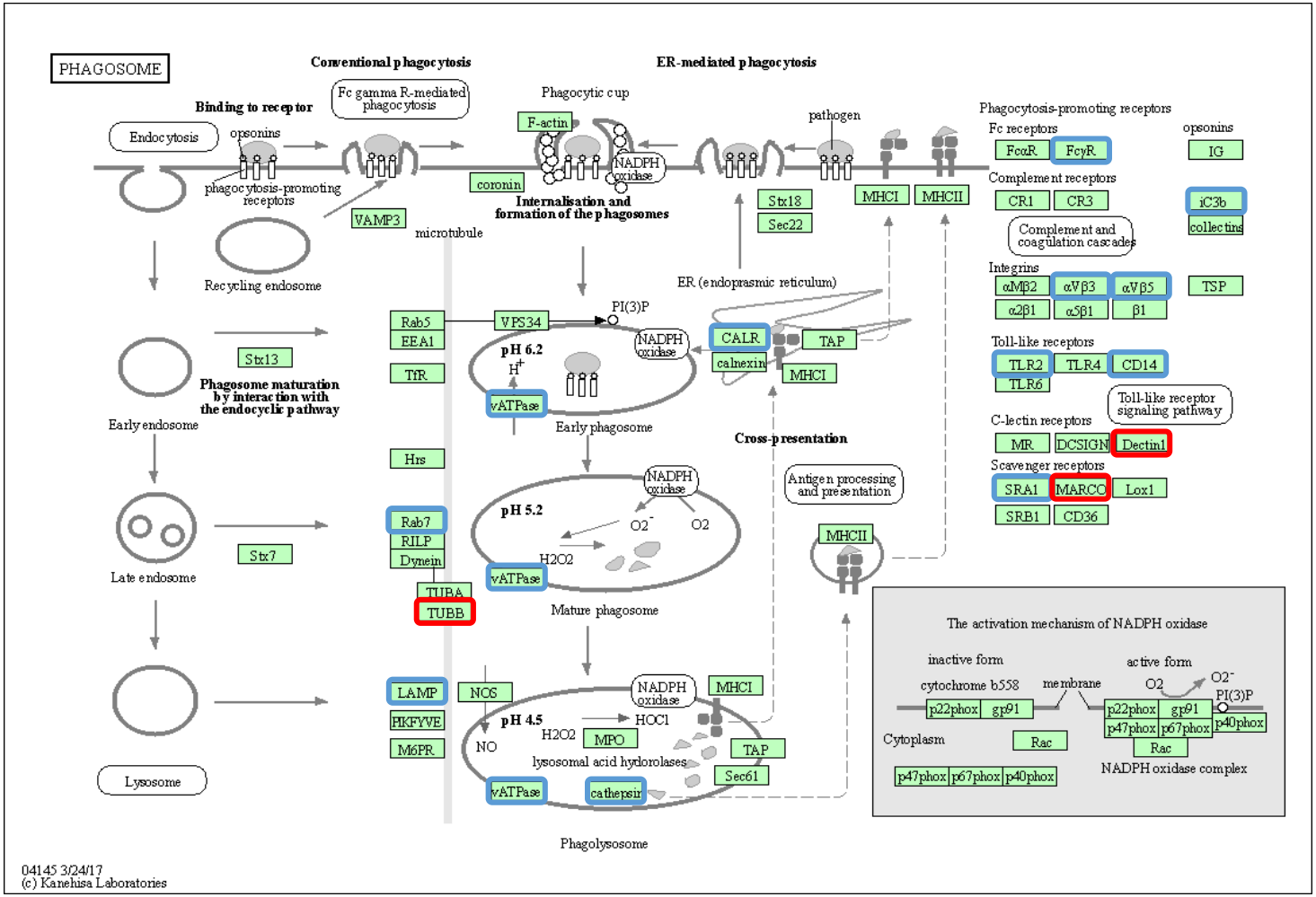

Figure 3.22 KEGG Phagosome Pathway

KEGG diagram showing dysregulated genes in spinal cord. Genes in blue were upregulated and those highlighted in red were downregulated

Alternative Gene Symbols:
MSR1= SRA1
iC3b = C3
CLEC7A = Dectin1

Natural Killer cell mediated cytotoxicity

The next pathway shared across the two data sets was the Natural Killer cell mediated cytotoxicity pathway Figure 3.24. Natural Killer (NK) cells are a type of lymphocyte and part of the innate immune system. NK cells form immune responses against both allogenic and autologous cells undergoing stress and kill these cells via the release of cytotoxic granules inducing apoptosis. The binding of MHC I to inhibitory receptors on the NK cell surface can override these signals preventing apoptosis, therefore loss of MHC I will result in targeted apoptosis. Under homeostatic conditions, NK cells are not routinely observed in the CNS. However, potentially following BBB breakdown, peripheral immune cells can cross into the CNS.

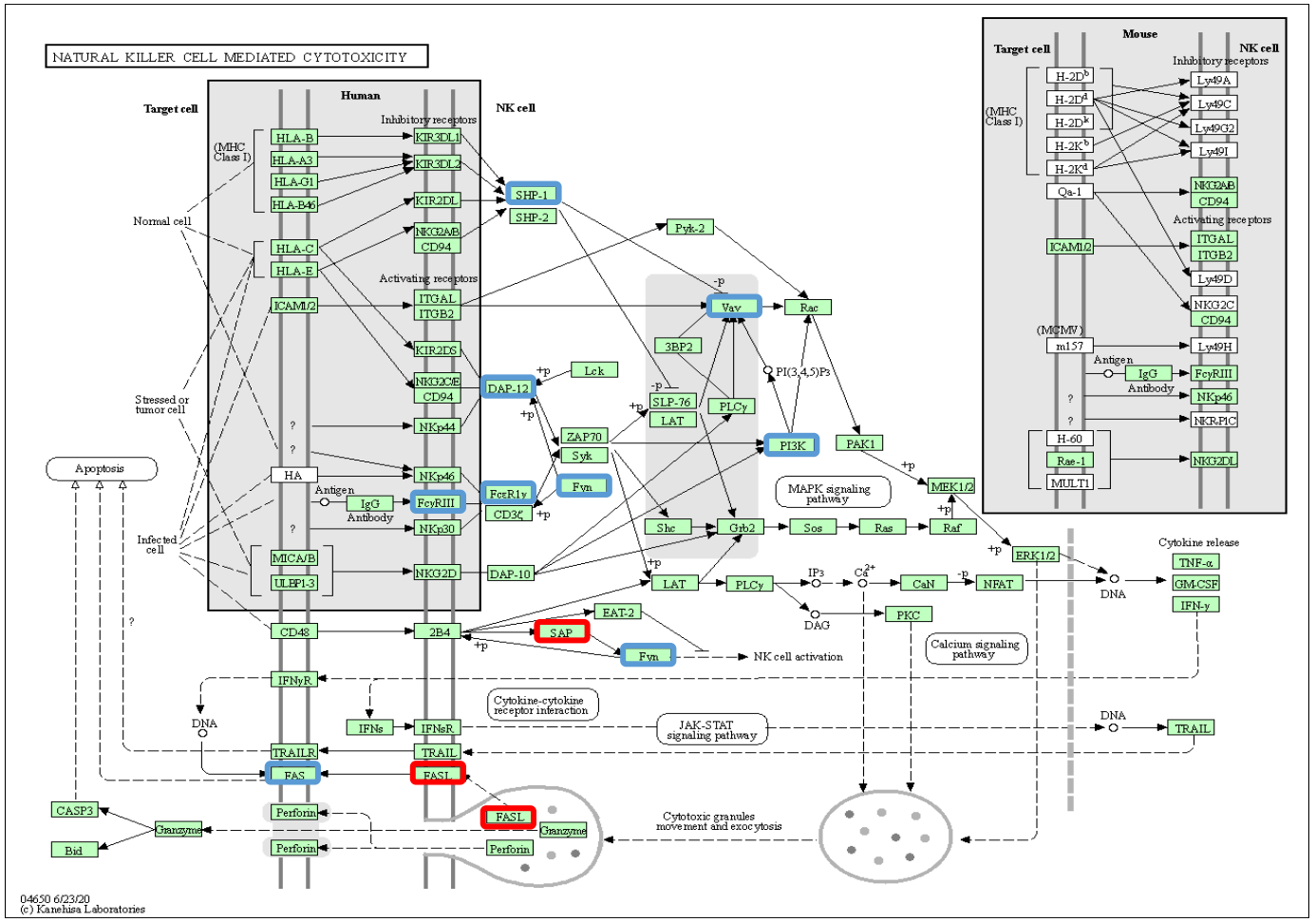

Figure 3.23 KEGG Natural Killer Cell Mediated Cytotoxicity Pathway

KEGG diagram showing dysregulated genes in spinal cord. Genes in blue were upregulated and those highlighted in red were downregulated

Alternative Gene Symbols:
PTPN6 = SHP1
TYROBP = DAP12
SH2D1A = SAP

NF-κB Signalling

The NF-κB signalling pathway was highlighted as key pathway in the Frozen data analysis (Figure 3.25).

NF-κB (nuclear factor kappa-light-chain-enhancer of activated B cells) is a protein complex that controls DNA transcription, cytokine production and cell survival, and is known as the master regulator of inflammation.

Although the NF-κB pathway was not one of the top-dysregulated pathways in the FFPE data, many genes were also dysregulated from the NF-κB pathway including *LTA, PTGS2 (COX2), TNFRSF1a*, and *NFκBIa*, highlighting the involvement of this pathway in sMND.

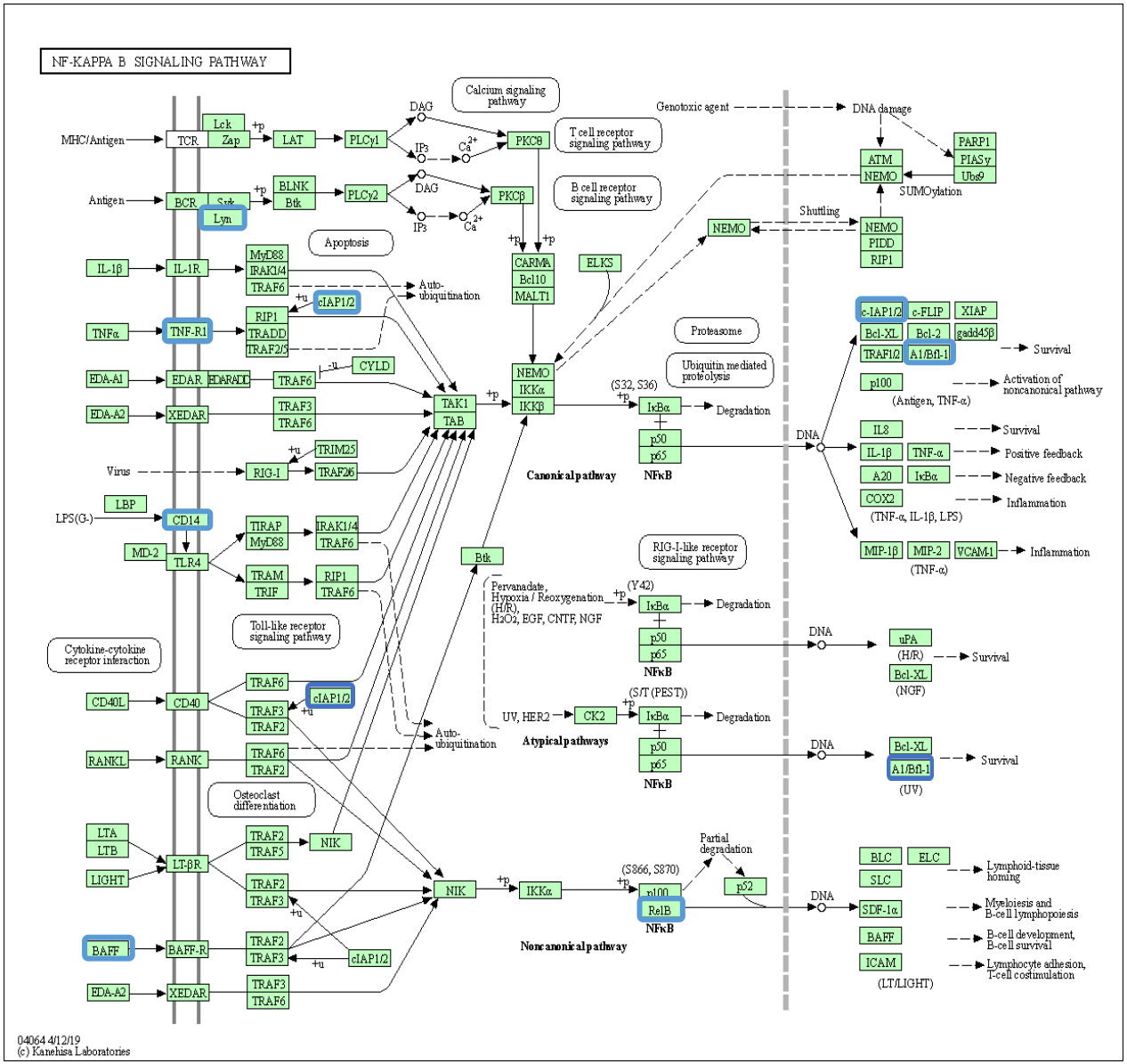

Figure 3.24 KEGG NF-Kappa B Signalling Pathway.

KEGG diagram showing dysregulated genes in frozen spinal cord. All genes were upregulated.

Alternative Gene Symbols:

BIRC3 = c-IAP1/2

TNFSF13B = BAFF

BCL2A1 = A1/Bf1-1

Finally, looking at the cytokine-cytokine mediated signalling pathway (Figure 3.26) highlights key pathways previously mentioned. These include genes associated with the *TNFα* and *TGFβ* pathway which were both dysregulated. As previously mentioned, the TNF pathway is a predominantly proinflammatory pathway.

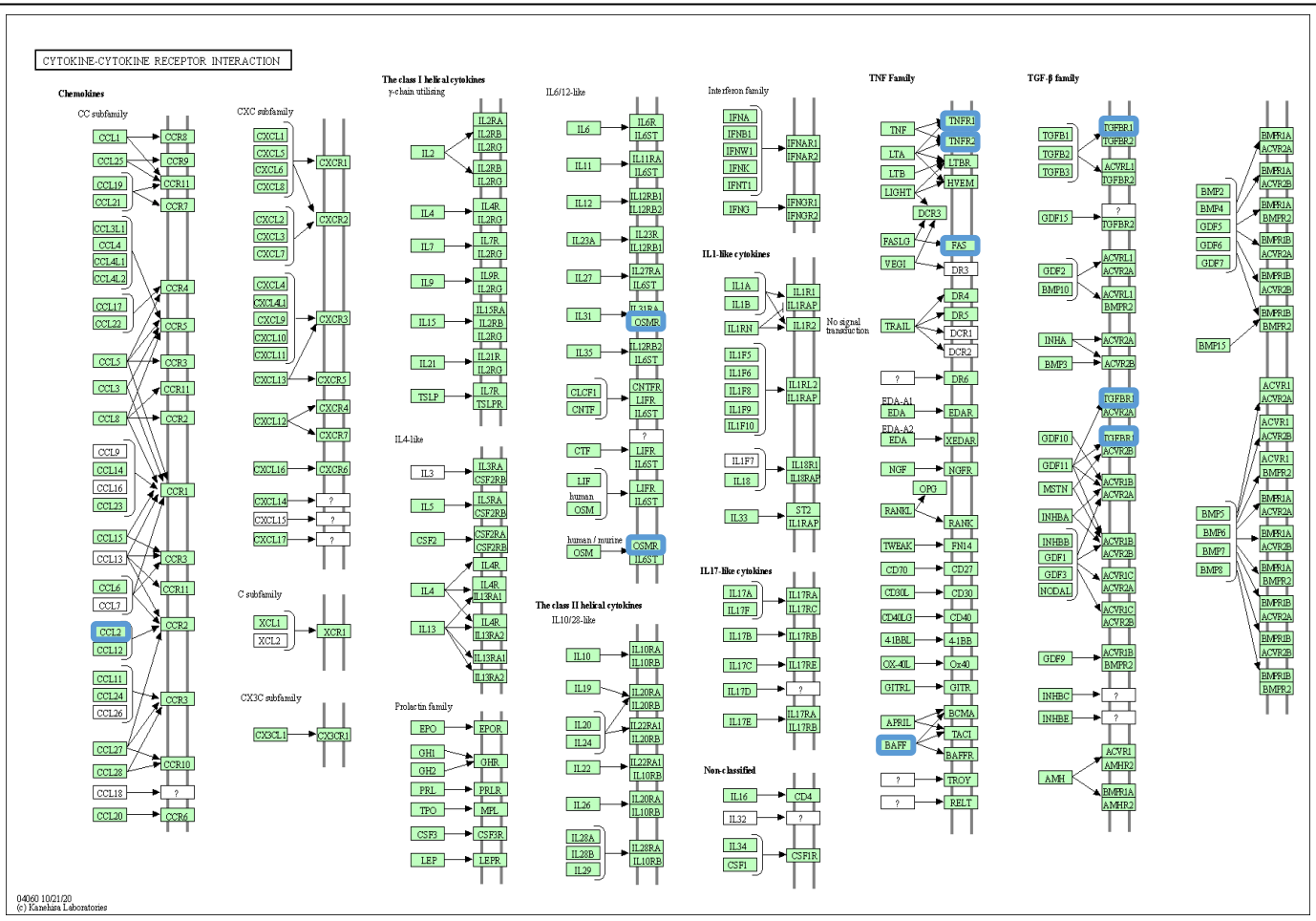

Figure 3.25 KEGG Cytokine-Cytokine Signalling Pathway with significantly dysregulated genes.

KEGG diagram displaying cytokine-cytokine signalling. All highlighted genes are upregulated.

EGFR was downregulated but no shown on image.

Alternative Gene Names
TNFSF13b = BAFF

3.8 Summary

In summary, characterisation of the neuroinflammatory transcriptome in sMND has revealed a significant upregulation of inflammation in the spinal cord. Comparatively little inflammation was observed in the motor cortex.

Examination of the spinal cord data sets has highlighted the following key themes:

- Increased immune activation as highlighted by genes associated with antigen presentation and processing.
- Phagocytosis.
- Increased proinflammatory signalling particularly TNF signalling.
- TREM2 signalling and APOE upregulation, as well as dysregulation of homeostatic and disease-associated microglial markers.
- NF-κB signalling with evidence of both the canonical and non-canonical pathways.
- Peripheral immune cell activation as indicated by NK cell mediated toxicity.

As such, the following targets were taken forward for further analysis by immunohistochemistry.

To assess microglial pathology in general, Ionized calcium binding adaptor molecule 1 (IBA1), MHCII/ HLA-DR, and CD68 were selected.

HLA-DR (Human Leukocyte Antigen – DR isotype, expressed by gene MHCII) is a protein involved in antigen presentation, the presentation of fragments of phagocytosed pathogens which triggers further inflammatory response in surrounding microglial cells (Jurga, Paleczna and Kuter, 2020). HLA-DR is generally

viewed within the CNS as a marker of activated inflammatory microglia and antigen presentation (Boche, Perry and Nicoll, 2013).

As a marker of microglial phagocytosis, CD68 was selected. The CD68 protein is a transmembrane protein localised in cellular, endosomal and lysosomal membranes of monocytes and macrophage cells (Jurga, Paleczna and Kuter, 2020). CD68 has the ability to internalise molecules from the cell surface to endosomes (Holness and Simmons, 1993).

From the results of the NanoString gene expression data the following specific targets were selected:

Cluster of Differentiation 163 (CD163) is a haptoglobin haemoglobin scavenger receptor, clearing oxidative haemoglobin for degradation resulting in, among other products, anti-inflammatory metabolites (Etzerodt and Moestrup, 2013). CD163 is primarily expressed by perivascular macrophages and microglia following blood-brain barrier breakdown (Borda *et al.*, 2008). In the current study *CD163* was upregulated in NanoString spinal cord data sets, furthermore, *CD163* was associated with longer patient survival (Cox proportional hazards regression coefficient = -1.874, log rank p = 0.004).

APOE is an apolipoprotein, whose main function is lipoprotein transport and regulation of cellular lipid plasma membranes (Sing and Davignon, 1985; Mahley, 1988; Bennet *et al.*, 2007), *APOE* was the most upregulated gene in the FFPE NanoString dataset, and the second most upregulated in the RNASeq spinal cord data set.

TREM2 and **TYROBP,** as discussed in Section 3.7.1 TREM2, TYROBP and APOE, upon stimulation, TREM2 engages with TYROBP to form a complex. This results in downstream changes in gene expression prompting changes in many cellular functions such as cell survival, phagocytosis, proinflammatory cytokine signalling, and cytoskeletal rearrangement (Humphrey, Xing and Titus, 2015).

Chapter 4 Results: Characterisation of Inflammatory Phenotype in sMND using Immunohistochemistry

4.1 Introduction

In the previous chapter, the neuroinflammatory transcriptome was characterised in the motor cortex and spinal cord of sMND and control cases. This revealed a significant inflammatory response in the spinal cord of sMND cases, which was not observed in the motor cortex. Furthermore, CD163, APOE, TREM2 and TYROBP were identified as targets for further investigation.

In the previous chapter the microglial/macrophage marker, CD163 was found to not only be upregulated in the spinal cord, but expression was found also to be significantly upregulated in those sMND cases with slower disease progression. CD163 is associated with anti-inflammatory microglial/ macrophage activation.

Furthermore, the transcriptomic analysis in Chapter 3, highlighted genes associated with the disease-associated microglial phenotype. In this pathway, activation of TREM2 via the binding of ligands, results in downstream upregulation of APOE through TYROBP.

Most research examining neuroinflammation and microglial pathology in MND have been limited to the precentral gyrus and spinal cord, given these are the most profound sites of neuronal degeneration associated with MND. However, as noted in the Section 1.5.2, MND-associated pathology has been observed in other motor regions such as the basal ganglia and across the cortex into non-motor regions.

To examine microglial morphology, and the expression of TREM2, TYROBP and APOE in sMND and control cases, across both motor and no-motor CNS regions, immunohistochemistry was allied with the use of tissue microarrays (TMAs).

The first modern TMAs were used for high throughput characterisation of cancer biopsies (Kononen *et al.*, 1998). A small core of formalin-fixed paraffin-embedded (FFPE) tissue was taken from several biopsies and embedded into a single paraffin block. This allowed the staining and characterisation of multiple cases on a single slide.

This method has several advantages over whole slide immunohistochemistry. Firstly, as multiple cases can be represented on a single slide, a whole cohort can be stained using a small number of slides. As such, staining is more efficient, both in terms of time and fewer reagents are required to produce data for the same cohort. Secondly, compiling whole cohorts onto one or two slides can reduce the effect of the inherent variability between staining batches observed in immunohistochemistry experiments. Finally, as a small core is taken to represent a larger section, the rest of the tissue can be used for other purposes, reducing the rate of resource exhaustion. This increases the amount of data that can be gained from such a finite resource.

This method has now been applied to neuropathology studies, for several purposes including diagnostics, antibody optimisation and morphological characterisation (Wang *et al.*, 2002). This method has been further optimised by members of our laboratory for the examination of microglial pathology (Heraty, 2019; Wilson *et al.*, 2021).

The following chapter characterises and quantifies microglial and monocyte pathology using a general marker (IBA1), phagocytic markers (CD68 and CD163) and antigen presentation markers (HLA-DR) as well as the three members of the APOE, TREM2, and TYROBP pathway in sMND compared to control cases by immunohistochemistry. This was done in both motor (spinal cord, precentral gyrus and basal ganglia) and non-motor regions (prefrontal, temporal and occipital cortices) of the CNS.

To this end, the following aims and hypothesis were examined:

Aims:

1. Characterise pathology through immunohistochemistry directed at IBA1, CD68, HLA-DR and CD163 across all CNS regions in control and sMND.
2. Characterise the expression of APOE, TREM2 and TYROBP in the CNS in control and sMND.
3. Compare the inflammatory reaction in spinal cord to precentral gyrus in sMND.
4. In sMND, examine the relationship between the expression of proteins of interest and clinical features such as the length of patient survival, and white matter pallor in the spinal cord.
5. Examine the cell and tissue- specific expression of all markers.

Hypotheses:

1. Expression of microglial markers will be increased in sMND compared to control cases. Microglia will display activated morphology characterised by

swelling of the processes and cell body, and/or the presence of ameboid microglia in sMND CNS regions.

2. TYROBP, TREM2 and TYROBP expression will be increased in the spinal cord in control cases compared to sMND cases.
3. There will be greater a microglial response and increased expression of target proteins in the spinal cord overall compared to cortical regions in sMND cases.
4. Expression of proteins of interest will be associated with survival, particularly in the spinal cord.
    a. Increased expression of microglial markers CD68 and IBA1 will be associated with faster progressing cases.
    b. Increased expression of CD163 will be associated with longer survival.
    c. Expression of TREM2, TYROBP and/or APOE will be associated a difference in survival.
5. The white matter pallor in the spinal cord corticospinal tract that is known to be associated with sMND will correlate with these measures.

4.2 Antibody Optimisation

To establish the optimum conditions for immunohistochemistry, the following conditions were examined: antigen retrieval method, buffer pH and antibody concentration. For all optimisation, an isotype control and negative control were also performed to identify non-specific staining. Previous optimisation of immunohistochemistry on TMAs had shown improved core retention using the pressure and heat method of antigen retrieval, compared to the microwave method (Heraty, 2019), As such, antibody optimisation was initially trialled using the antigen retrieval unit (pressure cooker). If optimal staining could not be achieved, the microwave was trialled.

4.2.1 Pre-optimised Antibodies

Most antibodies used had been optimised and were widely used in the laboratory prior to this project. As such, full re-optimisation was not carried out and instead the optimum condition was run with a negative and isotype control. The tissue used for optimisation was a well-characterised case, from a region of cortex surrounding a haemorrhagic stroke resulting in high levels of microglial activation The preoptimized antibodies include: IBA1 (Figure 4.1), CD68 (Figure 4.2), HLA-DR (Figure 4.3), CD163 (Figure 4.4) and APOE (Figure 4.5). For all antibodies, the positive conditions showed clear glial labelling with minimal background. Negative controls (primary antibody omitted) were free from immunoreactivity indicating the labelling observed in the positive controls was not the result of reactivity to the reagents or unspecific secondary antibody binding (Hewitt *et al.*, 2014). Similarly, the isotype controls, in which the primary antibody was replaced with immunoglobins of the

same species, were also negative. This indicated the labelling observed in the positive condition, was not the result of non-specific interactions of the antibody with the tissue (Hewitt *et al.*, 2014).

The APOE positive condition did show some parenchymal immunoreactivity, particularly in grey matter, however examination of the blood vessels in the main parenchyma and the meninges showed areas completely devoid of DAB labelling, indicating this was a genuine feature rather than an artifact.

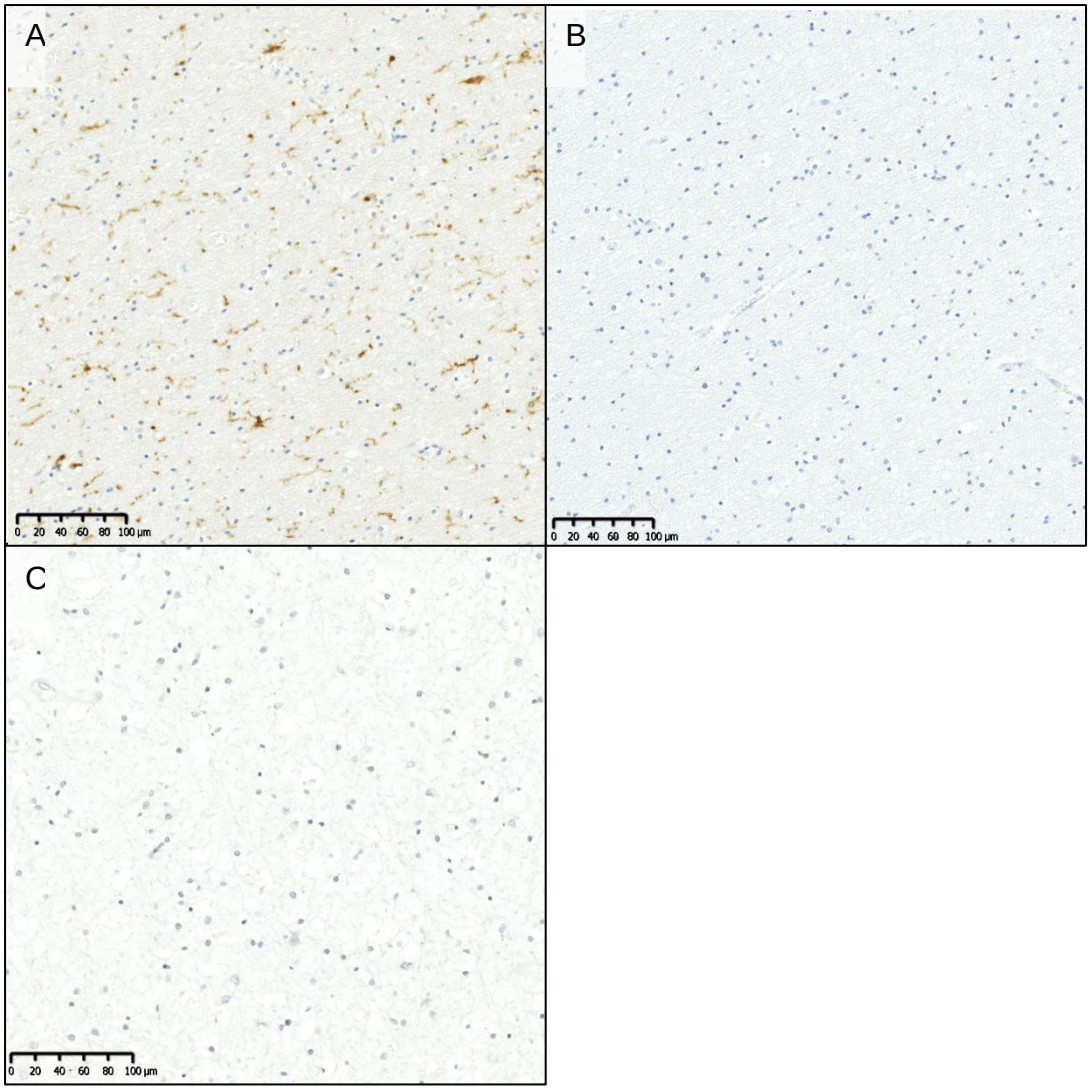

Figure 4.1 IBA1 Optimised Conditions

Antigen retrieval was performed using heat (microwave) with trisodium citrate buffer (pH 6). Primary antibody concentration was 1:200.

***A**) Optimised conditions showing clear staining with minimal background.*

***B**) Negative condition: primary antibody was omitted from staining. No non-specific staining was observed*

***C**) Isotype control: distinct staining was not observed, and very little non-specific staining of the background was observed.*

Scale bar = 100µm

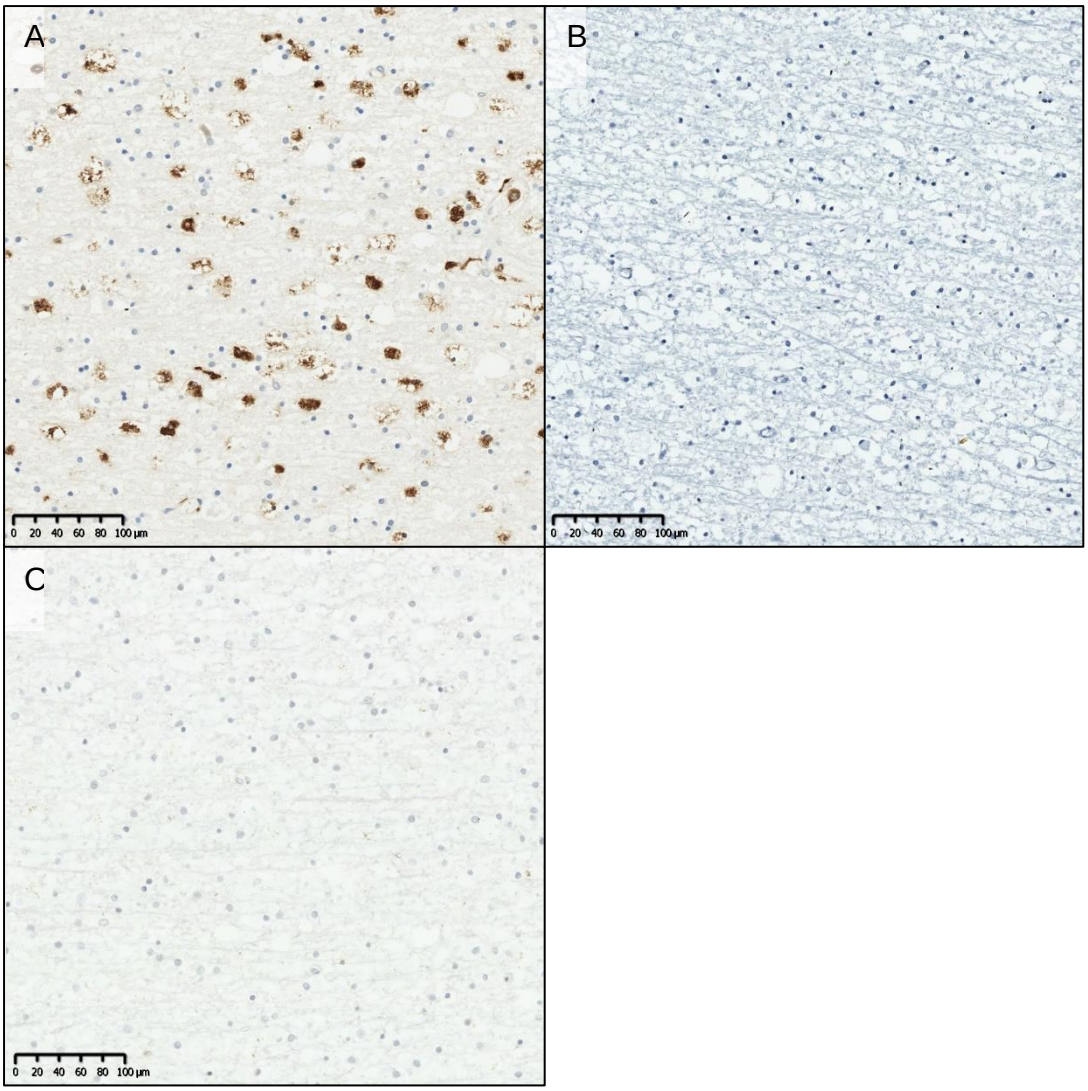

Figure 4.2 CD68 Optimised Conditions

Antigen retrieval was performed using heat (microwave) with trisodium citrate buffer (pH 6). Primary antibody concentration was 1:100.

***A**) Optimised conditions showing clear staining with minimal background.*

***B**) Negative condition: primary antibody was omitted from staining. No non-specific staining was observed*

***C**) Isotype control: distinct staining was not observed, and very little non-specific staining of the background was observed.*

Scale bar = 100µm

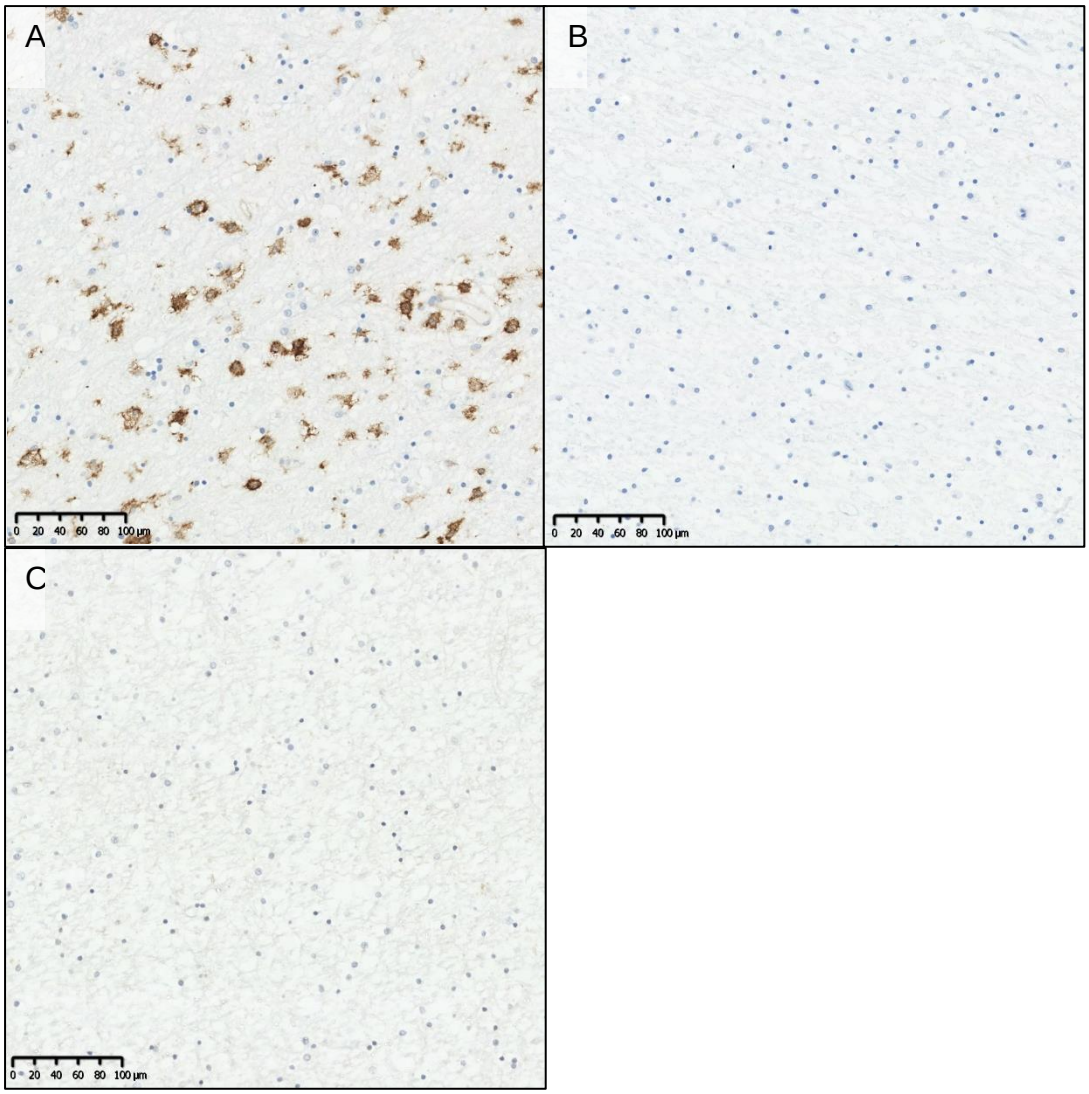

Figure 4.3 HLA-DR Optimised Conditions

Antigen retrieval was performed using the pressure cooker with reveal buffer (pH 6). Primary antibody concentration was 1:100.

***A**) Optimised conditions showing clear staining with minimal background.*

***B**) Negative condition: primary antibody was omitted from staining. No non-specific staining was observed*

***C**) Isotype control: distinct staining was not observed, and very little non-specific staining of the background was observed.*

Scale bar = 100µm

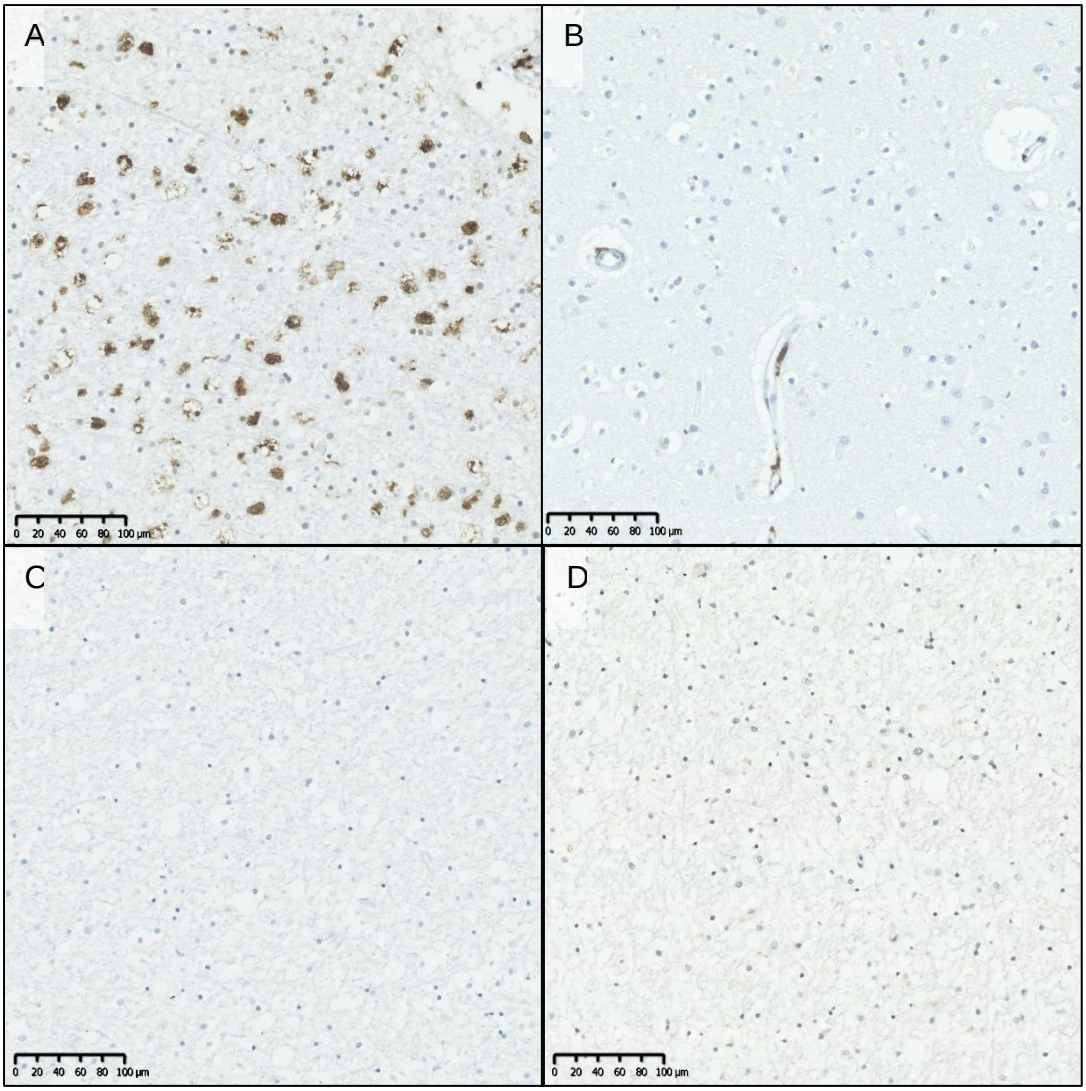

Figure 4.4 CD163 Optimised Conditions

Antigen retrieval was performed using the pressure cooker with reveal buffer (pH 6). Primary antibody concentration was 1:1000.

A *&* ***B****) Optimised conditions showing clear staining with minimal background. A) shows an area of high staining, and B) an area of low staining.*

C*) Negative condition: primary antibody was omitted from staining. No non-specific staining was observed.*

D*) Isotype control: distinct staining was not observed, and very little non-specific staining of the background was observed.*

Scale bar = 100µm

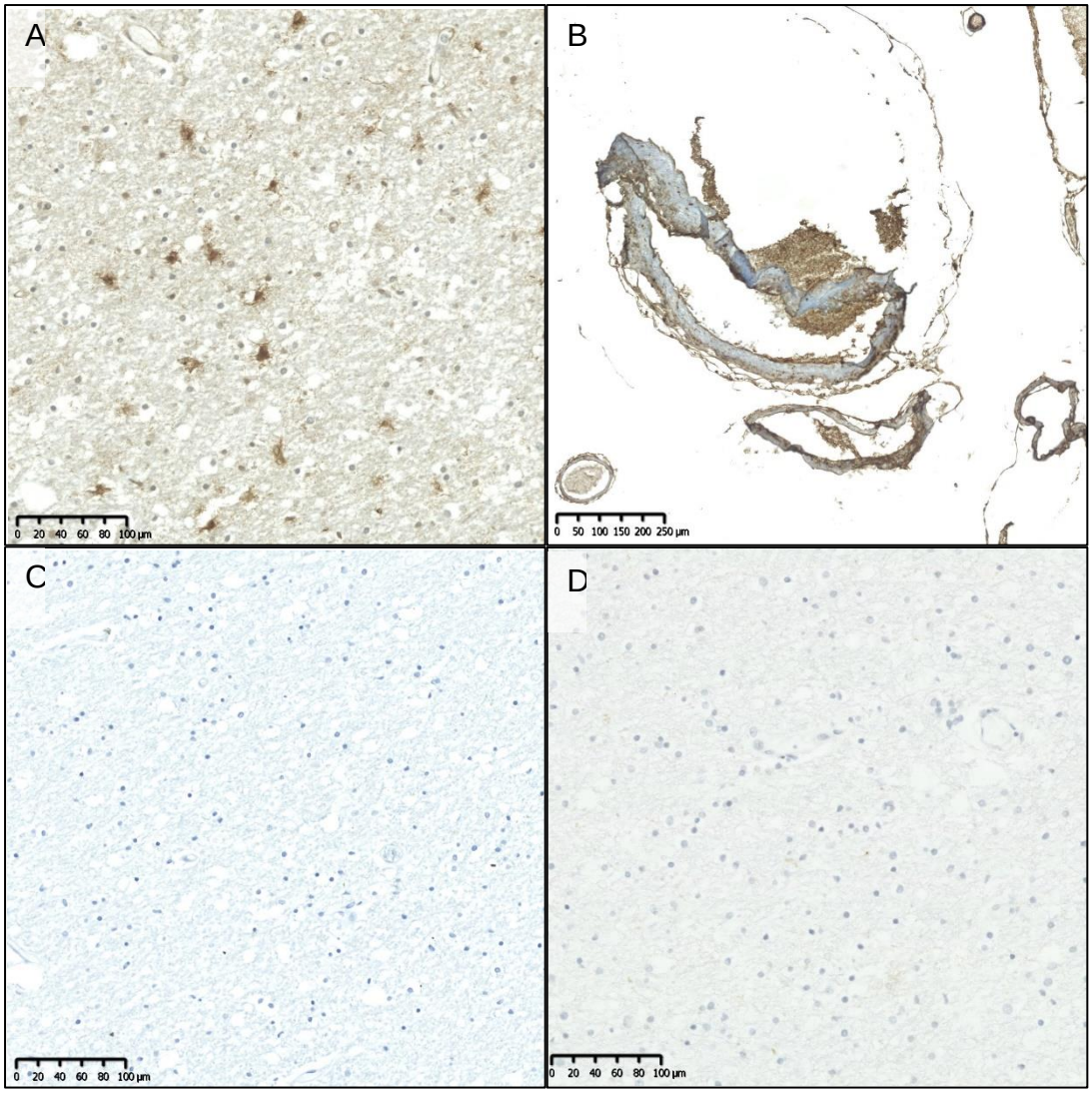

Figure 4.5 APOE Optimised Conditions

Antigen retrieval was performed using the pressure cooker with Borg buffer (pH 9.5). Primary antibody concentration was 1:1000.

***A**) Optimised conditions show distinct glial staining, there was some parenchymal staining, particularly in the grey matter.*

***B**) Smooth muscle of the tunica media of blood vessels were negative for immunoreactivity.*

***C**) Negative condition: primary antibody was omitted from staining. No non-specific staining was observed.*

***D**) Isotype control: distinct staining was not observed, and very little non-specific staining of the background was observed.*

Scale bar for figures A, C, D = 100µm, Scale bar for Figure B = 250µm

4.2.2 Optimisation of TREM2 and TYROBP

For both TYROBP (Figures 4.6 and 4.7) and TREM2 (Figures and 4.8 and 4.9), optimisation was carried out by performing antigen retrieval in the pressure cooker with titrated antibody concentrations. For TYROBP two pHs were trialled. Due to time limitations, TREM2 optimisation was carried out pH recommended by the manufactures only. The desired conditions for each antibody were those conditions which produced the highest contrast between desired labelling and minimal background immunoreactivity. Negative and isotype controls for the optimum conditions showed minimal reactivity for both antibodies.

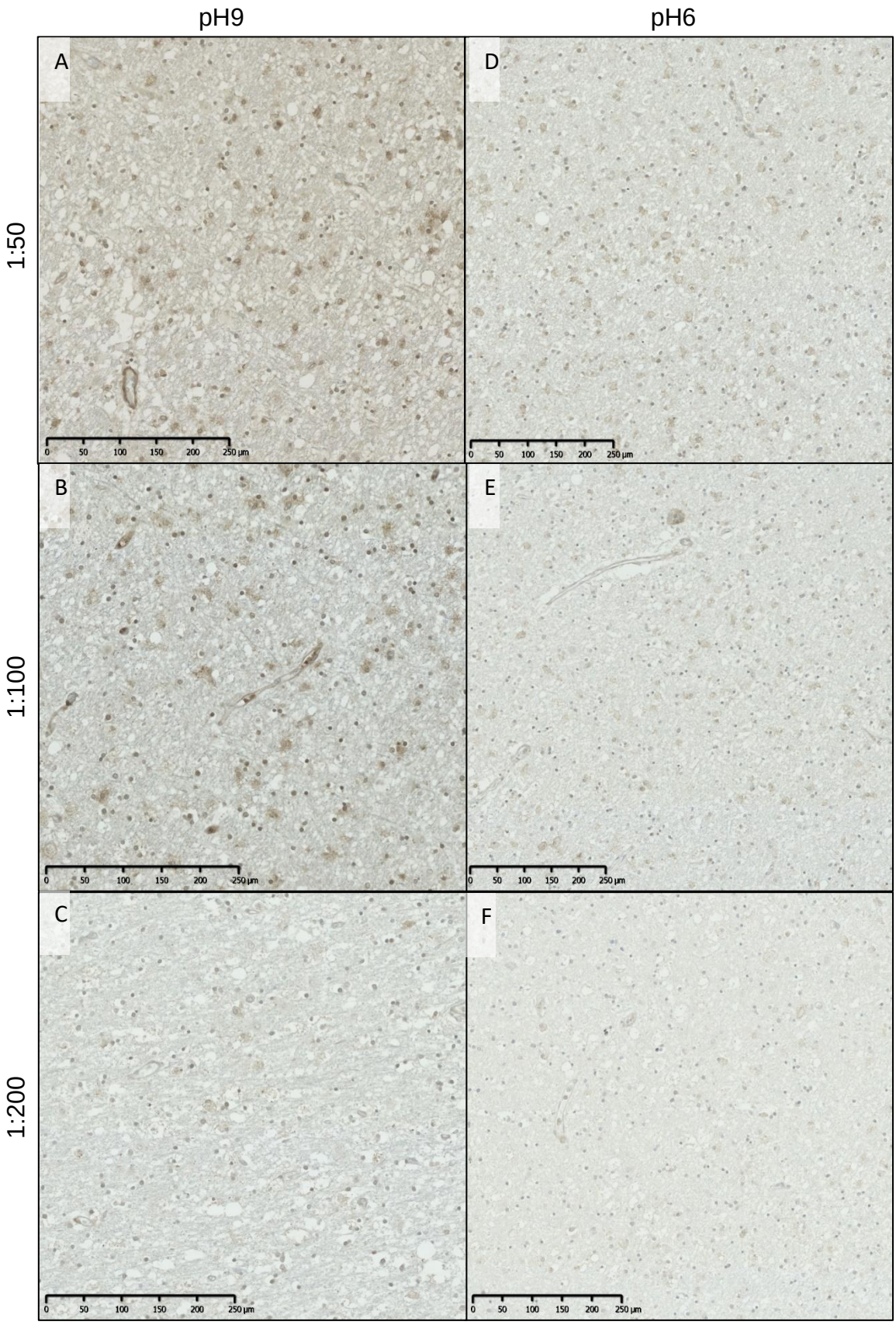

Figure 4.6 Optimisation of TYROBP

Overall immunoreactivity is lower in the pH6 antigen retrieval condition (D,E,F), compared to the pH9 condition (A,B,C). The optimum condition selected was pH9 with 1:100 antibody concentration (B): it showed clear labelling with low background. Scale bars= 250µm

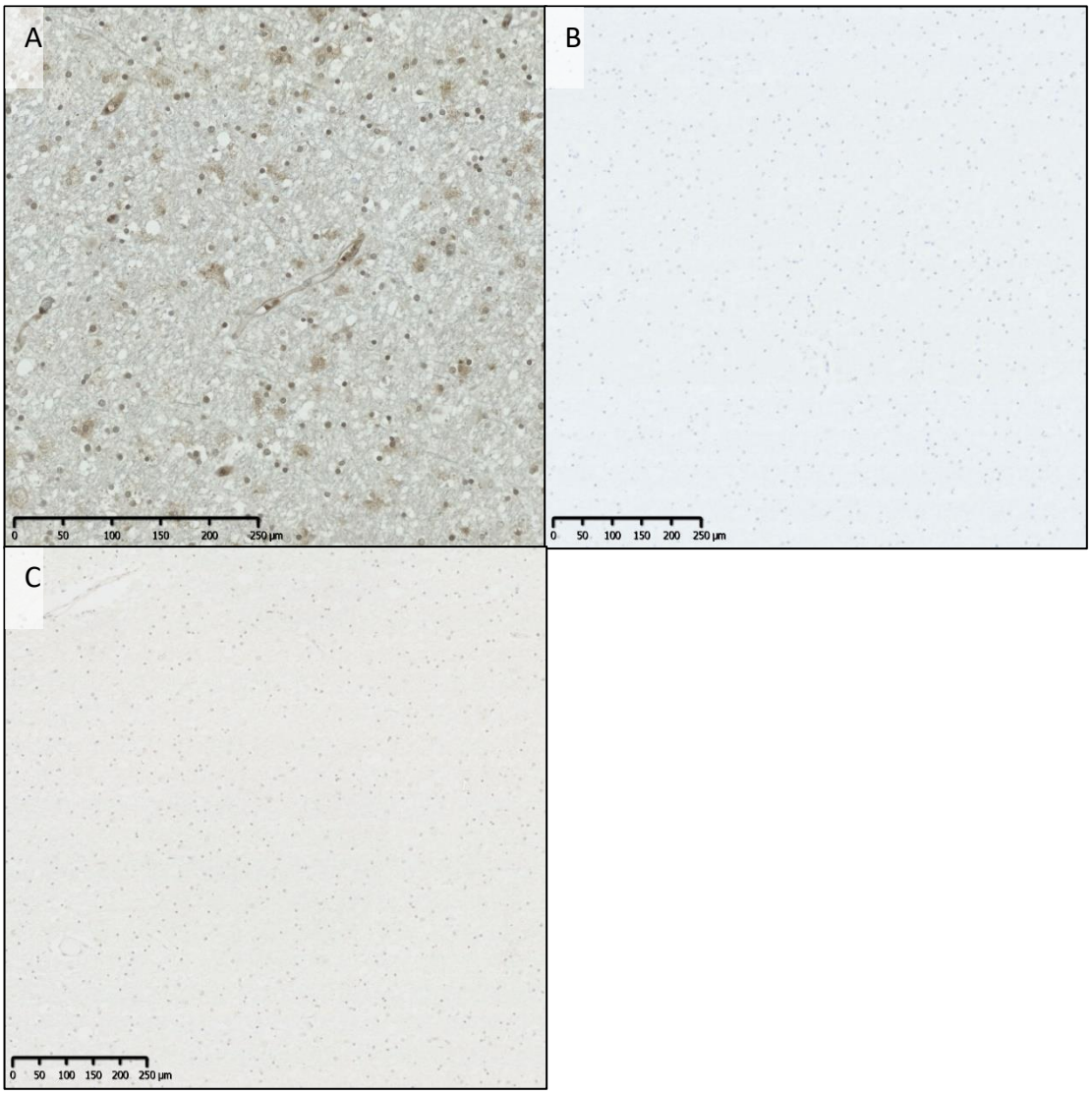

Figure 4.7 Optimised TYROBP Conditions with Negative and Isotype Control

A. *Optimised TYROBP condition (pressure cooker with pH9 buffer, antibody 1:1000 concentration. Provides clear labelling with high contrast to the main tissue parenchyma.*

B. *Negative control – omission of the primary antibody. Clear image indicates no interaction of the secondary antibody with the tissue or reagents.*

C. *Isotype control, shows some background reactivity, however this is relatively minimal*

Scale bars= 250µm

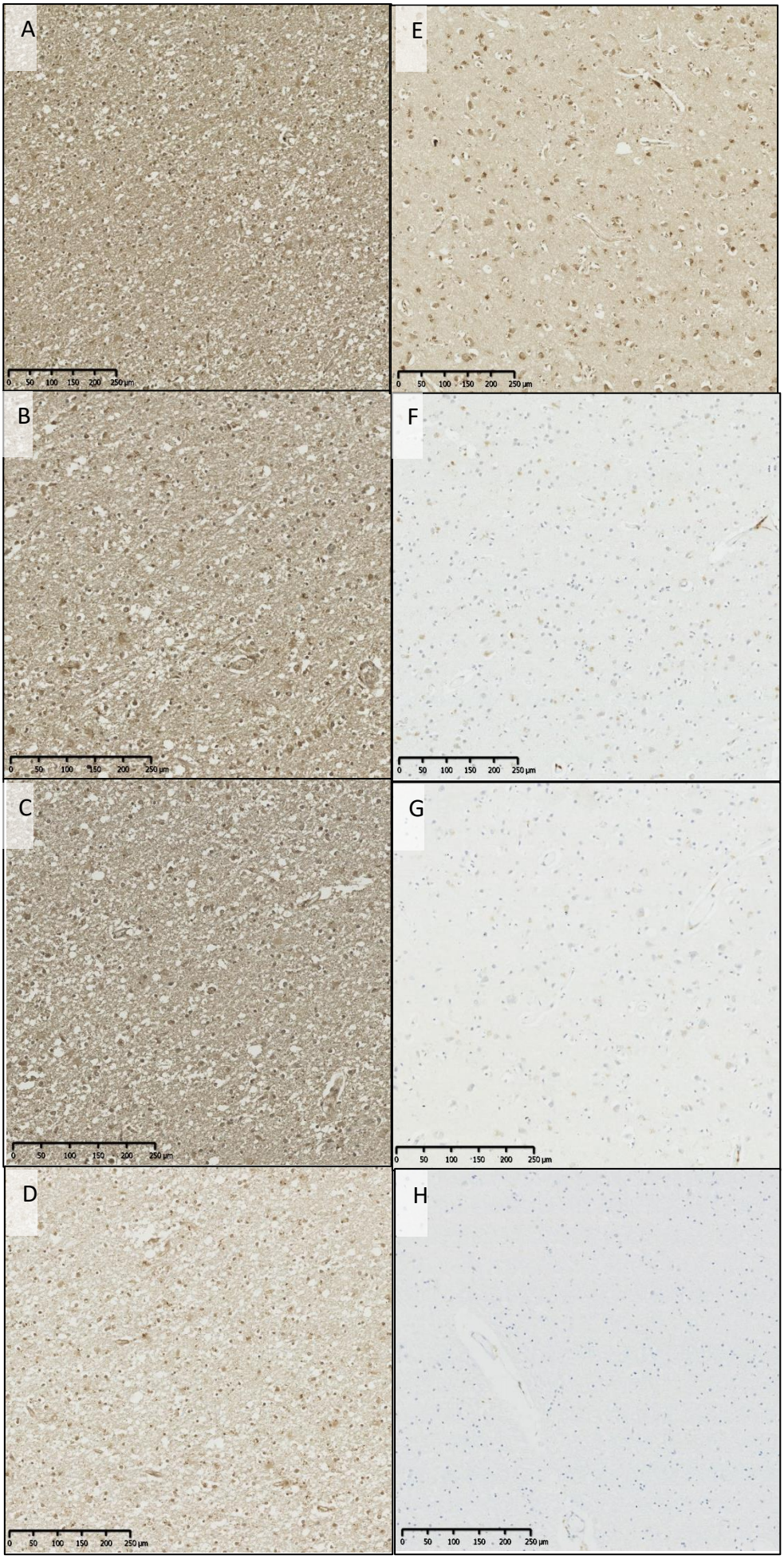
A
E
B
F
C
G
D
H
0 50 100 150 200 250 µm

Figure 4.8 Optimisation of TREM2

All TREM2 antibody optimisation was performed using the recommended pH6 buffer with the pressure cooker. Concentrations range from A) 1:50, B) 1:100, C) 1:200 D)1:400, E)1:800, F) 1:1600, G) 1:3200 and H)1:6400. The provided antibody concentration sheet recommended a 1:50 dilution. Dilutions 1:50 – 1:200 show such significant background staining, specific staining is difficult to see. The 1:1600 dilution was selected as it showed clear and distinct labelling with minimal background. Labelling was lost with further dilutions.

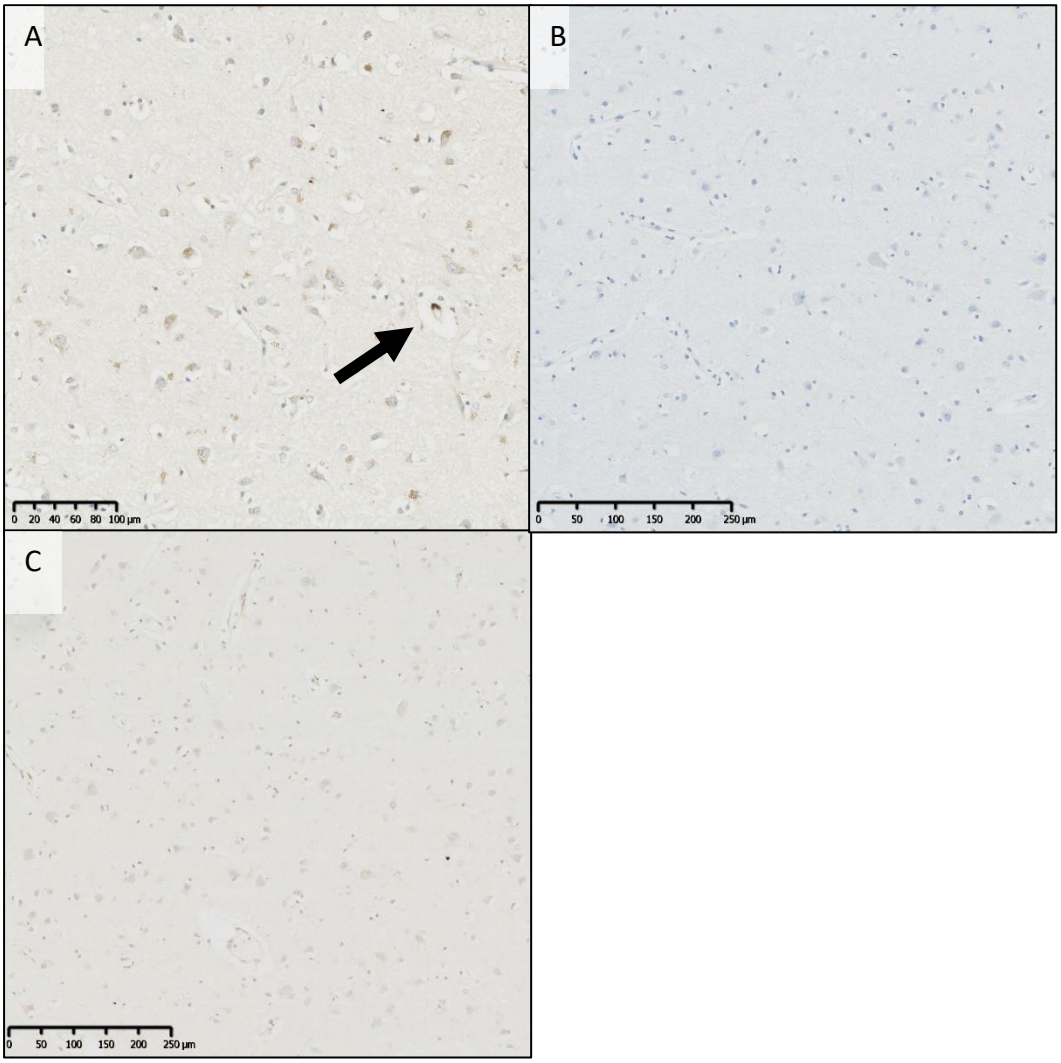

Figure 4.9 TREM2 Optimised Conditions

Optimised TREM2 condition (pressure cooker with pH6 buffer, antibody 1:1000 concentration.

A) Provides clear labelling with high contrast to the main tissue parenchyma. Arrow shows example of clear labelling

B) Negative control – omission of the primary antibody. Clear image indicates no interaction of the secondary antibody with the tissue or reagents.

C) Isotype control, shows some background reactivity, however this is relatively minimal

Scale bars= 250µm

4.3 Antibody Validation

Antibody validation aims to determine whether the primary antibody binds specifically to the desired protein and no other proteins in the tissue sample. There are several methods of doing this. First, western blotting can be used to determine whether the primary antibody binds to the protein of the expected protein weight. Specific antibodies would show specific bands at expected product mass. This method is not always appropriate. During western blotting, proteins are denatured to pass through the gel, and therefore do not have the same structure as those *in-situ.* Due the specificity of antibody binding, some antibodies used for immunohistochemistry may not be able to bind to proteins denatured during a western blot.

Secondly, an antibody absorption assay can be performed. This involves pre incubating the primary antibody with the target peptide, thus blocking the antibody. If the antibody is specific, it should block the ability of the antibody to bind to the tissue, resulting in a lack of labelling.

Thirdly, examining the pattern of immunoreactivity in tissue known to express the protein of interest can be used to test signal in various cell and tissue types against the expected pattern of expression. This is considered in section 4.9.

Antibody specificity may also be assessed using cell lines; The protein of interest may be over expressed and knocked down in cell lines which express the protein of interest. If the antibody binds to the desired protein, western blotting should show the expression of the protein of interest in in the cell line, overexpression line, and knockdown cell line. This was not possible in the scope of this project.

4.3.1 SDS-PAGE Western Blotting

APOE

APOE is 34kDa protein (Chou *et al.*, 2005; Shao *et al.*, 2020). A clear band at the desired weight was observed at 34kDa on the blot were 10ug was loaded (Figure 4.10). Time allowing further repeats would have been completed to confirm. For APOE, the electrophoresis was performed using 10% acrylamide gels.

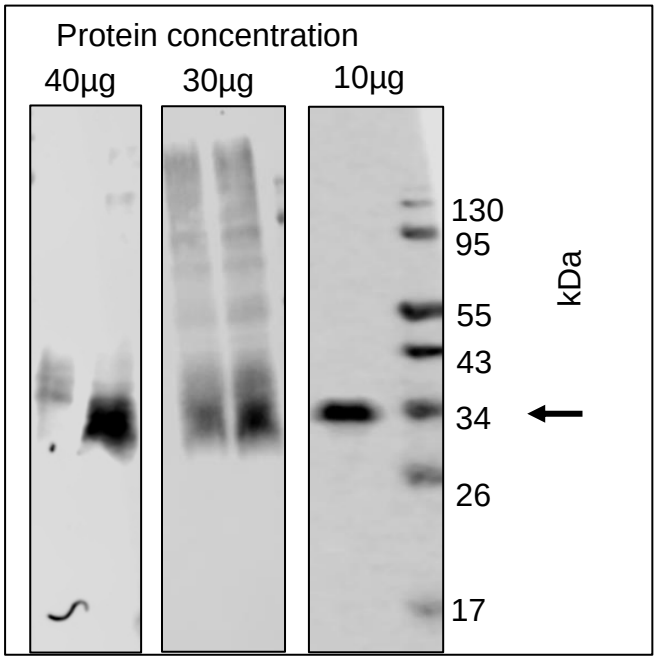

Figure 4.10 Western Blot Examining APOE Antibody Specificity

Western blotting of protein from human spinal cord, probed with APOE antibody, blots loaded with 10µg, 30µg, and 40ug of protein. The 10µg blot shows a single clear band at the desired weight of 34kDa. Higher protein loading concentrations lead to smearing. Arrow highlights expected protein weight.

TREM2

The TREM2 protein has several forms including a sheared form, a glycosylated and non-glycosylated form. The most widely cited protein weights are between 25k-45kDa (Sessa *et al.*, 2004; Zhong *et al.*, 2015). The expected product weight for the current antibody was not given by the producers. The spinal cord protein electrophoresis was run using 10% acrylamide gels. This antibody failed to produce a consistent band despite variations in protein loading amount and antibody concentration. Several bands were seen at approximately 55, 34 and 26kDA. From the inconsistency of these data, specificity of the antibody could not be confirmed.

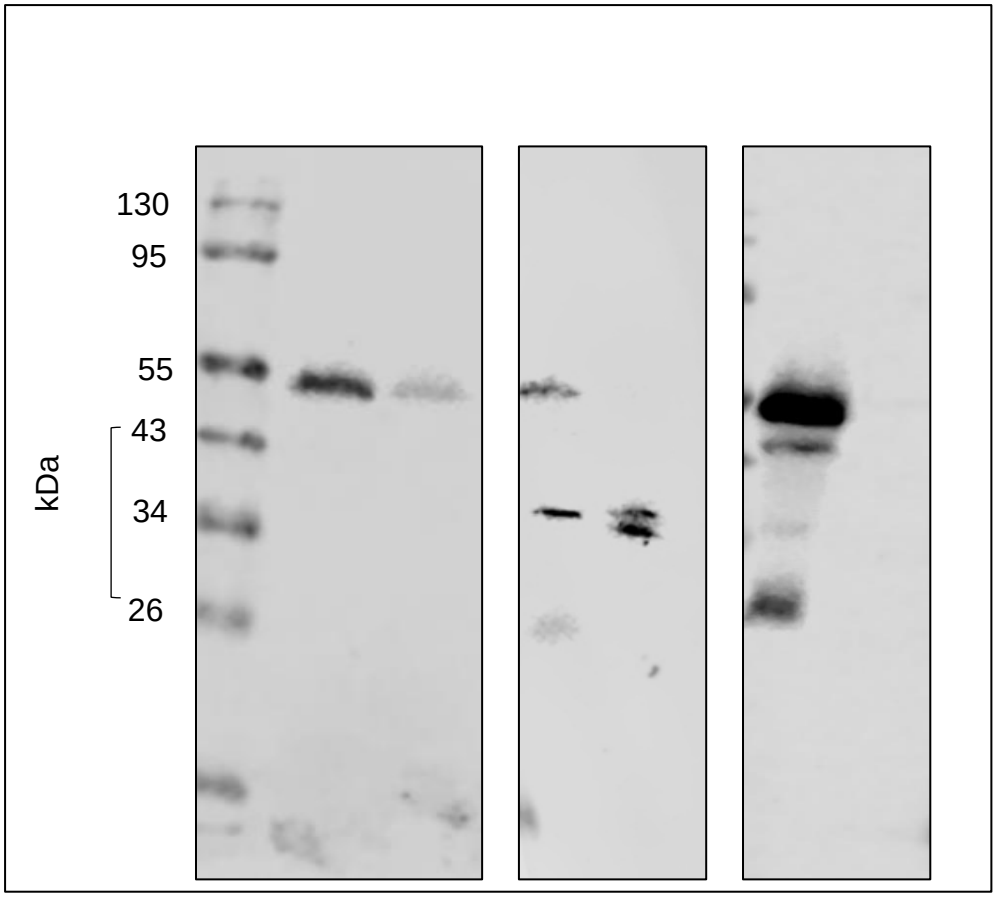

Figure 4.11 Western Blot Examining TREM2 Antibody Specificity

Western blotting of protein from human spinal cord homogenate, probed with the TREM2 antibody, blots loaded with 40µg, 50µg, and 50ug of protein. Antibody concentration was increased from 1:1000 to 1:500. Blots were very inconsistent. 55kDa band was out of the expected range, and as such unlikely to be TREM2. Bracket shows expected region for visualisation of protein of interest.

AB conc.= antibody concentration, Protein. = protein amount loaded

TYROBP

TYROBP is a 13kDa protein (Sessa *et al.*, 2004). Due to the smaller target protein, the electrophoresis was conducted using a higher density gel (15%) to ensure better separation of the lighter proteins. Several bands were observed surrounding the 55kDA mark, however these bands were too large and unlikely to be related to TYROBP protein (Figure 4.12).

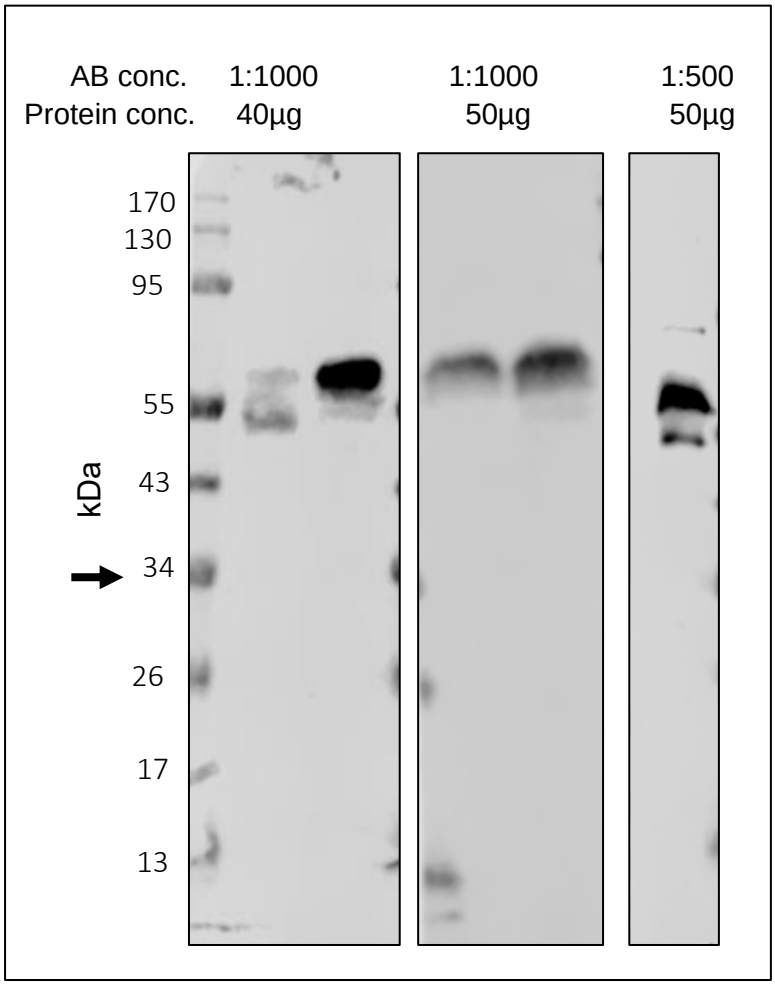

Figure 4.12 Western Blot Examining TYROBP Antibody Specificity

Western blotting of protein from human spinal cord homogenate, probed with the TYROBP antibody, blots loaded with 40µg, 50µg, and 50ug of protein. Antibody concentration was increased from 1:1000 to 1:500. Blots were very inconsistent. 55kDa band was out of the expected range, and as such unlikely to be TREM2. Arrow shows expected protein weight.

AB conc.= antibody concentration, Protein. = protein loaded (µg)

Due to the consistent presence of protein bands at 55kDa, a western blot was conducted where the primary antibody was omitted, to determine whether the secondary antibody binding non-specifically. For both the mouse and rabbit secondary antibodies, a band at 55kDa was observed (Figure 4.13). As such the bands observed at 55kDa in the TREM2 and TYROBP western blots were likely to be the result of non-specific binding. APOE is much more widely expressed compared to TYROBP and TREM2 in the spinal cord, and as the signal from off-target effects of the secondary were likely to have been comparatively low enough to have not been observed. We concluded that this antibody does not work for immunoblotting.

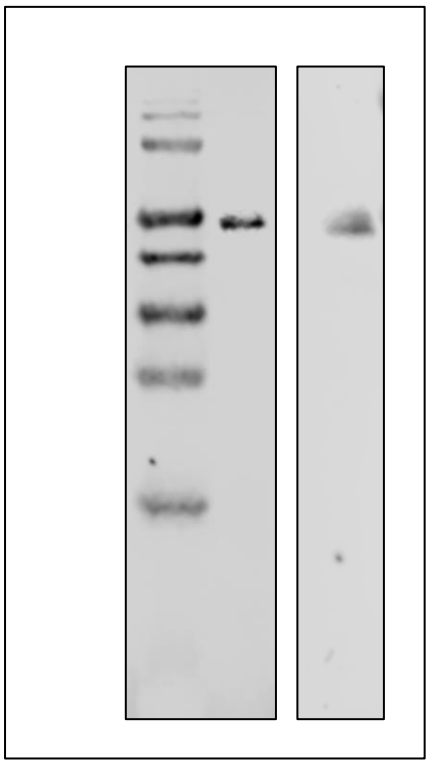

Figure 4.13 Negative Control Western Blots for Mouse and Rabbit Secondary Antibodies

Western blotting of protein from human spinal cord homogenate. Primary antibodies were omitted, to determine non-specific binding of secondary antibodies. Both the rabbit (Rb) and mouse (Ms) secondary antibodies produced bands at the 55kDa weight, indicating off target binding.

4.3.2 Antibody Pre-absorption

Antibody pre absorption was performed to further examine antibody specificity. Briefly, this involves blocking the epitope of the primary antibody with the target peptide prior to use. If the antibody is specific, this should block the action of the antibody preventing immunoreactivity. To do this, the antibody was incubated with the peptide overnight, and immunohistochemistry performed for APOE and TREM2 antibodies. The corresponding peptide for the TYROBP antibody was not available and as such, antibody absorption could not be performed for this antibody.

For both TREM2 and TRYOBP, the antibody as incubated with 10x the concentration of peptide to primary antibody to ensure complete blocking of the antibody. For both TREM2 and TYROBP, the peptide incubated conditions showed staining significantly darker than the non-protein condition. No immunoreactivity was observed in the negative control.

This may indicate the antibody-antigen complex was binding non-specifically. Alternatively, given the increase in immunoreactivity observed with the addition of the protein, the protein itself may also be able to bind to itself forming a complex, which results in increased signal (Burry, 2011).

4.4 Immunohistochemistry in Cervical Spinal Cord

4.4.1 IBA1

Qualitative Analysis

At lower magnification, IBA1 immunoreactivity was relatively evenly distributed across the spinal cord, and with little difference between control and sMND cases (Figure 4.14). Both perivascular macrophages and microglia within the parenchyma were positively stained for IBA1. Furthermore, IBA1- positive microglia were observed in both white and grey matter.

In control cases, staining was relatively even across the cord with microglia demonstrating mostly ramified morphology (Figure 4.15). In sMND cases, microglia tended to show ramified morphology, but with many cells showing thickened processes and some microglia with amoeboid morphology were also present (Figures 4.16 and 4.17). These features were seen in motor regions of the spinal cord (lateral corticospinal tract and ventral horn) and represent a microgliosis, which was not observed in control. Interestingly, an upregulation of IBA1 immunoreactivity was observed in almost all white matter tracts, including spinothalamic and spinocerebellar tracts with the only exception of the dorsal column, which was relatively spared.

Within sMND cases, both the extent of microgliosis and microglial morphology varied greatly between cases, particularly in the lateral corticospinal tract (Figure 4.19). Some cases showed much more extensive IBA1 immunoreactivity compared to other sMND cases. Furthermore, while all cases showed a mix of ramified and ameboid morphology, the relative proportions varied such that in some cases were

ramified microglia were predominant, with some amoeboid cells, while other cases were amoeboid microglia- predominant with few ramified microglia.

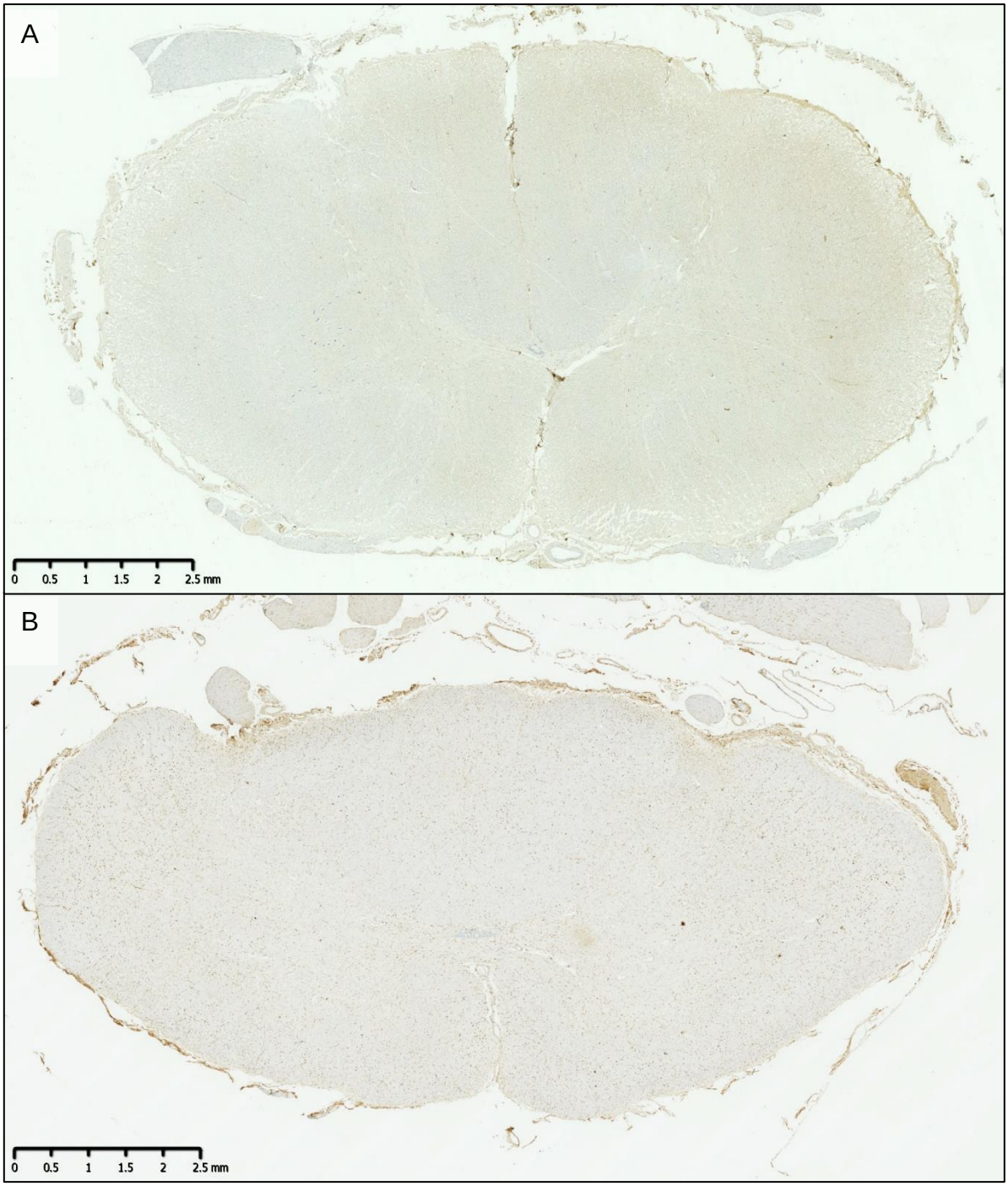

Figure 4.14 IBA1 Immunohistochemistry in control and sMND spinal cord

*Overview images of cervical spinal cord from control (**A**) and sMND (**B**) cases. In both, at low power, staining is difficult to discern, although present in both white and grey matter at high power.*

Scale bar represents 2.5mm

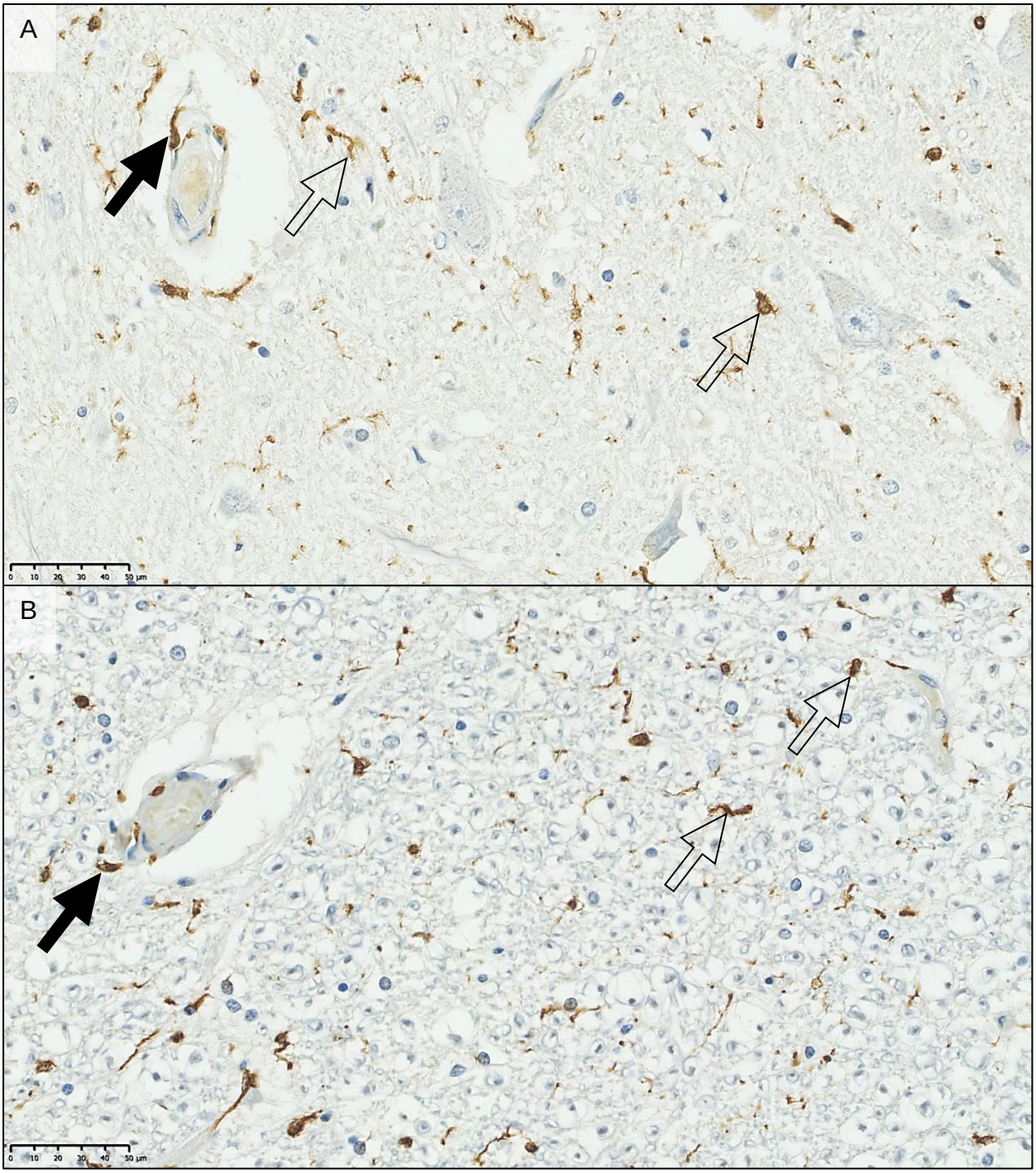

Figure 4.15 IBA1 Labels Predominantly Ramified Microglia and Perivascular Macrophages in Control Spinal Cord

In control spinal cord, IBA1 labels perivascular macrophages (black arrows), and microglia (open arrows). In control spinal cord, microglia tend to be ramified. Figure A shows IBA1 immunoreactivity in the ventral horn, and Figure B shows the lateral corticospinal tract.

Scale bars = 50µm

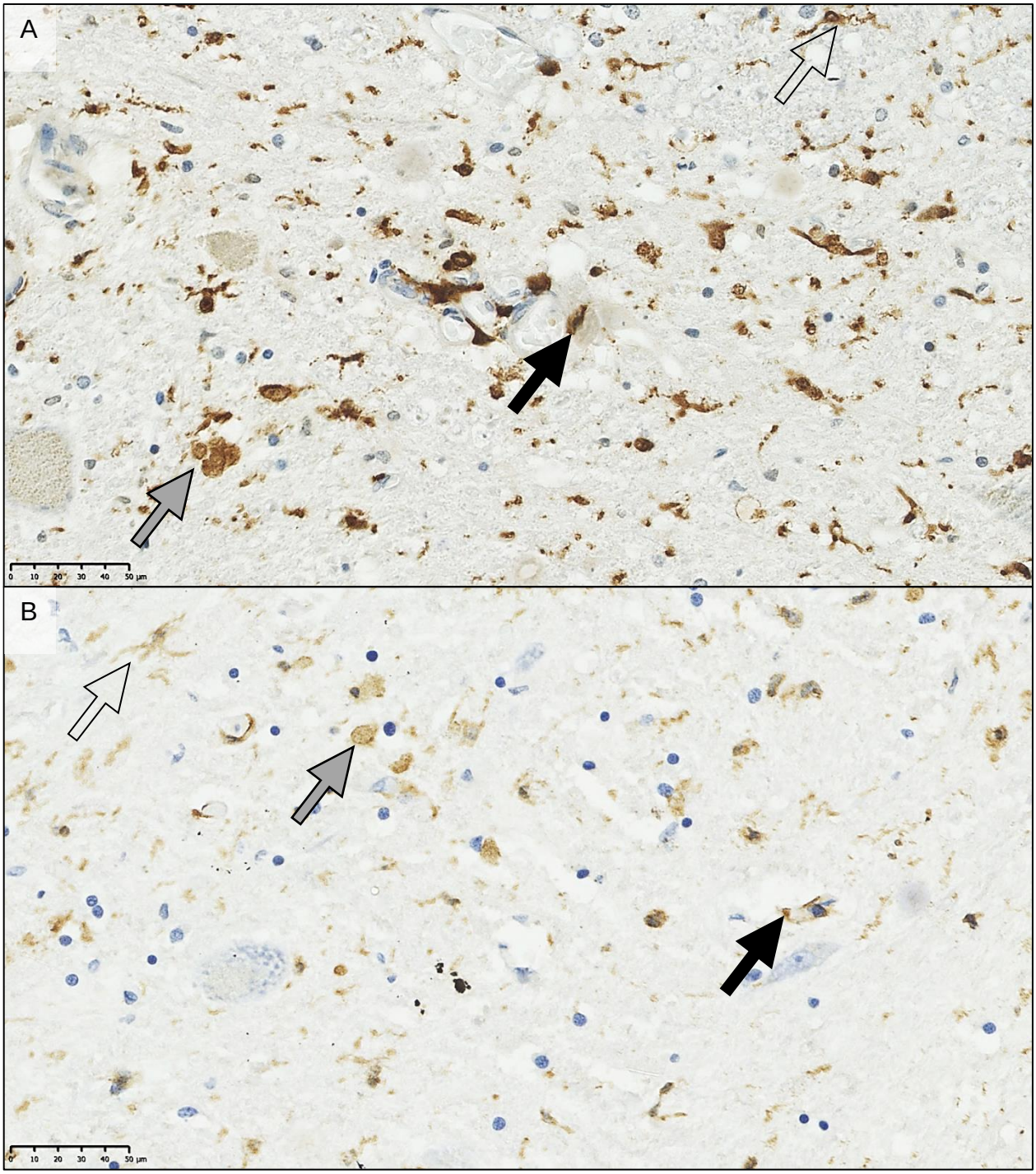

Figure 4.16 In sMND spinal cord, IBA1 Labels Perivascular Macrophages and Both Amoeboid and Ramified Microglia

*In sMND spinal cord, IBA1 labels perivascular macrophages and microglia. Perivascular macrophages (black arrows) were swollen in some cases compared to control. Microglia tended to show a mixture of ramified (open arrows) and amoeboid (grey arrows) morphology. Figure **A** shows ventral horn, and Figure **B** shows the lateral corticospinal tract.*

Scale bars= 50µm

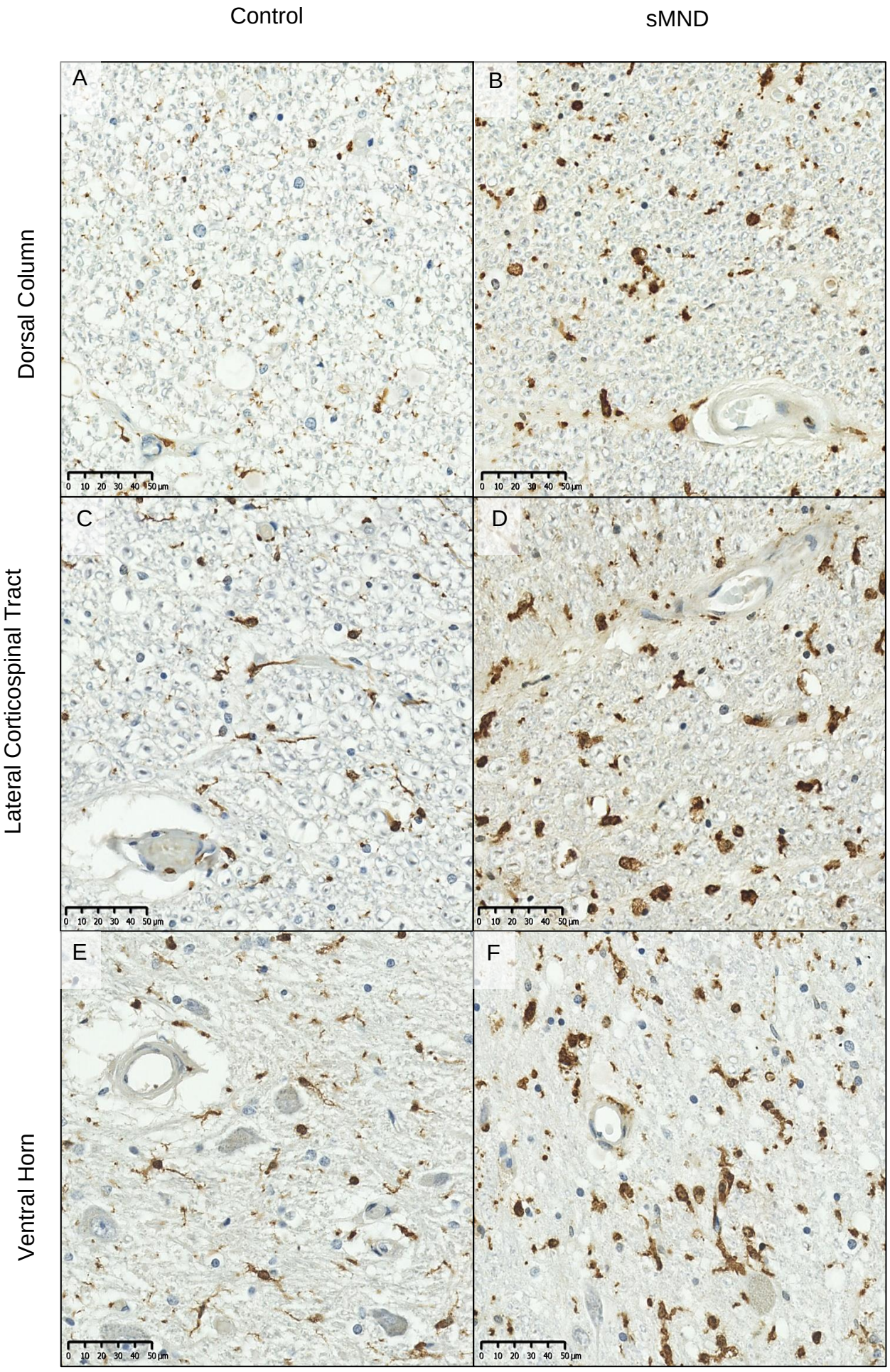
Control
sMND
Dorsal Column
Lateral Corticospinal Tract
Ventral Horn
A
B
C
D
E
F
0 10 20 30 40 50 µm

Figure 4.17 IBA1 Immunoreactivity in Control and sMND Spinal Cord

*IBA1 immunoreactivity in the dorsal column (**A&B**), lateral corticospinal tract (**C&D**), and ventral horn (**E&F**), in control (**A,C,E**) and sMND (**B,D,F**).*

Expression of IBA1 was increased across the spinal cord in sMND cases in both grey matter and white matter, compared to control. IBA1 immunoreactivity was most noticeably increased in the motor regions. In sMND cases, microgliosis was observed in the ventral horns and in the lateral corticospinal tract.

*In the dorsal column, although relatively spared, microglia were slightly more swollen in sMND cases (**B**) compared to control (**A**). However, overall little difference was observed between control and sMND cases in this spinal cord region*

*White matter (bar the dorsal column) showed a vast increase in IBA1 immunoreactivity in sMND cases. The lateral corticospinal tracts were the most affected region. Microglia were swollen, with larger cells bodies, and more microglia had adopted the amoeboid morphology in sMND cases (**D**) compared to control cases (**C**)*

*In the ventral horns, ramified microglia tended to have larger cell bodies and more swollen process in sMND cases (**F**) compared to control cases (**E**). Additionally, many more ameboid cells were present in sMND compared to control cases.*

Representative images were taken from one control and one sMND case at 40x magnification. Scale bars = 50µm.

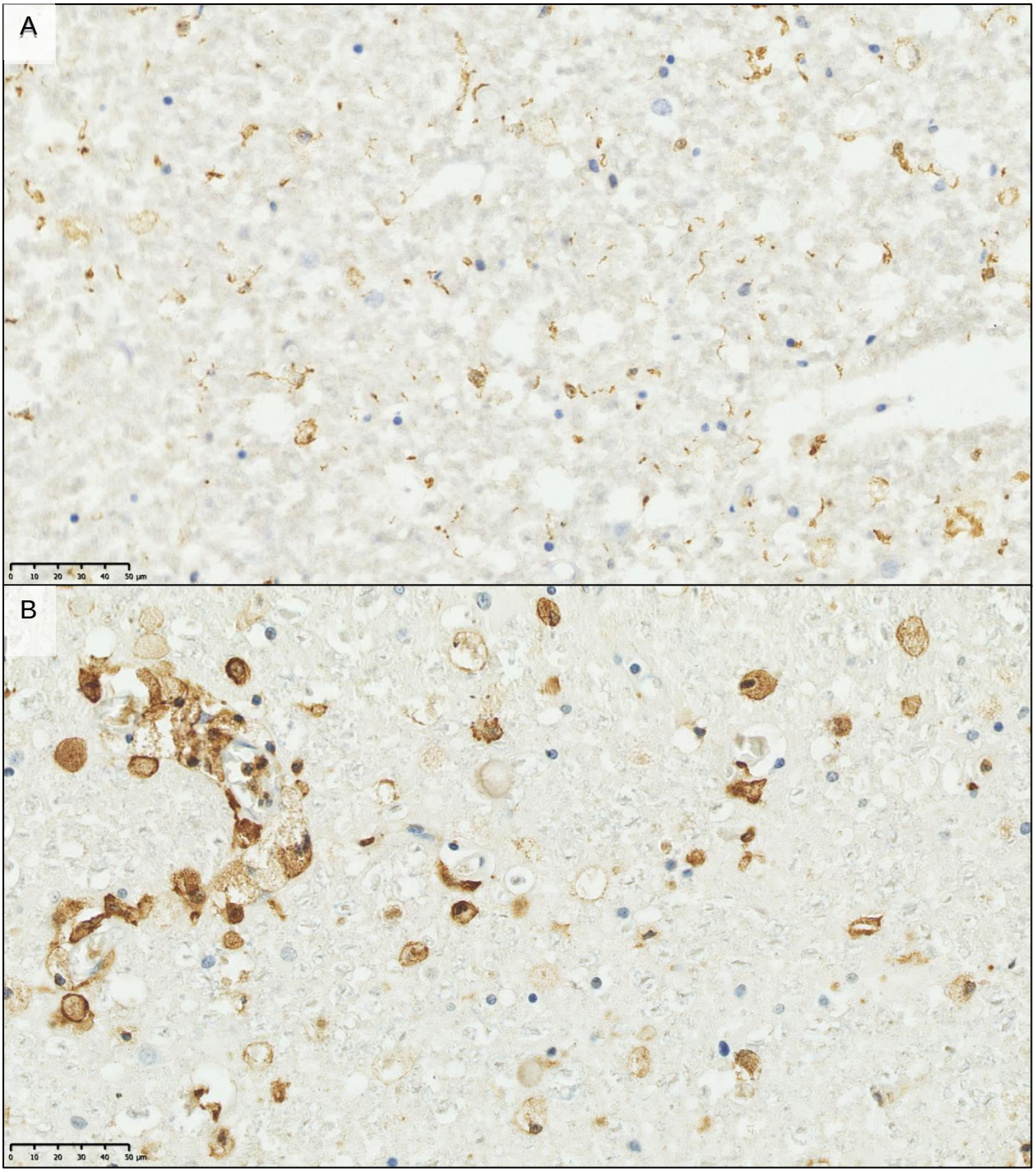

Figure 4.18 Microglial Morphology Varies in sMND cases

*Overall, IBA1 immunoreactivity was upregulated in sMND cases compared to control, however sMND cases varied greatly in microglial morphology. All sMND cases showed a mixture of ameboid and ramified morphology however some cases were predominantly ramified in their microglial morphology (illustrated by **A**), while others were predominantly ameboid, displaying very large and rounded microglia (as illustrated in **B**).*

Images were both taken in the lateral corticospinal tracts, from two sMND cases. Scale bars = 50 µm.

Quantitative Analysis

Visiopharm software was used to quantify the percentage area stained for IBA1 in the ventral horn, dorsal column, and lateral corticospinal tract in the control and sMND spinal cord cohort. A Kruskal-Wallis test showed a significant difference in the percentage area positive for IBA1 between sMND and control cases ($H(5)23.98$, $p=0.0002$). Pairwise comparisons were performed using one-tailed Mann-Whitney U tests (Figure 4.19), which revealed a significant increase in IBA1 staining density in sMND compared to control cases in the lateral corticospinal tract ($U=28$, $p=0.0033$), and in the ventral horn ($U=61$ $p=0.03$). There was no significant difference in IBA1 expression between control and sMND cases in the dorsal column ($U=75$, $p=0.096$). In all spinal cord regions, sMND regions showed great heterogeneity with IBA1 density varying greatly, as is evident in Figure 4.18.

A

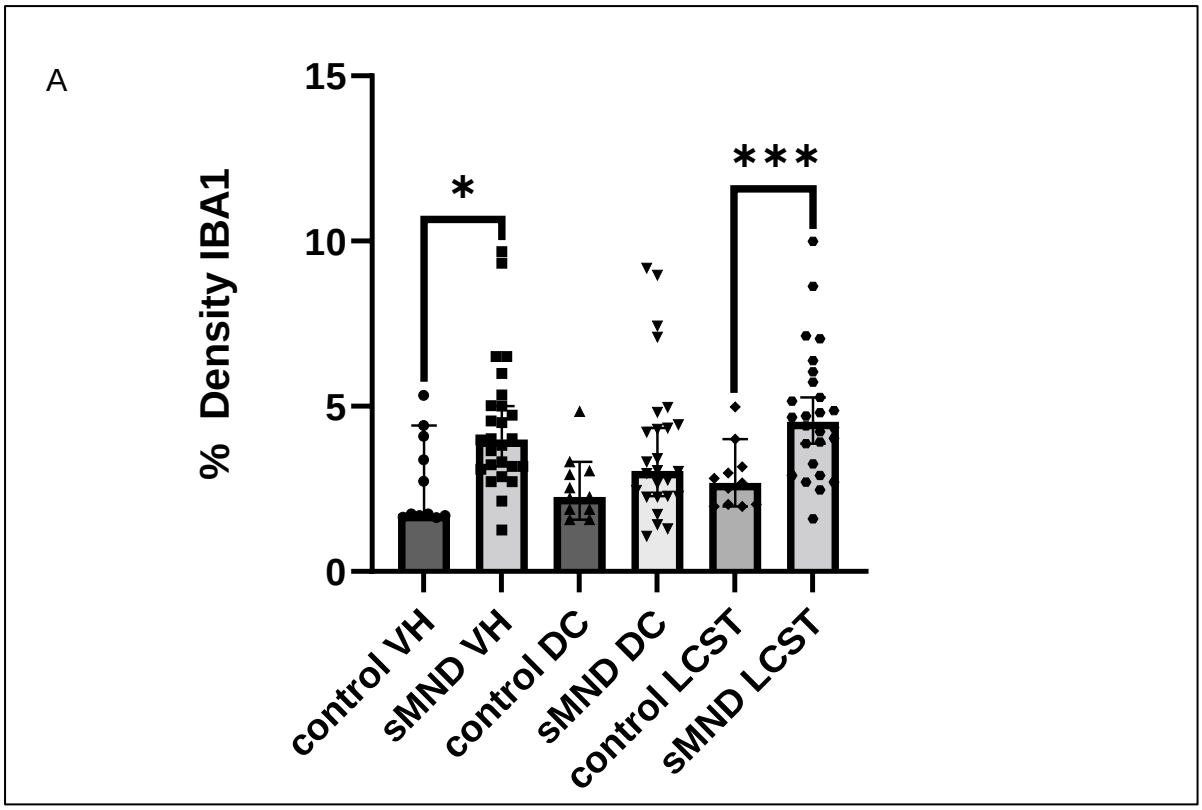

B

Spinal Cord Region	Disease Status	Median (% density)	95% Confidence Intervals (Lower, Upper)	Mann-Whitney U	P Value
Ventral Horn	Control	1.745	1.826, 3.649	61	0.03
	sMND	3.999	3.602, 5.192		
Dorsal Column	Control	2.253	1.905, 3.196	75	0.0963
	sMND	3.04	2.876, 3.196		
Lateral Corticospinal Tract	Control	2.683	2.195, 3.468	50	0.0007
	sMND	4.538	3.977, 5.546		

Figure 4.19 IBA1 Expression is Increased in the Lateral Corticospinal Tract in sMND.

A) Across the spinal cord, IBA1 staining was increased in sMND cases compared to control cases. A Kruskal-Wallis test found a significant difference between groups (H(5)50, p=0.0002). Pairwise comparisons using Mann-Whitney U analysis revealed a significant increase in IBA1 percentage density in sMND compared to control in the lateral corticospinal tract (U=28, p=0.0007) and the ventral horn (U=61, p=0.03). There was no significant difference between control and sMND cases in the ventral horn or dorsal column. Bars show the median value, error bars show 95% CI.

B) Table showing descriptive statistics (median % density and 95% confidence intervals), and results of the pairwise comparisons.

VH = ventral horn, DC = dorsal column, LCST = lateral corticospinal tract.

To examine whether IBA1 expression was associated with the length of patient survival, cases were split into fast or slow disease progression (months) using the median survival value (40 months). IBA1 density (%) was compared between groups using a Kruskal-Wallis test. No significant relationship difference was found between IBA1 density in the fast or slow progression sMND cases ($H(5)=10.38$, $p=0.065$).

4.4.2 CD68

Qualitative Analysis

At low magnification, CD68 immunoreactivity was not overtly visible in control cases. In sMND cases, some CD68 immunoreactivity was observable in the motor white matter tracts and ventral horns. In both control and sMND cases, the level of CD68 immunoreactivity was lower than that of IBA1.

CD68 immunohistochemistry labelled microglia within the parenchyma, and perivascular macrophages (Figure 4.20). In sMND cases, CD68 primarily labelled microglia with a rounded, amoeboid morphology (Figure 4.21). This is in line with previous literature (Korzhevskii and Kirik, 2016) given the role of the CD68 protein in the phagocytic functions of macrophages. Ramified microglia were observed in control cases, but more so in sMND cases. In sMND cases, microglial cells bodies tended to be larger than those from control cases, and microglia displaying ramified morphology had thicker processes compared to control cases, indicating microglial activation.

In sMND, microgliosis was observed in the ventral horns and in the white matter tracts (Figure 4.22). CD68 was upregulated consistently in the lateral corticospinal tracts, but some cases showed increased expression in all white matter (such as the spinothalamic tracts) except the dorsal column.

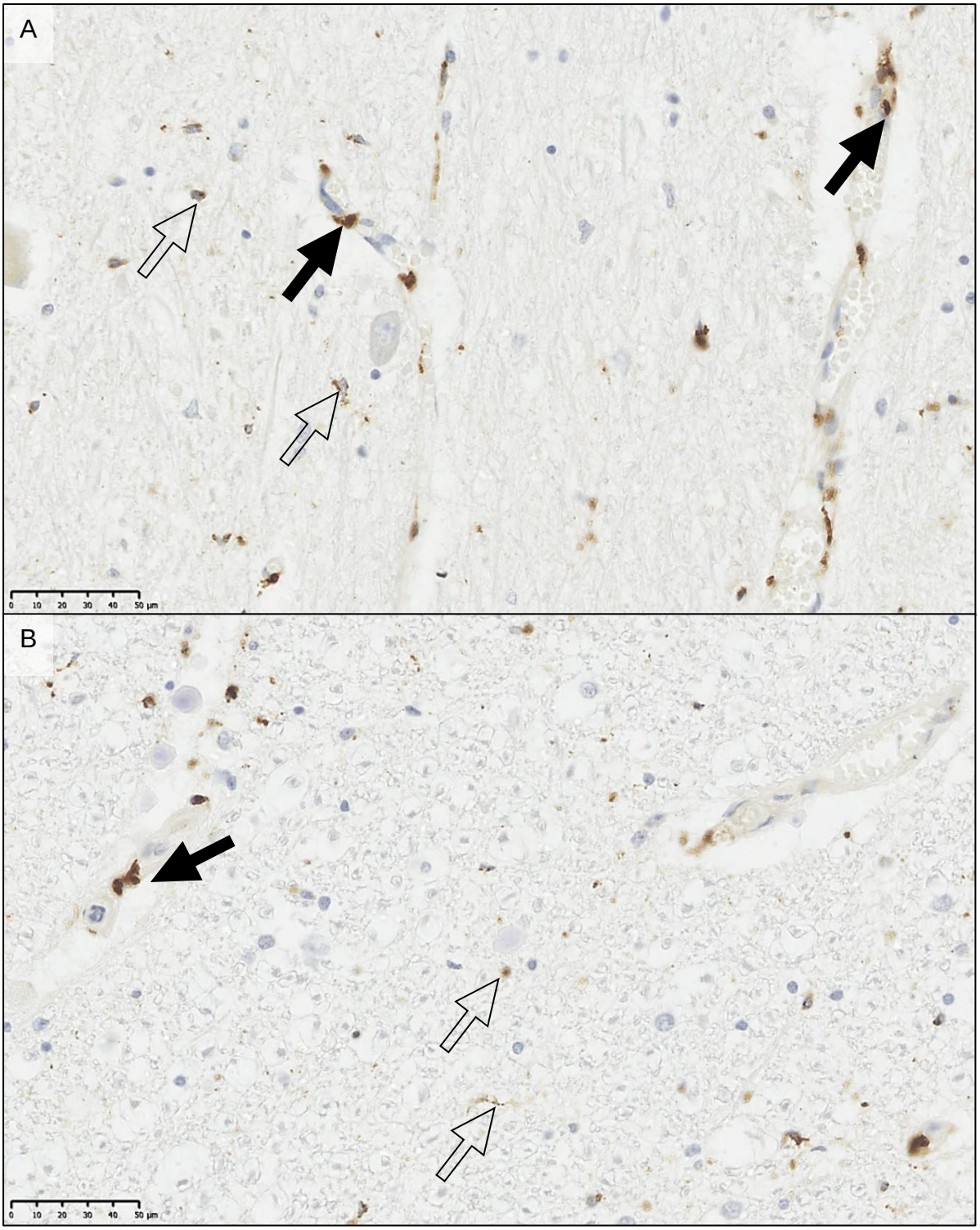

Figure 4.20 CD68 Labelled Perivascular Macrophages and a Small Number of Parenchymal Microglia in Control Spinal Cord.

*In the spinal cord of control cases, CD68 immunoreactivity is predominantly limited to perivascular macrophages (black arrows). Some smaller microglial cells were seen throughout the parenchyma. These microglial cells tended to have very small cells bodies (open arrows). Figure **A** shows CD68 immunoreactivity in the ventral horn, and Figure **B** shows the lateral corticospinal tract.*

Scale bars= 50µm

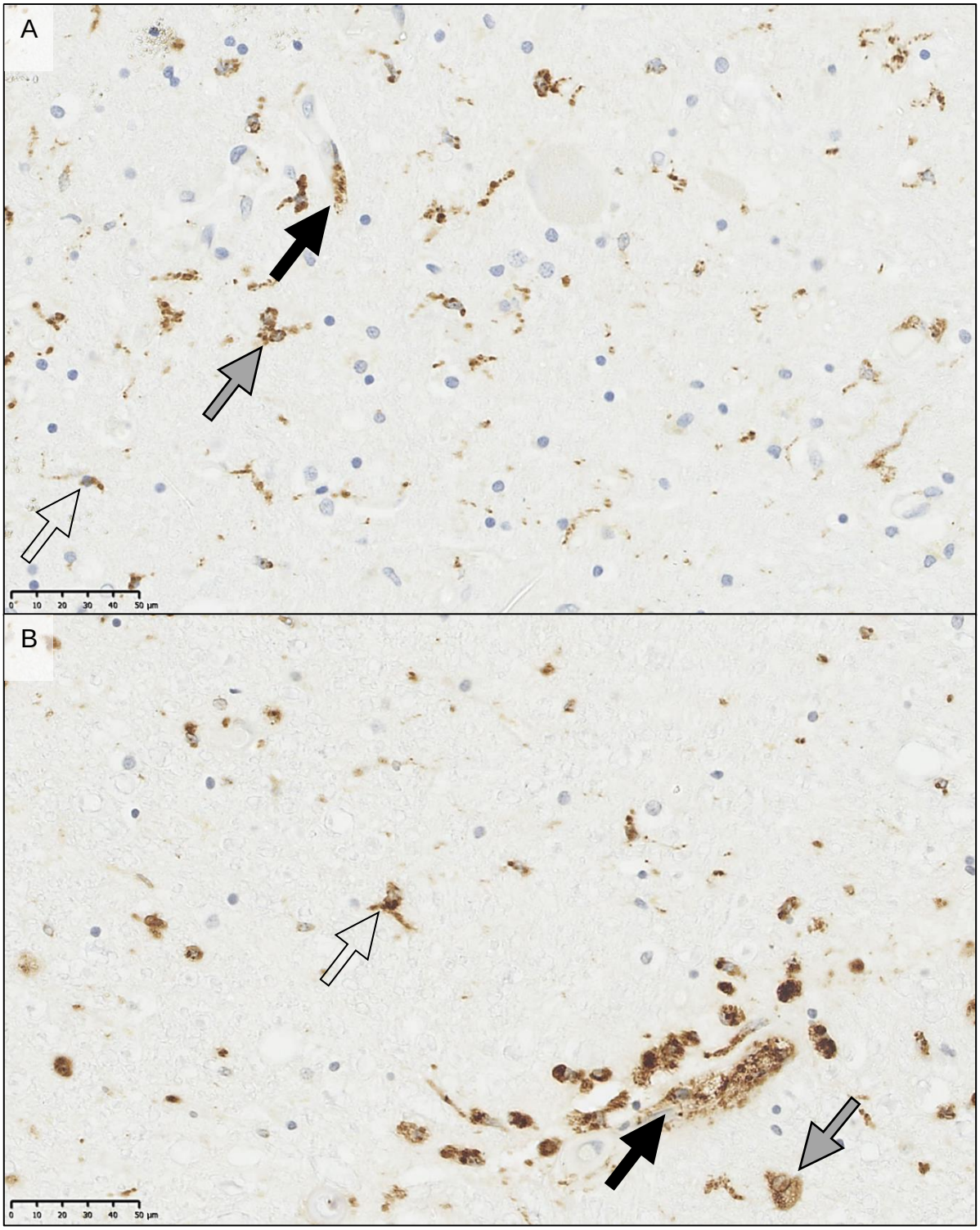

Figure 4.21 CD68 Labelled Perivascular Macrophages, and Ameboid and Ramified Microglia in sMND Spinal Cord.

In sMND, there is an increase in CD68 immunoreactivity. Perivascular macrophages (black arrows) were increased in number and size surround blood vessels. Microglia within the parenchyma had swollen cell bodies and varied from ramified (open arrows) to fully ameboid cell morphology (grey arrows).

Scale bars= 50µm

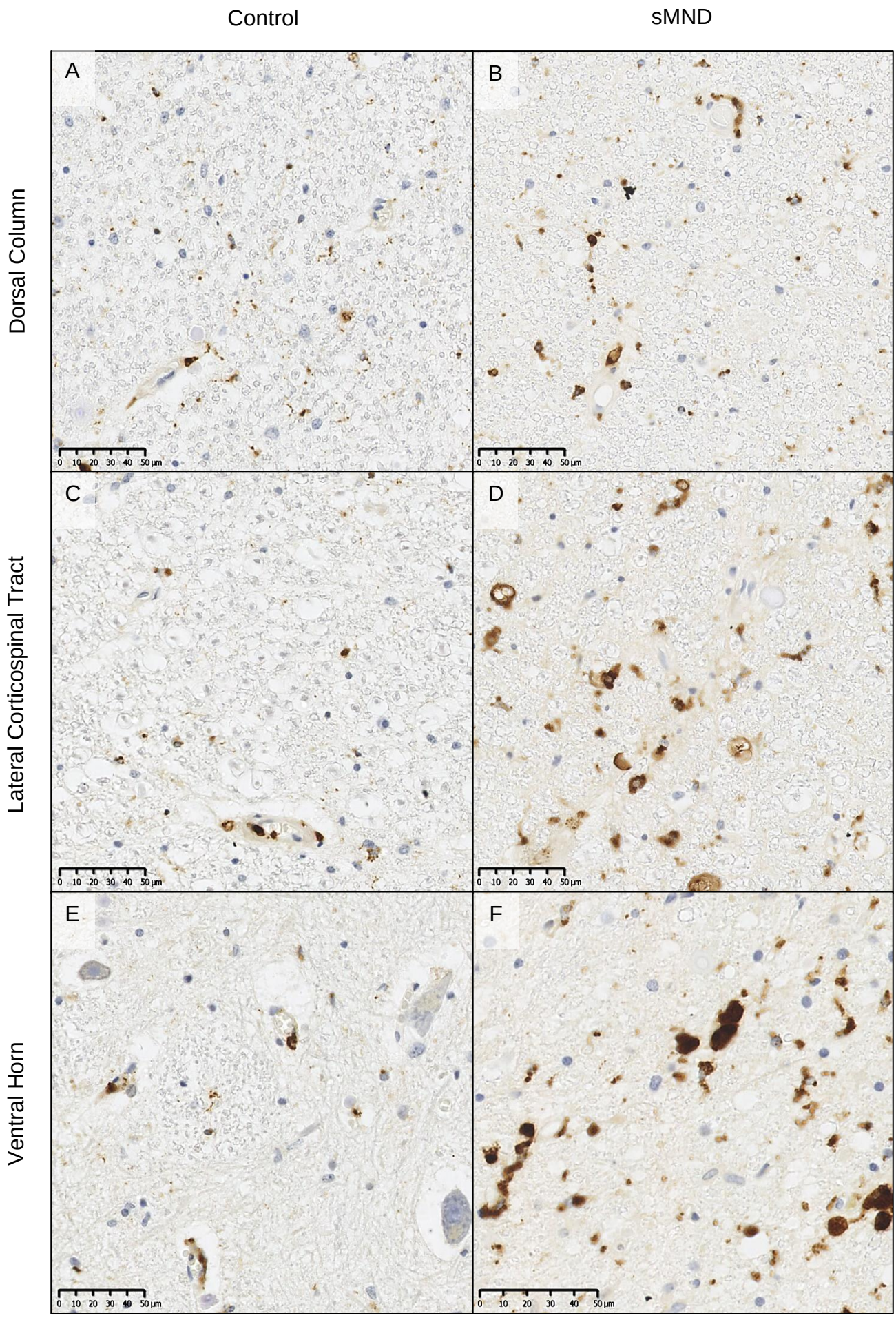
Control
sMND
Dorsal Column
Lateral Corticospinal Tract
Ventral Horn
A
B
C
D
E
F
0 10 20 30 40 50 µm

Figure 4.22 CD68 Immunoreactivity in Control and sMND Spinal Cord

*CD68 immunoreactivity in the dorsal column (**A&B**), lateral corticospinal tract (**C&D**), and ventral horn (**E&F**), in control (**A,C,E**) and sMND (**B,D,F**).*

Expression of CD68 was increased across the spinal cord in sMND cases in both grey matter and white matter, compared to control. CD68 immunoreactivity was increased in the motor regions. In sMND cases, microgliosis was observed in the ventral horns and in the lateral corticospinal tract.

*The dorsal column showed very little CD68 reactivity in control cases (**A**) and was mostly limited to some compact microglia and perivascular macrophages. In the sMND dorsal column, there was little increase in the number of cells expressing CD68, however parenchymal microglia were slightly larger.*

*In the white matter (bar the dorsal column) there was increased CD68 immunoreactivity in sMND cases. As with IBA1, the lateral corticospinal tracts were the most affected region. Microglia varied in their morphology ranging from ramified to fully swollen amoeboid in sMND cases (**D**). In control cases (**C**) microglia were compact and had small cells bodies compared to sMND cases.*

*In the ventral horns, there were an increased number of CD68 positive microglia in the parenchyma of sMND (**E**) cases compared to control (**F**). In sMND cases, microglia were largely ameboid*

Representative images were taken from one control and one sMND case at 40x magnification. Scale bars = 50µm.

Quantitative Analysis

Following quantification of CD68 immunoreactivity in cervical spinal cord using Visiopharm software, staining density was compared between control and sMND in the ventral horn, dorsal column, and lateral corticospinal tract. In all spinal cord regions, CD68 percentage staining density was increased in sMND. A Kruskal-Wallis test showed a significant difference in CD68 density between control and sMND ($H(5)=32.10$, $p<0.0001$). Pairwise comparisons were performed using one-tailed Mann-Whitney U tests, which revealed a significant increase in CD68 staining density in sMND cases compared to control, in the ventral horns ($U=24$, $p<0.0001$) and lateral corticospinal tract ($U=23$, $p<0.0001$). An increase in CD68 expression was also observed in the dorsal column ($U=56$, $p=0.014$), which was not noted in the qualitative analysis. In all spinal cord regions, sMND cases showed great heterogeneity as evidenced by the spread of data points in Figure 4.23.

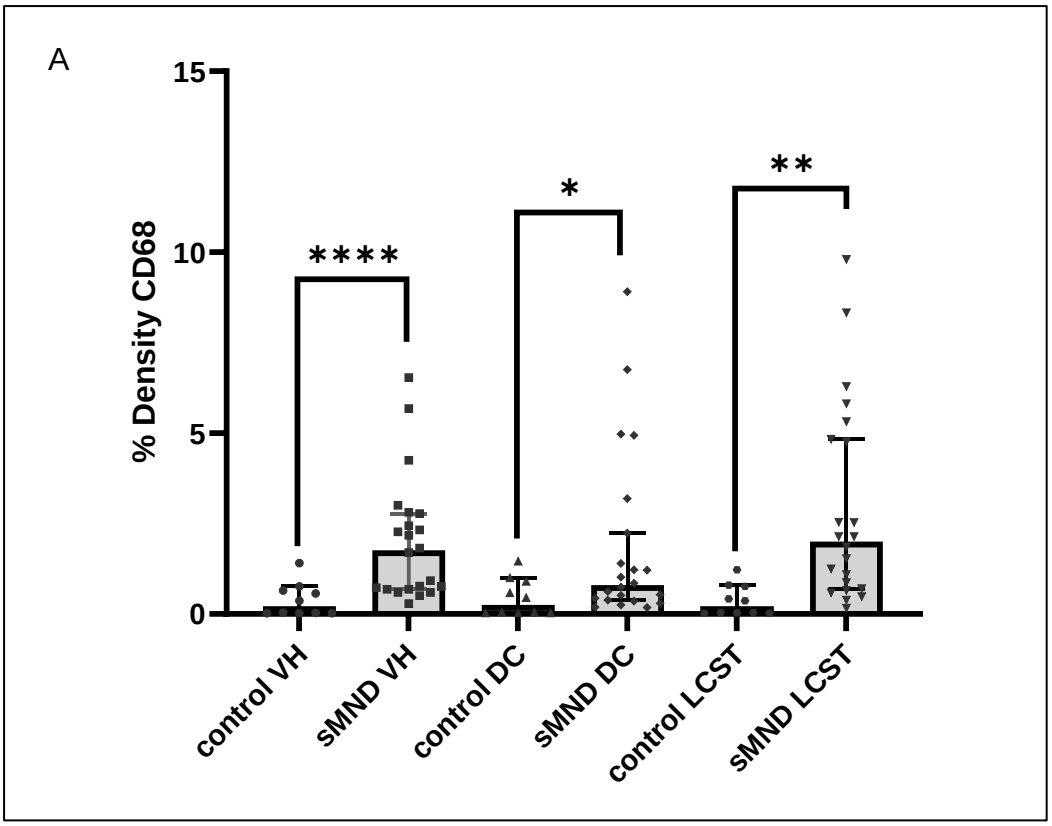

B

Spinal Cord Region	Disease Status	Median (%)	95% Confidence Intervals (Lower, Upper)	Mann-Whitney U	P Value
Ventral Horn	Control	0.206	0.059, 0.720	24	<0.0001
	sMND	1.761	1.264, 2.766		
Dorsal Column	Control	0.254	0.093, 0.831	56	0.0139
	sMND	0.798	0.810, 2.937		
Lateral Corticospinal Tract	Control	0.204	0.068, 0.0676	23	<0.0001
	sMND	2.000	1.690, 4.133		

Figure 4.23 CD68 staining is increased in sMND in the spinal cord.

A) Across the spinal cord, CD68 percentage staining density was compared in control and sMND. A Kruskall-Wallis test, revealed a significant difference between control and sMND, H(6)=32.10, p<0.0001. Pairwise comparisons found a significant increase in the ventral horn (VH), and lateral corticospinal tract (LCST), and in the dorsal column (DC). Bars show the median value, error bars are 95% CI.

B) Table showing descriptive statistics (median % density and 95% confidence intervals), and pairwise comparisons.

Note: VH= ventral horn, DC= dorsal column, LCST= lateral corticospinal tract

To examine whether CD68 expression was associated with the length of patient survival, cases were split into fast or slow disease progression (months) using the median expression value (38 months). CD68 density (%) was compared between fast and slow progressing sMND cases, using the Kruskall-Wallis test, no significant difference was found ($H(6)=4.904$, $p=0.428$).

4.4.3 HLA-DR

Qualitative Analysis

HLA-DR was widely expressed across the spinal cord and was visible even at low magnification (Figure 4.24). In both control and sMND cases, many cells were HLA-DR positive, comparatively more than observed in IBA1 and CD68.

Compared to control cases, HLA-DR expression was upregulated in sMND in the motor regions of the spinal cord (Figure 4.25), most noticeably in the corticospinal tracts but also in the anterior horns.

As with IBA1 and CD68, HLA-DR labelled microglia in the spinal cord parenchyma, and perivascular macrophages (Figure 4.26 and 4.27). HLA-DR-positive microglia showed a variety of morphologies. In control cases, microglia were predominantly ramified, with some amoeboid cells. In sMND cases, microglia tended to show more activated morphology, as indicated by enlarged cells bodies, thickened processes, and an increased proportion of amoeboid cells. Microglia in the white matter were predominantly amoeboid, with very few ramified cells. In the ventral horn, microglia were primarily ramified but did show thicker processes and rounder cell bodies compared to microglia in control ventral horn. In the dorsal column, although the density of staining did not differ between groups, microglia appeared to show slightly thicker processes with larger cell bodies with more amoeboid cells.

As with previous markers, sMND cases showed great heterogeneity in terms of the severity of HLA-DR positive microgliosis (Figure 4.28). HLA-DR expression was markedly increased in the white matter in sMND, with some cases showing upregulation across the entire white matter, bar the dorsal column. Some cases had predominantly ramified microglia with thickened processes and swollen cell bodies.

However, in a subset of cases, microglia were predominantly amoeboid and packed very densely.

HLA-DR immunoreactivity varied in the ventral horn. Some cases were barely distinguishable from control, only showing a slight increase in cell density with some thickening of microglial processes. However, other cases demonstrated much more extensive HLA-DR immunoreactivity and microglia were much larger, with thickened processes.

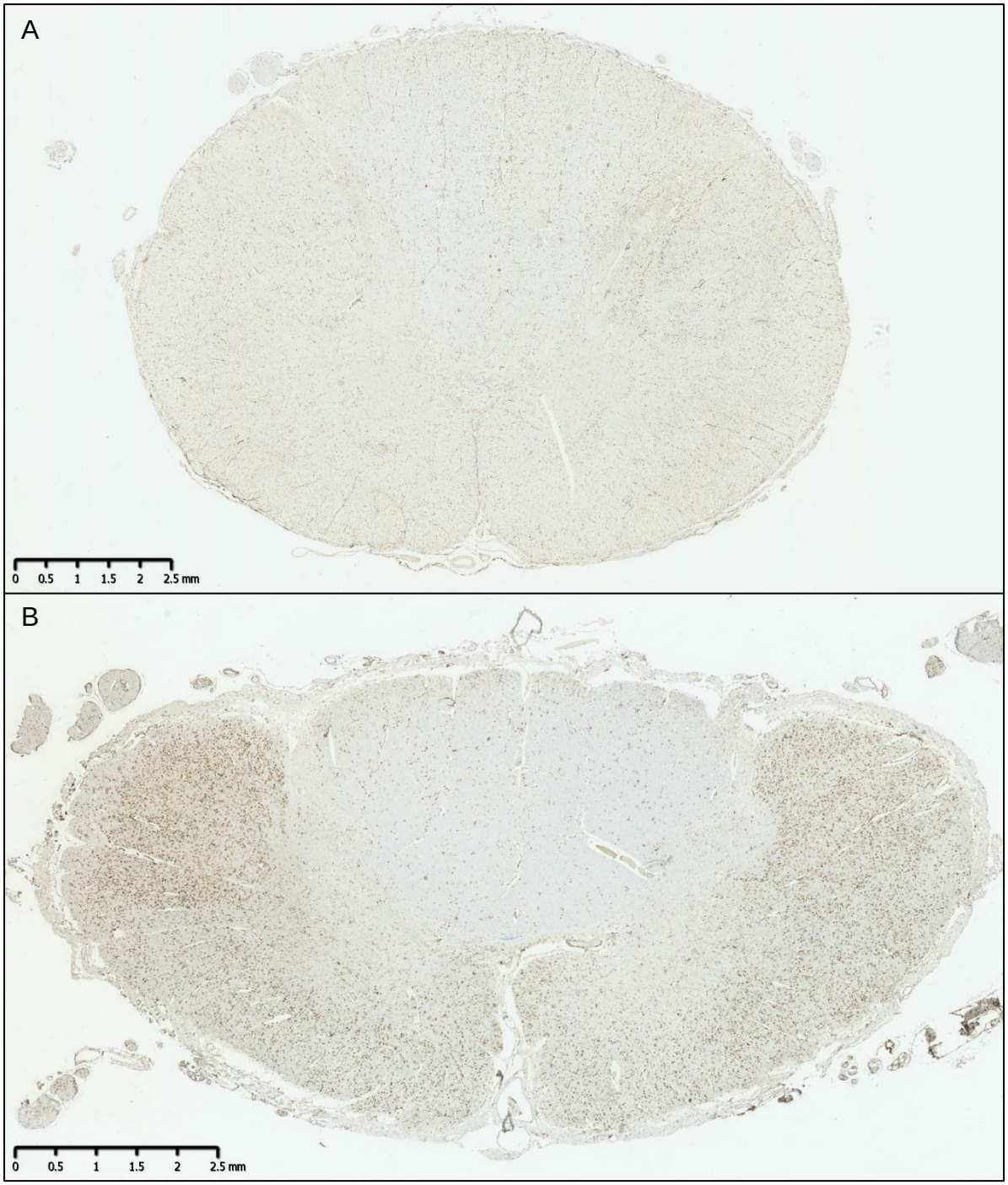

Figure 4.24 HLA-DR is Widely Expressed across the Spinal Cord

*HLA-DR expression was visible in both control (**A**) and sMND spinal cord (**B**) even at low magnification. Comparatively more cells were positive for HLA-DR, in relation to other microglial markers such as CD68. There was a striking upregulation of HLA-DR in the white matter of sMND cases, sparing the dorsal column.*

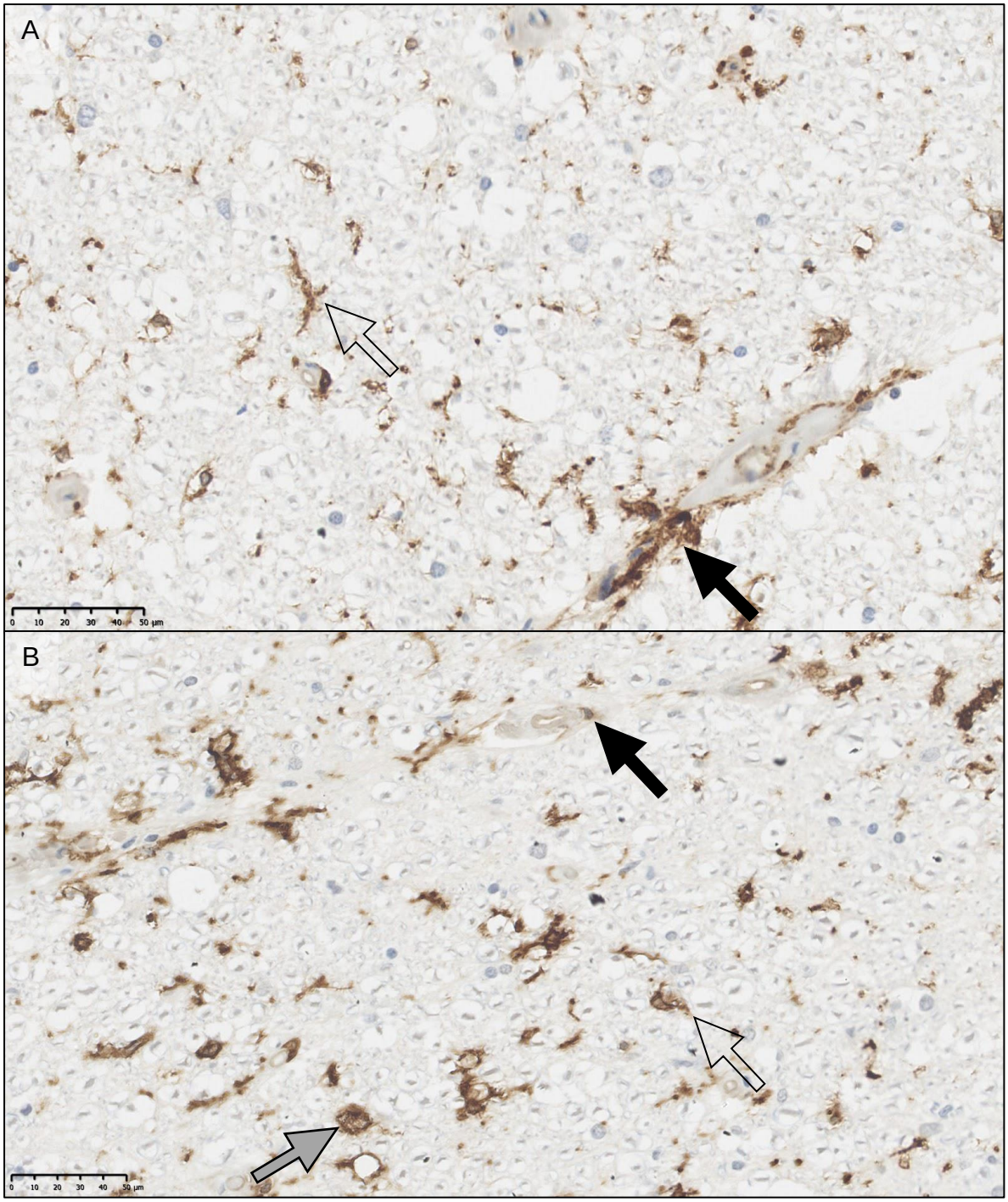

Figure 4.25 HLA-DR Labels Perivascular Macrophages and Microglia in the Parenchyma.

As with other microglial markers HLA-DR primarily labels microglia in the parenchyma and perivascular macrophages (black arrows).

In control cases (A), microglia were in their homeostatic ramified state (open arrow), In sMND cases (B) microglial morphology varies from ramified cells with thickened processes to full amoeboid cells (grey arrows)

Images were taken from the lateral cortical spinal tract. Scale bar = 50µm.

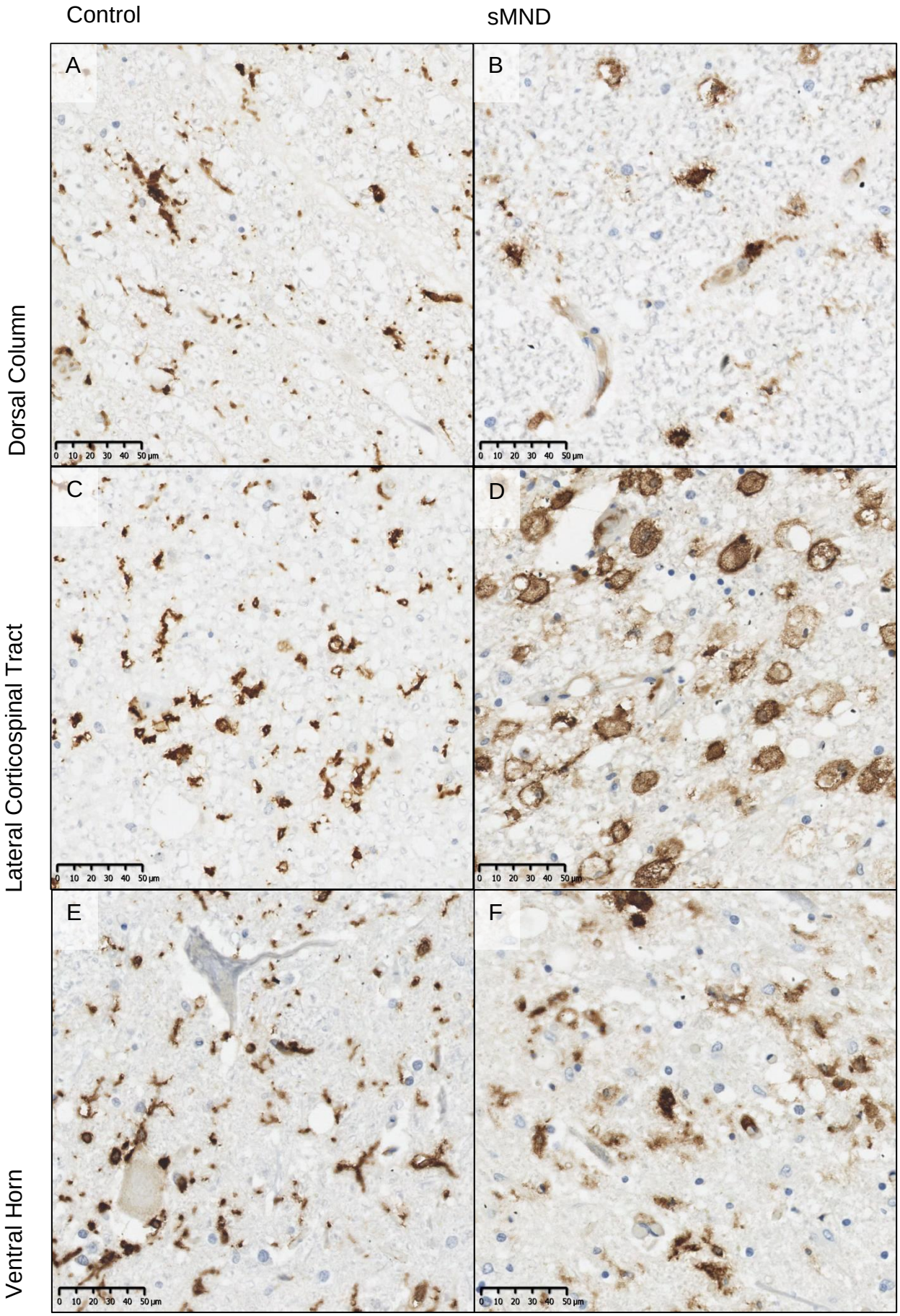
Control
sMND
A
B
C
D
E
F
Dorsal Column
Lateral Corticospinal Tract
Ventral Horn
0 10 20 30 40 50 µm

Figure 4.26 Comparison of HLA-DR Immunoreactivity Across the Spinal Cord in Control and sMND Cases.

*Comparison of IBA1 immunoreactivity in the dorsal column (**A&B**), lateral corticospinal tract (**C&D**), and ventral horn (**E&F**), in control (**A,C,E**) and sMND (**B,D,F**).*

Unlike other microglial markers, HLA-DR expression was widespread across the entire spinal cord in both control and sMND cases.

*The dorsal column did not show much excess HLA-DR immunoreactivity in sMND compared to control cases. Microglia did show a slight increase in the size, having slightly more swollen cell bodies in sMND (**B**) compared control cases in which microglia were predominantly in their homeostatic, ramified state (**A**).*

*Of all regions of the spinal cord, the most striking increase in HLA-DR expression in sMND cases was in the white matter particularly the corticospinal tracts. In many, cells were predominantly amoeboid and had very large cell bodies in the lateral corticospinal tract in sMND (**D**) compared to control cases (**C**).*

*In control cases (**E**), microglia in the ventral horns predominantly had ramified morphology with thin processes and small cells bodies. Little difference was observed in the number of microglia in the ventral horns in sMND cases (**F**), however microglia did look to be larger and more swollen. Additionally, a number of cells had adopted the fully amoeboid morphology.*

Scale bar=50µm.

sMND -Low Pathology Case

sMND -High Pathology Case

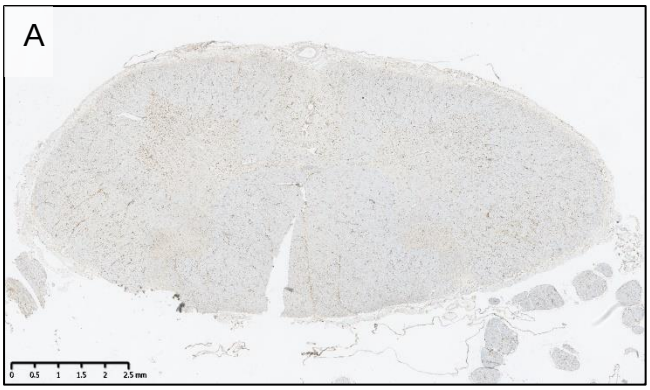

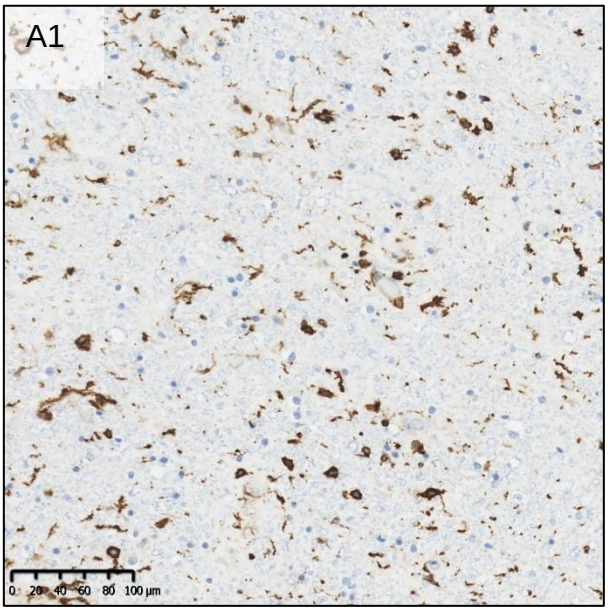

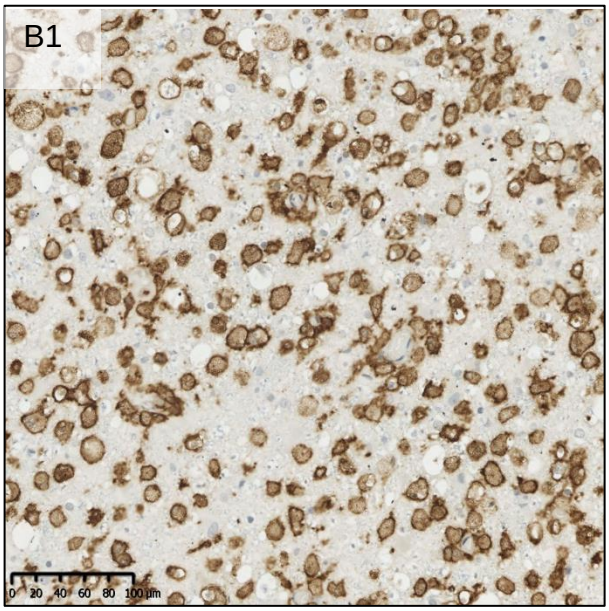

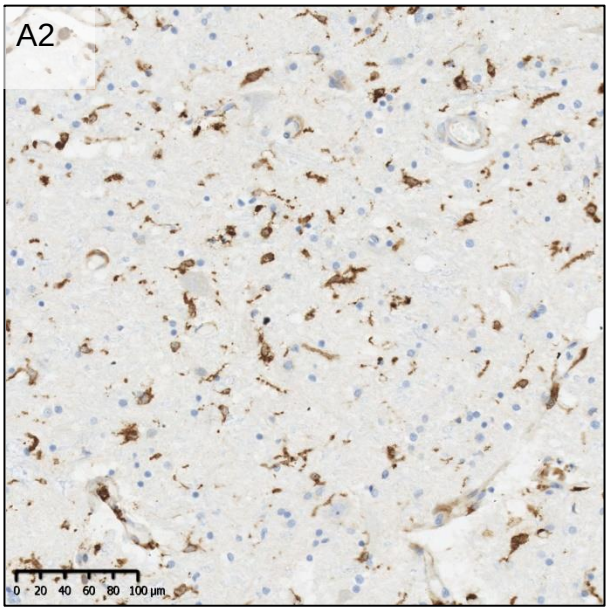

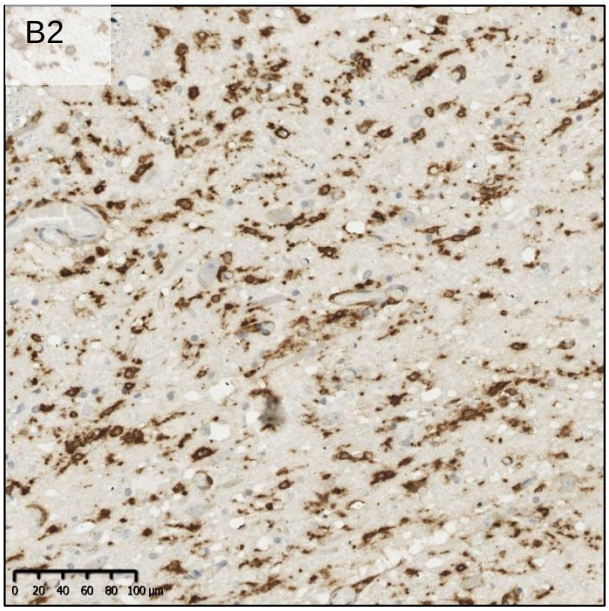

Figure 4.27 Heterogeneity of HLA-DR Immunoreactivity in sMND Cases

*In the spinal cord, sMND cases varied greatly in the level of HLA-DR staining present. Both cases (Figure **A** & **B**) are sMND cases. However, as visible from the low magnification image, these cases showed very different levels of HLA-DR positive microgliosis.*

*Figures **A1** and **B1** show higher magnification images of the lateral corticospinal tract for these cases. In the low pathology case (**A1**) microglia were rounded (when compared to control) and showed thickened processes. In the high pathology case (**B2**) microglia were completely rounded and showed much denser staining.*

*Figures **A2** and **B2** show higher magnification images of the ventral horn. In case A (low pathology) microglia again showed thick processes, swollen cell bodies and an increased number of HLA-DR positive microglia. In case B, HLA-DR positive microglia were much rounder, many becoming ameboid, and microgliosis was much more severe.*

A and B scale bars =2.5mm; A1, A2, B1 and B2 scale bars =100µm.

Quantitative Analysis

HLA-DR immunoreactivity in the spinal cord was quantified using the HLA-DR specific app in the Visiopharm analysis software. Staining density was compared between sMND and control cases using a one-way Kruskall-Wallis test, which indicated a significant difference in HLA-DR expression between groups ($H(5)=21.50$, $p=0.007$; Figure 4.28). Pairwise comparisons (one-tailed Mann-Whitney U test) indicated a significant increase in HLA-DR immunoreactivity in the lateral corticospinal tract in sMND cases (median = 4.581) compared to control cases (median = 8.549; $U=59$, $p=0.003$). HLA-DR staining density did not significantly differ in the ventral horn ($U=111$, $p=0.181$) or dorsal column ($U=131$, $p=0.412$) in comparison to control cases. sMND cases appeared to showed great variation in staining density, particularly in the lateral corticospinal tract and ventral horn.

A

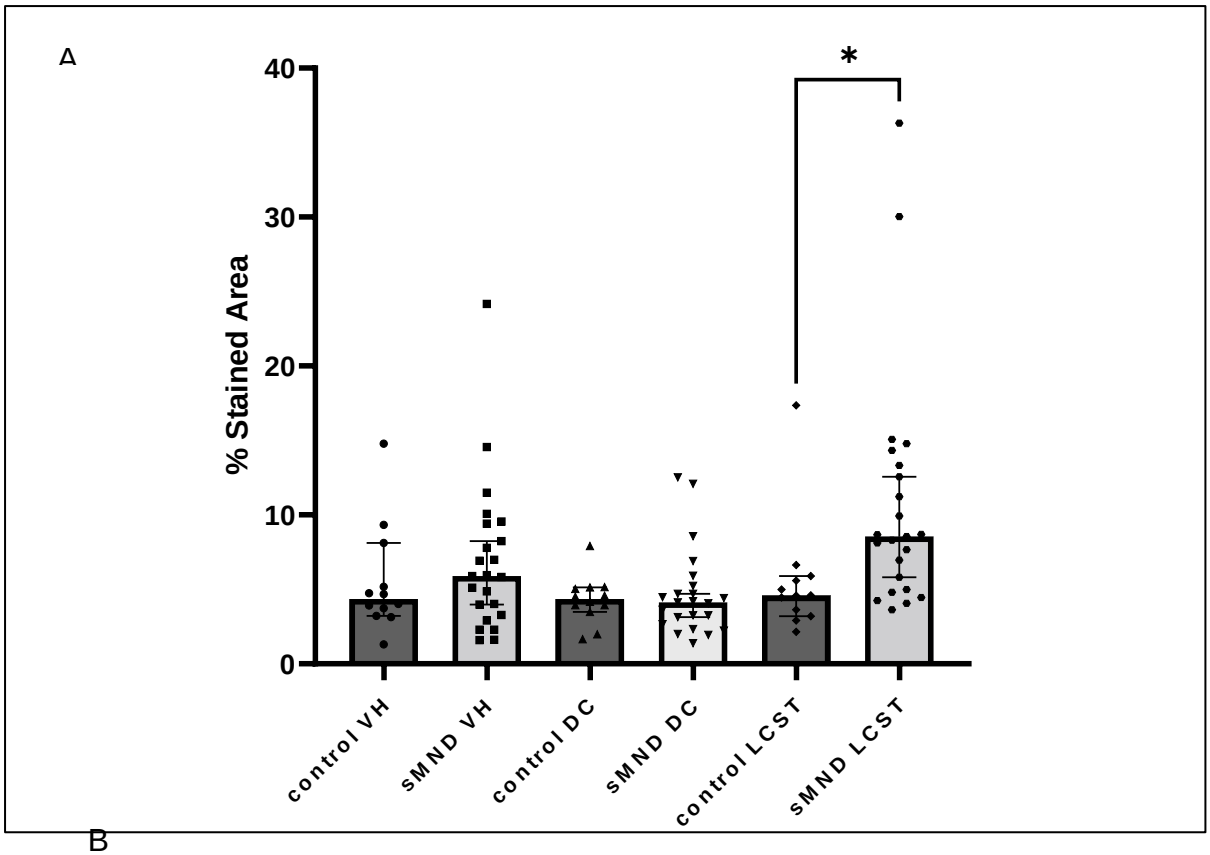

B

Spinal Cord Region	Disease Status	Median (%)	95% Confidence Intervals (Lower, Upper)	Mann-Whitney U	P Value
Ventral Horn	Control	4.351	3.203, 7.822	111	0.181
	sMND	5.898	4.730, 9.0088		
Dorsal Column	Control	4.343	3.272, 5.312	131	0.412
	sMND	4.122	3.422, 5.948		
Lateral Corticospinal Tract	Control	4.581	2.984, 8.008	59	0.003
	sMND	8.549	7.264, 14.170		

Figure 4.28 HLA-DR staining density is increased in the lateral corticospinal tract in sMND.

A) In cervical spinal cord, the percentage density of HLA-DR staining was compared between sMND and control cases using the Kruskal-Wallis test, indicating a significant difference between sMND and control cases ($H(5)=21.50$, $p<0.001$). Mann-Whitney tests revealed a significant increase in HLA-DR staining density in sMND lateral corticospinal tract compared to control cases ($U=59$, $p=0.003$. No significant difference was observed in the ventral horn or dorsal column. Bars show the median value, error bars show 95% CI.

B) Table showing descriptive statistics (median % density and 95% confidence intervals), and results of the pairwise comparisons.

VH= ventral horn, DC= dorsal column, LCST= lateral corticospinal tract.

To examine whether HLA-DR expression was associated with the length of patient survival, cases were split into fast or slow disease progression (months) using the median expression value (47 months). HLA-DR density (%) was compared between fast and slow progressing sMND cases, using a one-way Kruskall-Wallis test (Figure 4.29), which indicated there was a significant relationship between the rate of disease progression and HLA-DR staining density ($H(6)=23.31$, $p=0.0003$). Pairwise comparisons were performed using the two-tailed Mann-Whitney test, which revealed HLA-DR staining density was significantly increased in the ventral horns ($U=9$, $p=0.0148$), and in the lateral corticospinal tract ($U=6$, $p=0.005$), of fast progressing cases compared to slower progressing sMND cases. No relationship was found between the rate of disease progression and HLA-DR pathology in the dorsal column ($U=20$, $p=0.235$). As such, microglial immune activation is increased in the ventral horn and lateral corticospinal tracts in cases of faster progressing sMND.

A

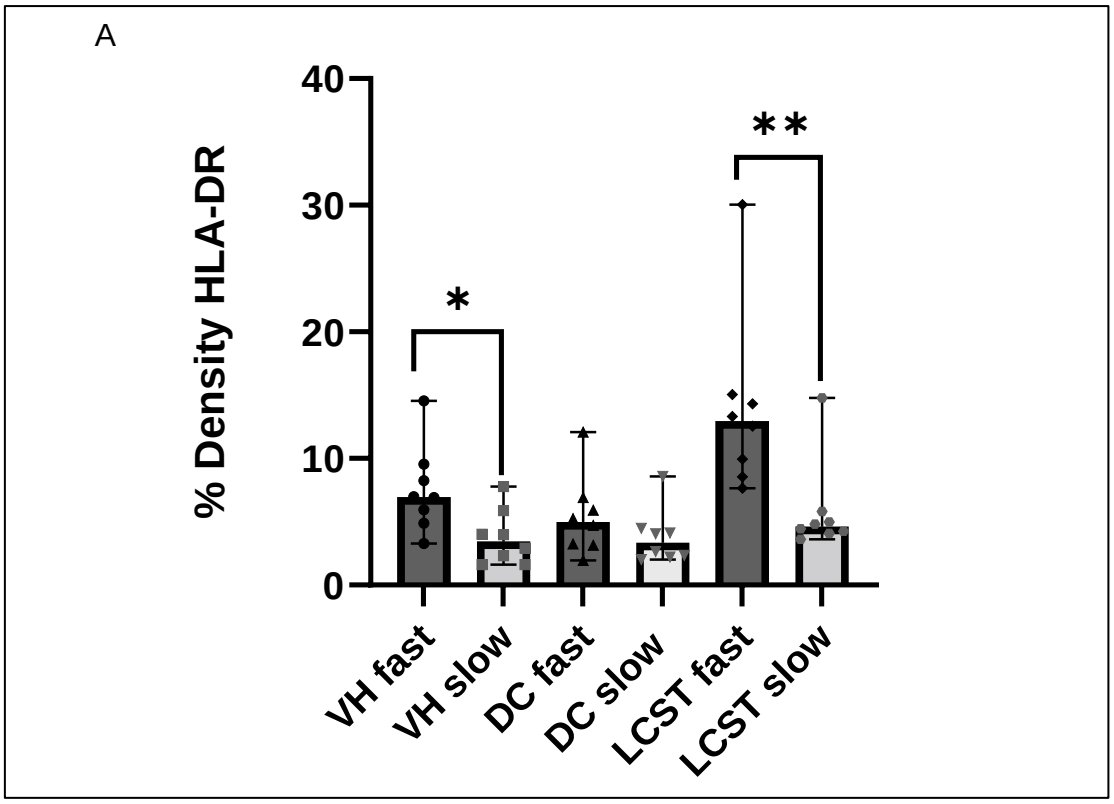

B

Spinal Cord Region	Disease Status	Median (%)	95% Confidence Intervals (Lower, Upper)	Mann-Whitney U	P Value
Ventral Horn	Control	4.351	3.203, 7.822	111	0.181
	sMND	5.898	4.73, 9.088		
Dorsal Column	Control	4.343	3.272, 5.312	131	0.412
	sMND	4.122	3.422, 5.948		
Lateral Corticospinal Tract	Control	4.581	2.984, 9.008	59	0.003
	sMND	8.549	7.264, 14.17		

Figure 4.29 HLA-DR Staining Density is Increased in Ventral Horn and Lateral Corticospinal Tract in Fast Progressing sMND Cases.

A) In sMND cervical spinal cord, a relationship between HLA-DR staining density was found to be related to the rate of disease progression ($H(5)=23.31$, $p=0.0003$). Pairwise comparisons revealed an increase in HLA-staining density in fast progressing cases, compared to slower progressing cases in the ventral horn ($p=0.0148$) and the lateral corticospinal tract ($p=0.005$). Bars show the median value, error bars show 95% CI.

B) Table showing descriptive statistics (median % density and 95% confidence intervals), and results of the pairwise comparisons.

Note: VH= ventral horn, DC= dorsal column, LCST= lateral corticospinal tract.

4.4.4 CD163

Qualitative Analysis

In control cases, CD163 immunoreactivity was not visible at low magnification (Figure 4.30). In sMND cases, the extent of immunoreactivity visible at low magnification varied: Some cases showed very little, with only mild upregulation across the lateral corticospinal tract and in the grey matter, while other cases showed much more significant upregulation in these regions.

In control spinal cord, expression of CD163 was primarily limited to perivascular macrophages surrounding blood vessels (Figure 4.31A). A small number of compact, round, amoeboid cells, likely microglia, were also CD163 positive throughout the main tissue parenchyma. Over different regions of the spinal cord, expression of CD163 appeared relatively even.

In sMND cases, there was an upregulation in the number of cells labelled by CD163, both perivascular macrophages and parenchymal cells (Figure 4.31B). In sMND cases, CD163 positive cells were much larger and rounded compared to control.

An increase in staining density was observed in the motor regions of the spinal cord, most noticeably in the lateral cortical spinal tracts (Figures 4.32). In control cases, very few cells present within the parenchyma were expressed CD163, however in sMND cases, CD163 positive cells were densely packed into this region of white matter.

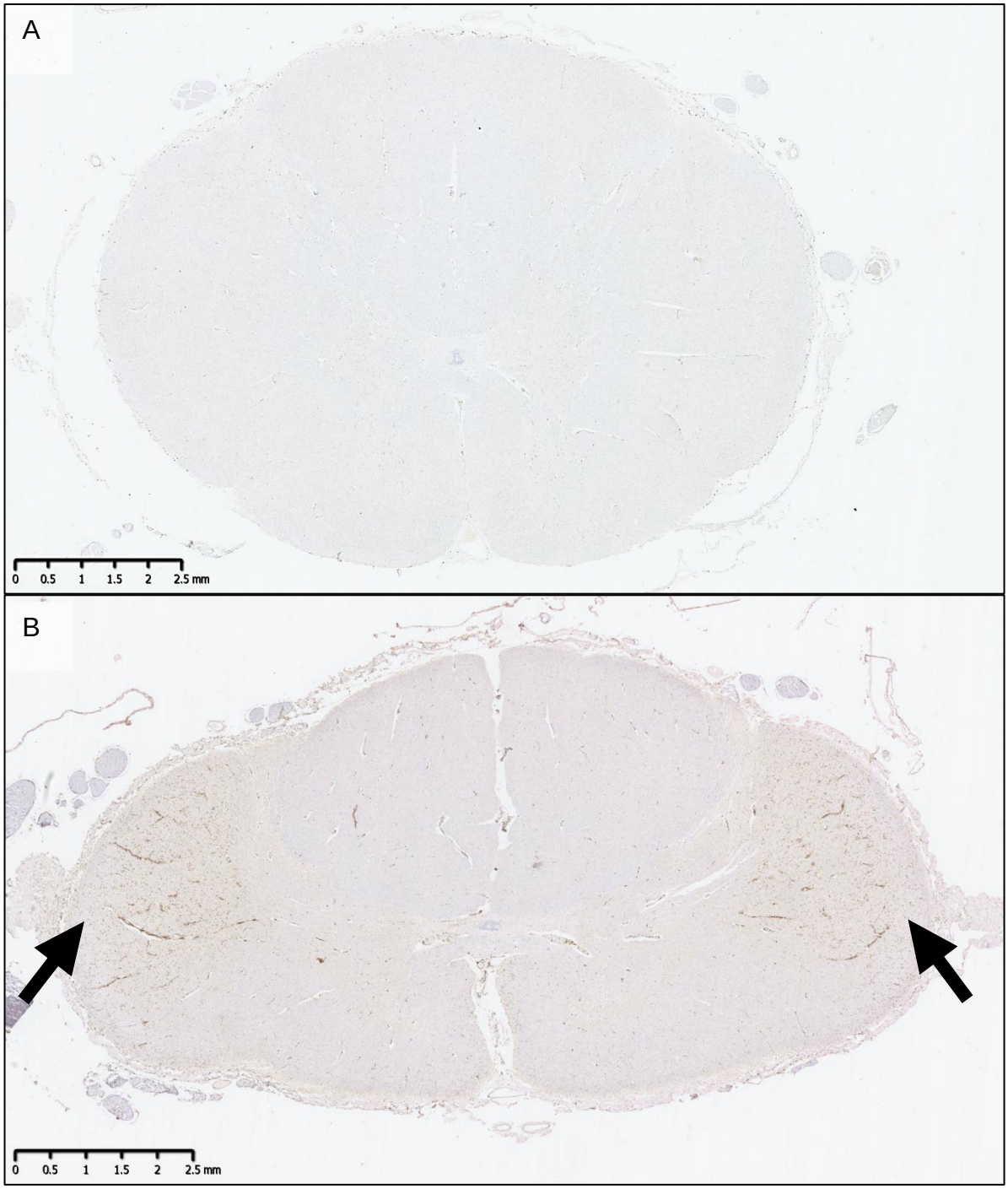

Figure 4.30 Low Power View of CD163 Expression in control and sMND Spinal Cord

*In control spinal cord (**A**) CD163 immunoreactivity was limited to perivascular macrophages and was not visible at low power. In sMND cases (**B**), CD163 expression was more widely expressed throughout the parenchyma, and was noticeably upregulated in the lateral corticospinal tracts (black arrows). In some cases, this upregulation was visible at low magnification.*

Scale bars = 2.5mm

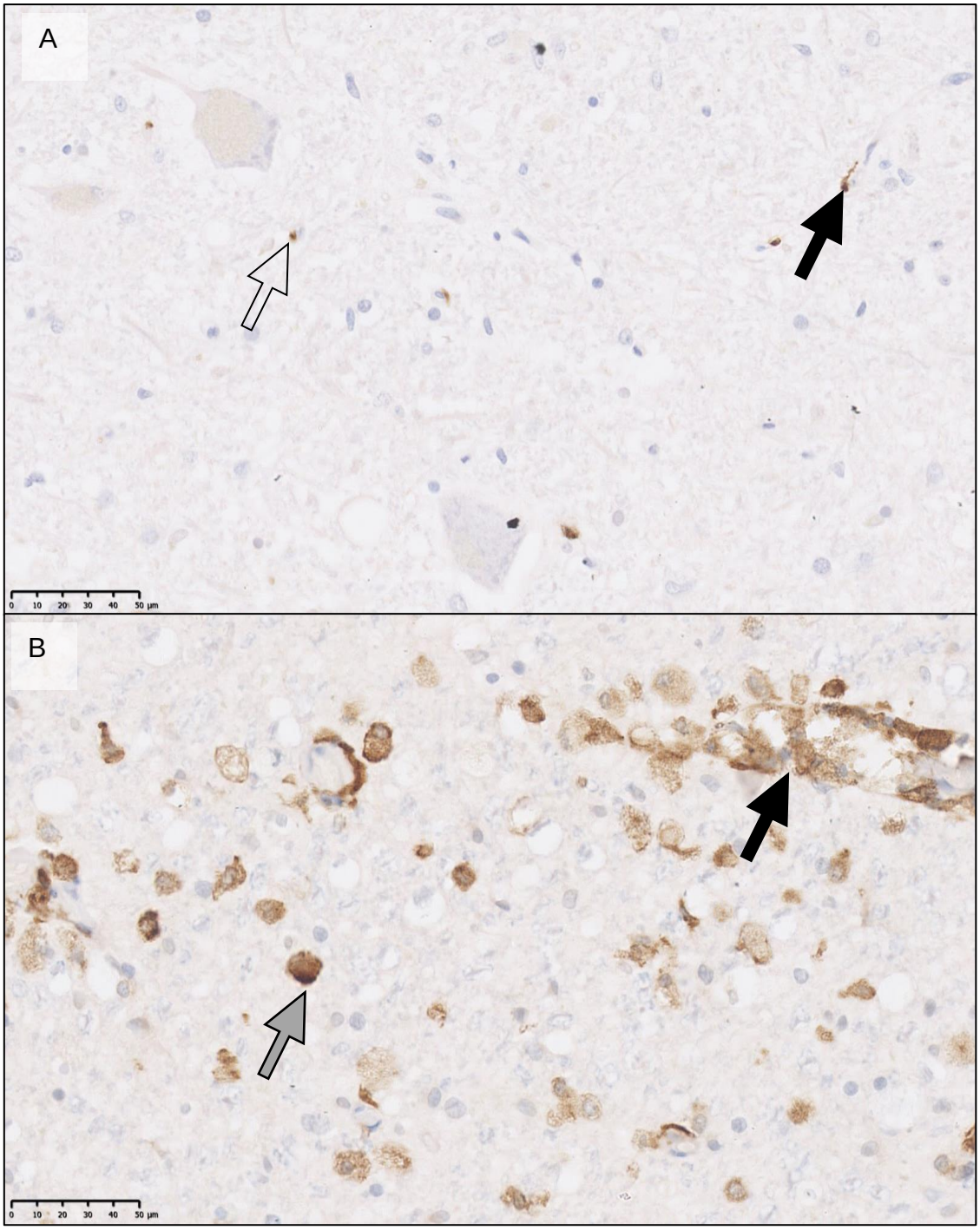

Figure 4.31 CD163 Expression Varies Between Control and sMND cases.

*In control cases (**A**), CD163 expression was mostly limited to perivascular macrophages (black arrow) but some sparse parenchymal microglia were also observed (open arrow). Expression of CD163 was relatively uniform across the cord in control cases.*

*In sMND spinal cord (**B**), CD163 expression is drastically increased. Perivascular macrophage (black arrow) expression is increased around most blood vessels. Most strikingly, expression of CD163 is hugely increased in the parenchyma, by large, rounded cells (grey arrow). These cells were likely of macrophage/monocyte lineage but could be microglia or infiltrating macrophages.*

Images taken in the ventral horn. Scale bars = 50µm.

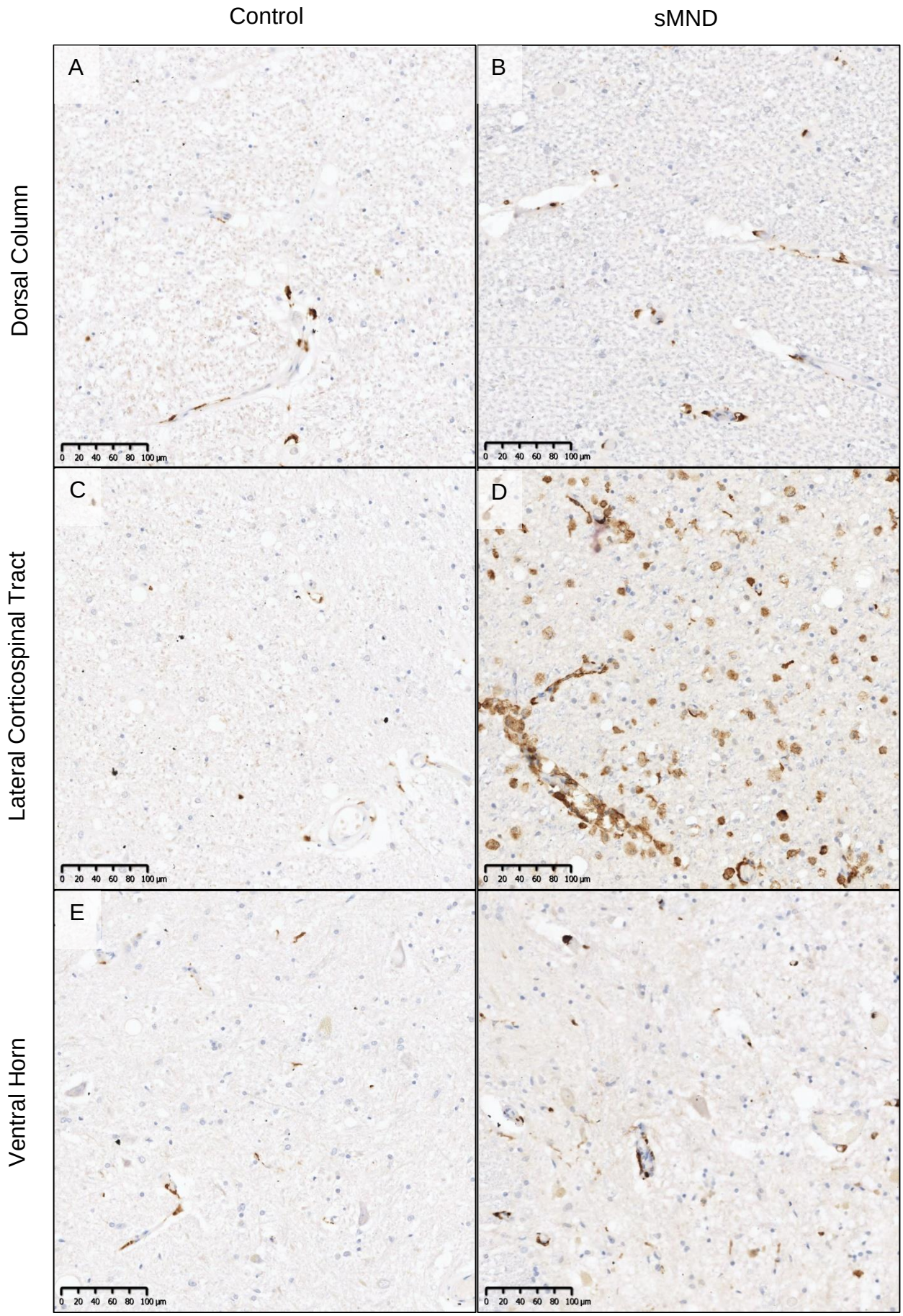
Control
sMND
Dorsal Column
Lateral Corticospinal Tract
Ventral Horn
A
B
C
D
E
0 20 40 60 80 100 µm

Figure 4.32 Comparison of CD163 immunoreactivity in control and sMND spinal cord.

*CD163 immunoreactivity in the dorsal column (**A&B**), lateral corticospinal tract (C**&D**), and ventral horn (E**&F**), in control (**A,C,E**) and sMND (**B,D,F**).*

*In control cases (**left column**), immunoreactivity was limited mostly to perivascular macrophages across the cord, with occasional positive cells in the parenchyma.*

*In sMND cases (**right column**), there was an increase in CD163 staining density primarily in the lateral corticospinal tracts [**D**], both in terms of number of parenchymal and perivascular cells. In sMND cases, CD163 positive cells become much larger had the rounded, amoeboid morphology.*

Scale bars =100µm.

Quantitative Analysis

Examination of CD163 expression data in the spinal cord revealed an outlying data point (Lateral corticospinal tract sMND, 041/2010). A box and whisker plot of all CD163 immunoreactivity data points from the spinal cord, indicated this point fell outside of the maximum range (75th percentile plus 25%) and was separated from all other data points (Figure 4.33). As such, this data point was removed from further analysis.

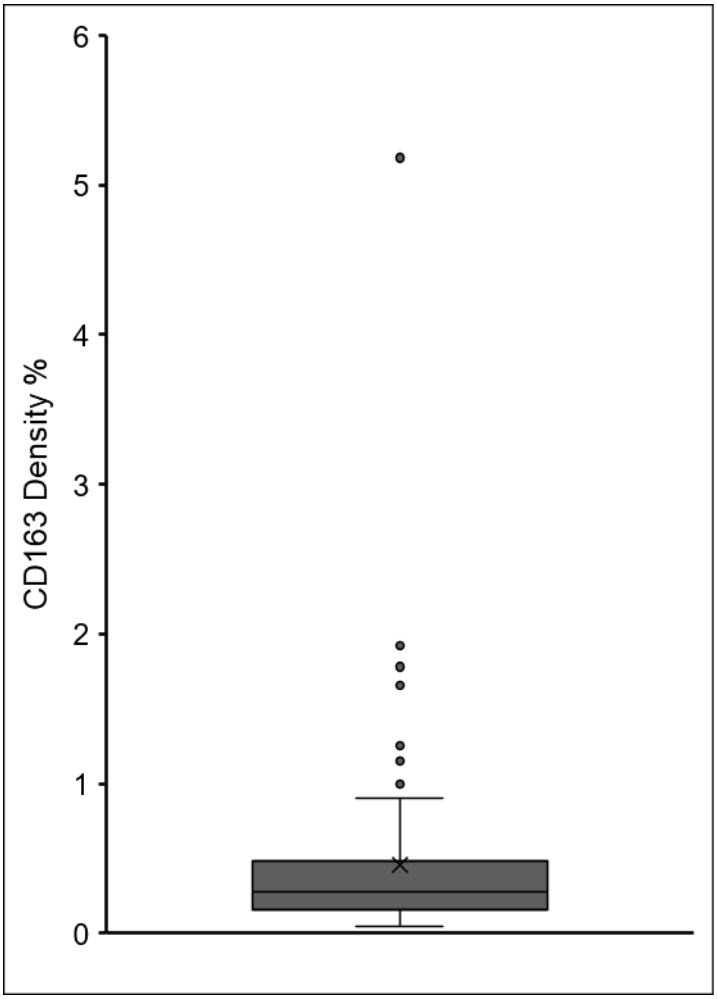

Figure 4.33 Outlier Removal from CD163 Spinal Cord Data

Box and whisker plot showing all datapoints (control and sMND) from the quantification of CD163 expression in the spinal cord. Case 041/2008 lateral cortical spinal tract (LCST, highlighted on the graph) was out of the maximum range shown by the top bar of the whisker plot, and was separate from all other data points. As such, this case was removed from further analysis.

Box plot shows the quartile 1, the median, and quartile 3. Whiskers range from the minimum (quartile 1 – 1.5x the interquartile range) to the maximum (quartile 3 +1.5x the interquartile range).

CD163 staining density was quantified in ventral horns, dorsal column and lateral corticospinal tracts using Visiopharm software. In all spinal cord regions, CD163 expression was increased in sMND cases compared to control (descriptive statistics are given in table in Figure 4.32B). A one-way Kruskal-Wallis test found there was a significant difference in CD163 staining density between disease and control cases ($H(5)=35.56$, $p<0.0001$). Pairwise comparisons were completed using one-tailed Mann-Whitney U tests (Figure 4.32A). CD163 immunoreactivity was significantly increased in sMND cases compared to control in the ventral horns ($U=14$, $p=0.0007$), and the lateral corticospinal tracts ($U=4$, $p<0.0001$). Interestingly, there was also a significant increase in CD163 expression in the dorsal column ($U=33$, $p=0.028$), which was not observed in the qualitative analysis.

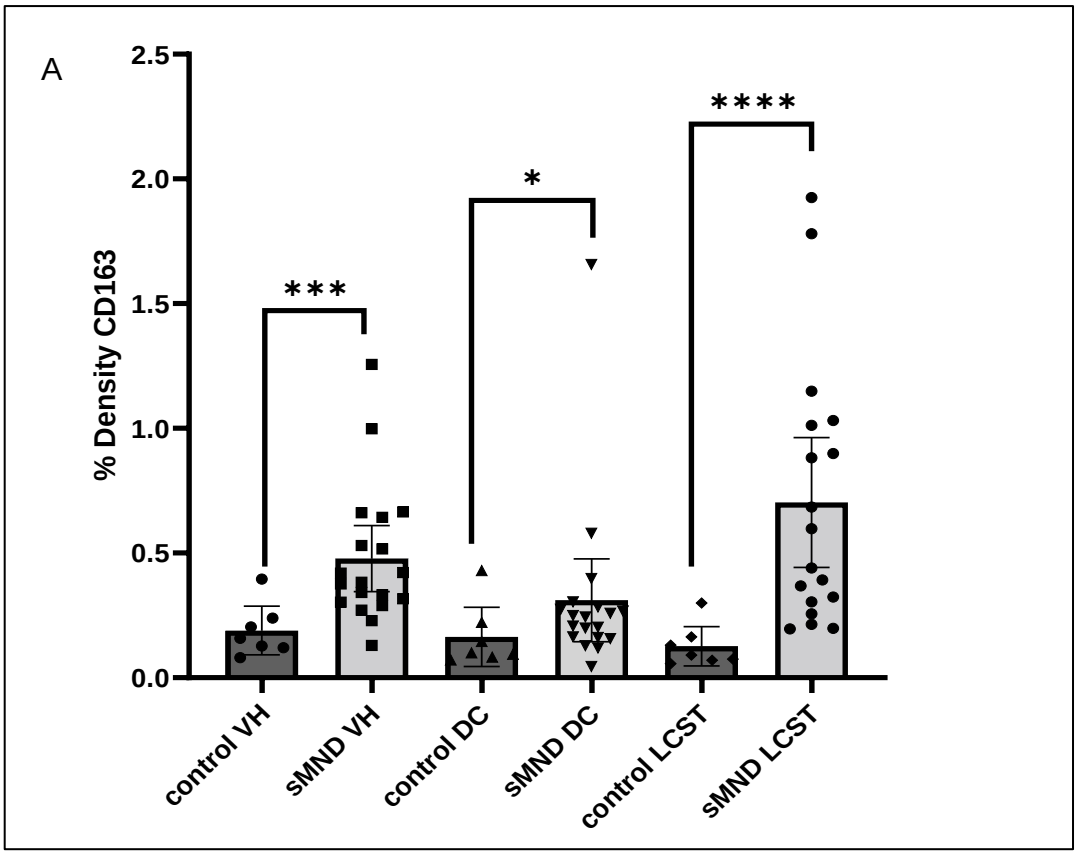

B

Spinal Cord Region	Disease Status	Median (%)	95% Confidence Intervals (Lower, Upper)	Mann-Whitney U	P Value
Ventral Horn	Control	0.158	0.092, 0.287	14	0.0007
	sMND	0.383	0.346, 0.611		
Dorsal Column	Control	0.100	0.045, 0.282	33	0.028
	sMND	0.244	0.144, 0.447		
Lateral Corticospinal Tract	Control	0.091	0.048, 0.205	4	<0.0001
	sMND	0.597	0.442, 0.963		

Figure 4.34 CD163 Staining is Increased Across the Spinal Cord in sMND.

A) CD163 expression in the spinal cord was increased in sMND cases compared to control cases (H(5)=36.66, p<0.0001). CD163 expression was increased in sMND dorsal column (U=33, p=0.028), ventral horns (U=14, p=0.0007), and most significantly in the lateral corticospinal tracts (U=4, p<0.0001). Bars show the median value, error bars show 95% CI.

B) Table showing descriptive statistics (median % density and 95% confidence intervals), and results of pairwise comparisons.

Note: VH= ventral horn, DC= dorsal column, LCST= lateral corticospinal tract.

In Section 3.5.2, increased expression of CD163 mRNA in the spinal cord was associated with longer patient survival time. To examine whether the extent of CD163 pathology present in the spinal cord was associated with the rate of disease progression, sMND cases where split into fast or slow progressing based on the median length of the survival (42 months), and CD163 staining density was compared using a Kruskal-Wallis test. A significant difference in staining density between fast and slow progressing sMND groups was observed ($H(5)=16.90$, $p=0.005$). However post-hoc analysis (one-tailed Mann-Whitney U tests), did not show any increase or decrease in CD163 staining density associated with the length of patient survival in any specific region.

4.4.5 APOE

Qualitative Analysis

APOE immunohistochemistry revealed staining of both the neuropil, and glial cells. At low magnification, the grey matter tended to show more signal than the white matter in both control and sMND cases (Figure 4.35). APOE immunoreactivity labelled branching glial cells- likely astrocytes or microglia (Figure 4.36). Furthermore, APOE immunoreactivity was also present in blood vessels, labelling the endothelial cells forming the intima (Figure 4.38). APOE also variably labelled motor neurons (Figure 4.37): Most motor neurons had a similar signal to the surrounding parenchyma. However, a subset of neurons had very intense labelling, and another very small group was completely devoid of APOE signal. The proportion of cells either highly expressing APOE or not expressing APOE did not differ based on sMND or control status and was highly variable between cases.

In sMND cases, there was a greater number of glial cells expressing APOE across the cord, but most notably in the lateral corticospinal tract and in the ventral horns (Figure 4.39). APOE immunoreactivity in the parenchyma was also greater in the ventral horn and to a lesser extent the lateral corticospinal tract in sMND cases compared to control cases.

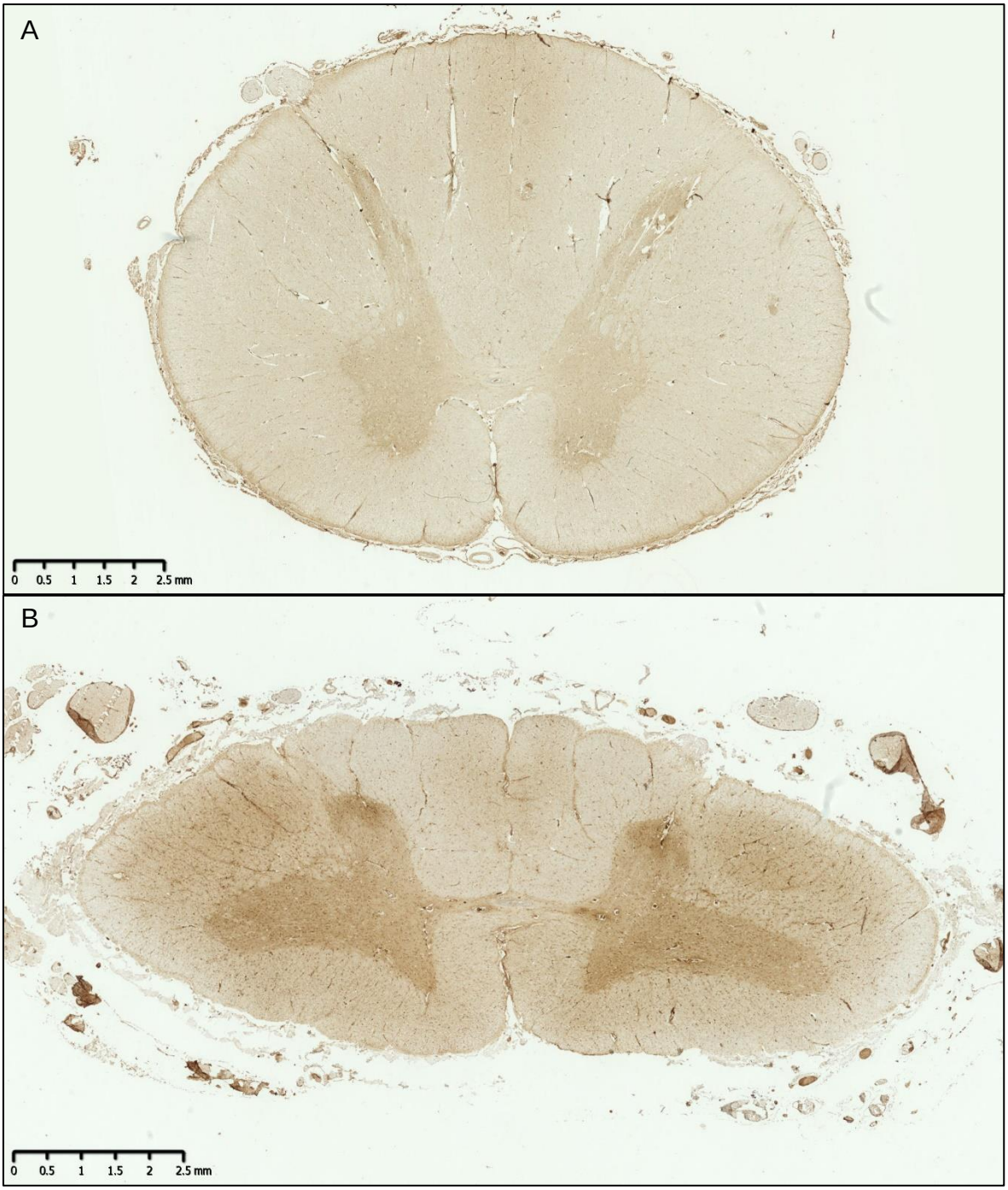

Figure 4.35 APOE Immunoreactivity in the Spinal Cord

*In control (**A**) and sMND (**B**) spinal cord, APOE immunoreactivity was present in the neuropil, in higher levels in the grey matter compared to the white matter. In sMND cases, APOE signal was increased in the motor regions, the corticospinal tract, and ventral horns.*

Scale bars= 2.5mm.

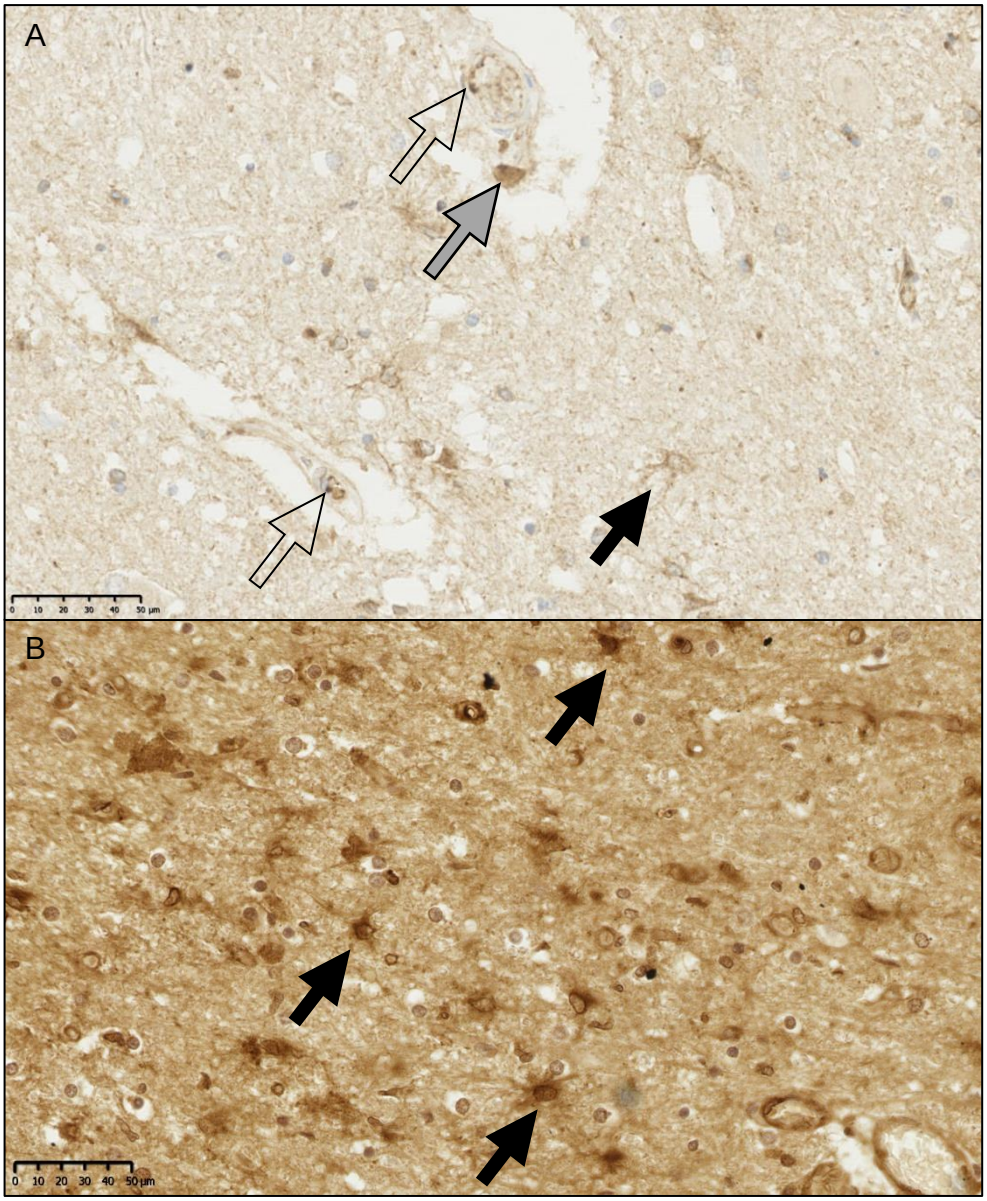

Figure 4.36 APOE Labels Glial Cells, Endothelial Cells, and Perivascular Cells

APOE immunohistochemistry labelled endothelial cells lining blood vessels (open arrows), and perivascular cells (grey arrow). Parenchymal cells may be astrocytes or microglia (black arrow). Figure A was taken from the ventral horn of a control case, Figure B the ventral horn of a sMND case.

Scale bar = 50 µm.

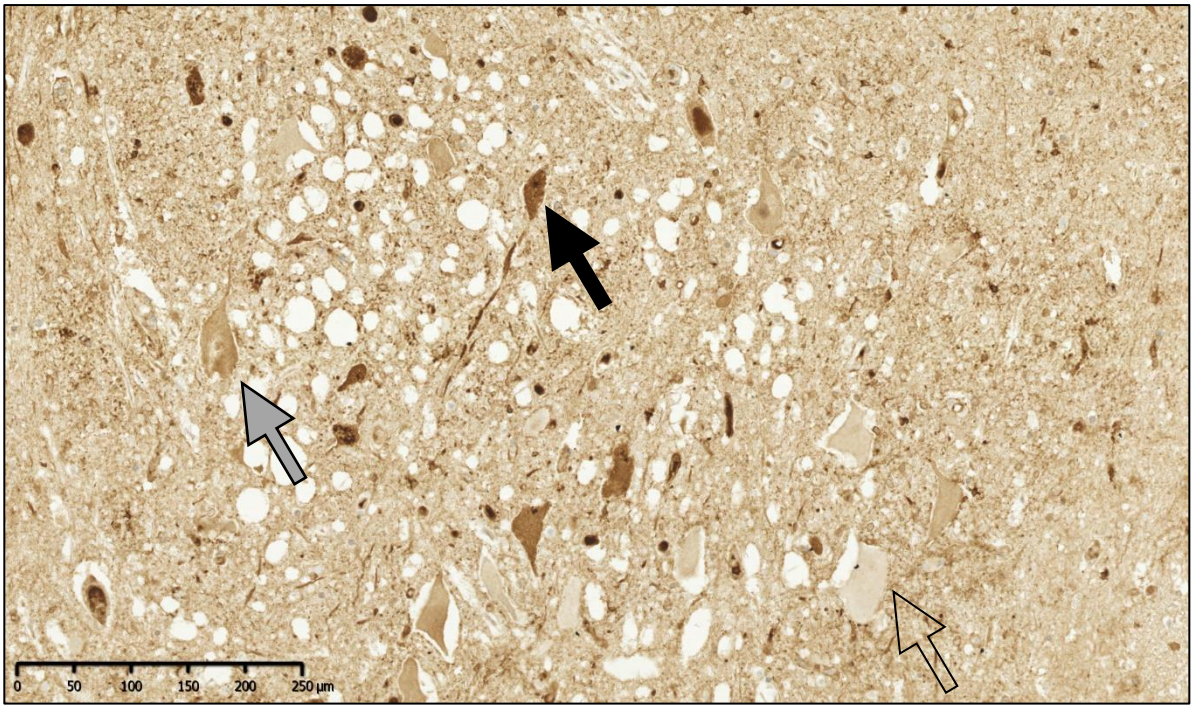

Figure 4.37 Neuronal Expression of APOE

APOE expression was found to vary between motor neurons with some having high DAB signal (black arrow), other motor neurons had similar DAB signal to the surrounding parenchyma (grey arrows) and a small number of neurons which did not show APOE immunoreactivity (open arrows). This differential APOE expression varied greatly between cases and was not associated with MND/control status.

Image of ventral horn. Scale bars represent 100µm.

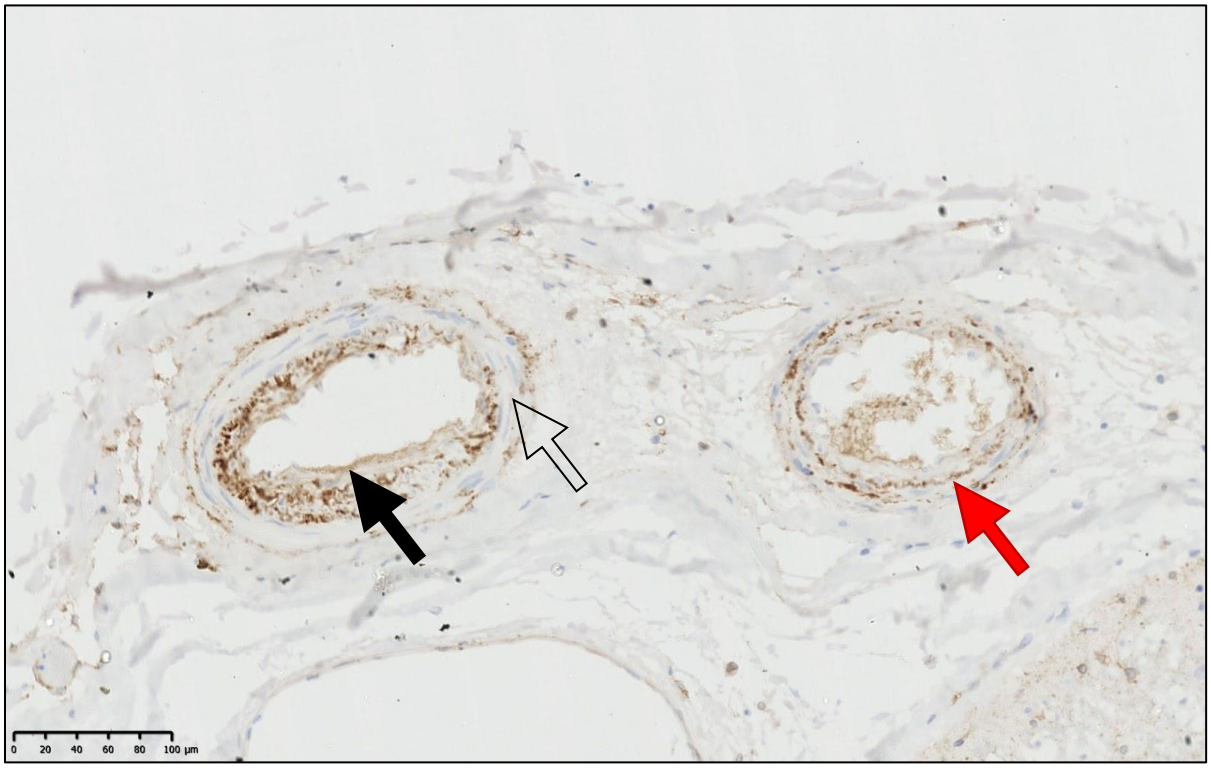

Figure 4.38 APOE Labels Blood Vessels

APOE was found to label different regions of blood vessels, including endothelial cells (black arrow) and the elastic laminae (red arrow). The smooth muscle surrounding the tunica media was free from staining (open arrow).

Scale bar= 100 µm.

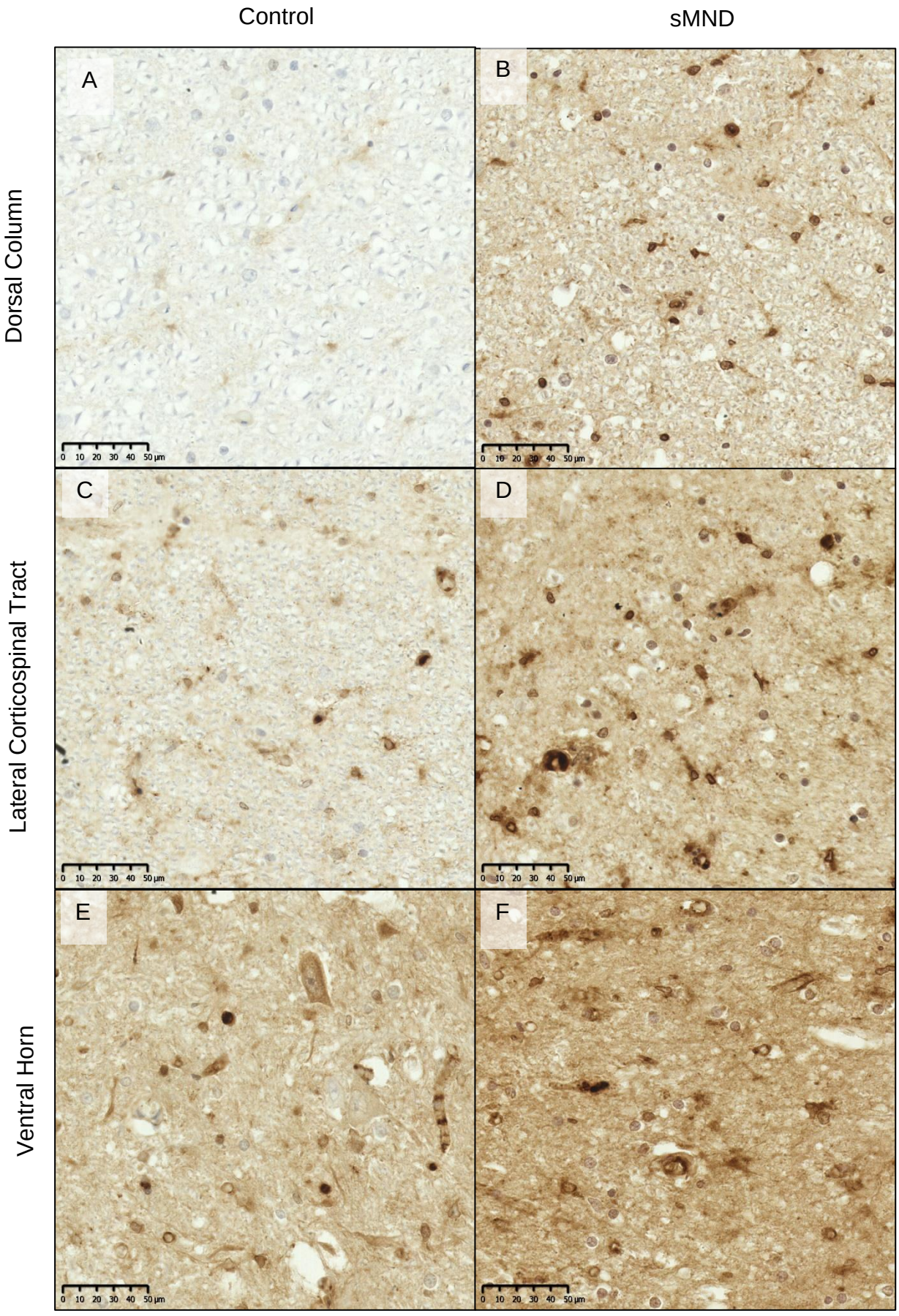
Control
sMND
Dorsal Column
Lateral Corticospinal Tract
Ventral Horn
A
B
C
D
E
F
0 10 20 30 40 50 µm

Figure 4.39 APOE Immunoreactivity in Control and sMND Spinal Cord

*APOE immunoreactivity in the dorsal column (**A&B**), lateral corticospinal tract (**C&D**), and ventral horn (**E&F**), in control (**A,C,E**) and sMND (**B,D,F**).*

*In control cases (**left column)** APOE labelled glial cells, subsets of neurons and endothelial cells surrounding blood vessels. Labelled glial cells have branched morphology like astrocytes.*

*In sMND cases (**right column**) there was un upregulation of glial staining across the cord but most reliably in the lateral corticospinal tracts (**C&D)** and in the ventral horn (**E&F)**.*

Scale bars = 50µm.

Quantitative Analysis

The percentage APOE density was compared between control and sMND cases, using the Kruskall-Wallis test, which revealed a significant difference between groups ($H(5)=27.57$, $p<0.0001$). Pairwise comparisons were completed using one-tailed Mann-Whitney U tests (Figure 4.40). Glial expression of APOE (% density) was significantly increased in sMND cases compared to control in the lateral corticospinal tract ($U=20$, $p=0.0003$), and in the ventral horn ($U=32$, $p=0.0036$). This was also observed in the qualitative analysis.

A

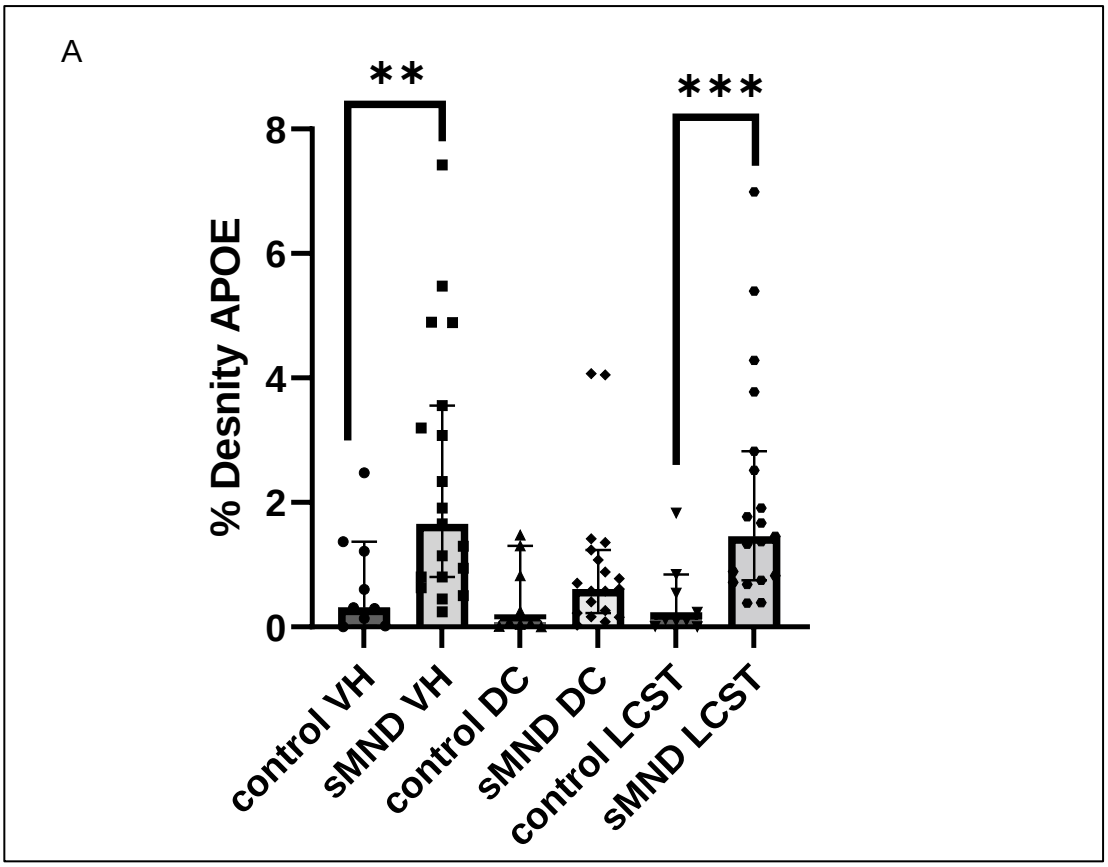

B

Spinal Cord Region	Disease Status	Median (%)	95% Confidence Intervals (Lower, Upper)	Mann-Whitney U	P Value
Ventral Horn	Control	0.3115	0.079, 1.349	32	0.0036
	sMND	1.659	1.394, 3.368		
Dorsal Column	Control	0.0838	-0.005, 0.906	51	0.0949
	sMND	0.6082	0.421, 1.543,		
Lateral Corticospinal Tract	Control	0.115	-0.0.039, 0.879	20	0.0003
	sMND	1.456	1.225, 2.979		

Figure 4.40 APOE Expression is Increased in the Lateral Corticospinal Tract in sMND.

APOE expression was significantly different between sMND and control cases ($H(5)=27.57$, $p<0.0001$). APOE immunoreactivity was significantly increased in the lateral corticospinal tract and the ventral horns. in sMND cases compared to control cases. Bars show the median value, error bars show 95% CI.

B) Table showing descriptive statistics (median % density and 95% confidence intervals), and results of pairwise comparisons.

VH= ventral horn, DC= dorsal column, LCST = lateral corticospinal tract.

To examine the effect of APOE expression on sMND patient survival, cases were split into fast or slow disease progressing groups based on median length of survival (44 months). APOE expression was compared between fast and slow progressing cases using a Kruskall-Wallis test, however no significant effect was found ($H(5)=11.01$, $p=0.051$, Table 4.1).

Table 4.1 Survival of sMND cases was not associated with APOE Expression

Spinal Cord Region	Rate of Disease Progression	Median (%)	95% Confidence Intervals (Lower, Upper)
Ventral Horn	Fast	1.975	1.144, 4.744
	Slow	1.660	0.950, 2.744
Dorsal Column	Fast	0.503	0.011, 2.252
	Slow	0.777	0.499, 1.189
Lateral Corticospinal Tract	Fast	2.095	1.029, 4.193
	Slow	1.330	0.6730, 2.397

Semi-Quantitative Analysis

Examination of the APOE cervical spinal cord slides indicated potential differences in the DAB staining present in the neuropil that were inconsistent with batch-to-batch differences in staining. The Visiopharm analysis does not measure neuropil staining therefore, semi-quantitative analysis was performed examining APOE DAB staining in the ventral horn, dorsal column, and lateral corticospinal tract.

Neuropil staining was assessed by two independent markers (BAA and MMM). Inter-rater reliability was assessed using a weighted Cohen's Kappa test. In the ventral horn, the observers score agreed in 28/33 cases (84.8%), which indicated substantial agreement between the observers (κw= 0.763, 95% confidence intervals 0.538 to 0.919). In the dorsal column, observers agreed on their scores in 30/33 cases (90.9%), this was scored as almost perfect agreement between observers by the Cohens κ test (κw= 0.85, 95% confidence intervals, 0.538 to 0.919). In the lateral corticospinal tract, observers agreed in 27/33 cases (84.8%). A weighted Cohens κ showed substantial agreement between the observers (κw= 0.83, 95% confidence intervals 0.597 to 0.953). All scores are summarised in Table 4.2.

Table 4.2 Inter-rater Reliability of APOE Immunoreactivity in Spinal Cord Neuropil

	Rater Score Agreement – All cases [/33(%)]	Rater Score Agreement – Control cases [/12 (%)]	Rater Score Agreement – sMND cases [/21 (%)]	Weighted Cohens Kappa	95% CI	Interpretation
Ventral Horn	28 (84.8%)	10 (83.3%)	18 (85.7%)	0.763	0.538 to 0.919	Substantial Agreement
Dorsal Column	30 (90.9%)	12 (100%)	18 (85.7%)	0.85	0.686 to 1	Almost Perfect Agreement
Lateral Corticospinal Tract	27 (84.8%)	11 (91.7%)	17 (81%)	0.83	0.597 to 0.953	Substantial Agreement

Neuropil staining was compared between control and sMND cases using a one-way Kruskal-Wallis test, which indicated APOE expression was significantly different between these control and sMND cases ($H(5)=21.14$, $p=0.0008$). Pairwise comparisons were completed using one-tailed Mann-Whitney U tests (Figure 4.41). APOE expression was significantly higher in sMND cases (median=3) compared to control (median=2) cases in the lateral corticospinal tract ($U=62$, $p=0.006$). No significant difference was found in the dorsal column ($U=113$, $p=0.354$) or the ventral horn ($U=109.5$, $p=0.264$).

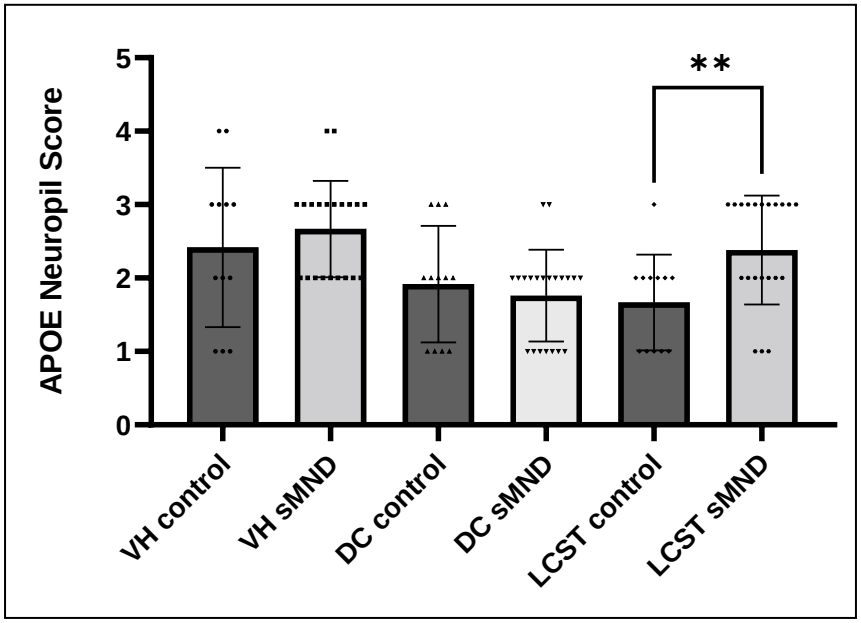

Figure 4.41 Expression of APOE in the Neuropil is Increased in the Lateral Corticospinal Tract in sMND.

Semi-quantitative analysis of APOE expression in the parenchyma across the spinal cord indicated a difference in expression between control and sMND cases ($H(5)=21.14$, $p=0.0008$). APOE expression was significantly increased in sMND cases in the lateral corticospinal tract compared to control cases. Bars show the median value, error bars show 95% confidence intervals.

VH= ventral horn, DC= dorsal column, LCST = lateral corticospinal tract.

A preliminary examination of motor neuronal expression of APOE was conducted by classifying motor neurons in the ventral horn as high or low APOE expressing for all sMND and control cases. The proportion of high to low expressing cells was expressed as a single value ($high\ expressing\ \div\ low\ expressing$). These values were compared between control and sMND cases using a two-tailed Mann-Whitney U test. No significant difference in the proportion of neurons expressing APOE was found between control (median = 0.931) and sMND (median=1.121) (Figure 4.42, $H(1)=93.50$, $p=0.816$).

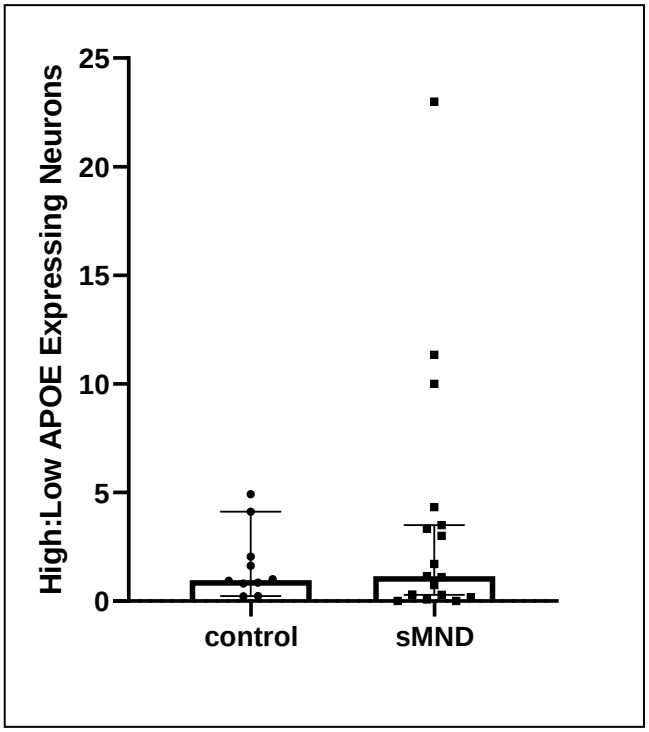

Figure 4.42 The Proportion of High and Low APOE Expressing Motor Neurons

The proportion of motor neurons in the ventral horn classified as high and low APOE expressing did not differ between control and sMND cases (H(1)=93.50, p=0.816). Bars show the median, error bars represent the 95% confidence intervals.

4.4.6 TYROBP

Qualitative Analysis

At low power, TYROBP immunohistochemistry labelled the neuropil and glial cells. There was greater expression in the grey matter compared to white in both control and sMND cases (Figure 4.43). Compared to control cases, sMND cases showed more glial staining in the corticospinal tracts, and in some cases ventral horn.

At higher power, TYROBP immunohistochemistry labelled neurons, as well as ramified and unramified glial cells which are likely microglial but could also be astrocytes (Figure 4.44). In both control and sMND spinal cord, TYROBP consistently labelled blood vessels. Endothelial cells were faintly labelled, with stronger labelling of the smooth muscle in the media of arterioles and arteries. Veins showed very little staining (Figure 4.45). As such, vascular labelling served as an internal positive control.

In control cases, the overall extent of staining varied greatly both in terms of the neuropil and the extent of neuronal staining (Figure 4.46).

In sMND cases, there was an increase of both perivascular and glial staining (Figure 4.46). Glial upregulation was particularly observed in the corticospinal tracts and the ventral horns. Glial immunoreactivity highlighted both amoeboid and activated cells. Ramified cells tended to be observed in the ventral horns and more amoeboid cells in the corticospinal tracts (Figure 4.47). Glial upregulation was especially marked in perivascular locations. This may represent an increase in TYROBP expression by perivascular macrophages or astrocyte end feet. This perivascular accentuation was not seen in controls (Figure 4.48).

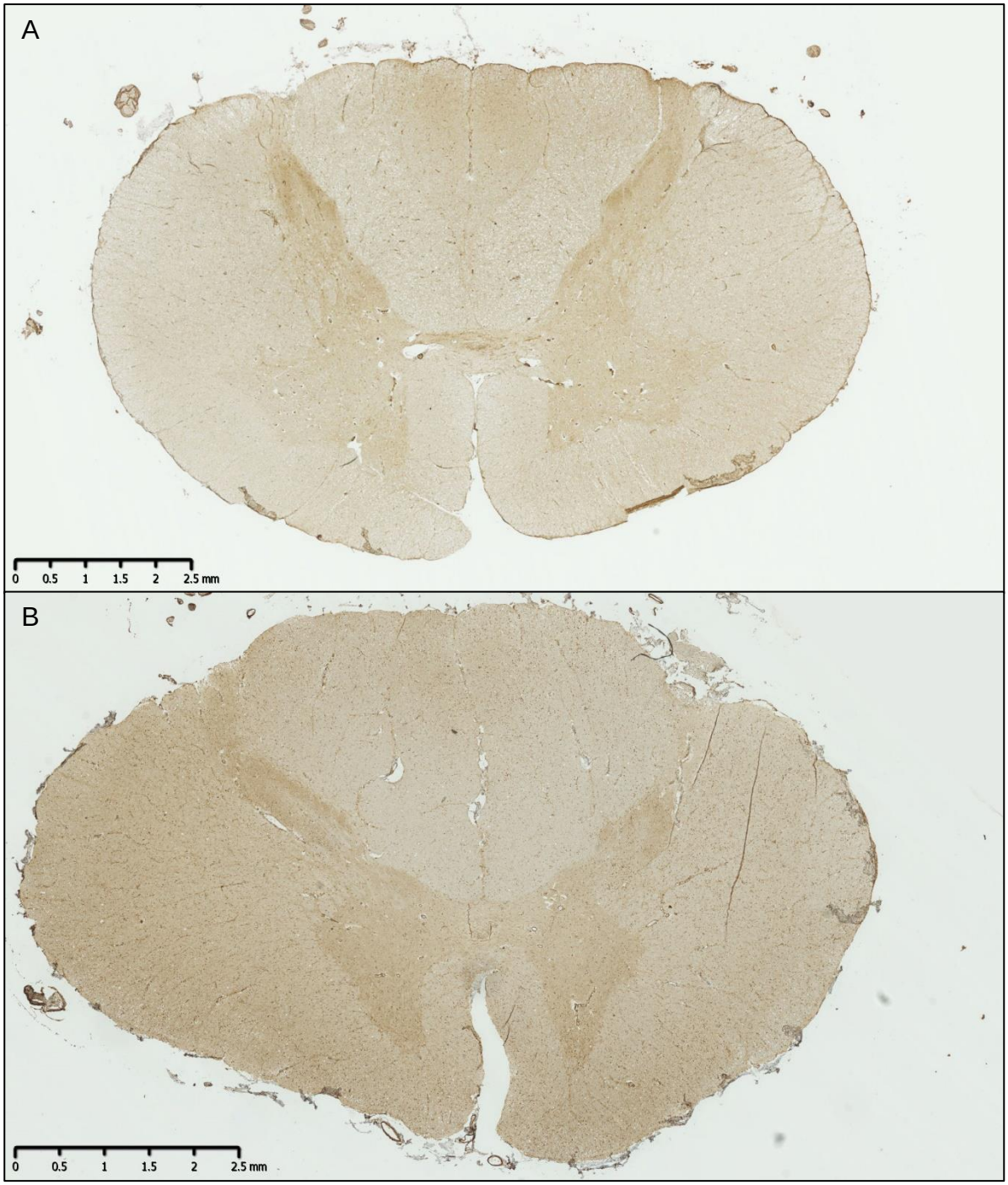

Figure 4.43 Expression of TYROBP is Greater in the Grey Matter of the Spinal Cord

*In control (**A**) and sMND (**B**) spinal cord, TYROBP immunoreactivity was present in the neuropil, in higher levels in the grey matter compared to the white matter. Glial staining in the white matter, particularly in the corticospinal tracts was increased in sMND cases.*

Scale bars= 2.5mm

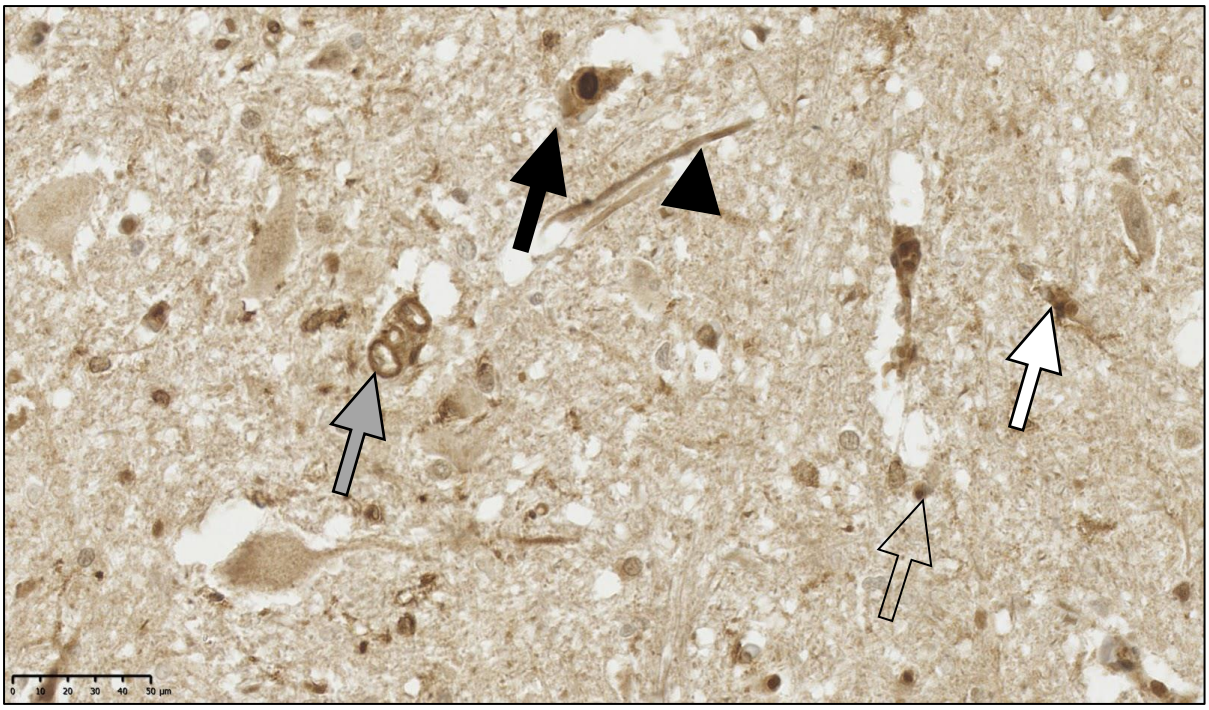

Figure 4.44 TYROBP Immunoreactivity Labelled Blood Vessels, Neurons, and Glia

TYROBP immunohistochemistry labelled motor neurons (both the soma- black arrow and some axons – black arrowhead) in the ventral horn, and blood vessels (grey arrow), as well as various ramified (white arrow) and unramified glia (open arrow). Image taken from the ventral horn. Scale bar =50µm.

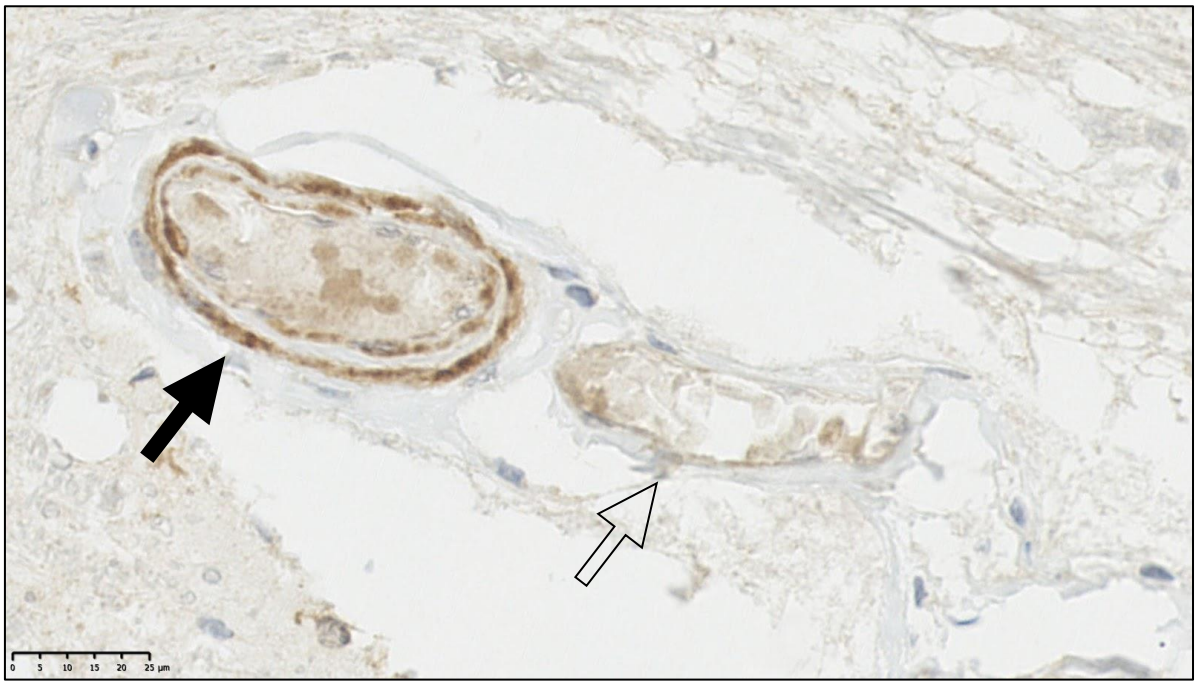

Figure 4.45 TYROBP labels Smooth Muscle and Endothelial Cells in Arterioles and Arteries

In both control and sMND, TYROBP consistently labelled blood vessels. There was faint staining of the endothelial cells, and strong labelling of the smooth muscle. As such arterioles and arteries (black arrow) were strongly labelled, while veins (open arrow) showed much less immunoreactivity. Scale bar =25µm.

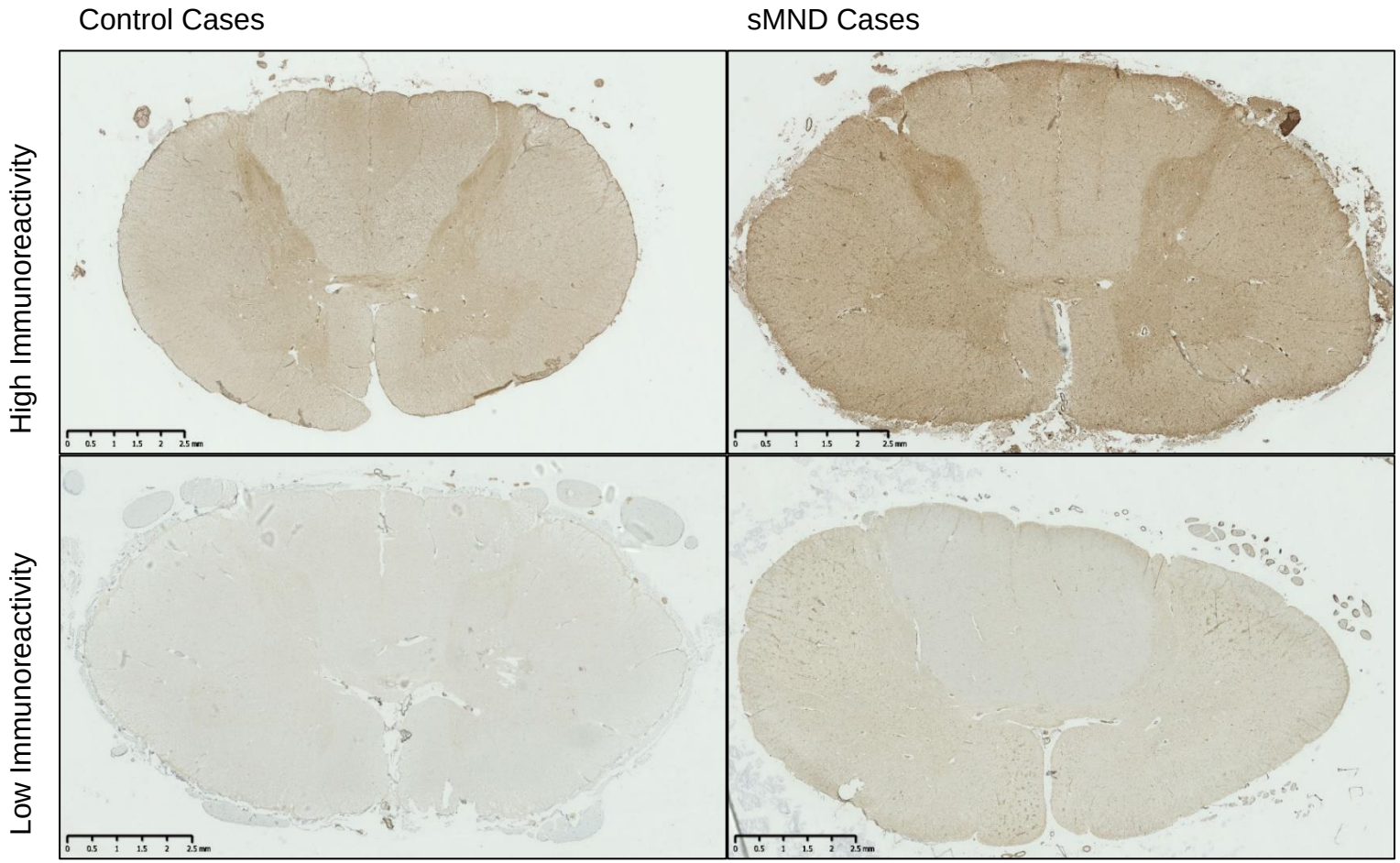

Figure 4.46 TYROBP Labelling Varied Greatly in both Control and sMND Cases

TYROBP immunoreactivity in the neuropil and glial labelling varied greatly between cases in both sMND and control cases. Vascular staining was present in all cases. Although the extent of labelling varied, sMND cases showed a strong increase in glial staining in the corticospinal tracts compared to control cases.

Scale bars = 2.5µm.

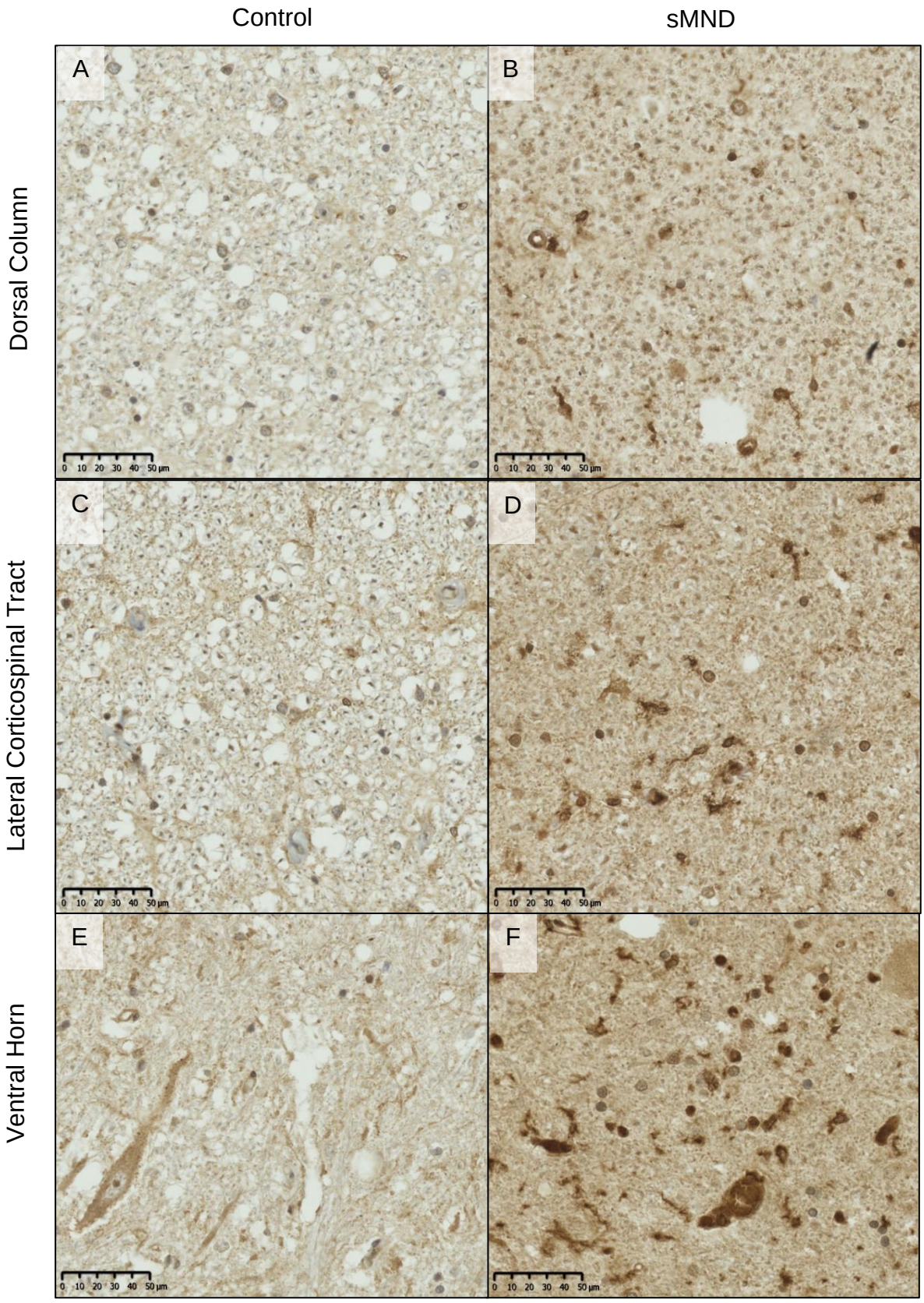
Control
sMND
Dorsal Column
Lateral Corticospinal Tract
Ventral Horn
A
B
C
D
E
F
0 10 20 30 40 50 µm

Figure 4.47 Comparison of TYROBP Immunoreactivity in Control and sMND spinal cord

*APOE immunoreactivity in the dorsal column (**A&B**), lateral corticospinal tract (**C&D**), and ventral horn (**E&F**), in control (**A,C,E**) and sMND (**B,D,F**).*

*In control cases (**left column)** APOE labelled glial cells, subsets of neurons and endothelial cells surrounding blood vessels. Labelled glial cells have branched morphology like astrocytes.*

*In sMND cases (**right column**) there was un upregulation of glial staining across the cord but most reliably in the lateral corticospinal tracts (**C&D)** and in the ventral horn (**E&F)**.*

Scale bars = 50µm.

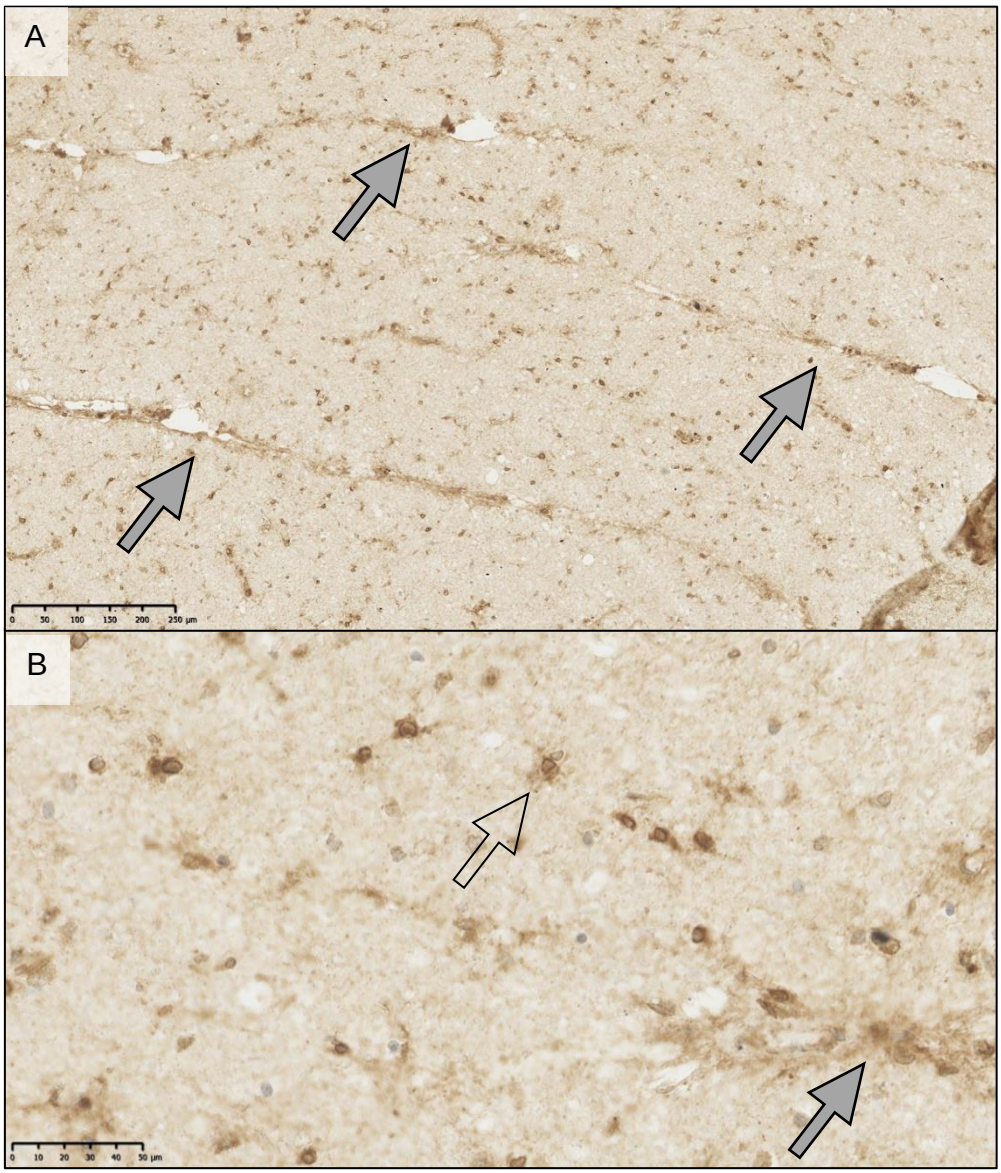

Figure 4.48 Glial Upregulation was Marked in Perivascular Locations

In sMND cases, perivascular glial cells showed an upregulation of TYROBP. This may represent an upregulation of TYROBP by perivascular macrophages or astrocyte end feet (grey arrows). Glial labelling in the parenchyma was also increased (open arrow). Figures A and B both show lateral cortical spinal tract.

Scale Bars, Figure A = 250µm, Figure B = 50 µm.

Quantitative Analysis

TYROBP immunoreactivity was compared between control and sMND cases, across the ventral horn, dorsal column and lateral corticospinal tract using a one-way Kruskal-Wallis test. This indicated a significant difference between groups ($H(5)=15.51$, $p=0.008$). Pairwise comparisons were completed using one-tailed Mann-Whitney U tests. TYROBP immunoreactivity was increased in sMND cases compared to control in the ventral horn ($U= 11$, $p=0.009$) and the lateral corticospinal tract ($U=12$, $p=0.018$). TYROBP expression did not differ in the dorsal column ($U=20$, $p=0.075$). Also of note, in both control and sMND cases, the staining density varied greatly across the spinal cord, as demonstrated in Figure 4.49.

A

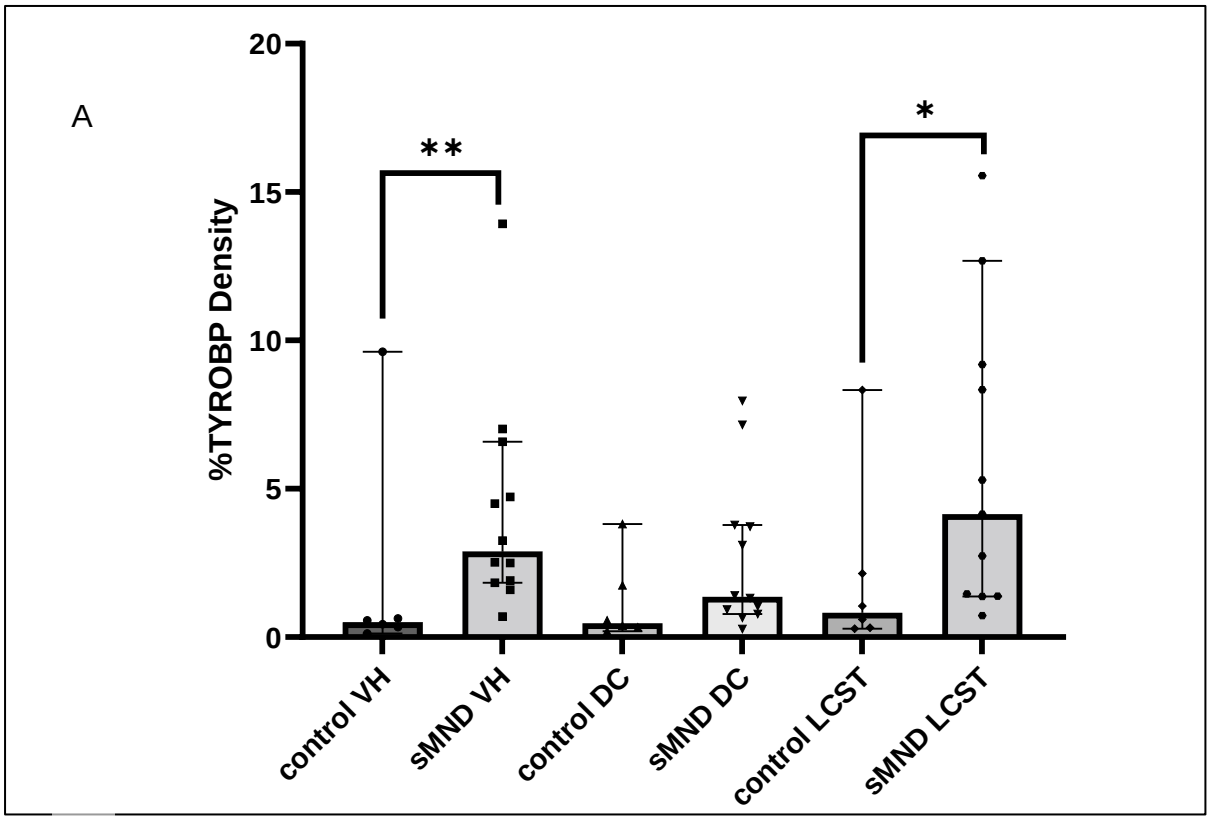

B

Spinal Cord Region	Disease Status	Median (%)	95% Confidence Intervals (Lower, Upper)	Mann-Whitney U	P Value
Ventral Horn	Control	0.496	-1.998, 5.896	11	0.009
	sMND	2.889	1.947, 6.564		
Dorsal Column	Control	0.4715	-0.306, 2.65	20	0.075
	sMND	1.364	1.038, 4.316		
Lateral Corticospinal Tract	Control	0.8215	-1.155, 5.395	12	0.018
	sMND	4.148	2.315, 9.119		

Figure 4.49 TYROBP Expression was Increased in the Ventral Horn and Lateral Corticospinal Tract in sMND

A) *TYROBP expression was significantly different between sMND and control cases (H(5)=15.51, p=0.008). TYROBP immunoreactivity was significantly increased in the lateral corticospinal tract and the ventral horns in sMND cases compared to control cases. Both sMND and control cases showed heterogeneity in the percentage of TYROBP density. Bars show the median value, error bars show 95% CI.*

B) *Table showing descriptive statistics (median % density and 95% confidence intervals), and results of pairwise comparisons.*

VH= ventral horn, DC= dorsal column, LCST = lateral corticospinal tract.

The expression of TYROBP in the ventral horn, lateral corticospinal tract and dorsal column was compared in fast and slow progressing sMND cases using a Kruskal-Wallis test, however no significant difference was observed between groups ($H(5)=1.33$, $p=0.932$, Table 4.3). MND cases were split into fast and slow progressing based on the median length of survival (44 months).

Table 4.3 TYROBP Immunoreactivity in the Spinal Cord is not Associated with sMND Patient Survival

Spinal Cord Region	Rate of Disease Progression	Median (%)	95% Confidence Intervals (Lower, Upper)
Ventral Horn	Fast	0.1013	0.322, 0.780
	Slow	0.06138	0.172, 0.846
Dorsal Column	Fast	0.04138	0.290 1.295
	Slow	0.06953	0.327, 1.306
Lateral Corticospinal Tract	Fast	0.08226	0.325, 1.142
	Slow	0.1041	0.296, 1.102

4.4.7 TREM2

Qualitative Analysis

TREM2 immunolabelling was minimal in the parenchyma of the spinal cord and showed some a slightly greater expression in the grey compared to white matter (Figure 4.50). In the spinal cord, TREM2 labelled a small number of perivascular macrophages (Figure 4.51). Motor neurons showed varying levels of TREM2 labelling within cases. Most motor neurons showed minimal immunoreactivity, but a subset showed greater staining (Figure 4.52). Artefactual staining of lipofuscin in motor neurons was also commonly observed (Figure 4.52).

Within the parenchyma, small granular staining was observed: some granules were associated with a nucleus, indicating they may be in a glial or monocyte cell. Other granules were located in the parenchyma, more densely in the white matter than the grey matter (Figure 4.53). Qualitatively, control and sMND cases showed similar patterns of TREM2 expression (Figure 4.54).

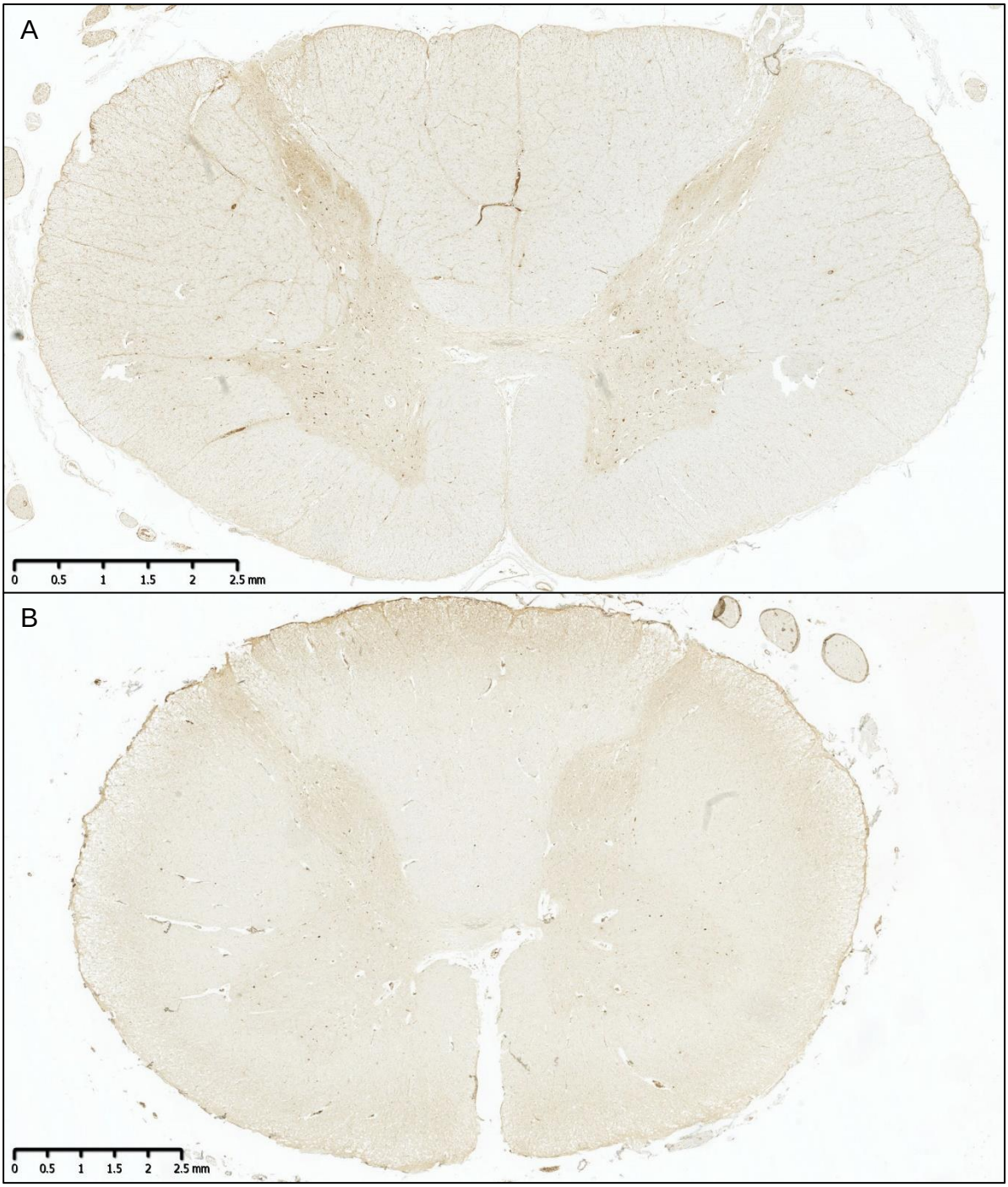

Figure 4.50 TREM2 Expression was Minimal in the Parenchyma

TREM2 immunoreactivity was minimal in the parenchyma, although some cases did show slightly greater labelling of the grey matter compared to white. At low power, there was little difference between control cases (A) and sMND cases (B). Scale bars = 2.5mm.

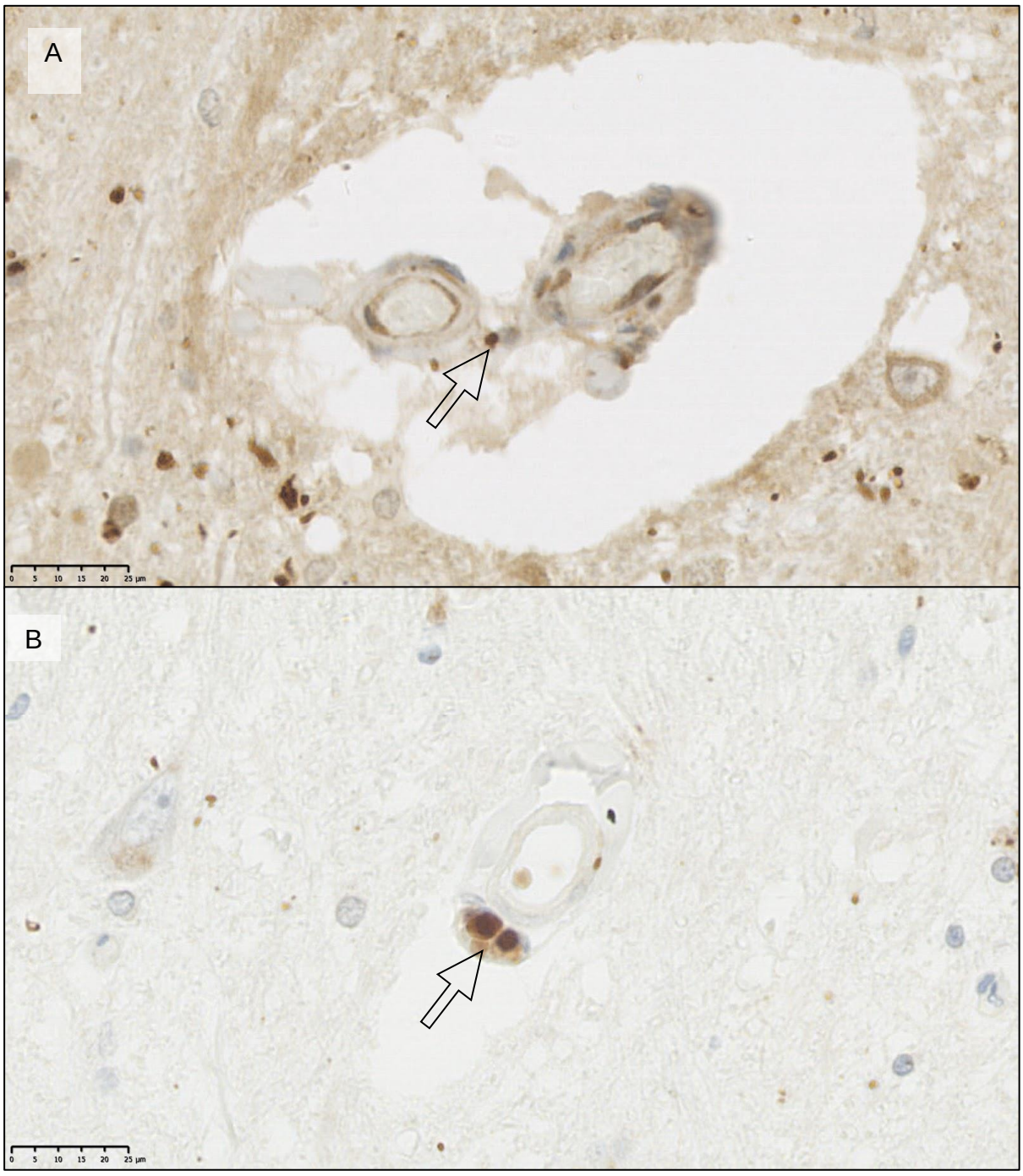

Figure 4.51 TREM2 Labelled a Subset of Perivascular Macrophages and Monocytes

TREM2 immunoreactivity labelled small, rounded cells likely monocytes (A) and perivascular macrophages (B). Positive cells were relatively rare and the number present varied between cases.

Scale bar= 25µm.

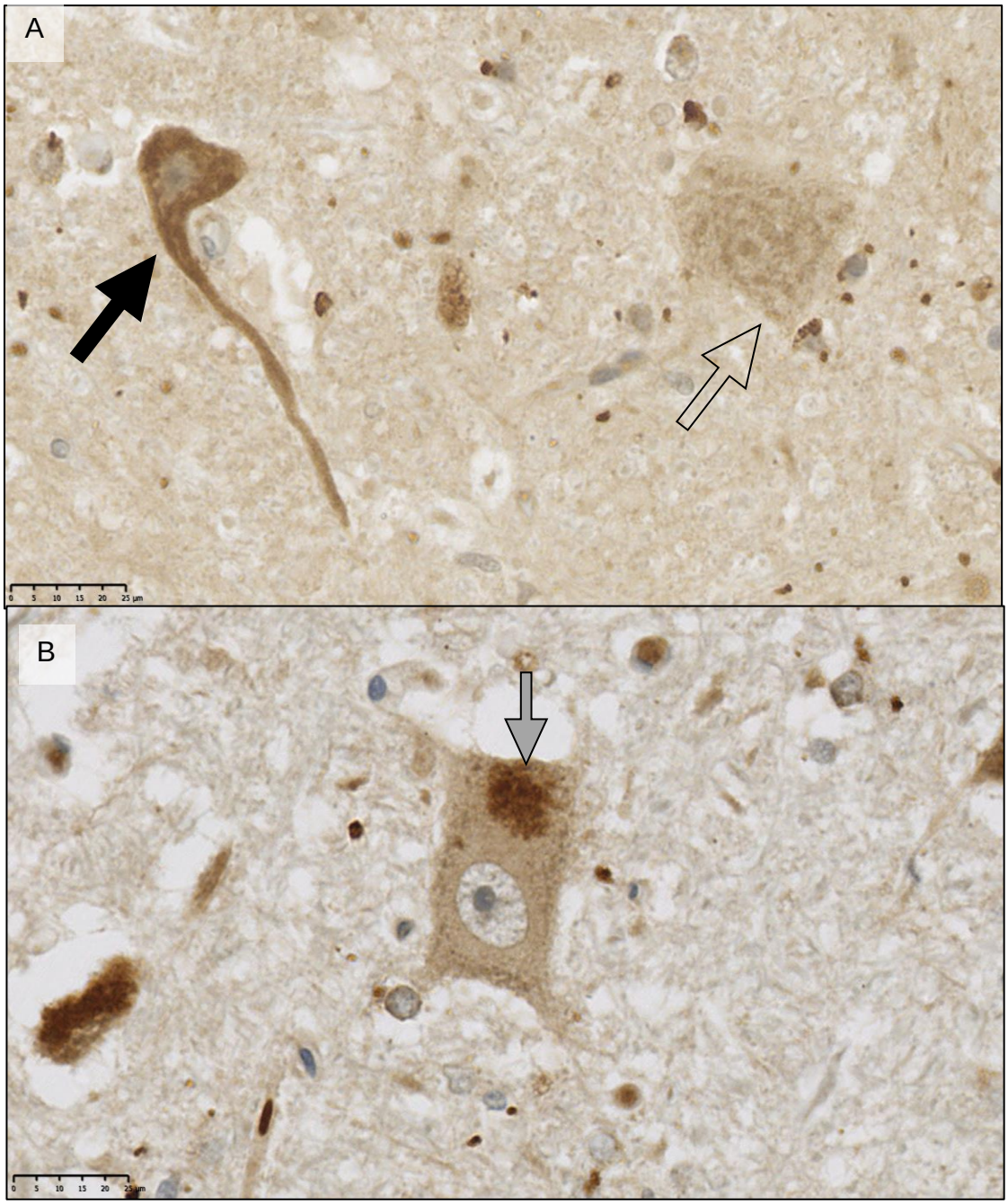

Figure 4.52 A Small Subset of Motor Neurons were TREM2 Positive

A) The majority of neurons showed minimal TREM2 signal (open arrow). However, TREM2 immunoreactivity did label a small number of motor neurons more strongly in the ventral horn. These (black arrow) were not present in all cases, and did not appear to be associated with either sMND or control cases specifically.

B) Artefactual lipofuscin reactivity (grey arrow) was also observed in motor neurons. This was present in both control and sMND cases.

Scale Bar = 25µm.

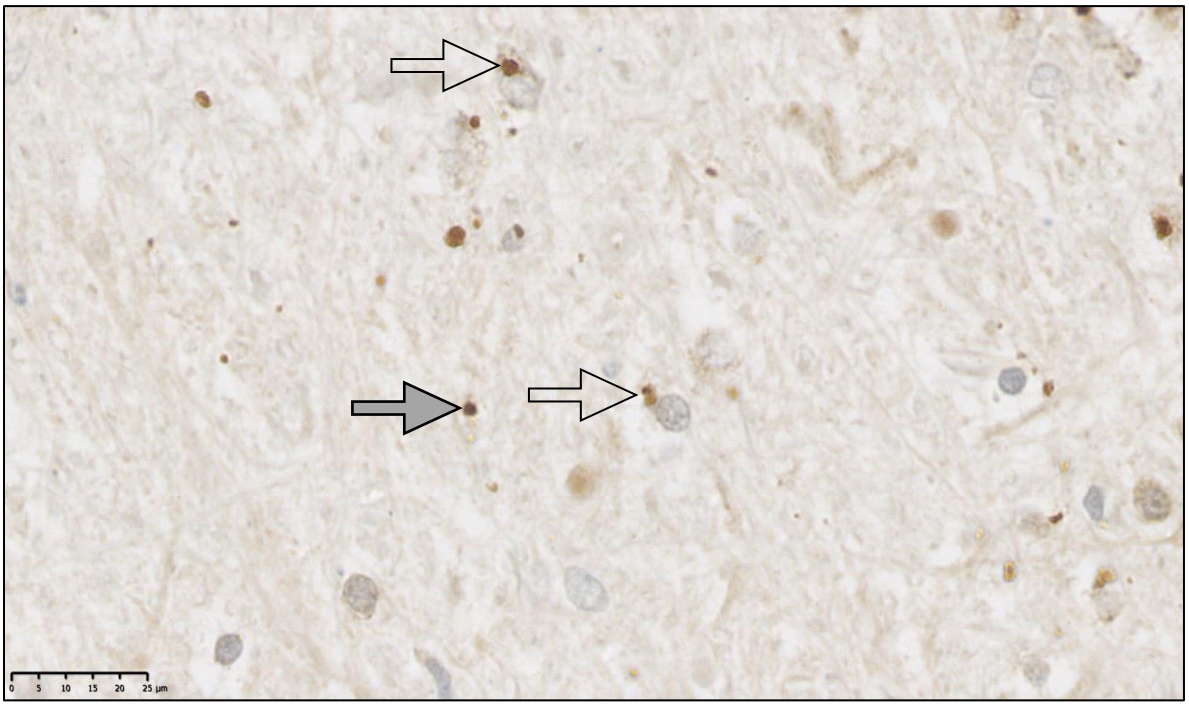

Figure 4.53 Granular TREM2 Positive Staining was Observed in the Parenchyma

In the main parenchyma, small TREM2^{+ve} granular staining was observed. Some granules were associated with a nucleus indicating these granules may be present in glial or monocyte cell (open arrow). Other granules were located in the parenchyma (grey arrow) and were observed slightly more in densely in the white matter compared to grey matter.

Scale bar = 25µm.

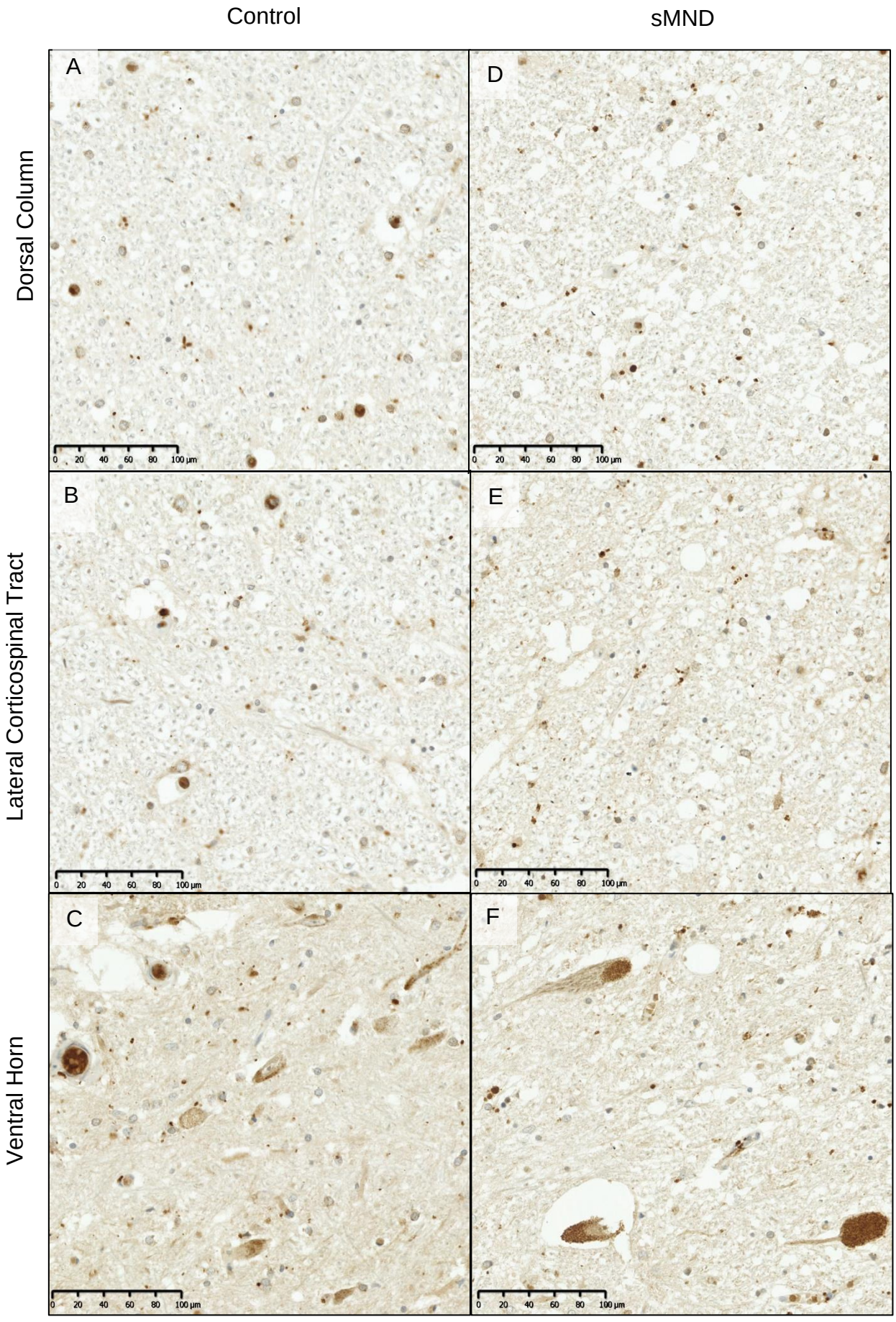
Control
sMND
Dorsal Column
Lateral Corticospinal Tract
Ventral Horn
A
B
C
D
E
F
0 20 40 60 80 100 µm

Figure 4.54 Comparison of TREM2 Immunoreactivity in sMND and Control Spinal Cord.

*TREM2 immunoreactivity in the dorsal column (**A&D**), lateral corticospinal tract (**B&E**), and ventral horn (**C&F**), in control (**A,B,C**) and sMND (**D,E,F**).*

*In the grey matter (ventral horns (**C&F**), the parenchyma tended to show slightly more immunoreactivity compared to white mater.*

Granular staining tended to be increased the in the lateral corticospinal tracts and dorsal column, compared to the ventral horn.

Between control and sMND no clear pattern of differential expression could be established in the spinal cord regions assessed.

Scale bars = 50µm.

Quantitative Analysis

TREM2 expression across the spinal cord was compared in control and sMND using a Kruskal-Wallis test, which did not find a difference between groups ($H(5)=8.449$, $p=0.133$). In the spinal cord, TREM2 immunoreactivity did not significantly differ by spinal cord region or sMND disease status (Figure 4.55).

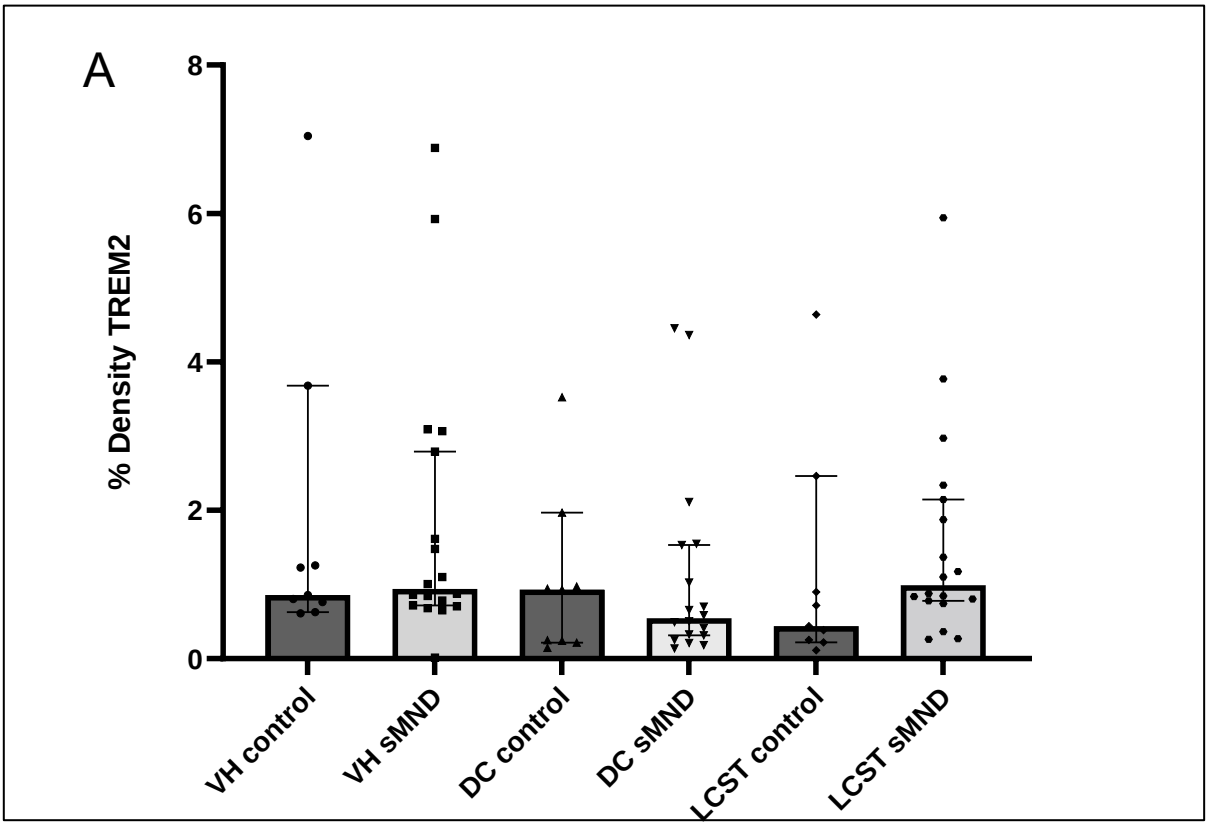

B

Spinal Cord Region	Disease Status	Median (%)	95% Confidence Intervals (Lower, Upper)
Ventral Horn	Control	0.860	0.214, 3.536
	sMND	0.942	0.903, 2.774
Dorsal Column	Control	0.930	0.171, 1.872
	sMND	0.545	0.445, 1.757
Lateral Corticospinal Tract	Control	0.439	-0.028, 2.277
	sMND	0.989	0.862, 2.301

Figure 4.55 TREM2 Immunoreactivity was not Significantly Altered in sMND Spinal Cord

***A**) TREM2 expression did not significantly different between sMND and control cases (H(5)=8.449, p=0.133). Expression of TREM2 in both control and sMND cases varied greatly. Bars show the median value, error bars show 95% confidence intervals.*

***B**) Table showing descriptive statistics (median % density and 95% confidence intervals).*

VH= ventral horn, DC= dorsal column, LCST = lateral corticospinal tract.

To examine relationship between the expression of TREM2 in the spinal cord and the rate of disease progression, sMND cases were split in fast and slow progressing sMND, based on the median length of disease duration (44 months). TREM2 expression was compared between fast and slow progressing sMND in the ventral horn, dorsal column and lateral corticospinal tract using a one-way Kruskal-Wallis test. This indicated a significant difference between groups ($H(5)=15.53$, $p=0.008$). Pairwise comparisons (two-tailed Mann-Whitney U tests) revealed TREM2 expression was significantly higher in the dorsal column ($U=11$, $p=0.008$) and lateral corticospinal tract ($U=15$, $p=0.024$) of slower progressing sMND cases compared to faster progressing cases (Figure 4.56). No difference was observed in the ventral horn ($U=27$, $p=0.258$). As such increased TREM2 expression in the spinal cord is associated with increased length of survival in sMND.

A

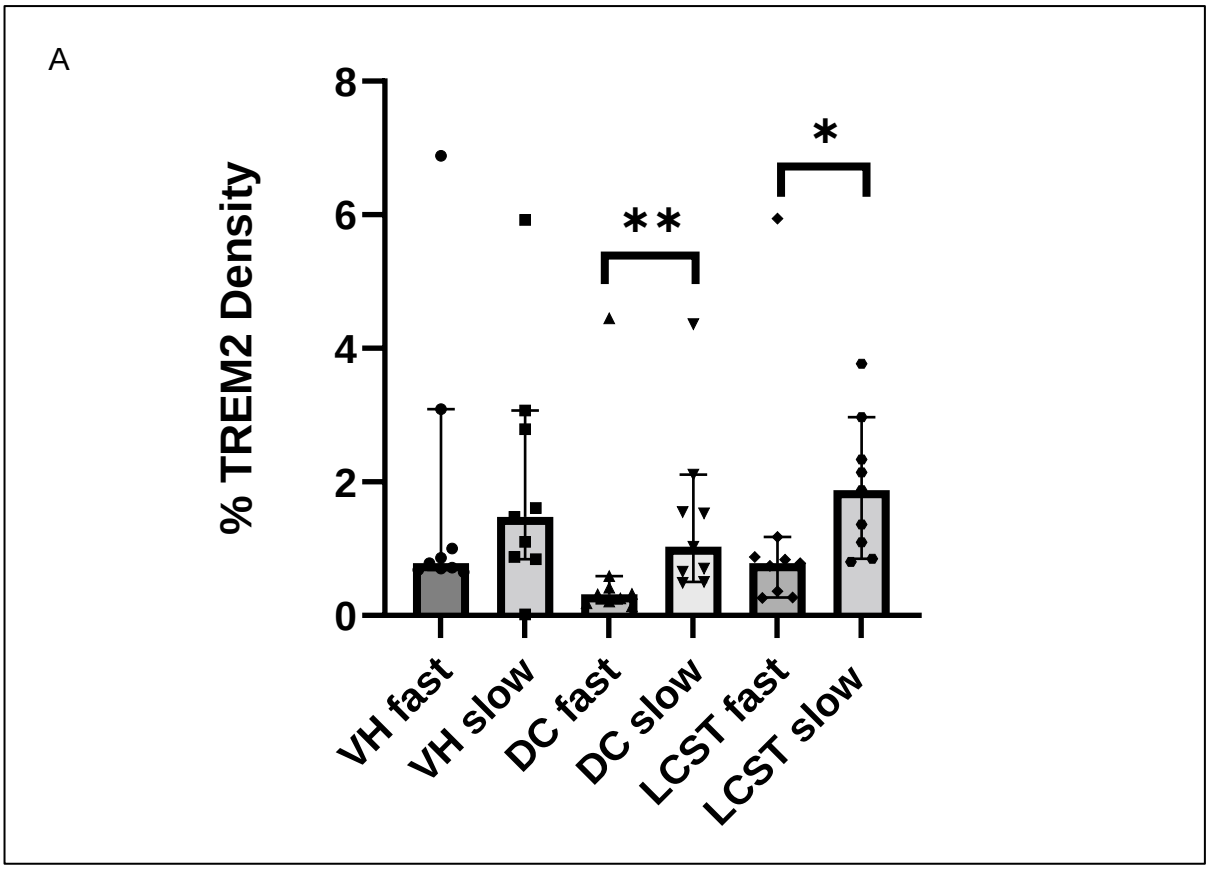

B

Spinal Cord Region	Rate of Disease Progression	Median (%)	95% Confidence Intervals (Lower, Upper)	Mann-Whitney U	p value
Ventral Horn	Fast	0.7819	0.103, 3.314	27	0.258
	Slow	1.48	0.612, 3.325		
Dorsal Column	Fast	0.3161	-0.304, 1.833	11	0.008
	Slow	1.027	0.491, 2.382		
Lateral Corticospinal Tract	Fast	0.78	-0.123, 2.623	15	0.024
	Slow	1.874	1.138, 2.687		

Figure 4.56 TREM2 Expression was Increased in Longer Surviving Patients

A) TREM2 expression in fast and slow progressing sMND cases significantly differed (H(6)=15.53, p=0.008. TREM2 expression was increased in the dorsal column and the lateral corticospinal tract of slow progressing sMND cases. Bars show the median TREM2 % density, error bars show 95% confidence intervals.

B) Table showing the median TREM2 density, 95% confidence intervals shown in Figure A, and the results of pairwise comparisons.

VH= ventral horn, DC= dorsal column, LCST= lateral corticospinal tract.

4.5 Quantification of White Matter Pallor in the Spinal Cord in sMND

Given the propensity for these inflammatory markers to show more marked upregulation in the lateral corticospinal tract in sMND, we wished to investigate whether this correlated with the myelin pallor that is classically seen here. Myelin was visualised using luxol fast blue stain. Regions of pallor were characterised as areas of white matter which had diminished staining compared to surrounding white matter. Pallor was quantified by image analysis in the lateral corticospinal tract and the dorsal column in control and sMND spinal cord and expressed as a percentage of the total area measured.

White Matter Pallor: Qualitative Analysis

Control cases showed minimal pallor (preserved myelin) compared to sMND cases (Figure 4.57). In sMND cases, pallor of varying severity was observed in the motor regions of the white matter, particularly the corticospinal tracts, both the lateral and ventral. Interestingly, some very mild pallor, was observed in the dorsal column.

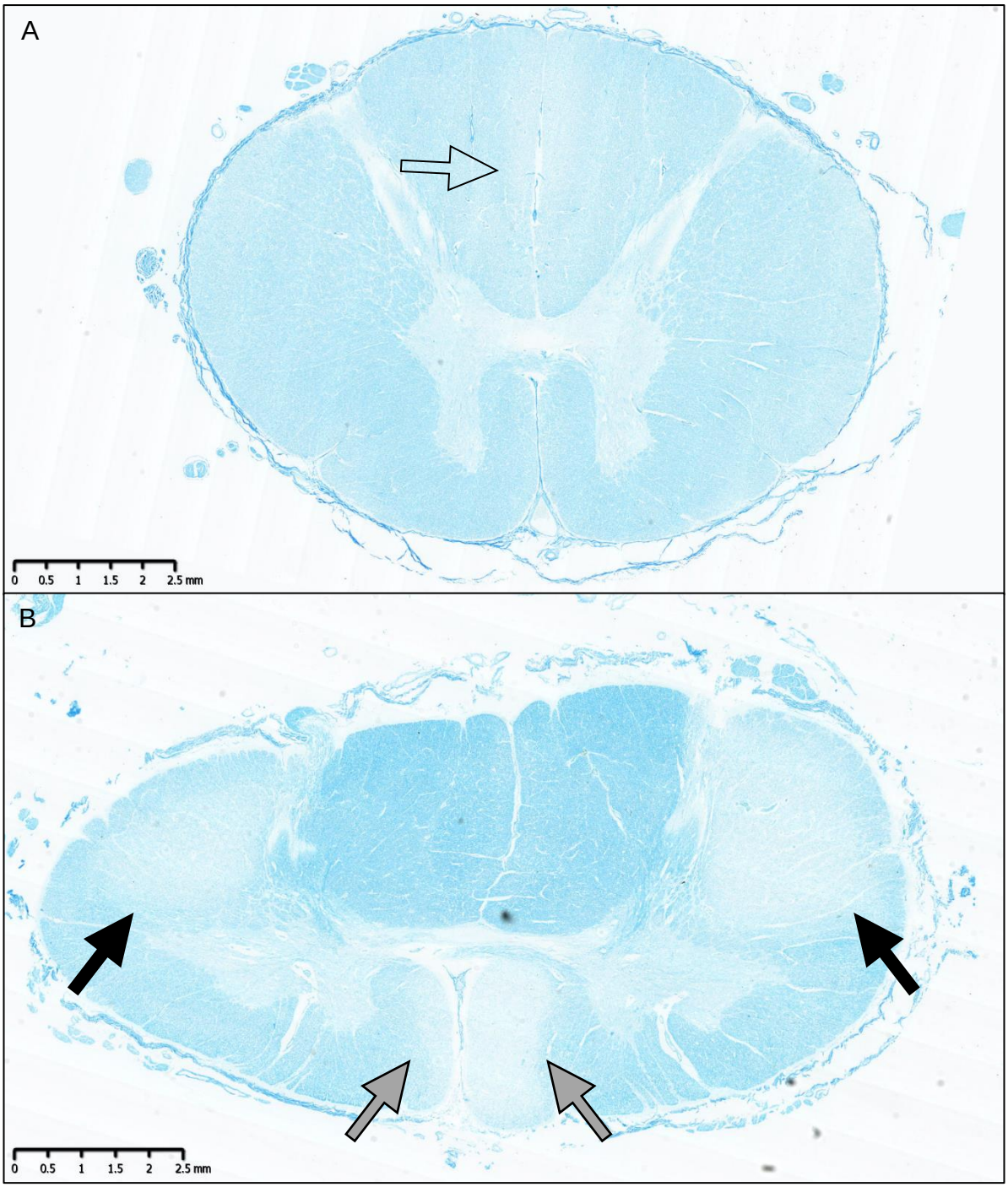

Figure 4.57 White Matter Pallor the Motor Regions of the White Matter in the Spinal Cord

***A**) Control cases showed very little evidence of pallor. For the cases that did have some evidence of low severity pallor, this tended to be in dorsal column (clear arrow).*

***B)** In sMND cases, the corticospinal tracts (both lateral [black arrows] and ventral [grey arrows]) showed evidence of more severe myelin loss. This varied in severity between cases, but the extent of pallor was increased compared to control cases. Some cases did have evidence of pallor in the dorsal column but this was equivocal to that observed in control cases.*

White Matter Pallor: Quantitative Analysis

A Kruskal-Wallis test indicated there was a significant difference between groups (spinal cord region and disease status, H(3)=8.758 p=0.032, Figure 4.58). Mann-Whitney U tests indicated pallor was significantly increased in the lateral corticospinal tract in sMND compared to control (U=54 p=0.012). No difference was observed in the dorsal column (U=109 p=0.666). Given the dorsal column did not appear to be impacted by myelin loss in sMND, only the lateral corticospinal tract was taken forward for further analysis.

A

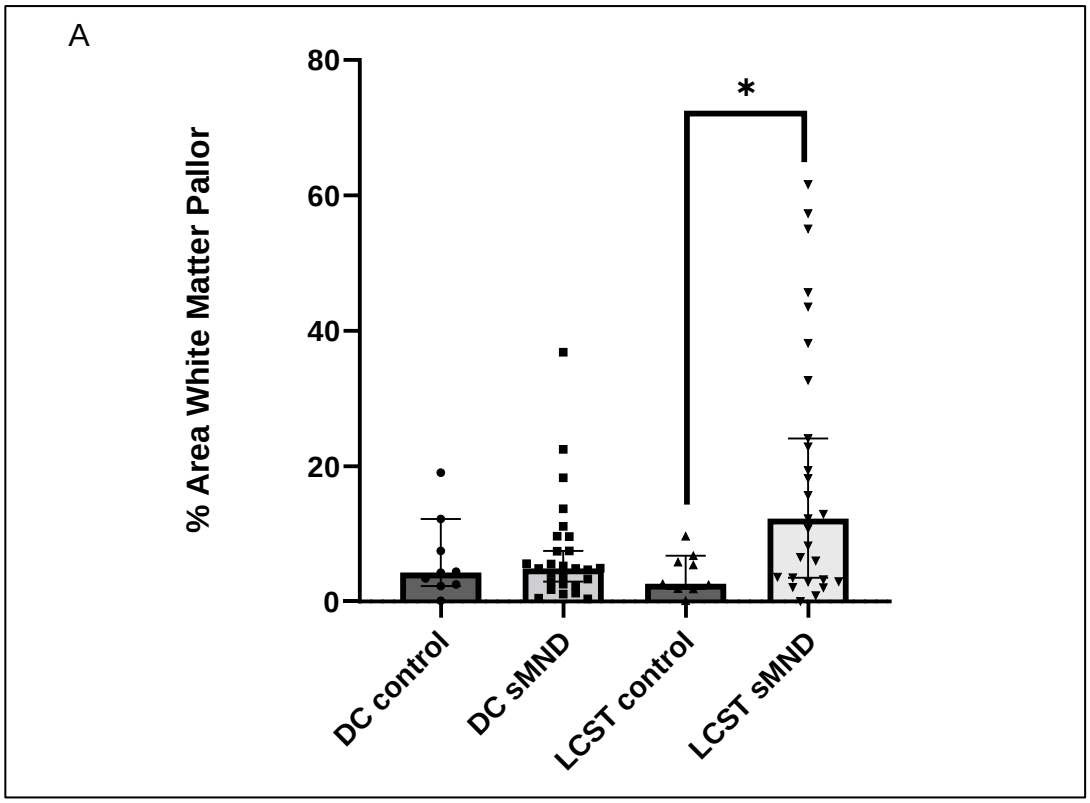

B

Spinal Cord Region	Disease Status	Median (%)	95% Confidence Intervals (Lower, Upper)	Mann-Whitney U	P Value
Dorsal Column	Control	4.259	1.617,10.77	109	0.666
	sMND	4.878	4.147, 10.41		
Lateral Corticospinal Tract	Control	2.61	1.74, 6.395	54	0.012
	sMND	12.27	11.38, 26.57		

Figure 4.58 White Matter Pallor is Observed in the Lateral Corticospinal tracts in sMND.

***A**) The area of white matter pallor was significantly increased in the lateral corticospinal tract in sMND compared control cases. The extent of white matter pallor the dorsal column did not differ between control and sMND. Bars give the median, error bars are (95% confidence intervals)*

***B**) Table showing the median, 95% confidence intervals, and the Mann-Whitney U and P values shown in Figure A.*

DC= Dorsal Column, LCST = Lateral Corticospinal Tract.

4.6 Immunohistochemistry in the Motor Cortex.

4.6.1 IBA1

Qualitative Analysis

As was observed in the spinal cord, IBA1 labels microglia and perivascular macrophages. In both sMND and control cases, the motor cortex showed great individual variation in the extent of immunoreactivity.

In control cases, microglia were ramified with fine processes and were qualitatively similar in both white and grey matter (Figure 4.59). In sMND cases, there was a greater degree of labelling. Activated microglia with thickened processes and amoeboid cells were observed in both the white and grey matter (Figure 4.60). The extent of microglial activation varied greatly between sMND cases.

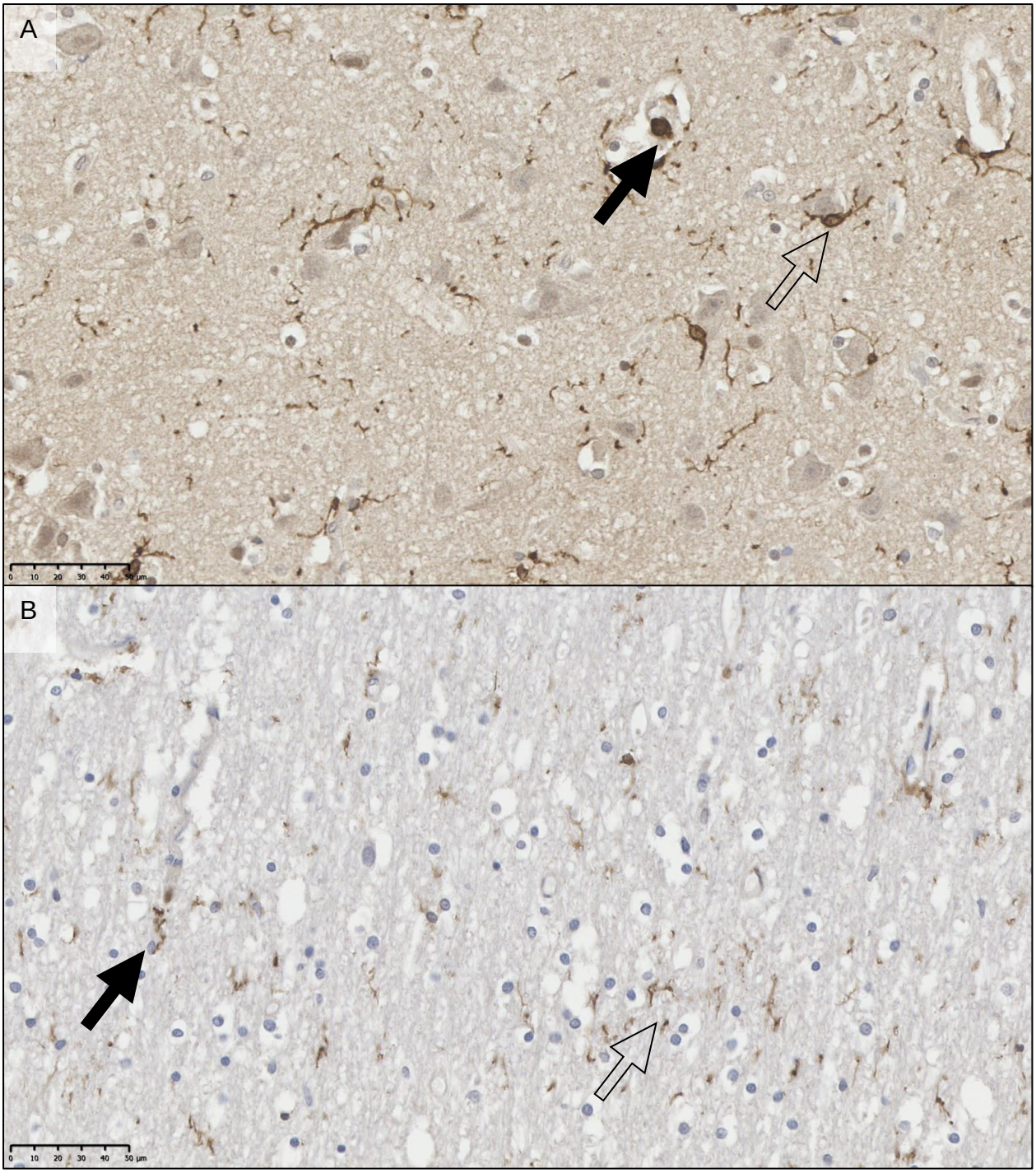

Figure 4.59 IBA1 Expression in Control Motor Cortex

*IBA1 labelled perivascular macrophages (black arrows) and microglia (open arrows). In control cases, microglia were ramified with small cell bodies and fine processes. Similar patterns of expression were observed in the grey matter (**A**) and white matter (**B**).*

Scale bar = 50µm.

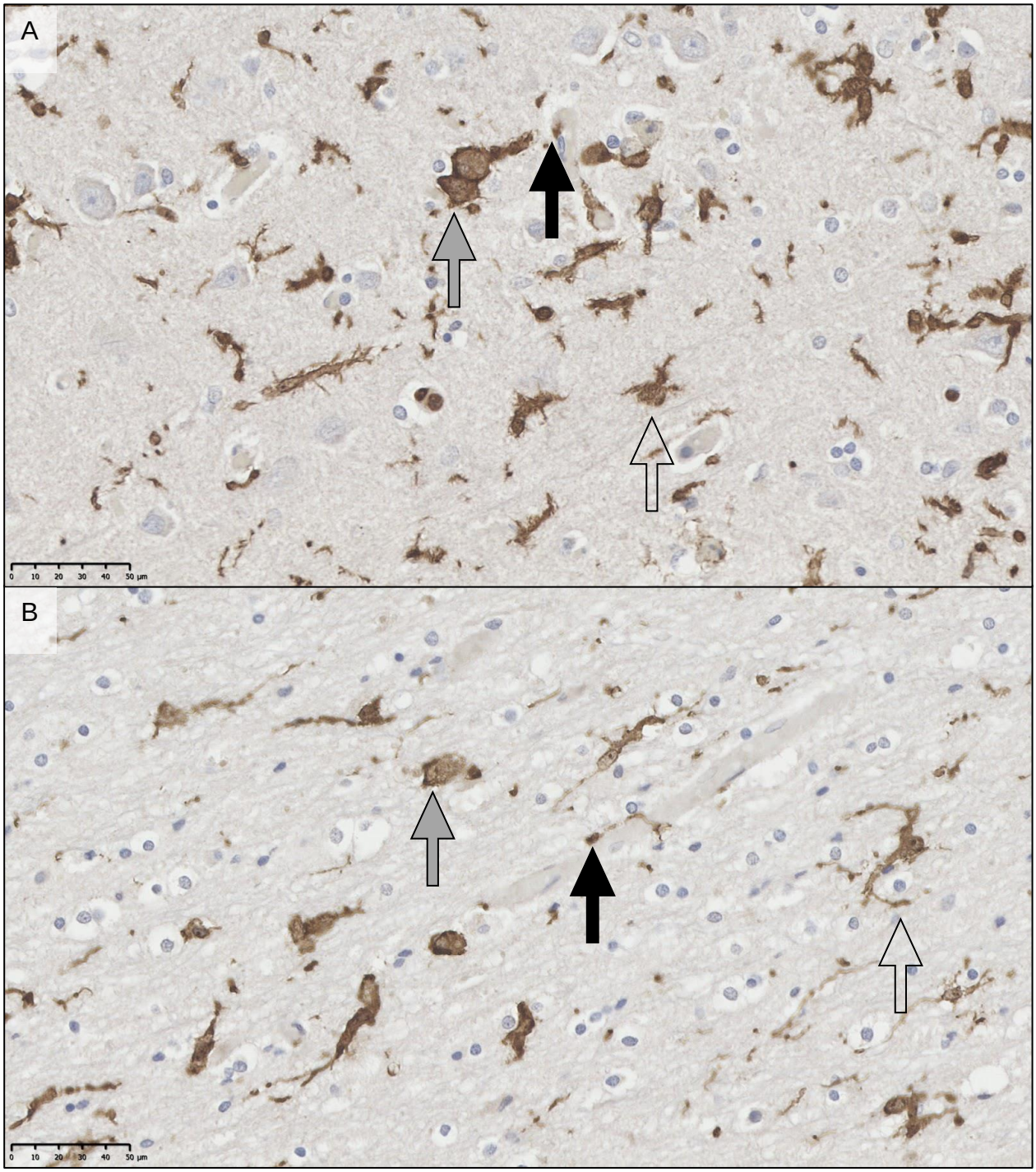

Figure 4.60 IBA1 Expression in sMND Motor Cortex

*IBA1 labelled microglia in sMND motor cortex were activated, with thicker cell bodies and swollen processes (open arrows), some microglia had also transitioned to the fully amoeboid state (grey arrows). Perivascular macrophages are labelled with black arrows. Expression was similar in grey matter (**A**) and white matter (**B**).*

Scale bar = 50µm.

Quantitative Analysis

IBA1 expression was quantified in the white and grey matter of the motor cortex using Visiopharm image analysis. IBA1 immunoreactivity was compared between sMND and control using a Kruskal Wallis test, which revealed no significant difference between groups ($H(3)=5.465$, $p=0.141$, descriptive statistics are given in Figure 4.60). IBA1 expression was highly heterogenous, in both the white and grey matter in both sMND and control cases (Figure 4.61).

A

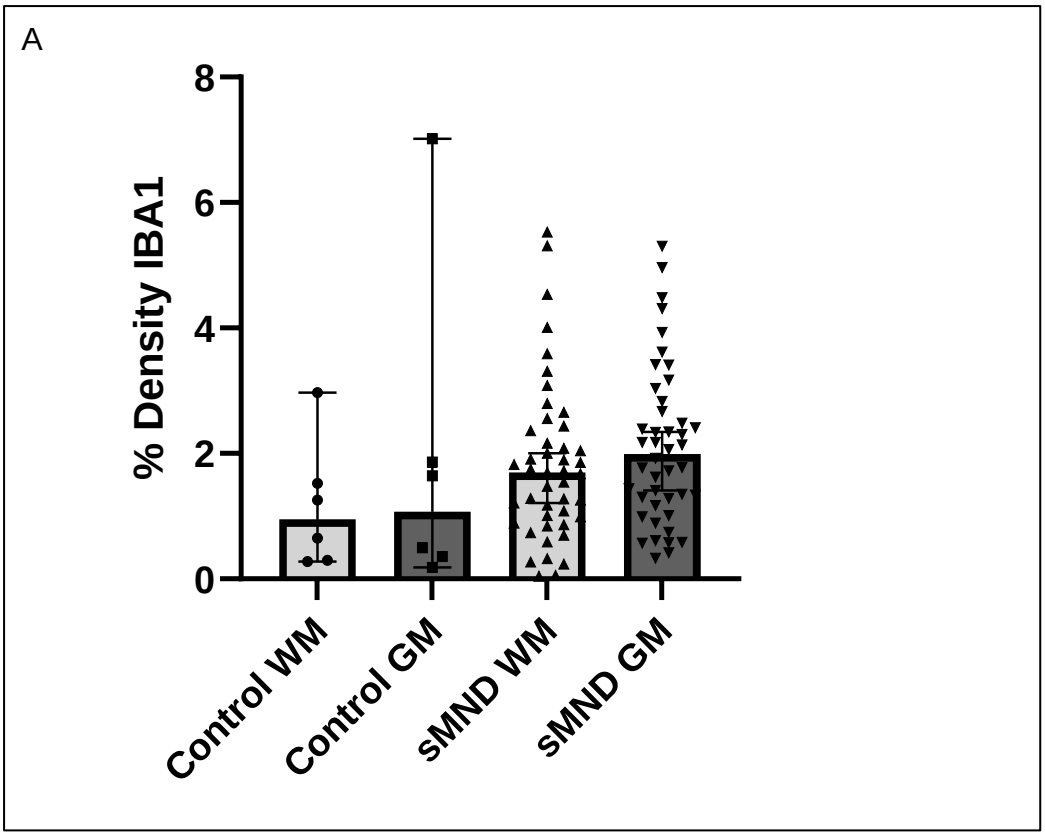

B

Motor Cortex	Disease Status	Median (% density)	95% Confidence Intervals (Lower, Upper)
White	Control	0.9523	0.090, 2.234
	sMND	1.694	1.452, 2.221
Grey	Control	1.07	-0.790, 4.644
	sMND	1.991	1.729, 2.489

Figure 4.61 IBA1 Expression was not Changed in sMND Motor Cortex

A) Expression of IBA1 was highly heterogeneous in the white and grey matter of both control and sMND cases. Bars show the median value, error bars show 95% confidence intervals

B) Table showing the median percentage area positive for IBA1 and 95% confidence intervals. IBA1 expression tended to be higher in sMND cases compared to control, but did not significantly differ in the white and grey matter (H(3)=5.465, p=0.141).

WM = White matter, GM = grey matter.

To examine the relationship between IBA1 expression in sMND and survival, cases were split into fast and slow disease progressing groups based on the median length of survival (26 months). IBA1 area density in the white and grey matter was compared between fast and slow progressing sMND in these regions using a one-way Kruskal-Wallis test. This found no significant relationship in the white or grey matter ($H[3]=1.015$, $p=0.798$, Figure 4.62).

A

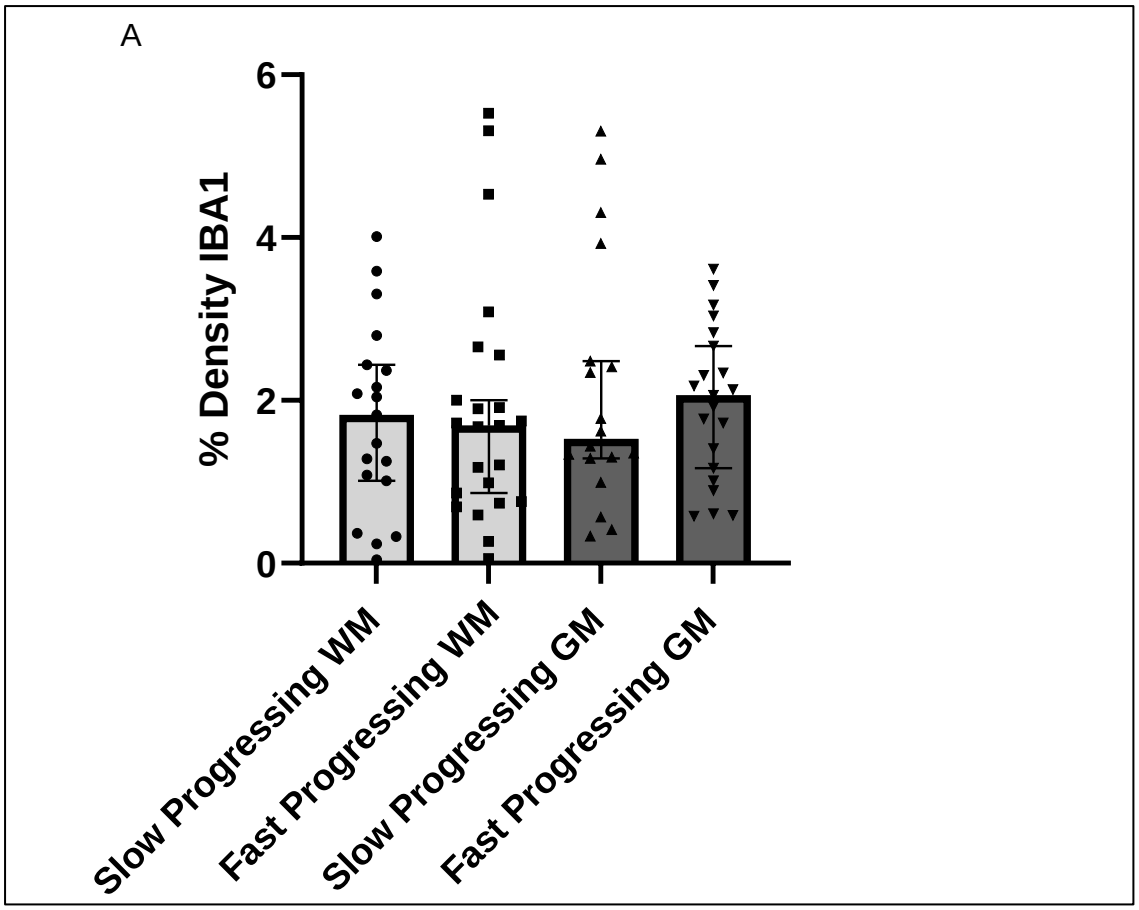

B

Motor Cortex	Rate of disease progression	Median (% density)	95% Confidence Intervals (Lower, Upper)
White Matter	Slow Progressing	1.825	1.218, 2.329
	Fast Progressing	1.694	1.253, 2.545
Grey Matter	Slow Progressing	1.53	1.360, 2.880
	Fast Progressing	2.062	1.543, 2.402

Figure 4.62 IBA1 Expression in the Motor Cortex was not Associated with the Rate of Disease Progression.

A) *Expression of IBA1 did not significantly differ between fast and slow progressing cases. IBA1 labelling varied greatly between sMND cases. Bars show the median, error bars show 95% confidence intervals.*

B) *Table showing median and confidence intervals displayed in Figure A.*

WM = White matter, GM = grey matter.

4.6.2 CD68

Qualitative Analysis

In control cases, CD68 immunohistochemistry labelled small number of perivascular macrophages, and physiological microglial in the parenchyma (Figure 4.63). The extent of CD68 labelling was similar in white and grey matter, but was much less than observed with IBA1. In sMND, there was a mild reaction in the grey matter if the motor cortex. Microglia showed thickened processes with some amoeboid cells too (Figure 4.64). A more marked reaction was observed in sMND white matter. Perivascular macrophages were larger and rounded, and interstitial microglia were activated, with a number of amoeboid cells.

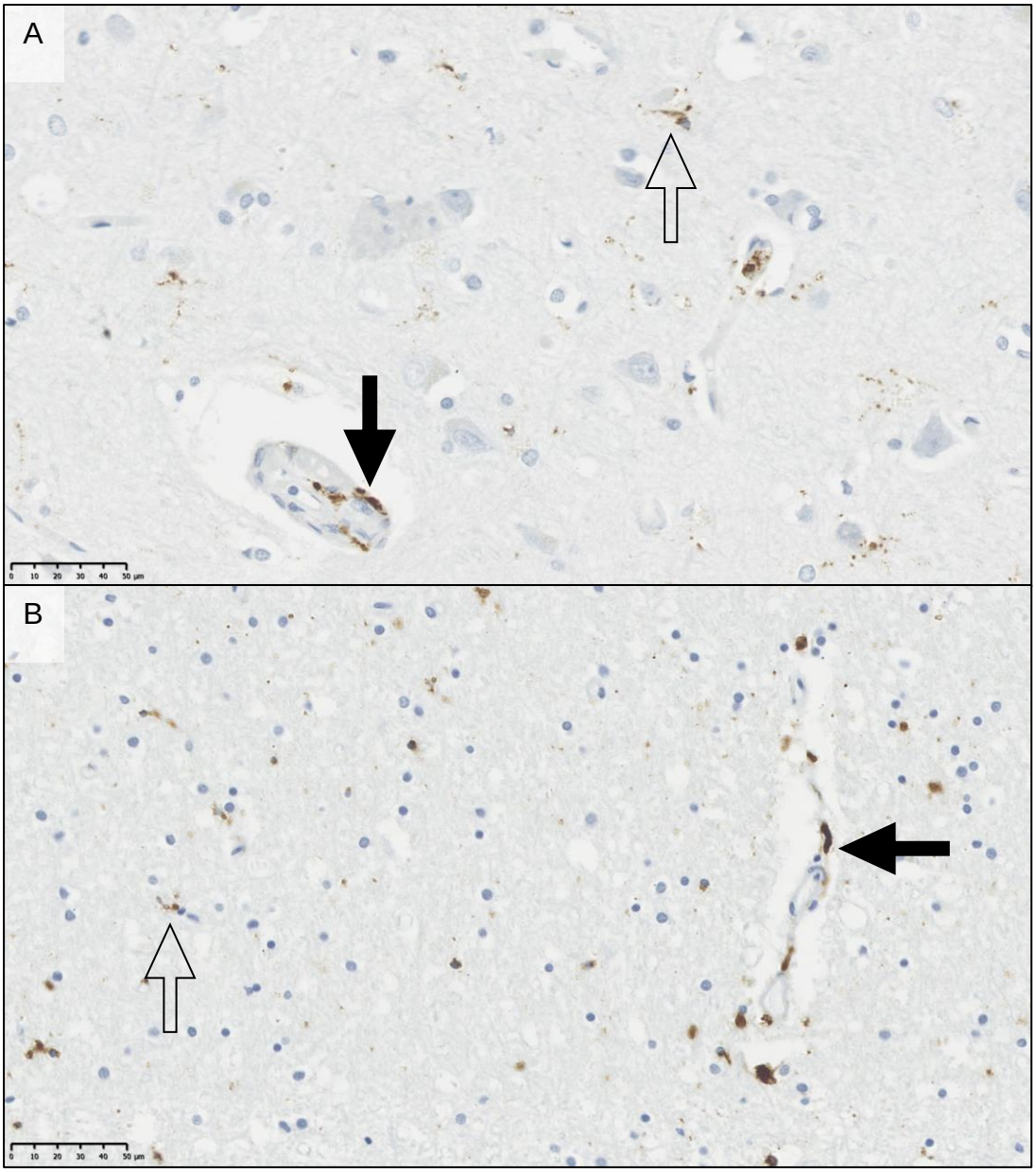

Figure 4.63 CD68 Expression in Control Motor Cortex

*Expression of CD68 in control motor cortex was limited to small perivascular macrophages (black arrow) and relatively few microglia (open arrows) in the parenchyma. In both grey (**A**) and white matter (**B**) microglia were very small with fine processes.*

Scale bar = 50µm.

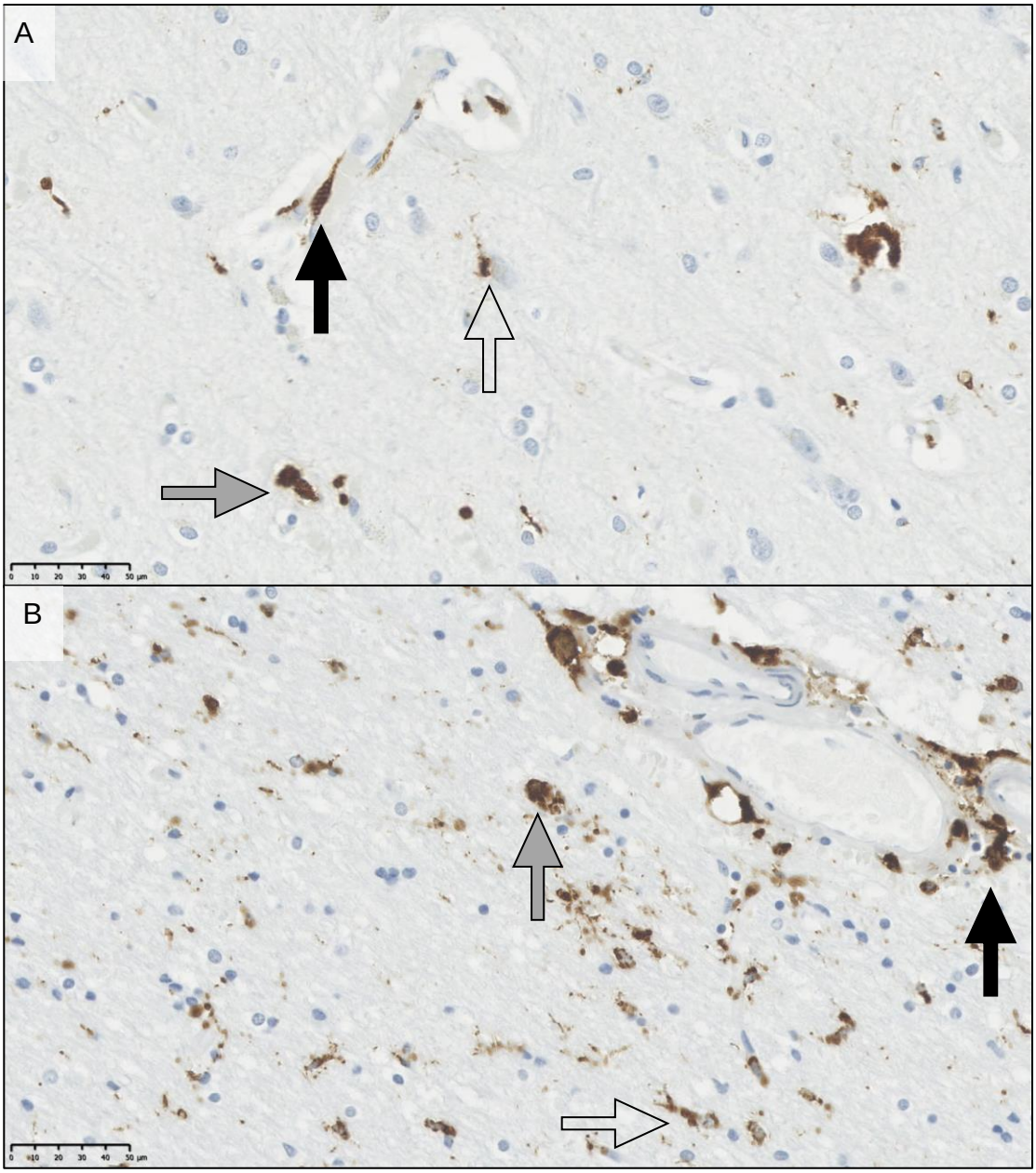

Figure 4.64 CD68 Expression in sMND Motor Cortex

*In grey matter (**A**), mild activation of CD68 positive cells was observed. Perivascular macrophages were larger (black arrows). Microglia showed some thickening of processes (open arrow), and amoeboid microglia were also observed (grey arrow).*

*A marked reaction was seen in the white matter (**B**), with an increase in the number of perivascular cells (black arrow), as well as activated (open arrow) and amoeboid (grey arrow) microglia.*

Scale bar = 50µm.

Quantitative Analysis

Expression of CD68 was quantified in the motor cortex white matter and grey matter in sMND and spinal cord cases. A Kruskall-Wallis test indicated there were significant differences in expression ($H(3)=8.383$, $p=0.0315$; Figure 4.65). Pairwise comparisons were completed using Mann-Whitney U tests. No difference was observed between control and sMND cases in the white matter ($U=138$, $p=0.663$) or grey matter ($U=142$, $p=0.684$). However, there was greater expression in the white compared to the grey matter in both sMND ($U=977.5$, $p=0.0098$) and control cases ($U=5$, $p=0.0411$). CD68 expression was highly variable in the motor cortex in across all conditions.

A

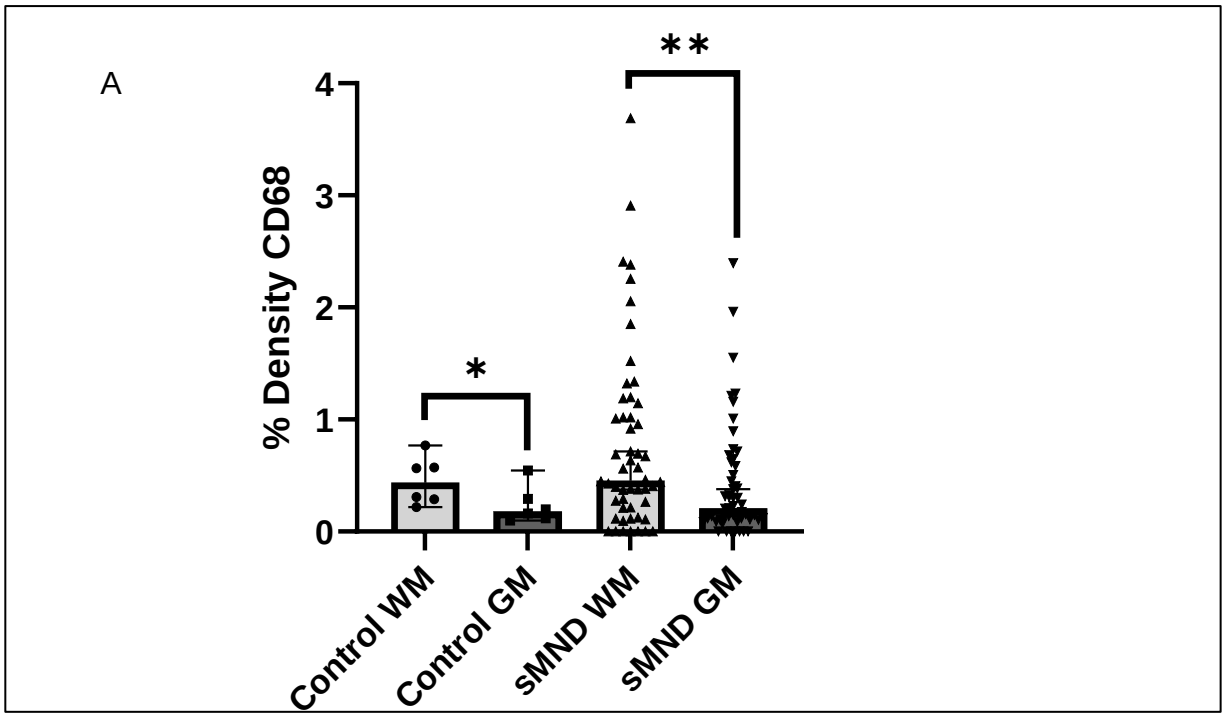

B

Disease Status	Motor Cortex:	Median (% density)	95% Confidence Intervals (Lower, Upper)	Mann-Whitney U	P Value
Control	White Matter	0.4376	0.229, 0.6786	977.5	0.0098
	Grey Matter	0.1784	0.060, 0.410		
sMND	White Matter	0.4555	0.553, 1.01	5	0.0411
	Grey Matter	0.2091	0.278, 0.558		

Figure 4.65 CD68 Expression is Increased in White Matter in the Motor Cortex

A) The percentage area positive for CD68 was significantly increased in the white matter compared to grey matter in both sMND cases and control cases, but no significant difference between sMND and control was observed. CD68 expression varied greatly between sMND cases. Bars represent median percentage staining density; error bars show 95% confidence intervals.

B) Table showing the median percentage staining area, 95% confidence intervals and Mann Whitney U comparisons of CD68 expression in white and grey matter in control and sMND cases.

To examine the relationship between CD68 expression in sMND and survival, the percentage of CD68 area density in the white and grey matter was compared between fast and slow progressing sMND by one-way Kruskal-Wallis test. Cases were split into fast and slow progressing groups of the median length of survival (26 months). There was a significant difference between groups (H[3]=12.37, p=0.006). However, pairwise comparisons (Table 4.4), completed using two-tailed Mann-Whitney U tests, indicated there was no significant difference in CD68 expression in the white (U=162, p=0.320) or grey (U=168.5, 0.319) matter between fast and slow progressing sMND cases.

Table 4.4 CD68 Expression in the Motor Cortex was not Associated with the Rate of Disease Progression

Motor Cortex	Rate of disease progression	Median (% density)	95% Confidence Intervals (Lower, Upper)	Mann-Whitney	P Value
White Matter	Slow Progressing	0.9597	0.731, 1.489	162	0.320
	Fast Progressing	0.5706	0.446, 1.247		
Grey Matter	Slow Progressing	0.3852	0.341 0.879	168.5	0.319
	Fast Progressing	0.2063	0.215, 0.594		

4.6.3 HLA-DR

Qualitative Analysis

In control motor cortex, HLA-DR labelled perivascular macrophages and parenchymal, ramified microglia with very fine long processes (Figure 4.66). In sMND cases, there was a possible increase in reactivity, although expression was so heterogenous between cases, this was difficult to determine. Compared to control, there appeared to be more perivascular macrophages, HLA-DR positive ramified and amoeboid microglia in sMND cases (Figure 4.67).

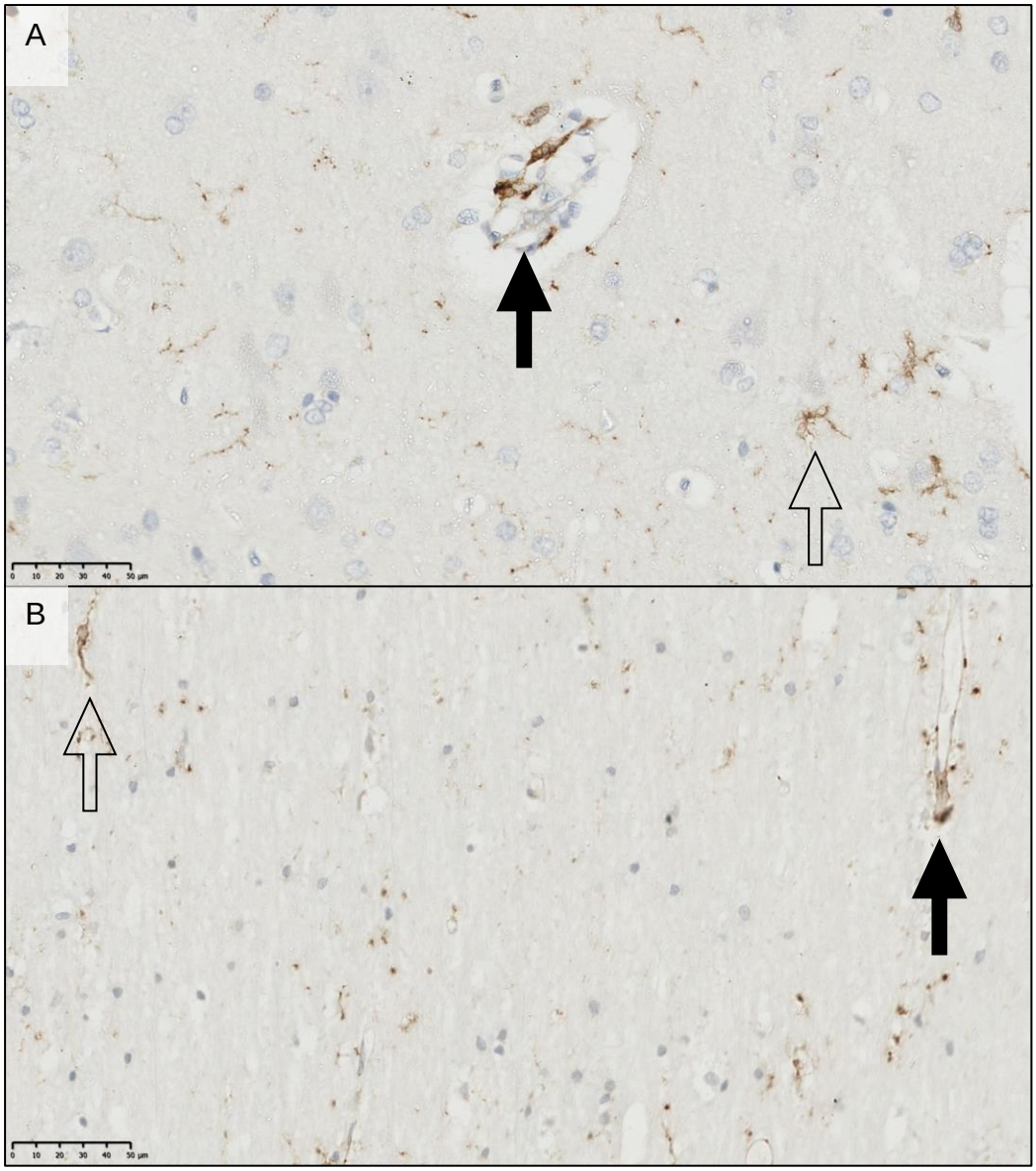

Figure 4.66 HLA-DR Immunoreactivity in Control Motor Cortex

*Compared to other microglial markers such as IBA1, HLA-DR immunoreactivity was comparatively minimal. HLA-DR labelled physiological microglia with fine spindly processes (open arrow). Perivascular macrophages were also labelled (black arrow). Similar levels of immunoreactivity were observed in grey (**A**) and white matter (**B**).*

Scale bar = 50µm.

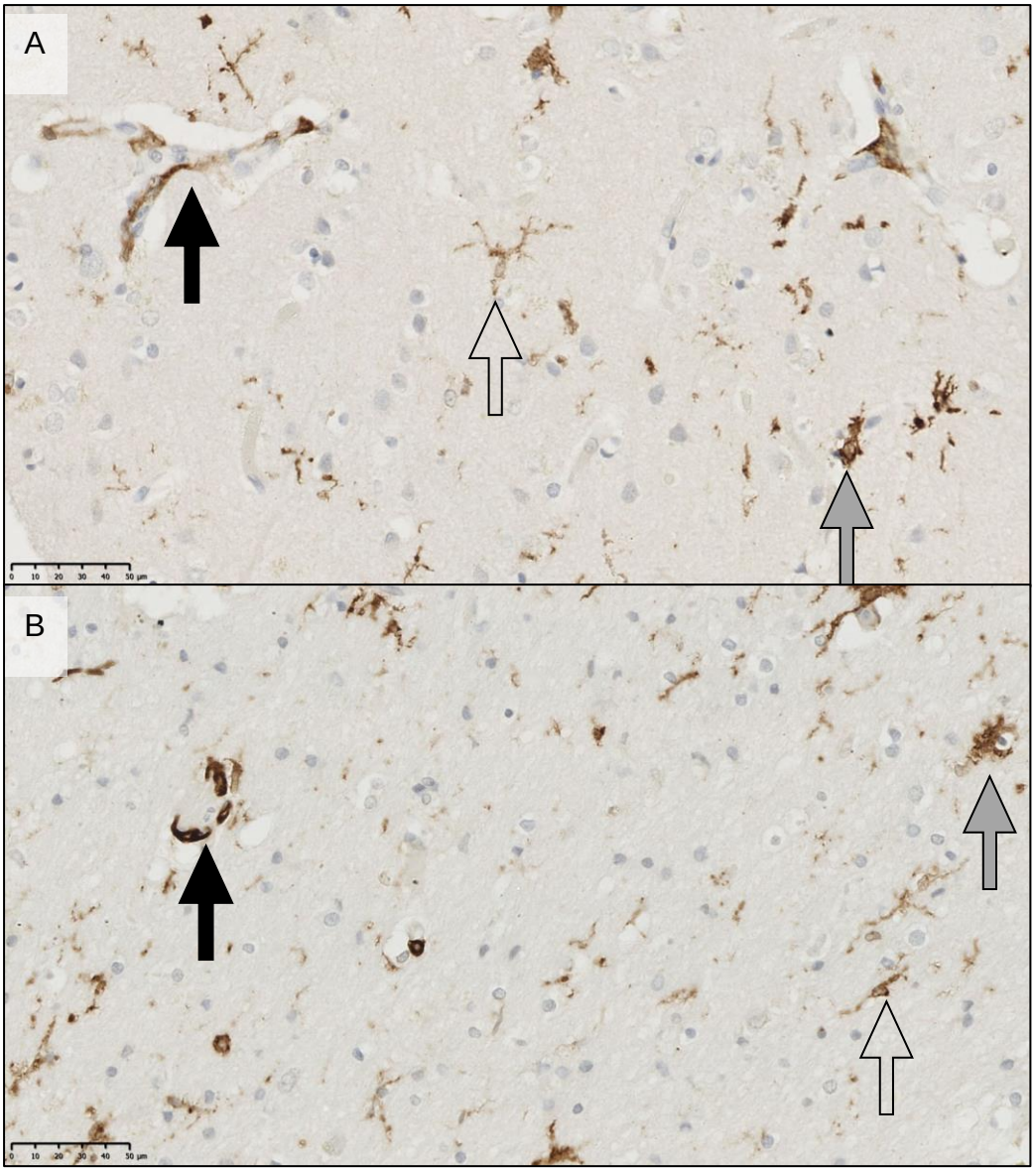

Figure 4.67 HLA-DR Expression in sMND Motor Cortex

*In both the grey matter (**A**) and white matter (**B**), HLA-DR immunoreactivity varied extensively between cases, making it difficult to ascertain whether there was a clear change in expression between control and sMND cases. sMND cases did tend to show an increase in the number of perivascular macrophages (black arrows). An increase in the number of ramified microglia (open arrows) were observed in the parenchyma, as well as more activated microglia with thickened processes (open arrows).*

Scale bar= 50µm.

Quantitative Analysis

The percentage area positive for HLA-DR was compared between control and sMND cases and white and grey matter using a Kruskal-Wallis test, which revealed there was no significant difference between groups ($H(3)=2.042$, $p=0.564$). HLA-DR expression varied greatly in sMND cases (Figure 4.68).

To examine the relationship between HLA-DR expression in sMND and the rate of disease progression, the percentage of HLA-DR immunoreactivity in the white and grey matter was compared between fast and slow progressing sMND using a one-way Kruskal-Wallis test. Cases were split into fast and slow progressing cases based on the median length of survival (26 months). This test indicated there was no significant difference in expression ($H(3)=3.415$, $p=0.332$).

A

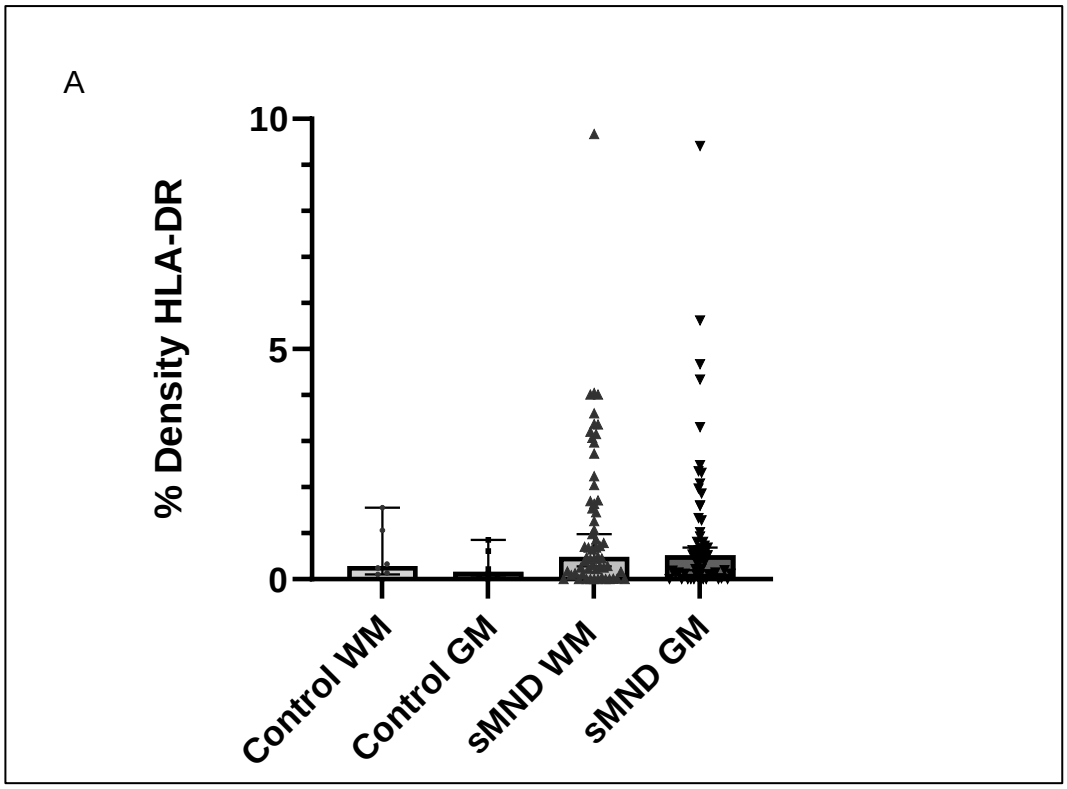

B

Disease Status	White or Grey Matter	Median (% density)	95% Confidence Intervals (Lower, Upper)
control	White	0.2883	-0.051, 1.196
	Grey	0.1659	-0.038, 0.670,
sMND	White	0.4885	0.0801, 1.678
	Grey	0.5236	0.0611, 1.508

Figure 4.68 HLA-DR Expression did not Differ Between Control and sMND in the Motor Cortex

***A**) HLA-DR expression in the motor cortex did not significantly differ between control and sMND cases, in the white or grey matter (H(3)=2.042, p=0.564). HLA-DR expression, particularly in the sMND cases varied greatly. Bars show the median, error bars show 95% confidence intervals.*

***B**) Table showing the median and confidence intervals given in Figure A.*

WM= white matter, GM= grey matter.

4.6.4 CD163

Qualitative Analysis

As was observed in the spinal cord, CD163 immunoreactivity was limited to perivascular macrophages in the control cases, in both white and grey matter with very little parenchymal staining. Very little difference qualitatively was observed between control and sMND case (Figure 4.69).

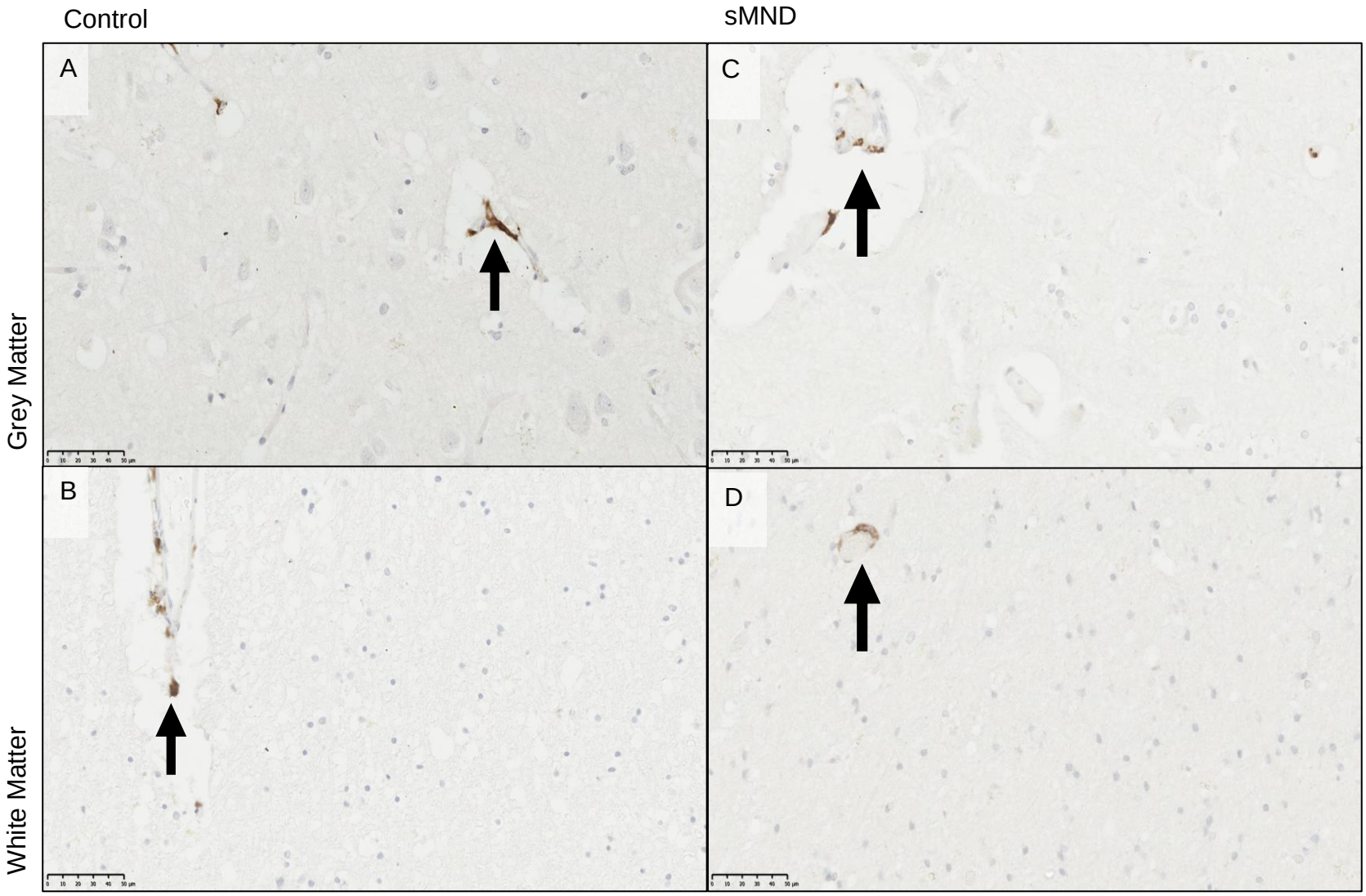
Control
sMND
A
C
B
D
Grey Matter
White Matter

Figure 4.69 CD163 Expression was Limited to Perivascular Macrophages in the Motor Cortex

CD163 labelled perivascular macrophages (black arrows), very little CD163 expression was observed in the general parenchyma. Expression was relatively uniform both in white (B&D) and grey (A&C) matter, and between control and sMND cases.

Scale bar = 50µm.

Quantitative Analysis

CD163 expression did not differ significantly between control and sMND cases in the motor cortex, as determined by one-way Kruskal-Wallis test (H(3)= 3.929, p=0.269, Table 4.5). Furthermore, CD163 expression did not differ between fast and slow progressing sMND cases in the white or the grey matter (one-way Kruskal-Wallis: H(3)=0.403, p=0.940, Table 4.6). Cases were split into fast and slow progressing cases for this analysis using the median length of survival (26 months).

Disease Status	White or Grey Matter	Median (% density)	95% Confidence Intervals (Lower, Upper)
control	White	0.06113	0.036, 0.0872
	Grey	0.05689	0.0215, 0.113
sMND	White	0.08528	0.084, 0.140
	Grey	0.07363	0.062, 0.136

Table 4.5 CD163 Expression in Control and sMND Motor Cortex

Table 4.6 CD163 Expression in the Motor Cortex in Fast and Slow Progressing sMND.

Motor Cortex	Rate of disease progression	Median (% density)	95% Confidence Intervals (Lower, Upper)
White Matter	Slow Progressing	0.002749	0.016, 0.074
	Fast Progressing	0.009848	0.028, 0.106
Grey Matter	Slow Progressing	0.002525	0.014, 0.075
	Fast Progressing	0.02342	0.019, 0.075

4.6.5 APOE

Qualitative Analysis

APOE immunohistochemistry labelling was similar in the motor cortex to that of the spinal cord. In control cases, subsets of neurons showed variable staining in the grey matter (Figure 4.70). Some glial staining was also present, as well as labelling of vascular structures. In white matter, there was APOE labelled a subset of axons. Glial labelling appeared greater in the white matter than the grey. Furthermore, staining of the neuropil was greater in the grey matter, than the white matter.

In sMND cases, labelling was quantitatively similar to controls, staining populations on neurons, glial cells vascular structures and the neuropil. In sMND grey matter, the neuropil showed greater immunoreactivity compared to white matter. Some neurons showed high levels of APOE expression; although, most were negative, or showed similar expression to the neuropil (Figure 4.71). As with control cases, the white matter showed more glial staining than the grey matter.

Both sMND and control cases showed great heterogeneity in the extent of APOE expression. As a result, there was not a clear qualitative separation between control and sMND cases.

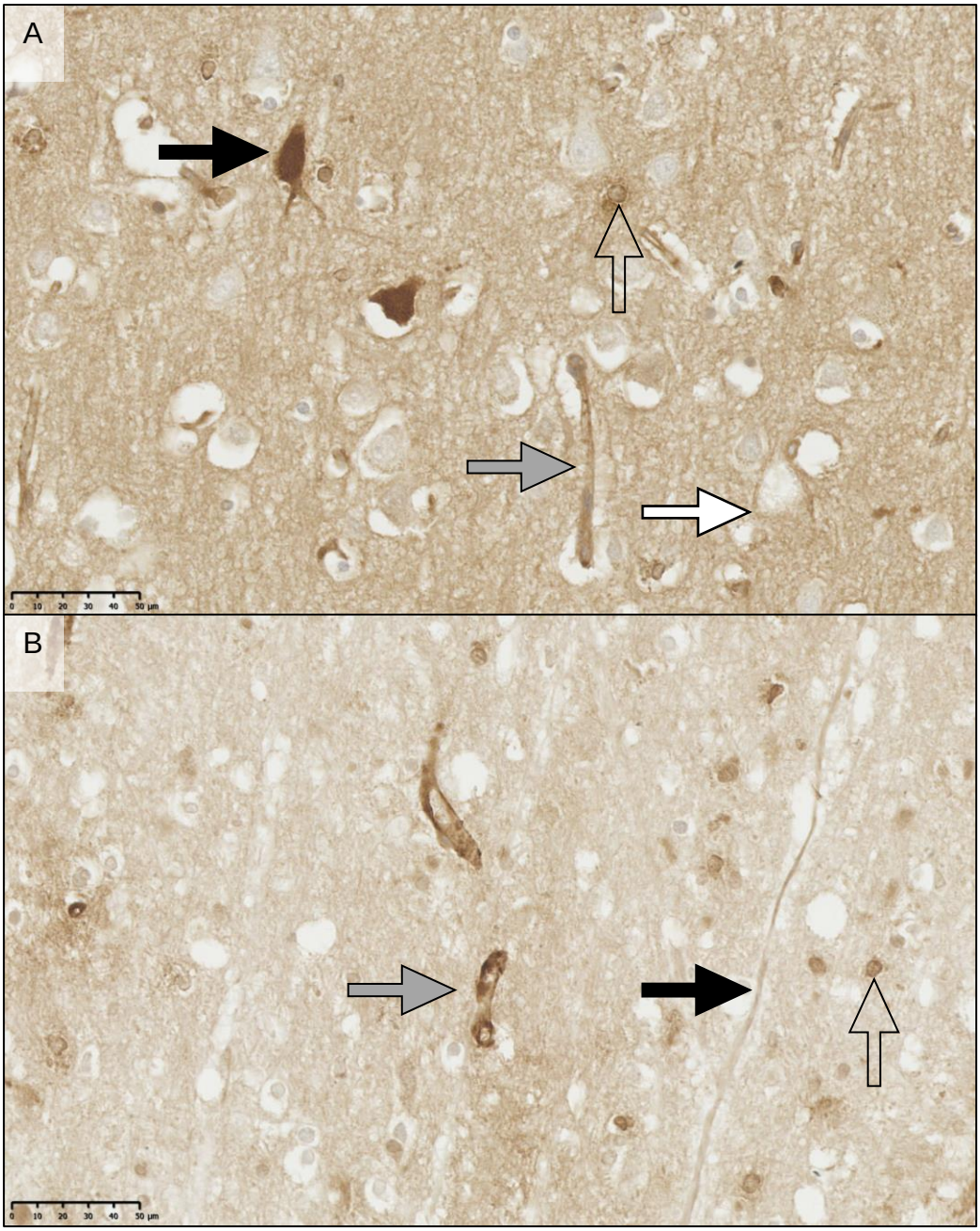

Figure 4.70 Expression of APOE in Control Motor Cortex

***A**) In the grey matter, subsets of neurons expressed high levels of APOE (black arrow), and other neuron populations were absent for any staining (white arrow). Some glial staining was also observed in the grey matter (open arrow), vascular structures were also labelled (grey arrow).*

***B**) In the white matter, the neuropil was generally less intensely stained. Blood vessels were stained (grey arrow). A number of glial cells were also positive for APOE (open arrow). A subset of axons were also APOE positive (black arrow).*

Scale bars= 50µ

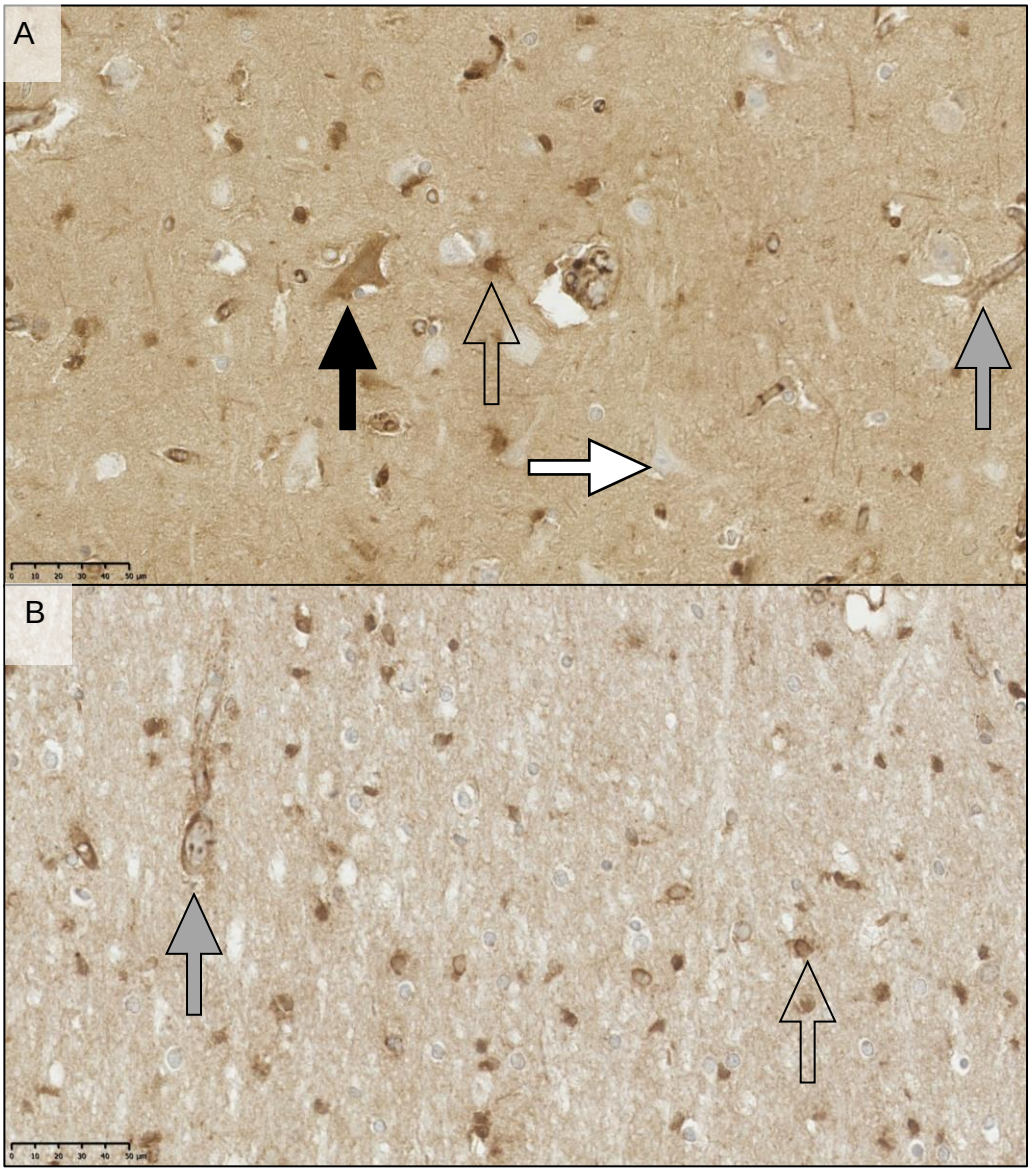

Figure 4.71 APOE Expression in sMND Motor Cortex

***A**) Grey matter showed greater APOE immunoreactivity than white matter. The majority of neurons had low levels of APOE expression (white arrow), but a small subset were significantly darker (black arrow). Glia (open arrow) and vascular structures (grey arrow) were also labelled*

***B**) White matter neuropil was less intensely stained than the grey matter. APOE expression in white matter predominantly labelled vascular structures (grey arrow), and glial cells (open arrow).*

Scale bars = 50µm.

Semi-Quantitative Analysis

Due to the high level of parenchymal APOE immunoreactivity in the cortex quantitative analysis was not possible using the Visiopharm data analysis software. Therefore, semi-quantitative analysis was performed.

Neuropil staining in the grey and white matter was assessed using the rating scale by two independent markers (BAA and JRH). A weighted Cohen's Kappa test was used to assess agreement between markers, which indicated there was near perfect agreement between markers in both the white matter and grey matter (Table 4.7).

Table 4.7 Inter-rater Reliability of APOE Immunoreactivity in the Motor Cortex

Motor Cortex Region	Cases Observers score agreed [/(%)]	Cases Observers score agreed - Control cases [/ (%)]	Cases Observers score agreed - sMND cases [/ (%)]	Weighted Cohens Kappa	95% CI	Interpretation
White Matter	51/55 (92.73%)	6/6 (100%)	45/49 (91.84%)	0.933	0.795 - 0.991	Almost perfect agreement
Grey Matter	57/59 (96.61%)	6/6 (100%)	51/53 (96.23%)	0.936	0.810-1.000	Almost perfect agreement

Neuropil staining was compared in control and sMND cases, in the white and grey matter using a one-way Kruskal-Wallis test. This indicated there was a significant difference between groups ($H(3)=60.96$, $p<0.000$, Figure 4.72). Pairwise comparisons, by two-tailed Mann-Whitney U tests, found no significant difference between control and sMND (white matter: $U=101.5$, $p=0.195$; grey matter: $U=152$, $p=1$). There was greater APOE expression in grey than white matter, in both control ($U=4$, $p=0.022$) and sMND ($U=257$, $p<0.0001$) cases.

A

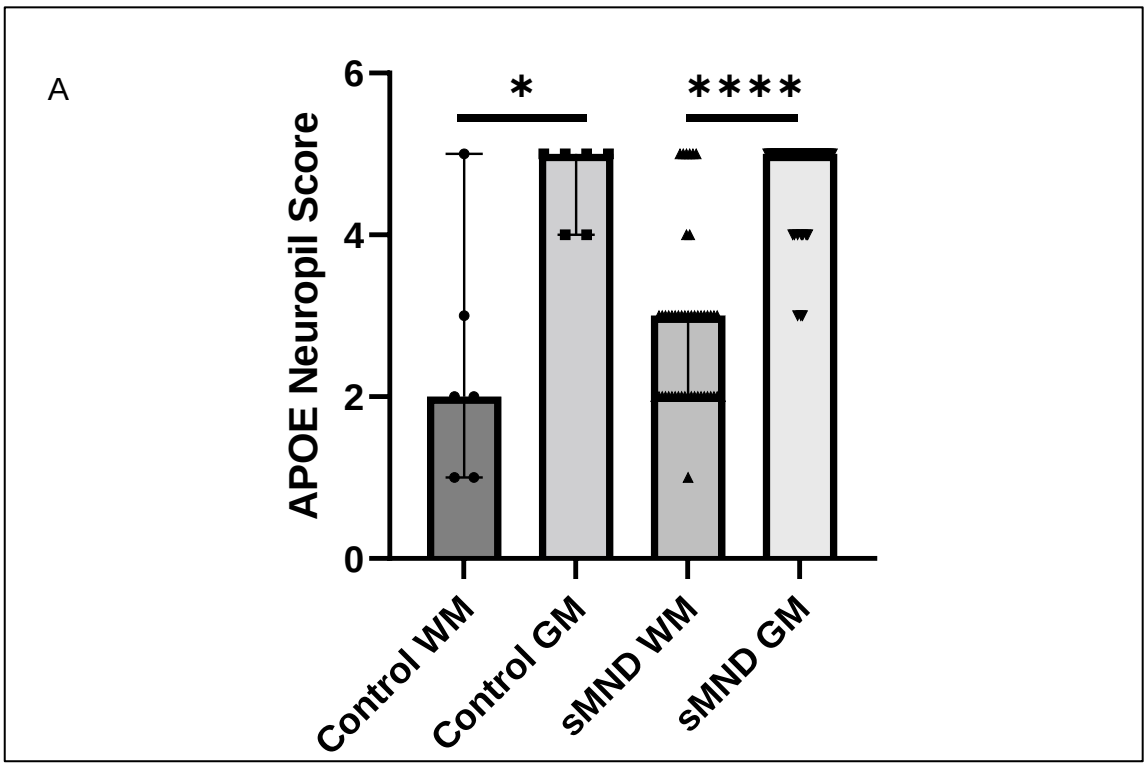

B

Disease Status	Motor Cortex:	Median (% Density)	95% Confidence Intervals (Lower, Upper)	Mann-Whitney U	P Value
Control	White Matter	2	0.753, 3.913	4	0.022
	Grey Matter	5	4.125, 5.209		
sMND	White Matter	3	2.525, 3.108	257	<0.0001
	Grey Matter	5	4.490, 4.831		
Control	White Matter	2	0.753, 3.913	101.5	0.195
sMND		3	2.525, 3.108		
Control	Grey Matter	5	4.125, 5.209	152	1
sMND		5	4.490, 4.831		

Figure 4.72 APOE Expression was increased in Grey Matter in the Motor Cortex

***A**) Expression of APOE in the parenchyma was significantly increased in the grey matter compared to white in both control and sMND cases. Disease status was not associated with APOE expression in the motor cortex. Bars show the median, error bars show 95% confidence intervals.*

***B**) Table showing the median percentage APOE density, 95% confidence intervals and Mann Whitney U comparisons of APOE expression in white and grey matter in control and sMND cases.*

The expression of APOE in the neuropil in white and grey matter was examined in relation the length of patient survival. sMND cases were divided into fast and slow progressing using the median length of survival (26 months), and APOE expression was compared using a using a one-way Kruskal-Wallis test. This indicated a significant difference between groups ($H(3)=43.96$, $p<0.0001$). However, pairwise comparisons (two-tailed Mann-Whitney U tests) did not find a significant difference in expression between fast and slow progressing cases in white ($U=206$ $p=0.932$) or grey matter ($U=195$ $p=0.660$).

4.6.6 TREM2

Qualitative Analysis

In the motor cortex, TREM2 was minimal for both control (Figure 4.73) and sMND (Figure 4.74) cases. TREM2 immunoreactivity was almost completely limited to perivascular macrophages. There was some minimal staining of neurons. The TREM2 positive granules observed in the spinal cord were not observed in the motor cortex.

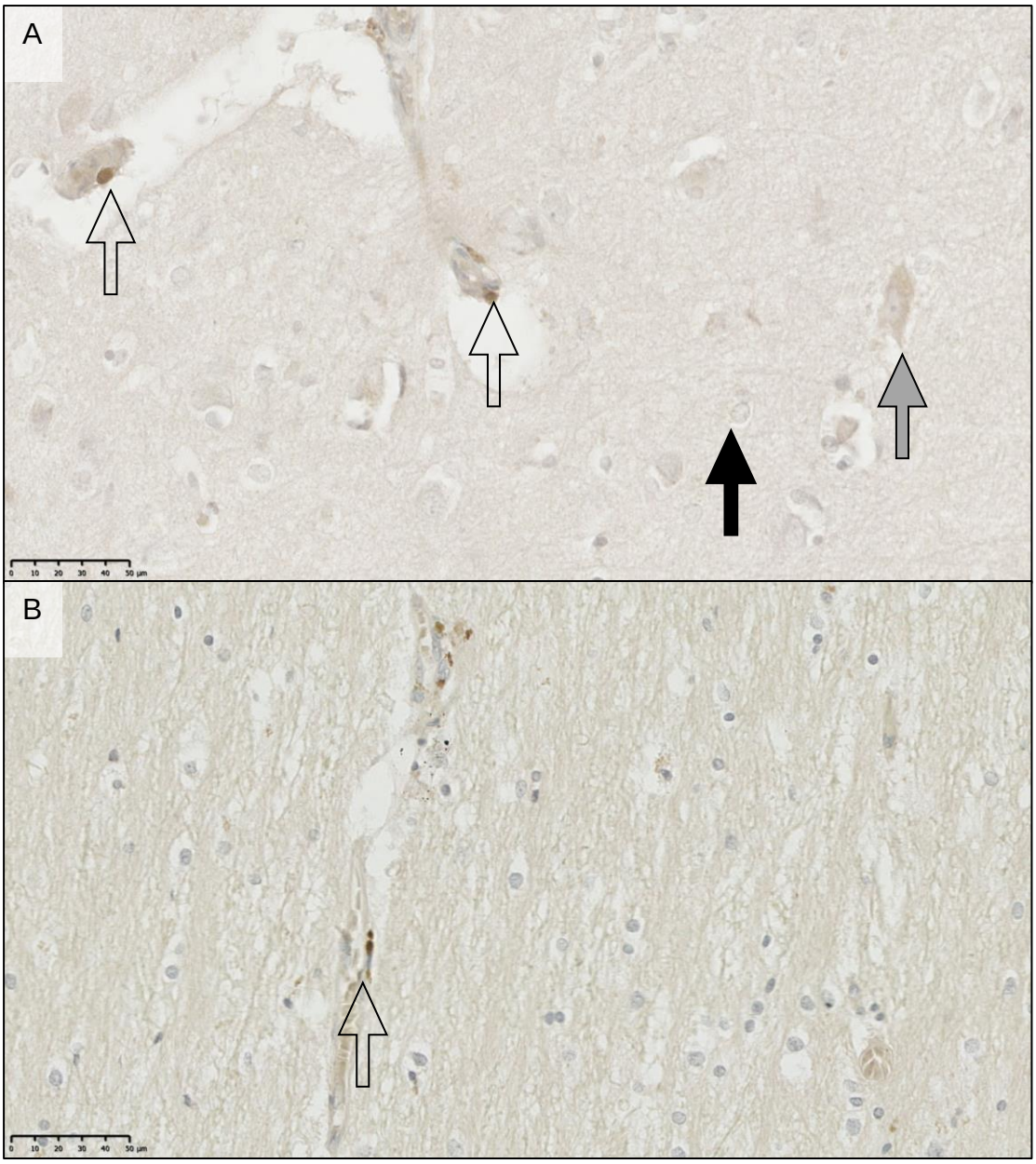

Figure 4.73 TREM2 Expression in Control Motor Cortex

In the motor cortex TREM2 primarily labelled perivascular macrophages (open arrows) in both grey (A) and white (B) matter. Staining of motor neurons (grey arrow) and glia (black arrow) was minimal.

Scale bars = 50µm.

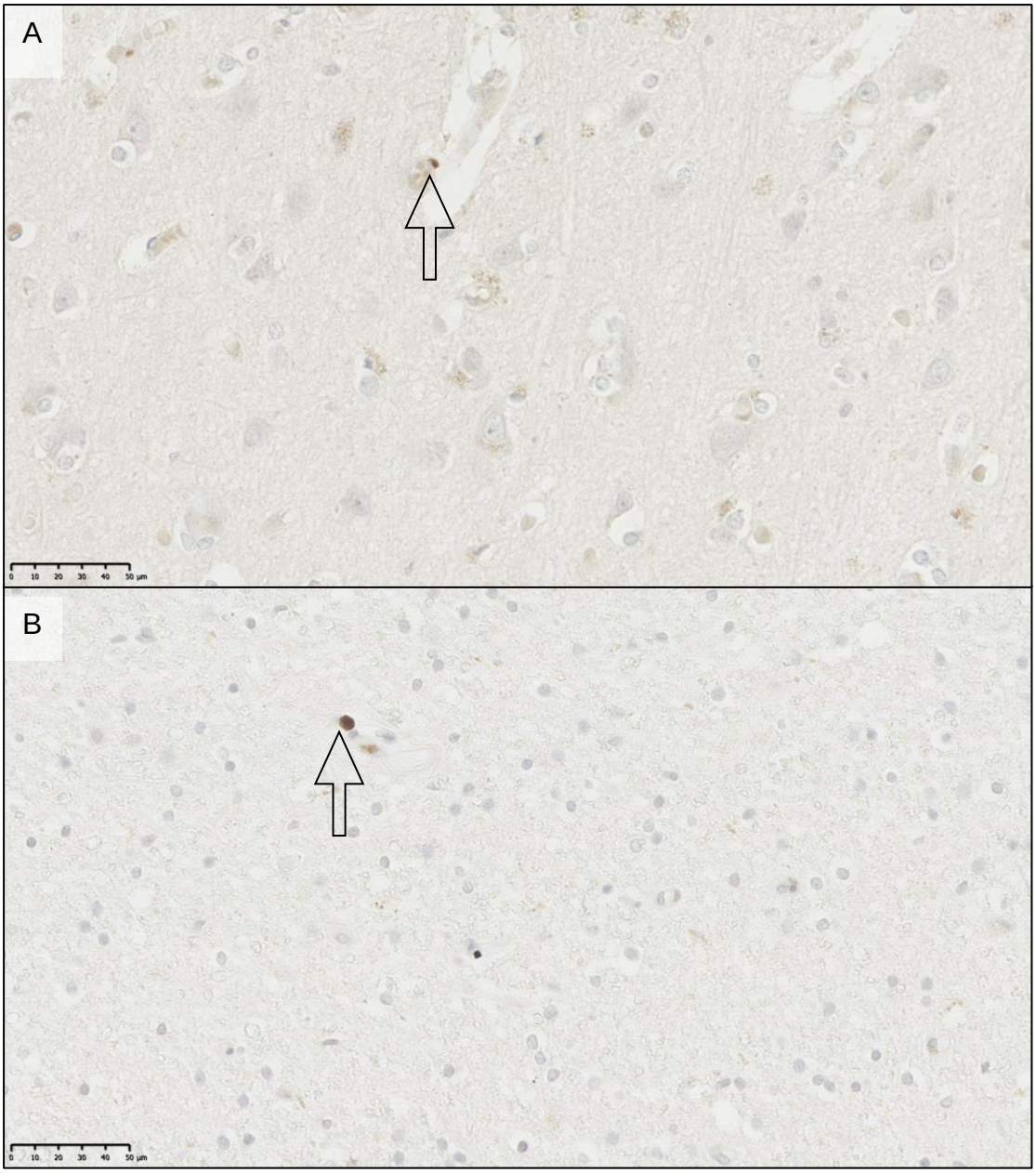

Figure 4.74 TREM2 Expression in sMND Motor Cortex

*TREM2 expression in the motor cortex did not differ between sMND and control. TREM2 labelling was primarily limited to perivascular macrophages (open arrows) in the grey (**A**) and white (**B**) matter.*

Scale bars = 50µm.

Quantitative Analysis

Examination of the TREM2 expression data in motor cortex revealed one outlying point (case 027/2008 grey matter, sMND). A box and whisker plot indicated this point fell outside the maximum (75th percentile plus 25%) and was separate from all other data points (Figure 4.75). As such, the decision was made to remove this point from the following analyses.

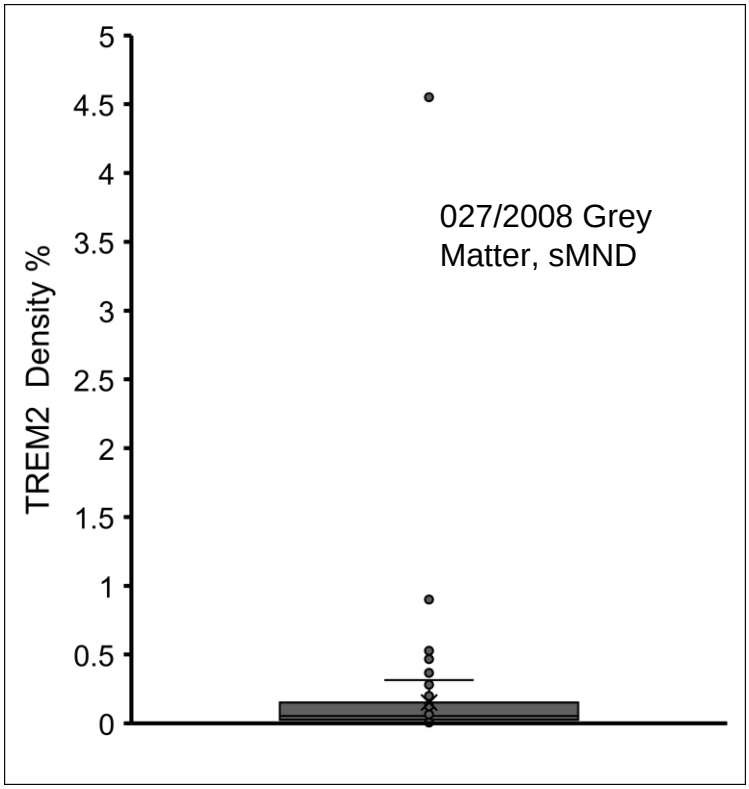

Figure 4.75 Detection of Outlying Point in Quantification of TREM2 Expression in Motor Cortex

Box and whisker plot showing all datapoints (control and sMND, white and grey matter) from the quantification of TREM2 expression in the motor cortex. Case 027/2008 grey matter (highlighted on the graph) was out of the maximum range shown by the top bar of the whisker plot and was separate from the main cluster of data points. As such, this case was removed from further analysis.

Box plot shows the quartile 1, the median, and quartile 3. Whiskers range from the minimum (quartile 1 – 1.5x the interquartile range) to the maximum (quartile 3 +1.5x the interquartile range).

TREM2 expression was compared control and sMND motor cortex, in white and grey matter using a one-way Kruskal-Wallis test, which indicated a significant difference between groups ($H(3)=37.21$, $p<0.0001$, Figure 4.76). Pairwise comparisons (two-tailed Mann-Whitney U) demonstrated no significant difference between control and sMND in white ($U=107$, $p= 0.392$) or grey ($U=144$, $p=0.948$) matter, or between white and grey matter in control cases ($U=7$, $p= 0.093$). However, there was greater TREM2 in the grey compared to white matter in sMND cases ($U=362$, $p<0.0001$).

A

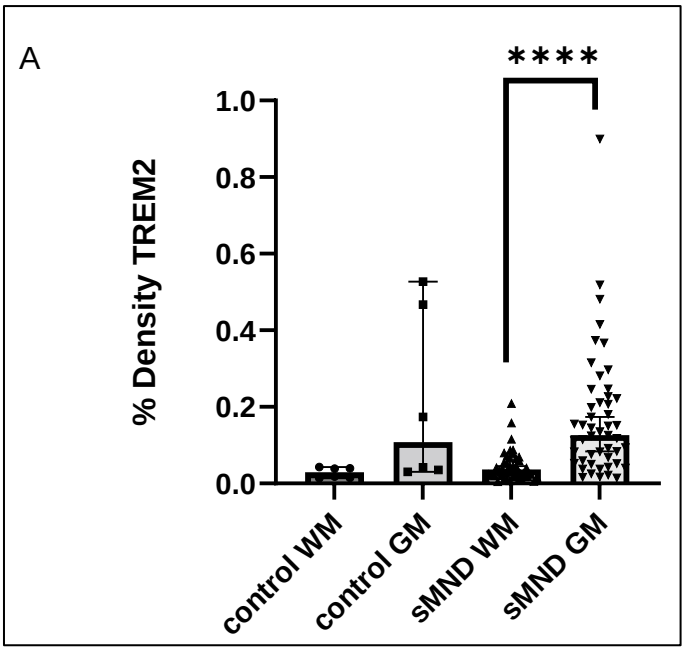

B

Disease Status	White or Grey Matter	Median (% density)	95% Confidence Intervals (Lower, Upper)
control	White	0.02863	0.014, 0.043
	Grey	0.1081	-0.026, 0.452
sMND	White	0.03592	0.032, 0.0559
	Grey	0.1264	0.125, 0.218

Figure 4.76 TREM2 Expression did not differ between Control and sMND

A) TREM2 expression was significantly increased in the white matter compared to grey (U=362, p<0.0001), in sMND cases, however, no difference in expression was observed between control and sMND. Bars show the median percentage TREM2 positive area, error bars are the 95% confidence intervals. WM = white matter, GM= grey matter.

***B**) Table showing the median percentage TREM2 positive area and 95% confidence intervals.*

The expression of TREM2 was compared between fast and slow progressing sMND cases using a one way-Kruskal-Wallis test. Cases were split into fast and slow progressing disease groups based on the median length of survival (26 months), which indicated a significant difference between groups ($H(3)=27.95$, $p<0.0001$). However, pairwise comparisons completed using two-tailed Mann-Whitney U tests, did not show a significant change in TREM2 expression between fast and slow progressing sMND cases in white ($U=212$, $p=0.673$) or grey ($U=148$, $p=0.072$) matter (Table 4.8).

Table 4.8 TREM2 Expression in the Motor cortex is not Associated with the Rate of sMND Disease Progression

Motor Cortex	Rate of disease progression	Median (% density)	95% Confidence Intervals (Lower, Upper)	Mann-Whitney U	P value
White Matter	Slow Progressing	0.0253	0.025, 0.059	212	0.673
	Fast Progressing	0.0375	0.029, 0.068		
Grey Matter	Slow Progressing	0.2067	0.0132, 0.365	148	0.075
	Fast Progressing	0.1026	0.085, 0.166		

4.6.7 TYROBP

Qualitative Analysis

TYROBP signal in the motor cortex was much less than that seen in the spinal cord but labelled similar cells and structures, including blood vessels, glia and some neuronal staining. Grey matter was slightly darker than white matter.

There was variable expression by motor neurons in the grey matter (Figure 4.77), with some faintly labelled and other neurons showing almost no expression. TYROBP also labelled glia in the grey matter. The white matter showed a very similar pattern of expression with TYROBP labelling branched glial cells. TYROBP signal intensity varied greatly between cases in both control and sMND. No qualitative difference was observed between control and sMND (Figure 4.78).

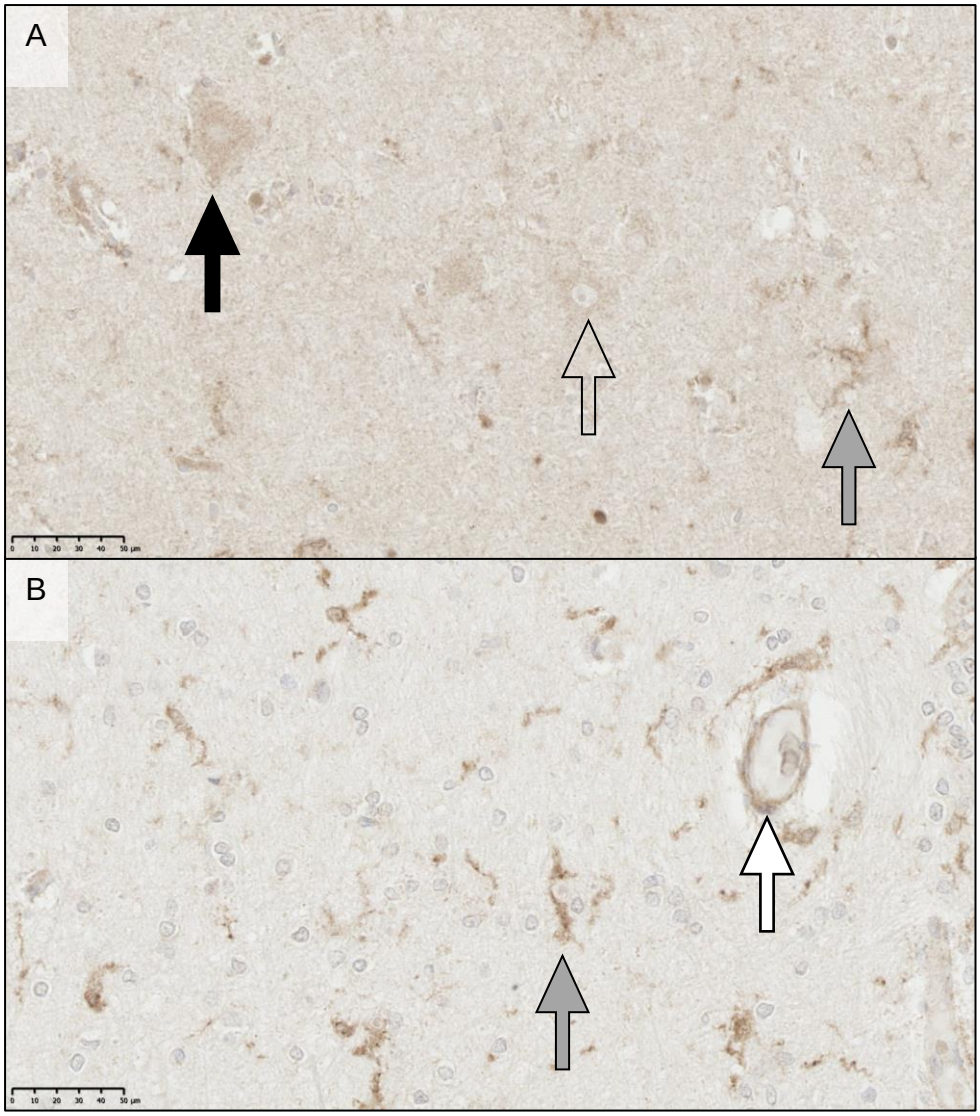

Figure 4.77 TYROBP Expression in the Motor Cortex

*Overall, in both grey (**A**) and white (**B**) matter TYROBP expression looked very similar. Signal intensity was much lower in the motor cortex compared to the spinal cord. No qualitative difference was observed between control and sMND.*

In the grey matter, TYROBP faintly labelled a subset of neurons with cases. Some showed darker expression (black arrow), while other neurons were almost completely absent of staining (open arrows). In both the white and grey matter, TYROBP labelled branched or ramified glia (grey arrows), and vasculature (white arrow).

Scale bars = 50µm.

Quantitative Analysis

Expression of TYROBP in the motor cortex was compared in white and grey matter between control and sMND cases using a one-way Kruskal-Wallis test, which indicated a significant difference between groups ($H(3)=21.58$, $p<0.0001$, Figure 4.78). Pairwise comparisons, completed using Mann-Whitney U tests, indicated a significant increase in TYROBP immunoreactivity in sMND compared to control in both the white matter ($U=58$, $p=0.018$) and the grey matter ($U=0.038$, $p=0.038$). Furthermore, TYROBP percentage density was greater in the grey matter compared to the white matter in sMND ($U=608$, $p=0.0002$).

A

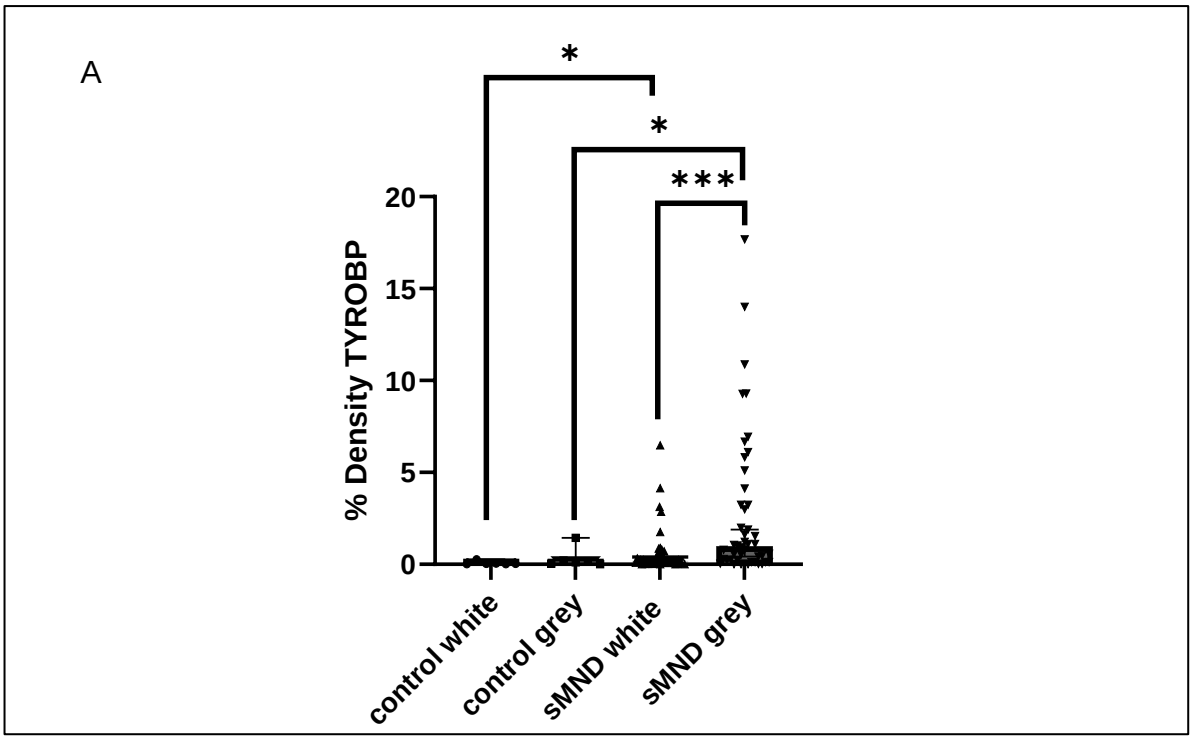

B

Disease Status	Motor Cortex	Median (% density)	95% Confidence Intervals (Lower, Upper)	Mann-Whitney U	P Value
Control	White Matter	0.0231	-0.048, 0.175	8	0.132
	Grey Matter	0.1389	-0.244, 0.905		
sMND	White Matter	0.1905	0.252, 0.965	608	0.0002
	Grey Matter	0.9676	1.521, 3.898		
control	White Matter	0.0231	-0.478, 0.175	58	0.018
sMND		0.1905	0.252, 0.965		
control	Grey Matter	0.1389	-0.244, 0.905	66	0.038
sMND		0.9676	1.521, 3.898		

Figure 4.78 TYROBP Immunoreactivity was Increased in the Motor Cortex in sMND Compared to Control

A) TYROBP expression was significantly increased in the grey matter compared to white (U=608, p=0.0002), in sMND cases, however, no difference in expression was observed between control and sMND. TYROBP was also increased in sMND compared to control in both white (U=58, p=0.018) and grey matter (U=58, p=0.018). Bars show the median percentage TYROBP positive area, error bars are the 95% confidence intervals. WM = white matter, GM= grey matter.

B) Table showing the median percentage TYROBP positive area and 95% confidence intervals.

To examine the relationship between TYROBP immunoreactivity and patient survival, sMND cases were divided into fast and slow progressing based on the median length of survival (26 months), and TYROBP expression was compared in the white and grey matter using a one-way Kruskal-Wallis test, which indicated a significant difference between groups (H(3)=12.44, p=0.006). However, pairwise comparisons completed using Mann-Whitney U tests Table 4.9), showed that TYROBP expression did not differ between fast and slow progressing sMND in the white (U=157, 0.077) or grey matter (U=168, p=0.293).

Table 4.9 sMND Patient Survival Time was not Associated with TYROBP Immunoreactivity

Motor Cortex	Rate of disease progression	Median (% density)	95% Confidence Intervals (Lower, Upper)	Mann-Whitney U	p value
White Matter	Slow Progressing	0.1177	-0.087, 1.353	157	0.077
	Fast Progressing	0.2406	0.203, 1.069		
Grey Matter	Slow Progressing	1.106	1.323, 6.009	168	0.293
	Fast Progressing	0.5641	0.403, 3.187		

4.7 Comparison of the Spinal Cord and Motor Cortex

In the Chapter 3, transcriptomic analysis in the spinal cord and motor cortex revealed the spinal cord to be an area of much greater inflammatory signalling. Little inflammation was observed in the motor cortex. Furthermore, differences between MND and controls were much more evident in the spinal cord than the motor cortex. As such, the following section aims to quantitatively compare expression of the target markers to determine whether such regional differences occurred at the translational level too. For these analyses the white matter underlying the motor cortex in the precentral gyrus was compared to the lateral corticospinal tracts in the spinal cord and motor cortex was compared to spinal cord ventral horn.

4.7.1 IBA1

IBA1 expression was compared between the white and grey matter in the motor cortex and spinal cord using a Kruskal-Wallis test, which indicated a significant difference between groups ($H(7)=71.56$, $p<0.0001$). Pairwise comparisons were completed using one-tailed Mann-Whitney U analyses, which revealed a significant increase in expression in the spinal cord compared to the precentral gyrus in control white matter, sMND grey matter, and sMND white matter (Figure 4.79).

A

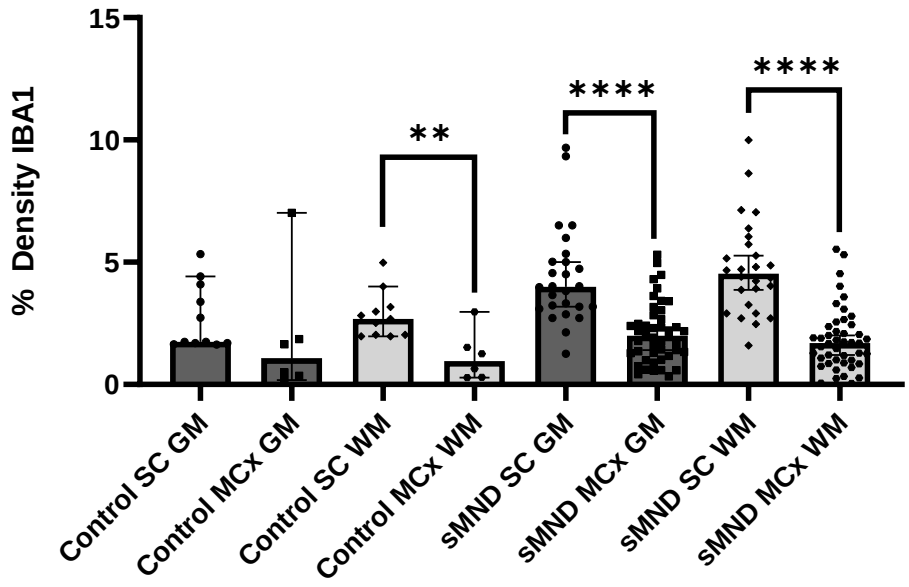

B

Disease Status	CNS Region		Median (% density)	95% Confidence Intervals (Lower, Upper)	Mann-Whitney U	P Value
Control	Spinal Cord	Grey Matter	1.745	1.826, 3.649	18	0.141
	Motor Cortex		1.07	-0.790, 4.644		
	Spinal Cord	White Matter	2.683	2.195, 3.468	7	0.006
	Motor Cortex		0.9523	0.090, 2.234		
sMND	Spinal Cord	Grey Matter	3.999	3.602, 5.192	157	<0.0001
	Motor Cortex		1.991	1.729, 2.489		
	Spinal Cord	White Matter	4.538	3.977, 5.546	102	<0.0001
	Motor Cortex		1.694	1.452, 2.221		

Figure 4.79 IBA1 Expression is Increased in the Spinal Cord Compared to the Motor Cortex

***A**) IBA1 expression was found to be significantly increased in the spinal cord compared to motor cortex, in control white matter, and sMND white and grey matter. Bars represent median, error bars 95% confidence intervals. SC= spinal cord, MCx= motor cortex, WM= white matter, GM= grey matter.*

***B**) Table showing the median percentage area positive for IBA1, 95% confidence intervals and the results of the Mann-Whitney U pairwise comparisons.*

4.7.2 CD68

CD68 expression was compared between white and grey matter in the motor cortex and spinal cord using a Kruskal-Wallis test, which indicated a significant difference between groups ($H(7)= 58.78$, $p<0.0001$). Pairwise comparisons using one-tailed Mann-Whitney U analyses, revealed a significant increase of CD68 expression in the spinal cord compared to the motor cortex in sMND grey and white matter (Figure 4.80). No significant difference was observed between the spinal cord and motor cortex in control cases.

A

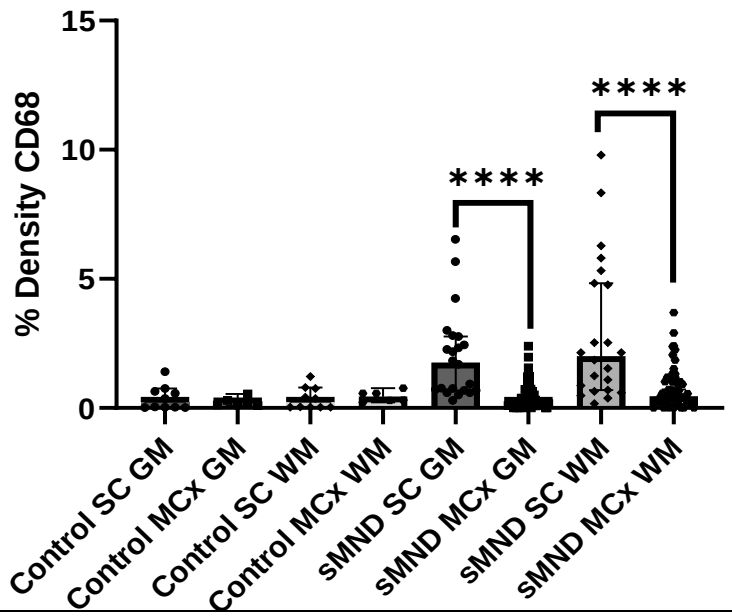

B

Disease Status	CNS Region		Median (% density)	95% Confidence Intervals (Lower, Upper)	Mann-Whitney U	P Value
Control	Spinal Cord	Grey Matter	0.2055	0.059, 0.720	29	0.958
	Motor Cortex		0.1784	0.060, 0.410		
	Spinal Cord	White Matter	0.204	0.068, 0.677	23	0.492
	Motor Cortex		0.4376	0.229, 0.679		
sMND	Spinal Cord	Grey Matter	1.761	1.264, 0.679	123	<0.0001
	Motor Cortex		0.2091	0.278, 0.558		
	Spinal Cord	White Matter	2	1.690, 4.133	228	<0.0001
	Motor Cortex		0.4555	0.553, 1.010		

Figure 4.80 CD68 Expression was Increased in sMND Spinal Cord compared to the Motor Cortex

***A**) CD68 expression was found to be significantly increased in the spinal cord compared to motor cortex, in sMND white and grey matter. A significant change in expression was not observed in control cases. Bars represent median, error bars 95% confidence intervals. SC= spinal cord, MCx= motor cortex, WM= white matter, GM= grey matter.*

***B**)* Table showing the median percentage area positive for CD68, 95% confidence intervals and the results of the Mann-Whitney U pairwise comparisons.

4.7.3 HLA-DR

HLA-DR expression was compared between the spinal cord and motor cortex, in white and grey matter, using a one-way Kruskal-Wallis test, which indicted a significant difference between groups ($H(7)=109.5$, $p<0.0001$). Pairwise comparisons (Figure 4.81), by Mann-Whitney U, highlighted a significant excess in HLA-DR in the spinal cord compared to motor cortex in both control white ($U=0$, $p=0.0001$) and grey matter ($U=0$, $p=0.0001$), and sMND white ($U=17$, $p<0.0001$) and grey matter ($U=68$, $P<0.0001$).

A

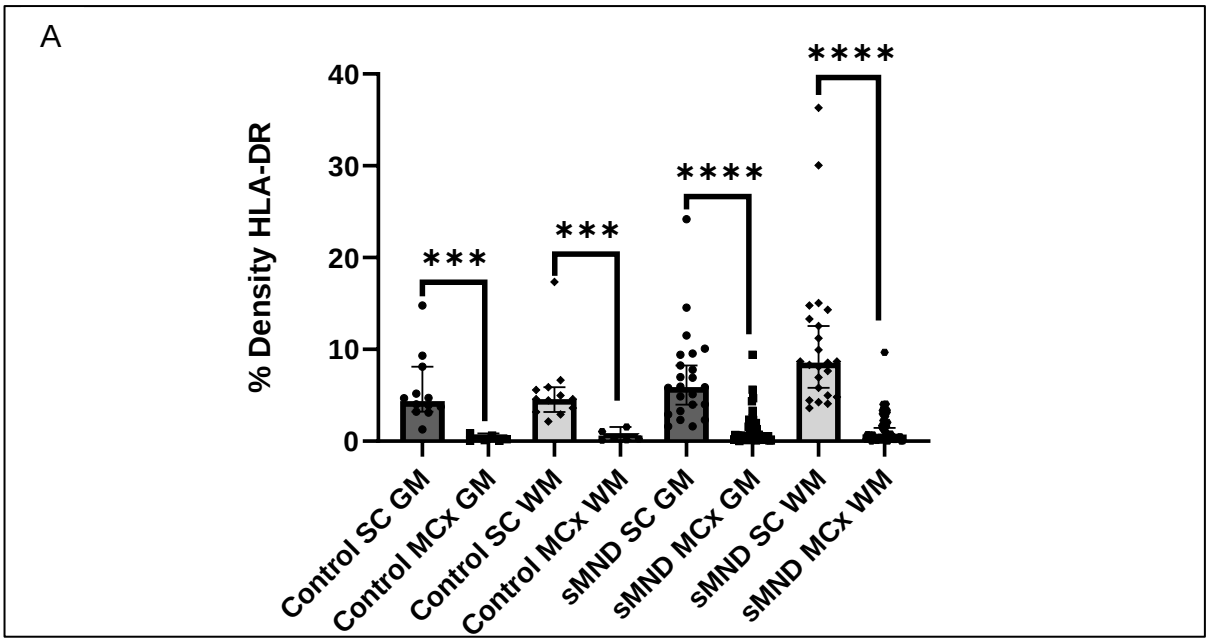

B

Disease Status	CNS Region		Median (% density)	95% Confidence Intervals (Lower, Upper)	Mann-Whitney U	P Value
Control	Spinal Cord	Grey Matter	4.351	3.203, 7.822	0	0.0001
	Motor Cortex		0.1659	-0.034, 0.670		
	Spinal Cord	White Matter	4.581	2.984, 8.008	0	0.0001
	Motor Cortex		0.2883	-0.051, 1.196		
sMND	Spinal Cord	Grey Matter	5.898	4.730, 9.088	68	<0.0001
	Motor Cortex		0.6251	0.7466, 1.778		
	Spinal Cord	White Matter	8.549	7.264, 14.17	17	<0.0001
	Motor Cortex		0.7057	0.947, 1.921		

Figure 4.81 HLA-DR Expression was Increased in the Spinal Cord compared to the Motor Cortex in both Control and sMND

***A**) HLA-DR expression was found to be significantly increased in the spinal cord compared to motor cortex, in the white and grey matter in both control and sMND cases. Bars represent median, error bars 95% confidence intervals. SC= spinal cord, MCx= motor cortex, WM= white matter, GM= grey matter.*

***B**) Table showing the median percentage area positive for HLA-DR, 95% confidence intervals and the results of the Mann-Whitney U pairwise comparisons.*

4.7.4 CD163

CD163 expression was compared between the spinal cord and motor cortex, in white and grey matter, using a one-way Kruskal-Wallis test, which indicted a significant difference between groups ($H(7)=83.81$, $p<0.0001$). Pairwise comparisons (Figure 4.82), by Mann-Whitney U, highlight greater CD163 expression in the spinal cord compared to motor cortex in control grey matter ($U=4$, $p=0.014$), and sMND white ($U=27$, $p<0.0001$) and grey matter ($U=68$, $P<0.0001$). No significant difference was observed in the white matter of control cases between the spinal cord and motor cortex ($U=9$, $p=0.101$).

A

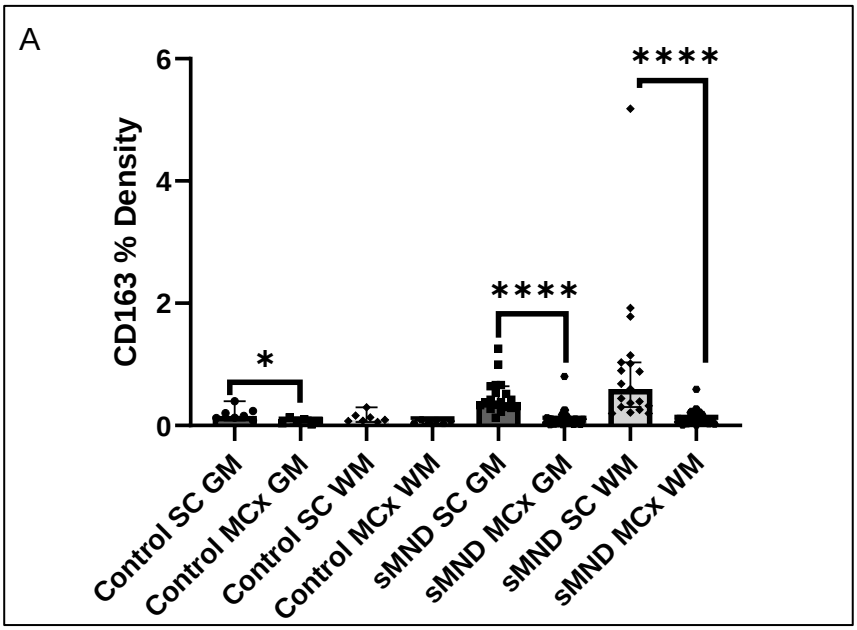

B

Disease Status	CNS Region		Median (% density)	95% Confidence Intervals (Lower, Upper)	Mann-Whitney U	P Value
Control	Spinal Cord	Grey Matter	0.1584	0.0917, 0.287	4	0.014
	Motor Cortex		0.05689	0.0215, 0.113		
	Spinal Cord	White Matter	0.09053	0.048, 0.205	9	0.101
	Motor Cortex		0.06113	0.036, 0.087		
sMND	Spinal Cord	Grey Matter	0.3834	0.346, 0.611	27	<0.0001
	Motor Cortex		0.07363	0.062, 0.136		
	Spinal Cord	White Matter	0.5973	0.386, 1.491	31	<0.0001
	Motor Cortex		0.08528	0.084, 0.140		

Figure 4.82 CD163 Expression was Increased in the Spinal Cord Compared to the Motor Cortex

***A**) CD163 expression was found to be significantly increased in the spinal cord compared to motor cortex, in the grey matter of control cases, and in both the white and grey matter sMND cases. Bars represent median, error bars 95% confidence intervals. SC= spinal cord, MCx= motor cortex, WM= white matter, GM= grey matter.*

***B**) Table showing the median percentage area positive for CD163, 95% confidence intervals and the results of the Mann-Whitney U pairwise comparisons.*

4.7.5 TREM2

TREM2 expression was compared between the spinal cord and motor cortex, in white and grey matter, using a one-way Kruskal-Wallis test, which indicted a significant difference between groups ($H(7)=111.1$, $p<0.0001$). Pairwise comparisons (Figure 4.83), by Mann-Whitney U, highlighted greater TREM2 expression in the spinal cord compared to precentral gyrus in control grey matter ($U=0$, $p=0.0004$) and white matter ($U=0$, $p=0.0004$), and sMND white ($U=56$, $p<0.0001$) and grey matter ($U=0$, $P<0.0001$).

A

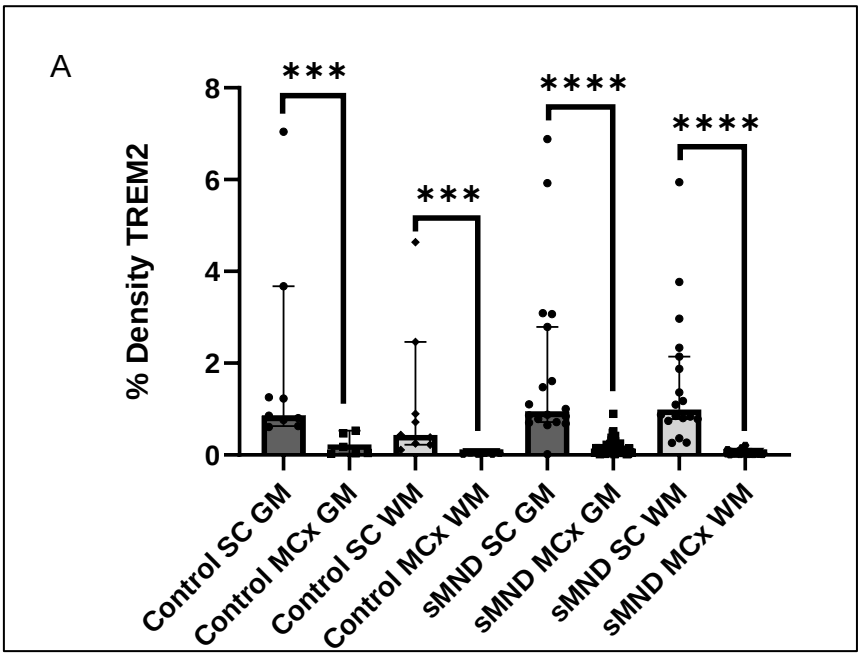

B

Disease Status	CNS Region		Median (% density)	95% Confidence Intervals (Lower, Upper)	Mann-Whitney U	P Value
Control	Spinal Cord	Grey Matter	0.8596	0.214, 3.536	0	0.0004
	Motor Cortex		0.1081	-0.261, 0.452		
	Spinal Cord	White Matter	0.439	-0.027, 0.452	0	0.0004
	Motor Cortex		0.02863	0.014, 0.043		
sMND	Spinal Cord	Grey Matter	0.9417	0.903, 2.774	56	<0.0001
	Motor Cortex		0.1264	0.125, 0.218		
	Spinal Cord	White Matter	0.9885	0.862, 2.301	0	<0.0001
	Motor Cortex		0.03592	0.032, 0.056		

Figure 4.83 TREM2 Expression is Increased in Spinal Cord compared to Motor Cortex

***A**) TREM2 expression was found to be significantly increased in the spinalcord compared to motor cortex, in the white and grey matter in both control and sMND cases. Bars represent median, error bars 95% confidence intervals. SC= spinal cord, MCx = motor cortex, WM= white matter, GM= grey matter*

***B**) Table showing the median percentage area positive for TREM2, 95% confidence intervals and the results of the Mann-Whitney U pairwise comparisons.*

4.7.6 TYROBP

TYROBP immunoreactivity was compared between the motor cortex and spinal cord in control and sMND cases, and in the white matter and grey matter, using a one-way Kruskal-Wallis test. This indicated a significant difference between groups ($H(7)=47.74$, $p<0.0001$, Figure 4.84). Pairwise comparisons using Mann-Whitney U tests indicated greater expression in the spinal cord than precentral gyrus in control white matter ($U= 0$, $p=0.002$) and both sMND white ($U=77$, $p<0.0001$) and grey matter ($U=147$, $p=0.012$), compared to the motor cortex. No significant difference was seen in control grey matter ($U=7$, $p=0.093$).

A

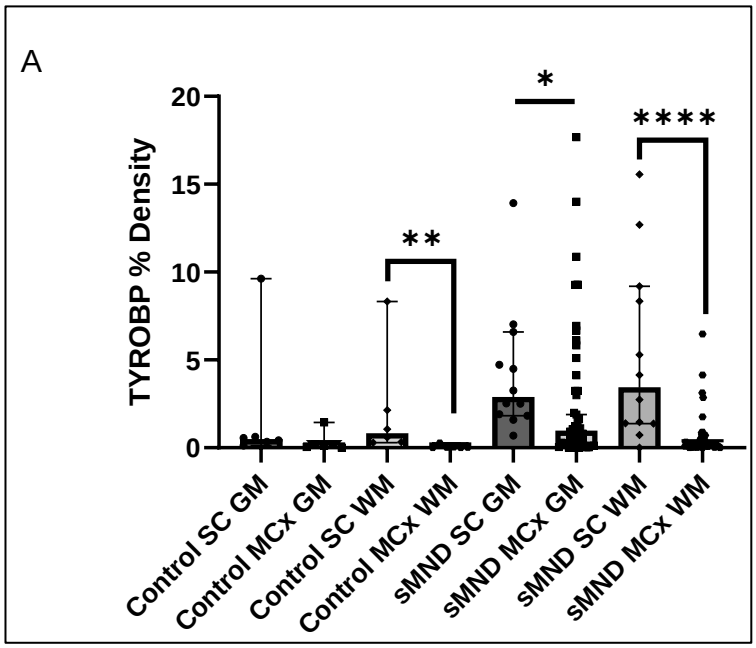

B

Disease Status	CNS Region		Median (% density)	95% Confidence Intervals (Lower, Upper)	Mann-Whitney U	P Value
Control	Spinal Cord	Grey Matter	0.496	-1.998, 5.896	7	0.0931
	Motor Cortex		0.1389	-0.244, 0.905		
	Spinal Cord	White Matter	0.8215	-1.155, 5.395	0	0.002
	Motor Cortex		0.02307	-0.048, 0.175		
sMND	Spinal Cord	Grey Matter	2.889	1.947, 6.564	147	0.012
	Motor Cortex		0.9676	1.521, 3.898		
	Spinal Cord	White Matter	3.443	1.999, 8.483	77	<0.0001
	Motor Cortex		0.1905	0.252, 0.964		

Figure 4.84 TYROBP Expression is Increased in the Spinal Cord Compared to the Motor Cortex in sMND.

***A**) TYROBP immunoreactivity significantly differed in the spinal cord and motor cortex, in control and sMND cases ($H(7)=47.74$, $p<0.0001$). Expression of TYROBP was increased in the spinal cord compared to the motor cortex in the white matter in control cases, and in both the white and grey matter of sMND cases. Bars show the median TYROBP staining density, error bars are the 95% confidence intervals. SC= spinal cord, MCx= motor cortex, WM= white matter, GM= grey matter*

***B)** Table showing the median and 95% confidence intervals given in Figure A, as well as the results of the pairwise comparisons.*

4.8 Immunohistochemistry in Extended Brain Regions

Having examined the main regions of the CNS associated with the development of sMND pathology, immunohistochemistry of the microglial markers and APOE was also performed on TMAs of other regions of the brain: the basal ganglia (putamen), and the prefrontal, temporal, and occipital cortices. Due to time constraints, TYROBP and TREM2 immunohistochemistry was not performed, and these data have not been quantified. However, a brief qualitative analysis is given below, within the context of the findings from the motor cortex.

4.8.1 IBA1

In both motor regions (motor cortex and basal ganglia) and extra-motor regions (prefrontal cortex, occipital, and temporal cortex), IBA1 immunohistochemistry highlighted microglia and perivascular macrophages. In control cases, both were present in low numbers in the white and grey matter. Microglia were broadly ramified, with small cell bodies and fine processes, however in some cases more reactive microglia with thickened processes or very occasionally ameboid cells were seen. There was also quite marked variability in the numbers of microglia including cases with very little microglial activity. Perivascular labelling was consistent throughout.

In sMND cases, the same cellular populations (perivascular macrophages and microglia) were present. Again, there was considerable inter individual variability. In the precentral gyrus, there appeared to be a greater degree of labelling. There were again the activated microglia with thickened processes and perivascular macrophages, possibly in greater numbers as well as occasional amoeboid

cells. The same cellular populations were also evident in the basal ganglia, and non-motor cortices. Without formal quantification, it is unclear if there is any increased microglial reaction in sMND cases. A comparison of IBA1 expression in high and low expressing cases, in control and sMND basal ganglia is given in Figure 4.84.

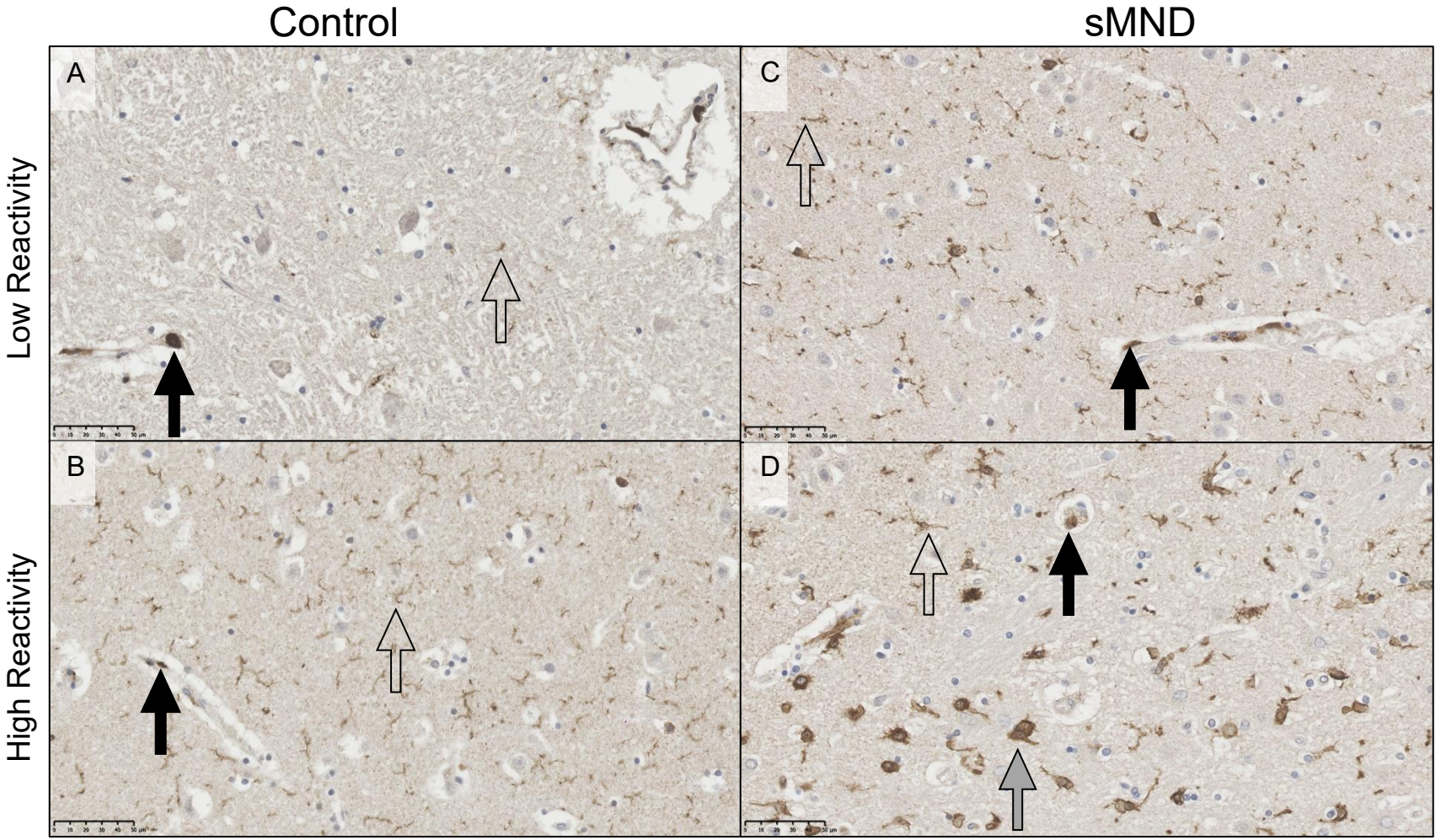

Figure 4.85 IBA1 Reactivity in the Basal Ganglia

IBA1 labelling in the basal ganglia varied greatly between both control and sMND cases. Figures A and B show areas of low (A) and high (B) reactivity in control cases. Figures C and D show areas of low (C) and high (D) reactivity in sMND cases. Black arrows show black perivascular macrophages, open arrows show ramified microglia, and they grey arrow shows ameboid microglia. Scale bars = 50µM

4.8.2 CD68

Overall CD68 labelling was reduced compared to IBA1 and HLA-DR overall. For control cases, labelling in the motor structures of the brain (motor cortex and basal ganglia) and non-motor brain structures this was largely limited to perivascular macrophages and occasional ramified microglia in the parenchyma.

In sMND motor cortex, a mild microglial reaction was observed, particularly in the grey matter compared to the white matter. More signal was observed overall, interstitial microglia had thickened processes plus some amoeboid microglia were observed in particularly activated cases. This reaction was not observed in the basal ganglia (Figure 4.85) or non-motor regions of the cortex in sMND individuals.

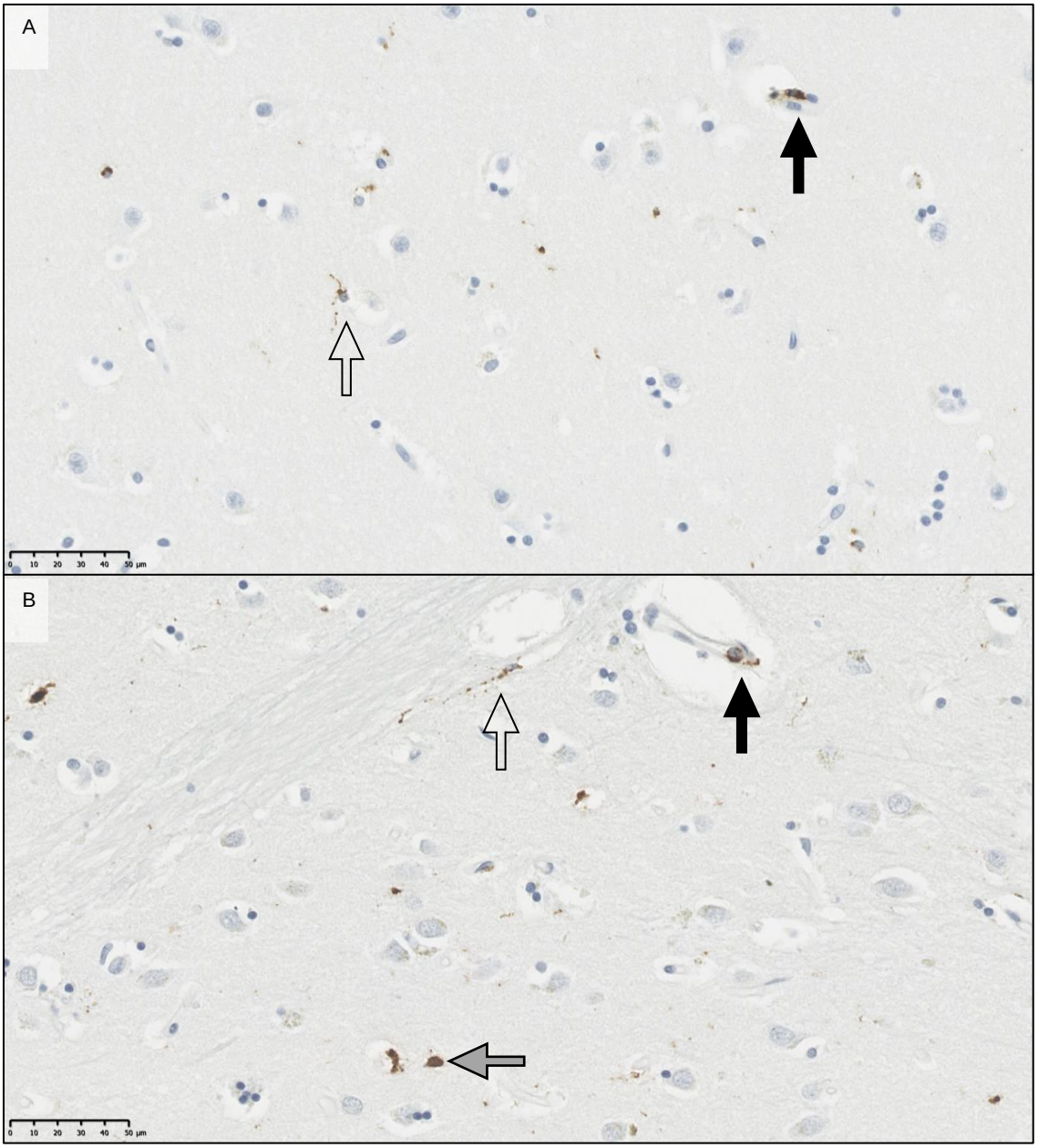

Figure 4.86 CD68 Expression in the Basal Ganglia

In control (A) and sMND (B) cases, CD68 reactivity was minimal compared to other microglial markers. CD68 labelled perivascular macrophages (black arrow) and some ramified microglia (open arrow) were observed in the main tissue parenchyma. A mild microglial response was observed in sMND cases characterised by more activated and ameboid microglia (grey arrow) in sMND parenchyma compared to control

Scale bars = 50µM

4.8.3 HLA-DR

Labelling was similar to that of IBA1, highlighting perivascular macrophages and microglia in the parenchyma. In control cases, HLA-DR labelling in all brain regions was similar to that observed in the motor cortex.

In sMND individuals, there was a possible increase in HLA-DR signal in both the motor and extra-motor regions of the brain, with increased labelling both activated ramified and ameboid microglia, and perivascular macrophages (basal ganglia shown in Figure 4.86). Quantification will be required to confirm this. Expression was highly variable between both control and sMND cases.

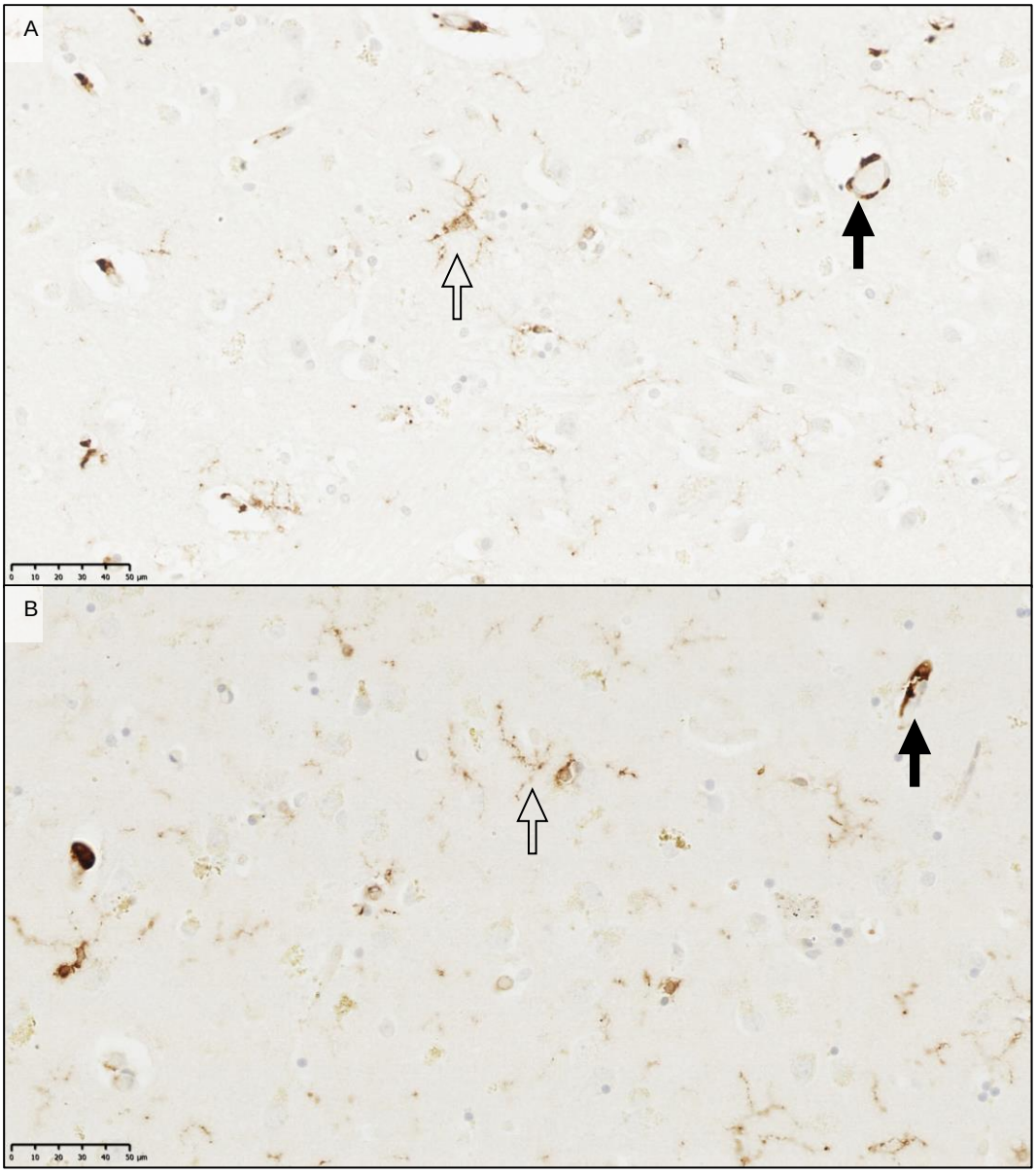

Figure 4.87 HLA-DR Expression in the Basal Ganglia

In control (A) and sMND (B) cases, HLA-DR labelled perivascular macrophages (black arrow) and ramified microglia (open arrow) were observed in the main tissue parenchyma. An increase in HLA-DR signal was observed in sMND compared to control, but cases showed great heterogeneity.

Scale bars = 50µM

4.8.4 CD163

As was observed in the motor cortex, CD163 labelling was reserved to perivascular macrophages, with negligible labelling of ramified microglia, across the basal ganglia and extra-motor brain regions. There was no obvious difference between control and sMND (Figure 4.87).

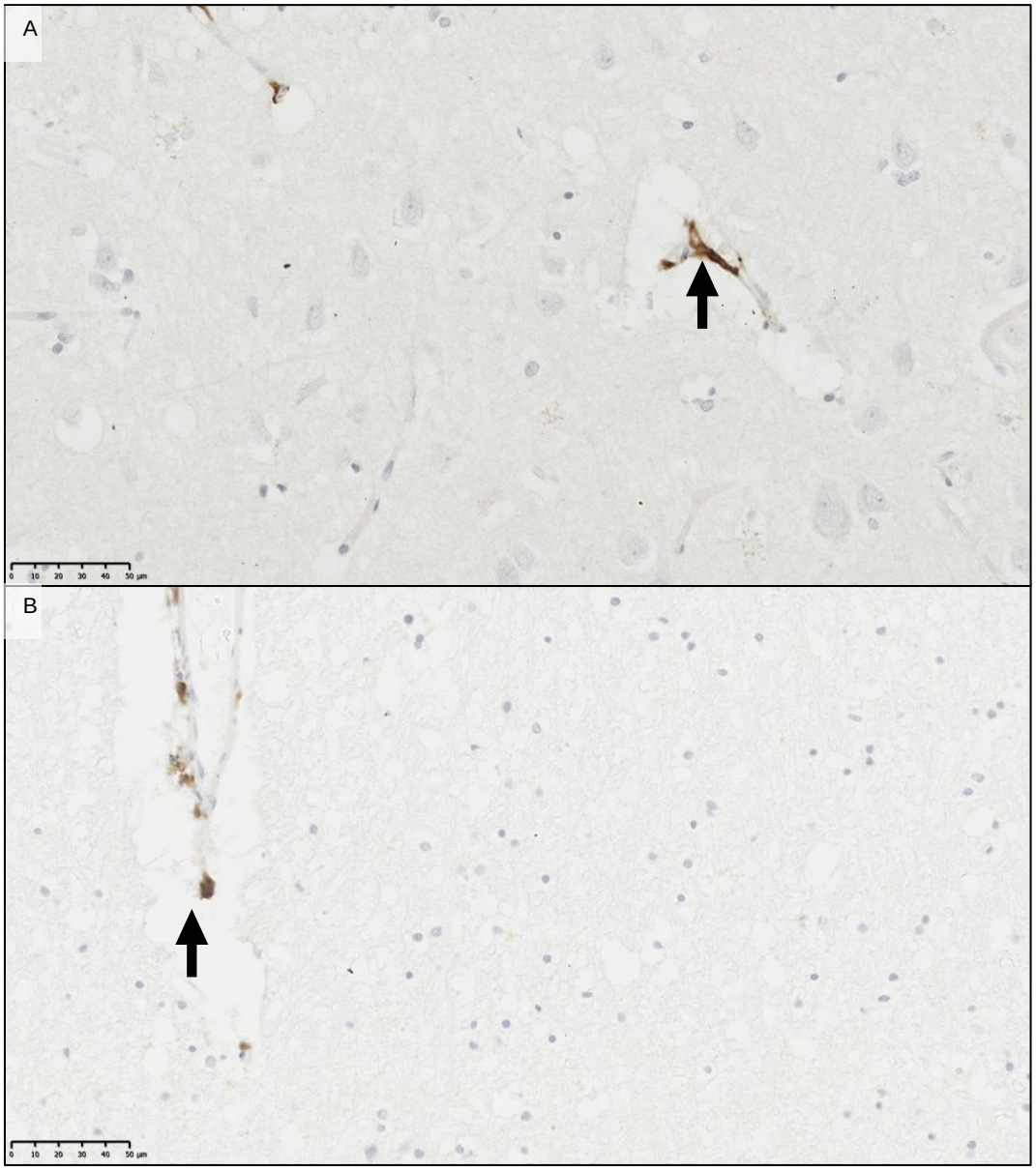

Figure 4.88 CD163 Expression in the Basal Ganglia

CD163 primarily labelled perivascular macrophages in the basal ganglia. Little difference was observed between control (A) and sMND (B) cases in the basal ganglia.

Scale bars = 50µM

4.8.5 APOE

As was observed in the spinal cord significant interpersonal variation in APOE expression was observed in the brain regions of both control and sMND individuals. As was observed in the spinal cord and motor cortex, there was some labelling of the neuropil which was generally darker in the grey matter compared to the white matter, as well as labelling of the blood vessels. In cortical regions and the basal ganglia (Figure 4.88), there was variable neuronal labelling as well as some glial cells labelled. Across the motor regions of the brain (motor cortex and basal ganglia) and non-motor regions, no noticeable difference the pattern of APOE expression was observed.

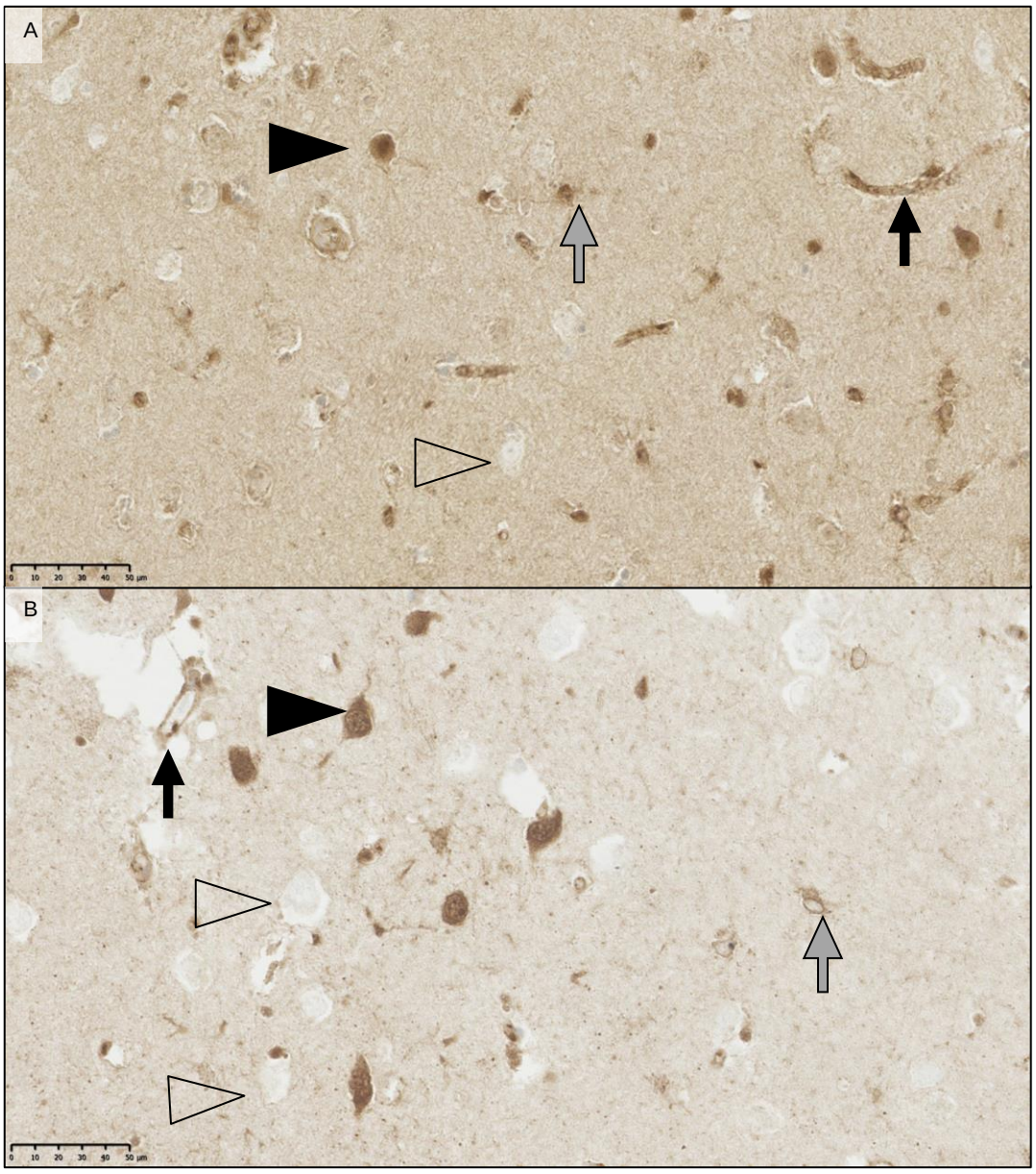

Figure 4.89 Expression of APOE in the Basal Ganglia

*In control (**A**) and sMND (**B**), APOE immunoreactivity labelled vascular structures (black arrows), as well as branched glia (grey arrow). Motor neurons were variably labelled with some showing high expression (black arrowhead), some neurons where devoid of any APOE expression (white arrow heads). No clear difference in immunolabeling was observed between control and sMND was observed, cases in both control and sMND varied greatly.*

Scale bars= 50µM.

4.9 Investigation of Cell-Specific Expression of TREM2, TYROBP and APOE.

Expression of APOE, TREM2 and TYROBP are thought to be expressed by a number of cells. To investigate the cell specific expression of these markers colocalization was performed with markers of astrocytes and microglia.

4.9.1 TREM2

In non-CNS tissue, TREM2 is primarily expressed by monocyte-type cells (Fahrenhold *et al.*, 2018). To confirm the antibody positively labels these, TREM2 expression was examined in bone marrow (Figure 4.90) and spleen (Figure 4.91). Both showed expression by rounded cells likely to be monocytes,

In the CNS, TREM2 expression is thought to be expressed primarily by microglia, however immunohistochemistry studies have failed to find evidence of microglial expression. Fahrenhold *et al. (2018)* failed to find expression of TREM2 in the parenchyma, unless following an infarct. The authors conclude these cells are likely to be recruited monocytes following blood brain barrier breakdown.

Spinal cord from sMND individuals was stained and imaged with TREM2, the stain chromophore dissolved, and the same slide re-stained with IBA1 as a marker of macrophage/monocyte cells. Several cells were positively stained for both TREM2 and IBA1, as well as many cells which were IBA1^{+ve} and TREM2^{-ve} (Figure 4.92).

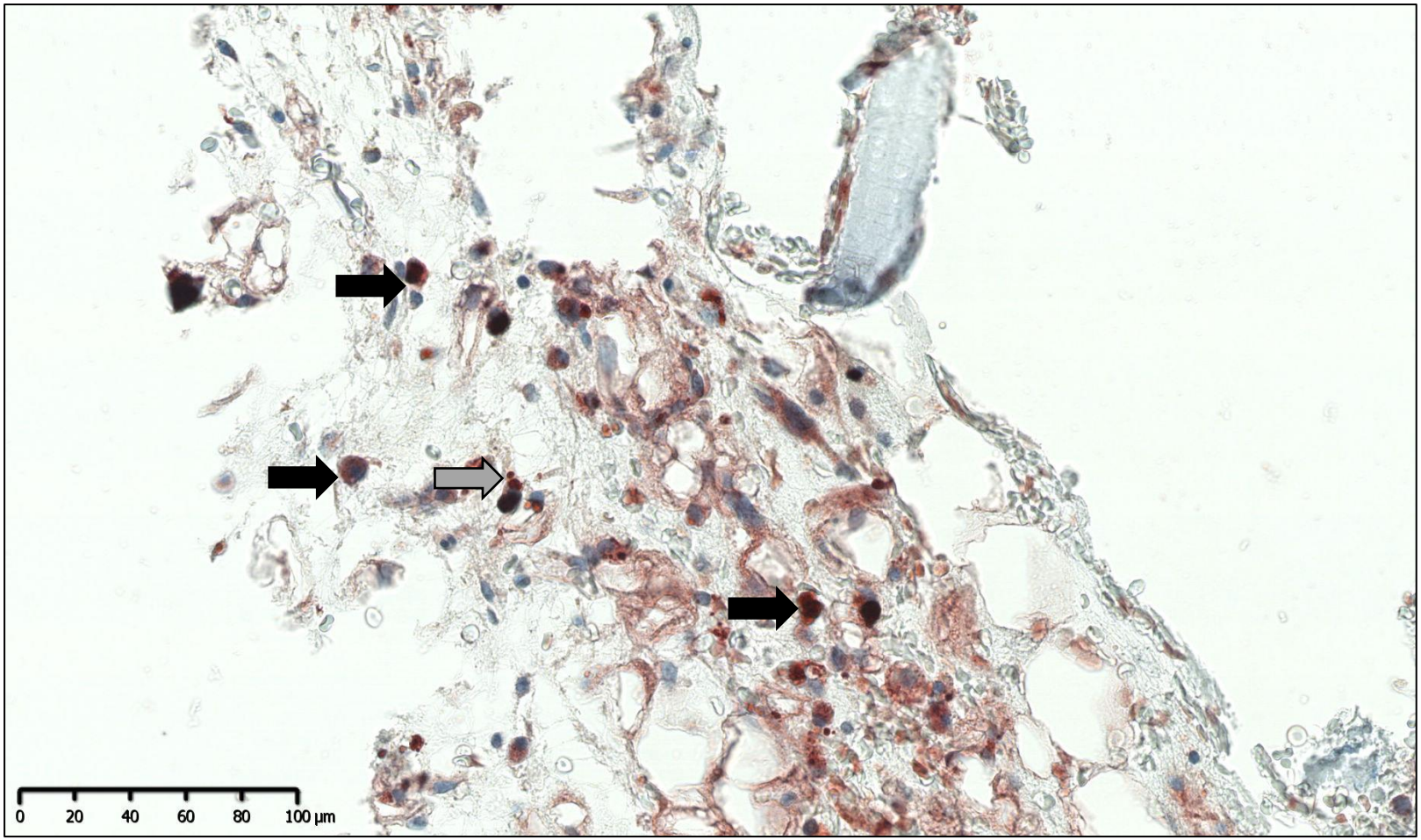

Figure 4.90 TREM2 Labelling in Bone Marrow

TREM2 labelling rounded cell with nuclei (black arrows), as well as the granules (grey arrow) observed in the spinal cord.

Scale bar= 100µm

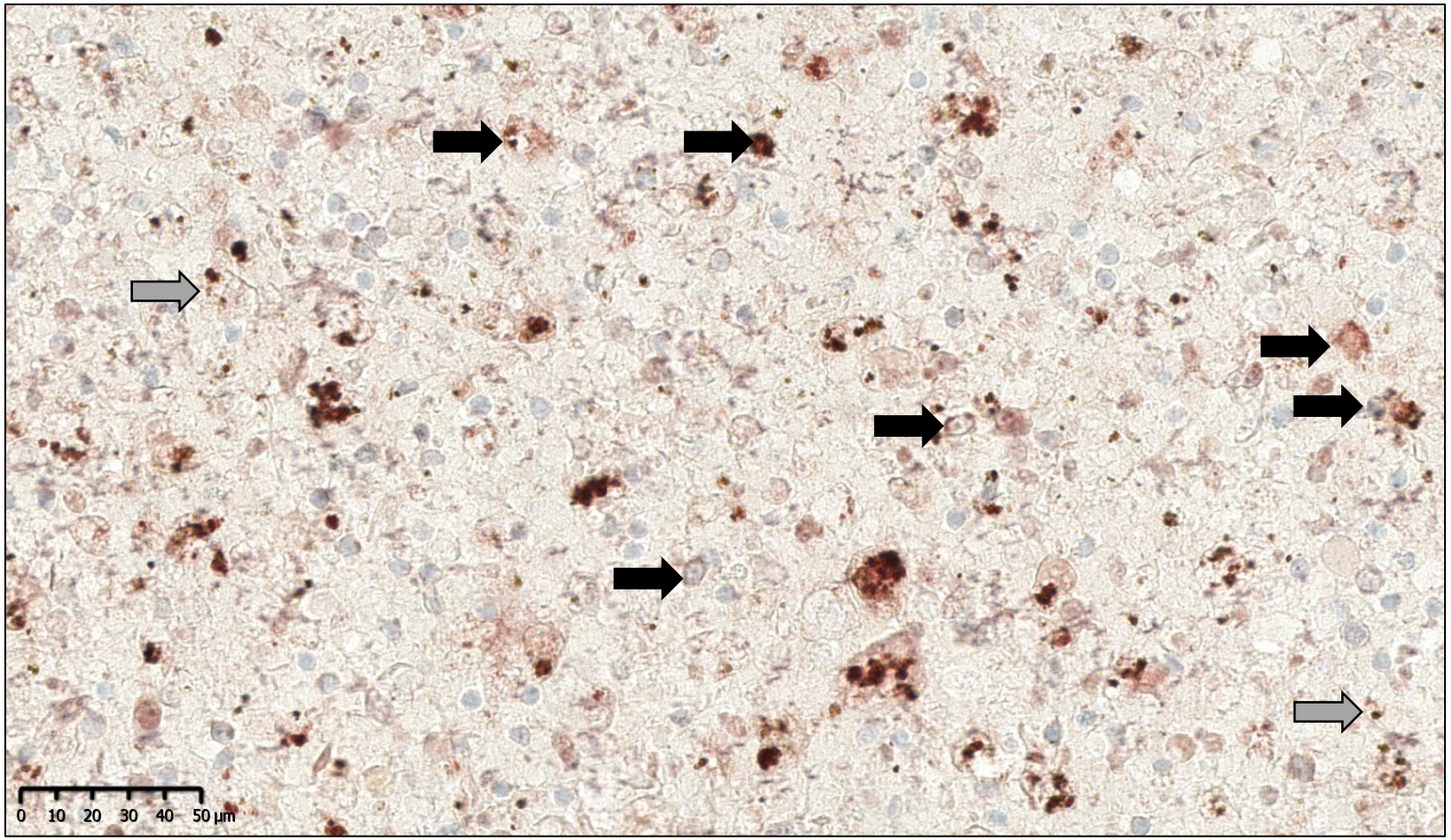

Figure 4.91 TREM2 Labelling in Spleen

Immunohistochemistry directed at TREM2 in the speel highlighted round cells with nuclei (black arrows) as well TREM2 positive granules.

Scale bar = 50µm.

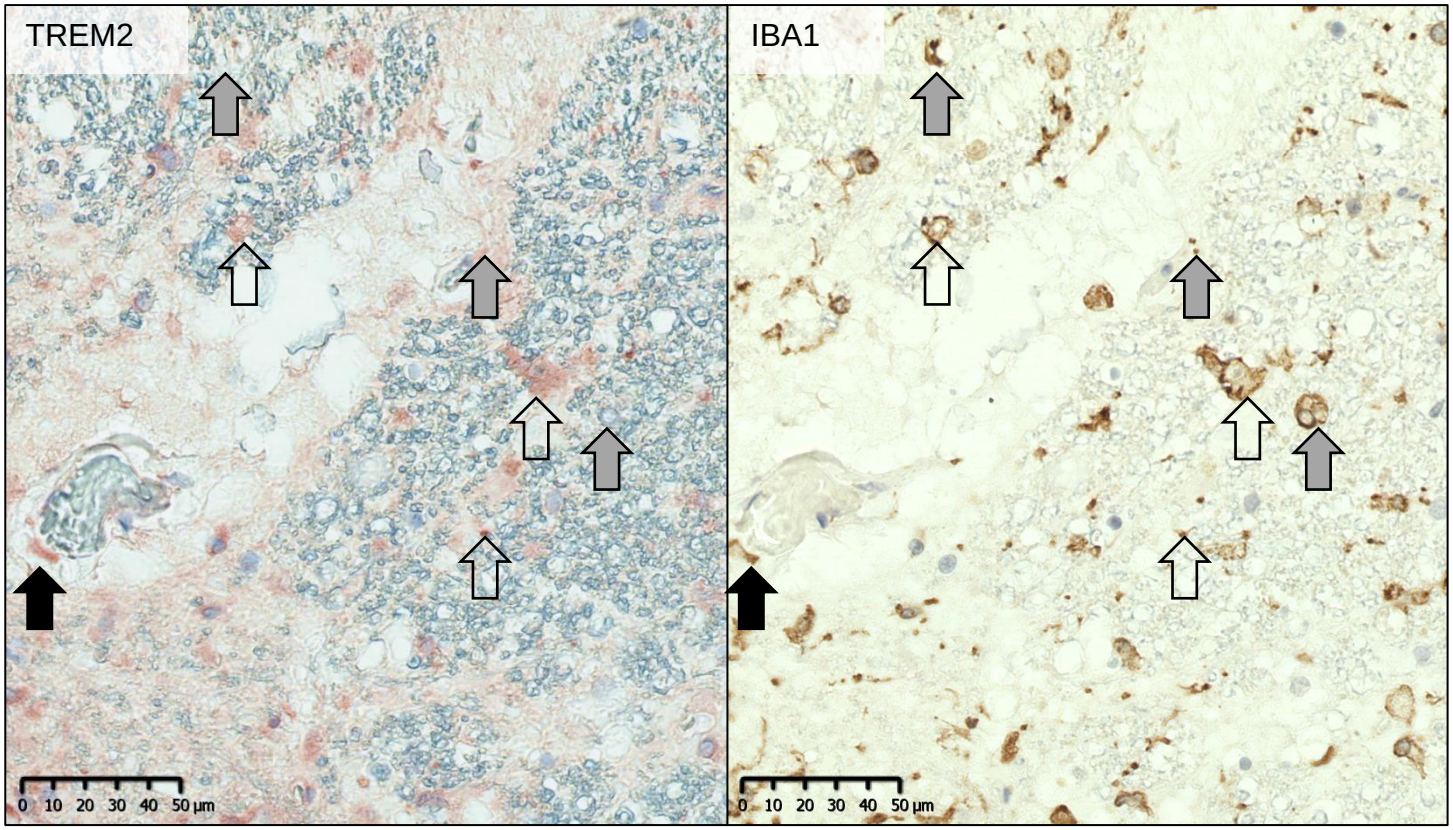

Figure 4.92 Colocalisation of TREM2 and IBA1 in sMND Spinal Cord

Staining and re-staining of TREM2 with IBA1 highlighted a subset of cells which were positive for both TREM2 and IBA1, some of which were perivascular (black arrow) and some in the main parenchyma (open arrow). Several cells were positive only for IBA1 (grey arrow).

Scale bar = 50µm.

4.9.2 TYROBP

TYROBP is largely thought to be expressed by microglia as well as perivascular macrophages and monocytes (Humphrey, Xing and Titus, 2015). Colocalisation was performed examining the expression of TYROBP with IBA1 by immunohistochemistry (Figures 4.93). TYROBP reactivity colocalised well with IBA1.

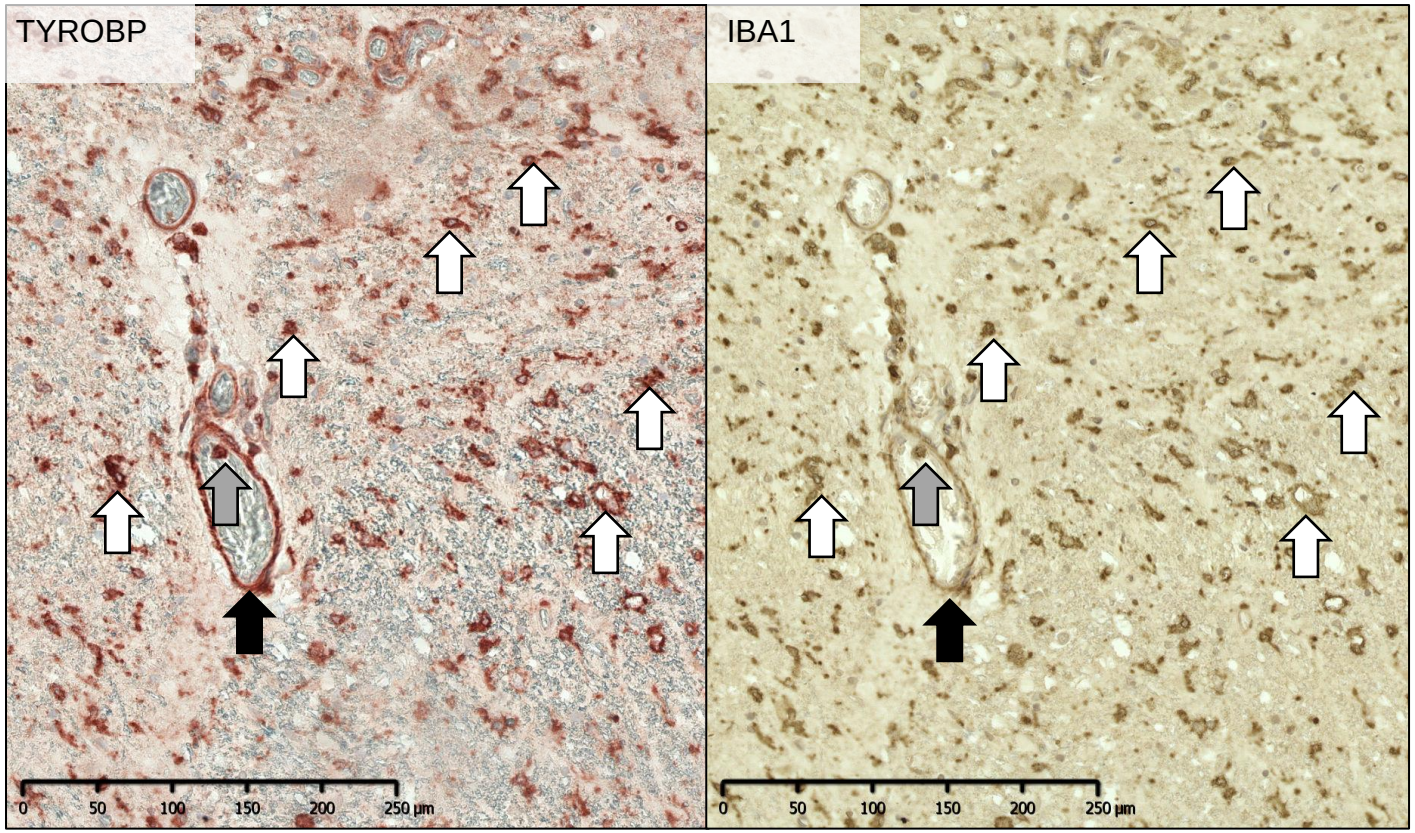

Figure 4.93 Colocalization of TYROBP and IBA1

Almost all TYROBP positive cells were also positive for IBA1. White arrows show parenchymal cells positive for IBA1 and TYROBP, the grey arrow highlights a monocyte within the blood vessel positive for TYROBP and IBA1. Black arrows show vascular labelling by both TRYOBP and IBA1.

Scale bar = 250µm.

4.9.3 APOE

APOE is thought to be expressed by both astrocytes and microglia in the CNS. The majority of cells expressing IBA1 also expressed APOE, and a number of IBA1 positive cells were APOE negative, indicating it is a subset of IBA1 positive cells which also express APOE (Figure 4.94).

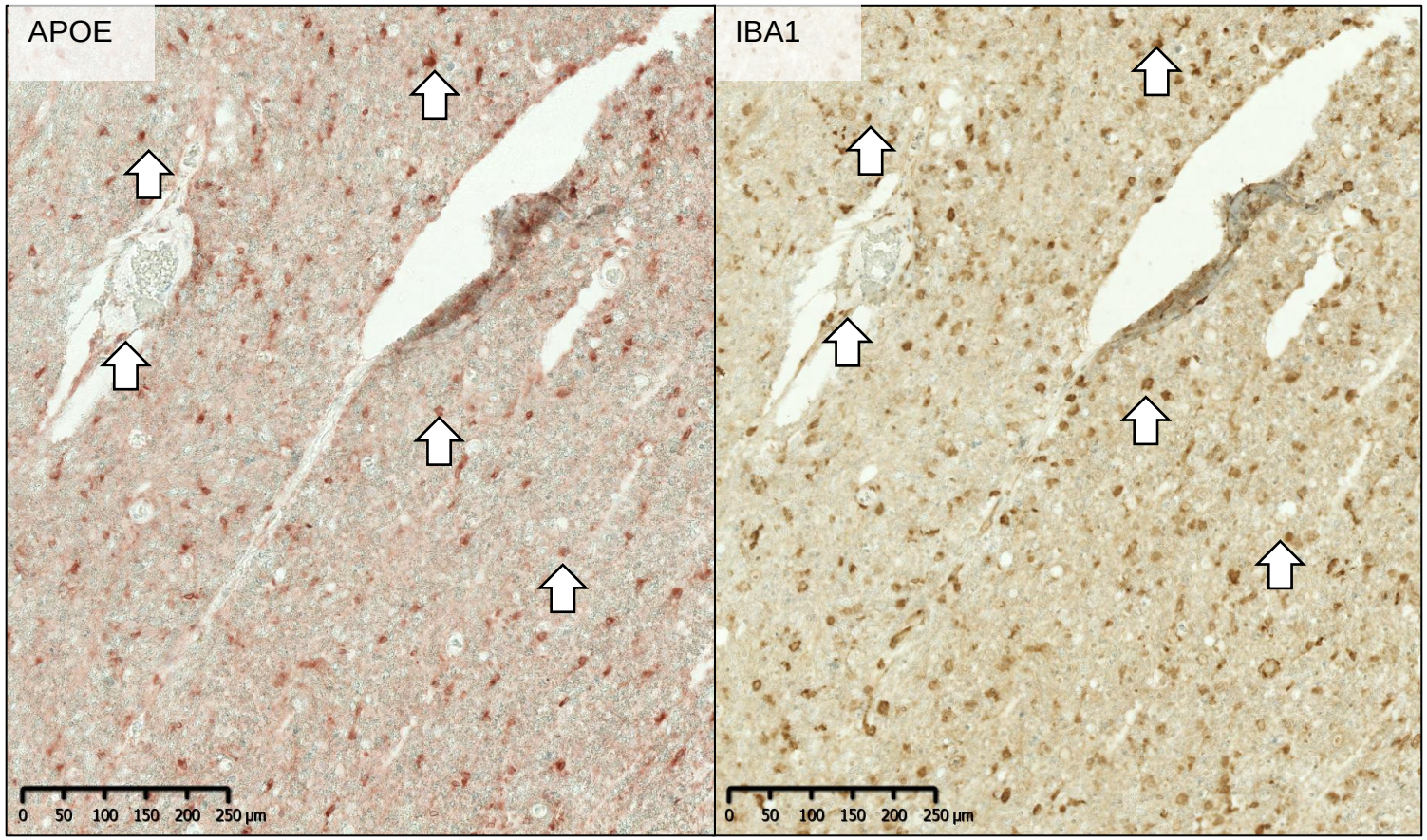

Figure 4.94 Colocalization of APOE and IBA1

In sMND spinal cord, most of the cells examined which were IBA1 positive were also APOE positive. A number IBA1 positive cells were negative for IBA1.

Scale bars = 250µm.

4.10 Real-Time Quantitative Polymerase Chain Reaction Quantification

Additional methods were sought to validate the expression of APOE, TREM2 and TYROBP in spinal cord. A novel method of RNA extraction was used known as Genome-wide RNA Analysis of Stalled Protein Synthesis (GRASPS) developed by Dr Guillame Hautbergue's Laboratory (unpublished). This method selectively isolates translating mRNA, by isolating ribosome-associated mRNA from the cytoplasm. By selecting the mRNA specifically which will be translated to protein, this should closer represent protein production than conventional mRNA. This method is still undergoing optimisation in human tissue and had not been performed in spinal cord *post-mortem* tissue prior.

4.10.1 RNA Extraction and cDNA Synthesis

Following RNA extraction, RNA concentration was assessed using the Nanodrop Spectrometer (Table 4.10). RNA concentration varied greatly, however did not vary significantly by disease status, or between input and GRASP status ($H(3)=2.385$, $p=0.539$). The optical density ratios (260:280 and 260:230) indicated some contamination of RNA samples. The ideal 260:280 for pure RNA is ~2.0. While most values did not reach this they were in an acceptable range (1.8-2.0). All 260:230 ratios were low (ideal value is between 2.0-2.2), which can indicate low RNA concentration or phenol contamination from the RNA extraction (Choi *et al.*, 2017).

Table 4.10 RNA Concentration and Quality Checks

	Sample Number	Case ID	Input			GRASP		
			RNA Concentration (ng/uL)	260:280	260:230	RNA Concentration (ng/uL)	260:280	260:230
Control	1	032/2000	39.4	1.85	0.17	62	1.79	0.15
	2	002/2000	40.8	1.87	0.38	51.7	1.57	0.12
	3	101/1992	44.1	1.8	0.26	72.5	1.8	0.21
sMND	4	135/1994	38.8	1.55	0.14	154.9	2	0.43
	5	089/1994	59	1.85	0.2	67.6	1.89	0.36
	6	1025/1989	72.4	1.87	0.21	11.4	1.47	0.03

Note. Highlighted cases show evidence of contamination

Following cDNA synthesis cDNA concentrations were taken again (Table 4.11). For pure DNA the 260:280 ratio is ~1.8. All values were low for both optical densities, indicating the presence of contaminants. This can artificially inflate concentration values.

Table 4.11 cDNA Concentration and Quality Checks

	sample Number	Case ID	Input			GRASP		
			cDNA concentration (ng/ul)	260:280	260:230	cDNA concentration (ng/ul)	260:280	260:230
Control	1	032/2000	277.3	1.37	0.47	203.7	1.44	0.49
	2	002/2000	277.7	1.35	0.44	212.0	1.43	0.61
	3	101/1992	262.9	1.45	0.50	264.3	1.44	0.59
sMND	4	135/1994	441.8	1.59	0.75	270.4	1.40	0.50
	5	089/1994	271.9	1.47	0.62	236.4	1.46	0.50
	6	1025/1989	187.6	1.43	0.36	233.7	1.44	0.45

4.10.2. Confirmation of cDNA Synthesis from Input and GRASPS RNA

To determine the success of cDNA synthesis, polymerase chain reaction (PCR) was performed on each cDNA sample using β Actin, and the product was run on an agarose gel. All samples produced a band at the desired product length 100 base pairs (Figure 4.95). The bands associated with input sample 4 and GRASPS sample 6 were dimmer compared to the other samples indicating a lower concentration of cDNA in these samples. The no template control (NTC) did not produce a band, indicating sample contamination had not occurred.

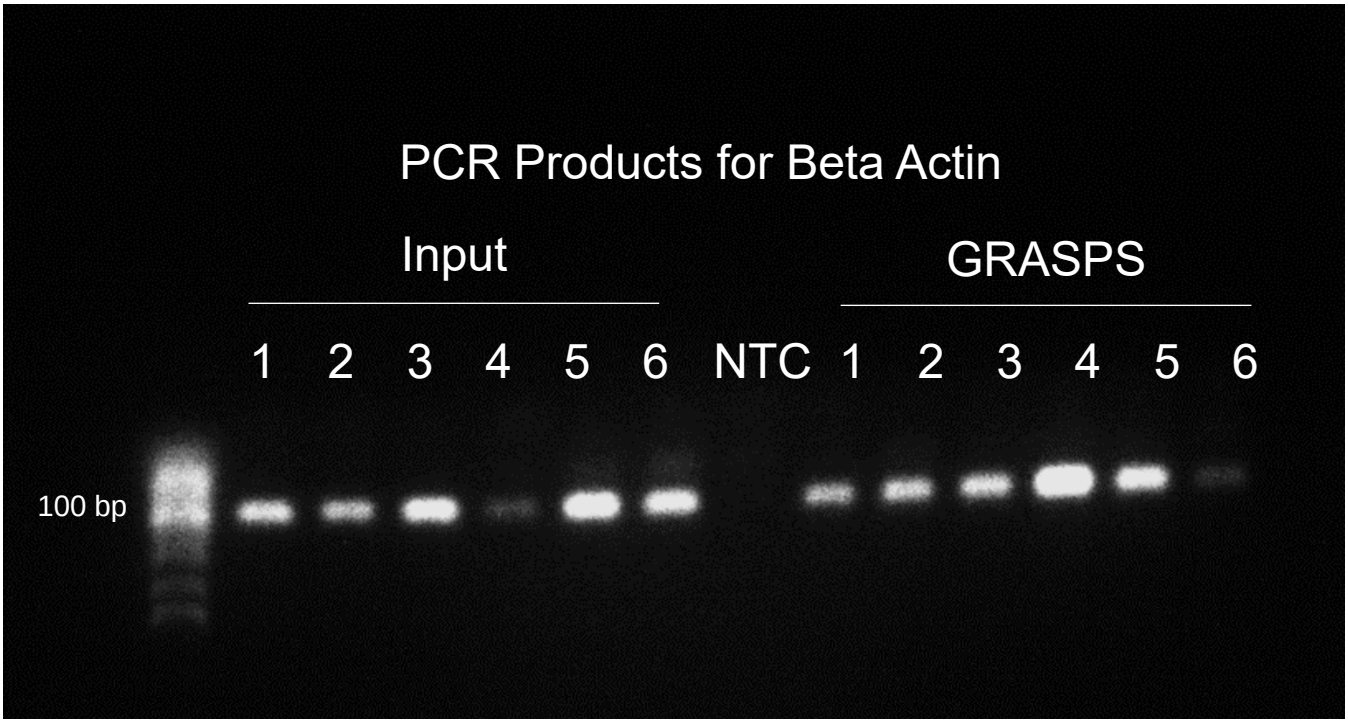

Figure 4.95 Agarose Gel Electrophoresis of RT-PCR Products for β Actin
β Actin was present in each of samples, however sample 4 input and sample 6 GRASPS show comparably less PCR product then the other samples indicating less cDNA was present in these samples. The no template control (NTC) did not show evidence of application, indicating contamination had not occurred.

4.10.3 Real-Time Quantitative Polymerase Chain Reaction

The expression of APOE, TREM2 and TYROBP were compared in control and sMND using real-time quantitative PCR (RT-qPCR), using both the cDNA generated

from the input mRNA and GRASPS RNA. Initially, 10ng of cDNA was used per reaction. Many samples did not reach the quantification threshold for the genes of interest, and the quantification cycle (Cq) values for the normalisation gene β Actin were high (ranging from 29.47-38.67) indicating insufficient starting cDNA quantity (the mean Cq values are given in Table 4.13). For all RT-qPCR experiments performed NTC's were also included whereby cDNA was omitted and the volume made up with ultra-pure dH_2O. The NTC did not generate a Cq value indicating undetectable levels of DNA or RNA contamination.

Table 4.12 Mean Cycle Quantification Values for the RT-qPCR using 10ng cDNA Input.

			Case	APOE	TREM2	TYRBOBP	β Actin
Input	sMND	1	032/2000	27.120	32.446	31.587	29.870
		2	002/2000	26.749	34.306	31.998	30.281
		3	101/1992	-	-	-	37.670
	Control	4	135/1994	-	-	37.337	36.125
		5	089/1994	26.393	31.457	30.343	29.879
		6	1025/1989	-	-	-	-
GRASPS	sMND	1	032/2000	-	-	37.824	32.627
		2	002/2000	-	-	-	-
		3	101/1992	27.774	32.759	31.969	29.819
	Control	4	135/1994	27.993	35.759	33.663	30.984
		5	089/1994	-	-	-	34.728
		6	1025/1989	-	-	-	-

As such, the cDNA input amount was increased to 50ng per reaction, which increased the number of samples which reached the quantification cycle and lowered the Cq values for the normalisation gene (Cq values ranged from 27.248-33.490, for Cq values see table 4.13). This said, samples 4 from the input cDNA and samples 4 and 6 from the GRASPS set of cDNA failed to reach the quantification cycle. NTCs did not generate a Cq value, indicating significant contamination had not

occurred. Time allowing the RT-qPCR would have been run again using a higher cDNA concentration, to bring all samples into the threshold of quantification.

Table 4.13 Mean Cycle Quantification Values for the RT-qPCR using 50ng cDNA Input.

			Case	APOE	TREM2	TYROBP	β Actin
Input	sMND	1	032/2000	26.780	31.658	29.645	28.310
		2	002/2000	26.759	31.363	29.236	28.130
		3	101/1992	27.344	30.415	30.205	28.030
	Control	4	135/1994	-	-	-	-
		5	089/1994	27.725	32.800	29.236	27.882
		6	1025/1989	27.046	33.624	29.042	27.248
GRASPS	sMND	1	032/2000	38.181	38.022	37.491	33.490
		2	002/2000	32.895	36.554	36.587	31.693
		3	101/1992	36.950	38.928	38.160	31.631
	Control	4	135/1994	-	-	-	-
		5	089/1994	38.591	-	38.160	32.193
		6	1025/1989	-	-	-	-

4.10.4 Gene Expression Analysis

Two of the GRASPS cDNA samples failed to produce usable Cq values, both of which were control samples (135/1994, 1025/1989). One control case from the input also failed to run (135/1994). As such, the input samples were selected for further analysis. However due to the low case numbers for each conditions statistical analysis was not performed. Genes of interest were normalised to the normalisation gene (β Actin) and ΔΔCq analysis performed and the relative concentration calculated ($2^{-\Delta\Delta Cq}$). Expression of APOE was 2.28x greater in sMND cases compared to control, TREM2 expression was 4.7x greater and TYROBP was 17.58 times greater in sMND cases compared to control (Figure 4.96). This is preliminary data, and due to low case and repeat number these data were not statistically analysed. However, these early findings do begin to corroborate the increased expression observed in the NanoString gene expression analysis, and

immunohistochemistry analysis. Further optimisation of the GRASPS method in human *post-mortem* spinal cord will be required.

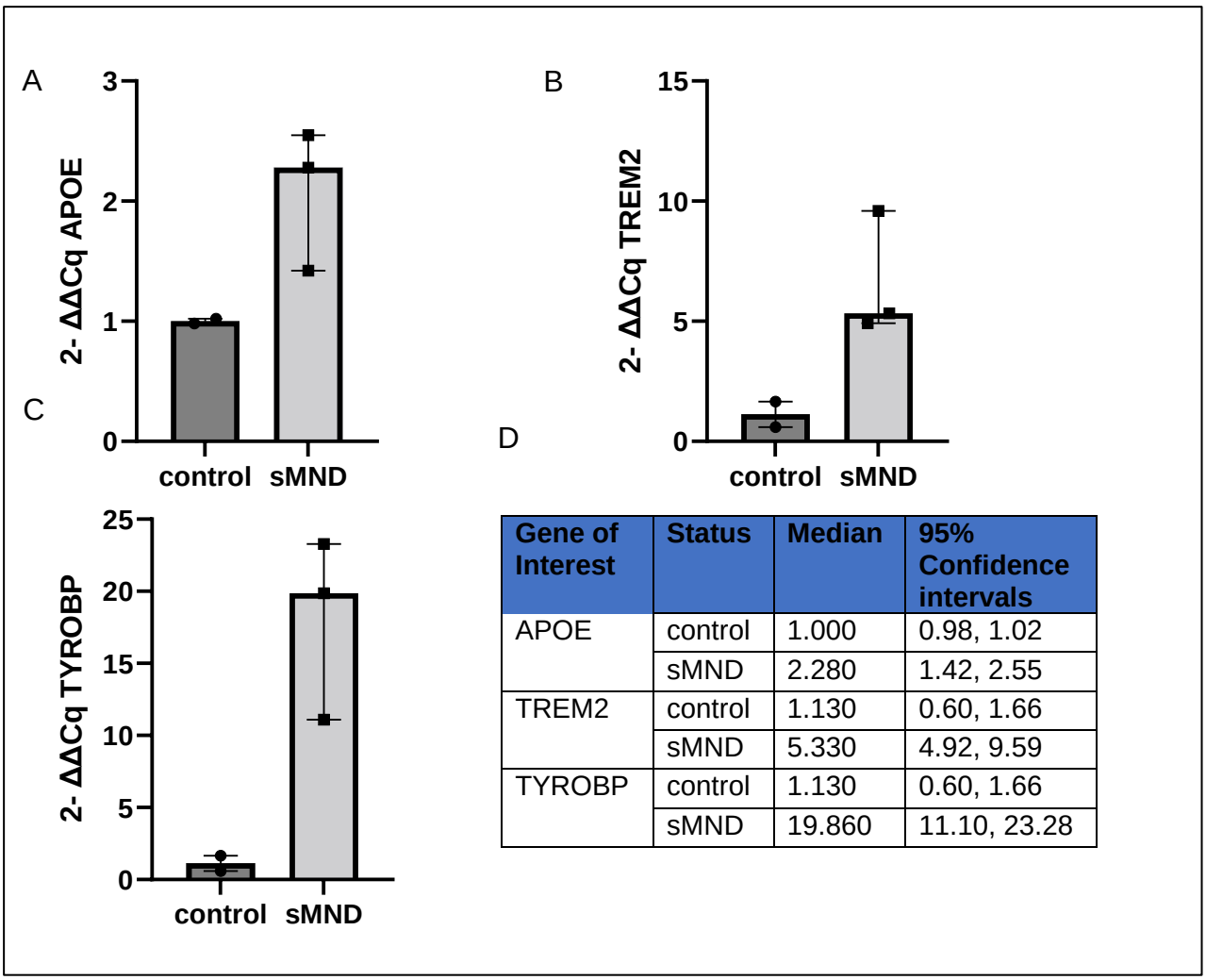

Gene of Interest	Status	Median	95% Confidence intervals
APOE	control	1.000	0.98, 1.02
	sMND	2.280	1.42, 2.55
TREM2	control	1.130	0.60, 1.66
	sMND	5.330	4.92, 9.59
TYROBP	control	1.130	0.60, 1.66
	sMND	19.860	11.10, 23.28

Figure 4.96 APOE, TREM2 and TYROBP mRNA were Increased in sMND

*Plots of $2^{-\Delta\Delta Cq}$ values for APOE (**A**), TREM2 (**B**), and TYROBP (**C**). In sMND cases, expression of APOE was 2.28x greater, TREM2 4.47x greater, and TYROBP was 17.58x greater compared to control cases. Bars show the median and error bars are 95% confidence intervals, these values are given in Table **D**.*

4.11 Summary

In this chapter, microglial pathology, and the expression of target proteins and microglial markers were characterised in control and sMND cases, in the spinal cord and motor cortex primarily, as well as the basal ganglia, and the prefrontal, temporal and occipital cortices.

In the spinal cord, expression of microglial markers was increased in the motor regions, particularly the lateral corticospinal tracts, in sMND compared to control. Microglia had transitioned from the homeostatic morphology observed in control to an activated phenotype. Expression of CD163 was limited to perivascular macrophages in control cases but extensive labelling was observed across the cord (although predominantly in the white matter) in sMND cases. Expression of HLA-DR was increased in the ventral horn and lateral corticospinal tracts in fast progressing sMND cases.

Expression of both APOE and TYROBP was increased in the motor regions of the spinal cord in sMND compared to control, but expression was not related to the length of survival. TREM2 expression in the spinal cord did not differ between control and sMND cases, but TREM2 expression was increased in the white matter (both dorsal column and lateral corticospinal tracts) of longer surviving sMND cases, indicating TREM2 may be protective in sMND.

The extent of white matter pallor in the lateral corticospinal tract of sMND cases was not associated with the expression of the assessed microglial markers of interest.

In the motor cortex, labelling with IBA1, CD68 and HLA-DR appeared to adopt a more activation-related morphological state with thicker processes and more amoeboid forms. However, no qualitative difference was observed between control

between control and sMND in terms of the percentage of tissue immunostained. CD163 expression did not differ between control and sMND cases. Both APOE and TREM2 showed little difference qualitatively or quantitatively between control and sMND cases. However, TYROBP labelling was increased in both the white and grey matter in sMND cases compared to control. No marker assessed in the motor cortex was associated with the length of patient survival.

Expression of markers was compared between spinal cord and motor cortex. For all markers assessed, expression was greater in the spinal cord compared to the motor cortex in sMND white and grey matter. This validates findings from Chapter 3, whereby the inflammatory response was significantly increased in the cord compared to the motor cortex in sMND.

In the basal ganglia, qualitative analysis (classical microscopy) indicated a potential microglial response in sMND. IBA1 labelling showed some highly reactive and even ameboid microglia in sMND cases. CD68 labelling showed a mild microglial reaction in sMND, with more microglia observed in the parenchyma in sMND compared to control. HLA-DR labelling showed a potential increase in labelling in sMND cases. No quantitative difference was observed in the basal ganglia between sMND and control for both CD163 and APOE. Extra-motor cortical regions overall showed very little change in expression of microglial markers and APOE on control and sMND cases.

It should be noted that in both sMND and control, there was great heterogeneity in the expression of all markers assessed and in all CNS regions. This highlights the necessity for adequately powered sample sizes when examining pathology in humans.

To investigate the cell-type associated with the expression of TREM2, TYROBP, and APOE, a co-localisation study was performed using IBA1 as a microglial marker and GFAP as an astrocyte marker. TREM2 labelling was first examined in tissues known to express TREM2 – bone marrow and spleen. These showed positive staining of rounded cells, likely monocyte type cells, and a similar pattern of staining as was observed in the spinal cord. Many cells labelled with both IBA1 and TREM2 including rounded cells in the parenchyma and perivascular regions. Many cells that labelled with IBA1 were not stained by TREM2 indicating that only a subpopulation of microglia express TREM2. Colocalisation of TYROBP with IBA1 and GFAP, indicated TYROBP in predominantly microglial, and not expressed by astrocytes, which is keeping with previous literature. APOE appeared to be highly expressed by IBA1-positive microglia.

To compliment the immunohistochemistry work, RT-qPCR was piloted using GRASPS, which selectively assesses ribosome-bound mRNA. This is hypothesised to better represent protein expression than total mRNA. RNA was successfully extracted, both regular, whole mRNA and GRASPS. Although underpowered, RT-qPCR for the input RNA did suggest an increase in APOE, TYROBP and TREM2 in sMND compared to control. Further repeats with greater sample sizes would be required to draw statistical conclusions.

Overall, expression microglial pathology was increased in sMND compared to control in the spinal cord, confirming our initial hypothesis. This was more marked in the white matter and involved pan-microglial markers as well as antigen presentation and phagocytosis markers as well as members of the APOE-TREM2-TYROBP pathway, confirming the findings of the previous chapter. The remaining motor regions, microglia did qualitatively appear activated however this was not always

observed quantitatively. Microglia activation was minimal in non-motor regions of the cortex in sMND cases, which did not confirm our hypothesis.

Chapter 5 Discussion

The inflammatory transcriptomic profile of sMND was characterised in the *post-mortem* spinal cord and motor cortex. This broadly showed an upregulation of inflammation in the spinal cord. The motor cortex did not show a significant dysregulation of inflammatory signalling in sMND. Cox-proportional hazards regression highlighted genes from both the motor cortex and the spinal cord, which were associated with the length of patient survival. Microglial/macrophage deconvolution analysis was performed to further explore the microglial signature. Pre-published data sets were re-analysed and compared with the NanoString data: CD163, APOE TREM2 and TYROBP were selected for further investigation.

The expression of these targets, along with markers of microglial activation, were compared in the spinal cord and motor cortex of control and sMND individuals, using immunohistochemistry. These data showed a similar pattern of expression. The motor regions of the spinal cord showed a strong inflammatory response in sMND, whereas the precentral gyrus qualitatively showed some microglial activation, but quantitatively very little inflammation was observed in sMND cases. Increased expression of TREM2 in the spinal cord, was associated with a slower rate of patient decline. The results of the gene expression analysis and immunohistochemistry for these markers are summarised in Table 5.1.

Further brain regions were examined qualitatively, however, these broadly showed little inflammatory response in sMND cases.

Table 5.1 Summary of Target Gene and Protein Expression in sMND Spinal Cord and Motor Cortex.

CNS Region	Data Set		IBA1	CD68	HLA-DR	CD163	APOE	TREM2	TYROBP
Spinal cord	FPPE NanoString		NC	NC	NC	↑ + ↑S	↑	↑	↑
	Frozen NanoString		NC	↑	NC	↑	↑	↑	↑
	RNA Seq.		NC	NC	NC	↑	↑	↑	↑
	IHC	VH	↑	↑	NC	↑	↑	NC	↑
		LCST	↑	↑	↑	↑	↑	NC + ↑S	↑
		DC	NC	↑	NC	↑	NC	NC + ↑S	NC
Motor Cortex	Frozen NanoString		NC	NC	NC	NC	NC	NC	NC
	Microarray		NC	NC	NC	NC	↑	↑	NC
	IHC	WM	NC	NC	NC	NC	NC	NC	↑
		GM	NC	NC	NC	NC	NC	NC	↑

Key: IHC = immunohistochemistry, VH= Ventral Horn, DC= Dorsal Column, LCST = LCST, NC= No change, ↑= upregulation, ↑S= upregulated in slower progressing sMND

5.1 Inflammation is Increased in sMND

The inflammatory transcriptome has been widely examined in the spinal cord in both human MND (Dangond *et al.*, 2004; Jiang *et al.*, 2005; Offen *et al.*, 2009; Figueroa-Romero *et al.*, 2012; Jones *et al.*, 2015; Brohawn, O'Brien and Bennett, 2016; Andrés-Benito *et al.*, 2017) and animal models of MND with SOD1, C9orf72, FUS and TDP-43 mutations (Yoshihara *et al.*, 2002; Schludi *et al.*, 2017; Funikov *et al.*, 2018; Hunter *et al.*, 2021). The precentral gyrus has been less widely examined however, given the motor cortex and spinal cord are both considered key sites of neuronal generation in MND, it was hypothesised inflammation would be increased in both regions. Both the gene expression and immunohistochemistry data indicated a significant inflammatory response in the spinal cord, but little inflammation was observed in the motor cortex, thus disproving the initial hypothesis.

The data surrounding inflammation in the motor cortex varies greatly. Wang *et al.* (2006) demonstrated a significant downregulation of inflammation in the motor cortex in human MND. Microarray analysis revealed 275 significantly differentially expressed genes, 265 of which were downregulated. However, this study may be considered rather underpowered, consisting of five MND cases and three controls. Lederer et al. (2007) used microarray technology to quantify gene expression in 11 sMND cases and 9 controls. Pathway analysis was performed using all genes significant at the uncorrected p value, which showed an upregulation of inflammatory and immune pathways. However, once more stringent corrections were applied, 57 genes were found to be significant, 40 of which were downregulated and 17 upregulated. The dysregulated genes were not associated with inflammatory signalling. Aronica *et al.* (2015), also used microarray technology to quantify gene expression in sMND motor cortex and found a significant upregulation of genes

associated with antigen presentation and processing, as well as cytokine release. In the current study, great heterogeneity was observed between cases, both in control and sMND, in the motor cortex, which could contribute to the different patterns of gene expression observed between studies. To remedy, this larger cohorts may be needed however this remains challenging with *post-mortem* tissue.

5.1.1 The Motor Cortex and Spinal Cord Represent Different Inflammatory Environments

The NanoString analysis, supported by immunohistochemistry has highlighted differences in the neuroinflammatory response between the motor cortex and spinal cord in sMND, indicating the motor regions have different disease environments. Wang and colleagues (2006), compared their gene expression findings from the motor cortex to MND *post-mortem* spinal cord gene expression data in the discussion of their paper (Dangond *et al.*, 2004), and found different groups of genes appeared to be of importance in these regions. The authors also commented on the lack of inflammation observed in the motor cortex compared to previous spinal cord findings. Lederer et al. (2007) compared the expression of 2266 genes detected via microarray in the motor cortex, to a previously published spinal cord data set, and did not find a correlation, suggesting the gene expression signature in these regions was very different. Of all the genes examined only 14 showed similar patterns of dysregulation between cord and cortex.

The differences in the inflammatory response in the motor regions of the CNS may be explained by differences in the pathology of these regions. Significant motor neuron loss is routinely observed in ventral horn of the spinal cord (Ince, Highley and

Wharton, 2015). Loss of neurons and the Betz cells has been described in the motor cortex (Murayama *et al.*, 1991; Brettschneider *et al.*, 2014). However, more rigorous and stereological studies, have shown no change in the number or size of motor neurons in the motor cortex in MND (Gredal *et al.*, 2000; Toft, Gredal and Pakkenberg, 2005). As such, the increased inflammatory and microglial reaction in the cord may reflect more active neuronal degeneration in the spinal cord compared to the motor cortex.

In the current study, increased immunolabelling of microglial markers was observed in the spinal cord in both the white and grey matter of sMND cases: indicating increased microglial activation, phagocytosis, and microglial-immune activity in the spinal cord. Interestingly, the microglial response has been shown to vary with by CNS region (Ritzel *et al.*, 2015). Microglia from the spinal cord tend to show a greater inflammatory response compared to microglia from the cortex following injury (Batchelor *et al.*, 2008). Spinal cord lesions have to been found to produce a greater microglial response and blood-brain-barrier dysfunction than cortical lesions (Schnell *et al.*, 1999; Bartanusz *et al.*, 2011). Microglia isolated from the spinal cord, were also more likely to show age-related deficits in phagocytosis compared to cortical microglia (Ritzel *et al.*, 2015). As such the increased inflammatory response in the spinal cord in sMND, may also result from spinal cord microglia having a lower threshold for activation compared to cortical microglia.

5.2 Inflammatory Pathways in sMND

Analysis of the transcriptomic data from sMND spinal cord highlighted several key genes and pathways which were taken forward for further analysis. These shall now be discussed in turn.

5.2.1 Phagocytosis

Phagocytosis is the process by which cells engulf and destroy large particles (Butler *et al.*, 2021). This is usually performed by specialised macrophage cells, in the CNS microglia are the primary phagocytes.

From the transcriptomic spinal cord data, the phagosome pathway was one of the most consistently upregulated pathways, as was Fc Gamma mediated phagocytosis. Furthermore, CD68 – the classical marker of phagocytic microglia was found to be upregulated. This was supported by immunolabelling of CD68, which showed significant upregulation in the motor regions and the dorsal column in sMND. This corroborates previous pathological reports which have shown increased $CD68^{+ve}$ pathology in the ventral horns and white matter tracts in MND (Graves *et al.*, 2004; Henkel *et al.*, 2004). In the corticospinal tract, increased CD68 positive pathology was associated with faster disease progression (Brettschneider, Toledo, *et al.*, 2012), however, the current study did not replicate these findings.

Similarly, increased IBA1 immunolabelling, was also observed in the motor regions of the spinal cord in the current study. IBA1 is key protein in the process of membrane ruffling, the formation of membranous protrusions used to engulf debris during phagocytosis (Ohsawa *et al.*, 2000). In *post-mortem* spinal cord, IBA1 labelled microglia were found to be upregulated in MND cases, particularly in the corticospinal tracts, and correlated positively with more rapid disease progression

(Brettschneider, Libon, *et al.*, 2012). Furthermore, Spencer *et al.* (2020), found that IBA1 immunoreactivity was reduced in those MND cases with longer disease duration. Here, IBA1 immunoreactivity was not associated with survival time.

Phagocytosis is a critical process for the maintenance of homeostasis in the brain. First, removing apoptotic cells prevents leakage of potentially toxic intracellular contents (Yu *et al.*, 2022). These intracellular contents not only directly cause toxicity, but act as DAMPS, triggering a further neurotoxic microglial phenotype. Clearance of apoptotic cells by microglia also suppresses the initiation of inflammatory signalling, inducing a more anti-inflammatory phenotype (De Simone, Ajmone-Cat and Minghetti, 2004; Fraser, Pisalyaput and Tenner, 2010)

Phagocytosis has been found to be dysfunctional in MND. Using sMND patient blood samples, Quek *et al.* (2022) developed monocyte-derived microglia-like cells (MDMi) to examine differences between microglia in sMND and control cases, and differences between fast and slow progressing cases. Compared to MDMis derived from control blood samples, sMND MDMis had significantly shorter processes, and reduced branching. Microglia-like cells from sMND had impaired phagocytic ability, that was worsened with faster disease progression (Noh *et al.*, 2020; Quek *et al.*, 2022).

Dysfunctional microglia may contribute to the pathological translocation of TDP-43 from the nucleus to the cytoplasm. Using a transgenic zebrafish model, which co-expresses green fluorescent protein with TDP-43 and microglia which express mCherry, Svahn *et al.* (2018) were able to visualise the nucleocytoplasmic transmission of TDP-43, and microglial dynamics *in-vivo*. After the initiation of motor neuron death via UV, microglia rapidly approached the damaged neuron and

phagocytosed the soma. Microglia were also shown to phagocytosed TDP-43 granules in the nucleus and break these particles down. Microglial populations were depleted via morpholinos targeted at the macrophage transcription factor, PU.1. After initiation of motor neuron death in the absence of functional microglia, motor neurons showed a more typical pattern of neurodegeneration characterised by swelling of the soma. Microglial depletion also resulted in the translocation of TDP-43 from the nucleus to the cytoplasm, a key feature of MND pathobiology. Although this is quite an artificial model of motor neuron death in MND, it indicates dysfunctional microglial phagocytosis may contribute to the typical TDP-43 pathology observed in models of MND and human pathology.

5.2.2 HLA-DR and Antigen Presentation

HLA-DR is a component of major histocompatibility complex class II (MHC-II) protein and is widely used as a marker of activated microglia, in CNS based pathological studies. HLA-DR is not specific to microglia and is also expressed by a number of peripheral leukocytes including monocytes.

Here, HLA-DR labelling was observed to be increased in the lateral corticospinal tracts the spinal cord in sMND. HLA-DR expression has been found to be upregulated in MND. Microglia expressing HLA-DR, along with other MHCII component proteins were found abundantly in the ventral horn of the spinal cord, and grey matter of the precentral gyrus, the full corticospinal tract, and the motor nuclei in the brain stem (Kawamata *et al.*, 1992). Qualitatively, the current study noted an increase in HLA-DR reactivity in sMND white and grey matter, however the extent of the microglial reaction varied greatly between cases and was not significant following quantification. HLA-DR expression has also been found to be increased in sMND

patient blood (Zhang *et al.*, 2005). Moreover, serum levels of HLA-DR correlated positively with the rate of patient decline. This likely reflects an increase in immune response in faster progressing cases, both in the CNS and peripheral immune system.

As a component of MHCII, HLA-DR is critical to the process of antigen presentation, the expression of surface antigens from pathogens to T-cells, as part of the adaptive immune response. In the current study, transcriptomic evidence demonstrated an upregulation of a number of genes involved in antigen presentation including CD74 and CD6, which a both critical for the presentation of antigens on the cell membrane.

In the healthy CNS, microglial antigen presentation for the stimulation of T-cells is rare due to the low number of T-cells in the CNS, as indicated by the relatively low expression of HLA-DR. However, T cell activity has been implicated in MND. Blood samples from MND patients show higher proportions of inflammatory Th1 and Th17 cells with lowered levels of anti-inflammatory Th2 and regulatory T (Treg) cells (Jin *et al.*, 2020). In mSOD1 mice, genetic deletion of T cells resulted in more rapid disease progression and increased microglial reactivity, indicating T cells may modulate microglial phenotype (Chiu *et al.*, 2008). Transfer of wild-type Tregs and effector T cells into mSOD1 mice lengthened survival. Amplification of Tregs through administration of low dose IL-2 has also shown reduced inflammation and increased neurotrophic factors in mSOD1 mice (Sheean *et al.*, 2018). Low dosage IL-2 has also been shown to be well tolerated in the first stages of human trials with MND patients, and has shown significant reduction in inflammatory signalling in patient leucocytes (Camu *et al.*, 2020; Giovannelli *et al.*, 2021).

5.2.3 CD163

CD163 mRNA was found to be upregulated in the spinal cord in all transcriptomic data sets and was found also to be significantly upregulated in those sMND cases with slower disease progression. In control cases, and sMND cortical regions, CD163 immunoreactivity was limited to perivascular macrophages. However, in the spinal cord of sMND individuals, large ameboid CD163^{+ve} cells were observed in the parenchyma of the ventral horn and extensively in the lateral corticospinal tracts. Interestingly, CD163 was also upregulated to a lesser extent in the non-motor regions of the spinal cord (dorsal column).

CD163 is a scavenger receptor for the haptoglobin-haemoglobin complex and is a marker of cells from the monocyte/ macrophage lineage. Broadly, CD163 is associated with phagocytic anti-inflammatory microglial/ macrophage activation. Increased CD163 expression in the spinal cord may represent a neuroprotective microglial/macrophage response. Liao *et al.* (2012) observed an increase in *CD163* along with other trophic factors such as *BDNF,* in mSOD1 mouse spinal cord prior to symptom onset.

In MS, CD163 immunoreactivity is absent from the parenchyma but labels microglia surrounding active plaques. These microglia were also positive for myelin basic protein indicating CD163^{+ve} cells had phagocytosed myelin (Zhang *et al.*, 2011). Incubation of Lipopolysaccharide (LPS)- stimulated proinflammatory macrophages with myelin significantly reduced pro-inflammatory cytokine expression, and induced expression of IL-10, an anti-inflammatory marker (Zhang *et al.*, 2011). Ingestion of myelin may induce an anti-inflammatory neuroprotective response.

CD163 expression in the CNS also increases following blood-brain-barrier breakdown (Pey *et al.*, 2014), which could suggest that CD163-positive cells could be the result of somatic macrophage infiltration.

5.2.4 TREM2 and TRYBOP

TREM2 is a cell surface receptor, associated with the regulation of the inflammatory phenotype in myeloid cells (Yamasaki *et al.*, 2014). The cytoplasmic domain of TREM2 alone does not have signalling capacity. TREM2 forms a complex with TYROBP which in turn signals through an immunoreceptor tyrosine activation motif (ITAM). The activation of the TREM2/TYROBP signalling complex by the binding of various ligands results in the activation of an anti-inflammatory phenotype and phagocytic behaviours in myeloid cells (Konishi and Kiyama, 2018).

Transcriptomic studies have consistently found an upregulation of TREM2 in human MND, and have associated the expression of soluble TREM2 with neuroprotection (Cady *et al.*, 2014; Cooper-Knock *et al.*, 2017). Here we have observed a significant upregulation of TREM2 mRNA in the sMND spinal cord. A significant difference in TREM2 immunoreactivity was not observed between sMND and control cases, however, increased expression in the white matter of the spinal cord was associated with slower disease progression, indicating a protective role for TREM2 in sMND.

Loss-of-function mutations in TREM2 are associated with several neurodegenerative conditions including Nasu-Hakola disease (Paloneva *et al.*, 2002), AD (Giraldo *et al.*, 2013; Jonsson *et al.*, 2013; Guerreiro *et al.*, 2013), FTD (Guerreiro *et al.*, 2013; Rayaprolu *et al.*, 2013; Le Ber *et al.*, 2014) and PD (Rayaprolu *et al.*, 2013), highlighting the role TREM2 plays in neurodegeneration.

In-vitro studies have highlighted the importance of TREM2 signalling in the anti-inflammatory response. Knockdown of TREM2 in microglia *in-vitro* dampened the anti-inflammatory response observed following IL-4 stimulation (Liu *et al.*, 2020). Furthermore, the reduction of TREM2 activity resulted in an increased neuroinflammatory response to LPS stimulation, characterised by increased production of inducible nitrous oxide synthase and IL-6 (Yin *et al.*, 2016).

TREM2 is also an important regulator of microglial phagocytic behaviour. In AD animal models, knockdown of TREM2 accelerated amyloidogenesis by reducing microglial phagocytic clearance of amyloid seeds (Parhizkar *et al.*, 2019). Xie *et al.* (2022) recently showed that, through a mouse model of TDP-43 proteinopathy, $TREM2^{-/-}$ microglia lost their ability to phagocytose TDP-43 inclusions, enhancing motor dysfunction compared to $TREM2^{+/+}$ mice. The authors went on to use immunoprecipitation to show that TREM2 interacts with TDP-43 in both mouse brain lysate and human spinal cord lysate. Structural analysis has shown many variants in TREM2 associated with neurodegeneration limit the ligand binding ability of TREM2 (Kober *et al.*, 2016), indicating disease-associated mutations may be associated with an inability of ligands to bind.

TYROBP expression in MND has not been as widely studied. Here we observed a significant upregulation of TYROBP mRNA in the spinal cord, as well as TYROBP labelling in the motor regions of the spinal cord and both the white and grey matter of the precentral gyrus in sMND cases.

Knockdown of TYROBP in a mouse model of hypoglossal nerve injury resulted in reduced production of proinflammatory cytokines, and a reduction in axotomy-induced motor neuron death (Kobayashi *et al.*, 2015), indicating TYROBP signalling

was detrimental. Similarly, TYROBP loss of function confers resistance to demyelination, in mouse models of demyelinating disease (Kaifu *et al.*, 2003). TYROBP deficiency in a mouse model of AD was protective, with less hyperphosphorylation of Tau protein, and a reduction in the severity of neuritic dystrophy (Haure-Mirande *et al.*, 2017).

Overall TREM2 signalling appears neuroprotective in MND and offers a strong therapeutic target. In contrast, TYROBP signalling is under-researched in MND but appears to confer a more neurotoxic microglial phenotype in other neurodegenerative conditions. Proteins from the sialic acid-binding immunoglobulin-type lectins (SIGLEC) family have also been found to associate with TYROBP through the ITAM region, which offers an alternative pathway for TYROBP signalling (Haure-Mirande *et al.*, 2022).

Microglial Expression of TREM2

TREM2 is widely expressed in the brain, and due to its expression by somatic human macrophages, and confirmed murine microglial expression, it has been assumed human microglia also express TREM2. Gene expression studies have found evidence of TREM2 mRNA in populations of isolated human microglia (Butovsky *et al.*, 2014; Zhou *et al.*, 2020). However, immunohistochemistry studies have failed to find TREM2 labelling of microglia in human *post-mortem* CNS material. Fahrenhold et al. (2018) observed TREM2^{+ve} intravascular monocytes. Satoh *et al.* (2013) observed the labelling of neurons, perivascular macrophages and intravascular monocytes. Raha-Chowdhury *et al.* (2019) found TREM2 immunoreactivity labelled erythrocytes, intravascular monocytes, perivascular macrophages, neurons, and choroid plexus epithelial cells. In the current study,

TREM2 was found to label intravascular monocytes, perivascular macrophages, neurons (cytoplasm), erythrocytes although this may potentially be artefactual, as well as glial staining, and granular staining throughout the parenchyma (findings summarised in Table 5.2). The glial labelling observed did not show identifiable microglial morphology. To compliment these data, colocalisation was performed with TREM2 and IBA1, which did show co-expression of IBA1 with TREM2.

The difficulty in confirming microglial expression of TREM2 in humans highlights potentially the need for further antibody trials and validation, but also underscores the difficulty in separating microglia from other cells of myeloid origin due to the lack of microglial-specific markers.

Table 5.2 Summary of TREM2 Labelling

	Erythrocytes	Intravascular monocytes	Perivascular macrophages	Neurons	Microglia	Parenchymal granules
Satoh *et al.* (2013)		+	+	+	-	
Raha-Chowdhury *et al.*, (2019)	+	+	+	+	-	
Fahrenhold *et al.* (2018)		+	-	-	-	
Current	+?	+	+	+	+?	+

Key. *+ = TREM2 positive, - = TREM2 negative, blank = not discussed, +? = validity uncertain*

5.2.5 APOE

APOE is a fat-binding protein, involved in lipid metabolism, and in the CNS is involved in lipid transport, neuronal survival and plasticity, and neurite outgrowth (Holtzman *et al.*, 1995; LaDu *et al.*, 2001; White *et al.*, 2001; Lanfranco *et al.*, 2021).

APOE expression is upregulated in *post-mortem* spinal cord of MND patients (Offen *et al.*, 2009; Andrés-Benito *et al.*, 2017; Oeckl *et al.*, 2020). Here we have shown an increase in APOE gene expression in the ventral horn, and through immunohistochemistry, we observed an upregulation of APOE in the motor regions of the spinal cord.

APOE allele type is one of the greatest risk factors for the development of AD (Liao, Yoon and Kim, 2017). In MND, APOE allele types have not been associated with an increased risk of developing MND (Moulard *et al.*, 1996; Siddique *et al.*, 1998; Govone *et al.*, 2014), however possession of different alleles has been linked to increased and decreased rate of disease progression (Praline *et al.*, 2011; Moulard *et al.*, 1996; Li *et al.*, 2004).

In the CNS, APOE facilitates the transfer of cholesterol between cells and is involved in cholesterol and lipid metabolism. In human MND, cholesterol metabolism shows deficits (Abdel-Khalik *et al.*, 2017). As neurons die through out disease progression, they release cholesterol. Glial metabolic pathways are unable to cope with this increase in cholesterol, resulting in increased neuronal toxicity, gliosis and increased inflammation (Bigini *et al.*, 2010).

APOE is also a ligand to the TREM2 receptor, as such APOE expression has been associated with the regulation of microglial phagocytosis and phenotype through the aforementioned pathway (Atagi *et al.*, 2015). Astrocyte-expressed APOE, has been suggested to act as an opsonin, triggering phagocytosis, to aid in the clearance of misfolded proteins and cellular debris (Pimenova, Marcora and Goate, 2017). Knockdown of APOE has also been shown to result in ineffective clearance of

neuronal debris by microglia in a model of prion pathology, indicating the importance of APOE in microglial phagocytosis (Pankiewicz *et al.*, 2021).

5.2.6 Disease-Associated Microglia

Together, APOE, TREM2 and TYRBOP also form a well-characterised pathway responsible for the Disease-Associated microglial (DAM) phenotype. Characterisation of microglia from several models of neurodegeneration and ageing led to the identification of a unique microglial common signature (Chiu *et al.*, 2013; Holtman *et al.*, 2015; Keren-Shaul *et al.*, 2017; Krasemann *et al.*, 2017; Friedman *et al.*, 2018; Spiller *et al.*, 2018). Through activation of the TREM2/TYROBP signalling complex, APOE is upregulated by microglia, resulting in the downregulation of Transforming Growth Factor β (TGFβ) mediated homeostatic microglial genes, and a simultaneous upregulation of the DAM genes (Figure 5.1).

Through the transcriptomic data collected in Chapter 3, we observed a significant increase in several of the genes associated with DAM in the spinal cord of sMND cases including APOE, TREM2 and TYROBP, as well as some downstream markers of DAM including ITGAX, SSP1 and CCL2 (Figure 5.1). However, the transcriptomic analysis reported little change in the expression of homeostatic markers. Using immunohistochemistry, we also showed an upregulation of APOE and TYRBOP in the motor regions of sMND spinal cord.

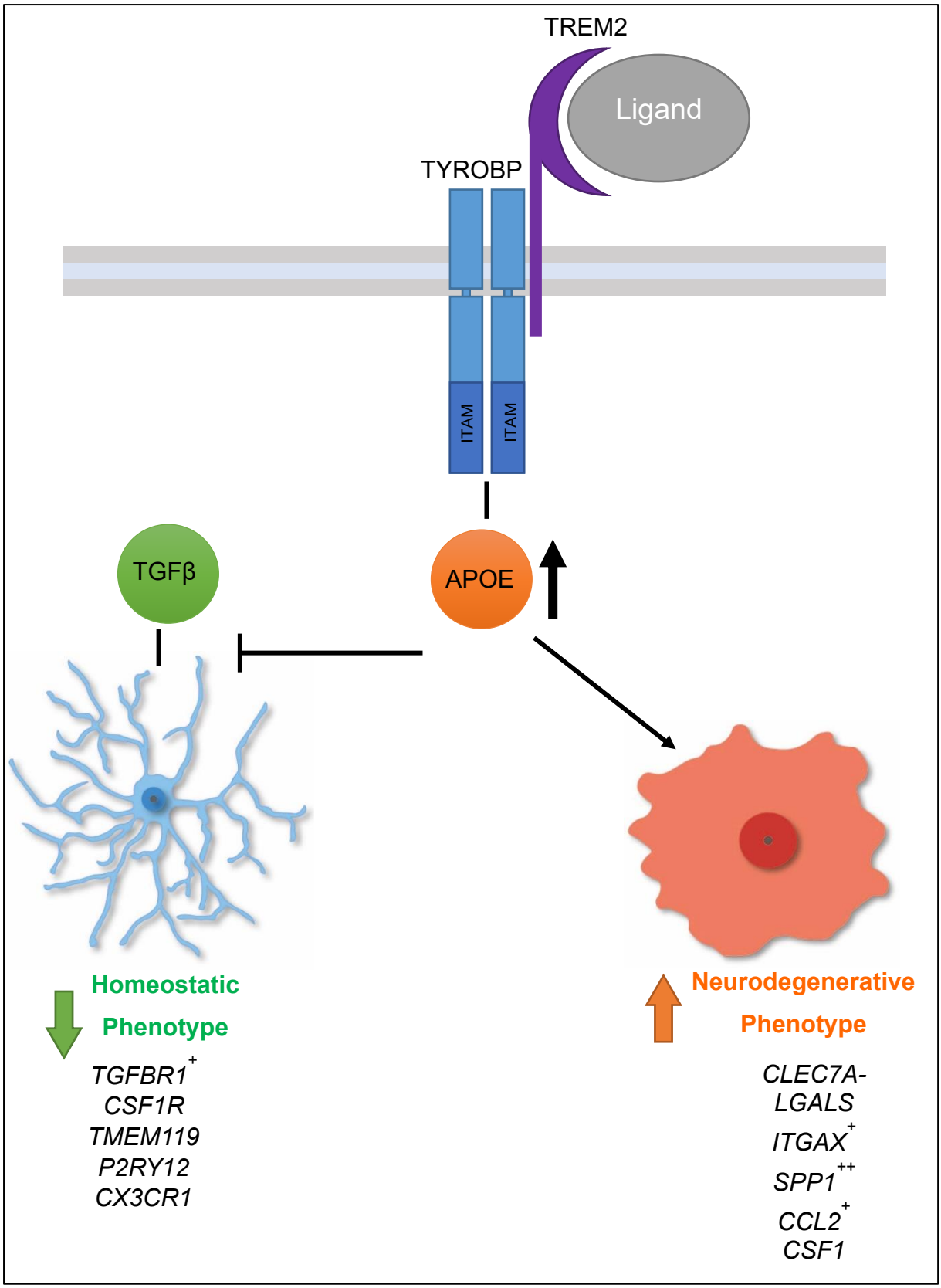

Figure 5.1 TREM2, TYROBP and APOE Regulate the Disease-Associated Microglial Phenotype

The gene expression signature of homeostatic microglia is mediated by TGFβ signalling and characterised by low expression of APOE. Microglial TREM2 receptors can be activated by various ligands This signalling cascade results in an upregulation of APOE which in turn downregulates the

homeostatic microglial phenotype and microglia switch to neurodegenerative disease phenotype referred to as Disease Associated Microglia or DAMs). This degenerative phenotype has been observed across murine models of various neurodegenerative diseases and aging.

***Key:** + = up regulated in our data, - = down regulated in our data, multiple symbols = significant in more than one data set.*

Broadly, the DAM phenotype is associated with an increase in phagocytic microglial activity and is thought to be beneficial despite increased inflammatory signalling (Deczkowska *et al.*, 2018). Others within the field, consider the DAM phenotype as a potentially damaging phenotype similar to senescent microglia: associated with loss of homeostatic functions and persistent inflammatory signalling (Krasemann *et al.*, 2017). This is a relatively newly discovered microglial phenotype, and its role in neurodegeneration is still undergoing characterisation.

5.3 Microglial phenotype in MND

Microglial phenotypes have widely been characterised into M1 (proinflammatory) or M2 (anti-inflammatory). This classification has offered a broad system to categorise microglial responses, however, it was quickly identified that this system did not capture the broad range of microglial functions and responses (Chiu *et al.*, 2013; Wes *et al.*, 2016). As such it was hypothesised microglial phenotype in sMND would not conform to M1/M2 phenotypes, and microglia would be associated with a range of both pro and anti-inflammatory functions. To this end, microglial/macrophage deconvolution analysis was performed on the FFPE and Frozen spinal cord transcriptomic data to isolate those genes associated with microglial/macrophage expression. Very few of the classical pro or anti-inflammatory cytokines were found to be differentially expressed in either spinal cord data set. Instead, the microglial phenotype appeared more complex, showing upregulation of cytokine and

chemokine receptors, as well as genes linked to phagocytosis and antigen presentation. Furthermore, genes associated both with inflammation (the complement pathway) and the regulation of inflammation were upregulated. As such, these data confirmed our hypothesis.

In generating their transcriptional database (which was used in the current study for assessing genes of probable microglial origin), Zhang *et al.* (2016), used immunopanning to isolate specific cell populations. This relies on the specific binding of proteins on the target cells' external membrane to antibodies bound to a dish, to isolate the target population from a mixed cell suspension (Zhang *et al.*, 2010). Zhang et al. (2016) used CD45 to isolate microglial populations. While this marker would separate microglia from other glial/ neuronal cells, it is not specific to microglia. As such the identified cell population likely contains other leukocytes.

5.4 MND: A Demyelinating Disease?

Here we have shown there is a significant microglial reaction in the white matter tracts of the spinal cord, namely the lateral corticospinal tracts, in sMND. In this region, activated microglia with amoeboid morphology were observed, expressing CD68, IBA1 and CD163 indicating an activated and phagocytic phenotype. This was accompanied by significantly increased expression of both APOE and TYROBP. For all markers assessed apart from TREM2, the pathology severity in the lateral corticospinal tract either matched or exceeded the reaction observed in the ventral horn. Furthermore, we noted significant white matter pallor in the corticospinal tracts of sMND cases.

Myelin loss in the white matter tracts is a well-established feature of human MND (Hayashi *et al.*, 2001; Kassubek *et al.*, 2009; Ishaque *et al.*, 2022). Myelin loss in MND is often recognized as a consequence of axonal death. However, animal models of MND have indicated changes in oligodendroglia take place early in disease, prior to symptom onset and evidence of myelin loss (Niebroj-Dobosz *et al.*, 2007). Furthermore, Pons *et al.* (2020) noted a significant loss of myelin basic protein in the corticospinal tract that was disproportionate to axon loss through western blotting, indicating myelin loss preceded axonal loss. Oligodendrocyte dysfunction was linked to impairment of mRNA transport. As such loss of white matter in MND appears to be separate from those processes driving axonal loss.

Inflammation and myelin loss with relative axonal sparing are characteristic of MS (Matthews, 2019). At the site of active lesions where demyelination is ongoing, microglia and macrophages appear large and rounded with an ameboid phenotype and show an upregulation of markers linked to proinflammation and phagocytosis such as CD68 and MHCII antigens such as HLA-DR, like observations made here in the corticospinal tract. Whether the microglial and immune response observed in the cortical spinal tracts actively causes demyelination in MND, or is a response to oligodendroglial dysfunction warrants further investigation.

5.5 Limitations

As a *post-mortem* study, this research provides data directly on human MND, which would not have been achievable through cellular or animal models of MND. However, there are limitations to *post-mortem*-based research. Primarily, this data provides a snapshot of the end stage of disease, and as such, we cannot monitor the development of disease or experimentally manipulate these data to determine

causation. However, *post-mortem* tissue provides a useful resource to identify targets for further functional studies in animal or cell models.

In human studies, there is less control over lifestyle factors compared to the relatively uniform and sterile conditions associated with animal models of disease. While this presents an opportunity to examine the potential contribution these lifestyle factors may have to risk across a population, it adds greater variability to the data.

The immunohistochemistry portion of this research highlighted great individual heterogeneity in both the control and sMND cohorts. All available and appropriate control cases from the Sheffield Brain and Tissue Bank (SBTB) were used to construct the control cohorts, however, it remains possibly underpowered.

During the immunohistochemical staining of spinal cord cases, some tissue was lost or damaged during the protocol, preventing data being collected from all cases within the spinal cord cohort. Due to time constraints, re-staining all missing cases was not feasible, therefore only control cases were repeated due to the low number of available control cases. As such, there was some variation in the cases used for each immunohistochemical marker for the spinal cord sMND cohorts. Therefore, separate cut offs were used during data analysis namely the median length of survival used to separate fast and slow progressing sMND cases in the survival analysis. This decision was made to account for the small changes between cohorts for each immunohistochemical marker.

Clinical information for each case in the SBTB was limited: For most cases, the available information was the age at diagnosis, and age at death, and from these data the length of disease progression was calculated. This estimation of survival

time may vary significantly from the true value and is a coarse measure of disease severity. Further clinical details such as scores for ALS Functional Rating Scale - revised (ALSFRS-r; Cedarbaum *et al.*, 1999) may provide a better measure of disease severity. Microglial activation has been linked to several clinical features of MND including upper motor neuron signs (Brettschneider, Libon, *et al.*, 2012). In the current study, histological analysis of cortical regions was collected. Access to neuropsychological data would have allowed examination of the relationship between these symptoms and pathology in the prefrontal and temporal cortices.

5.7 Further Work

5.7.1 Further Experimental Work.

If further time and resources were to be invested to take this project forward, the following work would be done.

Antibody Validation

In Chapter 4, immunoblotting was performed to validate antibody specificity. While these assays found no evidence of off-target antibody binding, the immunohistochemistry antisera did not work well in these Western blots and consequently did not confirm the specificity of the antibodies. Due to time constraints, full optimisation of the antibody concentration, and protein loading concentration could not be performed. For proteins such as TREM2, expression was relatively low in spinal cord homogenate, therefore the use of protein with higher concentrations of the relevant antigen may have given more useful data. The addition of the concentrated protein may also be necessary.

Secondly, an antibody absorption control was run, which showed a significant increase in DAB reactivity following blocking with the target protein, compared to the positive control. The presence of glial staining indicated non-specific binding of some component of the antibody-antigen complex. However, such high reactivity could indicate non-specific binding of the recombinant protein itself to the tissue. Further validation could have been performed using immunobeads coated with the specific peptide. Incubation with the immunobeads, would remove the antigen body- antigen complex from solution.

Quantitative Analysis of Extra Regions

Quantification of immunoreactivity was performed in the spinal cord and precentral gyrus; through this, we were able to validate the transcriptomic data at the translational level in the primary regions of neuronal degeneration. TMAs were generated for further regions including the prefrontal, temporal and occipital cortices and the basal ganglia. For these regions, immunohistochemistry began but was not completed for all markers, and these data were not quantified. Quantification of these data would allow comparison of inflammatory markers across regions of the brain associated with varying levels of MND-specific pathology.

GRASPS

Transcriptomic data provides information on the intention of the cell, however, there is often a significant difference between gene and protein expression. Analysis of RNA and protein concentrations isolated from human monocytes revealed a good correlation overall between RNA expression and protein quantity (Guo et al., 2008).

However, correlations varied greatly from gene to gene, with some genes with regulatory functions showing no correlation with protein.

Here, we piloted a method of isolating ribosomal mRNA from the cells of *post-mortem* spinal cord tissue. GRASPS aims to bridge this gap in transcriptional data to closer reflect protein expression.

Prior to this study, GRASPS had not been performed on human spinal cord and represents one of the first trials with post-mortem tissue. RNA isolation from *post-mortem* tissue is made more challenging by potential RNA degradation between death and preservation. However, the possibility of getting mRNA expression data that more closely correlates with protein quantitation is very exciting and thus, further optimisation of this method is ongoing.

Demyelination.

Given the above observations relating to demyelination and inflammation in MS, it would be useful to look for further parallels with MND. For example, an electron microscopy study to look at the “g” ratio, which indexes myelin sheath thickness. Secondly, immunohistochemistry for myelin components such as myelin basic protein, proteolipid protein or myelin associated glyocoprotein, allied with tinctorial histology combining luxol fast blue with periodic acid Schiff could be performed to detect myelin breakdown products in amoeboid macrophages (described above). If indeed there were further parallels with demyelinating processes, this raises the possibility that therapeutic strategies for immunomodulation or remyelination developed for MS, could be brought to bear on MND. Preserving oligodendrocytes could offer some neuroprotection for the pyramidal tract.

5.7.2 Further Functional Studies and Therapeutic Targets.

TREM2 as a Therapeutic Target

Here we have shown TREM2 expression was increased in the spinal cord white matter of longer surviving compared to shorter surviving sMND cases. TREM2 has been widely explored in animal models of AD. These studies highlight a role for TREM2 in the regulation of the microglial phenotype, particularly in regard to the phagocytic microglial response. Recent research has indicated TREM2 is able to interact with TDP-43 (Xie et al., 2022) and TDP-43 has also been shown to inhibit microglial phagocytosis (Rosa Paolicelli et al., 2017). As such, examining the impact of TREM2 overexpression and knockdown in TDP-43 mouse models, on microglial expression and survival may provide more data on the validity and potential mechanisms of TREM2 as a therapeutic target. This may allow developments from the field of AD to be transferred to MND.

Overexpression of APOE

Here we have observed a significant upregulation of APOE, associated with sMND in the spinal cord. Due to the association between APOE allele type and the risk of developing AD, much of the existing literature surrounding APOE has focused on the impact of allele type in both AD and MND. Differing allele types are associated with variability in protein stability and folding and domain interactions (Suri et al., 2013). Knock-down of APOE in models of AD results in reduced clearance of amyloid beta (Spires and Hyman, 2005). However, the impact of increased expression has not been examined in sMND. As such, examining the impact of APOE overexpression

on MND pathology and microglial reactivity in a TDP-43 mouse model would provide further data on the impact of APOE expression observed in sMND. Therapeutic strategies from the AD literature that are directed at APOE regulation may be applicable to MND.

Further, as noted above, the literature relating to APOE allele type and MND either as a risk factor or as a disease modifier remains equivocal (Serrano-Pozo, Das and Hyman, 2021). It would be beneficial to use a more powerful study (such as Project MinE; van der Spek *et al.*, 2019) to provide an answer.

5.8 Overall Conclusions

The inflammatory and microglial response is a key feature of human MND. Transcriptomic characterisation of inflammation in sMND using the NanoString system has shown a significant upregulation in the spinal cord but not the motor cortex highlighting a key difference between these disease environments in those regions. Analysis of key genes and pathways highlighted CD163, TREM2 and TYROBP signalling, and APOE, along with phagocytosis and antigen presentation as key inflammatory pathways in sMND. These pathways were examined further, using immunohistochemistry in the spinal cord and the precentral gyrus. A significant immune response was observed spinal cord but not the motor cortex in sMND cases, indicating the spinal cord and precentral gyrus represent different disease environments. A profound inflammatory response characterised by ameboid CD163 and CD68 positive microglia was observed in the motor regions of the spinal cord in sMND cases, indicative of pathology observed in MS. These data highlighted the lateral corticospinal tract as a key region in MND pathology, highlighting oligodendrocytic degeneration as a key feature of MND pathology. APOE and TYROBP showed significant upregulation, in the motor regions of the spinal cord. Increased TREM2 expression in the white matter of the spinal cord was associated with longer patient survival.

In conclusion, developing a greater understanding of the TREM2/ TYROBP/ APOE signalling pathway on microglial phenotype and the role of inflammation in white matter in sMND may be of importance in the development of potential therapeutic treatments.

References

Abdel-Khalik, J. *et al.* (2017) 'Defective cholesterol metabolism in amyotrophic lateral sclerosis', *Journal of Lipid Research*, 58(1), pp. 267–278. Available at: https://doi.org/10.1194/jlr.P071639.

Abe, K. *et al.* (2017) 'Safety and efficacy of edaravone in well defined patients with amyotrophic lateral sclerosis: a randomised, double-blind, placebo-controlled trial', *The Lancet Neurology*, 16(7), pp. 505–512. Available at: https://doi.org/10.1016/S1474-4422(17)30115-1.

Acevedo-Arozena, A. *et al.* (2011) 'A comprehensive assessment of the SOD1 G93A low-copy transgenic mouse, which models human amyotrophic lateral sclerosis', *DMM Disease Models and Mechanisms*, 4(5), pp. 686–700. Available at: https://doi.org/10.1242/DMM.007237/-/DC1.

Aebischer, J. *et al.* (2011) 'IFNγ triggers a LIGHT-dependent selective death of motoneurons contributing to the non-cell-autonomous effects of mutant SOD1', *Cell Death and Differentiation*, 18(5), p. 754. Available at: https://doi.org/10.1038/CDD.2010.143.

Afroz, T. *et al.* (2017) 'Functional and dynamic polymerization of the ALS-linked protein TDP-43 antagonizes its pathologic aggregation', *Nature Communications 2017 8:1*, 8(1), pp. 1–15. Available at: https://doi.org/10.1038/s41467-017-00062-0.

Ajami, B. *et al.* (2018) 'Single-cell mass cytometry reveals distinct populations of brain myeloid cells in mouse neuroinflammation and neurodegeneration models', *Nature Neuroscience 2018 21:4*, 21(4), pp. 541–551. Available at: https://doi.org/10.1038/s41593-018-0100-x.

Al-Chalabi, M. and Alsalman, I. (2018) 'Neuroanatomy, Posterior Column (Dorsal Column)', *StatPearls* [Preprint]. Available at: http://www.ncbi.nlm.nih.gov/pubmed/29939665 (Accessed: 12 August 2022).

Aloisi, F. (2001) 'Immune function of microglia', *Glia*, 36(2), pp. 165–179. Available at: https://doi.org/10.1002/glia.1106.

Alshikho, M.J. *et al.* (2016) 'Glial activation colocalizes with structural abnormalities in amyotrophic lateral sclerosis', *Neurology*, 87(24), pp. 2554–2561. Available at: https://doi.org/10.1212/WNL.0000000000003427.

Andersen, P.M. *et al.* (1995) 'Amyotrophic lateral sclerosis associated with homozygosity for an Asp90Ala mutation in CuZn-superoxide dismutase', *Nature Genetics*, 10(1), pp. 61–66. Available at: https://doi.org/10.1038/ng0595-61.

Andersen, P.M. *et al.* (1997) 'Phenotypic heterogeneity in motor neuron disease patients with CuZn-superoxide dismutase mutations in Scandinavia', *Brain : a journal of neurology*, 120 (Pt 10)(10), pp. 1723–1737. Available at: https://doi.org/10.1093/BRAIN/120.10.1723.

Andersson, M.K. *et al.* (2008) 'The multifunctional FUS, EWS and TAF15 proto-oncoproteins show cell type-specific expression patterns and involvement in cell

spreading and stress response', *BMC Cell Biology*, 9(1), pp. 1–17. Available at: https://doi.org/10.1186/1471-2121-9-37/FIGURES/7.

Andrés-Benito, P. *et al.* (2017) 'Amyotrophic lateral sclerosis, gene deregulation in the anterior horn of the spinal cord and frontal cortex area 8: Implications in frontotemporal lobar degeneration', *Aging*, 9(3), pp. 823–851. Available at: https://doi.org/10.18632/aging.101195.

April, C. *et al.* (2009) 'Whole-Genome Gene Expression Profiling of Formalin-Fixed, Paraffin-Embedded Tissue Samples', *PLoS ONE*. Edited by P. Tan, 4(12), p. e8162. Available at: https://doi.org/10.1371/journal.pone.0008162.

Arai, T. *et al.* (2006) 'TDP-43 is a component of ubiquitin-positive tau-negative inclusions in frontotemporal lobar degeneration and amyotrophic lateral sclerosis', *Biochemical and Biophysical Research Communications*, 351(3), pp. 602–611. Available at: https://doi.org/10.1016/J.BBRC.2006.10.093.

Aronica, E. *et al.* (2015) 'Molecular classification of amyotrophic lateral sclerosis by unsupervised clustering of gene expression in motor cortex', *Neurobiology of Disease*, 74, pp. 359–376. Available at: https://doi.org/10.1016/j.nbd.2014.12.002.

Arora, R.D. and Khan, Y.S. (2021) 'Motor neuron disease', in *StatPearls [Internet]*. StatPearls Publishing.

Ash, P.E.A. *et al.* (2013) 'Unconventional Translation of C9ORF72 GGGGCC Expansion Generates Insoluble Polypeptides Specific to c9FTD/ALS', *Neuron*, 77(4), pp. 639–646. Available at: https://doi.org/10.1016/J.NEURON.2013.02.004.

Ashford, B.A. *et al.* (2020) 'Microglia in Motor Neuron Disease', *Neuropathology and Applied Neurobiology*, p. nan.12640. Available at: https://doi.org/10.1111/nan.12640.

Atagi, Y. *et al.* (2015) 'Apolipoprotein E is a ligand for triggering receptor expressed on myeloid cells 2 (TREM2)', *Journal of Biological Chemistry*, 290(43), pp. 26043–26050. Available at: https://doi.org/10.1074/jbc.M115.679043.

Atanasio, A. *et al.* (2016) 'C9orf72 ablation causes immune dysregulation characterized by leukocyte expansion, autoantibody production and glomerulonephropathy in mice', *Scientific Reports*, 6(1), p. 23204. Available at: https://doi.org/10.1038/srep23204.

Ayala, V. *et al.* (2011) 'Cell stress induces TDP-43 pathological changes associated with ERK1/2 dysfunction: Implications in ALS', *Acta Neuropathologica*, 122(3), pp. 259–270. Available at: https://doi.org/10.1007/S00401-011-0850-Y/FIGURES/7.

Ayala, Y.M. *et al.* (2008) 'Structural determinants of the cellular localization and shuttling of TDP-43', *Journal of Cell Science*, 121(22), pp. 3778–3785. Available at: https://doi.org/10.1242/JCS.038950.

Ayers, J.I. *et al.* (2016) 'Prion-like propagation of mutant SOD1 misfolding and motor neuron disease spread along neuroanatomical pathways', 131(1), pp. 103–114. Available at: http://link.springer.com/10.1007/s00401-015-1514-0 (Accessed: 23 November 2018).

Azevedo, F.A.C. *et al.* (2009) 'Equal numbers of neuronal and nonneuronal cells make the human brain an isometrically scaled-up primate brain', *Journal of Comparative Neurology*, 513(5), pp. 532–541. Available at:

https://doi.org/10.1002/CNE.21974.

Babu, G.N. *et al.* (2008) 'Elevated inflammatory markers in a group of amyotrophic lateral sclerosis patients from northern India', *Neurochemical Research*, 33(6), pp. 1145–1149. Available at: https://doi.org/10.1007/s11064-007-9564-x.

Bankhead, P. *et al.* (2017) 'QuPath: Open source software for digital pathology image analysis', *Scientific Reports 2017 7:1*, 7(1), pp. 1–7. Available at: https://doi.org/10.1038/s41598-017-17204-5.

Barrett, T. *et al.* (2013) 'NCBI GEO: Archive for functional genomics data sets - Update', *Nucleic Acids Research*, 41(D1). Available at: https://doi.org/10.1093/nar/gks1193.

Bartanusz, V. *et al.* (2011) 'The blood–spinal cord barrier: Morphology and Clinical Implications', *Annals of Neurology*, 70(2), pp. 194–206. Available at: https://doi.org/10.1002/ANA.22421.

Batchelor, P.E. *et al.* (2008) 'Comparison of Inflammation in the Brain and Spinal Cord following Mechanical Injury', *https://home.liebertpub.com/neu*, 25(10), pp. 1217–1225. Available at: https://doi.org/10.1089/NEU.2007.0308.

Baumann, N. and Pham-Dinh, D. (2001) 'Biology of oligodendrocyte and myelin in the mammalian central nervous system', *Physiological Reviews*, 81(2), pp. 871–927. Available at: https://doi.org/10.1152/PHYSREV.2001.81.2.871/ASSET/IMAGES/LARGE/9J02101 33008.JPEG.

Beers, D.R. *et al.* (2006) 'Wild-type microglia extend survival in PU.1 knockout mice with familial amyotrophic lateral sclerosis', *Proceedings of the National Academy of Sciences*, 103(43), pp. 16021–16026. Available at: https://doi.org/10.1073/pnas.0607423103.

Benatar, M. (2007) 'Lost in translation: Treatment trials in the SOD1 mouse and in human ALS', *Neurobiology of Disease*, 26(1), pp. 1–13. Available at: https://doi.org/10.1016/J.NBD.2006.12.015.

Benbrika, S. *et al.* (2019) 'Cognitive, emotional and psychological manifestations in amyotrophic lateral sclerosis at baseline and overtime: A review', *Frontiers in Neuroscience*, 13, p. 951. Available at: https://doi.org/10.3389/FNINS.2019.00951/BIBTEX.

Bennet, A.M. *et al.* (2007) 'Association of apolipoprotein e genotypes with lipid levels and coronary risk', *Journal of the American Medical Association*, pp. 1300–1311. Available at: https://doi.org/10.1001/jama.298.11.1300.

Bennett, M.L. *et al.* (2016) 'New tools for studying microglia in the mouse and human CNS', *Proceedings of the National Academy of Sciences of the United States of America*, 113(12), pp. E1738–E1746. Available at: https://doi.org/10.1073/pnas.1525528113.

Le Ber, I. *et al.* (2014) 'Homozygous TREM2 mutation in a family with atypical frontotemporal dementia', *Neurobiology of Aging*, 35(10), pp. 2419.e23-2419.e25. Available at: https://doi.org/10.1016/J.NEUROBIOLAGING.2014.04.010.

Bertram, L. *et al.* (2007) 'Systematic meta-analyses of Alzheimer disease genetic

association studies: the AlzGene database', *Nature Genetics 2007 39:1*, 39(1), pp. 17–23. Available at: https://doi.org/10.1038/ng1934.

Beswick, E. *et al.* (2022) 'A systematic review of non-motor symptom evaluation in clinical trials for amyotrophic lateral sclerosis', *Journal of Neurology*, 269(1), pp. 411–426. Available at: https://doi.org/10.1007/S00415-021-10651-1/TABLES/4.

Beutner, C. *et al.* (2013) 'Unique transcriptome signature of mouse microglia', *Glia*, 61(9), pp. 1429–1442. Available at: https://doi.org/10.1002/glia.22524.

Bibikova, M. *et al.* (2004) 'Quantitative Gene Expression Profiling in Formalin-Fixed, Paraffin-Embedded Tissues Using Universal Bead Arrays', *The American Journal of Pathology*, 165(5), pp. 1799–1807. Available at: https://doi.org/10.1016/S0002-9440(10)63435-9.

Bigini, P. *et al.* (2010) 'Neuropathologic and Biochemical Changes During Disease Progression in Liver X Receptor β−/− Mice, A Model of Adult Neuron Disease', *Journal of Neuropathology & Experimental Neurology*, 69(6), pp. 593–605. Available at: https://doi.org/10.1097/NEN.0B013E3181DF20E1.

Bilsland, L.G. *et al.* (2010) 'Deficits in axonal transport precede ALS symptoms in vivo', *Proceedings of the National Academy of Sciences*, 107(47), pp. 20523–20528. Available at: https://doi.org/10.1073/pnas.1006869107.

Birdsill, A.C. *et al.* (2011) 'Postmortem interval effect on RNA and gene expression in human brain tissue', *Cell and Tissue Banking*, 12(4), pp. 311–318. Available at: https://doi.org/10.1007/s10561-010-9210-8.

Blinzinger, K. and Kreutzberg, G. (1968) 'Displacement of synaptic terminals from regenerating motoneurons by microglial cells', *Zeitschrift für Zellforschung und Mikroskopische Anatomie 1968 85:2*, 85(2), pp. 145–157. Available at: https://doi.org/10.1007/BF00325030.

van Blitterswijk, M. *et al.* (2015) 'Novel clinical associations with specific C9ORF72 transcripts in patients with repeat expansions in C9ORF72', *Acta neuropathologica*, 130(6), p. 863. Available at: https://doi.org/10.1007/S00401-015-1480-6.

Boche, D., Perry, V.H. and Nicoll, J.A.R. (2013) 'Review: Activation patterns of microglia and their identification in the human brain', *Neuropathology and Applied Neurobiology*, 39(1), pp. 3–18. Available at: https://doi.org/10.1111/nan.12011.

De Boer, E.M.J. *et al.* (2021) 'TDP-43 proteinopathies: a new wave of neurodegenerative diseases', *Journal of Neurology, Neurosurgery & Psychiatry*, 92(1), pp. 86–95. Available at: https://doi.org/10.1136/JNNP-2020-322983.

Boillée, S. *et al.* (2006) 'Onset and progression in inherited ALS determined by motor neurons and microglia.', *Science (New York, N.Y.)*, 312(5778), pp. 1389–92. Available at: https://doi.org/10.1126/science.1123511.

Borda, J.T. *et al.* (2008) 'CD163, a marker of perivascular macrophages, is up-regulated by microglia in simian immunodeficiency virus encephalitis after haptoglobin-hemoglobin complex stimulation and is suggestive of breakdown of the blood-brain barrier', *American Journal of Pathology*, 172(3), pp. 725–737. Available at: https://doi.org/10.2353/ajpath.2008.070848.

Bordeaux, J. *et al.* (2010) *Antibody validation*, *BioTechniques*. NIH Public Access.

Available at: https://doi.org/10.2144/000113382.

Borthwick, G.M. *et al.* (2006) 'Motor neuron disease in a patient with a mitochondrial tRNAIle mutation', *Annals of Neurology*, 59(3), pp. 570–574. Available at: https://doi.org/10.1002/ANA.20758.

Böttcher, C. *et al.* (2019) 'Human microglia regional heterogeneity and phenotypes determined by multiplexed single-cell mass cytometry', *Nature Neuroscience*, 22(1), pp. 78–90. Available at: https://doi.org/10.1038/s41593-018-0290-2.

Bozzo, F. *et al.* (2016) 'Structural insights into the multi-determinant aggregation of TDP-43 in motor neuron-like cells', *Neurobiology of Disease*, 94, pp. 63–72. Available at: https://doi.org/10.1016/J.NBD.2016.06.006.

Braak, H. *et al.* (2003) 'Staging of brain pathology related to sporadic Parkinson's disease.', *Neurobiology of aging*, 24(2), pp. 197–211. Available at: http://www.ncbi.nlm.nih.gov/pubmed/12498954 (Accessed: 22 July 2019).

Braak, H. and Braak, E. (1991) 'Neuropathological stageing of Alzheimer-related changes', *Acta Neuropathologica*, 82(4), pp. 239–259. Available at: https://doi.org/10.1007/BF00308809.

Brettschneider, J., Libon, D.J., *et al.* (2012) 'Microglial activation and TDP-43 pathology correlate with executive dysfunction in amyotrophic lateral sclerosis', *Acta Neuropathologica*, 123(3), pp. 395–407. Available at: https://doi.org/10.1007/s00401-011-0932-x.

Brettschneider, J., Toledo, J.B., *et al.* (2012) 'Microglial activation correlates with disease progression and upper motor neuron clinical symptoms in amyotrophic lateral sclerosis', *PLoS ONE*. Edited by L. Petrucelli, 7(6), p. e39216. Available at: https://doi.org/10.1371/journal.pone.0039216.

Brettschneider, J. *et al.* (2013) 'Stages of pTDP-43 pathology in amyotrophic lateral sclerosis', *Annals of Neurology*, 74(1), pp. 20–38. Available at: https://doi.org/10.1002/ana.23937.

Brettschneider, J. *et al.* (2014) 'TDP-43 pathology and neuronal loss in amyotrophic lateral sclerosis spinal cord', *Acta Neuropathologica*, 128(3), pp. 423–437. Available at: https://doi.org/10.1007/s00401-014-1299-6.

Brohawn, D.G., O'Brien, L.C. and Bennett, J.P. (2016) 'RNAseq analyses identify tumor necrosis factor-mediated inflammation as a major abnormality in ALS spinal cord', *PLoS ONE*, 11(8), p. e0160520. Available at: https://doi.org/10.1371/journal.pone.0160520.

Brooks, B.R. *et al.* (2000) 'El Escorial revisited: Revised criteria for the diagnosis of amyotrophic lateral sclerosis', *Amyotrophic Lateral Sclerosis*, 1(5), pp. 293–299. Available at: https://doi.org/10.1080/146608200300079536.

Bruijn, L.I. *et al.* (1997) 'ALS-Linked SOD1 Mutant G85R Mediates Damage to Astrocytes and Promotes Rapidly Progressive Disease with SOD1-Containing Inclusions', *Neuron*, 18(2), pp. 327–338. Available at: https://doi.org/10.1016/S0896-6273(00)80272-X.

Buchman, V.L. *et al.* (2013) 'Simultaneous and independent detection of C9ORF72 alleles with low and high number of GGGGCC repeats using an optimised protocol of

Southern blot hybridisation', *Molecular Neurodegeneration*, 8(1), pp. 1–6. Available at: https://doi.org/10.1186/1750-1326-8-12/FIGURES/3.

Burberry, A. *et al.* (2016) 'Loss-of-function mutations in the C9ORF72 mouse ortholog cause fatal autoimmune disease', *Science Translational Medicine*, 8(347), pp. 347–93. Available at: https://doi.org/10.1126/scitranslmed.aaf6038.

Burry, R.W. (2011) 'Controls for Immunocytochemistry: An Update', *Journal of Histochemistry and Cytochemistry*, 59(1), p. 6. Available at: https://doi.org/10.1369/JHC.2010.956920.

Butler, C.A. *et al.* (2021) 'Microglial phagocytosis of neurons in neurodegeneration, and its regulation', *Journal of Neurochemistry*, 158(3), pp. 621–639. Available at: https://doi.org/10.1111/JNC.15327.

Butovsky, O. *et al.* (2006) 'Microglia activated by IL-4 or IFN-γ differentially induce neurogenesis and oligodendrogenesis from adult stem/progenitor cells', *Molecular and Cellular Neuroscience*, 31(1), pp. 149–160. Available at: https://doi.org/10.1016/J.MCN.2005.10.006.

Butovsky, O. *et al.* (2014) 'Identification of a unique TGF-β-dependent molecular and functional signature in microglia', *Nature Neuroscience*, 17(1), pp. 131–143. Available at: https://doi.org/10.1038/nn.3599.

Cady, J. *et al.* (2014) 'TREM2 variant p.R47H as a risk factor for sporadic amyotrophic lateral sclerosis', *JAMA Neurology*, 71(4), pp. 449–453. Available at: https://doi.org/10.1001/jamaneurol.2013.6237.

Caldeira, C. *et al.* (2014) 'Microglia change from a reactive to an age-like phenotype with the time in culture', *Frontiers in Cellular Neuroscience*, 8(JUN), p. 152. Available at: https://doi.org/10.3389/FNCEL.2014.00152/XML/NLM.

Calvo, A. *et al.* (2018) 'Common polymorphisms of chemokine (C-X3-C motif) receptor 1 gene modify amyotrophic lateral sclerosis outcome: A population-based study', *Muscle & nerve*, 57(2), pp. 212–216. Available at: https://doi.org/10.1002/MUS.25653.

Camu, W. *et al.* (2020) 'Repeated 5-day cycles of low dose aldesleukin in amyotrophic lateral sclerosis (IMODALS): A phase 2a randomised, double-blind, placebo-controlled trial', *eBioMedicine*, 59, p. 102844. Available at: https://doi.org/10.1016/J.EBIOM.2020.102844.

Cardona, A.E. *et al.* (2006) 'Control of microglial neurotoxicity by the fractalkine receptor', *Nature Neuroscience*, 9(7), pp. 917–924. Available at: https://doi.org/10.1038/nn1715.

Cassina, P. *et al.* (2008) 'Mitochondrial Dysfunction in SOD1G93A-Bearing Astrocytes Promotes Motor Neuron Degeneration: Prevention by Mitochondrial-Targeted Antioxidants', *Journal of Neuroscience*, 28(16), pp. 4115–4122. Available at: https://doi.org/10.1523/JNEUROSCI.5308-07.2008.

Cedarbaum, J.M. *et al.* (1999) 'The ALSFRS-R: a revised ALS functional rating scale that incorporates assessments of respiratory function', *Journal of the Neurological Sciences*, 169(1–2), pp. 13–21. Available at: https://doi.org/10.1016/S0022-510X(99)00210-5.

Chan, W.Y., Kohsaka, S. and Rezaie, P. (2007) 'The origin and cell lineage of microglia—New concepts', *Brain Research Reviews*, 53(2), pp. 344–354. Available at: https://doi.org/10.1016/J.BRAINRESREV.2006.11.002.

Chapman, J. *et al.* (2001) 'APOE genotype is a major predictor of long-term progression of disability in MS', *Neurology*, 56(3), pp. 312–316. Available at: https://doi.org/10.1212/WNL.56.3.312.

Cherry, J.D., Olschowka, J.A. and O'Banion, M.K. (2014) 'Neuroinflammation and M2 microglia: The good, the bad, and the inflamed', *Journal of Neuroinflammation*. BioMed Central, p. 98. Available at: https://doi.org/10.1186/1742-2094-11-98.

Chiu, I.M. *et al.* (2008) 'T lymphocytes potentiate endogenous neuroprotective inflammation in a mouse model of ALS', *Proceedings of the National Academy of Sciences of the United States of America*, 105(46), pp. 17913–17918. Available at: https://doi.org/10.1073/pnas.0804610105.

Chiu, I.M. *et al.* (2013) 'A neurodegeneration-specific gene-expression signature of acutely isolated microglia from an amyotrophic lateral sclerosis mouse model', *Cell Reports*, 4(2), pp. 385–401. Available at: https://doi.org/10.1016/j.celrep.2013.06.018.

Choi, Y. *et al.* (2017) 'Optimization of RNA Extraction from Formalin-Fixed Paraffin-Embedded Blocks for Targeted Next-Generation Sequencing', *Journal of Breast Cancer*, 20(4), p. 393. Available at: https://doi.org/10.4048/jbc.2017.20.4.393.

Chou, C.Y. *et al.* (2005) 'Structural Variation in Human Apolipoprotein E3 and E4: Secondary Structure, Tertiary Structure, and Size Distribution', *Biophysical Journal*, 88(1), pp. 455–466. Available at: https://doi.org/10.1529/BIOPHYSJ.104.046813.

Cirulli, E.T. *et al.* (2015) 'Exome sequencing in amyotrophic lateral sclerosis identifies risk genes and pathways', *Science*, 347(6229), pp. 1436–1441. Available at: https://doi.org/10.1126/science.aaa3650.

Ciura, S. *et al.* (2013) 'Loss of function of C9orf72 causes motor deficits in a zebrafish model of Amyotrophic Lateral Sclerosis', *Annals of Neurology*, 74(2), p. n/a-n/a. Available at: https://doi.org/10.1002/ana.23946.

Clement, A.M. *et al.* (2003) 'Wild-type nonneuronal cells extend survival of SOD1 mutant motor neurons in ALS mice', *Science*, 302(5642), pp. 113–117. Available at: https://doi.org/10.1126/science.1086071.

Cohen, J. (1960) 'A Coefficient of Agreement for Nominal Scales', *Educational and Psychological Measurement*, 20(1), pp. 37–46. Available at: https://doi.org/10.1177/001316446002000104.

Cohen, J. (1968) 'Weighted kappa: Nominal scale agreement provision for scaled disagreement or partial credit', *Psychological Bulletin*, 70(4), pp. 213–220. Available at: https://doi.org/10.1037/H0026256.

Cohen, T.J. *et al.* (2012) 'Redox signalling directly regulates TDP-43 via cysteine oxidation and disulphide cross-linking', *The EMBO Journal*, 31(5), pp. 1241–1252. Available at: https://doi.org/10.1038/EMBOJ.2011.471.

Cooper-Knock, J. *et al.* (2017) 'A data-driven approach links microglia to pathology and prognosis in amyotrophic lateral sclerosis', *Acta neuropathologica*

communications, 5(1), p. 23. Available at: https://doi.org/10.1186/s40478-017-0424-x.

Coraci, I.S. *et al.* (2002) 'CD36, a class B scavenger receptor, is expressed on microglia in Alzheimer's disease brains and can mediate production of reactive oxygen species in response to β-amyloid fibrils', *American Journal of Pathology*, 160(1), pp. 101–112. Available at: https://doi.org/10.1016/S0002-9440(10)64354-4.

Costa, M.M.J. Da *et al.* (2014) 'A new zebrafish model produced by TILLING of SOD1-related amyotrophic lateral sclerosis replicates key features of the disease and represents a tool for in vivo therapeutic screening', *Disease Models & Mechanisms*, 7(1), pp. 73–81. Available at: https://doi.org/10.1242/DMM.012013.

Cragnolini, A. *et al.* (2020) 'Regional brain susceptibility to neurodegeneration: what is the role of glial cells?', *Neural Regeneration Research*, 15(5), p. 838. Available at: https://doi.org/10.4103/1673-5374.268897.

Cudkowicz, M.E. *et al.* (1997) 'Epidemiology of mutations in superoxide dismutase in amyotrophic lateral sclerosis', *Annals of Neurology*, 41(2), pp. 210–221. Available at: https://doi.org/10.1002/ana.410410212.

Cunningham, C.L., Martínez-Cerdeño, V. and Noctor, S.C. (2013) 'Microglia Regulate the Number of Neural Precursor Cells in the Developing Cerebral Cortex', *Journal of Neuroscience*, 33(10), pp. 4216–4233. Available at: https://doi.org/10.1523/JNEUROSCI.3441-12.2013.

Van Damme, P. *et al.* (2007) 'Astrocytes regulate GluR2 expression in motor neurons and their vulnerability to excitotoxicity', *Proceedings of the National Academy of Sciences of the United States of America*, 104(37), pp. 14825–14830. Available at: https://doi.org/10.1073/PNAS.0705046104.

Danbolt, N.C., Storm-Mathisen, J. and Kanner, B.I. (1992) 'An [Na+ + K+]coupledl-glutamate transporter purified from rat brain is located in glial cell processes', *Neuroscience*, 51(2), pp. 295–310. Available at: https://doi.org/10.1016/0306-4522(92)90316-T.

Dangond, F. *et al.* (2004) 'Molecular signature of late-stage human ALS revealed by expression profiling of postmortem spinal cord gray matter', *Physiological Genomics*, 16(2), pp. 229–239. Available at: https://doi.org/10.1152/physiolgenomics.00087.2001.

Das, R. and Chinnathambi, S. (2021) 'Microglial remodeling of actin network by Tau oligomers, via G protein-coupled purinergic receptor, P2Y12R-driven chemotaxis', *Traffic*, 22(5), pp. 153–170. Available at: https://doi.org/10.1111/TRA.12784.

Deczkowska, A. *et al.* (2018) 'Disease-Associated Microglia: A Universal Immune Sensor of Neurodegeneration', *Cell*, 173(5), pp. 1073–1081. Available at: https://doi.org/10.1016/J.CELL.2018.05.003.

Van Deerlin, V.M. *et al.* (2008) 'TARDBP mutations in amyotrophic lateral sclerosis with TDP-43 neuropathology: a genetic and histopathological analysis', *The Lancet Neurology*, 7(5), pp. 409–416. Available at: https://doi.org/10.1016/S1474-4422(08)70071-1.

DeJesus-Hernandez, M. *et al.* (2010) 'De novo truncating FUS gene mutation as a

cause of sporadic amyotrophic lateral sclerosis', *Human Mutation*, 31(5), pp. E1377–E1389. Available at: https://doi.org/10.1002/HUMU.21241.

DeJesus-Hernandez, M. *et al.* (2011) 'Expanded GGGGCC Hexanucleotide Repeat in Noncoding Region of C9ORF72 Causes Chromosome 9p-Linked FTD and ALS', *Neuron*, 72(2), pp. 245–256. Available at: https://doi.org/10.1016/j.neuron.2011.09.011.

Dols-Icardo, O. *et al.* (2014) 'Characterization of the repeat expansion size in C9orf72 in amyotrophic lateral sclerosis and frontotemporal dementia', *Human Molecular Genetics*, 23(3), pp. 749–754. Available at: https://doi.org/10.1093/hmg/ddt460.

Donnelly, C.J. *et al.* (2013) 'RNA Toxicity from the ALS/FTD C9ORF72 Expansion Is Mitigated by Antisense Intervention', *Neuron*, 80(2), pp. 415–428. Available at: https://doi.org/10.1016/J.NEURON.2013.10.015.

Dormann, D. *et al.* (2010) 'ALS-associated fused in sarcoma (FUS) mutations disrupt Transportin-mediated nuclear import', *The EMBO Journal*, 29(16), pp. 2841–2857. Available at: https://doi.org/10.1038/EMBOJ.2010.143.

Drepper, C. *et al.* (2011) 'C-terminal FUS/TLS mutations in familial and sporadic ALS in Germany', *Neurobiology of Aging*, 32(3), pp. 548.e1-548.e4. Available at: https://doi.org/10.1016/J.NEUROBIOLAGING.2009.11.017.

Ederle, H. and Dormann, D. (2017) 'TDP-43 and FUS en route from the nucleus to the cytoplasm', *FEBS Letters*, 591(11), pp. 1489–1507. Available at: https://doi.org/10.1002/1873-3468.12646.

Ellis, C.M. *et al.* (2001) 'Volumetric analysis reveals corticospinal tract degeneration and extramotor involvement in ALS', *Neurology*, 57(9), pp. 1571–1578. Available at: https://doi.org/10.1212/WNL.57.9.1571.

Ervin, J.F. *et al.* (2007) 'Postmortem delay has minimal effect on brain RNA integrity', *Journal of Neuropathology and Experimental Neurology*, 66(12), pp. 1093–1099. Available at: https://doi.org/10.1097/nen.0b013e31815c196a.

Essat, M. *et al.* (2022) 'Understanding the current nutritional management for people with amyotrophic lateral sclerosis - A mapping review', *Clinical Nutrition ESPEN*, 49, pp. 328–340. Available at: https://doi.org/10.1016/J.CLNESP.2022.03.026.

Etzerodt, A. and Moestrup, S.K. (2013) 'CD163 and inflammation: Biological, diagnostic, and therapeutic aspects', *Antioxidants and Redox Signaling*, pp. 2352–2363. Available at: https://doi.org/10.1089/ars.2012.4834.

Fahrenhold, M. *et al.* (2018) 'TREM2 expression in the human brain: a marker of monocyte recruitment?', *Brain Pathology*, 28(5), pp. 595–602. Available at: https://doi.org/10.1111/bpa.12564.

Farg, M.A. *et al.* (2014) 'C9ORF72, implicated in amytrophic lateral sclerosis and frontotemporal dementia, regulates endosomal trafficking', *Human molecular genetics*, 23(13), pp. 3579–3595. Available at: https://doi.org/10.1093/HMG/DDU068.

Fedor, H.L. and De Marzo, A.M. (2005) 'Practical Methods for Tissue Microarray Construction', in G.H. Su (ed.) *Pancreatic Cancer: Methods and Protocols*. Totowa,

NJ: Humana Press, pp. 89–101. Available at: https://doi.org/10.1385/1-59259-780-7:089.

Feiler, M.S. *et al.* (2015) 'TDP-43 is intercellularly transmitted across axon terminals', *Journal of Cell Biology*, 211(4), pp. 897–911. Available at: https://doi.org/10.1083/JCB.201504057.

Fernandez, C.G. *et al.* (2019) 'The role of apoE4 in disrupting the homeostatic functions of astrocytes and microglia in aging and Alzheimer's disease', *Frontiers in Aging Neuroscience*, 10(FEB), p. 14. Available at: https://doi.org/10.3389/FNAGI.2019.00014/XML/NLM.

Ferraiuolo, L. *et al.* (2011) 'Dysregulation of astrocyte–motoneuron cross-talk in mutant superoxide dismutase 1-related amyotrophic lateral sclerosis', *Brain*, 134(9), pp. 2627–2641. Available at: https://doi.org/10.1093/BRAIN/AWR193.

Ferrari, R. *et al.* (2011) 'FTD and ALS: a tale of two diseases', *Current Alzheimer research*, 8(3), p. 273. Available at: https://doi.org/10.2174/156720511795563700.

Figueroa-Romero, C. *et al.* (2012) 'Identification of Epigenetically Altered Genes in Sporadic Amyotrophic Lateral Sclerosis', *PLOS ONE*, 7(12), p. e52672. Available at: https://doi.org/10.1371/JOURNAL.PONE.0052672.

Fleige, S. and Pfaffl, M.W. (2006) 'RNA integrity and the effect on the real-time qRT-PCR performance', *Molecular Aspects of Medicine*, 27(2–3), pp. 126–139. Available at: https://doi.org/10.1016/J.MAM.2005.12.003.

Ford, A.L. *et al.* (1995) 'Normal adult ramified microglia separated from other central nervous system macrophages by flow cytometric sorting. Phenotypic differences defined and direct ex vivo antigen presentation to myelin basic protein-reactive CD4+ T cells compared.', *The Journal of Immunology*, 154(9).

Foster, L.A. and Salajegheh, M.K. (2019) 'Motor Neuron Disease: Pathophysiology, Diagnosis, and Management', *American Journal of Medicine*. Elsevier, pp. 32–37. Available at: https://doi.org/10.1016/j.amjmed.2018.07.012.

Fraser, D.A., Pisalyaput, K. and Tenner, A.J. (2010) 'C1q enhances microglial clearance of apoptotic neurons and neuronal blebs, and modulates subsequent inflammatory cytokine production', *Journal of Neurochemistry*, 112(3), pp. 733–743. Available at: https://doi.org/10.1111/J.1471-4159.2009.06494.X.

Frenkel, D. *et al.* (2013) 'Scara1 deficiency impairs clearance of soluble amyloid-β by mononuclear phagocytes and accelerates Alzheimer's-like disease progression', *Nature Communications*, 4(1), p. 2030. Available at: https://doi.org/10.1038/ncomms3030.

Friedman, B.A. *et al.* (2018) 'Diverse Brain Myeloid Expression Profiles Reveal Distinct Microglial Activation States and Aspects of Alzheimer's Disease Not Evident in Mouse Models.', *Cell reports*, 22(3), pp. 832–847. Available at: https://doi.org/10.1016/j.celrep.2017.12.066.

Funikov, S.Y. *et al.* (2018) 'FUS(1-359) transgenic mice as a model of ALS: pathophysiological and molecular aspects of the proteinopathy', 19(3), pp. 189–204. Available at: https://doi.org/10.1007/s10048-018-0553-9.

Galatro, T.F. *et al.* (2017) 'Transcriptomic analysis of purified human cortical

microglia reveals age-associated changes', *Nature Neuroscience*, 20(8), pp. 1162–1171. Available at: https://doi.org/10.1038/nn.4597.

García-Redondo, A. *et al.* (2013) 'Analysis of the C9orf72 Gene in Patients with Amyotrophic Lateral Sclerosis in Spain and Different Populations Worldwide', *Human Mutation*, 34(1), pp. 79–82. Available at: https://doi.org/10.1002/HUMU.22211.

Gautier, E.L. *et al.* (2012) 'Gene-expression profiles and transcriptional regulatory pathways that underlie the identity and diversity of mouse tissue macrophages', *Nature Immunology*, 13(11), pp. 1118–1128. Available at: https://doi.org/10.1038/ni.2419.

Gendron, T.F. *et al.* (2013) 'Antisense transcripts of the expanded C9ORF72 hexanucleotide repeat form nuclear RNA foci and undergo repeat-associated non-ATG translation in c9FTD/ALS', *Acta Neuropathologica*, 126(6), pp. 829–844. Available at: https://doi.org/10.1007/S00401-013-1192-8/FIGURES/7.

Georgoudaki, A. *et al.* (2015) 'CD244 is expressed on dendritic cells and regulates their functions', *Immunology & Cell Biology*, 93(6), pp. 581–590. Available at: https://doi.org/10.1038/icb.2014.124.

Giovannelli, I. *et al.* (2021) 'Amyotrophic lateral sclerosis transcriptomics reveals immunological effects of low-dose interleukin-2', *Brain Communications*, 3(3). Available at: https://doi.org/10.1093/BRAINCOMMS/FCAB141.

Giraldo, M. *et al.* (2013) 'Variants in triggering receptor expressed on myeloid cells 2 are associated with both behavioral variant frontotemporal lobar degeneration and Alzheimer's disease', *Neurobiology of Aging*, 34(8), pp. 2077.e11-2077.e18. Available at: https://doi.org/10.1016/J.NEUROBIOLAGING.2013.02.016.

Gitcho, M.A. *et al.* (2008) 'TDP-43 A315T mutation in familial motor neuron disease', *Annals of neurology*, 63(4), pp. 535–538. Available at: https://doi.org/10.1002/ANA.21344.

Gong, Y.H. *et al.* (2000) 'Restricted Expression of G86R Cu/Zn Superoxide Dismutase in Astrocytes Results in Astrocytosis But Does Not Cause Motoneuron Degeneration', *Journal of Neuroscience*, 20(2), pp. 660–665. Available at: https://doi.org/10.1523/JNEUROSCI.20-02-00660.2000.

Gosselin, D. *et al.* (2017) 'An environment-dependent transcriptional network specifies human microglia identity', *Science*, 356(6344), pp. 1248–1259. Available at: https://doi.org/10.1126/SCIENCE.AAL3222/SUPPL_FILE/AAL3222_GOSSELIN_TABLES6.XLSX.

Govone, F. *et al.* (2014) 'Lack of association between APOE gene polymorphisms and amyotrophic lateral sclerosis: A comprehensive meta-analysis', *Amyotrophic Lateral Sclerosis and Frontotemporal Degeneration*, 15(7–8), pp. 551–556. Available at: https://doi.org/10.3109/21678421.2014.918149.

Grabert, K. *et al.* (2016) 'Microglial brain region-dependent diversity and selective regional sensitivities to aging', *Nature Neuroscience*, 19(3), pp. 504–516. Available at: https://doi.org/10.1038/nn.4222.

Gravel, M. *et al.* (2016) 'IL-10 Controls Early Microglial Phenotypes and Disease

Onset in ALS Caused by Misfolded Superoxide Dismutase 1.', *The Journal of neuroscience : the official journal of the Society for Neuroscience*, 36(3), pp. 1031–48. Available at: https://doi.org/10.1523/JNEUROSCI.0854-15.2016.

Gredal, O. *et al.* (2000) 'Unchanged total number of neurons in motor cortex and neocortex in amyotrophic lateral sclerosis: a stereological study', *Journal of Neuroscience Methods*, 95(2), pp. 171–176. Available at: https://doi.org/10.1016/S0165-0270(99)00175-2.

Griffiths, I. *et al.* (1998) 'Axonal swellings and degeneration in mice lacking the major proteolipid of myelin', *Science*, 280(5369), pp. 1610–1613. Available at: https://doi.org/10.1126/SCIENCE.280.5369.1610/ASSET/D522FCE4-FDA0-46A2-8068-99D37D205650/ASSETS/GRAPHIC/SE2386559004.JPEG.

Guerreiro, R. *et al.* (2013) 'TREM2 Variants in Alzheimer's Disease ', *New England Journal of Medicine*, 368(2), pp. 117–127. Available at: https://doi.org/10.1056/NEJMOA1211851/SUPPL_FILE/NEJMOA1211851_DISCLOSURES.PDF.

Guerreiro, R.J. *et al.* (2013) 'Using Exome Sequencing to Reveal Mutations in TREM2 Presenting as a Frontotemporal Dementia–like Syndrome Without Bone Involvement', *JAMA Neurology*, 70(1), pp. 78–84. Available at: https://doi.org/10.1001/JAMANEUROL.2013.579.

Guneykaya, D. *et al.* (2018) 'Transcriptional and Translational Differences of Microglia from Male and Female Brains.', *Cell reports*, 24(10), pp. 2773-2783.e6. Available at: https://doi.org/10.1016/j.celrep.2018.08.001.

Guo, H. *et al.* (2003) 'Increased expression of the glial glutamate transporter EAAT2 modulates excitotoxicity and delays the onset but not the outcome of ALS in mice', *Human Molecular Genetics*, 12(19), pp. 2519–2532. Available at: https://doi.org/10.1093/HMG/DDG267.

Gurney, M.E. *et al.* (1994) 'Motor neuron degeneration in mice that express a human Cu,Zn superoxide dismutase mutation.', *Science (New York, N.Y.)*, 264(5166), pp. 1772–5. Available at: http://www.ncbi.nlm.nih.gov/pubmed/8209258 (Accessed: 20 December 2018).

Haeusler, A.R. *et al.* (2014) 'C9orf72 nucleotide repeat structures initiate molecular cascades of disease', *Nature 2014 507:7491*, 507(7491), pp. 195–200. Available at: https://doi.org/10.1038/nature13124.

Haidet-Phillips, A.M. *et al.* (2011) 'Astrocytes from familial and sporadic ALS patients are toxic to motor neurons', *Nature Biotechnology 2011 29:9*, 29(9), pp. 824–828. Available at: https://doi.org/10.1038/nbt.1957.

Hall, E.D., Oostveen, J.A. and Gurney, M.E. (1998) 'Relationship of microglial and astrocytic activation to disease onset and progression in a transgenic model of familial ALS.', *Glia*, 23(3), pp. 249–56. Available at: http://www.ncbi.nlm.nih.gov/pubmed/9633809 (Accessed: 19 December 2018).

Hall, J.S. *et al.* (2012) 'Enhanced stability of microRNA expression facilitates classification of FFPE tumour samples exhibiting near total mRNA degradation', *British Journal of Cancer*, 107(4), pp. 684–694. Available at: https://doi.org/10.1038/bjc.2012.294.

Hambardzumyan, D., Gutmann, D.H. and Kettenmann, H. (2016) 'The role of microglia and macrophages in glioma maintenance and progression.', *Nature neuroscience*, 19(1), pp. 20–7. Available at: https://doi.org/10.1038/nn.4185.

Harris, F.M. *et al.* (2004) 'Astroglial regulation of apolipoprotein E expression in neuronal cells: Implications for Alzheimer's disease', *Journal of Biological Chemistry*, 279(5), pp. 3862–3868. Available at: https://doi.org/10.1074/jbc.M309475200.

Haure-Mirande, J.V. *et al.* (2017) 'Deficiency of TYROBP, an adapter protein for TREM2 and CR3 receptors, is neuroprotective in a mouse model of early Alzheimer's pathology', *Acta Neuropathologica*, 134(5), pp. 769–788. Available at: https://doi.org/10.1007/S00401-017-1737-3/FIGURES/7.

Haure-Mirande, J.V. *et al.* (2022) 'Microglial TYROBP/DAP12 in Alzheimer's disease: Transduction of physiological and pathological signals across TREM2', *Molecular Neurodegeneration 2022 17:1*, 17(1), pp. 1–15. Available at: https://doi.org/10.1186/S13024-022-00552-W.

Hayashi, H. *et al.* (2004) 'Glial lipoproteins stimulate axon growth of central nervous system neurons in compartmented cultures.', *The Journal of biological chemistry*, 279(14), pp. 14009–15. Available at: https://doi.org/10.1074/jbc.M313828200.

Hayashi, S. *et al.* (2001) 'Pathological study of the diffuse myelin pallor in the anterolateral columns of the spinal cord in amyotrophic lateral sclerosis', *Journal of the Neurological Sciences*, 188(1–2), pp. 3–7. Available at: https://doi.org/10.1016/S0022-510X(01)00531-7.

Hayes, G.M., Woodroofe, M.N. and Cuzner, M.L. (1987) 'Microglia are the major cell type expressing MHC class II in human white matter', *Journal of the neurological sciences*, 80(1), pp. 25–37. Available at: https://doi.org/10.1016/0022-510X(87)90218-8.

Henkel, J.S. *et al.* (2004) 'Presence of Dendritic Cells, MCP-1, and Activated Microglia/Macrophages in Amyotrophic Lateral Sclerosis Spinal Cord Tissue', *Annals of Neurology*, 55(2), pp. 221–235. Available at: https://doi.org/10.1002/ana.10805.

Henkel, J.S. *et al.* (2006) 'The chemokine MCP-1 and the dendritic and myeloid cells it attracts are increased in the mSOD1 mouse model of ALS', *Molecular and Cellular Neuroscience*, 31(3), pp. 427–437. Available at: https://doi.org/10.1016/J.MCN.2005.10.016.

Hennig, S. *et al.* (2015) 'Prion-like domains in RNA binding proteins are essential for building subnuclear paraspeckles', *The Journal of Cell Biology*, 210(4), p. 529. Available at: https://doi.org/10.1083/JCB.201504117.

Hensley, K. *et al.* (2002) 'Temporal patterns of cytokine and apoptosis-related gene expression in spinal cords of the G93A-SOD1 mouse model of amyotrophic lateral sclerosis', *Journal of Neurochemistry*, 82(2), pp. 365–374. Available at: https://doi.org/10.1046/j.1471-4159.2002.00968.x.

Heraty, L. (2019) *Tissue Microarrays to assess TDP-43 and Microglial Pathologyin Motor Neurone Disease*. University of Sheffiled.

Herculano-Houzel, S. (2014) 'The glia/neuron ratio: How it varies uniformly across brain structures and species and what that means for brain physiology and

evolution', *Glia*, 62(9), pp. 1377–1391. Available at: https://doi.org/10.1002/GLIA.22683.

Hergesheimer, R.C. *et al.* (2019) 'The debated toxic role of aggregated TDP-43 in amyotrophic lateral sclerosis: a resolution in sight?', *Brain*, 142(5), p. 1176. Available at: https://doi.org/10.1093/BRAIN/AWZ078.

Hewitt, S.M. *et al.* (2014) 'Controls for Immunohistochemistry: The Histochemical Society's Standards of Practice for Validation of Immunohistochemical Assays', *Journal of Histochemistry and Cytochemistry*, 62(10), p. 693. Available at: https://doi.org/10.1369/0022155414545224.

Hickey, W.F. and Kimura, H. (1988) 'Perivascular microglial cells of the CNS are bone marrow-derived and present antigen in vivo.', *Science (New York, N.Y.)*, 239(4837), pp. 290–2. Available at: https://doi.org/10.1126/SCIENCE.3276004.

Hickman, S. *et al.* (2018) 'Microglia in neurodegeneration', *Nature Neuroscience*, 21(10), pp. 1359–1369. Available at: https://doi.org/10.1038/s41593-018-0242-x.

Hickman, S.E. *et al.* (2013) 'The microglial sensome revealed by direct RNA sequencing', *Nature Neuroscience*, 16(12), pp. 1896–1905. Available at: https://doi.org/10.1038/nn.3554.

Hickman, S.E., Allison, E.K. and El Khoury, J. (2008) 'Microglial dysfunction and defective beta-amyloid clearance pathways in aging Alzheimer's disease mice.', *The Journal of neuroscience : the official journal of the Society for Neuroscience*, 28(33), pp. 8354–60. Available at: https://doi.org/10.1523/JNEUROSCI.0616-08.2008.

Hobson, E. V. *et al.* (2016) 'Clinical aspects of motor neurone disease', *Medicine*, 44(9), pp. 552–556. Available at: https://doi.org/10.1016/J.MPMED.2016.06.004.

Holness, C.L. and Simmons, D.L. (1993) 'Molecular cloning of CD68, a human macrophage marker related to lysosomal glycoproteins', *Blood*, 81(6), pp. 1607–1613. Available at: https://doi.org/10.1182/blood.v81.6.1607.1607.

Holtman, I.R. *et al.* (2015) 'Induction of a common microglia gene expression signature by aging and neurodegenerative conditions: a co-expression meta-analysis', *Acta neuropathologica communications*, 3(1), p. 31. Available at: https://doi.org/10.1186/s40478-015-0203-5.

Holtzman, D.M. *et al.* (1995) 'Low density lipoprotein receptor-related protein mediates apolipoprotein E-dependent neurite outgrowth in a central nervous system-derived neuronal cell line.', *Proceedings of the National Academy of Sciences*, 92(21), pp. 9480–9484. Available at: https://doi.org/10.1073/PNAS.92.21.9480.

Hong, S. *et al.* (2016) 'Complement and microglia mediate early synapse loss in Alzheimer mouse models.', *Science (New York, N.Y.)*, 352(6286), pp. 712–716. Available at: https://doi.org/10.1126/science.aad8373.

Hoshiko, M. *et al.* (2012) 'Deficiency of the Microglial Receptor CX3CR1 Impairs Postnatal Functional Development of Thalamocortical Synapses in the Barrel Cortex', *Journal of Neuroscience*, 32(43), pp. 15106–15111. Available at: https://doi.org/10.1523/JNEUROSCI.1167-12.2012.

Howland, D.S. *et al.* (2002) 'Focal loss of the glutamate transporter EAAT2 in a transgenic rat model of SOD1 mutant-mediated amyotrophic lateral sclerosis (ALS)',

Proceedings of the National Academy of Sciences, 99(3), pp. 1604–1609. Available at: https://doi.org/10.1073/PNAS.032539299.

Huang, D.W., Sherman, B.T. and Lempicki, R.A. (2009) 'Systematic and integrative analysis of large gene lists using DAVID bioinformatics resources', *Nature Protocols*, 4(1), pp. 44–57. Available at: https://doi.org/10.1038/nprot.2008.211.

Humphrey, M.B., Xing, J. and Titus, A. (2015) 'The TREM2-DAP12 signaling pathway in Nasu–Hakola disease: a molecular genetics perspective', *Research and Reports in Biochemistry*, 5, p. 89. Available at: https://doi.org/10.2147/rrbc.s58057.

Hunter, M. *et al.* (2021) 'Microglial transcriptome analysis in the rNLS8 mouse model of TDP-43 proteinopathy reveals discrete expression profiles associated with neurodegenerative progression and recovery', *Acta Neuropathologica Communications*, 9(1). Available at: https://doi.org/10.1186/s40478-021-01239-x.

Ince, P.G. *et al.* (2003) 'Corticospinal tract degeneration in the progressive muscular atrophy variant of ALS', *Neurology*, 60(8), pp. 1252–1258. Available at: https://doi.org/10.1212/01.WNL.0000058901.75728.4E.

Ince, P.G., Highley, J.R. and Wharton, S.B. (2015) 'Motor Neuron Disorders', in S. Love et al. (eds) *Greenfield's Neuropathology*. 9th edn. Oxford Academic, pp. 817–848. Available at: https://doi.org/10.1093/jnen/74.12.1185.

Ishaque, A. *et al.* (2022) 'Distinct patterns of progressive gray and white matter degeneration in amyotrophic lateral sclerosis', *Human Brain Mapping*, 43(5), pp. 1519–1534. Available at: https://doi.org/10.1002/HBM.25738.

Ishigaki, S. and Sobue, G. (2018) 'Importance of functional loss of FUS in FTLD/ALS', *Frontiers in Molecular Biosciences*, 5(MAY), p. 44. Available at: https://doi.org/10.3389/FMOLB.2018.00044/XML/NLM.

Jaarsma, D. *et al.* (2001) 'CuZn superoxide dismutase (SOD1) accumulates in vacuolated mitochondria in transgenic mice expressing amyotrophic lateral sclerosis-linked SOD1 mutations', *Acta Neuropathologica 2001 102:4*, 102(4), pp. 293–305. Available at: https://doi.org/10.1007/S004010100399.

Jäkel, S. and Dimou, L. (2017) 'Glial cells and their function in the adult brain: A journey through the history of their ablation', *Frontiers in Cellular Neuroscience*, 11, p. 24. Available at: https://doi.org/10.3389/FNCEL.2017.00024/XML/NLM.

Javed, K. and Lui, F. (2018) *Neuroanatomy, Lateral Corticospinal Tract*, *StatPearls*. StatPearls Publishing. Available at: https://www.ncbi.nlm.nih.gov/books/NBK534818/ (Accessed: 12 August 2022).

Jiang, J. *et al.* (2016) 'Gain of Toxicity from ALS/FTD-Linked Repeat Expansions in C9ORF72 Is Alleviated by Antisense Oligonucleotides Targeting GGGGCC-Containing RNAs', *Neuron*, 90(3), pp. 535–550. Available at: https://doi.org/10.1016/J.NEURON.2016.04.006.

Jiang, Y.M. *et al.* (2005) 'Gene expression profile of spinal motor neurons in sporadic amyotrophic lateral sclerosis', *Annals of Neurology*, 57(2), pp. 236–251. Available at: https://doi.org/10.1002/ana.20379.

Jin, M. *et al.* (2020) 'Peripheral proinflammatory Th1/Th17 immune cell shift is linked

to disease severity in amyotrophic lateral sclerosis', *Scientific Reports 2020 10:1*, 10(1), pp. 1–13. Available at: https://doi.org/10.1038/s41598-020-62756-8.

Johnson, J.K. *et al.* (2005) 'Frontotemporal Lobar Degeneration: Demographic Characteristics of 353 Patients', *Archives of Neurology*, 62(6), pp. 925–930. Available at: https://doi.org/10.1001/ARCHNEUR.62.6.925.

Jones, A.R. *et al.* (2015) 'Stratified gene expression analysis identifies major amyotrophic lateral sclerosis genes', *Neurobiology of Aging*, 36(5), pp. 2006.e1-2006.e9. Available at: https://doi.org/10.1016/J.NEUROBIOLAGING.2015.02.017.

Jonsson, T. *et al.* (2013) 'Variant of *TREM2* Associated with the Risk of Alzheimer's Disease', *New England Journal of Medicine*, 368(2), pp. 107–116. Available at: https://doi.org/10.1056/NEJMoa1211103.

Jordan, B.D. *et al.* (1997) 'Apolipoprotein E ∈4 Associated With Chronic Traumatic Brain Injury in Boxing', *JAMA*, 278(2), pp. 136–140. Available at: https://doi.org/10.1001/JAMA.1997.03550020068040.

Jurga, A.M., Paleczna, M. and Kuter, K.Z. (2020) 'Overview of General and Discriminating Markers of Differential Microglia Phenotypes', *Frontiers in Cellular Neuroscience*, 14, p. 198. Available at: https://doi.org/10.3389/fncel.2020.00198.

Kaifu, T. *et al.* (2003) 'Osteopetrosis and thalamic hypomyelinosis with synaptic degeneration in DAP12-deficient mice', *The Journal of Clinical Investigation*, 111(3), pp. 323–332. Available at: https://doi.org/10.1172/JCI16923.

Kamelgarn, M. *et al.* (2016) 'Proteomic analysis of FUS interacting proteins provides insights into FUS function and its role in ALS', *Biochimica et Biophysica Acta (BBA) - Molecular Basis of Disease*, 1862(10), pp. 2004–2014. Available at: https://doi.org/10.1016/J.BBADIS.2016.07.015.

Kamphuis, W. *et al.* (2016) 'Transcriptional profiling of CD11c-positive microglia accumulating around amyloid plaques in a mouse model for Alzheimer's disease', *Biochimica et Biophysica Acta (BBA) - Molecular Basis of Disease*, 1862(10), pp. 1847–1860. Available at: https://doi.org/10.1016/J.BBADIS.2016.07.007.

Kang, S.H. *et al.* (2013) 'Degeneration and impaired regeneration of gray matter oligodendrocytes in amyotrophic lateral sclerosis', *Nature Neuroscience 2013 16:5*, 16(5), pp. 571–579. Available at: https://doi.org/10.1038/nn.3357.

Kano, O. *et al.* (2012) 'Peripheral nerve inflammation in ALS mice: cause or consequence.', *Neurology*, 78(11), pp. 833–5. Available at: https://doi.org/10.1212/WNL.0b013e318249f776.

Karlsborg, M. *et al.* (2004) 'Corticospinal tract degeneration and possible pathogenesis in ALS evaluated by MR diffusion tensor imaging', *Amyotrophic Lateral Sclerosis and Other Motor Neuron Disorders*, 5(3), pp. 136–140. Available at: https://doi.org/10.1080/14660820410018982.

Kassubek, J. *et al.* (2009) 'Global brain atrophy and corticospinal tract alterations in ALS, as investigated by voxel-based morphometry of 3-D MRI', *http://dx.doi.org/10.1080/14660820510038538*, 6(1 SUPPL. 1), pp. 213–220. Available at: https://doi.org/10.1080/14660820510038538.

Kawamata, H. *et al.* (2014) 'Abnormal Intracellular Calcium Signaling and SNARE-Dependent Exocytosis Contributes to SOD1G93A Astrocyte-Mediated Toxicity in Amyotrophic Lateral Sclerosis', *Journal of Neuroscience*, 34(6), pp. 2331–2348. Available at: https://doi.org/10.1523/JNEUROSCI.2689-13.2014.

Kawamata, T. *et al.* (1992) 'Immunologic reactions in amyotrophic lateral sclerosis brain and spinal cord tissue.', *The American Journal of Pathology*, 140(3), p. 691. Available at: /pmc/articles/PMC1886170/?report=abstract (Accessed: 9 August 2022).

Kawamura, M.F. *et al.* (2012) 'Impaired recruitment of neuroprotective microglia and T cells during acute neuronal injury coincides with increased neuronal vulnerability in an amyotrophic lateral sclerosis model', *Experimental Neurology*, 234(2), pp. 437–445. Available at: https://doi.org/10.1016/j.expneurol.2012.01.015.

Keren-Shaul, H. *et al.* (2017) 'A Unique Microglia Type Associated with Restricting Development of Alzheimer's Disease', *Cell*, 169(7), pp. 1276-1290.e17. Available at: https://doi.org/10.1016/j.cell.2017.05.018.

El Khoury, J. *et al.* (1996) 'Scavenger receptor-mediated adhesion of microglia to β-amyloid fibrils', *Nature*, 382(6593), pp. 716–719. Available at: https://doi.org/10.1038/382716a0.

Kigerl, K.A. *et al.* (2014) 'Pattern recognition receptors and central nervous system repair', *Experimental Neurology*, 258, pp. 5–16. Available at: https://doi.org/10.1016/J.EXPNEUROL.2014.01.001.

Kim, H.J. *et al.* (2016) 'Deficient autophagy in microglia impairs synaptic pruning and causes social behavioral defects', *Molecular Psychiatry 2016 22:11*, 22(11), pp. 1576–1584. Available at: https://doi.org/10.1038/mp.2016.103.

Klein, S.L. and Flanagan, K.L. (2016) 'Sex differences in immune responses', *Nature Reviews Immunology*, 16(10), pp. 626–638. Available at: https://doi.org/10.1038/nri.2016.90.

Kobayashi, M. *et al.* (2015) 'A DAP12-Dependent signal promotes pro-inflammatory polarization in microglia following nerve injury and exacerbates degeneration of injured neurons', *Glia*, 63(6), pp. 1073–1082. Available at: https://doi.org/10.1002/GLIA.22802.

Kober, D.L. *et al.* (2016) 'Neurodegenerative disease mutations in TREM2 reveal a functional surface and distinct loss-of-function mechanisms', *eLife*, 5(DECEMBER2016). Available at: https://doi.org/10.7554/ELIFE.20391.

Kodavati, M., Wang, H. and Hegde, M.L. (2020) 'Altered Mitochondrial Dynamics in Motor Neuron Disease: An Emerging Perspective', *Cells 2020, Vol. 9, Page 1065*, 9(4), p. 1065. Available at: https://doi.org/10.3390/CELLS9041065.

Konishi, H. and Kiyama, H. (2018) 'Microglial TREM2/DAP12 signaling: A double-edged sword in neural diseases', *Frontiers in Cellular Neuroscience*, 12, p. 206. Available at: https://doi.org/10.3389/FNCEL.2018.00206/XML/NLM.

Könnecke, H. and Bechmann, I. (2013) 'The role of microglia and matrix metalloproteinases involvement in neuroinflammation and gliomas.', *Clinical & developmental immunology*, 2013, p. 914104. Available at:

https://doi.org/10.1155/2013/914104.

Kononen, J. *et al.* (1998) 'Tissue microarrays for high-throughput molecular profiling of tumor specimens', *Nature Medicine*, 4(7), pp. 844–847. Available at: https://doi.org/10.1038/nm0798-844.

Korpetinou, A. *et al.* (2014) 'Serglycin: At the crossroad of inflammation and malignancy', *Frontiers in Oncology*. Frontiers Research Foundation. Available at: https://doi.org/10.3389/fonc.2013.00327.

Krasemann, S. *et al.* (2017) 'The TREM2-APOE Pathway Drives the Transcriptional Phenotype of Dysfunctional Microglia in Neurodegenerative Diseases', *Immunity*, 47(3), pp. 566-581.e9. Available at: https://doi.org/10.1016/j.immuni.2017.08.008.

Krumbholz, M. *et al.* (2006) 'Chemokines in multiple sclerosis: CXCL12 and CXCL13 up-regulation is differentially linked to CNS immune cell recruitment', *Brain*, 129(1), pp. 200–211. Available at: https://doi.org/10.1093/brain/awh680.

Kushner, P., Stephenson, D.T. and Wright, S. (1991) 'Reactive astrogliosis is widespread in the subcortical white matter of amyotrophic lateral sclerosis brain', *Journal of Neuropathology and Experimental Neurology*, 50(3), pp. 263–277. Available at: https://doi.org/10.1097/00005072-199105000-00008.

Kwiatkowski, T.J. *et al.* (2009) 'Mutations in the FUS/TLS gene on chromosome 16 cause familial amyotrophic lateral sclerosis.', *Science (New York, N.Y.)*, 323(5918), pp. 1205–8. Available at: https://doi.org/10.1126/science.1166066.

Lacomblez, L. *et al.* (1996) 'Dose-ranging study of riluzole in amyotrophic lateral sclerosis. Amyotrophic Lateral Sclerosis/Riluzole Study Group II', *Lancet (London, England)*, 347(9013), pp. 1425–1431. Available at: https://doi.org/10.1016/S0140-6736(96)91680-3.

LaDu, M.J. *et al.* (2001) 'Apolipoprotein E and apolipoprotein E receptors modulate Aβ-induced glial neuroinflammatory responses', *Neurochemistry International*, 39(5–6), pp. 427–434. Available at: https://doi.org/10.1016/S0197-0186(01)00050-X.

Landis, J.R. and Koch, G.G. (1977) 'The Measurement of Observer Agreement for Categorical Data', *Biometrics*, 33(1), p. 159. Available at: https://doi.org/10.2307/2529310.

Lanfranco, M.F. *et al.* (2021) 'Expression and secretion of apoE isoforms in astrocytes and microglia during inflammation', *Glia*, 69(6), pp. 1478–1493. Available at: https://doi.org/10.1002/GLIA.23974.

Lappe-Siefke, C. *et al.* (2003) 'Disruption of Cnp1 uncouples oligodendroglial functions in axonal support and myelination', *Nature Genetics 2003 33:3*, 33(3), pp. 366–374. Available at: https://doi.org/10.1038/ng1095.

Lattante, S., Rouleau, G.A. and Kabashi, E. (2013) 'TARDBP and FUS Mutations Associated with Amyotrophic Lateral Sclerosis: Summary and Update', *Human Mutation*, 34(6), pp. 812–826. Available at: https://doi.org/10.1002/HUMU.22319.

Law, C.W. *et al.* (2014) 'Voom: Precision weights unlock linear model analysis tools for RNA-seq read counts', *Genome Biology*, 15(2), pp. 1–17. Available at: https://doi.org/10.1186/GB-2014-15-2-R29/FIGURES/11.

Lederer, C.W. *et al.* (2007) 'Pathways and genes differentially expressed in the motor cortex of patients with sporadic amyotrophic lateral sclerosis', *BMC Genomics*, 8, p. 26. Available at: https://doi.org/10.1186/1471-2164-8-26.

Lee, Y. *et al.* (2012) 'Oligodendroglia metabolically support axons and contribute to neurodegeneration', *Nature 2012 487:7408*, 487(7408), pp. 443–448. Available at: https://doi.org/10.1038/nature11314.

Li, Y.J. *et al.* (2004) 'Apolipoprotein E is associated with age at onset of amyotrophic lateral sclerosis', *Neurogenetics*, 5(4), pp. 209–213. Available at: https://doi.org/10.1007/S10048-004-0193-0/FIGURES/1.

Liao, B. *et al.* (2012) 'Transformation from a neuroprotective to a neurotoxic microglial phenotype in a mouse model of ALS', *Experimental Neurology*, 237(1), pp. 147–152. Available at: https://doi.org/10.1016/j.expneurol.2012.06.011.

Liao, F., Yoon, H. and Kim, J. (2017) 'Apolipoprotein E metabolism and functions in brain and its role in Alzheimer's disease', *Current Opinion in Lipidology*, 28(1), p. 60. Available at: https://doi.org/10.1097/MOL.0000000000000383.

Liu, J., Gao, L. and Zang, D. (2015) 'Elevated Levels of IFN-γ in CSF and Serum of Patients with Amyotrophic Lateral Sclerosis', *PLOS ONE*. Edited by D.R. Borchelt, 10(9), p. e0136937. Available at: https://doi.org/10.1371/journal.pone.0136937.

Liu, W. *et al.* (2020) 'Trem2 promotes anti-inflammatory responses in microglia and is suppressed under pro-inflammatory conditions', *Human Molecular Genetics*, 29(19), pp. 3224–3248. Available at: https://doi.org/10.1093/HMG/DDAA209.

Liu, Y.J. *et al.* (2015) 'Activation of AMP-activated protein kinase α1 mediates mislocalization of TDP-43 in amyotrophic lateral sclerosis', *Human Molecular Genetics*, 24(3), pp. 787–801. Available at: https://doi.org/10.1093/HMG/DDU497.

Longinetti, E. and Fang, F. (2019) 'Epidemiology of amyotrophic lateral sclerosis: an update of recent literature', *Current Opinion in Neurology*, 32(5), p. 771. Available at: https://doi.org/10.1097/WCO.0000000000000730.

Lopez-Lopez, A. *et al.* (2014) 'CX3CR1 Is a Modifying Gene of Survival and Progression in Amyotrophic Lateral Sclerosis', *PLoS ONE*. Edited by C. Raoul, 9(5), p. e96528. Available at: https://doi.org/10.1371/journal.pone.0096528.

Love, M.I., Huber, W. and Anders, S. (2014) 'Moderated estimation of fold change and dispersion for RNA-seq data with DESeq2', *Genome Biology*, 15(12), p. 550. Available at: https://doi.org/10.1186/s13059-014-0550-8.

Ludolph, A. *et al.* (2015) 'A revision of the El Escorial criteria - 2015', *https://doi.org/10.3109/21678421.2015.1049183*, 16(5–6), pp. 291–292. Available at: https://doi.org/10.3109/21678421.2015.1049183.

Lutz, C. (2018) 'Mouse models of ALS: Past, present and future', *Brain Research*, 1693(Pt A), pp. 1–10. Available at: http://www.ncbi.nlm.nih.gov/pubmed/29577886 (Accessed: 22 January 2019).

MacDonald, A. *et al.* (2021) 'Single Cell Transcriptomics of Ependymal Cells Across Age, Region and Species Reveals Cilia-Related and Metal Ion Regulatory Roles as Major Conserved Ependymal Cell Functions', *Frontiers in Cellular Neuroscience*, 15, p. 268. Available at: https://doi.org/10.3389/FNCEL.2021.703951/BIBTEX.

Mackenzie, I.R., Rademakers, R. and Neumann, M. (2010) ‘TDP-43 and FUS in amyotrophic lateral sclerosis and frontotemporal dementia’, *The Lancet Neurology*. Elsevier, pp. 995–1007. Available at: https://doi.org/10.1016/S1474-4422(10)70195-2.

Mackenzie, I.R.A. and Neumann, M. (2016) ‘Molecular neuropathology of frontotemporal dementia: insights into disease mechanisms from postmortem studies’, *Journal of neurochemistry*, 138 Suppl 1, pp. 54–70. Available at: https://doi.org/10.1111/JNC.13588.

Mackenzie, I.R.A.A. *et al.* (2007) ‘Pathological TDP-43 distinguishes sporadic amyotrophic lateral sclerosis from amyotrophic lateral sclerosis with SOD1 mutations’, *Annals of Neurology*, 61(5), pp. 427–434. Available at: https://doi.org/10.1002/ana.21147.

Madji Hounoum, B. *et al.* (2017) ‘Wildtype motoneurons, ALS-Linked SOD1 mutation and glutamate profoundly modify astrocyte metabolism and lactate shuttling’, *GLIA*, 65(4), pp. 592–605. Available at: https://doi.org/10.1002/glia.23114.

Mahley, R.W. (1988) ‘Apolipoprotein E: Cholesterol transport protein with expanding role in cell biology’, *Science*, pp. 622–630. Available at: https://doi.org/10.1126/science.3283935.

Mahley, R.W. (2016) ‘Central nervous system lipoproteins: ApoE and regulation of cholesterol metabolism’, *Arteriosclerosis, Thrombosis, and Vascular Biology*, 36(7), pp. 1305–1315. Available at: https://doi.org/10.1161/ATVBAHA.116.307023.

Majounie, E. *et al.* (2012) ‘Frequency of the C9orf72 hexanucleotide repeat expansion in patients with amyotrophic lateral sclerosis and frontotemporal dementia: A cross-sectional study’, *The Lancet Neurology*, 11(4), pp. 323–330. Available at: https://doi.org/10.1016/S1474-4422(12)70043-1.

Masrori, P. and Van Damme, P. (2020) ‘Amyotrophic lateral sclerosis: a clinical review’, *European Journal of Neurology*, 27(10), pp. 1918–1929. Available at: https://doi.org/10.1111/ENE.14393.

Mathis, S. *et al.* (2019) ‘Genetics of amyotrophic lateral sclerosis: A review’, *Journal of the Neurological Sciences*, 399, pp. 217–226. Available at: https://doi.org/10.1016/J.JNS.2019.02.030.

Matthews, P.M. (2019) ‘Chronic inflammation in multiple sclerosis — seeing what was always there’, *Nature Reviews Neurology 2019 15:10*, 15(10), pp. 582–593. Available at: https://doi.org/10.1038/s41582-019-0240-y.

Mazaheri, F. *et al.* (2014) ‘Distinct roles for BAI1 and TIM-4 in the engulfment of dying neurons by microglia’, *Nature Communications 2014 5:1*, 5(1), pp. 1–11. Available at: https://doi.org/10.1038/ncomms5046.

McCauley, M.E. *et al.* (2020) ‘C9orf72 in myeloid cells suppresses STING-induced inflammation’, *Nature*, 585(7823), pp. 96–101. Available at: https://doi.org/10.1038/S41586-020-2625-X.

Michelucci, A. *et al.* (2009) ‘Characterization of the microglial phenotype under specific pro-inflammatory and anti-inflammatory conditions: Effects of oligomeric and fibrillar amyloid-β’, *Journal of Neuroimmunology*, 210(1–2), pp. 3–12. Available at:

https://doi.org/10.1016/j.jneuroim.2009.02.003.

Miller, R.G., Mitchell, J.D. and Moore, D.H. (2012) 'Riluzole for amyotrophic lateral sclerosis (ALS)/motor neuron disease (MND)', *Cochrane Database of Systematic Reviews* [Preprint], (3). Available at: https://doi.org/10.1002/14651858.CD001447.pub3.

Mitchell, J. *et al.* (2010) 'Familial amyotrophic lateral sclerosis is associated with a mutation in D-amino acid oxidase', *Proceedings of the National Academy of Sciences of the United States of America*, 107(16), pp. 7556–7561. Available at: https://doi.org/10.1073/PNAS.0914128107/SUPPL_FILE/PNAS.200914128SI.PDF.

Mitchell, R.M. *et al.* (2009) 'A CSF biomarker panel for identification of patients with amyotrophic lateral sclerosis.', *Neurology*, 72(1), pp. 14–9. Available at: https://doi.org/10.1212/01.wnl.0000333251.36681.a5.

Mittelbronn, M. *et al.* (2001) 'Local distribution of microglia in the normal adult human central nervous system differs by up to one order of magnitude', *Acta Neuropathologica 2000 101:3*, 101(3), pp. 249–255. Available at: https://doi.org/10.1007/S004010000284.

Miyamoto, A. *et al.* (2016) 'Microglia contact induces synapse formation in developing somatosensory cortex', *Nature Communications 2016 7:1*, 7(1), pp. 1–12. Available at: https://doi.org/10.1038/ncomms12540.

Monje, M.L., Toda, H. and Palmer, T.D. (2003) 'Inflammatory blockade restores adult hippocampal neurogenesis.', *Science (New York, N.Y.)*, 302(5651), pp. 1760–5. Available at: https://doi.org/10.1126/science.1088417.

Moreno-García, A. *et al.* (2018) 'An overview of the role of lipofuscin in age-related neurodegeneration', *Frontiers in Neuroscience*, 12(JUL), p. 464. Available at: https://doi.org/10.3389/FNINS.2018.00464/BIBTEX.

Mori, K. *et al.* (2013) 'The C9orf72 GGGGCC repeat is translated into aggregating dipeptide-repeat proteins in FTLD/ALS', *Science*, 339(6125), pp. 1335–1338. Available at: https://doi.org/10.1126/SCIENCE.1232927/SUPPL_FILE/PAPV2.PDF.

Motataianu, A., Barcutean, L. and Balasa, R. (2020) 'Neuroimmunity in amyotrophic lateral sclerosis: focus on microglia', *Amyotrophic Lateral Sclerosis and Frontotemporal Degeneration*, 21(3–4), pp. 159–166. Available at: https://doi.org/10.1080/21678421.2019.1708949.

Moulard, B. *et al.* (1996) 'Apolipoprotein E genotyping in sporadic amyotrophic lateral sclerosis: evidence for a major influence on the clinical presentation and prognosis', *Journal of the Neurological Sciences*, 139(SUPPL.), pp. 34–37. Available at: https://doi.org/10.1016/0022-510X(96)00085-8.

Mrdjen, D. *et al.* (2018) 'High-Dimensional Single-Cell Mapping of Central Nervous System Immune Cells Reveals Distinct Myeloid Subsets in Health, Aging, and Disease', *Immunity*, 48(2), pp. 380-395.e6. Available at: https://doi.org/10.1016/J.IMMUNI.2018.01.011.

Mueller, T.D. *et al.* (2002) 'Structure, binding, and antagonists in the IL-4/IL-13 receptor system', *Biochimica et Biophysica Acta (BBA) - Molecular Cell Research*, 1592(3), pp. 237–250. Available at: https://doi.org/10.1016/S0167-4889(02)00318-X.

Müller, K. *et al.* (2022) 'De novo mutations in SOD1 are a cause of ALS', *Journal of neurology, neurosurgery, and psychiatry*, 93(2), pp. 201–206. Available at: https://doi.org/10.1136/jnnp-2021-327520.

Murayama, S. *et al.* (1991) 'A unique pattern of astrocytosis in the primary motor area in amyotrophic lateral sclerosis', *Acta Neuropathologica 1991 82:6*, 82(6), pp. 456–461. Available at: https://doi.org/10.1007/BF00293379.

Nagai, M. *et al.* (2007) 'Astrocytes expressing ALS-linked mutated SOD1 release factors selectively toxic to motor neurons', *Nature Neuroscience 2007 10:5*, 10(5), pp. 615–622. Available at: https://doi.org/10.1038/nn1876.

NanoString Technologies (2016) *nCounter XT Assay User Manual*. Available at: https://www.nanostring.com/support/product-support/support-documentation (Accessed: 7 July 2019).

Naumann, M. *et al.* (2019) 'Phenotypes and malignancy risk of different FUS mutations in genetic amyotrophic lateral sclerosis', *Annals of Clinical and Translational Neurology*, 6(12), pp. 2384–2394. Available at: https://doi.org/10.1002/acn3.50930.

Nelson, P.T. *et al.* (2019) 'Limbic-predominant age-related TDP-43 encephalopathy (LATE): consensus working group report', *Brain*, 142(6), pp. 1503–1527. Available at: https://doi.org/10.1093/BRAIN/AWZ099.

Neumann, M. *et al.* (2006) 'Ubiquitinated TDP-43 in frontotemporal lobar degeneration and amyotrophic lateral sclerosis', *Science*, 314(5796), pp. 130–133. Available at: https://doi.org/10.1126/science.1134108.

Niebroj-Dobosz, I. *et al.* (2007) 'Myelin composition of spinal cord in a model of amyotrophic lateral sclerosis (ALS) in SOD1^{G93A} transgenic rats', *Folia Neuropathologica*, 45(4), pp. 236–241.

Nikodemova, M. *et al.* (2014) 'Spinal but not cortical microglia acquire an atypical phenotype with high VEGF, galectin-3 and osteopontin, and blunted inflammatory responses in ALS rats', *Neurobiology of Disease*, 69, pp. 43–53. Available at: https://doi.org/10.1016/j.nbd.2013.11.009.

Nimmerjahn, A., Kirchhoff, F. and Helmchen, F. (2005) 'Resting microglial cells are highly dynamic surveillants of brain parenchyma in vivo.', *Science (New York, N.Y.)*, 308(5726), pp. 1314–8. Available at: https://doi.org/10.1126/science.1110647.

Noh, M.-Y. *et al.* (no date) 'Defective phagocytic function of induced microglia-like cells is correlated with rapid progression of sporadic ALS'. Available at: https://doi.org/10.21203/rs.3.rs-29976/v1.

Nugent, A.A. *et al.* (2020) 'TREM2 Regulates Microglial Cholesterol Metabolism upon Chronic Phagocytic Challenge', *Neuron*, 105(5), pp. 837-854.e9. Available at: https://doi.org/10.1016/j.neuron.2019.12.007.

O'Rourke, J.G. *et al.* (2016) 'C9orf72 is required for proper macrophage and microglial function in mice', *Science*, 351(6279), pp. 1324–1329. Available at: https://doi.org/10.1126/science.aaf1064.

Oeckl, P. *et al.* (2020) 'Proteomics in cerebrospinal fluid and spinal cord suggests UCHL1, MAP2 and GPNMB as biomarkers and underpins importance of

transcriptional pathways in amyotrophic lateral sclerosis', *Acta Neuropathologica*, 139(1), pp. 119–134. Available at: https://doi.org/10.1007/s00401-019-02093-x.

Offen, D. *et al.* (2009) 'Spinal cord mRNA profile in patients with ALS: Comparison with transgenic mice expressing the human SOD-1 mutant', *Journal of Molecular Neuroscience*, 38(2), pp. 85–93. Available at: https://doi.org/10.1007/s12031-007-9004-z.

Ohsawa, K. *et al.* (2000) 'Involvement of Iba1 in membrane ruffling and phagocytosis of macrophages/microglia', *Journal of Cell Science*, 113(17), pp. 3073–3084. Available at: https://journals.biologists.com/jcs/article/113/17/3073/26221/Involvement-of-Iba1-in-membrane-ruffling-and (Accessed: 12 May 2021).

Olsen, M.K. *et al.* (2001) 'Disease mechanisms revealed by transcription profiling in SOD1-G93A transgenic mouse spinal cord', *Annals of Neurology*, 50(6), pp. 730–740. Available at: https://doi.org/10.1002/ana.1252.

Ou, S.H. *et al.* (1995) 'Cloning and characterization of a novel cellular protein, TDP-43, that binds to human immunodeficiency virus type 1 TAR DNA sequence motifs', *Journal of virology*, 69(6), pp. 3584–3596. Available at: https://doi.org/10.1128/JVI.69.6.3584-3596.1995.

Paloneva, J. *et al.* (2002) 'Mutations in two genes encoding different subunits of a receptor signaling complex result in an identical disease phenotype', *American Journal of Human Genetics*, 71(3), pp. 656–662. Available at: https://doi.org/10.1086/342259.

Pankiewicz, J.E. *et al.* (2021) 'Absence of Apolipoprotein E is associated with exacerbation of prion pathology and promotes microglial neurodegenerative phenotype', *Acta Neuropathologica Communications*, 9(1), pp. 1–30. Available at: https://doi.org/10.1186/S40478-021-01261-Z/FIGURES/12.

Paolicelli, R.C. *et al.* (2011) 'Synaptic pruning by microglia is necessary for normal brain development.', *Science (New York, N.Y.)*, 333(6048), pp. 1456–8. Available at: https://doi.org/10.1126/science.1202529.

Pardo, A.C. *et al.* (2006) 'Loss of the astrocyte glutamate transporter GLT1 modifies disease in SOD1G93A mice', *Experimental Neurology*, 201(1), pp. 120–130. Available at: https://doi.org/10.1016/J.EXPNEUROL.2006.03.028.

Parhizkar, S. *et al.* (2019) 'Loss of TREM2 function increases amyloid seeding but reduces plaque-associated ApoE', *Nature Neuroscience 2019 22:2*, 22(2), pp. 191–204. Available at: https://doi.org/10.1038/s41593-018-0296-9.

Parkhurst, C.N. *et al.* (2013) 'Microglia Promote Learning-Dependent Synapse Formation through Brain-Derived Neurotrophic Factor', *Cell*, 155(7), pp. 1596–1609. Available at: https://doi.org/10.1016/J.CELL.2013.11.030.

Pey, P. *et al.* (2014) 'Phenotypic profile of alternative activation marker CD163 is different in Alzheimer's and Parkinson's disease', *Acta Neuropathologica Communications*, 2(1). Available at: https://doi.org/10.1186/2051-5960-2-21.

Philips, T. *et al.* (2013) 'Oligodendrocyte dysfunction in the pathogenesis of amyotrophic lateral sclerosis', *Brain*, 136(2), pp. 471–482. Available at:

https://doi.org/10.1093/BRAIN/AWS339.

Philips, T. and Rothstein, J.D. (2015) ‘Rodent models of amyotrophic lateral sclerosis’, *Current Protocols in Pharmacology*, 2015(9), pp. 5.67.1-5.67.21. Available at: https://doi.org/10.1002/0471141755.ph0567s69.

Phukan, J., Pender, N.P. and Hardiman, O. (2007) ‘Cognitive impairment in amyotrophic lateral sclerosis’, *The Lancet Neurology*, 6(11), pp. 994–1003. Available at: https://doi.org/10.1016/S1474-4422(07)70265-X.

Pimenova, A.A., Marcora, E. and Goate, A.M. (2017) ‘A Tale of Two Genes: Microglial Apoe and Trem2’, *Immunity*. Cell Press, pp. 398–400. Available at: https://doi.org/10.1016/j.immuni.2017.08.015.

Pitas, R.E. *et al.* (1987) ‘Astrocytes synthesize apolipoprotein E and metabolize apolipoprotein E-containing lipoproteins’, *Biochimica et Biophysica Acta (BBA)/Lipids and Lipid Metabolism*, 917(1), pp. 148–161. Available at: https://doi.org/10.1016/0005-2760(87)90295-5.

Pons, A.L. *et al.* (2020) ‘Oligodendrocyte pathology exceeds axonal pathology in white matter in human amyotrophic lateral sclerosis’. Available at: https://doi.org/10.1002/path.5455.

Praline, J. *et al.* (2011) ‘APOE ε4 allele is associated with an increased risk of bulbar-onset amyotrophic lateral sclerosis in men’, *European Journal of Neurology*, 18(8), pp. 1046–1052. Available at: https://doi.org/10.1111/J.1468-1331.2010.03330.X.

Prasad, A. *et al.* (2019) ‘Molecular mechanisms of TDP-43 misfolding and pathology in amyotrophic lateral sclerosis’, *Frontiers in Molecular Neuroscience*, 12, p. 25. Available at: https://doi.org/10.3389/FNMOL.2019.00025/BIBTEX.

Quek, H. *et al.* (2022) ‘ALS monocyte-derived microglia-like cells reveal cytoplasmic TDP-43 accumulation, DNA damage, and cell-specific impairment of phagocytosis associated with disease progression’, *Journal of Neuroinflammation*, 19(1), pp. 1–21. Available at: https://doi.org/10.1186/S12974-022-02421-1/FIGURES/7.

R Core Team (2016) ‘R: A language and environment for statistical computing.’ Vienna, Austria.

R Core Team (2019) ‘R: A language and environment for statistical computing.’ Vienna, Austria: R Foundation for Statistical Computing. Available at: https://www.r-project.org/.

R Core Team (2020) ‘R: A language and environment for statistical computing.’ Vienna, Austria: R Foundation for Statistical Computing. Available at: https://www.r-project.org/.

Raha-Chowdhury, R. *et al.* (2019) ‘Choroid Plexus Acts as Gatekeeper for TREM2, Abnormal Accumulation of ApoE, and Fibrillary Tau in Alzheimer’s Disease and in Down Syndrome Dementia’, *Journal of Alzheimer’s Disease*, 69(1), pp. 91–109. Available at: https://doi.org/10.3233/JAD-181179.

Ramesh, T.M., Shaw, P.J. and McDearmid, J. (2014) ‘A zebrafish model exemplifies the long preclinical period of motor neuron disease.’, *Journal of neurology, neurosurgery, and psychiatry*, 85(11), pp. 1288–9. Available at:

https://doi.org/10.1136/jnnp-2014-308288.

Rayaprolu, S. *et al.* (2013) 'TREM2 in neurodegeneration: evidence for association of the p.R47H variant with frontotemporal dementia and Parkinson's disease', *Molecular Neurodegeneration*, 8(1), p. 19. Available at: https://doi.org/10.1186/1750-1326-8-19.

Reaume, A.G. *et al.* (1996) 'Motor neurons in Cu/Zn superoxide dismutase-deficient mice develop normally but exhibit enhanced cell death after axonal injury', *Nature genetics*, 13(1), pp. 43–47. Available at: https://doi.org/10.1038/NG0596-43.

Renton, A.E. *et al.* (2011) 'A hexanucleotide repeat expansion in C9ORF72 is the cause of chromosome 9p21-linked ALS-FTD', *Neuron*, 72(2), pp. 257–268. Available at: https://doi.org/10.1016/j.neuron.2011.09.010.

Ripps, M.E. *et al.* (1995) 'Transgenic mice expressing an altered murine superoxide dismutase gene provide an animal model of amyotrophic lateral sclerosis.', *Proceedings of the National Academy of Sciences of the United States of America*, 92(3), pp. 689–93. Available at: https://doi.org/10.1073/pnas.92.3.689.

Ritchie, M.E. *et al.* (2015) 'limma powers differential expression analyses for RNA-sequencing and microarray studies.', *Nucleic acids research*, 43(7), p. e47. Available at: https://doi.org/10.1093/nar/gkv007.

Ritzel, R.M. *et al.* (2015) 'Age- and location-related changes in microglial function', *Neurobiology of Aging*, 36(6), pp. 2153–2163. Available at: https://doi.org/10.1016/J.NEUROBIOLAGING.2015.02.016.

Rizzu, P. *et al.* (2016) 'C9orf72 is differentially expressed in the central nervous system and myeloid cells and consistently reduced in C9orf72, MAPT and GRN mutation carriers', *Acta neuropathologica communications*, 4(1), p. 37. Available at: https://doi.org/10.1186/S40478-016-0306-7/TABLES/3.

Rojas, P. *et al.* (2020) 'Amyotrophic Lateral Sclerosis: A Neurodegenerative Motor Neuron Disease With Ocular Involvement', *Frontiers in Neuroscience*, 14, p. 976. Available at: https://doi.org/10.3389/FNINS.2020.566858/BIBTEX.

Rosen, D.R. *et al.* (1993) 'Mutations in Cu/Zn superoxide dismutase gene are associated with familial amyotrophic lateral sclerosis', *Nature*, 362(6415), pp. 59–62. Available at: https://doi.org/10.1038/362059a0.

Rosso, S.M. *et al.* (2003) 'Frontotemporal dementia in The Netherlands: patient characteristics and prevalence estimates from a population-based study', *Brain*, 126(9), pp. 2016–2022. Available at: https://doi.org/10.1093/BRAIN/AWG204.

Rothstein, J.D. *et al.* (1995) 'Selective loss of glial glutamate transporter GLT-1 in amyotrophic lateral sclerosis', *Annals of Neurology*, 38(1), pp. 73–84. Available at: https://doi.org/10.1002/ANA.410380114.

Rothstein, J.D., Martin, L.J. and Kuncl, R.W. (1992) 'Decreased Glutamate Transport by the Brain and Spinal Cord in Amyotrophic Lateral Sclerosis', *New England Journal of Medicine*, 326(22), pp. 1464–1468. Available at: https://doi.org/10.1056/nejm199205283262204.

Rowland, L.P. (2001) 'How Amyotrophic Lateral Sclerosis Got Its Name: The Clinical-Pathologic Genius of Jean-Martin Charcot', *Archives of Neurology*, 58(3), pp.

512–515. Available at: https://doi.org/10.1001/ARCHNEUR.58.3.512.

RStudio Team (2020) ‘RStudio: Integrated Development for R.’ RStudio, PBC, Boston, MA. Available at: http://www.rstudio.com/.

Saberi, S. *et al.* (2015) ‘Neuropathology of Amyotrophic Lateral Sclerosis and Its Variants’, *Neurologic Clinics*, 33(4), pp. 855–876. Available at: https://doi.org/10.1016/j.ncl.2015.07.012.

Santoni, G. *et al.* (2015) ‘Danger- and pathogen-associated molecular patterns recognition by pattern-recognition receptors and ion channels of the transient receptor potential family triggers the inflammasome activation in immune cells and sensory neurons’, *Journal of Neuroinflammation*, 12(1). Available at: https://doi.org/10.1186/s12974-015-0239-2.

Sasabe, J. *et al.* (2012) ‘D-Amino acid oxidase controls motoneuron degeneration through D-serine’, *Proceedings of the National Academy of Sciences of the United States of America*, 109(2), pp. 627–632. Available at: https://doi.org/10.1073/PNAS.1114639109/SUPPL_FILE/PNAS.201114639SI.PDF.

Satoh, J. ichi *et al.* (2016) ‘TMEM119 marks a subset of microglia in the human brain’, *Neuropathology*, 36(1), pp. 39–49. Available at: https://doi.org/10.1111/neup.12235.

Satoh, J.I. *et al.* (2013) ‘A survey of TREM2 antibodies reveals neuronal but not microglial staining in formalin-fixed paraffin-embedded postmortem Alzheimer’s brain tissues’, *Alzheimer’s Research and Therapy*, 5(4), pp. 1–3. Available at: https://doi.org/10.1186/ALZRT184/FIGURES/3.

Schafer, D.P. *et al.* (2012) ‘Microglia Sculpt Postnatal Neural Circuits in an Activity and Complement-Dependent Manner’, *Neuron*, 74(4), pp. 691–705. Available at: https://doi.org/10.1016/J.NEURON.2012.03.026.

Schetters, S.T.T. *et al.* (2018) ‘Neuroinflammation: Microglia and T cells get ready to tango’, *Frontiers in Immunology*, 8(JAN), p. 1905. Available at: https://doi.org/10.3389/FIMMU.2017.01905/BIBTEX.

Schiffer, D. *et al.* (1996) *Reactive astrogliosis of the spinal cord in amyotrophic lateral sclerosis*, *Journal of the Neurological Sciences*. Elsevier. Available at: https://doi.org/10.1016/0022-510X(96)00073-1.

Schilling, M. *et al.* (2005) ‘Predominant phagocytic activity of resident microglia over hematogenous macrophages following transient focal cerebral ischemia: An investigation using green fluorescent protein transgenic bone marrow chimeric mice’, *Experimental Neurology*, 196(2), pp. 290–297. Available at: https://doi.org/10.1016/J.EXPNEUROL.2005.08.004.

Schludi, M.H. *et al.* (2017) ‘Spinal poly-GA inclusions in a C9orf72 mouse model trigger motor deficits and inflammation without neuron loss’, *Acta Neuropathologica*, 134(2), pp. 241–254. Available at: https://doi.org/10.1007/s00401-017-1711-0.

Schnell, L. *et al.* (1999) ‘Acute inflammatory responses to mechanical lesions in the CNS: differences between brain and spinal cord’, *European Journal of Neuroscience*, 11(10), pp. 3648–3658. Available at: https://doi.org/10.1046/J.1460-9568.1999.00792.X.

Scotland, R.S. *et al.* (2011) ‘Sex differences in resident immune cell phenotype underlie more efficient acute inflammatory responses in female mice’. Available at: https://doi.org/10.1182/blood-2011-03-340281.

Scotter, E.L., Chen, H.J. and Shaw, C.E. (2015) ‘TDP-43 Proteinopathy and ALS: Insights into Disease Mechanisms and Therapeutic Targets’, *Neurotherapeutics : the journal of the American Society for Experimental NeuroTherapeutics*, 12(2), pp. 352–363. Available at: https://doi.org/10.1007/S13311-015-0338-X.

Seelaar, H. *et al.* (2007) ‘TDP-43 pathology in familial frontotemporal dementia and motor neuron disease without Progranulin mutations’, *Brain*, 130(5), pp. 1375–1385. Available at: https://doi.org/10.1093/BRAIN/AWM024.

Sellier, C. *et al.* (2016) ‘Loss of C9ORF72 impairs autophagy and synergizes with polyQ Ataxin-2 to induce motor neuron dysfunction and cell death’, *The EMBO Journal*, 35(12), pp. 1276–1297. Available at: https://doi.org/10.15252/EMBJ.201593350.

Serrano-Pozo, A., Das, S. and Hyman, B.T. (2021) ‘APOE and Alzheimer’s Disease: Advances in Genetics, Pathophysiology, and Therapeutic Approaches.’, *The Lancet. Neurology*, 20(1), p. 68. Available at: https://doi.org/10.1016/S1474-4422(20)30412-9.

Sessa, G. *et al.* (2004) ‘Distribution and signaling of TREM2/DAP12, the receptor system mutated in human polycystic lipomembraneous osteodysplasia with sclerosing leukoencephalopathy dementia’, *European Journal of Neuroscience*, 20(10), pp. 2617–2628. Available at: https://doi.org/10.1111/J.1460-9568.2004.03729.X.

Shao, Y. *et al.* (2020) ‘Presence of the apolipoprotein E-ε4 allele is associated with an increased risk of sepsis progression’, *Scientific Reports*, 10(1). Available at: https://doi.org/10.1038/S41598-020-72616-0.

Sharma, K. *et al.* (2015) ‘Cell type– and brain region–resolved mouse brain proteome’, *Nature Neuroscience*, 18(12), pp. 1819–1831. Available at: https://doi.org/10.1038/nn.4160.

Shaw, M.P. *et al.* (2018) ‘Stable transgenic C9orf72 zebrafish model key aspects of the ALS/FTD phenotype and reveal novel pathological features’, *Acta Neuropathologica Communications*, 6(1), p. 125. Available at: https://doi.org/10.1186/s40478-018-0629-7.

Sheean, R.K. *et al.* (2018) ‘Association of regulatory T-Cell Expansion with progression of amyotrophic lateral sclerosis a study of humans and a transgenic mouse model’, *JAMA Neurology*, 75(6), pp. 681–689. Available at: https://doi.org/10.1001/jamaneurol.2018.0035.

Shi, Y. *et al.* (2018) ‘Haploinsufficiency leads to neurodegeneration in C9ORF72 ALS/FTD human induced motor neurons’, *Nature Medicine 2018 24:3*, 24(3), pp. 313–325. Available at: https://doi.org/10.1038/nm.4490.

Shibata, N. (2001) ‘Transgenic mouse model for familial amyotrophic lateral sclerosis with superoxide dismutase-1 mutation’, *Neuropathology*, 21(1), pp. 82–92. Available at: https://doi.org/10.1046/j.1440-1789.2001.00361.x.

Shigemoto-Mogami, Y. *et al.* (2014) 'Microglia Enhance Neurogenesis and Oligodendrogenesis in the Early Postnatal Subventricular Zone', *Journal of Neuroscience*, 34(6), pp. 2231–2243. Available at: https://doi.org/10.1523/JNEUROSCI.1619-13.2014.

Shiraishi, W. *et al.* (2021) 'Clearance of peripheral nerve misfolded mutant protein by infiltrated macrophages correlates with motor neuron disease progression', *Scientific Reports*, 11(1), pp. 1–16. Available at: https://doi.org/10.1038/s41598-021-96064-6.

Siddique, T. and Ajroud-Driss, S. (2011) 'Familial amyotrophic lateral sclerosis,a historical perspective', *Acta Myologica*, 30(2), p. 117. Available at: /pmc/articles/PMC3235825/ (Accessed: 20 August 2022).

Siddique, Teepu *et al.* (1998) 'Lack of association between apolipoprotein E genotype and sporadic amyotrophic lateral sclerosis', *Neurogenetics 1998 1:3*, 1(3), pp. 213–216. Available at: https://doi.org/10.1007/S100480050031.

Sierra, A. *et al.* (2010) 'Microglia Shape Adult Hippocampal Neurogenesis through Apoptosis-Coupled Phagocytosis', *Cell Stem Cell*, 7(4), pp. 483–495. Available at: https://doi.org/10.1016/J.STEM.2010.08.014.

De Simone, R., Antonietta Ajmone-Cat, M. and Minghetti, L. (2004) 'Atypical Antiinflammatory Activation of Microglia Induced by Apoptotic Neurons Possible Role of Phosphatidylserine-Phosphatidylserine Receptor Interaction', *Molecular Neurobiology*, 29.

Simpson, J.E. *et al.* (2007) 'White matter lesions in an unselected cohort of the elderly: Astrocytic, microglial and oligodendrocyte precursor cell responses', *Neuropathology and Applied Neurobiology*, 33(4), pp. 410–419. Available at: https://doi.org/10.1111/j.1365-2990.2007.00828.x.

Sing, C.F. and Davignon, J. (1985) 'Role of the apolipoprotein E polymorphism in determining normal plasma lipid and lipoprotein variation', *American Journal of Human Genetics*, 37(2), pp. 268–285.

Sofroniew, M. V. and Vinters, H. V. (2010) 'Astrocytes: Biology and pathology', *Acta Neuropathologica*, 119(1), pp. 7–35. Available at: https://doi.org/10.1007/S00401-009-0619-8/FIGURES/9.

Sparkman, N.L. and Johnson, R.W. (2008) 'Neuroinflammation associated with aging sensitizes the brain to the effects of infection or stress', *NeuroImmunoModulation*. NIH Public Access, pp. 323–330. Available at: https://doi.org/10.1159/000156474.

van der Spek, R.A.A. *et al.* (2019) 'The project MinE databrowser: bringing large-scale whole-genome sequencing in ALS to researchers and the public', *Amyotrophic Lateral Sclerosis and Frontotemporal Degeneration*, 20(5–6), pp. 432–440. Available at: https://doi.org/10.1080/21678421.2019.1606244/SUPPL_FILE/IAFD_A_1606244_SM5246.DOCX.

Spiller, K.J. *et al.* (2018) 'Microglia-mediated recovery from ALS-relevant motor neuron degeneration in a mouse model of TDP-43 proteinopathy', *Nature Neuroscience*, 21(3), pp. 329–340. Available at: https://doi.org/10.1038/s41593-018-0083-7.

Sreedharan, J. *et al.* (2008) 'TDP-43 mutations in familial and sporadic amyotrophic lateral sclerosis', 319(5870), pp. 1668–1672. Available at: https://pubmed.ncbi.nlm.nih.gov/18309045/ (Accessed: 1 December 2018).

Sudria-Lopez, E. *et al.* (2016) 'Full ablation of C9orf72 in mice causes immune system-related pathology and neoplastic events but no motor neuron defects', *Acta Neuropathol*, 3, pp. 145–147. Available at: https://doi.org/10.1007/s00401-016-1581-x.

Suk, T.R. and Rousseaux, M.W.C. (2020) 'The role of TDP-43 mislocalization in amyotrophic lateral sclerosis', *Molecular Neurodegeneration*, 15(1), pp. 1–16. Available at: https://doi.org/10.1186/S13024-020-00397-1/FIGURES/2.

Sullivan, P.M. *et al.* (2016) 'The ALS/FTLD associated protein C9orf72 associates with SMCR8 and WDR41 to regulate the autophagy-lysosome pathway', *Acta neuropathologica communications*, 4(1), p. 51. Available at: https://doi.org/10.1186/S40478-016-0324-5.

Sun, S. *et al.* (2015) 'ALS-causative mutations in FUS/TLS confer gain and loss of function by altered association with SMN and U1-snRNP', *Nature Communications*, 6(1), p. 6171. Available at: https://doi.org/10.1038/ncomms7171.

Süssmuth, S.D. *et al.* (2010) 'CSF glial markers correlate with survival in amyotrophic lateral sclerosis', *Neurology*, 74(12), pp. 982–987. Available at: https://doi.org/10.1212/WNL.0b013e3181d5dc3b.

Tan, R.H. *et al.* (2015) 'TDP-43 proteinopathies: pathological identification of brain regions differentiating clinical phenotypes', *Brain : a journal of neurology*, 138(Pt 10), pp. 3110–3122. Available at: https://doi.org/10.1093/BRAIN/AWV220.

Tateishi, T. *et al.* (2010) 'CSF chemokine alterations related to the clinical course of amyotrophic lateral sclerosis', *Journal of Neuroimmunology*, 222(1–2), pp. 76–81. Available at: https://doi.org/10.1016/J.JNEUROIM.2010.03.004.

Tenger, C. and Zhou, X. (2003) 'Apolipoprotein E modulates immune activation by acting on the antigen-presenting cell', *Immunology*, 109(3), pp. 392–397. Available at: https://doi.org/10.1046/J.1365-2567.2003.01665.X.

Thermoscientific (2012) *Assessment of Nucleic Acid Purity*, *Thermo Fisher Scientific: Technical Bulletin NanoDrop Spectrophotometers*. Available at: www.thermoscientific.com (Accessed: 8 February 2021).

Therrien, M. *et al.* (2013) 'Deletion of C9ORF72 results in motor neuron degeneration and stress sensitivity in C. elegans', *PLoS ONE*. Edited by D. Dupuy, 8(12), p. e83450. Available at: https://doi.org/10.1371/journal.pone.0083450.

Toft, M.H., Gredal, O. and Pakkenberg, B. (2005) 'The size distribution of neurons in the motor cortex in amyotrophic lateral sclerosis', *Journal of Anatomy*, 207(4), pp. 399–407. Available at: https://doi.org/10.1111/J.1469-7580.2005.00465.X.

Turner, M.R. *et al.* (2004) 'Evidence of widespread cerebral microglial activation in amyotrophic lateral sclerosis: An [11C](R)-PK11195 positron emission tomography study', *Neurobiology of Disease*, 15(3), pp. 601–609. Available at: https://doi.org/10.1016/j.nbd.2003.12.012.

Turner, M.R. *et al.* (2010) 'Pattern of spread and prognosis in lower limb-onset ALS',

Amyotrophic lateral sclerosis : official publication of the World Federation of Neurology Research Group on Motor Neuron Diseases, 11(4), p. 369. Available at: https://doi.org/10.3109/17482960903420140.

Ueno, M. *et al.* (2013) 'Layer V cortical neurons require microglial support for survival during postnatal development', *Nature Neuroscience 2013 16:5*, 16(5), pp. 543–551. Available at: https://doi.org/10.1038/nn.3358.

Ugolino, J. *et al.* (2016) 'Loss of C9orf72 Enhances Autophagic Activity via Deregulated mTOR and TFEB Signaling', *PLoS genetics*, 12(11). Available at: https://doi.org/10.1371/JOURNAL.PGEN.1006443.

Vance, C. *et al.* (2009) 'Mutations in FUS, an RNA processing protein, cause familial amyotrophic lateral sclerosis type 6.', *Science (New York, N.Y.)*, 323(5918), pp. 1208–1211. Available at: https://doi.org/10.1126/science.1165942.

Vargas, M.R. *et al.* (2006) 'Increased glutathione biosynthesis by Nrf2 activation in astrocytes prevents p75NTR-dependent motor neuron apoptosis', *Journal of Neurochemistry*, 97(3), pp. 687–696. Available at: https://doi.org/10.1111/J.1471-4159.2006.03742.X.

Vargas, M.R. *et al.* (2008) 'Transcriptional profile of primary astrocytes expressing ALS-linked mutant SOD1', *Journal of Neuroscience Research*, 86(16), pp. 3515–3525. Available at: https://doi.org/10.1002/jnr.21797.

Venegas, C. *et al.* (2017) 'Microglia-derived ASC specks cross-seed amyloid-β in Alzheimer's disease', *Nature*, 552(7685), pp. 355–361. Available at: https://doi.org/10.1038/nature25158.

Verdone, B.M. *et al.* (2022) 'A mouse model with widespread expression of the C9orf72-linked glycine–arginine dipeptide displays non-lethal ALS/FTD-like phenotypes', *Scientific Reports 2022 12:1*, 12(1), pp. 1–17. Available at: https://doi.org/10.1038/s41598-022-09593-z.

Vitek, M.P., Brown, C.M. and Colton, C.A. (2009) 'APOE genotype-specific differences in the innate immune response', *Neurobiology of Aging*, 30(9), pp. 1350–1360. Available at: https://doi.org/10.1016/J.NEUROBIOLAGING.2007.11.014.

Wakselman, S. *et al.* (2008) 'Developmental Neuronal Death in Hippocampus Requires the Microglial CD11b Integrin and DAP12 Immunoreceptor', *Journal of Neuroscience*, 28(32), pp. 8138–8143. Available at: https://doi.org/10.1523/JNEUROSCI.1006-08.2008.

Walker, D.G. and Lue, L.F. (2015) 'Immune phenotypes of microglia in human neurodegenerative disease: Challenges to detecting microglial polarization in human brains', *Alzheimer's Research and Therapy*. BioMed Central Ltd. Available at: https://doi.org/10.1186/s13195-015-0139-9.

Waller, R. *et al.* (2019) 'Iba-1 - /CD68 + microglia are a prominent feature of age-associated deep subcortical white matter lesions', *PLoS ONE*, 14(1). Available at: https://doi.org/10.1371/journal.pone.0210888.

Wang, H. *et al.* (2002) 'Tissue microarrays: Applications in neuropathology research, diagnosis, and education', in *Brain Pathology*. John Wiley & Sons, Ltd (10.1111), pp. 95–107. Available at: https://doi.org/10.1111/j.1750-3639.2002.tb00426.x.

Wang, J. *et al.* (2002) ‘Fibrillar inclusions and motor neuron degeneration in transgenic mice expressing superoxide dismutase 1 with a disrupted copper-binding site’, *Neurobiology of Disease*, 10(2), pp. 128–138. Available at: https://doi.org/10.1006/nbdi.2002.0498.

Wang, Jiaying *et al.* (2019) ‘Targeting microglia and macrophages: A potential treatment strategy for multiple sclerosis’, *Frontiers in Pharmacology*, 10(MAR), p. 286. Available at: https://doi.org/10.3389/fphar.2019.00286.

Wang, L. *et al.* (2009) ‘The effect of mutant SOD1 dismutase activity on non-cell autonomous degeneration in familial amyotrophic lateral sclerosis’, *Neurobiology of Disease*, 35(2), pp. 234–240. Available at: https://doi.org/10.1016/j.nbd.2009.05.002.

Wang, L., Gutmann, D.H. and Roos, R.P. (2011) ‘Astrocyte loss of mutant SOD1 delays ALS disease onset and progression in G85R transgenic mice’, *Human Molecular Genetics*, 20(2), pp. 286–293. Available at: https://doi.org/10.1093/HMG/DDQ463.

Wang, X.S. *et al.* (2006) ‘Differential expression of genes in amyotrophic lateral sclerosis revealed by profiling the post mortem cortex’, *Amyotrophic Lateral Sclerosis*, 7(4), pp. 201–216. Available at: https://doi.org/10.1080/17482960600947689.

Weinhard, L. *et al.* (2018) ‘Microglia remodel synapses by presynaptic trogocytosis and spine head filopodia induction’, *Nature Communications*, 9(1), p. 1228. Available at: https://doi.org/10.1038/s41467-018-03566-5.

Wes, P.D. *et al.* (2016) ‘Next generation transcriptomics and genomics elucidate biological complexity of microglia in health and disease’, *Glia*, 64(2), pp. 197–213. Available at: https://doi.org/10.1002/glia.22866.

White, F. *et al.* (2001) ‘Impaired Neuronal Plasticity in Transgenic Mice Expressing Human Apolipoprotein E4 Compared to E3 in a Model of Entorhinal Cortex Lesion’, *Neurobiology of Disease*, 8(4), pp. 611–625. Available at: https://doi.org/10.1006/NBDI.2001.0401.

White, K. *et al.* (2018) ‘Effect of Postmortem Interval and Years in Storage on RNA Quality of Tissue at a Repository of the NIH NeuroBioBank’, *Biopreservation and Biobanking*, 16(2), pp. 148–157. Available at: https://doi.org/10.1089/bio.2017.0099.

Wilson, L. (2018) *Tissue Microarray Reliability Assessment of Microglial Morphology Within White Matter Lesions, Motor Neuron Disease Spinal Cord and Motor Neuron Disease Cortex.* University of Sheffield.

Wilson, L.A. *et al.* (2021) ‘Tissue microarray (TMA) use in post mortem neuropathology’, *Journal of Neuroscience Methods*, 347. Available at: https://doi.org/10.1016/j.jneumeth.2020.108963.

Witting, A. *et al.* (2000) *Phagocytic Clearance of Apoptotic Neurons by Microglia/Brain Macrophages In Vitro: Involvement of Lectin-, Integrin-, and Phosphatidylserine-Mediated Recognition*, *J. Neurochem*. Available at: https://onlinelibrary.wiley.com/doi/pdf/10.1046/j.1471-4159.2000.0751060.x (Accessed: 31 December 2018).

Wolf, Y. *et al.* (2013) ‘Microglia, seen from the CX3CR1 angle’, *Frontiers in Cellular*

Neuroscience, 7, p. 26. Available at: https://doi.org/10.3389/fncel.2013.00026.

Wong, P.C. *et al.* (1995) 'An adverse property of a familial ALS-linked SOD1 mutation causes motor neuron disease characterized by vacuolar degeneration of mitochondria', *Neuron*, 14(6), pp. 1105–1116. Available at: https://doi.org/10.1016/0896-6273(95)90259-7.

Wood-Allum, C. and Shaw, P.J. (2010) 'Motor neurone disease: a practical update on diagnosis and management.', *Clinical medicine (London, England)*, 10(3), pp. 252–8. Available at: https://doi.org/10.7861/CLINMEDICINE.10-3-252.

Wu, S.Y. and Watabe, K. (2017) 'The roles of microglia/macrophages in tumor progression of brain cancer and metastatic disease', *Frontiers in bioscience (Landmark edition)*, 22(10), p. 1805. Available at: https://doi.org/10.2741/4573.

Xiao, Q. *et al.* (2007) 'Mutant SOD1 ^{G93A} microglia are more neurotoxic relative to wild-type microglia', *Journal of Neurochemistry*, 102(6), pp. 2008–2019. Available at: https://doi.org/10.1111/j.1471-4159.2007.04677.x.

Xie, M. *et al.* (2022) 'TREM2 interacts with TDP-43 and mediates microglial neuroprotection against TDP-43-related neurodegeneration', *Nature Neuroscience*, 25(1), pp. 26–38. Available at: https://doi.org/10.1038/s41593-021-00975-6.

Xu, C. *et al.* (2017) 'Mesenchymal stem cells maintain the microenvironment of central nervous system by regulating the polarization of macrophages/microglia after traumatic brain injury', *http://dx.doi.org/10.1080/00207454.2017.1325884*, 127(12), pp. 1124–1135. Available at: https://doi.org/10.1080/00207454.2017.1325884.

Xu, Q. *et al.* (2000) 'Isolation and characterization of apolipoproteins from murine microglia. Identification of a low density lipoprotein-like apolipoprotein J-rich but E-poor spherical particle.', *The Journal of biological chemistry*, 275(41), pp. 31770–7. Available at: https://doi.org/10.1074/jbc.M002796200.

Yamanaka, K. *et al.* (2008) 'Astrocytes as determinants of disease progression in inherited amyotrophic lateral sclerosis', *Nature Neuroscience 2008 11:3*, 11(3), pp. 251–253. Available at: https://doi.org/10.1038/nn2047.

Yamanaka, K. and Komine, O. (2018) 'The multi-dimensional roles of astrocytes in ALS', *Neuroscience Research*, 126, pp. 31–38. Available at: https://doi.org/10.1016/J.NEURES.2017.09.011.

Yamasaki, R. *et al.* (2014) 'Differential roles of microglia and monocytes in the inflamed central nervous system', *Journal of Experimental Medicine*, 211(8), pp. 1533–1549. Available at: https://doi.org/10.1084/jem.20132477.

Yang, M. *et al.* (2016) 'A C9ORF72/SMCR8-containing complex regulates ULK1 and plays a dual role in autophagy', *Science Advances*, 2(9). Available at: https://doi.org/10.1126/SCIADV.1601167/SUPPL_FILE/1601167_SM.PDF.

Yasuda, K. *et al.* (2013) 'The RNA-binding protein Fus directs translation of localized mRNAs in APC-RNP granules', *Journal of Cell Biology*, 203(5), pp. 737–746. Available at: https://doi.org/10.1083/JCB.201306058.

Yin, J. *et al.* (2016) 'Vps35-dependent recycling of Trem2 regulates microglial function', *Traffic*, 17(12), pp. 1286–1296. Available at: https://doi.org/10.1111/TRA.12451.

Yoshihara, T. *et al.* (2002) 'Differential expression of inflammation- and apoptosis-related genes in spinal cords of a mutant SOD1 transgenic mouse model of familial amyotrophic lateral sclerosis', *Journal of Neurochemistry*, 80(1), pp. 158–167. Available at: https://doi.org/10.1046/j.0022-3042.2001.00683.x.

Yu, F. *et al.* (2022) 'Phagocytic microglia and macrophages in brain injury and repair', *CNS Neuroscience & Therapeutics*, 28(9), pp. 1279–1293. Available at: https://doi.org/10.1111/CNS.13899.

Zarei, S. *et al.* (2015) 'A comprehensive review of amyotrophic lateral sclerosis', *Surgical Neurology International*, 6(1). Available at: https://doi.org/10.4103/2152-7806.169561.

Zhang, R. *et al.* (2005) 'Evidence for systemic immune system alterations in sporadic amyotrophic lateral sclerosis (sALS)', *Journal of Neuroimmunology*, 159(1–2), pp. 215–224. Available at: https://doi.org/10.1016/j.jneuroim.2004.10.009.

Zhang, R. *et al.* (2009) 'Circulating endotoxin and systemic immune activation in sporadic amyotrophic lateral sclerosis (sALS)', *Journal of Neuroimmunology*, 206(1–2), pp. 121–124. Available at: https://doi.org/10.1016/J.JNEUROIM.2008.09.017.

Zhang, X.M. *et al.* (2010) 'Immunopanning purification and long-term culture of human retinal ganglion cells', *Molecular Vision*, 16, p. 2867. Available at: /pmc/articles/PMC3012647/ (Accessed: 26 September 2022).

Zhang, Xu *et al.* (2013) 'Cyclic GMP-AMP Containing Mixed Phosphodiester Linkages Is An Endogenous High-Affinity Ligand for STING', *Molecular Cell*, 51(2), pp. 226–235. Available at: https://doi.org/10.1016/J.MOLCEL.2013.05.022.

Zhang, Y. *et al.* (2016) 'Purification and Characterization of Progenitor and Mature Human Astrocytes Reveals Transcriptional and Functional Differences with Mouse', *Neuron*, 89(1), pp. 37–53. Available at: https://doi.org/10.1016/j.neuron.2015.11.013.

Zhang, Z. *et al.* (2011) 'Parenchymal accumulation of CD163+ macrophages/microglia in multiple sclerosis brains', *Journal of Neuroimmunology*, 237(1–2), pp. 73–79. Available at: https://doi.org/10.1016/J.JNEUROIM.2011.06.006.

Zhao, W. *et al.* (2010) 'Extracellular mutant SOD1 induces microglial-mediated motoneuron injury', *Glia*, 58(2), pp. 231–243. Available at: https://doi.org/10.1002/glia.20919.

Zhong, L. *et al.* (2015) 'DAP12 stabilizes the C-terminal fragment of the triggering receptor expressed on myeloid cells-2 (TREM2) and protects against LPS-induced pro-inflammatory response', *Journal of Biological Chemistry*, 290(25), pp. 15866–15877. Available at: https://doi.org/10.1074/jbc.M115.645986.

Zhong, L. *et al.* (2017) 'Soluble TREM2 induces inflammatory responses and enhances microglial survival', *Journal of Experimental Medicine*, 214(3), pp. 597–607. Available at: https://doi.org/10.1084/JEM.20160844.

Zhou, Y. *et al.* (2020) 'Human and mouse single-nucleus transcriptomics reveal TREM2-dependent and TREM2-independent cellular responses in Alzheimer's disease', *Nature Medicine*, 26(1), pp. 131–142. Available at: https://doi.org/10.1038/s41591-019-0695-9.

Ziff, O.J. *et al.* (2022) ‘Meta-analysis of human and mouse ALS astrocytes reveals multi-omic signatures of inflammatory reactive states’, *Genome Research*, 32(1), pp. 71–84. Available at: https://doi.org/10.1101/GR.275939.121.

Zinszner, H. *et al.* (1997) ‘TLS (FUS) binds RNA in vivo and engages in nucleo-cytoplasmic shuttling’, *Journal of Cell Science*, 110(15), pp. 1741–1750. Available at: https://doi.org/10.1242/JCS.110.15.1741.

Appendices

Appendix A Motor Cortex Microarray Cohort Data from Aronica et al. (2015)

Case Name	Sex	Disease Status	Age at death (Years)	Survival time from date of onset (months)	*Post-mortem* interval (hours)	Location of onset
1	Male	Control	31	n/a	8	n/a
3	Male	Control	39	130	8	n/a
6	Male	Control	44	96	9	n/a
5	Male	Control	48	72	4	n/a
8	Male	Control	58	48	7	n/a
12bis	Male	Control	59	n/a	7	n/a
9	Male	Control	60	60	6.5	n/a
14	Male	Control	68	n/a	8	n/a
15bis	Female	Control	71	n/a	9	n/a
17	Male	Control	73	n/a	10	n/a
63	Male	sMND	38	38	7	leg onset
21	Female	sMND	40	n/a	5	arm onset
23	Male	sMND	41	49	3	trunk onset
25bis	Male	sMND	41	71	10	arm onset
67	Male	sMND	43	43	6	leg onset
61	Male	sMND	45	31	6.5	leg onset
55	Female	sMND	46	n/a	7	arm onset
27bis	Male	sMND	46	52	7.5	trunk onset
29	Male	sMND	51	90	4	arm onset
59	Female	sMND	51	42	7	leg onset
53	Male	sMND	51	29	8	trunk onset
65	Male	sMND	54	29	3	leg onset
31	Male	sMND	54	52	8	arm onset
51bis	Male	sMND	55	27	6	leg onset
41	Female	sMND	57	n/a	4	arm onset
45	Male	sMND	59	23	8	leg onset
49	Male	sMND	61	31	3	leg onset
71	Female	sMND	61	22	6	leg onset

69bis	Female	sMND	61	27	10	leg onset
57	Male	sMND	63	38	7.5	trunk onset
33	Female	sMND	64	7	5.3	leg onset
83	Male	sMND	65	n/a	6.5	arm onset
35	Female	sMND	65	30	7	leg onset
37bis	Female	sMND	67	30	8	trunk onset
73	Male	sMND	67	13	8	arm onset
77	Male	sMND	68	n/a	6	arm onset
79	Male	sMND	68	20	7	arm onset
75	Female	sMND	68	18	8	trunk onset
39	Female	sMND	69	11	9	leg onset
81	Male	sMND	69	38	10	leg onset
43	Female	sMND	70	18	4	trunk onset

***Appendix B**: Spinal Cord RNAseq Data Cohort from* Brohawn, O'Brien and Bennett (2016)

Case Name	***Sex***	***Disease Status***	***Age at death (Years)***
CTL6	male	control	80
CTL8	female	control	67
CTL16	female	control	66
CTL22	male	control	54
CTL23	female	control	65
CTL24	male	control	83
CTL25	male	control	59
CTL27	female	control	84
ALS1	male	sMND	70
ALS2	male	sMND	67
ALS3	female	sMND	80
ALS9	female	sMND	75
ALS10	female	sMND	64
ALS14	male	sMND	61

Note. *Post-mortem* delay, length of survival and location of symptom onset was not given.

Middle Frontal

Case Number	Block Number	Disease Status
027/2008	n	sMND
043/2005	p	sMND
088/2006	m	sMND
074/2009	v	sMND
034/2005	s	sMND
099/2009	m	sMND
042/2005	p	sMND
064/2009	d	sMND
098/2008	f	sMND
096/2008	o	sMND
014/2008	l	sMND
075/2008	e	sMND
099/2003	l	sMND
023/2010	p	sMND
041/2011	d	sMND
054/2015	a4	sMND
064/2010	d	sMND
082/2010	f	sMND
005/2010	d	sMND
094/2006	j	sMND
008/2013	a4	sMND
005/2011	d	sMND
036/2012	a16	sMND
048/2012	a16	sMND
046/2014	a4	sMND
058/2012	a16	sMND
049/2006	f	sMND
060/2016	a16	sMND
054/2005	n	sMND
049/2005	i	sMND
102/2005	p	sMND
094/2006	p	sMND
039/2005	d	sMND

Case Number	Block Number	Disease Status
070/2007	c	control
007/2009	h	control
098/2007	c	control
224/2016	a15	control
085/2007	l	control
118/1996	e	control
058/2022	a26	control

Temporal Cortex

Case Number	Block Number	Disease Status
027/2008	o	sMND
043/2005	q	sMND
102/2005	q	sMND
088/2006	n	sMND
077/2011	e	sMND
099/2009	n	sMND
042/2005	q	sMND
009/2008	b	sMND
098/2008	e	sMND
098/2008	h	sMND
096/2008	p	sMND
014/2008	o	sMND
075/2008	g	sMND
099/2003	g	sMND
023/2010	q	sMND
041/2010	q	sMND
054/2015	a7	sMND
064/2010	e	sMND
014/2011	j	sMND
005/2010	g	sMND
094/2006	ah	sMND
008/2013	a6	sMND
005/2011	g	sMND
024/2008	e	sMND
048/2012	a17	sMND
046/2013	a10	sMND
074/2009	w	sMND

049/2006	k	sMND
060/2016	a17	sMND
054/2005	l	sMND
049/2005	j	sMND
026/2013	a6	sMND
175/1995	h	sMND
187/1991	x1	sMND

Case Number	Block Number	Disease Status
007/2009	i	control
224/2016	a33	control
018/2009	c	control
098/2007	g	control
070/2007	n	control
058/2022	a36	control
005/2007	t	control
085/2007	e	control

Basal Ganglia

Case Number	Block Number	Disease Status
027/2008	g	sMND
043/2005	i	sMND
087/1992	v1	sMND
088/2006	j	sMND
034/2005	r	sMND
099/2009	j	sMND
042/2005	h	sMND
064/2009	m	sMND
098/2008	k	sMND
096/2008	j	sMND
014/2008	n	sMND
075/2008	m	sMND
099/2003	d	sMND
023/2010	i	sMND
041/2010	j	sMND
054/2015	a12	sMND
064/2010	i	sMND
082/2010	j	sMND
005/2010	k	sMND
097/2006	d	sMND
008/2013	a11	sMND
005/2011	n	sMND
036/2012	a10	sMND
048/2012	aa	sMND
046/2013	a8	sMND
058/2012	a10	sMND
049/2005	e	sMND

060/2016	a8	sMND
054/2005	o	sMND
049/2006	o	sMND
261/1990	r1	sMND
175/1995	p	sMND
187/1991	d2	sMND

Case Number	Block Number	Disease Status
005/2007	aa	control
007/2009	m	control
135/2018	a10	control
070/2007	h	control
098/2007	h	control
058/2022	a30	control
085/2007	d	control
097/1997	h	control
118/1996	v	control
224/2016	a17	control

Occipital Cortex

Case Number	Block Number	Sex	Disease Status	Age at death
141/1993	D	F	sMND	66
206/1993	Z		sMND	
082/1994	B1	M	sMND	57
138/1994	T	M	sMND	75
203/1994	P	F	sMND	57
089/1995	Z	F	sMND	56
088/1996	X	M	sMND	66
137/1996	V	F	sMND	56
212/1999	W	M	sMND	60
054/2005	D	M	sMND	
064/2005	O	M	sMND	64
072/2005	R	M	sMND	66
014/2008	U	F	sMND	76
075/2008	I	F	sMND	61
063/2009	R	M	sMND	60
064/2009	H	M	sMND	67
074/2009	Y	M	sMND	
046/2011	H	M	sMND	77
046/2012	A10	M	sMND	47
008/2013	A8	M	sMND	71
025/2013	A18	F	sMND	72
026/2013	A8	M	sMND	62
033/2013	A18	F	sMND	58

046/2013	A15	M	sMND	78
104/2014	A6	M	sMND	63
105/2014	A6	M	sMND	
128/2014	A6	F	sMND	29
138/2014	A6	M	sMND	78
054/2015	A6	F	sMND	62
194/2015	A6	M	sMND	
062/2016	A6	M	sMND	72
060/2016	A18	M	sMND	75
168/2018	A11	F	sMND	

Case	Block Reference	Clinical diagnosis
085/2007	O	Control
098/2007	F	Control
007/2009	J	Control
018/2009	E	Control
224/2016	A36	Control
135/2018	A18	Control

CCC Marketplace™

This is a License Agreement between Bridget A. Ashford ("User") and Copyright Clearance Center, Inc. ("CCC") on behalf of the Rightsholder identified in the order details below. The license consists of the order details, the Marketplace Order General Terms and Conditions below, and any Rightsholder Terms and Conditions which are included below.

All payments must be made in full to CCC in accordance with the Marketplace Order General Terms and Conditions below.

Order Date	28-Sep-2022	Type of Use	Republish in a thesis/dissertation
Order License ID	1273687-1		
ISSN	1365-2990	Publisher	BLACKWELL PUBLISHING
		Portion	Chart/graph/table/figure

LICENSED CONTENT

Publication Title	Neuropathology & applied neurobiology	Publication Type	e-Journal
		Start Page	179
Article Title	Review: Microglia in motor neuron disease	End Page	197
		Issue	2
Author/Editor	British Neuropathological Society	Volume	47
Date	01/01/1999	URL	http://onlinelibrary.wiley.com/journal/10.1111/(ISSN)1365-2990
Language	English		
Country	United Kingdom of Great Britain and Northern Ireland		
Rightsholder	John Wiley & Sons - Books		

REQUEST DETAILS

Portion Type	Chart/graph/table/figure	Distribution	Worldwide
Number of charts / graphs / tables / figures requested	3	Translation	Original language of publication
		Copies for the disabled?	No
Format (select all that apply)	Print, Electronic	Minor editing privileges?	Yes
Who will republish the content?	Academic institution	Incidental promotional use?	No
Duration of Use	Life of current and all future editions	Currency	GBP
Lifetime Unit Quantity	Up to 499		
Rights Requested	Main product		

NEW WORK DETAILS

Title	Neuroinflammation in Human Motor Neuron Disease	Institution name	Unviersity of Sheffield
		Expected presentation date	2022-10-06
Instructor name	Bridget Ashford/ Robin Highley		

ADDITIONAL DETAILS

Sheffield Brain Tissue Bank

Management Board review of Application/Extension for Access to Tissue

Name and institution of researcher(s):	Robin Highley, SITraN, The University of Sheffield
Project title:	Microglial Pathology in Human Motor Neuron Disease
Date of request:	

Table 1. Management Board - Internal Comments	
1. Has the researcher: **a.** provided adequate information in the *Application/Extension for Access to Data* for the Committee to form an opinion; **and** b. Fully completed and signed the *Agreement for Data Use*?	Yes
2. Does the research fit within the REC-approved research aims of the SBTB (outlined below)? • Neurodegeneration, neurological disease, or normal ageing -related studies investigating the genetic causes and potential environmental predispositions of the disease. • Neurodegeneration, neurological disease, or normal ageing -related studies that will facilitate and support the improvements in clinical care and advance the knowledge of clinicians and researchers in attempt to find new treatments and methods of improving life for patients. • Studies looking for specific trends or correlations in the data, aiding in understanding of the disease progression and phenotype, and investigating potential therapeutic benefits or targets for future therapies. • Studies to enable Biomathematicians to build probabilistic models that can link clinical data to environmental risk factors and genetic risk factors. *If No, but the further review questions are favourable, it is possible for the researcher(s) to access tissue if project-specific REC approval is received. The SBTB must be in receipt of the REC approval and all associated documents before the Management Board can approve release of any tissue.*	Yes
3. Will the research develop new scientific knowledge, which has the potential benefit to patients?	Yes/
4. Is there a potential conflict with any currently ongoing research? If Yes, Please give details:	No

FOR SBTB OFFICE USE

Project no. 18/005

AUTHORISATION TO USE TISSUE RESOURCE FROM THE SHEFFIELD BRAIN TISSUE BANK (SBTB)

FOLLOWING CONSIDERATION BY THE SBTB MANAGEMENT BOARD:

Proposed Study Title: "nanoString analysis of neuroinflammation in MND"

Head of proposed study:

Title: Dr Initials: JR

Surname: Highley

Position: Senior Clinical Lecturer

Organisation: SITraN

Address: 385a Glossop Road, Sheffield, S10 2HQ

Telephone No: **07866 108125** Fax No.: 0114 222 2290

Email: **, robin.highley@sheffield.ac.uk**

SBTB PROJECT REQUEST NUMBER: 18/005

This project was reviewed by the SBTB Management Board and approval to release tissue under REC **08/MRE00/103** was granted.

Professor Stephen Wharton
Professor of Neuropathology and
Consultant Neuropathologist

Date: 6/4/18.

SBTB Issue and version / word : 01/02/2008

FOR SBTB OFFICE USE

Project no. 18/007

AUTHORISATION TO USE TISSUE RESOURCE FROM THE SHEFFIELD BRAIN TISSUE BANK (SBTB)

FOLLOWING CONSIDERATION BY THE SBTB MANAGEMENT BOARD:

Proposed Study **Title:** Generation of Tissue Microarrays for neurodegeneration research using brain bank material.

Head of proposed study

Title: Dr Initials: JR

Surname: Highley

Position: Senior Clinical Lecturer in Neuropathology

Organisation: SITraN

Address: 385a Glossop Road, Sheffield, S10 2HQ

Telephone No: 0114 222 2241 Fax No: 0114 222 2290

Email: robin.highley@sheffield.ac.uk

SBTB PROJECT REQUEST NUMBER: 18/007

This project was reviewed by the SBTB Management Board and approval to release tissue under REC **08/MRE00/103** was granted.

Professor Stephen Wharton
Professor of Neuropathology and
Consultant Neuropathologist

Date. 25/6/18.

SBTB Release authorisation / ver1 01/02/2008

FOR SBTB OFFICE USE:

Project no. 17/010

AUTHORISATION TO USE TISSUE RESOURCE FROM THE SHEFFIELD BRAIN TISSUE BANK (SBTB)

FOLLOWING CONSIDERATION BY THE SBTB MANAGEMENT BOARD:

Proposed Study Title: Tissue microarrays, microglia and neuropathology research

Head of proposed study

Title Dr Initials JR

Surname Highley

Position: Senior Clinical Lecturer in Neuropathology

Organisation: STTaN, University of Sheffield

Address. 385a Glossop Road, Sheffield, S10 2HQ

Telephone No: 0114 222 2244 Fax No....

Email: robin.highley@sheffield.ac.uk

SBTB PROJECT REQUEST NUMBER: 17/010

This project was reviewed by the SBTB Management Board and approval to release tissue under REC **08/MRE00/103** was granted.

Professor Stephen Wharton
Professor of Neuropathology and
Consultant Neuropathologist

20/11/12
Date:

FOR SBTB OFFICE USE

Project no. 18/007

AUTHORISATION TO USE TISSUE RESOURCE FROM THE SHEFFIELD BRAIN TISSUE BANK (SBTB)

FOLLOWING CONSIDERATION BY THE SBTB MANAGEMENT BOARD:

Proposed Study **Title:** Generation of Tissue Microarrays for neurodegeneration research using brain bank material.

Head of proposed study

Title: Dr Initials: JR

Surname: Highley

Position: Senior Clinical Lecturer in Neuropathology

Organisation: SITraN

Address: 385a Glossop Road, Sheffield, S10 2HQ

Telephone No: 0114 222 2241 Fax No: 0114 222 2290

Email: robin.highley@sheffield.ac.uk

SBTB PROJECT REQUEST NUMBER: 18/007

This project was reviewed by the SBTB Management Board and approval to release tissue under REC **08/MRE00/103** was granted.

Professor Stephen Wharton
Professor of Neuropathology and
Consultant Neuropathologist

Date. 25/6/18.

Appendix F. Kaplan Meir Diagrams for Length of Survival Analysis from FFPE Spinal Cord Data

The proportion of cases (shown on the y-axis) against the time of survival in months (shown on the x-axis), for each gene with a significant association with the length of survival.

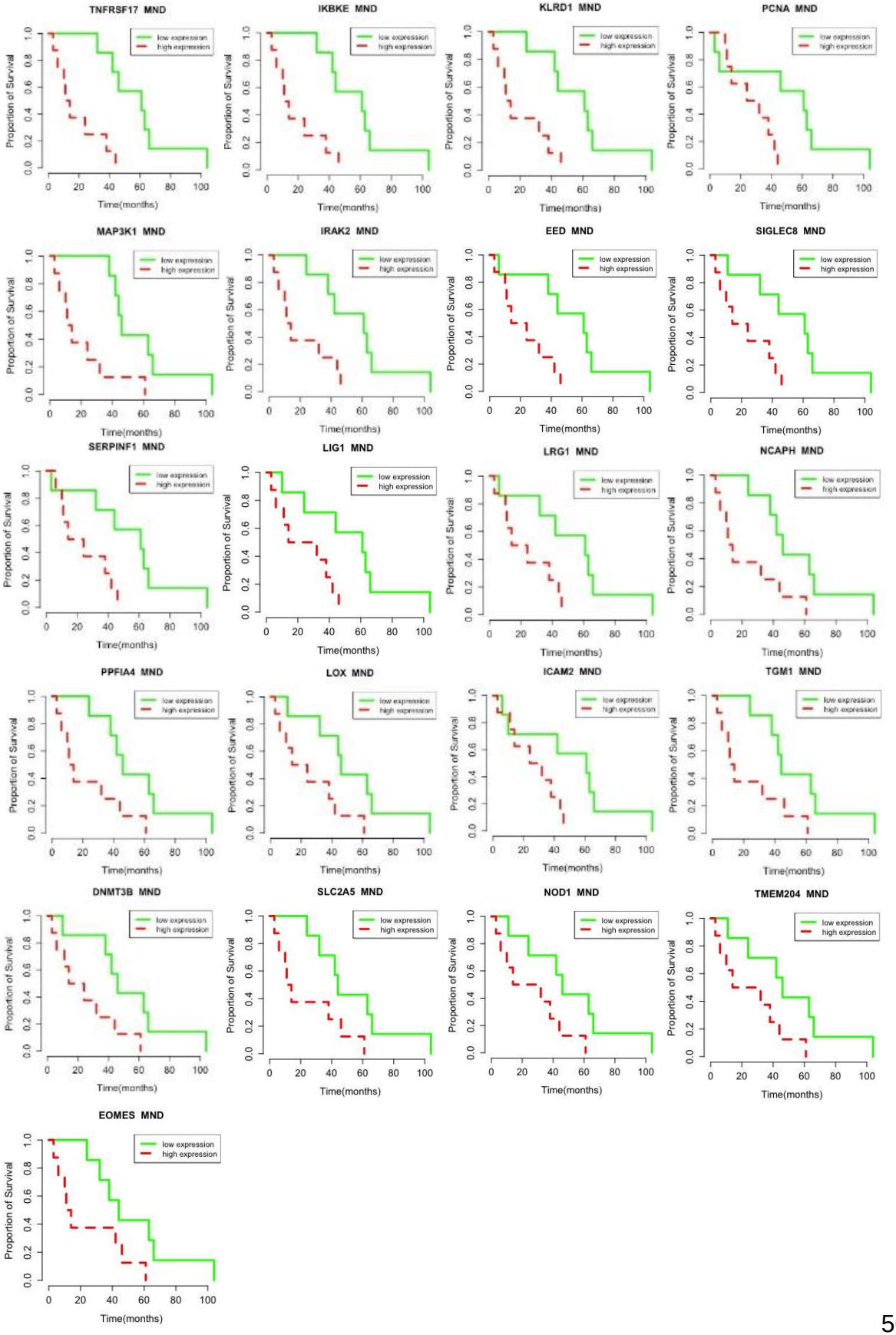

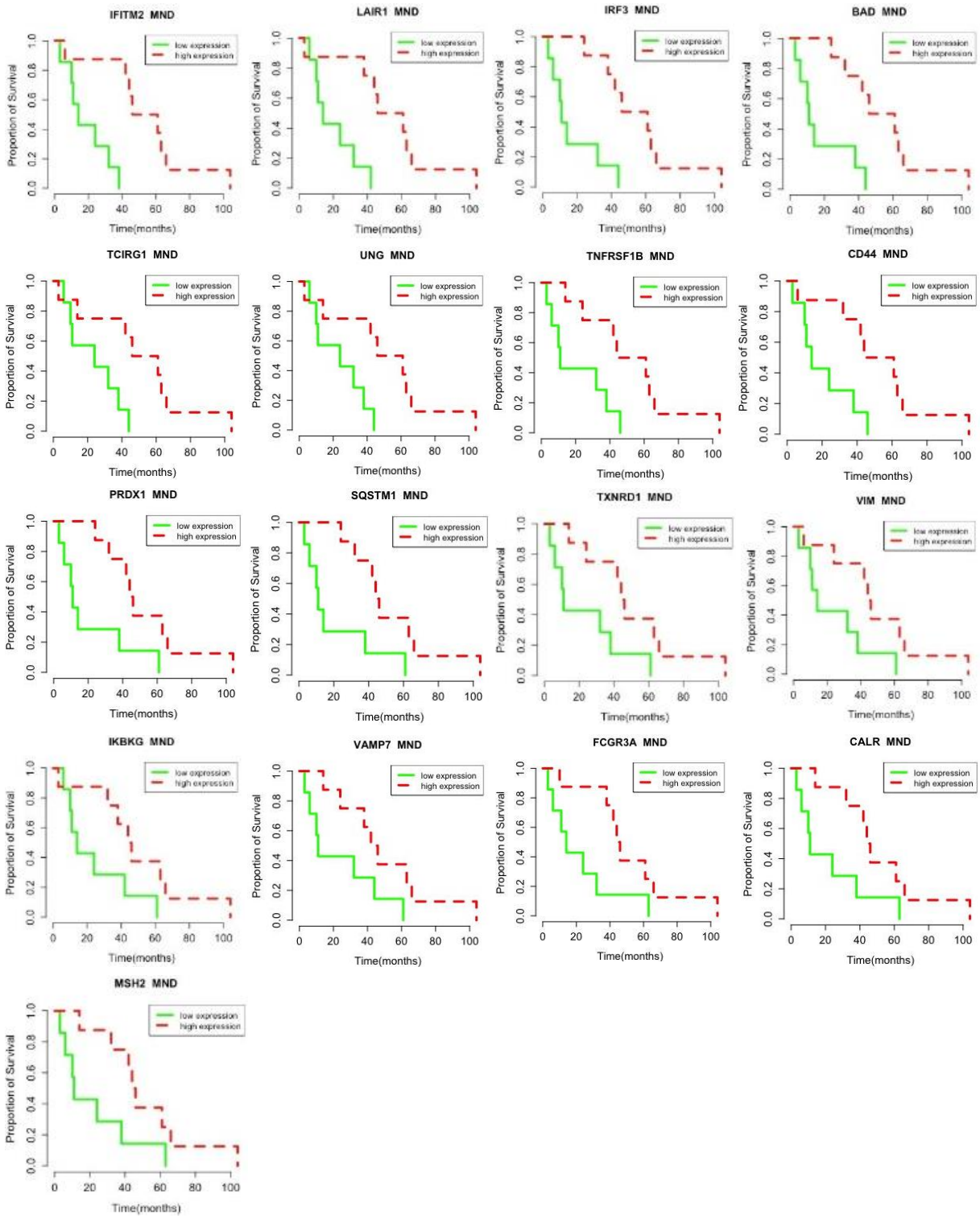
IFITM2 MND
LAIR1 MND
IRF3 MND
BAD MND
TCIRG1 MND
UNG MND
TNFRSF1B MND
CD44 MND
PRDX1 MND
SQSTM1 MND
TXNRD1 MND
VIM MND
IKBKG MND
VAMP7 MND
FCGR3A MND
CALR MND
MSH2 MND
low expression
high expression
Proportion of Survival
Time(months)

Appendix G. Kaplan Meir Diagrams for Length of Survival Analysis from Frozen Spinal Cord Data

The proportion of cases (shown on the y-axis) against the time of survival in months (shown on the x-axis), for each gene with a significant association with the length of survival.

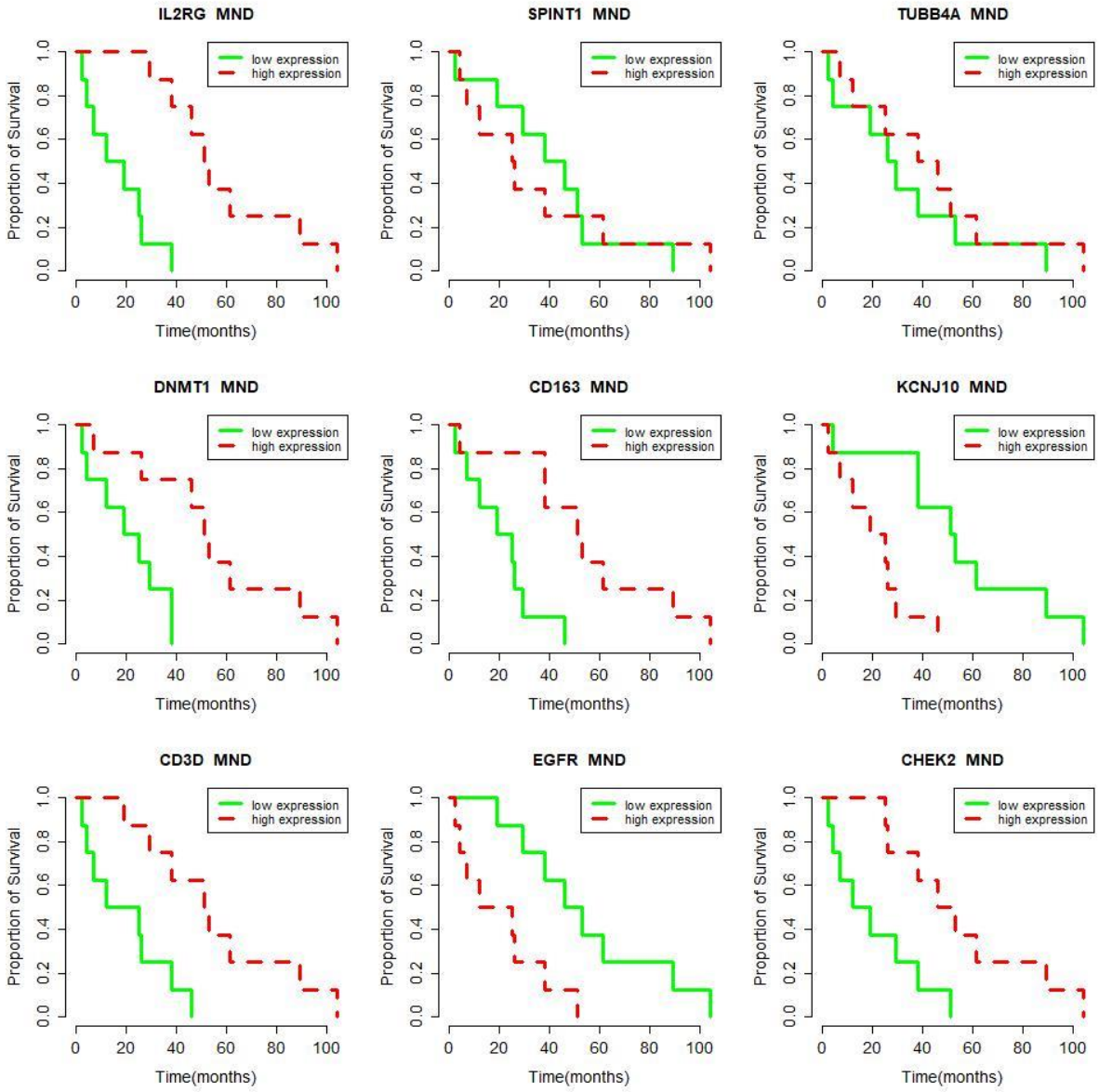

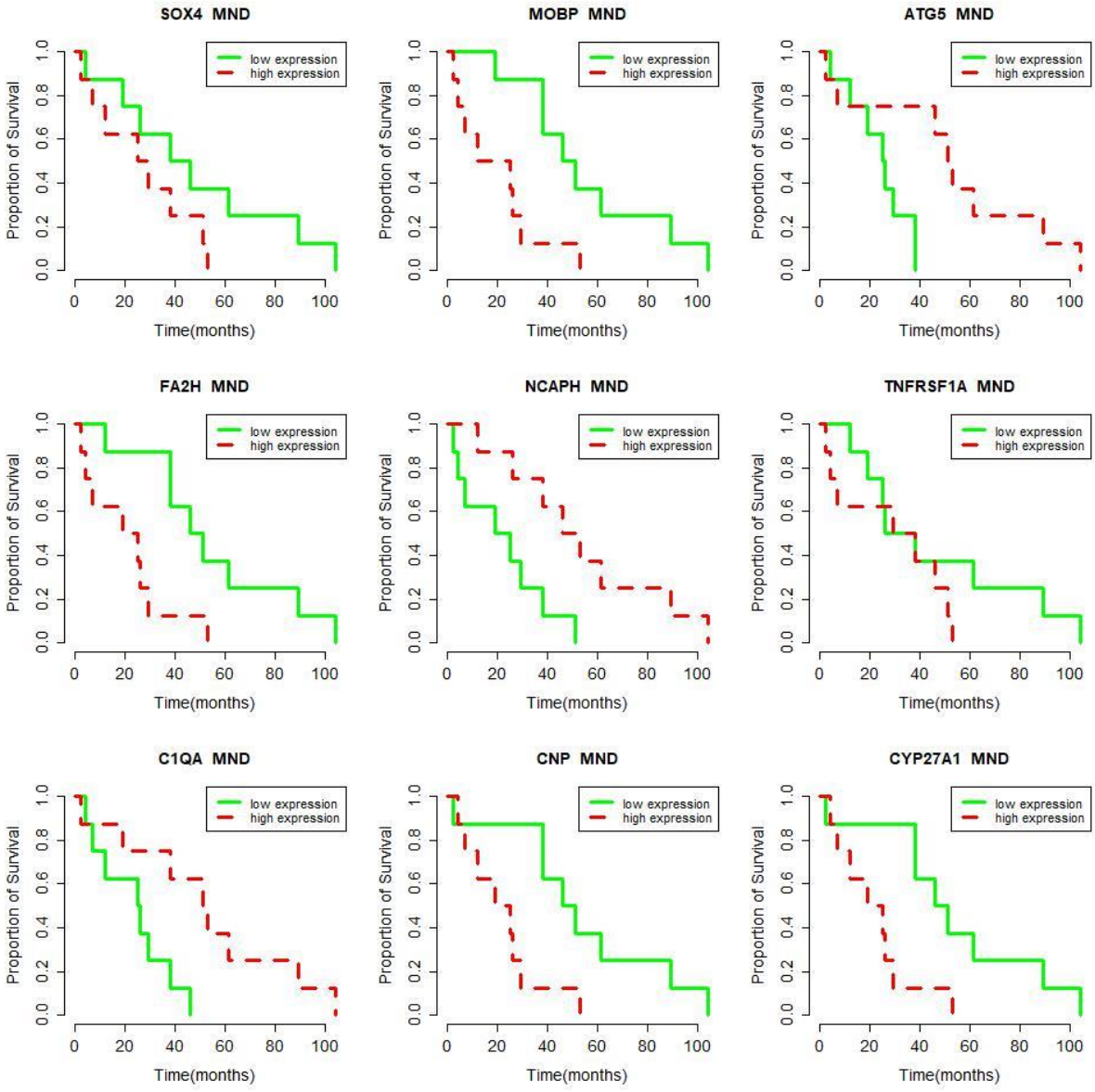
SOX4 MND
MOBP MND
ATG5 MND
FA2H MND
NCAPH MND
TNFRSF1A MND
C1QA MND
CNP MND
CYP27A1 MND
low expression
high expression
Proportion of Survival
Time(months)
0.0
0.2
0.4
0.6
0.8
1.0
0
20
40
60
80
100

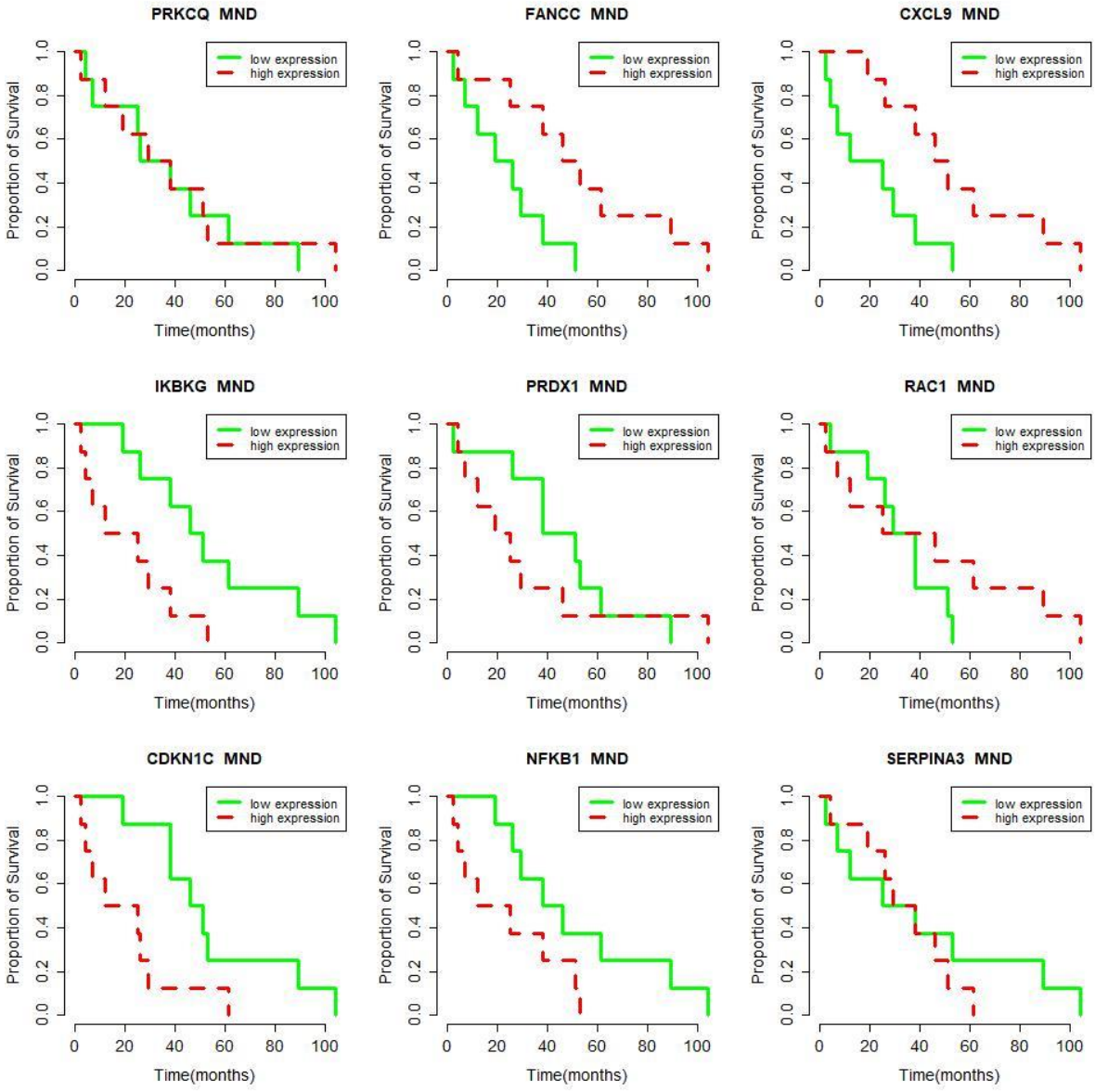
PRKCQ MND
FANCC MND
CXCL9 MND
IKBKG MND
PRDX1 MND
RAC1 MND
CDKN1C MND
NFKB1 MND
SERPINA3 MND
low expression
high expression
Proportion of Survival
Time(months)
0.0
0.2
0.4
0.6
0.8
1.0
0
20
40
60
80
100

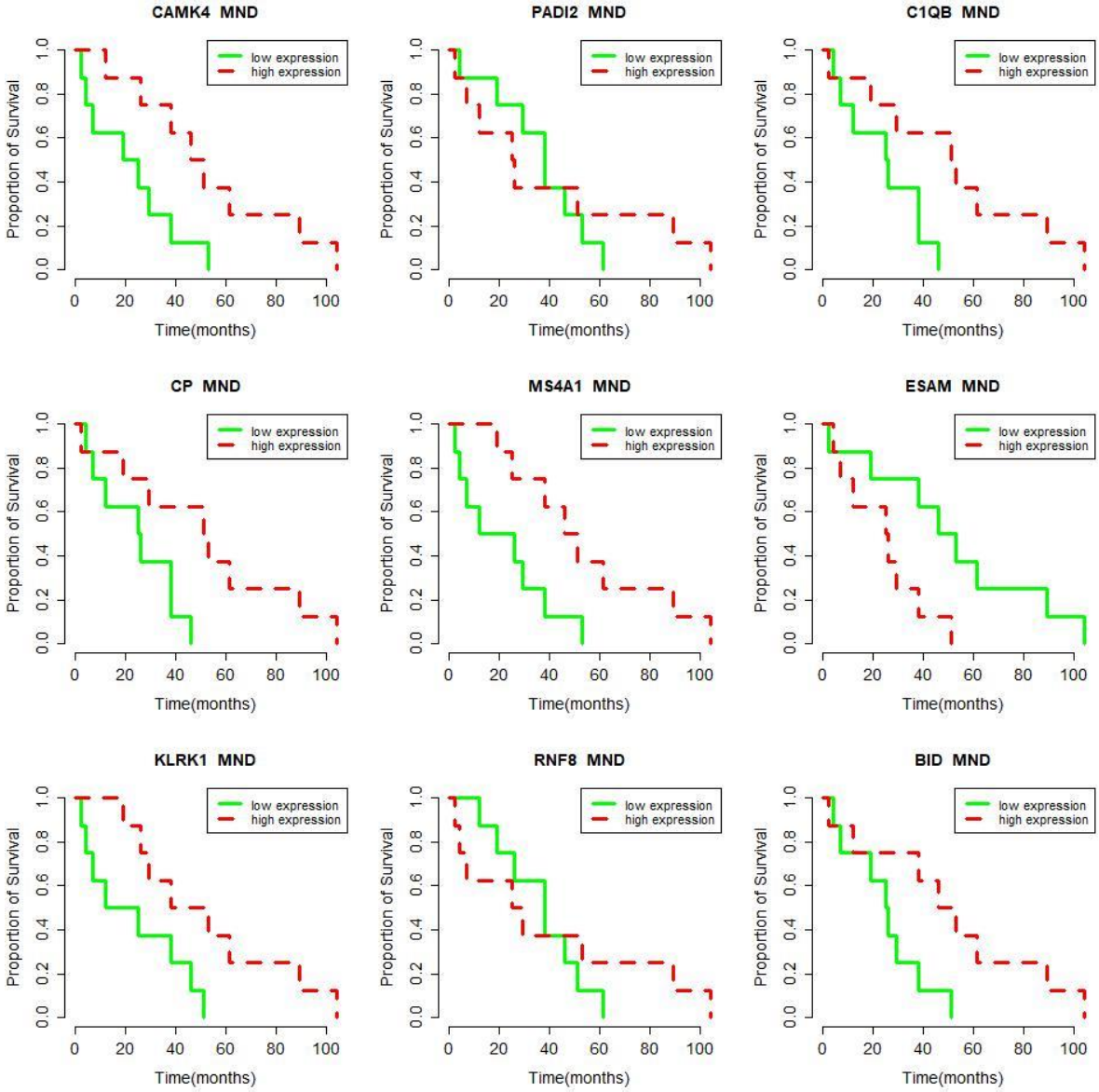
CAMK4 MND
PADI2 MND
C1QB MND
CP MND
MS4A1 MND
ESAM MND
KLRK1 MND
RNF8 MND
BID MND
low expression
high expression
Proportion of Survival
Time(months)
0.0
0.2
0.4
0.6
0.8
1.0
0
20
40
60
80
100

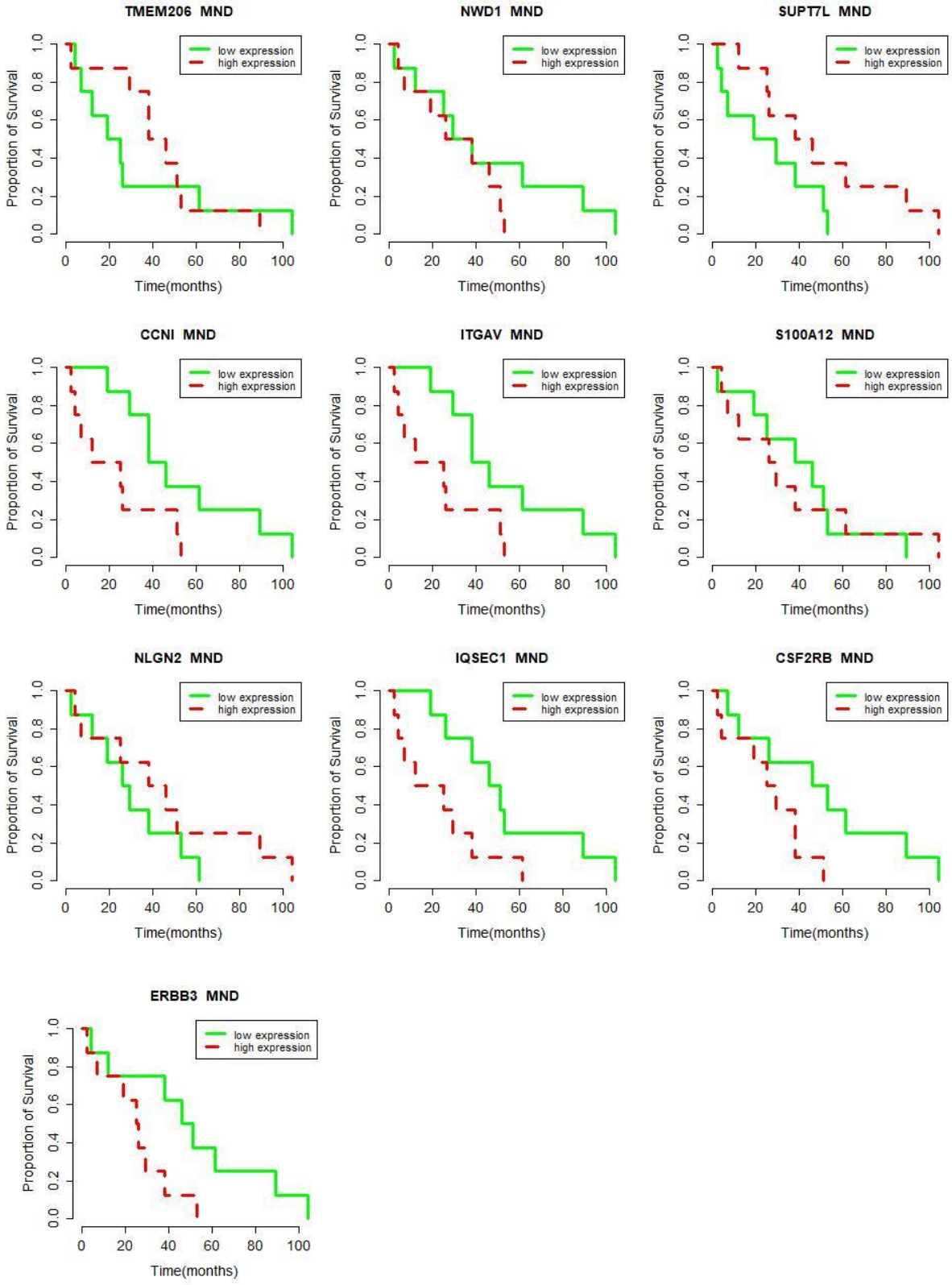
TMEM206 MND
NWD1 MND
SUPT7L MND
CCNI MND
ITGAV MND
S100A12 MND
NLGN2 MND
IQSEC1 MND
CSF2RB MND
ERBB3 MND
low expression
high expression
Proportion of Survival
Time(months)
0.0
0.2
0.4
0.6
0.8
1.0
0
20
40
60
80
100

Appendix H. Kaplan Meir Diagrams for Length of Survival Analysis from Frozen Motor Cortex

The proportion of cases (shown on the y-axis) against the time of survival in months (shown on the x-axis), for each gene with a significant association with the length of survival.

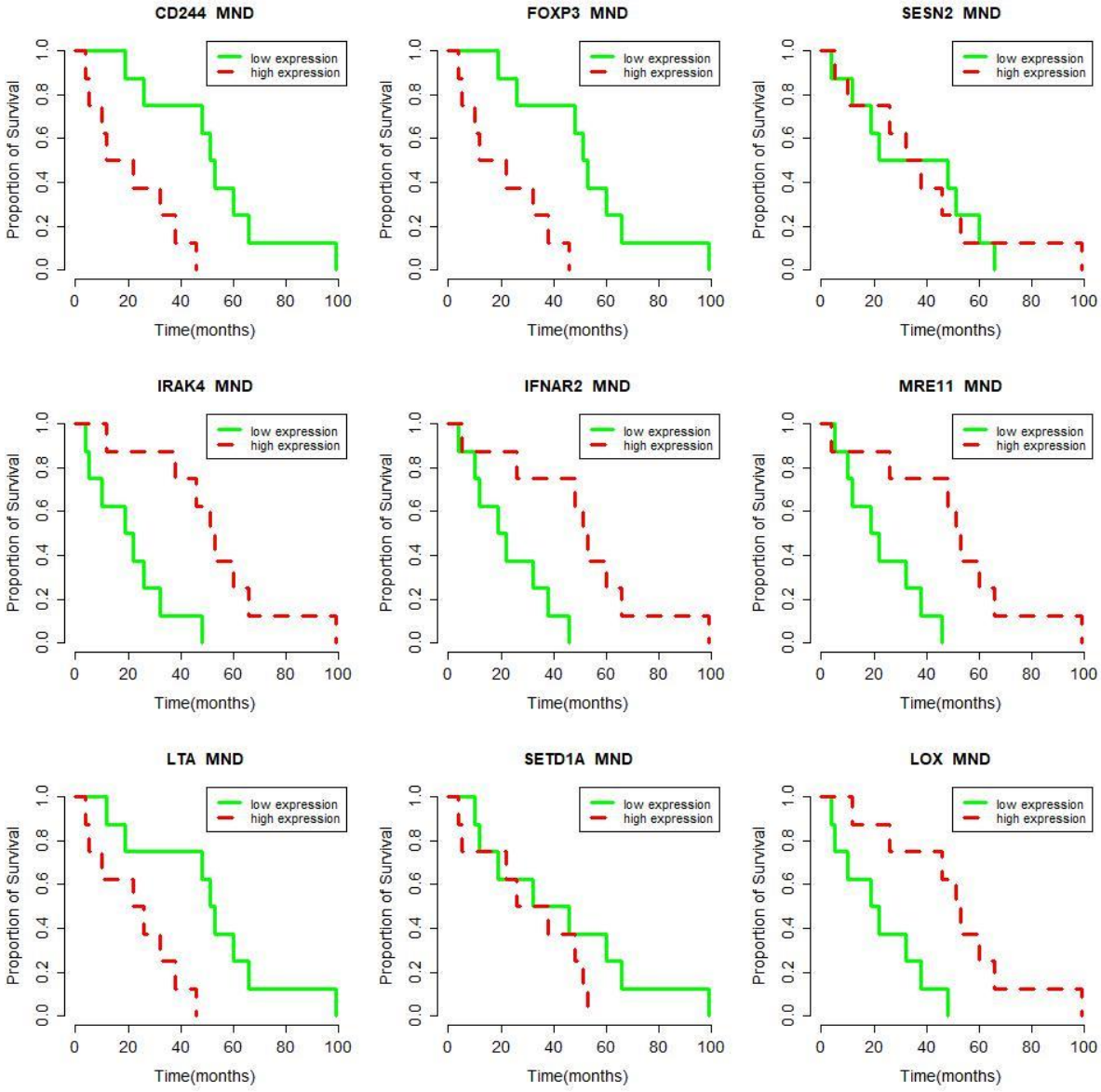

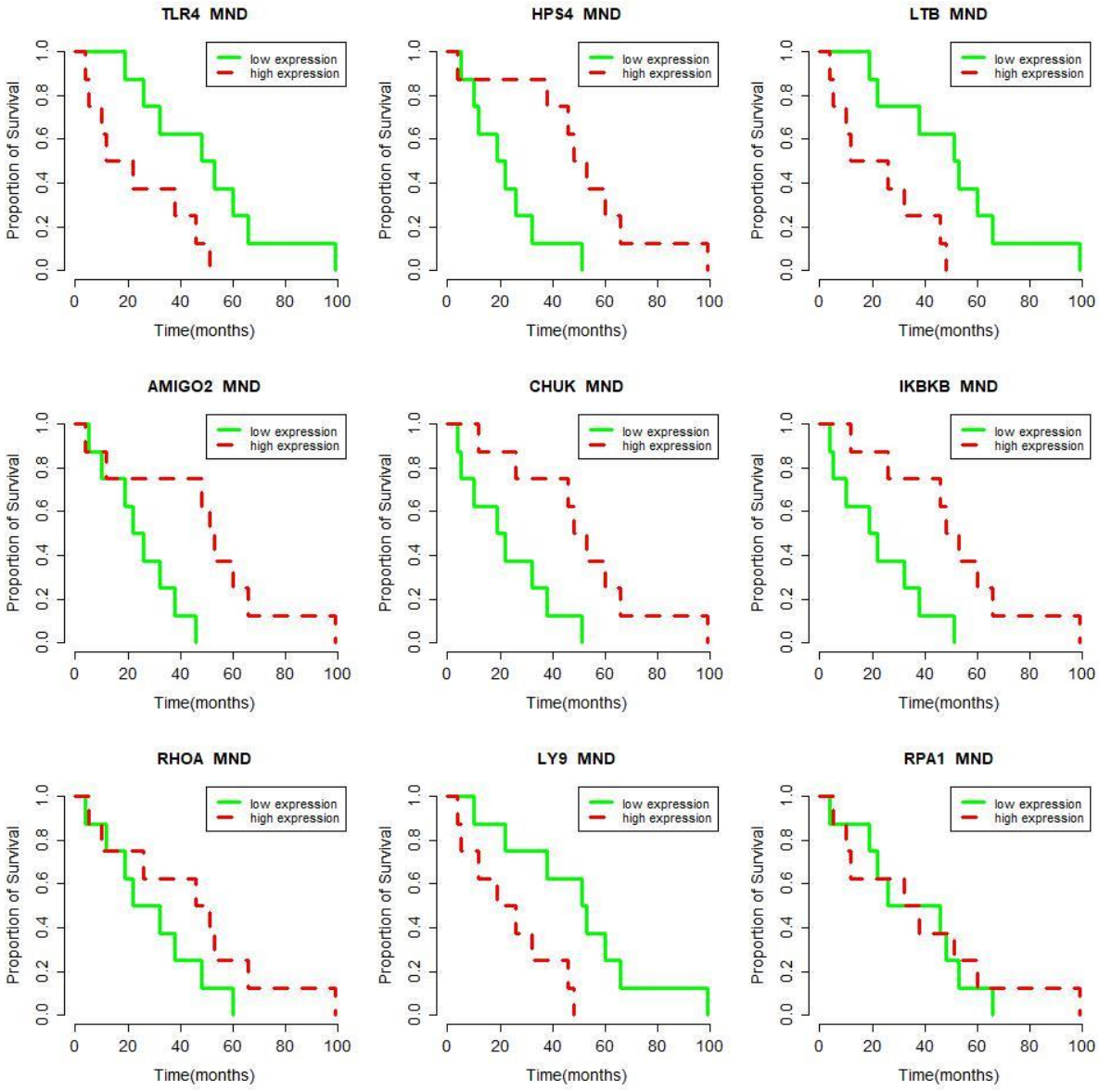
TLR4 MND
HPS4 MND
LTB MND
AMIGO2 MND
CHUK MND
IKBKB MND
RHOA MND
LY9 MND
RPA1 MND
low expression
high expression
Proportion of Survival
Time(months)
0.0
0.2
0.4
0.6
0.8
1.0
0
20
40
60
80
100

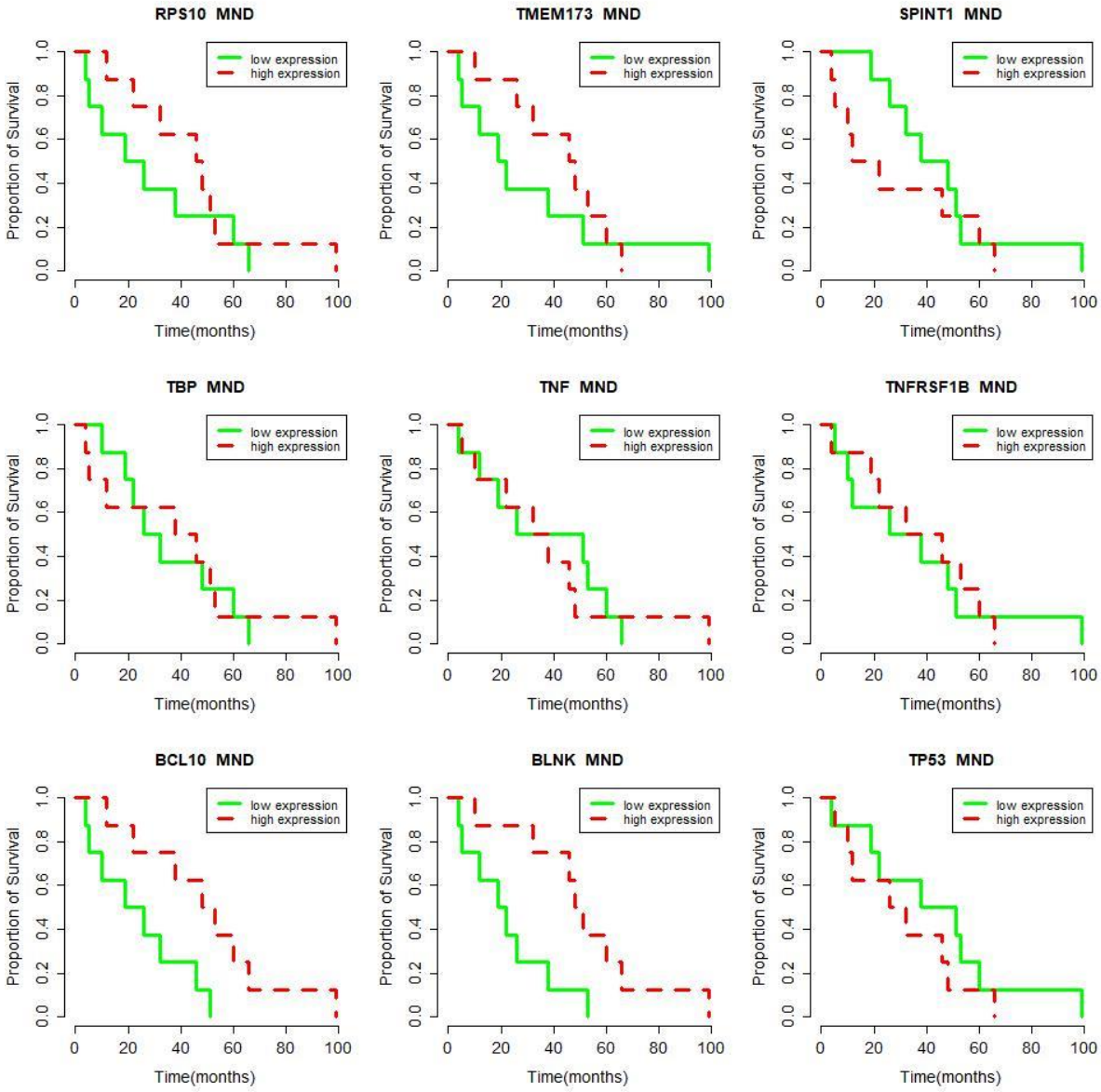
RPS10 MND
TMEM173 MND
SPINT1 MND
TBP MND
TNF MND
TNFRSF1B MND
BCL10 MND
BLNK MND
TP53 MND
low expression
high expression
Proportion of Survival
Time(months)
0.0
0.2
0.4
0.6
0.8
1.0
0
20
40
60
80
100

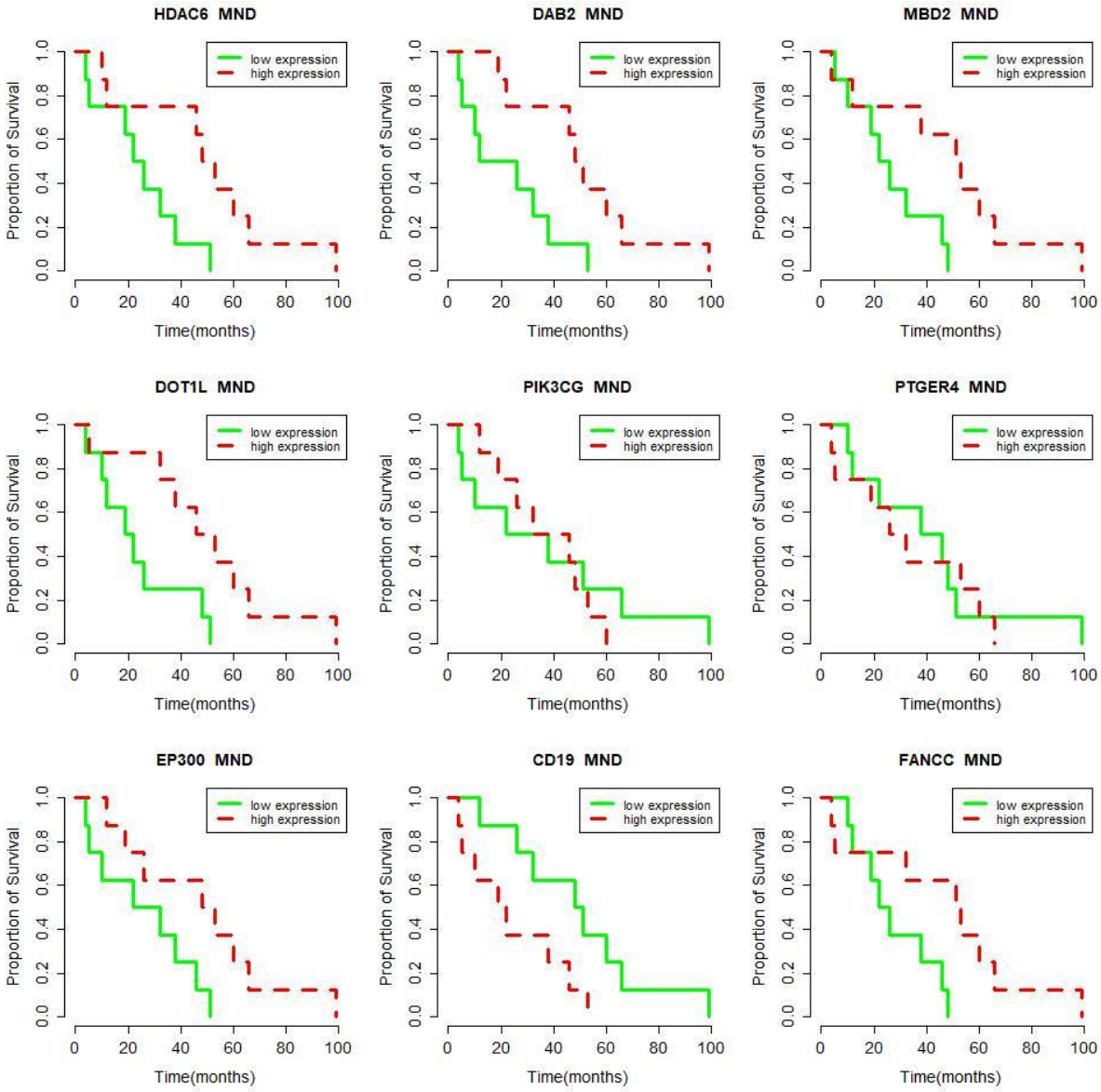
HDAC6 MND
DAB2 MND
MBD2 MND
DOT1L MND
PIK3CG MND
PTGER4 MND
EP300 MND
CD19 MND
FANCC MND
low expression
high expression
Proportion of Survival
Time(months)
0.0
0.2
0.4
0.6
0.8
1.0
0
20
40
60
80
100

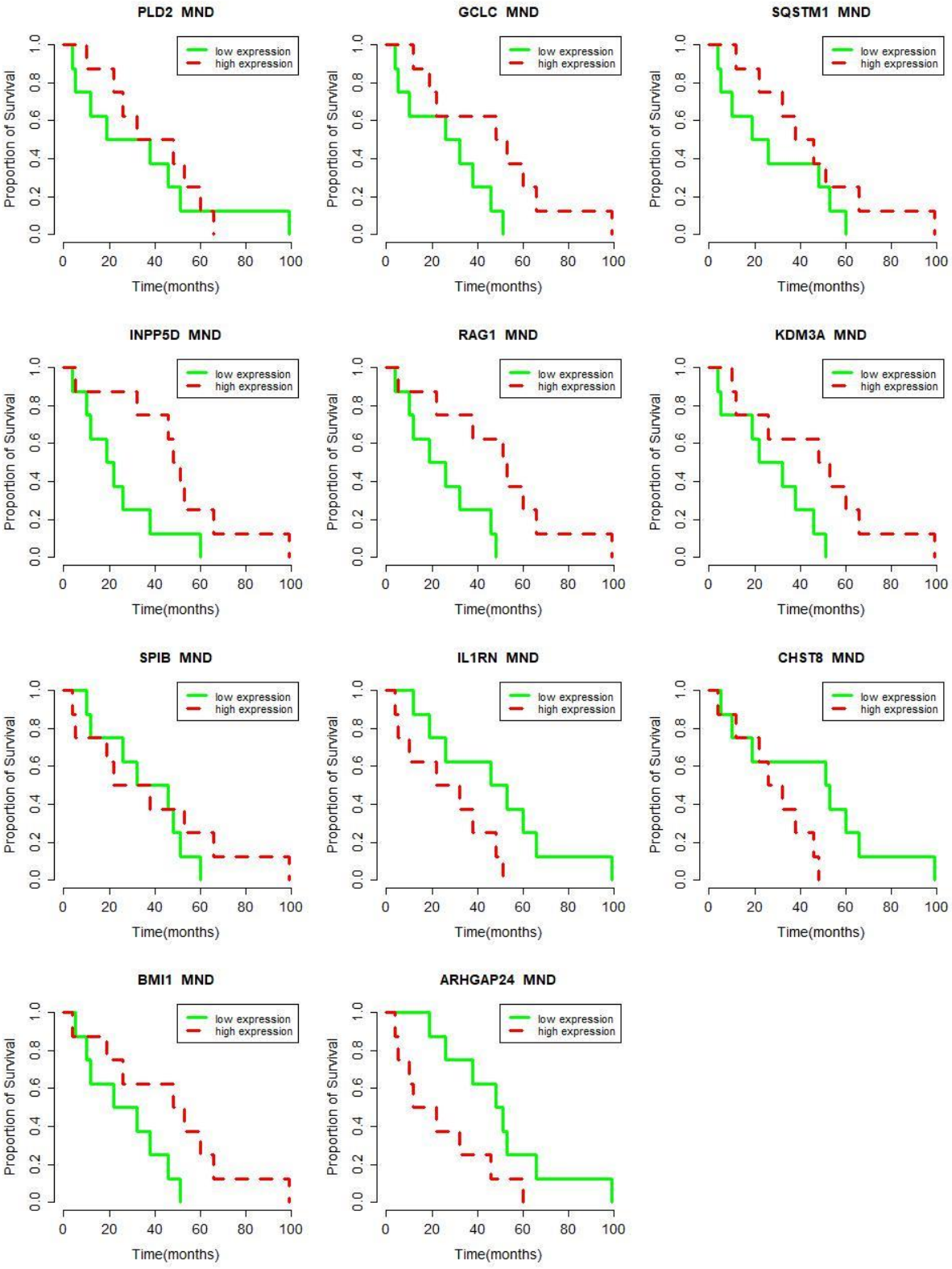
PLD2 MND
GCLC MND
SQSTM1 MND
INPP5D MND
RAG1 MND
KDM3A MND
SPIB MND
IL1RN MND
CHST8 MND
BMI1 MND
ARHGAP24 MND
low expression
high expression
Proportion of Survival
Time(months)
0.0
0.2
0.4
0.6
0.8
1.0
0
20
40
60
80
100